A STUDY OF X-RAY, GAMMA AND NEUTRON SHIELDING PARAMETERS IN SOME ALLOYS AND COMPOSITES



Thesis submitted to Bharathidasan University
in partial fulfillment of the requirements for the degree of
Doctor of Philosophy in Physics

Submitted by

SATHISH K V

(Ref. No. 06975/Ph. D-K3/Physics/PT/April 2019)

Part time Research Scholar in Physics St. Joseph's College (Autonomous) Tiruchirappalli

Under the guidance of

Supervisor

Dr. S. ALFRED CECIL RAJ

Associate Professor of Physics St. Joseph's College (Autonomous) Tiruchirappalli – 620 002 Tamilnadu **Co-Supervisor**

Dr. H.C. MANJUNATHA

Associate Professor of Physics Government College for Women Kolar – 563 101 Karnataka



Department of Physics

St. Joseph's College (Autonomous)
(Affiliated to Bharathidasan University)
Tiruchirappalli-620 002

MAY 2022

Dr. S. Alfred Cecil Raj, M Sc., M.Phil., Ph.D.

Associate Professor

Department of Physics

St. Joseph's College (Autonomous)

Tiruchirappalli- 620 002

CERTIFICATE

This is to certify that the thesis entitled "A STUDY OF X-RAY, GAMMA

AND NEUTRON SHIELDING PARAMETERS IN SOME ALLOYS AND

COMPOSITES" submitted to the Bharathidasan University, Tiruchirappalli in partial

fulfillment of the requirements for the award of the degree of Doctor of Philosophy in

Physics, is a bonafide record of the work done by Sathish K V (Ref.No.06975/Ph.D.-

K3/Physics/PT/April 2019) from May 2019 to May 2022 under my supervision and

guidance. This is an independent work on the part of the candidate under my

guidance.

(Dr. S. Alfred Cecil Raj)

Supervisor

Place: Tiruchirappalli

Date:

Dr. H.C. Manjunatha, M.Sc., M.Phil., Ph.D.

Associate Professor

Department of Physics

Govt. College for Women

Kolar- 563 101

CERTIFICATE

This is to certify that the thesis entitled "A STUDY OF X-RAY, GAMMA

AND NEUTRON SHIELDING PARAMETERS IN SOME ALLOYS AND

COMPOSITES" submitted to the Bharathidasan University, Tiruchirappalli in partial

fulfillment of the requirements for the award of the degree of Doctor of Philosophy in

Physics, is a bonafide record of the work done by Sathish K V (Ref. No. 06975/Ph. D-

K3/Physics/PT/April 2019) from May 2019 to May 2022 under my supervision and

guidance. This is an independent work on the part of the candidate under my

guidance.

(Dr. H.C. Manjunatha)

Co-Supervisor

Place: Kolar

Date:

DECLARATION

I hereby declare that the thesis entitled "A STUDY OF X-RAY, GAMMA

AND NEUTRON SHIELDING PARAMETERS IN SOME ALLOYS AND

COMPOSITES" embodies the results of my research work carried out under the

guidance and supervision of Dr. S. Alfred Cecil Raj, M.Sc., M.Phil., Ph.D.

Supervisor, Associate Professor, Department of Physics, St. Joseph's College

(Autonomous), Tiruchirappalli & Dr. H.C. Manjunatha, M.Sc., M.Phil., Ph.D.

Co-Supervisor, Associate Professor, Department of Physics, Govt. College for

Women, Kolar. I have not submitted the above thesis to any University for any

Degree, Diploma, Fellowship or any other similar titles previously.

(SATHISH K V)

Place: Tiruchirappalli

Date:

Department of Physics St. Joseph's College (Autonomous)

(Affiliated to Bharathidasan University) Tiruchirappalli-620002



CERTIFICATE OF PLAGIARISM CHECK

1.	Name of the Research Scholar	SATHISH K V (Ref. No. 06975/Ph. D-K3/Physics/PT/April2019)
2.	Course of study	Ph.D. Physics
3.	Title of the Thesis	A STUDY OF X-RAY, GAMMA AND NEUTRON SHIELDING PARAMETERS IN SOME ALLOYS AND COMPOSITES
4.	Name of the Supervisor	Dr. S. Alfred Cecil Raj, M.Sc., M.Phil., Ph.D
5	Name of the Co-Supervisor	Dr. H.C. Manjunatha, M.Sc., M.Phil., Ph.D
6.	Department/Institution/ Research Centre	Department of Physics St. Joseph's College (Autonomous) Tiruchirapalli -620 002
7.	Acceptable Maximum Limit	10%
8.	Percentage of similarity of content identified	1%
9.	Software Used	Ouriginal
10.	Date of Verification	23.05.2022

Report on plagiarism check, item with % of similarity is attached.

Signature of the Co-Supervisor

Signature of the Supervisor

Signature of the Candidate



Document Information

Analyzed document Sathish KV.pdf (D137587698)

Submitted 2022-05-23T07:03:00.0000000

Submitted by Dorairajan

Submitter email manavaidorai@gmail.com

Similarity 1%

Analysis address manavaidorai.stjct@analysis.ouriginal.com

Sources included in the report

W

URL: https://teachers.yale.edu/curriculum/viewer/initiative_18.04.04_u

Fetched: 2021-05-09T21:34:52.7530000

11

ACKNOWLEDGEMENT

I would like to express my sincere gratitude to my Supervisor **Dr. S. Alfred Cecil Raj**, Associate Professor, Department of Physics, St. Joseph's College (Autonomous), Tiruchirappalli for his continuous support of my Ph.D. work. As my research Supervisor, the valuable guidance given during the course of this investigation helped me to complete my Ph.D. work successfully. I thank my Supervisor for the extended support and encouragement over these years.

With immense pleasure and a deep sense of gratitude, I wish to express my sincere thanks to my Co-Supervisor **Dr. H.C. Manjunatha**, Associate Professor, Department of Physics, Government College for Women, Kolar, without his motivation, continuous encouragement, and suggestions, this research would not have been successfully completed.

I would like to extend my special thanks to Doctoral Committee Members **Dr. A.J. Clement Lourduraj**, Assistant Professor, St. Joseph's College (Autonomous), Tiruchirappalli, and **Dr. C. Ravidhas**, Associate Professor & Head, Department of Physics, Bishop Heber College (Autonomous), Tiruchirappalli, for their valuable and inspiring guidance which enabled me to bring out this research successfully.

I am grateful to **Rev. Dr. M. Arockiasamy Xavier S.J.,** Principal, St. Joseph's College (Autonomous), Tiruchirappalli for providing me with the facilities and many other resources needed for my research. I am extremely grateful to **Dr. N. Ravi,** HOD, and all the faculty members of the Department of Physics, St. Joseph's College (Autonomous), Tiruchirappalli for their consent, encouragement, and support in my research.

My sincere thanks to research colleagues Dr. L. Seenappa, Dr. K.N. Sridhar, Dr. N. Sowmya, Prof. Srinivas. M.G, Prof. G.R. Sridhara, Prof. N. Nagaraja, and Prof. Nagaraja. A.M, Dr. Y.S. Vidya and Prof. B. Chinnappa Reddy, fellow researchers Mr. P.S. Damodara Gupta, Mr. N. Manjunath, Mr. R.Munirathnam, and Mr. B. Mahesh and Miss. S. Deepthi for their cooperation, support, and encouragement during the research work.

My sincere thanks to the Principal, H.O.D, and faculties of the Physics department, Government First Grade College, Kolar. I wish to extend my profound sense of gratitude to my family members and friends for all the sacrifices they made during my research and also for providing me with moral support and encouragement whenever required.

CONTENTS

LIST	OF FI	GURES	iv
LIST	OF TA	ABLES	xi
ABS'	TRACT	,	xii
1	Intro	duction	1
1.1	Mass	attenuation coefficient (μ/ρ) and linear attenuation coefficient (μ)	3
1.2	Effect	tive atomic number (Z_{eff})	15
1.3	Effect	tive electron density(\mathbf{N}_{el})	18
1.4	Photo	on Buildup factor(PBF)	19
	1.4.1	Energy absorption buildup factor (B_{en})	20
	1.4.2	Exposure buildup factor (B_{ex}) :	21
1.5	Relati	ive dose (RD) of photon	27
1.6	Neutr	ron shielding parameters (NSP)	27
1.7	Objec	ctive of the present study	29
2	Photo	on interaction with matter	30
2.1	Photo	pelectric effect (PEE)	30
	2.1.1	Derivation of analytical equation for photoelectric cross section	34
2.2	Pair I	Production	39
	2.2.1	Semi empirical formula for cross section of pair production in nuclear	
		field (σ_{ppn})	40
	2.2.2	Semi empirical formula for cross section of pair production in the elec-	
		tric field(σ_{ppe})	42
2.3	Cohe	rent Scattering	43
	2.3.1	Rayleigh Scattering	43
	2.3.2	Thomson Scattering	43
	2.3.3	. "Delbruck" Scattering	43

	2.3.4	Semi-empirical formula for coherent scattering (σ_{coh})	43
2.4	Incoh	erent Scattering (σ_{incoh})	44
2.5	Gamr	na Ray Attenuation	45
3	Estin	nation of X-ray, gamma shielding parameters in alloys and composites	48
3.1	Theor	y	48
	3.1.1	Gamma/X-ray shielding parameters	48
	3.1.2	Absorption buildup factor	49
	3.1.3	Neutron shielding parameters (NSP)	50
	3.1.4	Kerma coefficients from partial photon interactions	50
	3.1.5	Relative dose	51
	3.1.6	Specific absorbed fraction of energy (φ)	52
3.2	Resul	ts	52
	3.2.1	Iron boron alloys	52
	3.2.2	Silicon - alloys	58
	3.2.3	Gallium alloys	67
	3.2.4	Lead Alloys	70
	3.2.5	Aluminium alloys	79
	3.2.6	Silicon-boron alloys	90
	3.2.7	Zinc alloys	99
3.3	Silico	n Germanium alloys	100
4	Synth	esis and characterization of nano compounds	110
4.1	Synth	esis	110
	4.1.1	Synthesis of Barium-Nickel-Iron Oxide NanoComposite	110
	4.1.2	Synthesis of Aluminium-Barium-zinc oxide Nonocomposite	111
	4.1.3	Synthesis of Leadaluminoborate nanocomposite	112
4.2	Chara	acterization	113
	4.2.1	Characterization Ba-Fe-Ni Oxide NanoComposite	113
	4.2.2	Characterization of Aluminium-Barium-zinc oxide Nonocomposite	118
	4.2.3	Characterization of Leadaluminoborate nanocomposite	123
5	Meas	urements of shielding values of X, γ radiation of Ba–Ni–Fe oxide,Aluminium	n-
	Rarin	m-Zinc oxide and Leadaluminoborate Nanocomposites	128

5.1	Expe	riment to measure $\mathbf{X},\!\gamma$ radiation shielding dimensions $\dots\dots\dots\dots$	128
5.2	Analy	vsis	130
	5.2.1	Analysis of measured X-ray / gamma ray shielding properties of Bar-	
		ium-Nickel-Iron oxide Nanocomposites	130
	5.2.2	Analysis of of measured X/γ ray shielding properties of Aluminium-	
		Barium-Zinc oxide Nanocomposites.	133
	5.2.3	Study of shielding properties of \mathbf{X} , γ radiation of Leadaluminoborate	
		Nanocomposites	136
6	Sumi	mary and conclusion	139
6.1	Crite	ria for selection of good absorber of X-ray/gamma radiation	139
6.2	Select	tion of good shielding material	139
	6.2.1	Iron-Boron alloys	139
	6.2.2	Silicon alloys	140
	6.2.3	Gallium alloys	140
	6.2.4	Lead alloys	140
	6.2.5	Aluminium alloys	141
	6.2.6	Silicon-Boron alloys	141
	6.2.7	Zinc alloys	141
	6.2.8	Silicon-Germanium alloys	142
6.3	Comp	parison of shielding parameter amoung studied alloys	142
6.4	Select	ted good shielding material among the studied alloys	148
6.5	Resul	ts on studies of shielding parameters of nano-composites	148
6.6	Scope	e of research work	150
	REFE	RENCES	150
	I IST	OF PURI ICATIONS	10/

List of Figures

2.1	Variation of logarithmic photoelectric cross section with logarithmic energy for	
	different energy ranges in case of Hydrogen element. Continuous line represents	
	the values produced by the present formula, Circles represents the data available in	
	the linterature	34
2.2	Variation of average percentage error of $\log \sigma$ as a function Z	38
3.1	Variation of mass attenuation coefficient with energy for the studied iron boron	
	alloys	53
3.2	Variation of tenth value layer (TVL) with energy for the studied iron boron alloys	53
3.3	Variation of half value layer (HVL) with energy for the studied iron boron alloys .	54
3.4	Variation of mean free path with energy for the studied iron boron alloys	54
3.5	Variation of effective atomic number with energy for the studied iron boron alloys	55
3.6	Variation of effective electron density with energy for the studied iron boron alloys	55
3.7	Comparison of specific gamma ray constant for the studied iron boron alloys,	
	$Fe_{0.95}B_{0.05}\left(A\right),Fe_{0.9}B_{0.1}\left(B\right),Fe_{0.8}B_{0.2}\left(C\right),Fe_{0.7}B_{0.3}\left(D\right),Fe_{0.6}B_{0.4}\left(E\right)\ and\ Fe_{0.5}B_{0.5}$	
	$(F) \ \dots $	56
3.8	Comparison of material line and the first transfer the state of the st	
	Comparison of neutron shielding parameters for the studied iron boron alloys,	
	Comparison of neutron shielding parameters for the studied from boron alloys, $Fe_{0.95}B_{0.05}$ (A), $Fe_{0.9}B_{0.1}$ (B), $Fe_{0.8}B_{0.2}$ (C), $Fe_{0.7}B_{0.3}$ (D), $Fe_{0.6}B_{0.4}$ (E) and $Fe_{0.5}B_{0.5}$	
	·	56
3.9	$Fe_{0.95}B_{0.05}$ (A), $Fe_{0.9}B_{0.1}$ (B), $Fe_{0.8}B_{0.2}$ (C), $Fe_{0.7}B_{0.3}$ (D), $Fe_{0.6}B_{0.4}$ (E) and $Fe_{0.5}B_{0.5}$	56
3.9	$Fe_{0.95}B_{0.05}\left(A\right), Fe_{0.9}B_{0.1}\left(B\right), Fe_{0.8}B_{0.2}\left(C\right), Fe_{0.7}B_{0.3}\left(D\right), Fe_{0.6}B_{0.4}\left(E\right) \text{ and } Fe_{0.5}B_{0.5}$ $(F) \dots \dots \dots \dots \dots \dots \dots \dots \dots $	56 57
	$Fe_{0.95}B_{0.05}\left(A\right), Fe_{0.9}B_{0.1}\left(B\right), Fe_{0.8}B_{0.2}\left(C\right), Fe_{0.7}B_{0.3}\left(D\right), Fe_{0.6}B_{0.4}\left(E\right) \text{ and } Fe_{0.5}B_{0.5}$ (F)	
3.10	$Fe_{0.95}B_{0.05}\left(A\right), Fe_{0.9}B_{0.1}\left(B\right), Fe_{0.8}B_{0.2}\left(C\right), Fe_{0.7}B_{0.3}\left(D\right), Fe_{0.6}B_{0.4}\left(E\right) \text{ and } Fe_{0.5}B_{0.5}$ (F)	57
3.10 3.11	$Fe_{0.95}B_{0.05}$ (A), $Fe_{0.9}B_{0.1}$ (B), $Fe_{0.8}B_{0.2}$ (C), $Fe_{0.7}B_{0.3}$ (D), $Fe_{0.6}B_{0.4}$ (E) and $Fe_{0.5}B_{0.5}$ (F)	57 58
3.10 3.11 3.12	$Fe_{0.95}B_{0.05}$ (A), $Fe_{0.9}B_{0.1}$ (B), $Fe_{0.8}B_{0.2}$ (C), $Fe_{0.7}B_{0.3}$ (D), $Fe_{0.6}B_{0.4}$ (E) and $Fe_{0.5}B_{0.5}$ (F)	57 58 59
3.10 3.11 3.12 3.13	Fe _{0.95} B _{0.05} (A), Fe _{0.9} B _{0.1} (B), Fe _{0.8} B _{0.2} (C), Fe _{0.7} B _{0.3} (D), Fe _{0.6} B _{0.4} (E) and Fe _{0.5} B _{0.5} (F)	57 58 59

3.16	Variation of total mass attenuation coefficient with photon energy for Al- 355 alloy.	62
3.17	Comparison of Half value layer (HVL), Tenth value layer (TVL) and mean free	
	$path(\lambda)$ for aluminium silicon alloys (1.Al-47, 2.Al-32s, 3.Al-43, 4-Ferro Silicon,	
	5.Al-355, 6. Al-356 and 7.Al A-355)	62
3.18	Variation of effective atomic number and effective electron density with energy for	
	different aluminium silicon alloys.	63
3.19	Variation of exposure buildup factors with energy for different mean free paths for	
	aluminum silicon alloys.	64
3.20	Variation of exposure buildup factors with mean free path at different energies for	
	different aluminium silicon alloys.	65
3.21	Comparison of exposure buildup factors with energy for different aluminium sil-	
	icon alloys (1-Al-47, 2-Al-32S, 3-Al-43, 4-Ferro silicon, 5-Al-355, 6-Al-356, 7-	
	Al-A355)	65
3.22	Comparison of evaluated coherent neutron scattering length (λ_{nc}) , incoherent neu-	
	tron scattering lengths (λ_{inc}), coherent neutron scattering cross section (σ_{nc}), in-	
	coherent neutron scattering cross sections (σ_{inc}), total neutron scattering cross	
	section (σ_{tot}) and neutron absorption cross sections (σ_a) for different aluminium	
	silicon alloys (1-Al-47, 2-Al-32S, 3-Al-43, 4-Ferro silicon, 5-Al-355, 6-Al-356,	
	7-Al-A355)	66
3.23	Comparison of neutron attenuation parameters among the studied aluminium sil-	
	icon alloys (1-Al-47, 2-Al-32S, 3-Al-43, 4-Ferro silicon, 5-Al-355, 6-Al-356, 7-	
	Al-A355)	66
3.24	Variation of energy exposure buildup factors with energy for the studied gallium	
	alloys at different mean free	67
3.25	Variation of energy exposure buildup factors with mean free path for the studied	
	gallium alloys at different energies	68
3.26	Variation of φ with energy for the studied gallium alloys at different mean free paths.	68
3.27	Variation of φ with mean free path for the studied gallium alloys at different energies.	69
3.28	Comparison of EBF and SAF among the studied alloys for 10 mfp (1- Gallium	
	alloy, 2- Galfenol and 3- Galinstan) at different energies	70
3.29	Variation of mass attenuation coefficient with gamma energy for the (a) FD, (b)	
	LT, (c) MC and (d) MT binary / tertiary / quaternary alloys respectively	71

3.30	Variation of mass attenuation coefficient with gamma energy for the (e) ST, (f) TU,	
	(g) TM and (h) WM binary / tertiary / quaternary alloys respectively	72
3.31	Comparison of HVL of FD, LT, MC, MT, ST, TU, TM and WM binary / tertiary	
	/ quaternary alloys at different photon energies	73
3.32	Variation of (a) Z_{eff} , (b) N_e , (c) RPE and (d) Kerma with photon energy for FD,	
	LT, MC, MT, ST, TU, TM and WM binary / tertiary / quaternary alloys	74
3.33	Variation of (a) ABF with photon energy, (b) ABF with λ for MC binary alloy,	
	(c) ABF with photon energy, (d) ABF with λ , (e) $SAFE$ with photon energy, (f)	
	SAFE with λ , (g) Relative dose with photon energy, (h) Relative dose with λ for	
	FD, LT, MC, MT, ST, TU, TM and WM binary / tertiary / quaternary alloys	75
3.34	Comparison of $SAFE$ and relative dose for FD, LT, MC, MT, ST, TU, TM and	
	WM binary, tertiary, quaternary alloys at different photon energies	76
3.35	Variation of (a) φ and (b) RD with distance (r) for FD, LT, MC, MT, ST, TU, TM	
	and WM binary / tertiary / quaternary alloys	77
3.36	Comparison of neutron shielding parameters for the FD, LT, MC, MT, ST, TU, TM	
	and WM binary / tertiary / quaternary alloys	78
3.37	Comparison of neutron attenuation parameters (NAP) for the FD, LT, MC, MT,	
	ST, TU, TM and WM binary / tertiary / quaternary alloys	78
3.38	Variation of $\frac{\mu}{\rho}$ versus E for the studied Al alloys	79
3.39	A plot of HVL versus E for the studied Al alloys	80
3.40	A plot of mean free path (λ) versus energy E for the studied Al alloys	81
3.41	Effective electron density (N_e) versus E for the studied Al alloys	82
3.42	Radiation protection energy (RPE) versus E for the studied Al alloys at different	
	thickness	83
3.43	Comparison of different shielding parameters such as (a) μ , (b) HVL, (c) λ , (d)	
	N_e , (e) RPE and (f) KERMA coefficient for the studied Al alloys at an energy of	
	661 keV. Name of the alloys are given in section 3.2.5.1	84
3.44	Comparison of gamma dose rate of the studied Al alloys for distinct energies rang-	
	ing from 0.123MeV to 1.33MeV. Name of the alloys are given in section 3.2.5.1.	85
3.45	Correlation of studied (a) (λ_{co}) and $(b)(\lambda_{inc})$. A comparison of (c) coherent (σ_{co})	
	(d) incoherent (σ_{inc}), (e) total (σ_{tot}) and (f) neutron absorption cross sections (σ_{ab})	
	for aluminium alloys. Name of the alloys are given in section 3.2.5.1	85

3.46	Comparison of shielding effectiveness for electromagnetic radiation at different	
	frequency range from radio waves to infrared radiations in different studied alu-	
	minium alloys. Name of the alloys are given in section 3.2.5.1	87
3.47	Variation of Bremsstrahlung efficiency as a function of maximum energy of beta	
	emitters for the studied aluminium alloys. Name of the alloys are given in section	
	3.2.5.1	88
3.48	Comparison of Bremsstrahlung dose rate for the different studied aluminium al-	
	loys in (a) ¹⁶⁹ Er at an energy of 0.351MeV, (b) ⁴⁷ Sc at an energy of 0.6MeV, (c)	
	$^{89}\mathrm{Sr}$ at an energy of 1.495MeV and (d) $^{76}\mathrm{As}$ at an energy of 2.962MeV. Name of	
	the alloys are given in section 3.2.5.1	88
3.49	Comparison of probability of energy loss during Bremsstrahlung interaction for	
	the studied aluminium alloys in different beta emitters i.e (a) $^{169}\mathrm{Er}$ at an energy of	
	0.351MeV , (b) $^{47} \text{Sc}$ at an energy of 0.6MeV , (c) $^{89} \text{Sr}$ at an energy of 1.495MeV	
	and (d) $^{76}\mathrm{As}$ at an energy of 2.962MeV. Name of the alloys are given in section	
	3.2.5.1	90
3.50	Variation of mass attenuation coefficient (cm^2g^{-1}) as a function of energy (MeV)	91
3.51	Variation of half value layer (HVL) (cm) as a function of energy (MeV)	92
3.52	Variation of tenth value layer (TVL) (cm) as a function of energy (MeV)	92
3.53	Variation of mean free path (λ) (cm) as a function of energy (MeV)	93
3.54	Variation of effective atomic number (Z_{eff}) as a function of energy (MeV)	93
3.55	Variation of electron density (N_e) as a function of energy (MeV) $\ldots \ldots$	94
3.56	Variation of B_{en} with that of energy for different mean free paths and for different	
	boron concentrations	94
3.57	Variation of RPE of various alloys with that of thickness of alloys at different	
	energies in keV	95
3.58	Variation of KERMA with that of energy for different boron concentrations	96
3.59	Variation of (a) μ/ρ , (b) TVL, (c) HVL, (d) λ , (e) Z_{eff} , (f) N_e , (g) RPE, (h) SGR	
	(Γ) and (i) KERMA with that of boron concentrations for different energies	97
3.60	Variation of lead equivalent distance (d_{Pb}) with that of energy for different boron	
	concentrations	97
3.61	Variation of SET with that of boron concentrations for different frequencies / en-	
	ergies	98

3.62	Variation of neutron shielding parameters with different silicon boron alloys (SB1,	
	SB2, SB3, SB4, SB5 and SB6)]	99
3.63	Comparison of $SAF(\varphi)$ for the studied alloys at a particular energy	100
3.64	Comparison of RD for the studied alloys at a particular energy	100
3.65	Variation of $\mathrm{SAF}(\varphi)$ and RD with energy for the studied alloy of composition (Cu	
	70 %, Ni 15 %, Zn 15%)	101
3.66	Variation of mass attenuation coefficient with photon energy for (a) SG1, (b) SG2,	
	(c) SG3, (d) SG4, (e) SG5 and (f) SG6 Si-Ge alloys respectively	102
3.67	Variation of (a) HVL, (b) TVL, (c) mean free path (λ) , (d) specific gamma ray	
	constant (Γ), (e) Effective atomic number (Z_{eff}), (f) effective electron density	
	(N_e) , (g) radiation protection efficiency (RPE) and (h) KERMA with photon	
	energy respectively for SG1, SG2, SG3, SG4, SG5 and SG6 alloys	103
3.68	Variation of (a) (B_{en}) with energy at different λ , (b) B_{en} with mean free path (λ)	
	at different energies, (c) SAFE with energy at different λ , (d) relative dose with	
	energy at different λ for SG1 alloy, (e) B_{en} with Z_{eff} at different energies, (f)	
	SAFE with Z_{eff} at different energies for SG1, SG2, SG3, SG4, SG5 and SG6 alloy	s106
3.69	Comparison of neutron shielding parameters for SG1, SG2, SG3, SG4, SG5 and	
	SG6 alloys	107
3.70	Comparison of neutron attenuation parameters (NAP) for SG1, SG2, SG3, SG4,	
	SG5 and SG6 Si-Ge alloys	108
3.71	Diagram showing the absorption of radiation by SG1 alloy and ordinary concrete	
	combination at different energies	108
4.1	Flowchart for the synthesis of BFNONC	111
4.2	Flowchart for the synthesis of ZABNONC	112
4.3	Pictorial representation for the synthesis of LABNC	113
4.4	PXRD pattern of BFNONC	114
4.5	SEM image (a-c) at different magnifications and EDAX spectra (d) of BFNONC .	115
4.6	(a) FTIR spectra and (b) Wood and Tauc's plot (UV-Visible absorption spectra) of	
	BFNONC	116
4.7	Energy band diagram	117
4.8	PXRD pattern of ZABNONC	119
4.9	SEM images (a-b) of ZABNONC	120

4.10	EDAX (Elemental composition) of ZABNONC	120
4.11	FTIR spectrum of Aluminium-Barium-zinc oxide Nonocomposite	121
4.12	UV-Visible absorption spectrum of ZABNONC	122
4.13	Wood and Tauc's plot of ZABNONC	122
4.14	Energy band diagram	123
4.15	(a) PXRD pattern and (b) W-h plot of LABNC	123
4.16	SEM image (a-c) and EDAX (Inset: Elemental composition) (d) of LABNC	124
4.17	(a) FTIR spectra and (b) Wood and Tauc's plot (Inset: UV-Visible absorption spec-	
	tra) of LABNC	125
4.18	Schematic representation of Energy band diagram of LABNC	126
5.1	Schematic diagram of the Experimental Setup (S: Source position, T: Target sam-	
	ple, L: Lead shielding, D: Detector, PM: Photomultiplier)	129
5.2	Measured Gamma ray spectra in BFNONC NPs using different sources such as	
	Ba-133, Co-60, Cs-137 and Na-22 for different thickness	131
5.3	Comparison of measured shielding properties for BFNONC such as (a) μ/ρ , (b) μ ,	
	(c) λ , (d)HVL, (e)TVL, (f) \mathbf{Z}_{eff} , (g) N_e , (h) EABF, (i) KERMA, (j) SGR, (k) SAF	
	and (l) RPE with that of the theoretical values in the energy range 0.081-1.332 MeV	132
5.4	Measured Gamma ray spectra in ZABNONC NPs using different sources such as	
	Ba-133, Co-60, Cs-137 and Na-22 for different thickness	133
5.5	Comparison of measured shielding properties for ZNBNONC such as (a) μ/ρ , (b)	
	μ , (c) λ , (d)HVL, (e)TVL, (f) Z_{eff} , (g) N_{el} , (h) EABF, (i) KERMA, (j) SGR, (k)	
	SAF and (l) RPE with that of the theoretical values in the energy range 0.081-1.332	
	MeV	135
5.6	Measured Gamma ray spectra in LABNC using different sources such as Ba-133,	
	Co-60, Cs-137 and Na-22 for different thickness.	136
5.7	Comparison of measured shielding properties for LABNC of such as (a) μ/ρ , (b)	
	μ , (c) λ , (d)HVL, (e)TVL, (f) Z_{eff} , (g) N_{el} , (h) EABF, (i) KERMA, (j) SGR, (k)	
	SAF and (l) RPE with that of the theoretical values in the energy range 0.081-1.332	
	MeV	137
6.1	Comparison of (a) mass attenuation coefficient, (b) mean free path, (c) tenth value	
	layer, (d) effective atomic number, (e) specific gamma ray constant, (f) radiation	
	protection efficiency and (g) KERMA with that of energy for the studied alloys	143

6.2	Comparison of buildup factors of the studied alloys with that of photon energy at	
	penetration depths of (a) 5 cm, (b) 10 cm, (c) 20 cm and (d) 40 cm	145
6.3	Comparison of specific absorption fraction of energy of the studied alloys as a	
	function of photon energy at penetration depths of (a) 5 cm, (b) 10 cm, (c) 20 cm	
	and (d) 40 cm	145
6.4	Comparison of relative dose of the studied alloys with that of photon energy at	
	penetration depths of (a) 5 cm, (b) 10 cm, (c) 20 cm and (d) 40 cm	146

List of Tables

2.1	Value for degree of polynomial (n) to obtain the photoelectric cross section for	
	different energy regions	35
2.2	Fitting parameters for photoelectric cross sections formula	36
2.3	Fitting parameters to find the Photo electric cross section near X-ray absorption	
	edges	37
2.4	Correlation of Photoelectric cross sections of current work and literature	39
2.5	Fitting parameters of pair production (in nuclear field)	41
2.6	Fitting parameters of pair production (in electric field)	42
2.7	Values of a,b for fitting(coherent scattering)	44
2.8	a,b fitting values (Incoherent scattering)	45
3.1	Tabulation of type of alloy, X-ray edge, element and its corresponding energy(MeV).	80
3.2	Tabulation of gamma shielding parameters for selected Ni-Ti-Al alloy	83
5.1	Comparison of measured mass attenuation co-efficient with that of NIST data	130
5.2	Comparison of measured X-ray / gamma shielding properties for BFNONC with	
	that of the theory.	131
5.3	Comparison of measured X-ray / gamma shielding properties of ZABNONC with	
	that of the theory.	134
5.4	Comparison of measured X-ray/gamma shielding properties of LABNC with that	
	of the theory.	138
6.1	X-ray/gamma energy at which shielding efficiency becomes minimum $(E_m^{\mathcal{S}})$ and	
	corresponding λ, Z_{eff} , HVL and RPE (%)	147
6.2	X-ray/gamma energy at which shielding efficiency becomes maximum $(E_{\it opt.})$ and	
	corresponding Z_{eff} , HVL and RPE (%)	147

ABSTRACT

The current investigation focus on the X-ray and gamma radiation shielding parameters such as mass attenuation coefficient (μ/ρ) , linear attenuation coefficient (μ) , mean free path (λ) , tenth value layer (TVL), effective atomic number (Z_{eff}), specific gamma ray constant (Γ), radiation protection efficiency (RPE), Kinetic energy released in matter (KERMA), buildup factor, specific absorption fraction (ϕ) and relative dose (RD). The different alloys such as Iron-Boron, Iron-Silicon, Gallium, lead, Aluminium, Silicon-Boron, Zinc and Silicon-Germanium are investigated. The good absorber of X-ray and Gamma radiation among each category is selected. Among the studied iron-boron alloys, Fe0.95B0.05 was found to be good absorber of X-ray and Gamma radiation. Similarly, Ferro-Silicon (Fe0.21Si0.79), Galinstan (Ga0.685In0.215Sn0.1), Molybdochalkos (Cu0.1Pb0.9), Ni-Ti-Al (Ti0.4Al0.1Ni0.50), Silicon-Boron alloy (Si0.95B0.05), Zinc alloy (Cu0.7Ni0.15Zn0.15) and Silicon-Germanium alloy (Si0.1Ge0.9) are found to be good absorber among the Iron-Silicon, Gallium, lead, Aluminium, Silicon-Boron, Zinc and Silicon-Germanium respectively. Furthermore, to select the suitable alloy for X-ray and Gamma radiation shielding, we have studied shielding properties of these selected alloys of different categories in detail. The detail investigation shows Molybdochalkos (Cu0.1Pb0.9) is a good absorber with larger value of μ/ρ , Z_{eff} , Γ , RPE, KERMA, buildup factor, specific absorption fraction and relative dose, meanwhile smaller value of λ and TVL. As a result, Molybdochalkos alloy is an effective X-ray/Gamm a radiation shielding material among all the studied alloys. In addition to this nanocomposites such as for the first time Ba-Fe-Ni oxide nanocomposite (BFNONC), Aluminium-Barium-Zinc oxide nanocomposite (ZABNONC) and Lead alumino borate (PbAlBO4) nanocomposite (LABNC) were synthesized using solution combustion method. The synthesized sample was characterized using the techniques such as powder X-ray diffraction (PXRD), scanning electron microscopy (SEM), Fourier transmission infrared spectroscopy (FTIR) and UV-Visible spectrophotometer. Further, the X-ray/gamma ray shielding properties were measured in the energy range 0.081–1.332 MeV using NaI (Tl) detector and multi channel analyser (MCA) were measured. The measured shielding parameters are compared with the theory. The synthesized nano composites were may be used in the field of radiation shielding.

CHAPTER 1

Introduction

Reduction of radiation by introducing a shield of absorbing material between any radioactive source and a person, work area or radiation-sensitive device is known as radiation shielding. X-ray/Gamma radiation shielding has got much concentration of researchers in recent times since, in day to day life many aspects especially in research, industries, medical environments etc., are correlated with X-ray/Gamma radiation[1]. Ionizing radiation is commonly employed in business and medicine, yet it can pose a serious health hazardous by causing microscopic tissue damage. Neutral radiation shielding (X-ray, gamma, neutron) has long been a fascinating field for developing effective shielding materials. Higher atomic materials are required for X,γ radiation shielding. Lower atomic materials, a mix of lower atomic and higher atomic elements, are required for neutron shielding [2]. On top of that Lead was chosen as the most prominent element which is used as shielding material, taking in combination form with other materials in different proportions and became prime candidate for many researchers [3–5].

Furthermore, shielding at nuclear reactors and nuclear research centers requires shielding environments against high energetic γ radiations in order to bring them into acceptable range [6, 7]. The kinds of radiation, radioisotope activity, cost effectiveness, and exposure rate etc influence the thickness required for shielding. A strong shielding material causes considerable attenuation and decreases the risk of additional hazardous radiation emission as much as feasible [8]. Due to

several disadvantages with shielding materials which are from beginning, researchers are investigating to find new kind of materials namely polymers of glass etc [9–11]. Hence there is need of new types of alloys which will produce radiation shielding ability and good mechanical properties as well as high heat resistant properties [12].

Study of structural properties of Al–Si alloys obtained by fast cooling of a levitated melt by taking samples by rapid cooling of levitated melts of various compositions from 11.5 to 35 wt.% Si [13]. High energetic radiation shielding properties of Fe based alloys was done by Manjunatha et al., [14].X, γ radiation,neutron interaction characteristics of various alloys with different concentrations was studied by Seenappa et al.,[15]. Further mechanically alloyed Mo–Si–B alloys with a continuous α -Mo matrix and improved mechanical properties of Mechanical Alloying (MA) followed by cold iso-static pressing (CIPing) was studied by Krüger et al., [16]. On top of that Song et al., [17] investigated the structural and mechanical, anisotropic and optical properties of Si–Ge alloys in the C^2 /m phase were studied.LinHe et al., [18] Using the Vacuum Induction Melting (VIM) method, researchers evaluated the impact of titanium content on the microstructure and mechanical characteristics of high boron Fe–B alloys. Moreover reviews on the influences of alloying elements on the micro structure and mechanical properties of Aluminum alloys was performed by Rana et al., [19]. Further study of mechanical properties of magnetostrictive irongallium alloys was done by Kellogg et al., [20].

The effects of Zn on the microstructure, mechanical property and corrosion behavior of the as cast Mg–Zn alloys were studied using direct observations, tensile testing, immersion tests and electro chemical evaluations by ShuhuaCai et. al., [21]. Finally lead has become prime candidate for many researchers, one among that the microstructure and mechanical properties of Pb-free solder alloys for low-cost electronic assembly was studied by Glaze et al.,[22]. Previous researchers [23–32] have studied all radiation shelding properties with different combinations of metals. Fur-

thermore, the study of effect of X,γ radiation with Gallium based alloys done by Seenappa et al.,[33]. Earlier researchers studied effect of X,γ radiation with Aluminium based alloys and Si based polymers. [31, 34].

1.1 Mass attenuation coefficient (μ/ρ) and linear attenuation coefficient (μ)

The fundamental criteria for determining the penetrations of X/γ -rays in the material medium are μ/ρ and μ is a probability of a photon interaction per unit length. This parameter plays a vital role in radiation shielding and depends on the shielding material. With their application in various fields such as medical diagnostic, therapy computations, industrial irradiation and monitoring, X-ray crystallographic technique, health physics and many more fields, shielding parameters like photon interaction cross-section (σ), photon μ/ρ , μ , Z_{eff} and N_{el} have become highly significant. Real values of these parameters are useful in determining the regions of significance of theoretically dependent parameterization. Gerard et al., [35] developed a WinXCom program to explain importance of μ/ρ

The term "alloy" refers to a material that is made up of several different metals. However, it can also be a mixture of a metal and a nonmetallic element. The absolute composition of an alloy material plays very important role to meet certain application requirements. These alloys have a variety of implications on mechanical, physical and chemical properties. Recently research work has been carried out on different composition of alloys. Still, Nuclear engineers and radiation physicists are continually looking for new materials with higher radiation absorption capabilities. In this view, Akman et.al., [3, 35–37] The gamma shielding ability of triad alloys comprising Cr, Fe, and Ni in various percentages was examined.

A layer of heavy metals such as few meters of concrete and lead are used to get protection from gamma / X-ray radiations. However, due to the strong heat generated after long exposure

to radiation, these materials with insufficient characteristics restrict their shielding capacity and radiation leaks might occur. Even though, lead is a radiation shielding material, poor features such as low melting point, low mechanical strength and toxic effect made the researchers to focus on new alternative materials [38–40]. Alloys, metal composites, glasses, polymers etc., have been proposed as appropriate shielding materials for radiation fields since they are eco-friendly, safe and non-toxic in comparison to lead [15, 31, 34, 41–43]. The μ/ρ of organic compounds containing the elements H, C and O have been determined by Kataeb and Hamidi et al., [44]. Photon interaction with solutions of certain compounds was also investigated by Gagandeep et al., [45, 46] and Singh et al., [47]. Lead based alloys are conventional materials used as a primary shielding material due to superior attenuation properties against ionizing X-rays / gamma, its high atomic number and density. Combination of one or two other elements with lead, improves certain advanced properties were studied by Agar et al., Saritha and Rao measured the linear attenuation coefficient (μ) and μ/ρ using NaI (Tl) scintillation detector at energies 662 keV and 59.5 keV.

Tran et al., [48] used the XERT to calculate silicon μ/ρ 's and compared the results with experimental values. The radiation interaction properties of different materials have been established Shivaramu and Ramprasath, [49] to determine the most appropriate materials for use of radiation shielding in various fields and radiation measurements. There is a lot of research in previous work Gerward et al., [35] observed that comprehensive data sets available on photon interaction in the elements as well as extensive data sets on photon interaction in the elements. The μ/ρ 's of molybdenum have been estimated by Jonge et al., [50–63]. Huseyin et al., [55] determined mass attenuation coefficients of the concrete sample as building materials using MCNP-X different photon energies has been tested using NaI(Tl) detector and compared the values obtained from the XCOM and Monte Carlo data. Calculated values well agrees with each other. Singh et al., [64] reported the physical properties and gamma rays shielding parameters for some Lead-Copper bi-

nary alloys. Akman et al.,[36] investigated the gamma ray shielding performance of ternary alloys.

Şakar et al.,[65] determined the radiation shielding properties of leaded brasses using a HPGe detector and a ¹³³Ba radioactive source. Agar et al.,[7] studied the photon interaction features for some alloys containing Palladium and Silver alloys to use it as an alternative gamma radiations shielding material. Manjunatha et al.,[31] studied the X-ray and gamma radiation shielding parameters for the Al-based glassy alloys. Liu et al.,[66] investigated the effects of Yittrium and Zinc additions on electrical conductivity and electromagnetic shielding effectiveness of Mg-Y-Zn alloys. Kaur et al.,[67] made an attempt to summarize the various investigations made so far on visualizing the feasibility of alloys as radiation shielding material. Kaçal et al.,[68] determined the gamma-ray attenuation characteristics of eight different polymers using high resolution HPGe detector and different radioactive sources. Dong et al.,[69] calculated the shielding parameters of some boron containing resources for gamma ray and fast neutron. Aygün et al.,[10] studied the fabrication of Nickel alloys, Chromium and Tungsten reinforced new alloyed stainless steels for radiation shielding applications. Khobkham et al.,[70] studied the Photon interaction behavior of Zirconium alloy materials by using WinXCom program in the energy range 1 keV to 100 MeV.

Han and Demir [71] determined the total μ/ρ 's of Ti and Ni alloys at various photon energies of 22.1, 25.0, 59.5, and 88.0 keV. Kerur et al., [72] and Nagabhushan et al., [73] explored the problems associated with the intermediate energy resolution detector when measuring the mass attenuation coefficient of X-rays. The utilitarian value of γ rays exposure has been increased in petroleum plants, medicine, science and technology, industry, medicine, agriculture and energy sectors etc. Gamma-ray sources with energies ranging from 0.2 MeV to 1.5 MeV are often used in medical diagnostic fields such as radiography, archaeometry, chemotherapy, and Compton scatter images. High-density materials such as lead, tungsten, concrete and building materials can absorb gamma rays.

X-ray and gamma ray attenuation and absorption in materials are calculated using the energy absorption coefficients (EAC) and the μ/ρ . The ratio of incoming energy converted to kinetic energy (KE) of a charged particle is expressed by the mass absorption coefficient by hubble [50]. The EAC, μ/ρ and μ are the most important parameters for determining X-ray and gamma-ray penetrations in the material medium. The chance of a photon interaction per unit length is called the linear attenuation coefficient. This parameter is important in radiation shielding and is determined by the shielding material. Hubble and Seltzer [74] calculated the photon μ/ρ , N_{el} and Z_{eff} of a variety of thermoluminescent dosimetric substances by applying an interpolation method with a hyper pure germanium detector. Gerward mentioned μ/ρ for elements and compounds require a lot of lengthy computations to address this challenge he created the WinXCom programme for the elements in the periodic table of atomic numbers from 1 to 100. The mixture rule was established and used by Teli et al., [75] and measured the attenuation coefficient of several inorganic and organic substances at energies of 662 keV and 59.5 keV. Saritha and Nageswara Rao used a NaI (Tl) scintillation detector to assess the μ and μ/ρ by using experimental and theoretical data, Saritha and Rao et al.,[76] were able to determine the μ/ρ of complex biological molecules such as wood samples containing H, C, N and O components. Shielding parameters such as photon interaction cross-section, photon μ/ρ , Z_{eff} and N_{el} have become extremely important in a variety of fields including medical diagnostics, therapy computations, industrial irradiation and monitoring, X-ray crystallographic technique, health physics and many other fields. The real values of these parameters are abdel 2000 effect helpful in defining the theoretically dependent parameterizations significant regions. Gowda et al.,[77] Jonge et al., [78] determined the μ/ρ of molybdenum spanning the energy spectrum 13.5–41.5 keV. The μ/ρ have been determined in a variety of ways both experimentally and theoretically when compared to shielding materials such as lead, lead glass and concrete. Khanna et al., [53] studied the gamma-ray μ/ρ of borate glasses at energy 0.662 MeV and discovered that these glasses have a wide range of uses as transparent radiation shielding materials. Huseyin et al., [55] used MCNP-X to calculate the μ/ρ of concrete samples used as building materials. The calculated numbers are in good agreement with Manteo Carlo data. Due to the high radiation dose in applications such as nuclear reactors and medical treatments, it is critical to decrease the radiation exposure at places and on people. The (μ/ρ) observations were made using an Ultra Ge detector at photon energies of 81, 276, 302, 356, and 383 keV emitted from a 133Ba radioactive source. The experimental results were compared to the values acquired by the WinX-COM application and they were found to be perfectly in agreement. The average track length of incoming photons inside six different alloys was calculated sayyed et al.,[79] using the Monte Carlo simulation (MCNP-5) code. Other essential gamma-ray shielding characteristics were estimated based on the simulated track length. The alloys encoding MAR-302 and MAR-247 with mass attenuation coefficients ranging from 0.035 to 72.94 and 0.035 to 71.98 cm2g1, respectively had the highest μ/ρ in this study. For carbon steel (AISI 1018), austenitic (304 SS) and duplex (2507 SS) stainless steel alloys, various nuclear characteristics and corrosion behaviour were determined. Sadway et al., [80] calculated the cm1 and μ/ρ (cm2g1) of gamma rays using three types of neutron energies as well as nine γ -ray energy lines (121.78–1407.92 keV). Various electro chemical techniques were used to investigate the corrosion behaviour of 2O5-Na2O-CaO-K2O-MgO (PNCKM) was developed and tested as a new bio active glass system for use in radiation shielding applications and shielding parameters were calculated.

Gamma rays were first discovered by Becquerel and Villard in 1900 as a component of uranium and radium radiation with a significantly higher permeability than α and β particles. Gamma rays have the highest energy of all the radiation in the electromagnetic spectrum and can almost pierce any medium. It is a kind of ionising radiation with a high intensity but no electric charge. They are not affected by electric or magnetic fields, therefore they have a character similar to light

but with a considerably higher energy. They may interact with the absorbent as a particle but they will also act as a wave. In some alloys such as AL-6XN, nicrosil, nisil, terfenol-D, elektron and ferro-boron, X-ray and γ -radiation shielding parameters and σ_{coh} , σ_{incoh} , b_{coh} , b_{incoh} , b_{tot} , σ_{tot} and σ_{abs} were studied by seenappa et al., [29]. The μ/ρ , HVL, TVL and B_{ex} were used to calculate the alloys gamma shielding efficacy. The partial density method was used to compute the alloys fast neutron removal cross section. Cupero-Nickel was discovered to be the best γ -ray shielding material, studied by singh et al., [81] . This research could be useful in the construction of nuclear reactor cores and other sectors looking for appropriate radiation shielding materials. Furthermore the shielding parameters for photon energies accessible for the predefined energies can be calculated by csakar et al.,[82]. After registering with the Phy-X platform the radiation shielding effects of hardened epoxy resin samples containing ferrochromium slag were studied with the help of freely available online by korkut et al., [83]. Five separate samples were created, each with varying amounts of epoxy resin and ferrochromium slag. Epoxy-ferrochromium slag composites were subjected to X, γ , neutron particle transmission studies. In addition, absorbed dosages were determined using FLUKA Monte Carlo simulations. As a result, increasing the amount of ferrochromium slag in epoxy, improves radiation shielding efficacy. Using the WinX-Com programme and the MCNP5 code, μ/ρ , Z_{eff} , N_{el} , λ and HVL were studied by sayyed et al., [84]. Both the MCNP5 code and the WinXCom software produced similar μ/ρ results. In both BaO/SrOBi₂O₃B₂O₃ and BaO/SrOBi₂O₃B₂O₃ glass systems, adding Bi₂O₃ results in higher Z_{eff} values. The investigations of mechanical properties of the alloys place a very important role to reveal their possible use for alloy design through a hardness test and a tensile test [85]. The alloys are easy to process on relatively unsophisticated machinery because of their low melting points and relatively high mechanical properties soon after casting [86]. Alloys posses good mechanical properties [85]. studies on mechanical properties are also important when these are used for the

purpose of shielding [86, 87].Different parameters such as (MAC), (HVL), (Z_{eff}), (N_e) and (EBF) can be used to evaluate the shielding efficacy of materials. Each parameter provides important information about the radiation shielding capacity of the substances. There has been reports on the shielding properties of various materials. [9, 31, 64, 65, 82]. The high atomic number materials are most suitable for radiation shielding material whereas low atomic number materials such as Boron are the suitable choice for neutron shielding applications. The combination of high and low atomic number metals with different composition shows better gamma / X-ray / neutron / EMI shielding properties compared to other materials. Boron compounds or combinations are utilised in reactors for shut-down or power operating systems in various ways [1, 88–90]. Li et.al., [91] prepared the composite by incorporating Boron carbide to polyamide and investigated the neutron shielding properties. Singh et.al., [1, 92] investigated the shielding characteristics of some boron containing materials. Even though research work has been carried out on shielding properties of boron based alloys, radiation shielding properties of Silicon boron based alloys are not yet reported.

Hubble reviews [93] underline the importance of more biological attenuation observations, particularly at energies that might provide a key test of current theory. As a result, it is thought to be beneficial to do a rigorous analysis of photon interaction, such as the mass attenuation coefficient in compounds. Ylmaz et al., [94] measured the μ/ρ 's of p-type and n-type semiconducting samples in an external magnetic field by bombarding the samples with gamma-rays released from radioactive sources at varying energies of 59.5 keV, 80.1 keV, 121.8 keV and 244.7 keV.

The μ/ρ 's of Junior et al., [95] computed X-rays in several barite concretes used in radiation safety. Using the MCNP4C code, MiladVahabi et al. [96] calculated the μ/ρ for certain polymers. The findings were compared to experimental data and XCOM software predictions using gamma ray energies. Kaur et al., [9] experimentally investigated the finest thickness needed to measure

 μ/ρ 's for some Sn–Pb alloy systems at 122, 511 and 662 keV incident photon energies. El-Khayatt [97] designed a SEF for calculation of γ -ray kerma coefficient . Koehl et al., [98] measured μ/ρ 's of fission product isotopes and compared the results with that of EGS5 Monte Carlo computer code. Obaid, et al., [99] measured the mass attenuation coefficient for seven rocks which were collected from different regions of India. Dehghani et al., [100] calculated the γ -ray irradiation on molecular structure, optical properties and of colloidal gold nanoparticles. Mass attenuation coefficients are evaluated and the result shows that γ -ray irradiation has an impact on radiation absorption coefficients of colloidal gold nanoparticles. Mirji and Lobo [101] used a second degree polynomial equation and a logarithmic interpolation formula to calculate the γ -ray μ/ρ s of ten synthetic polymeric materials at various γ -photon energies ranging from 14.4 keV to 1332 keV. Third degree polynomial fitting is considered to be well suited for lower γ - photon energies.

Tarim et al. [102] created a basic Monte Carlo code to calculate the μ/ρ s of nine distinct gamma-ray energies in soil samples. The obtained findings were found to be very similar to the values obtained from the XCOM data base. The energy absorption coefficients and μ/ρ are used to calculate X-ray and γ attenuation and absorption in materials. The estimation of number of collisions between incident photons and the medium in a given volume is termed as mass attenuation coefficient. It is expressed as ratio of incident energy converted in to kinetic energy of a charged particle.

Seenappa et al., [103] studied the X-ray and gamma radiation shielding and neutron shielding properties of polymer concretes. Kacal et al., [104] carried out the experimental studies of radiation shielding properties for some ceramics. Ripin et al., [105] were studied the X-ray shielding behavior of kaolin derived mullite-barite ceramics. manjunath et al., [106, 107]. Earlier workers [108] studied the biological samples to compute their specific absorbed fraction of energy. A number of researchers gave the data for buildup factor for designing the shielding of radiation and

other such applications were studied [109–113]. Sidhu et al., [114] investigated how exposure buildup factors varies with the energy of incident photon and effective atomic number (Z_{eff}) in biological samples. Traditionally elements with higher atomic numbers and concrete were used for shielding. There have been investigated on concrete with different amounts of lead [115]. The alternative shielding materials, alloys, binary-alloys,tertiary alloys have gained the major importance in literature were studied.

Traditional shielding materilas used at nuclear plants include lead, many layers single slabs made up of Al, concrete etc [67]. These traditional materials were famous in reducing γ rays, X-rays and neutron beam exposure, easy in fabrication cost factor is being less. Lead can effectively attenuate certain kinds of radiation like X-rays and γ rays because of its high density and high atomic number. On top that Concrete can be a good replacement for lead due to it toxicity [116]. Rezaei et al., [115] investigated the γ ray shielding properties by considering the effect of concrete on different percentage of lead. They concluded that, if the powder of lead to cement ratio of 90 % by weight is added in the concrete mixture, the concrete can be used as a suitable shield against γ rays. Akkurt et. al., [117] studied the improvisation of shielding parameters of gamma rays by the addition of concrete aggregates into marbles. In order to overcome all these drawbacks, research is going on by using alloys as an alternative γ ray shielding material.

Alloying provides an opportunity to tune the chemical, mechanical and physical properties of metals. Kaur et. al., [118] made an attempt to prepare by using different combinations of cadmium, lead, tin and zinc white alloys as shielding materials and investigated their feasibility. Ekinci et al., [119] examined the shielding properties of rhenium-based super alloys. Akman et. al., [120] investigated the photon shielding parameters of Ag/Cu alloys with different compositions. Kaewkhao et. al., [121] studied gamma rays shielding parameters of Cu/Zn alloy. Various investigations has been reported in the literature for the gamma ray interaction with alloys

[31, 64, 122, 123]. As a result, changing the composition of alloys or selecting alternative alloys and comparing them to existing shielding materials becomes an exciting subject of study.

The fundamental shielding parameters such as mass attenuation coefficient (μ_m), mean free path (λ), half value thickness (HVL), tenth value thickness (TVL), effective atomic number (Z_{eff}), effective electron number (N_e) and exposure buildup factor (R_{ex}) are base concepts for radiation shielding. Enormous work has been reported relevant to investigations of shielding parameters. The determination of exact values of μ/ρ in very important for mny practical applications [57, 124, 125]. Elmahroug et.al., [126] determines the neutron and gamma-ray shielding parameters using a new computer program called ParShield. The mass attenuation coefficient parameter mainly depends on incident photon energy and chemical composition of the material. R_{eff} is an important parameter to complex media for visualizing photon interactions. Several methods have been adopted for measuring the R_{eff} of composite materials. Hosamani and Badiger [127, 128] determined the R_{eff} of composite materials by measuring the back scattered gamma photons at 180° and in back scattered beta particles.

Generally, logarithmic interpolation method, geometric-progression (GP) fitting method [129], iterative method [130], Monte Carlo method [131] are available in literature. Bulk reports have been available on B_{en} for polymers [132], human tissues [133], fattyacids, aminoacids, carbohydrates [134] and also for low atomic number elements [135] but very few reports are available for high atomic number elements such as glasses and alloys. In the present study, Si-Ge alloy of different composition viz., silicon germanium alloys such as $Si_{0.1}Ge_{0.9}(SG1)$, $Si_{0.2}Ge_{0.8}$ (SG2), $Si_{0.4}Ge_{0.6}$ (SG3), $Si_{0.6}Ge_{0.4}$ (SG4), $Si_{0.8}Ge_{0.2}$ (SG5) and $Si_{0.9}Ge_{0.1}$ (SG6) are used for examining the shielding properties of gamma/X-ray and neutrons. Since Silicon acts as a hybrid elastomer and has various applications [136]. Whereas, Germanium is preferred due to its atomic number being much higher than silicon and which increases the probability of gamma ray interaction.

Nuclear shielding for X-rays, gamma and neutrons is an important concern in the field of radiation physics. The mass attenuation coefficient and its derivable are fundamental parameters for the collection of shielding materials for X-ray and gamma radiation. Tekina et al.,[137] were studied the μ/ρ and calculated shielding parameters (for example: effective atomic number (Zeff), HVL, TVL, effictive electron density (Nel), average free path, and photon transport factors.

 X,γ radiation attenuation and absorption in materials are calculated using the energy absorption co-efficients (EAC) and the μ/ρ . Mass absorption coefficient is the ratio of incident energy converted into kinetic energy of charged particles. The EAC, (μ/ρ) and linear attenuation coefficient (μ) are the basic requirements for calculating the penetration of X, γ radiation in the material medium. The linear attenuation coefficient plays a pivotal role in radiation shielding. Radiation shielding properties like μ/ρ , Z_{eff} and N_{el} have become highly significant to study radiation shielding materials. Lobascio et al., [138] have measured the response to simulated heavy-ion cosmic radiation of Kelvar and Nextel materials and compared it to polythene, lucite and aluminium. From this study they have observed that Nextel is less efficient as a radiation shielding against X-ray and gamma rays. Tijani et al., [139] studied erbium doped tellurite glass at diagnostic energy range in order to produce a high potential substitute for lead. Azeez et al., [140] measured the μ of lead and green tungsten-brass composites and found that it is a good shielding material than lead. Caner et al., [141] measured the μ of aluminium alloys and stainless steel and found that aluminium alloys have high mechanical strength, it can be used in aviation vechiles. Hubble et al., [50] tabulated the mass attenuation coefficient and mass absorption coefficient of 40 elements having atomic number ranging from 1 to 92. The photon mass attenuation coefficient, Z_{eff} and N_{el} of some dosimeteric compounds are measured by Gowda et al.,[77]. Berger et al., [berger1999xcom] have designed XCOM software to calculate μ/ρ of some compounds. Gerward et al., [gerward2004winxcom] developed a WINXCOM software to calculate X-ray attenuation coefficients of mixture of compounds. Kateeb et al.,[142] studied the μ/ρ of some materials containing H, O and C elements. Attenuation coefficients of aqueous solutions of Li, Na and K chlorides having different concentrations have been studied at different energies by Kaur et al., [45]. Singh et al., [143] have been measured the μ of solutions of some compounds at 662 keV, they are good in agreement with values from XCOM calculations. Gagandeep et al., [47] have measured the total (μ/ρ) of aqueous solutions of urea at different concentrations at 662 KeV. Telli et al., [75] developed a solution technique for the measurement of μ and (μ/ρ) of salts containing carbonates and sulphates, results obtained have excellent agreement with the theoretical values. Saritha et al., [144] have studied the (μ/ρ) Of biological molecule containing H, C and O elements experimentally and compared the results with calculated values. Azeez et al., [145] have measured the radiation shielding properties of concrete samples of different thickness using Cs137 and Co60 sources. Photon attenuation coefficients of barite concrete have been determined by Akkurt et al.,[146]. Basher azeez et al.,[147] examined the dependence of γ -ray absorption coefficient on steel slag, iron filings and steel balls incorporated concrete using γ -spectrometer of NaI(Tl)detector and Cs-137 source at 0.662MeV energy. Tran et al., [48] have compared experimental X-ray total (μ/ρ) of Silicon with the X-ray extended-range technique from 5keV to 20keV. The total μ/ρ , Z_{eff} and N_{el} for different compounds at 59.54keV has been studied by Ozdemir et al., [148]. The Z_{eff} and N_{el} have been determined by mixture rule. The (μ/ρ) of molybdenum in the energy range 13.5-41.5 keV has been measured using X-ray extended range technique by Martin et al.,. [149]. Hubbel measured the (μ/ρ) and B_{en} for 23 elements and 13 compounds from 10 keV to 100 GeV.

1.2 Effective atomic number (Z_{eff})

The Z_{eff} of a composite material is a number that has the same effect as an individual element when it interacts with photons. It is very much helpful in the design of radiation shielding and in calculating of absorbed dose. This number is not constant for a multi element. Depending on the relative value of the interaction mechanisms, it varies with photon energy. It is an energy dependent variable that has been determined from Z values of the elements in a given compound/mixture weighed according to various photon interaction processes. Limkitjaroenporn et al., [150] determined the μ/ρ and Z_{eff} for Inconel 738 alloy for different energies obtained from Compton scattering. Ozdemir and Kurudirek et al., [148] studied the total μ/ρ 's, Z_{eff} and N_{el} of several inorganic and organic substances at 0.05954 MeV. The Z_{eff} of composite materials varies with energy. For the understanding of X-ray attenuation by a compound medium like any biological tissue, studies on Z_{eff} and N_{el} are needed. Shivaramu et al., [151] measured the EAN's for low atomic number substances. The theoretical values of Z_{eff} were determined by Jackson et al., [152].

In this way, it provides fundamental details about the properties of multi-element materials. As a more useful parameter, it is used in a variety of applications, including the nuclear industry, architecture, radiation shielding design, absorbed dose and BF measurements, space research projects and a variety of science applications [153]. The incident energy as well as the atomic number of the constituent elements define this number. It denotes the number of electrons in the sample that are directly participating in the photon–atom interaction [154]. Z_{eff} is also a useful parameter in many case namely B_{en} , absorbed dose etc. The Z_{eff} represents the interaction of radiation with material medium [154]. Several researchers have made lot of contribution to determine the Z_{eff}) in various alloys [71, 155, 156]. But, these studies appear to be restricted to a narrow

range of energies. Hubble and Seltzer., [51] have determined the photon μ/ρ , Nel and Zeff of certain thermoluminescent dosimetric compounds of different energies using hyper pure germanium detector by interpolation method.

Murat Kurudirek et al., [157] used mass attenuation coefficients from the WinXCom computer programme to investigate the Z_{eff} s of different alloys. Exact values of μ/ρ 's for X, γ - radiations in various materials are critical in many sectors, including radiation dosimetry, nuclear and radiation physics, agriculture, biology, medicine, the environment and industry. These values are significant in both basic physics and many application fields. Creagh et al., [158] found key information and issues linked with the determing the high energy radiation attenuation constants. It has a physical meaning and permits various properties of a material to be represented numerically. This value is a very useful parameter in space research programs, technology, nuclear industry, engineering and many other scientific domains especially, such as calculation of the dose in radiation therapy. The estimation of μ/ρ values for gamma ray interaction by the transmission method is a regularly used way of determining an Z_{eff} of a material consisting of multiple elements in specific proportions. Arif Bastug et al., [159] measured the Z_{eff} 's of some composite mixtures including borax. This number is determined by the incident energy as well as the atomic number (Z) of its constituents. It represents the average number of electrons in a material that are actively involved in the photonatom interaction. As a result, the Z_{eff} is commonly utilised in mass energy absorption coefficient calculations and Kerma in radiation dosimetry. Manjunatha and Umesh et al., [160]. Prasanna Kumar and Umesh et al., [161] investigated the Z_{eff} of composite materials in the gamma ray range 280-1115 keV for the Compton effect.

Accurate understanding of Z_{eff} 's is critical in medical radiation dosimetry, as well as technical and engineering applications. There have been several efforts to develop a method for calculating the effective atomic numbers of composite materials [151, 162]. Certain empirical formulae have

been designed and published in the literature [163]. However, its applicability is restricted to the experimental circumstances utilized in the specific paper. Cevik et al., [164] gives out data for the μ/ρ 's of bulky and thin film CuInSe₂ samples at various energies. If certain constants are known, the energy absorption in a particular material may be estimated. These required constants are the medium's effective atomic number and electron density. Many technical applications make use of Z_{eff} 's and N_{el} 's. Previous workers [164, 165] have conducted substantial research on effective atomic numbers in a wide range of composite materials such as polymers, alloys, compounds, mixtures, superconductors, semiconductors and thermoluminescent dosimetric compounds. The effective atomic number has an interesting application in security screening of aviation passenger luggage for chemical explosives, particularly for low crystalline substances. Gounhalli et al., [166] published research on the Z_{eff} 's and N_{el} 's of several chemical explosives.

Eritenko et al., [167] analysed the analytical effect of Z_{eff} on matter and radiation energy in the 10–1000 keV range. Hosamani and Badiger et al., [127] estimated the Z_{eff} of composite materials by measuring the back scattered γ - photons at 180° . Richter and Greilich et al., [168] used dual-energy computed tomography to assess the relative electron density and Z_{eff} . Dual-energy computed tomography can increase accuracy in radiotherapy treatment planning.

Sakata et al., [169] showed that dual-energy computed tomography imaging can measure the Z_{eff} as well as N_{el} . They concluded that a dual-energy computed tomography provides an excellent prediction for the Z_{eff} . Sathiyaraj et al., [170] investigated metal nanoparticle doped polymer gel effective atomic number and buildup factor estimations. Willem and Langeveld [171] demonstrated that dual-energy imaging, spectroscopy and statistical waveform analysis can be utilized to estimate the Z_{eff} from X-ray transmission data because the μ/ρ depend on both energy and atomic number.

Renu Sharma et al., [172] calculated the Z_{eff} 's for certain binary alloys using the gamma ray

backscattering technique. For the Z_{eff} 's of all studied alloys, there was good agreement between theoretically estimated and experimentally observed values. Levelt et al., [173] measured the buildup factor, total atomic cross-section, N_{el} and Z_{eff} of some compounds for various sources. Measured values of μ/ρ s were determined using an energetic dispersive X-ray spectroscopy apparatus, while the theoretical values were computed using the WinXCom computer tool.

1.3 Effective electron density(N_{el})

Depending on the application, the N_{el} is most beneficial in selecting an alternate composite material instead of an element for that energy. Singh et al., [174] developed a WinXCom software, it is used to calculate the μ/ρ , N_{el} , and Z_{eff} of carbon and stainless steels. Photon energies ranging from 5000 eV to a few MeV are often used in medical and biological applications. The amount of X-ray attenuation data available, however, is limited to biological samples Singh et al., [174] computed the μ/ρ , Z_{eff} and effective electron density of carbon steel and stainless steels by using the WinXcom program. Seven et al., [175] measured the total μ/ρ for Co, Cu, Ni elements and Co-Cu, Co-Cu-Ni alloys at different energies using transmission arrangement. Levet et al., [173] measured the effective electron numbers, σ , Z_{eff} and BF of certain elements using various radiation sources. Mass attenuation coefficients are useful for calculating $N_{\it el}$ and Z_{eff}. Bursalioğlu et al., [176] measured trace element concentrations and electron density in human blood serum after radioiodine therapy in differentiated thyroid cancer patients. [177]. Kaewkhao et al., [121] computed the total interaction cross-sections, μ/ρ 's, N_{el} 's, effective atomic numbers and average paths of Cu/Zn alloy using mixture rule at different gamma-ray energies. Kurudirek and Onaran [178] used an interpolation method to calculate the N_{el} 's and Z_{eff} 's of some important biomolecules for total electron(e⁻), proton and an α -particle interaction. Alteration in electron densities seems to be more or less the same with the alteration in effective atomic numbers for the given materials. More et al., [179]. studied the properties of electron density and effective atomic number of amino acids. Wu [180] developed a technique for electron density measurements in the atmosphere. The Z_{eff} and N_{el} of some samarium compounds are calculated using the experimental total μ/ρ values around the K edge by Akman et al.,

1.4 **Photon Buildup factor(PBF)**

The use of X-radiation and gamma in radiation therapy and radiation imaging requires sufficient understanding of the interactions of radiation with matter. When photons penetrate the target medium, their energy degrades and builds up in the medium, causing secondary radiation to be emitted, which may be estimated using a factor known as the BF. Calculation of the energy absorbed in a medium depends on the contribution of the un-collided photons from the source and also on the contribution from collided and secondary photons. The energy absorbed in a medium is computed by multiplying the un-collided photon contribution by the B_{en} , The photon buildup factor determines how much secondary photons add to the total amount of photons at that location. The build-up factor is the ratio of the overall value of a particular radiation quantity at any place in a medium to the contribution to that value from radiation reaching the same point without colliding. The B_{ex} and B_{en} are the two forms of buildup factors. The absorbed / deposited energy in the material/medium is expressed by B_{en} . The energy deposited in the air is represented by the B_{ex} Lalit et al., [181] have been employed monte carlo simulation method to study X ray,gamma ray buildup factor for graphite and water in the energy range 4-10 Mev upto 5 λ . Kurudirek et al.,[182] have inferred from the findings that the build-up of photons was smaller in case of NaCl relative to other materials at lower penetration depth(PD). The build up factors for homogeneous samples of iron, air and water have been calculated by chilton et al., [110] using moments method code.

1.4.1 Energy absorption buildup factor (\mathbf{B}_{en})

The energy absorption buildup factors employed in shielding calculations, nuclear engineering and nuclear medicine. Singh et al. [183] investigated the energy B_{en} factors for gel dosimeters, which may be used to calculate the effective dosage to human organs.

Mann et al., [184] measured the double layered transmission exposure buildup factor for Aluminium-Lime stone and it has been observed that the Aluminium-Lime stone shield provides the highest protection against gamma-rays. Levet et al., [173] measured N_{el} , μ/ρ , Z_{eff} and buildup factor (BF) for some oxygen and hydrogen based compounds. Singh et al., [183] determined γ -ray energy B_{en} for optically stimulated luminescence materials using the GP fitting method and it is useful in the medical diagnostics and therapy, accident dosimetry, space dosimetry and personnel surveillance.

Park et al., [185] analyzed uncertainties in the weighted least square fitted BF's in the point kernel method. Kucuk et al., [186] developed a model of γ -ray B_{en} 's for thermo-luminescent dosimetric materials. Kurudirek and Özdemir determined the B_{ex} and B_{en} for some carbohydrates amino acids and fatty acids. Manohara et al., [187] calculated the B_{en} and tissue equivalent for thermoluminescent dosimetry materials. Mann et al., [188] studied the μ/ρ and B_{ex} of some low atomic number materials as a building materials. Atak et al., [189] calculated photon buildup factors using Monte Carlo code MCNP5. Kurudirek et al., [133]measured gamma-ray B_{ex} and B_{en} 's of human tissues. Singh et al., [190] calculated certain regularly used solvents for the variation of B_{en} with incident photon energy and penetration depth. Mann et al., [191] determined gamma-ray buildup factors in some silicates up to 100λ penetration depth. Gamma-rays and X-radiations are widely used in medical imaging and radiation therapy. The BF is an important parameter in the distribution of photon energy in all objects. In branchy therapy, radioactive seeds are implanted in the patient's body to destroy cancer cells. The PBF is important in calculating the radiation

dosage received by cancer cells. Sardari et al., used the Monte Carlo approach to calculate the buildup factor of γ and X-ray photons in water and soft tissue by Kavaz et al., [192] studied the EB_{en} for certain chemotherapy medications in the energy range 15 keV-15 MeV for penetration depths up to 40 λ are calculated using the GP fitting model. This is useful in radiation dosimetry and therapy, both of which are utilized in cancer treatment. Hernández et al., [193] introduced a semi-empirical method for the correction of photon self-absorption gamma spectrometry of environment low energy range. Hirayama et al., [194] calculated B_{ex} of high energy γ -rays for water, lead, iron and concrete using Monte Carlo code in the energy range 0.01keV to 0,1 keV up to a penetration depth of 10 mpf. Kulwinder., [191] calculated γ -ray buildup factors for silicate sample in the energy range 15keV to 15 MeV up to penetration depth of 100 λ using G P fitting formula. Kulwinder Singh mann et al., [184] explained a comparative study of γ ray double layered transmission B_{ex} s of some engineering materials. The B_{en} for thermoluminescent dosimitric materials using G P fitting formula in the energy range 15keV to 15 MeV for penetration depth up to 40λ by Manohar et al., [187]. Morris [195] measured the B_{en} for water and aluminum and for B_{ex} concrete using point isotropic gamma-ray sources in the energy range 0.03 to 10 MeV up to a penetration depth of 50 λ . The photon interaction parameters such as μ/ρ , Z_{eff} , N_{el} and BF for different alloys have been measured by Levet [173] using $^{137}\mathrm{Ba},\,^{157}\mathrm{Gd}$ and $^{241}\mathrm{Am}$ $\gamma\text{-rays}$ sources.

1.4.2 Exposure buildup factor (\mathbf{B}_{ex}):

Manjunatha et al., [196, 197] evaluated the photon relative dose distribution and buildup factors in various parts of teeth. Manjunatha and Rudraswamyet et al., [197] studied energy absorption buildup factors as well as exposure buildup factors in hydroxyapatite. Previous researchers used exposure buildup factors for the investigation of secondary radiation dose like bremsstrahlung manjunath et al., [106, 107] By injecting radioactive seeds into the patient's body,

cancerous tumors can be destroyed in brachy therapy williamson et al., [198, 199]. Cancerous tumors can be destroyed by multiplying the contribution of un collided photons with the energy absorption buildup factors [200, 201] for designing the shielding of radiation, previous researchers gave the data for buildup factors [110–113]. In the computations of radiation dose absorbed by the cancer cells it is necessary to assume photon buildup factors. The shielding parameters in silicon boron alloys of different composition $Si_{0.95}B_{0.05}$ (SB1), $Si_{0.9}B_{0.1}$ (SB2), $Si_{0.8}B_{0.2}$ (SB3), $Si_{0.7}B_{0.3}$ (SB4), $Si_{0.6}B_{0.4}$ (SB5) and $Si_{0.5}B_{0.5}$ (SB6) has been studied. A detailed study was done on Silicon-boron alloy to get better radiation shielding results compared to other materials. So far, as per our knowledge X-ray / gamma ray, neutron and EMI shielding investigation on Silicon -Boron alloys are limited. Due to the desirable corrosion characteristics and biocompatibility, Zinc alloys can be used as the biodegradable metals. The specific absorbed fraction (SAF) of energy, energy absorption buildup factors (B_{en}s) and relative dose (RD) in the energy range 15keV-15 MeV for zinc alloys of different composition such as alloy A (Cu 20%, Ni 40 %, Zn 40 %), alloy B (Cu 30 %, Ni 35 %, Zn 35%), alloy C (Cu 40 %, Ni 30 %, Zn 30%), alloy D (Cu 50 %, Ni 25%, Zn 25%), alloy E (Cu 60 %, Ni 20%, Zn 20%) and alloy F (Cu 70%, Ni 15 %, Zn 15%) has been investigated up to the penetration depth (PD) of 40 λ using GP fitting method. It is found that both SAF and RD are larger for alloy F (Cu 70 %, Ni 15 %, Zn 15%) than the other studied zinc alloys.. Hence, we can conclude that the alloy F (Cu 70 %, Ni 15 %, Zn 15%) is a good absorber of X-rays, neutrons and gamma among the investigated zinc alloys. This work finds its usefulness in the radiation dosimetry and shielding of radiation. Kurdirek et al., [134] calculated the Ben and B_{ex} for some essential amino acids, fatty acids and carbohydrates in the energy region 0.015–15 MeV up to a penetration depth of 40 λ . Shimizu et al., [202] observed small discrepancies for elements of lower atomic numbers up to 10 λ when the buildup factors obtained by three methods viz., Monte Carlo method, invariant embedding, and GP fitting are compared. Singh et al., [190] investigated how exposure buildup factors varies with the energy of incident photon. The present work focusses on the estimation of buildup factor as explained by Manjunatha et al., [23] and specific absorbed fractions in some gallium alloys such as Gallium alloy [Al-50%, Ga-50%], Galfenol [Fe-30%, Ga-70%] and Galinstan [Ga-68.5%, In-21.5%, Sn-10%]. The exposure buildup factor calculation is important for estimating the effective dose to human organs and simulating the dosage for radiation treatment and other medical fields. The study of exposure buildup factor (B_{en}) is very helpful in radiation biology. Murat Kurudirek et al., [133] have been determined the B_{en} and B_{en} of human teeth by utilizing the GP fitting approximation in the energy range 0.015–15 MeV up to 40λ . Vishwanath et al., [203] studied the B_{en}'s of some Oxide Dispersion Strengthened (ODS) steels, observed that ODS steel is the superior neutron and γ -ray shielding materials, this study is very much useful in designing of shielding materials and future reactor technologies. chibani et al., [204] has developed a new Monte Carlo code to calculate B_{ex} in media. the results from monte carlo code the results good agreement with SNID code results for materials for low atomic number.

The concept of BF was first presented by White et al., [205] and Fano et al., [206], who recognized its relevance in attenuation studies. Hirayama et al., [207] studied the impact of coherent and incoherent scattering on low energy gamma ray exposure buildup factor. The impact of linear polarization and Doppler widening on low-energy gamma ray B_{en} 's were investigated by Namito et al., [208]. Hirayama et al., [209] investigated the impact of photon cross sections and air energy absorption coefficients on the γ - ray B_{en} .

Considering the need of complete investigations of BF's, Brar et al. [210] investigated the EB_{en} of H, C, and O materials as a function of fractional weights of H, C and O. Manjunatha and Rudraswamy et al., [196, 197] also calculated the BF's and photon relative dose distribution in various areas of teeth, which can be used in dental diagnosis.manjunatha et al., [108]

researchers computed BF's for estimating specific absorbed fractions of energy (SAFE) in biological samples. Previous studies [106, 107] used the B_{en} to calculate secondary radiation doses such bremsstrahlung in bone. Sathiyaraj et al., [170] computed the Z_{eff} and BF for metal nanoparticle doped with polymer gel. In the medical as well as biological fields, the γ -ray BF is important in the Photon energy distribution (PE) and radiation dose (RD) estimate for biological samples, in biological materials like proteins, fatty acids, and amino acids [211]. While photons in the keV range are significant in medical diagnostics, radiation biology, and therapy, photons in the MeV range play a vital role in medical imaging and radiography [154, 212].

There are several ways for calculating the buildup factor, sayyed et al., [213] including the invariant embedding method [111, 202, 214] and the GP fitting approach [215] provides BF data for 23 elements, one chemical, two mixtures sayyed et al., [213]. The proposed GP fitting formula has been shown to be accurate to within a few percentage points Harima [200, 216] has conducted a thorough analysis of the state of BF calculations and applications. Sidhu et al., [217] investigated the energy B_{en} of several biological samples. Sayyed et al., [213] investigated the B_{en} 's for several types of smart polymers in the energy range of 0.015–15 MeV using the GP fitting approach. The shielding performance of the polymers is found to be comparable to that of regularly used polymers, and the outcomes of this research should be valuable for radiation shielding applications. such as nuclear, medical and industrial fields. Angular B_{en} 's for photons from a combined energy source through aluminum, steel and lead shielding blocks were measured by Geguchadze. Topcuoglu et al., [218] computed the Z_{eff} and N_{el} of human teeth in the energy range 1 keV–20 MeV for total photon interaction and photon energy absorption.

Khabaz et al.,[219] Using the Monte Carlo code MCNPX, they investigated the gamma ray exposure and relative dose buildup factor for five sites isotropic multi-energy sources up to a depth of $10~\lambda$ for iron, lead, concrete, aluminum, tungsten and uranium. The dose BF values

were parameterized as a function of λ using the GP analytical formula and the parameters were derived for various gamma sources. Kavaz et al., [220] determined the γ -ray B_{en} and B_{en} values of barite-doped, limonite-doped and serpentine-doped for incident photon energies ranging from 0.015 MeV to 15 MeV and penetration depths up to 40 λ . The addition of minerals with very similar atomic numbers improves the lithium borate glasses.

Al-Ani and Jawad et al., [221] investigated the γ -ray BF for two shielding materials, graphite (Z = 6) and water (Z_{eff} = 7.42) for isotropic plane sources usually incident within the energy range 4 MeV-10 MeV and up to 5mfp. Lokhande et al., [222] computed radiological parameters of some amine group bio material containing C- H- N- O with the γ -ray count by narrow beam geometry in the energy range 122–1330 keV. It is found that amino acid has the highest EB_{en} value at 0.1 MeV, and the estimated radiological data of biological material is used in dosimetry and medical physics.

Sharaf and Saleh [223] employed characteristics such as μ/ρ , Z_{eff} , penetration depth and B_{en} to assess the shielding qualities of three different construction designs and building materials typically used in Jordan. Bakos and Tsagas et al., [224] defined and calculated the angular exposure dose build up factor for combined energies disc geometry sources ranging from 1.43 to 2.75 MeV. Rajkumar et al.,[225] explained the comparative study of the μ/ρ , γ , Z_{eff} , N_{el} and HVL for manufactured spinel ferrites is carried out using NIST-XCOM and Geant4 at 122–1330 keV.

The X-ray and gamma radiation shielding parameters in Al-Si alloys (Al-47, Al–32S, Al–43, Fe–Si, Al-356, Al-355, and Al-A355) including μ/ρ , μ , HVL, TVL, Z_{eff} , B_{ex} and Γ has been measured. In addition, the NSPs in Al-Si alloys has been investigated by manjunatha et al.,[23] such as b_{coh} , b_{inc} , σ_{coh} , σ_{inc} , σ_{tot} and σ_{abs} . The shielding capabilities of the aluminium silicon alloys under investigation were compared. According to the findings, the ferro-silicon alloy has the minimum mean free path, HVL, TVL and the maximum B_{ex} . Thus, ferro-silicon alloy is a good

X-ray and γ radiation absorber. For ferro silicon alloy, neutron attenuation parameters are considerable. As a result, we believe that ferro silicon alloys are the best X-ray, gamma and neutron shielding materials.

Khayatt et al., [226] calculated the photon shielding parameters such as Z_{eff} , N_{el} photon interaction and photon energy absorption and gamma-ray kerma coefficient for seven polyethylenebased neutron shielding materials in the energy range 1keV to 100MeV. Tekin and Kilicoglu investigated the gamma-ray and neutron shielding properties of different type of Ga additive in Pd-Mn binary alloys. Earlier researchers [1, 81, 227, 228] were studied the gamma and neutron shielding and γ -ray interaction properties in alloys, polymers and boron containing elements. The synthesis and characterization of nanocomposite magnetite films were effectively used by Badway et al., [229]. The neutron shielding properties (NSP) of a sample consists of $\mathbf{b}_{coh}, b_{inc}, \sigma_{coh}, \sigma_{inc}, \sigma_{tot}$ and σ_{abs} and these are calculated by using the following mixture rule. Nuclear shielding for X-ray, γ -rays and neutrons is an important concern in the field of radiation physics. The μ/ρ and its derivable are fundamental parameters for the collection of shielding materials for X-ray and gamma radiation. Hayashi et al.,[230] have shown that the capability of neutron shielding is increased by the combination of steel and Zr(BH4)4. The polymers, plastic materials and polyvinyl alcohol / iron oxide polymer composite were extensively used to measure radiation shielding properties[15, 31, 35, 231–233]. It is important to replace the lead shielding material by nontoxic and low cost materials. Seenappa et al.,[15] studied the X-ray, gamma radiation shielding parameters and neutron shielding parameters in some alloys such as AL-6XN, nicrosil, nisil, terfenol-D, elektron and ferro-boron. Kaur et al., [6, 234] studied the scope of Pb-Sn and Pb-Zn binary alloy in gamma ray shielding. Further the physical properties and shielding parameters were discussed in detail. Singh et al., [235] computed various photon interaction parameters for different compositions of Cu-Pb binary alloys in the wide energy regime of 1 keV to 100 GeV.

1.5 Relative dose (RD) of photon

The study of relative dose of gamma radiation has become significant importance for radiation dosimetry due to the continuous use of X-rays and gamma rays in medical imaging and radiation therapy. The photon buildup factor must be included when calculating the radiation BF, attenuation coefficient and distance from the point source determines the dose of gamma radiation and it is given by $D_{\gamma} = D_0 \exp\left(-\mu r\right) \frac{B}{r^2}$. Here D_0 is initial dose delivered by the point gamma source, μ is the linear mass attenuation coefficient for the Photon energy and B is the BF. The RD distribution at a distance r is given by $\frac{D_{\gamma}}{D_0} = \exp\left(-\mu r\right) \frac{B}{r^2}$.

1.6 Neutron shielding parameters (NSP)

Following properties are considered as shielding parameters for neutrons.

Coherent neutron scattering cross section (σ_{coh}): The ability of an interacting material to scatter neutrons without causing energy loss is known as Coherent neutron scattering cross section.

In-coherent neutron scattering cross sections (σ_{incoh}): The ability of an interacting material to scatter neutrons with causing minimum energy loss is known as In-Coherent neutron scattering cross section.

Total neutron scattering cross section (σ_{tot}): The ability of the interacting medium to scatter neutrons through coherent and incoherent process.

Neutron absorption cross sections (σ_{abs}): The ability of interacting medium to absorb neutrons is called neutron absorption cross sections.

Coherent neutron scattering length (b_{coh}): It is the distance covered by the neutron in an interacting medium between two coherent.

Incoherent neutron scattering length (b_{inc}): It is the distance covered by the neutron in an interacting medium between two incoherent events.

The neutron shielding properties (NSP) of a sample consists of b_{coh} , b_{inc} , σ_{coh} , σ_{inc} , σ_{tot} and σ_{abs} and these are calculated by using

$$(NSP)_{sample} = \sum f_i(NSP)_i \tag{1.1}$$

Here (NSP)i is neutron shielding parameter of i^{th} element in the concrete and f_i is the fractional abundance (a mass fraction of the i^{th} element in the molecule). From the calculated neutron cross sections, attenuation parameter of neutron is evaluated using the relation;

$$\textbf{Attenuation Parameter} \ = \frac{\sum XN_A}{A}cm^2/glabeleq - Attenuation parameter - c1$$
 (1.2)

Here A and N_A are evaluated atomic mass and Avogadro number respectively.

Nuclear scientists are continually experimenting with different materials to determine how different radiation shielding parameters affect their ability to utilise radiation efficiently in a variety of applications. Due to the shortcomings of traditional shielding materials, several researchers have proposed using metallic alloys as an alternative for X-ray/Gamma ray shielding material. As a result, it is necessary to first investigate various alloys in terms of radiation shielding capabilities,

categorization, and fabrication techniques which gave us motive in writing this paper.

1.7 **Objective of the present study**

- To investigate the X-ray/gamma shielding properties, the proper understanding of mechanism of interaction of X-ray/gamma with atoms are essential such as Photo electric effect, Compton scattering and pair production. As a part of this study, the semi empirical formula is developed for Photo electric cross section. This enable us to study Z-dependence of Photoelectric process. Similarly, the Z-dependence of Compton and pair production.
- Theoretical study of different shielding properties in various alloys such as Aluminiumsilicon alloy, Gallium alloy, Silicon-Boron alloy, Lead alloy, Aluminium alloy, Zinc alloy, Silicon-Germanium alloy and Iron-Boron alloy.
- Synthesis and characterization of nanocomposites which consist of Ba, Fe, Ni, Al, Zn, B and Pb.
- Evaluation of X, γ shielding characteristics.
- Identification of suitable alloy/nanocomposite for X-ray/gamma radiation shielding.

CHAPTER 2

Photon interaction with matter

Shielding of X-ray,gamma depends on the attenuation which in turn depend on interaction with matter Gamma rays interact with matter mainly through absorption and scattering. Absorption and scattering process such as Photoelectric effect,Compton scattering, pair production are important in the radiation shielding parameters.

2.1 Photoelectric effect (PEE)

In this process, an incident photon striking an atom ejects one of the orbital electrons of the atom. During this process, the gamma ray disappears, its entire energy being given to the electron. It is found both experimentally and theoretically that about 80 percent of the photoelectric absorption processes take place in the K-shell, photon energy $h\nu$ clearly more than the K-shell energy. The energy of the ejected photo electron is given by $T=h\nu$ - B_e , where B_e is binding energy of the ejected electron. After the atomic electron is ejected via the photoelectric effect, the vacancy in that shell is filled up by another electron from an outer shell. This is followed by the emission of X-rays or Auger electrons consuming the binding energy B_e .

The protection against ionising radiation is important all over the world [236]. The photoelectric effect (PEE), Compton scattering, pair production and triplet formation are the most important ways when radiation interacts with matter. In PEE photon is absorbed by a target atom,

an atomic electron is released or promoted to a bound open orbital, leaving the leftover ion or atom in an excited state [237]. When photon energies are as high as the electron rest energy, the Compton scattering may take place. Above twice this energy pair production is also more likely. Even if the PEE is the preferred reaction for a specific interaction of a single photon with a bound electron, the outcome is susceptible to quantum statistics and hence cannot be guaranteed. The probability of the PEE occurring is measured by the cross section of the interaction, σ .

Quantitative information on the Photo electric cross section is required for practical applications including material analysis, astronomy, photon research, and biomedical physics. For the appropriate assessment of total photon absorption and photon transport processes, as well as the construction of shielding and a range of radiation detection systems, a precise value of photoelectric cross-section in different materials is required [238]. For the calculation of PEE differential and total cross sections, including all polarisation correlations, a numerical algorithm has been developed [238]. Different codes / models are used and compared the calculated cross sections with NIST standard values [239]. Brysk et.al., [240] computed Photoelectric coss section using bound-state wave functions and potentials from a relativistic Dirac-Slater self-consistent-field program. Many other Monte Carlo simulation packages such as SPECT and PET are developed mainly for nuclear medical imaging research have been described in the literature [241–243].

There has been a renewed interest in measuring photon interaction cross-sections at low energies (keV photons), particularly at energies close to the element absorption boundaries. Bhattacharya et. al., [244] measured the total mass attenuation coefficients for 11 elements with atomic numbers ranging from 41 - 92 for photon energies between 59.5 and 43.0 keV, as well as Photoelectric coss section. The high-energy Photoelectric coss section is usually calculated from total absorption coefficient measurements by subtracting the scattering cross section per atom from the total interaction cross section [245]. This Photoelectric coss section is inversely proportional to

the atomic number as well as energy. According to Pratt et.al., [238], The total photo electric cross section for unpolarized photons of low energy is given by

$$\sigma = \frac{32\sqrt{2}\pi e^2 a^5}{3k^{\frac{7}{2}}}\tag{2.1}$$

For higher energies,

$$\sigma = \frac{4\pi e^2 a^5}{k} \tag{2.2}$$

where $a = Ze^2$ and k is the polarization vector. Bethel et.al., [246] was given straightforward polynomial fits to the X-ray photoelectric cross-sections (0.03 keV E 10 keV). According to him, the Photoelectric coss section is given by

$$\sigma(E) = 10^{-24} (C_0 + C_1 E + C_2 E^2) E^{-3} cm^2$$
(2.3)

where E is the X-ray energy and c_0 , c_1 , and c_2 are the coefficients. But few discrepancy between theoretical and currently accepted data for the Photoelectric coss section motivated researchers to develop a correction factor which would be able to correct the theoretical expressions in order to account for the currently accepted data. In this view, Legarda et. al., [247] adopted correction factor for Photoelectric coss section. The actual photo electric cross section given by the Legarda et. al., [247] is expressed as;

$$\sigma(k,z) = \frac{F(k,Z)}{\delta} \sigma_0 Z^5 \alpha^4 2\sqrt{2} \frac{(k-I+\mu)^4}{\mu^{\frac{1}{2}} k^{\frac{T}{2}}}$$
(2.4)

where F(k) is the function for each of the Z values, I; energy value near the absorption edge, k; energy value, σ_0 ; Thomson scattering cross section, α ; fine structure constant; μ ; electron

rest-mass energy and δ is quotient defined by previous worker [248]. Recently Fornalski et. al., [236] represented the cross section formulas for the photoelectric effect, Compton scattering, pair and triplet production in the intermediate and high photon energy spectrum for carbon where he applied the correction factor.

$$\sigma = c[f + f_{corr}] \tag{2.5}$$

where c; the constant usually related to atomic number Z, f; is the classical cross section relation for each process [249] and f_{corr} is the correction function which is calculated by using the classical Gaussian regression method. For low energies (k < 0.9) equation for Photoelectric coss section was given by

$$\sigma(E) = 3 \cdot 10^{12} \frac{Z^4}{E_{\gamma}^{3.5}} \tag{2.6}$$

For higher energies (k>0.9) equation for Photoelectric coss section was given by

$$\sigma(ph) = Z^{5} \left[\left(\sum_{i=1}^{4} \frac{a_{n} + b_{n}Z}{1 + c_{n}Z} k^{-p_{n}} \right) + f_{corr,ph} \right]$$
 (2.7)

where f_{corr} is given by

$$f_{corr} = exp[1.47628 \cdot 10^{-5} ln \ k^6 - 6.81543 \cdot 10^{-4} ln \ k^5 + 1.2797 \cdot 10^{-2} ln \ k^4$$

$$- 0.125606 ln \ k^3 + 0.68583 ln \ k^2 - 3.0079 ln \ k - 18.209]$$
(2.8)

Eventhough, several Photoelectric coss section calculations based on both theoretical and empirical approaches are available, some of them examined, while others have been implemented and subjected to validation tests to estimate whether they could improve the accuracy of particle trans-

port codes [240, 250–259]. In the present study, We have attempted to construct semi empirical formula for Photoelectric cross section by giving inputs Z and E for atoms whose atomic number varying between 1 to 100 in the energy region from 1keV < E < 100GeV.

2.1.1 Derivation of analytical equation for photoelectric cross section

To derivation of analytical equation for photoelectric cross section, the variation of Photoelectric cross section with energy was taken into account. From this observation we have designed followed formula

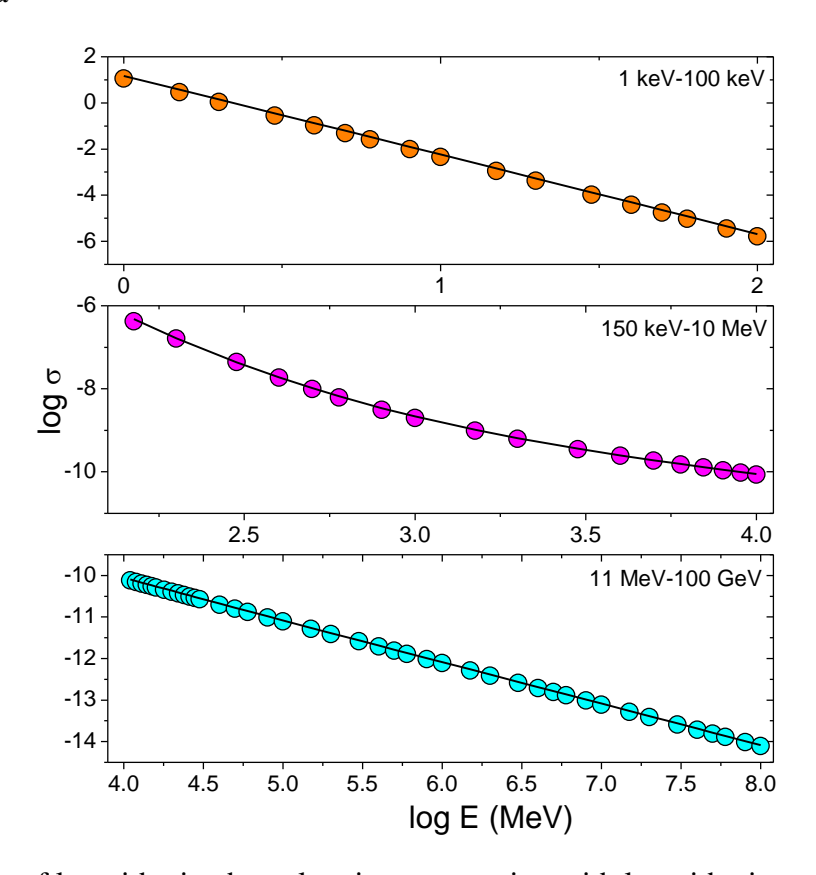


Fig. 2.1 Variation of logarithmic photoelectric cross section with logarithmic energy for different energy ranges in case of Hydrogen element. Continuous line represents the values produced by the present formula, Circles represents the data available in the linterature

$$\log \sigma_{pe} = f(\log (E)) \tag{2.9}$$

By plotting a graph the $\log{(\sigma)}$ vs $\log{(E)}$, $\log{(E)}$ was calculated and fitted the suitable relation

Table 2.1 Value for degree of polynomial (n) to obtain the photoelectric cross section for different energy regions

Z	E (KeV)	n	Z	E (KeV)	n	Z	E (KeV)	n	Z	E (KeV)	n
1-19	1-100	2	41-50	4-20	1	61-69	8-50	1	81-90	15-100	1
20-30	1-6	1	41-50	30-100	1	61-69	60-100	1	91-100	1-3	1
20-30	8-100	1	51-60	1-5	1	70-80	1-10	2	91-100	4-15	1
31-40	1-10	2	51-60	6-30	1	70-80	15-100	2	91-100	20-100	1
31-40	15-100	1	51-60	40-100	1	81-90	1-2	1	1-100	$150-10^3$	3
41-50	1-3	2	61-69	1-6	1	81-90	3-10	1	1-100	$10^3 - 10^5$	3

between $\log{(\sigma)}$ and $\log{(E)}$ such a way that this equation should have coefficient of determination is almost equal to one and minimum residual sum of squares. For hydrogen same graph was represented in figure 2.1. Same kind of graphs were plotted and variation of $\log{(\sigma)}$ with $\log{(E)}$ was studied and an equation is given below.

$$\log\left(\sigma\right) = \sum_{i=0}^{n} A_i (\log E)^i \tag{2.10}$$

here "n" is the order of the polynomial. The value for degree of polynomial (n) to obtain the photoelectric cross section for different energy regions are valuated and it is give in table 2.1. A_i is fitting constant, given by followed equation.

$$A_i = A_i(Z) (2.11)$$

To construct the function for A_i , we have studied the variation of A_i with Z, an equation is given below

$$A_i = \sum_{j=0}^m B_j Z^j \tag{2.12}$$

Table 2.2 Fitting parameters for photoelectric cross sections formula

Z	E		B_0	B_1	B_2	B_3	Z	E		B_0	B_1	B_2	B_3	B_4		
	Fitting parameters for energy range (1-100 keV) A ₀ -0.52251 1.922323 -0.23895 0.010675						A_0	8.563926	-0.06616	0.000439	-	-				
			-0.52251	1.922323	-0.23895	0.010675		1-10 keV	A_1	-80.8367	2.091742	-0.01353	-	-		
1-10	1-100 keV	A_1	-3.52012	0.141445	-0.00788	0.000269	70-80		A_2	109.3536	-2.89114	0.018833	-	-		
		A_2	0.01744	-0.0421	0.00344	-0.00144	70-80	15-100 keV	A_0	-49.5294	1.736492	-0.01208	-	-		
		A_0	4.616359	0.090072	-	-			A_1	84.73463	-2.65743	0.01865	-	-		
11-19	11-19 1-100 keV	A_1	-2.9278	0.02999	-	-	1		A_2	-34.7089	1.03888	-0.00725	-	-		
		A_2	-0.1661	-0.00317	-	-		1-2 keV	A_0	4.634041	0.019786	-	-	-		
	1-6 keV	A_0	4.266364	0.064127	-	-		1-2 KC V	A_1	-2.52812	0.006268	-	-	-		
20-30	1-0 Ke v	A_1	-2.85475	0.009003	-	-	81-90	3-10 keV	A_0	5.972166	0.012436	-	-	-		
20-30	8-100 keV	A_0	5.792546	0.051102	-	-	01-90	3-10 KC V	A_1	-2.95937	0.007723	-	-	-		
	0-100 KC V	A_1	-3.24903	0.012913	-	-	1	15-100 keV	A_0	15.31134	-0.09187	-	-	-		
		A_0	10.9586	-0.14712	-	-		15-100 KeV	A_1	-7.92963	0.065232	-	-	-		
	1-10 keV	A_1	-18.8479	0.518605	-	-	91-100	1-3 keV	A_0	5.19278	0.013636	-	-	-		
31-40	-40	A_2	10.06733	-0.32578	-	-		1-3 Ke V	A_1	-3.33482	0.014613	-	-	-		
	15-100 keV	A_0	6.386046	0.033726	-	-		4-15 keV	A_0	6.025833	0.012047	-	-	-		
	13-100 Ke v	A_1	-3.1625	0.008535	-	-		4-13 KC V	A_1	-2.67946	0.004118	-	-	-		
		A_0	4.196176	0.045345	-0.0001	-		20-100 keV	A_0	13.31152	-0.06015	-	-	-		
	1-3 keV	A_1	-87.8766	3.457518	-0.03485	-	1		A_1	-6.52754	0.044129	-	-	-		
		A_2	310.3076	-12.549	0.126579	-		Fitting p	aram	ameters for energy range (150 keV-10 MeV)						
41-50	4-20 keV	A_0	6.050309	0.019048	-	-		150 keV -10MeV	A_0	11.8634	-4.26E-01	2.50E-01	-2.66E-02	7.92E-04		
	4-20 Ke v	A_1	-3.45503	0.017323	-	-	1-10		A_1	-16.5344	3.463285	-8.43E-01	8.41E-02	-2.89E-03		
	30-100keV	A_0	7.167155	0.016824	-	-			A_2	4.014211	-1.16662	2.87E-01	-2.87E-02	9.94E-04		
	30-100ke v	A_1	-3.31432	0.01093	-	-	1		A_3	-3.49E-01	1.26E-01	-3.13E-02	3.16E-03	-1.11E-04		
	1-5 keV	A_0	5.442881	0.01634	-	-			A_0	13.95754	8.71E-02	-3.04E-03	3.26E-05	-1.37E-07		
	1-3 Ke V	A_1	-3.87157	0.028548	-	-	11-100	150 keV -10MeV	A_1	-12.6149	1.22E-01	-8.94E-04	4.28E-06	2.05E-09		
51-60	6-30keV	A_0	6.926477	0.005493	-	-	11-100	130 KeV -10MeV	A_2	2.693512	-3.52E-02	2.66E-04	-1.27E-06	-3.21E-10		
31-00	0-30Ke v	A_1	-3.8171	0.021077	-	-			A_3	-0.20584	3.20E-03	-2.36E-05	1.01E-07	9.21E-11		
	40-100 keV	A_0	7.133064	0.018084	-	-		Fitting p	aram	eters for ener	gy range (11	MeV-100 M	eV)			
	40-100 Ke v	A_1	-3.08606	0.006053	-	-	1-10		A_0	-7.68147	2.79141	-5.16E-01	4.89E-02	-1.75E-03		
	1-6 keV	A_0	7.979171	-0.02171	-	-				-1.9591	2.41E-01	-4.12E-03	3.79E-05	-1.35E-07		
	1-0 Ke V	A_1	-7.14401	0.075576	-	-	11 100	11- 100 MeV	A_1	-1.33274	-9.89E-03	8.51E-05	-5.94E-07	1.83E-09		
61.60	61.60 0.501.17	A_0	13.00309	-0.08848	-	-	11-100		A_2	5.17E-02	1.51E-03	-1.23E-05	7.78E-08	-2.16E-10		
61-69	8-50 keV	A_1	-7.47155	0.076653	-	-	1		A_3	-2.65E-03	-7.75E-05	6.74E-07	-4.77E-09	1.50E-11		
	60 100 1-37	A_0	7.61909	0.010663	-	-				'	'					
	60-100 keV	A_1	-3.15553	0.006868	-	-	1									

here here "m" is the order of the polynomial. The value for degree of polynomial (m) to obtain the fitting parameter A's for different energy regions. In the above equation, B_j are fitting parameters, table 2.2 gives required fitting parameters for equation (2.12). The formula presented in the equation (2.10) with fitting parameters defined in the equation (2.12) is the present formula for photo electric cross section. This formula produces the cross sections successfully for photoelectric interaction except near the X-ray absorption edges. The photoelectric cross sections near the X-ray absorption edges (K, L1, L2, L3, M1, M2, M3, M4, N1, N2, N3) are also constructed and it is given as follows;

$$\sigma_{XPE} = ak^b \tag{2.13}$$

Where k = Z/E and E in MeV. The variation of photoelectric cross section near M_5 X-ray absorption edge is different than other X-ray absorption edges and hence we have constructed

Table 2.3 Fitting parameters to find the Photo electric cross section near X-ray absorption edges.

Type	a	b
K	9.79E-03	1.849284
L1	1.62E-02	1.761063
L2	3.62E-02	1.667448
L3	3.32E-01	1.404392
M1	8.24E-02	1.561367
M2	6.17E-02	1.592018
M3	2.23E-01	1.471953
M4	1.879134	1.252384
M5 $(60 < Z < 75)$	-3.27E+10	1203188
M5(76 < Z < 84)	79285.57	-27740.9
M5(85 < Z < 100)	2.64E-06	2.559688
N1	3.06355	1.18079
N2	3.211146	1.183953
N3	197.8709	8.33E-01

separate equation for M_5 X-ray absorption edge. The photoelectric cross sections near the M_5 X-ray absorption edge is also constructed and it is given as follows;

$$\sigma_{XPEMS} = \begin{cases} \frac{a}{k} + b & \text{for } 60 < Z < 75\\ \frac{ak}{(k-b)} & \text{for } 76 < Z < 84\\ ak + b & \text{for } 85 < Z < 100 \end{cases}$$
 (2.14)

a,b in the above equations are the fitting constants are given in table 2.3.

From the thorough literature [35, 253] survey a semi empirical formula was designed. This formula also successfully produces photoelectric cross sections near the x-ray absorption edges. It is observed that present formula produces exact values of Photoelectric coss section present in the literature [35]. Using equation 2.15. The deviation for Photoelectric cross section calculated and it gives $\pm 5\%$. This validate the present work.

$$\Delta \sigma_{pe}(\%) = \frac{\log \sigma_{data} - \log \sigma_{formula}}{\log \sigma_{data}} \times 100$$
 (2.15)

In the above equation, σ_{data} is the Photoelectric cross section available in the literature [35] and $\sigma_{formula}$ is from current work.

fig. 2.2 represents the % deviation for photoelectric cross sections for range oof energies 1keV < E < 100keV, 150keV < E < 10MeV and 11MeV < E < 100GeV and same is found to be less than $\pm 5\%$.

To validate the present work, the values produced by the present formula is compared with

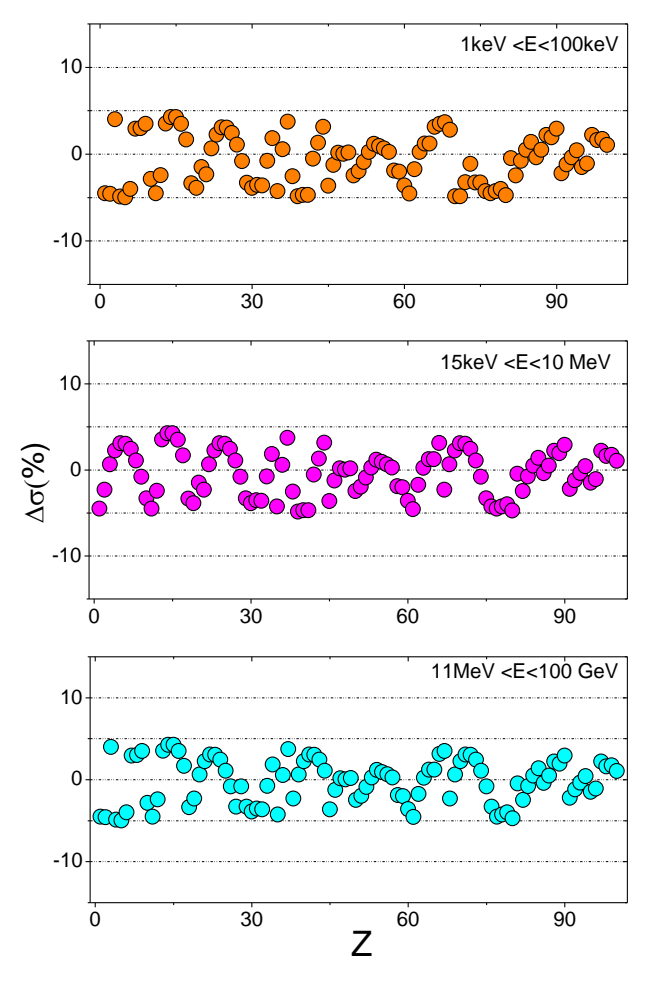


Fig. 2.2 Variation of average percentage error of $\log \sigma$ as a function Z.

that of experiments and other data and formulae available in the literature [35, 236, 245–247]. This comparison is as shown in table 2.4. First column of this table represents the target element. Second column of this table represents the energy. Third column represents the experimental values corresponds to that energy. Photoelectric cross sections of the current work is presented in

Table 2.4 Correlation of Photoelectric cross sections of current work and literature

Element	Photon energy	_	_	σ_{Winxom}	$\sigma_{fornal.}$	σ_{Titus}	$\sigma_{Bethell}$	σ_{Legard}
Element	(keV)	$\sigma_{Expt.}$	$\sigma_{Present}$	[35]	[236]	[245]	45 [246]	[247]
	4	0.105 [260]	0.106	0.105	0.112	0.108	0.101	0.111
	5	0.049 [260]	0.049	0.049	0.054	0.08	0.01	0.089
Hydrogen	5.41	0.056±5.58 [261] 0.037 [260]	-	-	0.121	0.067	0.089	0.147
	5.895	0.028 [260]	0.026	0.026	0.058	0.014	0.052	0.038
	8.39	0.012 ± 0.43 [261]	0.0097	0.0098	0.14	0.0018	0.0025	0.078
	6.47	162.4±3.3 [256]	210.306	210.3	218.21	212.32	230.2.75	215.25
Carbon	14.41	12.3±0.3 [256]	11.139	11.14	14.68	13.54	16.48	15.24
	21.12	-	4.341	4.341	6.89	5.14	5.96	6.47
	6.47	4073±80 [256]	5789.739	5119	5263.21	5180.21	5154.36	5140.32
Aluminium	14.41	377±8 [256]	336.703	336.7	401.65	408.32	399.54	408.64
	21.12	116.6±2.6 [256]	138.901	138.9	105 0.112 0.108 0.101 049 0.054 0.08 0.01 - 0.121 0.067 0.089 026 0.058 0.014 0.052 0098 0.14 0.0018 0.0025 0.3 218.21 212.32 230.2.75 1.14 14.68 13.54 16.48 341 6.89 5.14 5.96 119 5263.21 5180.21 5154.36 36.7 401.65 408.32 399.54 38.9 142.32 141.97 140.35 200 11306.21 11250.65 11254.32 95.8 725.32 710.24 706.54 34.9 340.25 338.21 339.15 1250 30244 30100 30508 797 3401.21 3304 3250	140.35	144.54	
	6.47	9021±180 [256]	9267.194	11200	11306.21	11250.65	11254.32	11248.21
Sulphur	14.41	885±18 [256]	795.808	795.8	725.32	710.24	706.54	702.21
	21.12	279±5.8 [256]	334.881	334.9	340.25	338.21	339.15	340.21
	6.47	28042±550 [256]	30583.62	30250	30244	30100	30508	30301
Sulphur	14.41	3125±60 [256]	2797.03	2797	3401.21	3304	3250	3150
	21.12	103±20 [23]	1219.019	1219	1244	1250	1248	1238

Fourth column of this table. Photoelectric cross sections produced by the winxcom code [σ_{Winxom} [35]] which are based on the Hubbel data [262]are represented in the fifth coloumn of this table. The photoelectric cross sections produced by the other formulae such as σ_{fornal} . [236], σ_{Titus} [245], $\sigma_{Bethell}$ [246] and σ_{Legard} [247] are presented in the last four coloumns of this table. Table 2.5 confirms that values of current work is close in agrrement with that of experimental values. Hence it validates present formula for producing photoelectric cross section. This simple pocket formula will be useful in the determination of Photoelectric cross section (barn/atom) which intern useful in the radiation and nuclear physics.

2.2 Pair Production

When a photon having energy greater than 1.02MeV strikes a material of high atomic number (Z), it is found that the photon is completely absorbed and a pair of negatron and positron is produced. This process is known as pair production. Thus,

$$h\nu = T_{+} + m_{0}C^{2}T_{-} + m_{0}C^{2}$$
(2.16)

where $h\nu$ is the total energy of the incident photon, T_- and T_+ are the kinetic energies of the negatron and positron respectively and $+m_0c_2 = 0.511 \text{MeV}$ is the electronic rest energy. The process occurs only in the field of charged particles, mainly in the nuclear field but also to some degree in the field of an electron. The presence of this particle is necessary for momentum conservation. The cross-section of pair production varies as Z.

Semi empirical formula for cross section of pair production in nuclear field (σ_{ppn}) 2.2.1

The Semi empirical formula for pair production with in energy range 1.25*10⁶eV to 10*10⁶eV is given as

$$\sigma_{ppn} = \alpha exp(\beta/E) \tag{2.17}$$

Here α and β 's are fitting parameters with in the energy range of 1.25*10⁶ eV to 10*10⁶ eV which depends on parent nuclei atomic number, same were given by

$$\alpha = \begin{cases} \alpha_1 Z^{\alpha_2} & \text{Energy } 1.25 \text{MeV} \le E \le 10 \text{MeV}, 1 \le Z \le 50, \\ \alpha_1 / Z + \alpha_2 & \text{Energy } 1.25 \text{MeV} \le E \le 10 \text{MeV}, 51 \le Z \le 75, \\ \alpha_1 Z + \alpha_2 & \text{Energy } 1.25 \text{MeV} \le E \le 10 \text{MeV}, 76 \le Z \le 100 \end{cases}$$
 (2.18)

$$\beta = \begin{cases} \beta_1 Z + \beta_2 & \text{Energy } 1.25 \text{MeV} \le E \le 10 \text{MeV}, \ 1 \le Z \le 50, \\ \beta_1 / Z + \beta_2 & \text{Energy } 1.25 \text{MeV} \le E \le 10 \text{MeV}, \ 51 \le Z \le 75, \\ \beta_1 \sqrt{Z} + \beta_2 & \text{Energy } 1.25 \text{MeV} \le E \le 10 \text{MeV}, \ 76 \le Z \le 100 \end{cases}$$

$$(2.19)$$
The pair

Here α_1 , α_2 , β_1 and β_2 are the constant with in $1 \le Z \le 100$ as shown in table. 2.5. The pair

Table 2.5 Fitting parameters of pair production (in nuclear field).

Energy	Z	Fitting parameters								
range		α_1	α_2	β_1	β_2					
	1-25	0.004312	1.963863	0.008659	-6.406237148					
1.25 - 10 MeV	26 -50	0.006124	1.858944	0.018519	-6.658275091					
1.23 - 10 Me v	51-75	-1327.624332	34.94021	-92.46209706	-3.918039391					
	76-100	0.386338	-11.33707533	0.421056	-8.78627238					
	Z	δ_1	δ_2	Δ_1	Δ_2					
	1-25	0.009362	1.922957	0.448805	-7.075955309					
11 MeV- 100GeV	26-50	0.01104	1.871779	-3.804551218	-8.847991045					
11 IVIE v- 100GE V	51-75	0.015997	1.778576	0.006064	-5.688792957					
	76-100	0.02158	1.709163	-0.001920755593	-5.06585504					

production (in nuclear field) from 11 MeV to 100 GeV.

$$\sigma_{ppn} = \delta \exp \Delta / E(MeV) \tag{2.20}$$

Here δ and $\Delta's$ are the fitting constants from 11 MeV - 100 GeV which depends on the parent nuclei atomic number , as follows

$$\delta = \delta_1 Z^{\delta_2} \text{for} 11 MeV \le E \le 100 GeV \text{ and} 1 \le Z \le 100, \tag{2.21}$$

$$\Delta = \begin{cases} \Delta_1 \ln(Z) + \Delta_2 & \text{for } 11\text{MeV} \le E \le 100\text{GeV and } 1 \le Z \le 25 \\ \Delta_1 Z / (Z + \Delta_2) & \text{for } 11\text{MeV} \le E \le 100\text{GeV and } 26 \le Z \le 50 \\ \Delta_1 Z + \Delta_2 & \text{for } 11\text{MeV} \le E \le 100\text{GeV and } 51 \le Z \le 100 \end{cases}$$
 (2.22)

Here δ_1 , δ_2 , Δ_1 and Δ_2 are the fitting constants in the atomic number range of $1 \le Z \le 100$ were also tabulated in Table 2.5.

Table 2.6 Fitting parameters of pair production (in electric field).

Energy	Z	Fitting parameters								
range		ξ_1	ξ_2	ψ_1	ψ_1					
	1-10	2.6357929959	317.0109234	0.07957569032	-8.678053655					
3-100 MeV	11-25	3.514478883	427.3932769	0.08592197619	-8.685070414					
	26-100	5.937707263	746.0395743	0.07586591351	-8.625412801					
150 MeV- 100 GeV	1-25	0.01111255097	0.9215112224	1.661164945	-17.55823018					
130 Me v- 100 Ge v	26-100	3.792914618	431.2069716	0.3959115352	-13.70217717					

2.2.2 Semi empirical formula for cross section of pair production in the electric field (σ_{ppe})

The semi empirical formula for pair production ,electric field is given by

$$\sigma_{ppe} = \xi E_{MeV}^{(\psi/E_{MeV})} \tag{2.23}$$

Here ξ and ψ 's are the fitting parameters energy range from $3MeV \leq E \leq 100GeV$ which depends on the parent nuclei atomic number. These fitting parameters are as follows

$$\xi = \begin{cases} \xi_1 Z / (Z + \xi_2) & \text{for } 3 \text{MeV} \le E \le 100 \text{MeV and } 1 \le Z \le 100, \\ \xi_1 Z^{\xi_2} & \text{for } 150 \text{MeV} \le E \le 100 \text{GeV and } 1 \le Z \le 25, \\ \xi_1 Z / (Z + \xi_2) & \text{for } 150 \text{MeV} \le E \le 100 \text{GeV and } 26 \le Z \le 100. \end{cases}$$
 (2.24)

$$\psi = \begin{cases} \psi_1 Z + \psi_2 & \text{for 3MeV} \le E \le 100 \text{MeV and } 1 \le Z \le 100, \\ \psi_1 \ln(Z) + \psi_2 & \text{for 150MeV} \le E \le 100 \text{MeV and } 1 \le Z \le 25, \\ \psi_1 \sqrt{Z} + \psi_2 & \text{for 150MeV} \le E \le 100 \text{MeV and } 26 \le Z \le 100. \end{cases}$$
 (2.25)

Here ξ_1, ξ_2, ψ_1 and ψ_2 are the fitting constants from $1 \le Z \le 100$ were tabulated in Table 2.6.

2.3 Coherent Scattering

Here the scattered X-ray energy is nearly the same as the incident energy except for very small recoil energy taken up by the scattering atom. There are four types of elastic scattering.

2.3.1 Rayleigh Scattering

This occurs at energies of 0.1MeV and above. For large $h\nu$ and small Z, Rayleigh scattering is negligible. Rayleigh scattering is greatest at small scattering angles.

2.3.2 Thomson Scattering

It is a coherent scattering from the nucleus as a whole. It is independent of energy and is proportional to \mathbb{Z}^4 .

2.3.3 . "Delbruck" Scattering

This process also known as Elastic Nuclear Potential Scattering. This effect is very small at low energies

2.3.4 Semi-empirical formula for coherent scattering (σ_{coh})

The variation of log $\log\left(\sigma_{coh}\right)$ versus $\ln(E)$ is represented using following equation;

$$\log\left(\sigma_{coh}\right) = a\ln\left(E\right) + b \tag{2.26}$$

where a,b are the fitting constants depends on Z

$$a = a_1 \ln(Z) + a_2 \tag{2.27}$$

$$b = b_1 \ln (Z) + b_2 \tag{2.28}$$

On substitution of a_1 , a_2 , b_1 and b_2 from table 2.7.into the equations (2.27),(2.28), (2.26), coherent

Table 2.7 Values of a,b for fitting(coherent scattering)

Fitting	Energy range							
parameters	1-100keV	100keV-100GeV						
a_1	0.062205	0.001726						
a_2	-0.67478	-0.87237						
b_1	0.866216	1.172743						
b_2	0.140565	0.786349						

scattering cross section (σ_{coh})(in mb) becomes

$$\sigma_{coh} = 10^{[a_1 \ln(Z) + a_2] + [b_1 \ln(Z) + b_2]}$$
(2.29)

2.4 Incoherent Scattering (σ_{incoh})

In this process the incident gamma quantum is scattered by an atomic electron at energies much greater than the binding energies of the electron, the photon being scattered as if the electrons were free and at rest. Around 1Mev it is the dominant mode of interaction. Semi empirical formula for different energy regions are given as

$$\ln \sigma_{incoh} = \sum_{i=0}^{i=3} a_i (\log E)^i 1 keV < E < 100 keV$$
 (2.30)

$$\ln \sigma_{incoh} = \sum_{i=0}^{i=3} a_i (\log E)^i 100 keV < E < 100 GeV$$
 (2.31)

where a_i and b_i are fitting constants that are functions of a given atom. The fitting parameters can be expressed as

$$a_{i} = \begin{cases} a_{1} = a_{11}\sqrt{Z} + a_{12} \\ a_{2} = a_{21}/Z + a_{22} & \text{for} \quad 1 < E < 100 \text{keV} \\ a_{3} = a_{31}\ln(Z) + a_{32} \end{cases}$$
 (2.32)

$$b_{i} = \begin{cases} b_{1} = b_{11}Z + b_{12} \\ b_{2} = b_{21}Z + b_{22} \\ b_{3} = b_{31}Z + b_{32} \\ b_{4} = b_{41}\ln(Z) + b_{42} \end{cases}$$
 for $E > 100 \text{keV}$ (2.33)

where a_{11} , a_{12} , a_{21} , a_{22} , a_{31} , a_{32} , b_{11} , b_{12} , b_{21} , b_{22} , b_{31} , b_{32} , b_{41} and b_{42} values are given in the table 2.8.

Table 2.8 a,b fitting values (Incoherent scattering).

Fitting Parameters	a ₁₁	a ₁₂	a ₂₁	a ₂₂	a ₃₁	a ₃₂	b ₁₁	b_{12}	b_{21}	b_{22}	b ₃₁	b ₃₂	b ₄₁	b ₄₂
Value	0.039827	-1.1652	-0.17048	3.2371	0.59722	-2.2359	2.92E-05	0.02698	-5.01E-04	-0.45336	2.77E-03	0.92148	8.62E-01	-0.61216

2.5 Gamma Ray Attenuation

Consider a narrow bean of gamma rays, such that I is the intensity of photon falling perpendicularly on a slab of elemental material of thickness Δx . Then the number of photons ΔI removed from the beam due to the interaction of gamma rays with matter is proportional to the thickness Δx and the incident photons I.

$$\Delta I = -\mu I \Delta x \tag{2.34}$$

where μ is the proportionality constant known as the total linear attenuation coefficient. The intensity of gamma rays thus decreases with the absorber thickness. The attenuation coefficient μ depends on the material and on the energy of gamma rays. For a given material and monochromatic gamma rays μ will be constant and we can integrate the expression for I. Thus we get,

$$I = I_0 e^{-\mu x} (2.35)$$

Where I_0 is the intensity of the incident beam while I is the intensity of the beam after traversing a distance x in the absorber More usually a total mass attenuation coefficient μ m is used. The mass attenuation coefficient is the ratio of the linear coefficient to the density, i.e., $\mu_m = \mu/\rho$. This can be converted into cross sections in barns/atom by the use of

$$\sigma = \frac{\mu}{\rho} \left(\frac{A}{N} \right) 10^{24} \tag{2.36}$$

where ρ is the density, A is the atomic weight and N is the Avagadro's Number. The primary attenuation of gamma rays in chemical compounds or other mixtures of elements is assumed to depend only upon the sum of cross-section presented by all the atoms in the mixture. Because chemical bonds are only of the order of a few electron volts, they have no significant effect on the Compton, photoelectric and pair production interactions. It can be shown that an absorber where bulk density is ρ and which is made up of mixture of elements whose mass attenuation coefficients are (μ_1/ρ_1) , (μ_2/ρ_2) ,..... will have an overall mass attenuation coefficient given by,

$$\mu/\rho = (\mu_1/\rho_1)W_1 + (\mu_2/\rho_2)W_2 \tag{2.37}$$

Where W_1 , W_2 are the fractions by weight of the element which make up the absorber. The total attenuation cross-section σ_{comp} of a compound system in terms of the cross-section σ_i of its various atomic constituents is $\sigma_{comp} = \sum n_i \sigma_i$, where n_i is the number of atoms of the i^{th} element present in the compound .The cross sections obtained from different semi empirical formulae for various process such as PEE, Pair production, coherent scattering and incoherent scattering can be used to evaluate corresponding mass attenuation coefficient, total mass attenuation coefficients is sum of these form,

$$\frac{\mu}{\rho} = \left(\frac{\mu}{\rho}\right)_{Photoelectriceff} + \left(\frac{\mu}{\rho}\right)_{PairProduction} + \left(\frac{\mu}{\rho}\right)_{coherent} + \left(\frac{\mu}{\rho}\right)_{incoherent} \tag{2.38}$$

CHAPTER 3

Estimation of X-ray, gamma shielding parameters in alloys and composites

3.1 **Theory**

3.1.1 Gamma/X-ray shielding parameters

3.1.1.1 Mass attenuation coefficient and its derivables

Theoretically, the $\mu l \rho$ in the energy range from 1 keV to 100 GeV are generated WinXCom code [263]. The total μ can be calculated by multiplying the density of the compounds with (μ_m) [23]. For shielding purpose, the optimum thickness of material plays a very important role. It is necessary to have the knowledge of Half Value Layer (HVL) and Tenth Value layer (TVL). Like the attenuation coefficient, the values of HVL and TVL are dependent on the energy of the photon radiation and the type of material/alloy. Both HVL and TVL are inversely proportional to μ . HVL is determined by the ratio of 0.693 to the μ whereas TVL is determined by the ratio of 2.303 to the μ . The reciprocal of μ gives the average distance travelled by the photon in the target material before it can be absorbed or scattered. It is called as photon mean free path λ . The ratio of total atomic cross section σ_a to the total electronic cross section σ_e gives the effective atomic number (Z_{eff}). The σ_a can be derived from the values of the $\mu l \rho$. The number of electrons per unit mass gives the another interaction parameter called electron density and is calculated from the measured Z_{eff} . Larger the electron density, more are the chances of photon interaction [264].

Previous researchers [26, 196, 197, 263, 265–271] clearly demonstrated the method and equations used in estimating the σ_a , σ_e , Z_{eff} and N_e .

3.1.1.2 Specific gamma ray constant (Γ)

The gamma ray constant is an exposure rate (in R/h) due to photons at a distance of one meter from a source with an activity of 1 Curie. It is determined by the relation

$$\Gamma = 657.68 \times E_{\gamma} \left(\frac{\mu_{en}}{\rho}\right) \frac{R.m^2}{Ci.hr}$$
(3.1)

3.1.1.3 Radiation protection efficiency(RPE)

The protection of people from harmful effects of ionizing radiation and the method for achieving this is called radiation protection, calculated using below equation

$$(1 - \frac{I}{I_0}) \times 100\% = (1 - e^{-\mu t}) \times 100\%$$
(3.2)

where μ is the measure of linear attenuation coefficient. I and I_0 are the intensities of the radiation for thickness t and t=0 respectively.

3.1.2 **Absorption buildup factor**

The interaction of γ ray with material depends upon photon energy and element compositions of alloy. The strength of γ ray beam through the medium depends on Lambert Beer law under three conditions: (i) monochromatic rays, (ii) thin absorbing material and (iii) narrow beam geometry. If the conditions set out above are not satisfied, then the law is no longer applicable. In order to apply the law, a correction factor called "build up factor" is used. A dimensionless multiplication factor that corrects the response of the un-collided photon beam is the build-up factor. Buildup

factor gives the information on the quantity of secondary radiations produced in the medium and energy deposited/absorbed in the medium. In the present work, the B_{en} has been estimated using geometric progression (GP) fitting method. Geometric progression parameters were evaluated for SG1, SG2, SG3, SG4, SG5 and SG6 as explained by manjunatha et. al., [23] for different penetration depths and energy is varying between 5 - 40 cm and 0.5 - 15 MeV respectively.

3.1.3 Neutron shielding parameters (NSP)

The neutron shielding parameters such as b_{co} , σ_{coh} , σ_{inc} , σ_{tot} and σ_{abs} in different compositions were calculated using the equations as explained in Manjunatha et.al.,[23]. From the computed neutron cross sections, attenuation parameter of neutron is evaluated using the relation

Attenuation parameter =
$$\frac{\sigma_{abs} \times N_A}{A} cm^2/g$$
 (3.3)

where N_A and A are Avogadro number, atomic weight respectively and σ_{abs} is the evaluated absorption cross section.

3.1.4 Kerma coefficients from partial photon interactions

For the energy fluence φ of uncharged radiation of energy E, the kerma K is given by [97]

$$K = \Phi E(\mu_{tr}/\rho) \tag{3.4}$$

where (μ_{tr}/ρ) is the mass energy transfer coefficient of the material for this radiation. The kerma coefficient k is given by [97]

$$k = K/\Phi = E(\mu_{tr}/\rho) \tag{3.5}$$

To determine the kerma coefficient k(E) at certain photon energy E we need a) The partial cross section for the photoelectric process, Compton scattering and pair production and b) The energy deposition fraction from each of the partial photon interaction. γ -ray kerma coefficient is given by

$$k(E) = k_D \Sigma_i w^i [\sigma_r^i E + \sigma_{Ca}^i E + \sigma_k^i (E - 1.022)] \quad Gycm^2/photon$$
(3.6)

where σ_r^i , σ_k^i and σ_{Ca}^i are photoelectric, pair production and Compton energy absorption cross sections (cm^2/g) for the i^{th} element at photon energy E respectively,k(E) is the photon kerma coefficient at energy E, w^i is the weight fraction of the i^{th} element and k_D is the energy conversion coefficient from MeV to Gy.g.

3.1.5 **Relative dose**

The ratio of delivered dose rate to planned dose rate is termed as relative dose intensity. Dose distribution at a distance r is given by

$$D_r = D_0 e^{-\mu r} B/r \tag{3.7}$$

where μ denotes the linear attenuation coefficient for the appropriate photon energy and B is the exposure build-up factor. D_0 is the initial dose delivered by the gamma ray source. The relative dose distribution at a distance r is

$$\frac{D_r}{D_0} = e^{-\mu r} B/r \tag{3.8}$$

The relative dose distribution can be calculated by using the estimated exposure build-up factor for different penetration depths.

3.1.6 Specific absorbed fraction of energy (φ)

The specific absorbed fraction of energy (φ) is the fraction of emitted energy from the source organ that is absorbed by the target organ per unit mass of target organ. The φ at distance x from the point source is given by

$$\varphi(x) = \frac{\mu_{en} \exp(-\mu x) B_{en}}{4\pi r^2 \rho}$$
(3.9)

Here μ_{en} is linear absorption coefficient of photons of given energy, μ is linear attenuation coefficient of photons of given energy, B_{en} is energy absorption build up factor; ρ is density of the medium. The energy absorption build up factors are computed and are used to evaluate φ for various distances.

3.2 **Results**

3.2.1 Iron boron alloys

3.2.1.1 Variation of mass attenuation coefficient with photon energy

The Fig. 3.1 shows the variation of μ/ρ values for various iron boron alloys in the energy range 1 keV-100 GeV. The μ/ρ values for iron boron alloys are larger in the low energy region and decreases gradually. Because of the dominant photoelectric interaction, the μ/ρ is observed to be high in the low energy region. Again, the Compton scattering is dominant in the high-energy field, which is linearly dependent on nuclear numbers. Hence, μ/ρ value becomes minimum value.

3.2.1.2 Gamma/X-ray interaction parameters

For various iron boron alloys, we have measured HVL, TVL and λ . The variation of TVL is presented in Fig. 3.2 Similarly, HVL and λ for different iron boron alloys with that of energy are

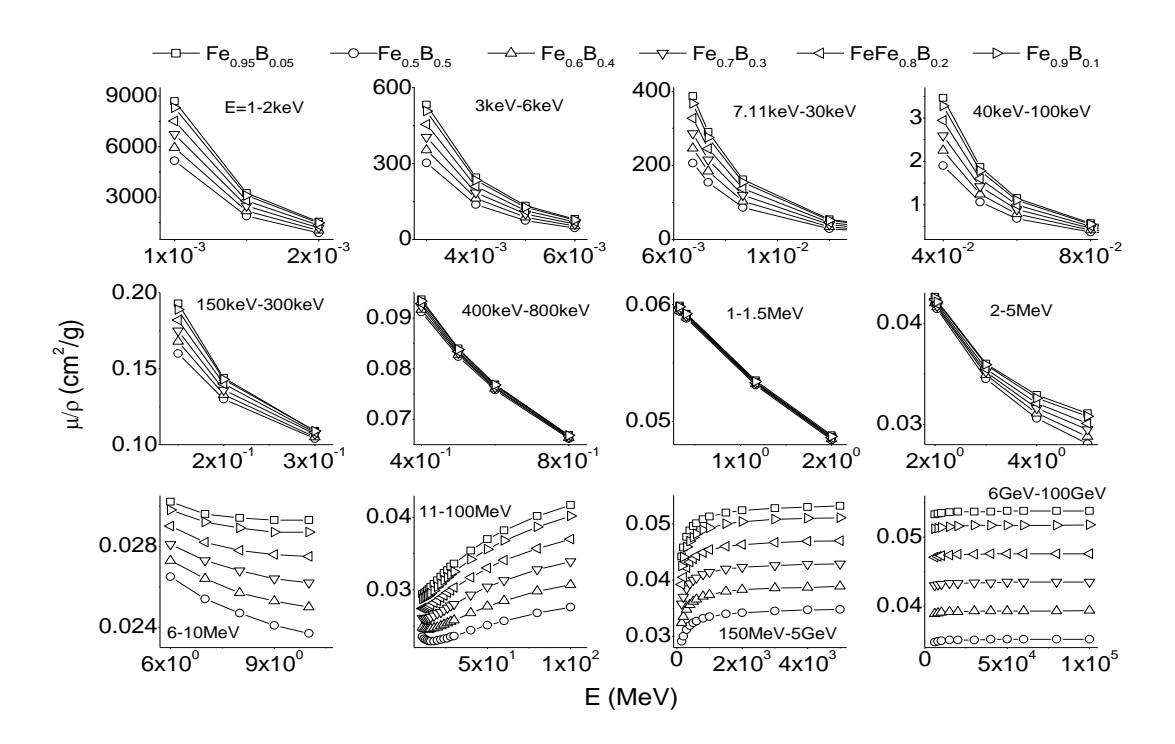


Fig. 3.1 Variation of mass attenuation coefficient with energy for the studied iron boron alloys

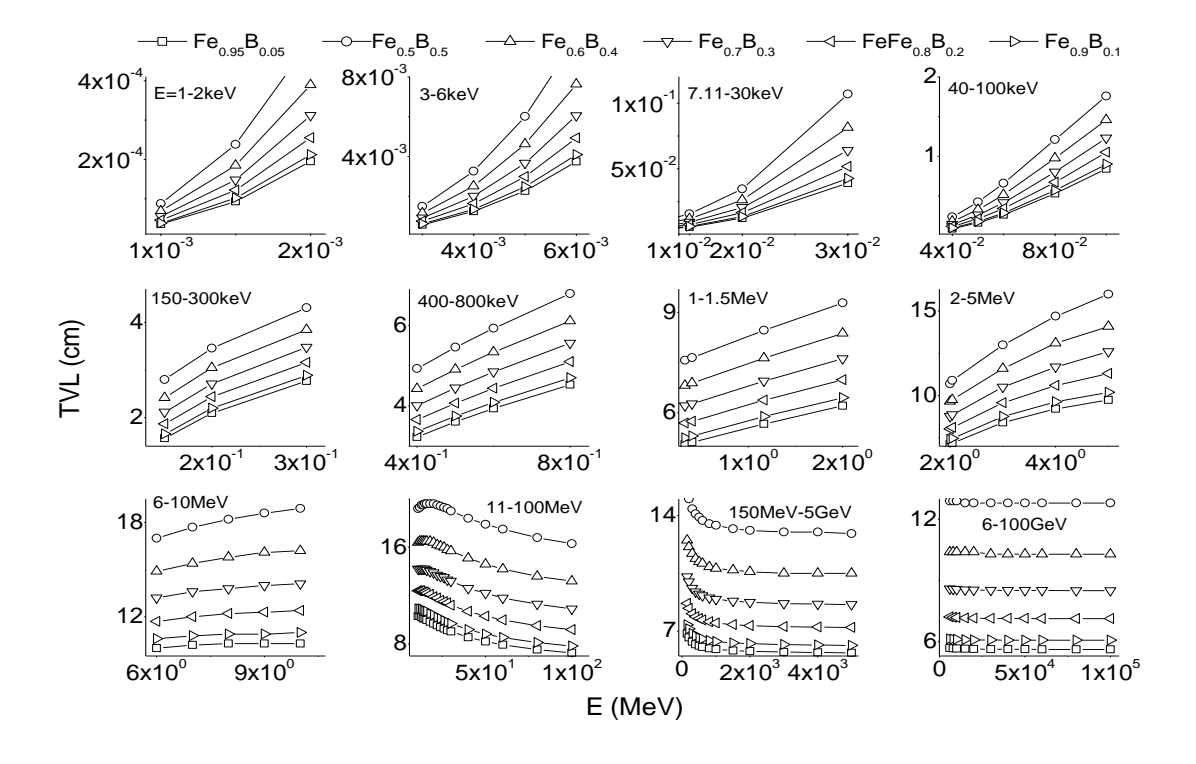


Fig. 3.2 Variation of tenth value layer (TVL) with energy for the studied iron boron alloys as shown in Figs. 3.3 and 3.4 respectively. From the figure, it is observed that the iron boron alloy $Fe_{0.95}B_{0.05}$ is having maximum TVL, HVL and λ values when compared to all other alloys studied.

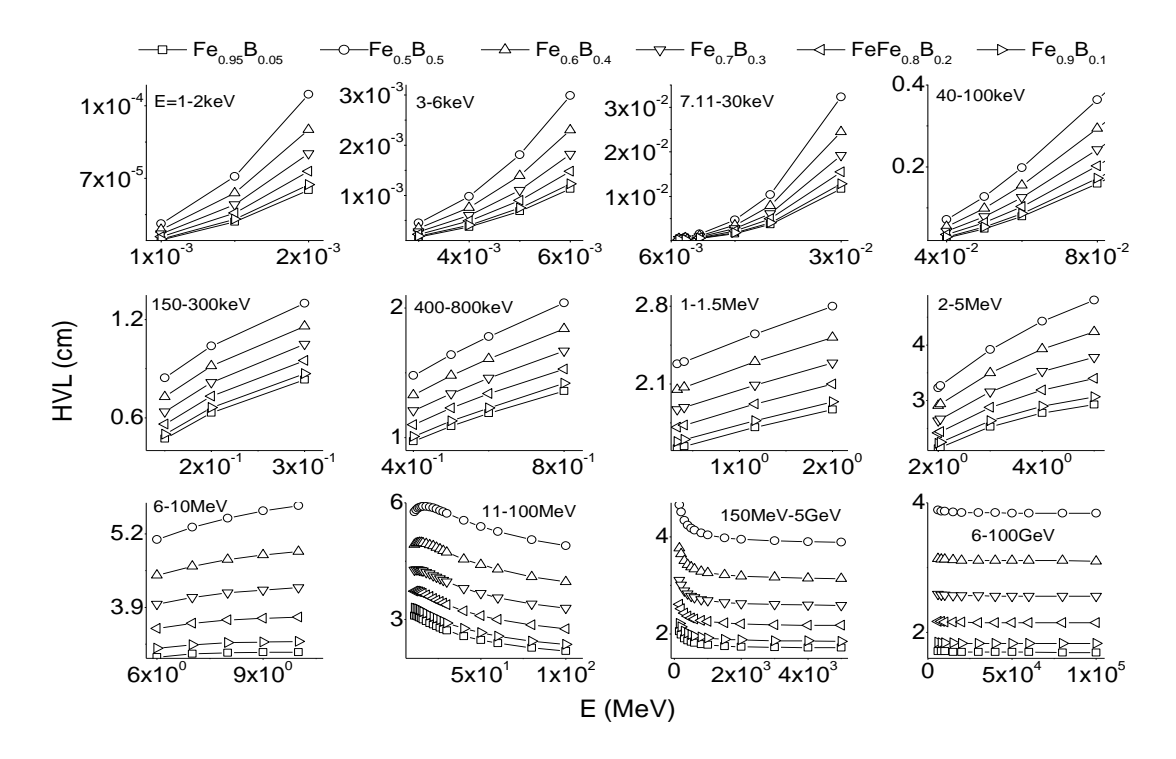


Fig. 3.3 Variation of half value layer (HVL) with energy for the studied iron boron alloys

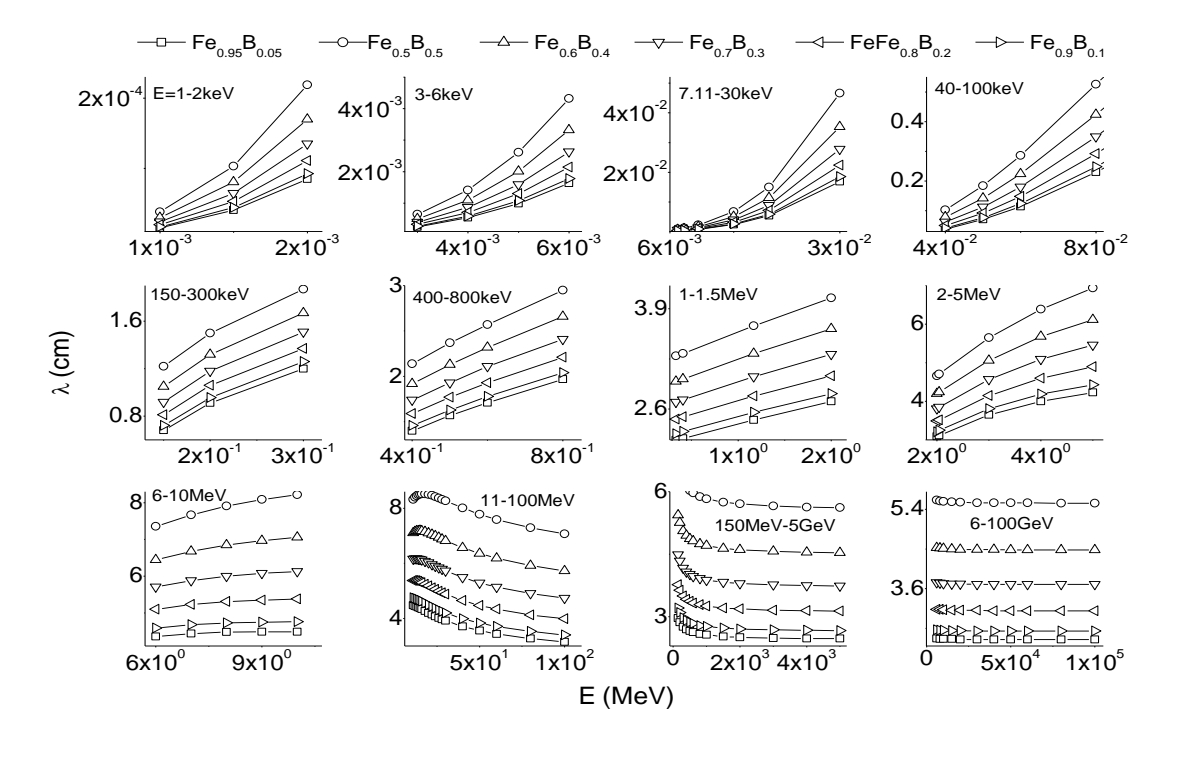


Fig. 3.4 Variation of mean free path with energy for the studied iron boron alloys

Which indicates that the iron boron alloy $Fe_{0.95}B_{0.05}$ will have less penetration for the gamma / X ray than the other iron boron alloys studied. The Figs. 3.5 and 3.6 shows the variation of Z_{eff} and N_{el} with energy for the studied iron boron alloys. The studied parameters for iron boron alloys are

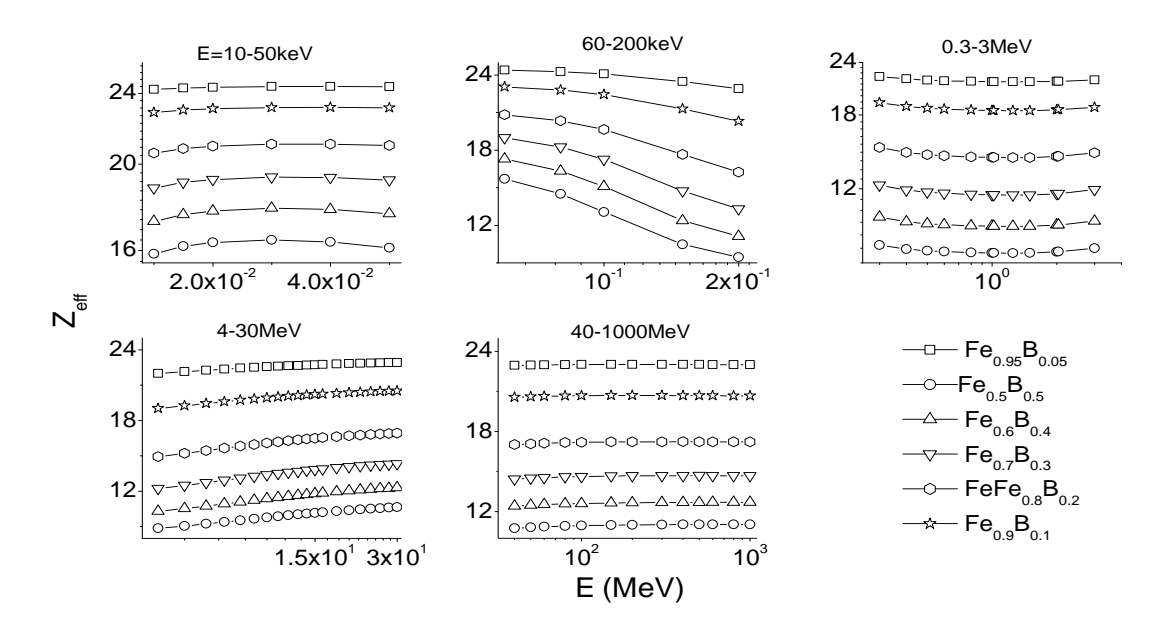


Fig. 3.5 Variation of effective atomic number with energy for the studied iron boron alloys

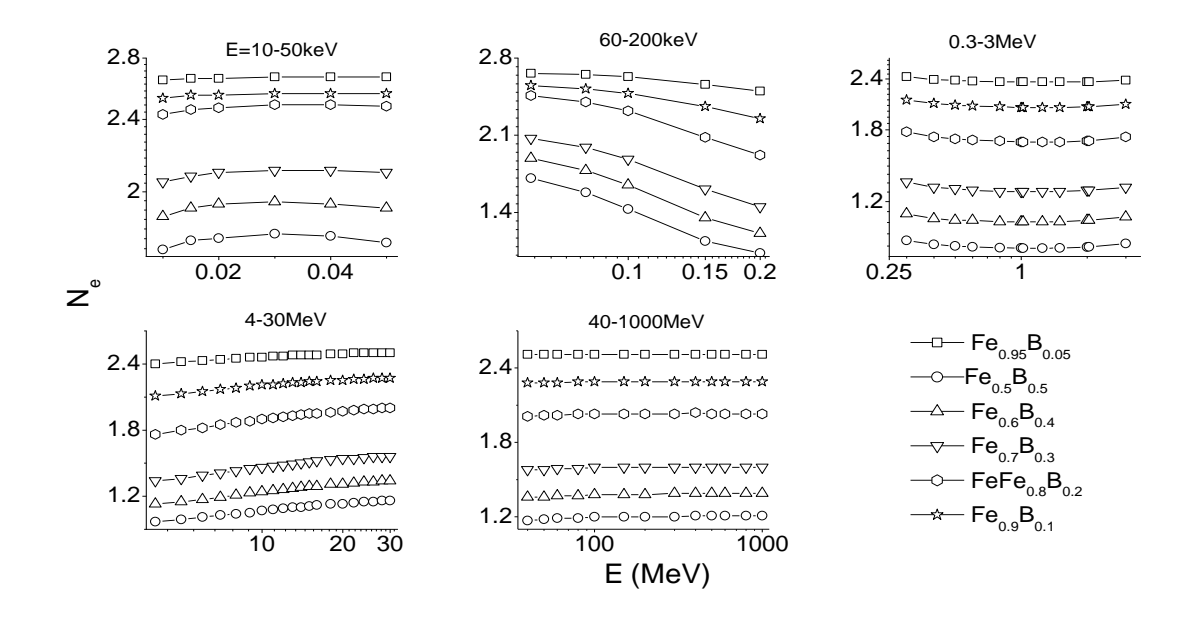


Fig. 3.6 Variation of effective electron density with energy for the studied iron boron alloys large in the low energy region (due to photo electric effect) and decreases gradually with energy.

3.2.1.3 **Specific Gamma Ray Constant**(Γ)

The evaluation of Γ for studied iron boron alloys, $Fe_{0.95}B_{0.05}$ (A), $Fe_{0.9}B_{0.1}$ (B), $Fe_{0.8}B_{0.2}$ (C), $Fe_{0.7}B_{0.3}$ (D), $Fe_{0.6}B_{0.4}$ (E) and $Fe_{0.5}B_{0.5}$ (F) are depicted in Fig. 3.7. From this comparison, it confirms that Γ is higher for the iron boron alloy $Fe_{0.95}B_{0.05}$ than the other studied alloys.

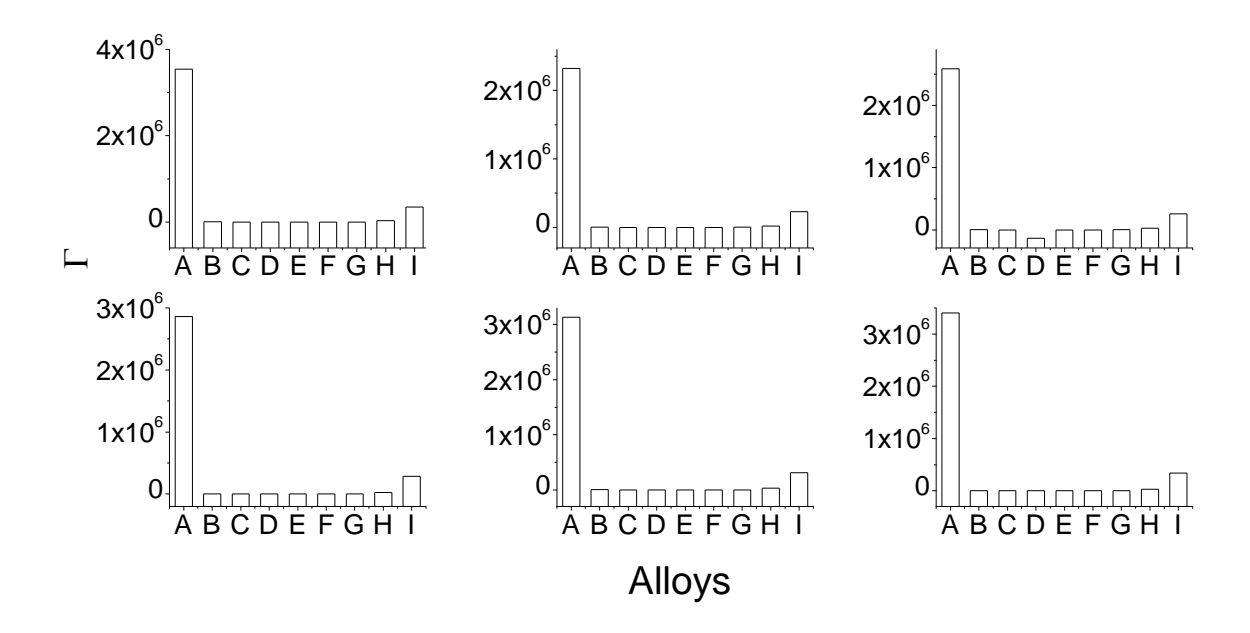


Fig. 3.7 Comparison of specific gamma ray constant for the studied iron boron alloys, $Fe_{0.95}B_{0.05}$ (A), $Fe_{0.9}B_{0.1}$ (B), $Fe_{0.8}B_{0.2}$ (C), $Fe_{0.7}B_{0.3}$ (D), $Fe_{0.6}B_{0.4}$ (E) and $Fe_{0.5}B_{0.5}$ (F)

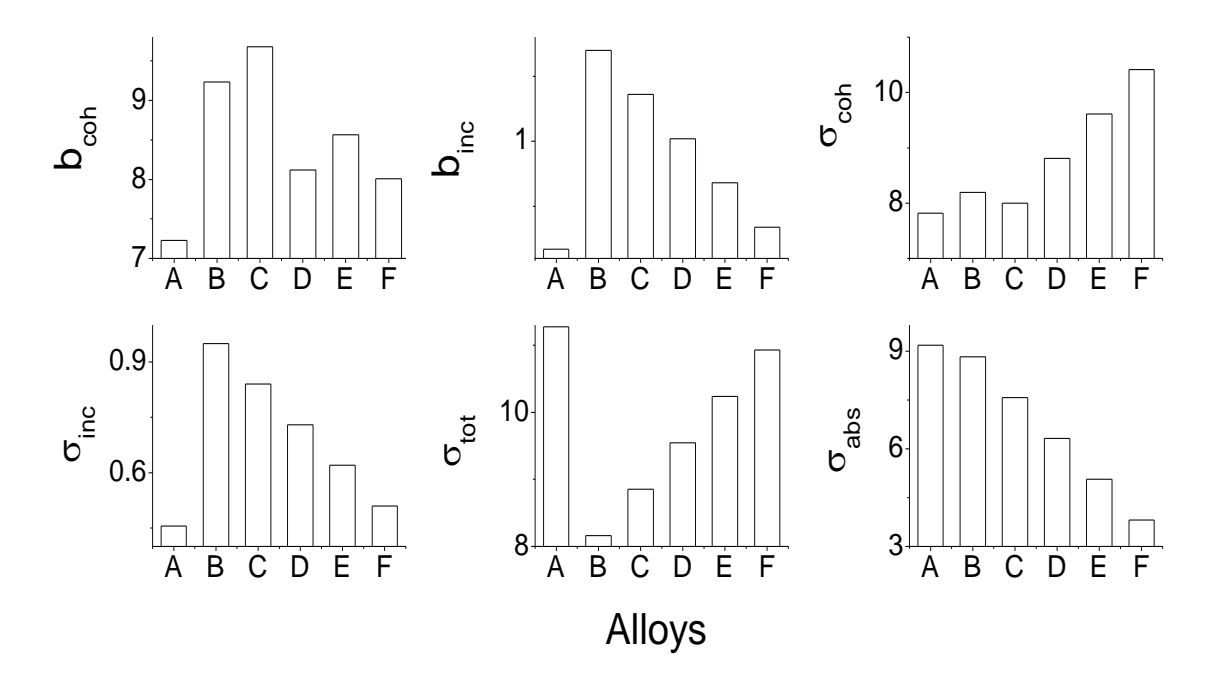


Fig. 3.8 Comparison of neutron shielding parameters for the studied iron boron alloys, $Fe_{0.95}B_{0.05}$ (A), $Fe_{0.9}B_{0.1}$ (B), $Fe_{0.8}B_{0.2}$ (C), $Fe_{0.7}B_{0.3}$ (D), $Fe_{0.6}B_{0.4}$ (E) and $Fe_{0.5}B_{0.5}$ (F)

3.2.1.4 **Neutron shielding Properties**

The Fig. 3.8 shows the comparison of b_{coh} , b_{inc} , σ_{coh} , σ_{inc} , σ_{tot} and σ_{abs} for different iron boron alloys. From the figure, it is evident that the b_{coh} and b_{inc} are minimum for the iron boron

alloy $Fe_{0.95}B_{0.05}$ than the other studied iron boron alloys. The σ_{coh} and σ_{tot} are minimum for the iron boron alloy $Fe_{0.95}B_{0.05}$. From the figure it is also observed that the σ_{abs} is maximum for the iron boron alloy $Fe_{0.95}B_{0.05}$ when compared to all other alloys studied.

3.2.1.5 Radiation protection efficiency(RPE)

The studied RPE for iron boron alloys at different thickness for different energies (32 keV, 84 keV, 662 keV, 1170 keV and 1330 keV) are shown in Fig. 3.9. From the figure it is observed that the RPE is maximum for the iron boron alloy $Fe_{0.95}B_{0.05}$ than the other studied iron boron alloys.

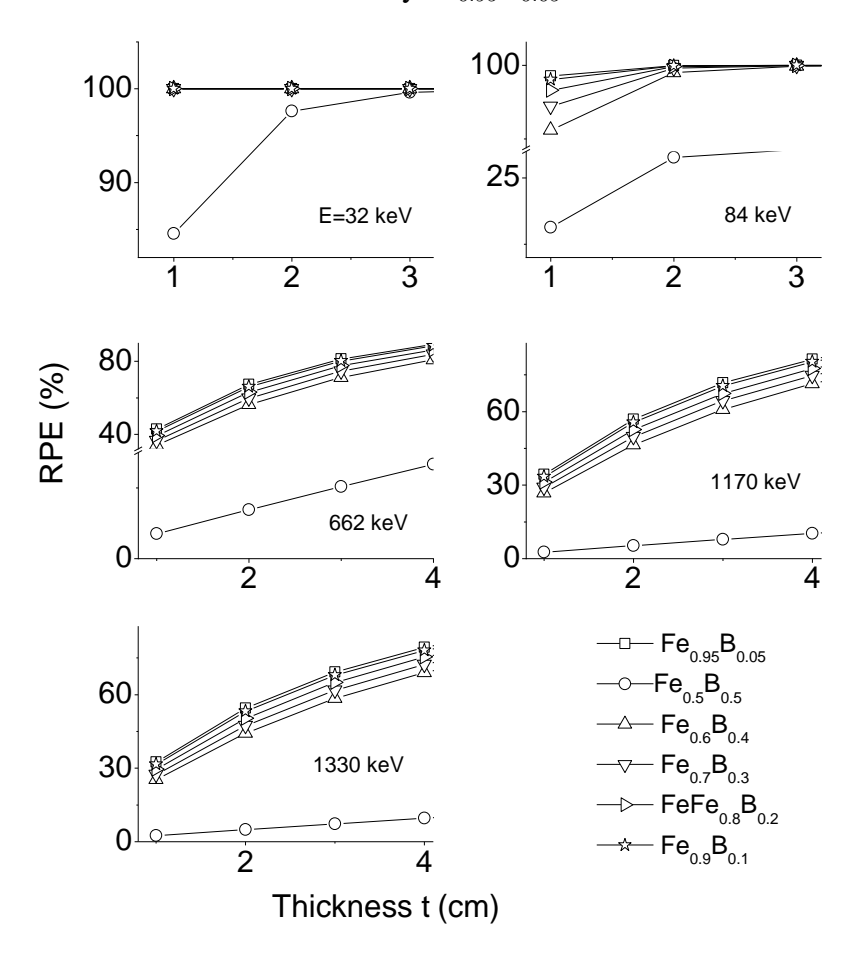


Fig. 3.9 Variation of radiation protection efficiency of the studied iron boron alloys with that of thickness of the studied alloys at different energies in keV

3.2.2 Silicon - alloys

3.2.2.1 Variation of mass attenuation coefficient with photon energy

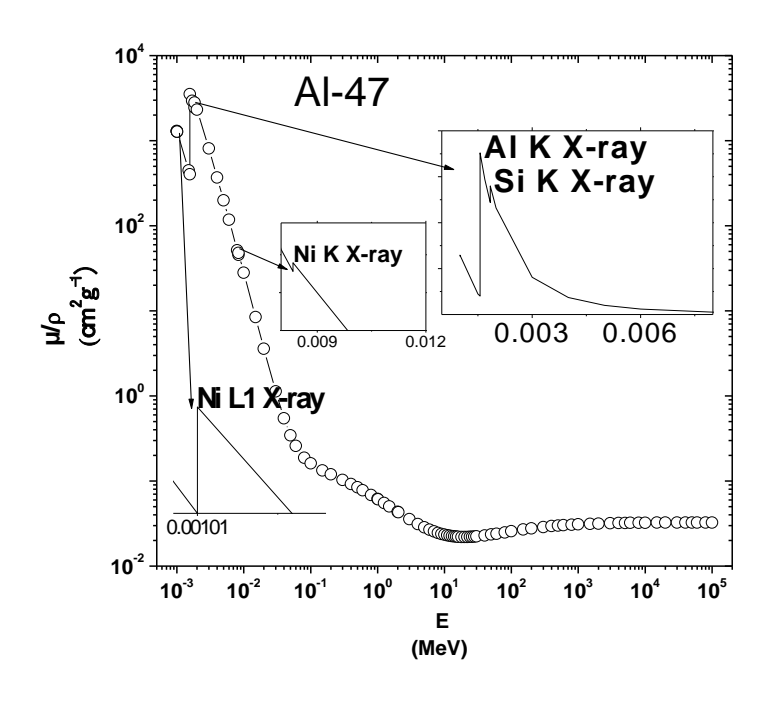


Fig. 3.10 Variation of total mass attenuation coefficient with photon energy for Al-47 alloy.

We have studied the X-ray and gamma radiation shielding parameters in aluminum silicon alloys (Al-47, Al– 32S, Al-43, Fe–Si, Al-356, Al-355 and Al-A355). The calculated $\mu l \rho$ for aluminium silicon alloys is graphically represented. There are two values of $\mu l \rho$ at same energies due to the presence of X-ray absorption edges. The variation of $\mu l \rho$ with photon energy for Al-47 alloy is as shown in figure 3.10. In case of Al 47 alloy, there are 4 X-ray absorption edges those are Ni L1, Al K, Si K and Ni K X are observed at energies 1.01, 1.56, 1.84 and 8.33 keV respectively. These identified X-ray absorption edges are highlighted in the fig 3.10. the $\mu l \rho$ values of aluminium silicon alloys are large in the low energy region and decreases progressively. In the low energy region, mass attenuation coefficient is observed to be maximum, because of dominant photoelectric interaction which depends on atomic number as Z^{4-5} . In the intermediate energy region (0.8 < E < 5MeV), Compton scattering becomes dominant which depends linearly with atomic number. Hence, the $\mu l \rho$ values become minimum. In the high energy region (> 10MeV),

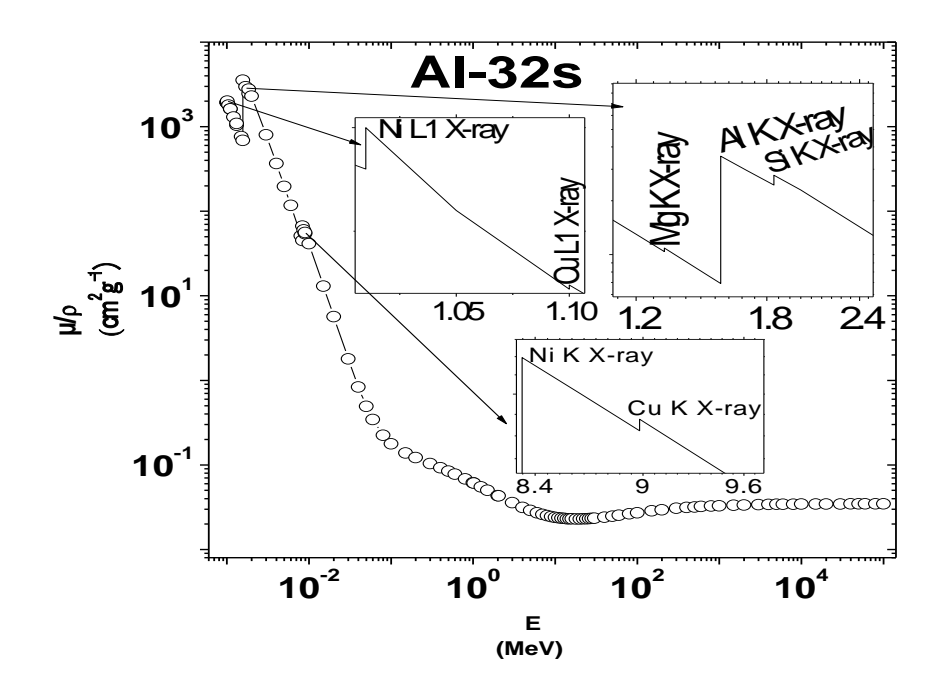


Fig. 3.11 Variation of total mass attenuation coefficient with photon energy for Al-32s alloy.

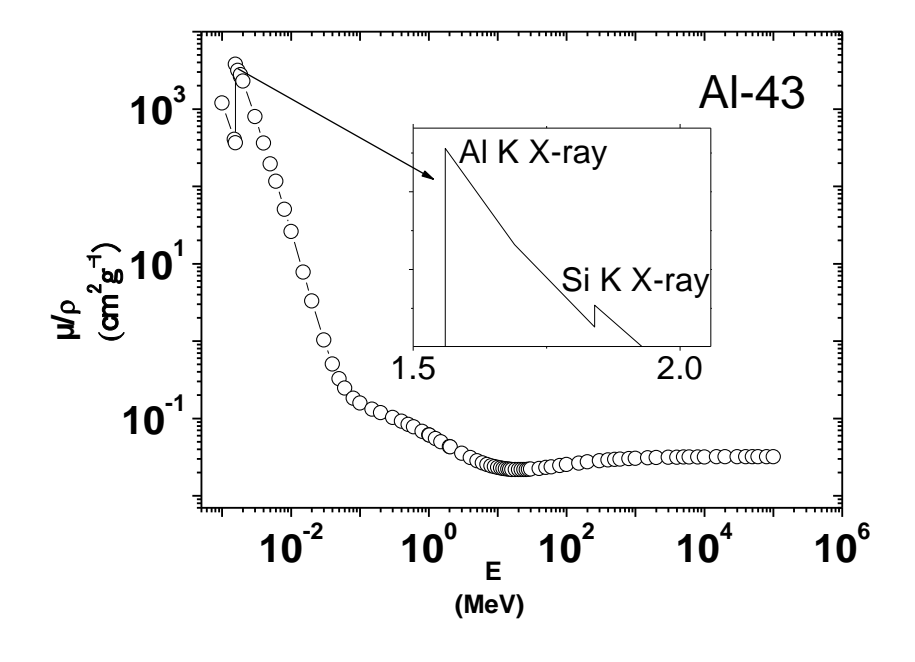


Fig. 3.12 Variation of total mass attenuation coefficient with photon energy for Al-43 alloy μ/ρ values again increases because of pair production which is proportional to Z^2 . The variation of μ/ρ with photon energy for Al-32S is as shown in fig 3.11. There are 5 X-ray absorption edges observed in Al-32 S those are Ni L1, Cu L1, Mg K, Al K and Si K,Ni k, Cu k X ray at energies 1.01, 1.10, 1.31, 1.56 and 1.84 keV respectively.

The variation of μ/ρ with photon energy for Al-43 alloy is as shown in fig 3.12. There are 2

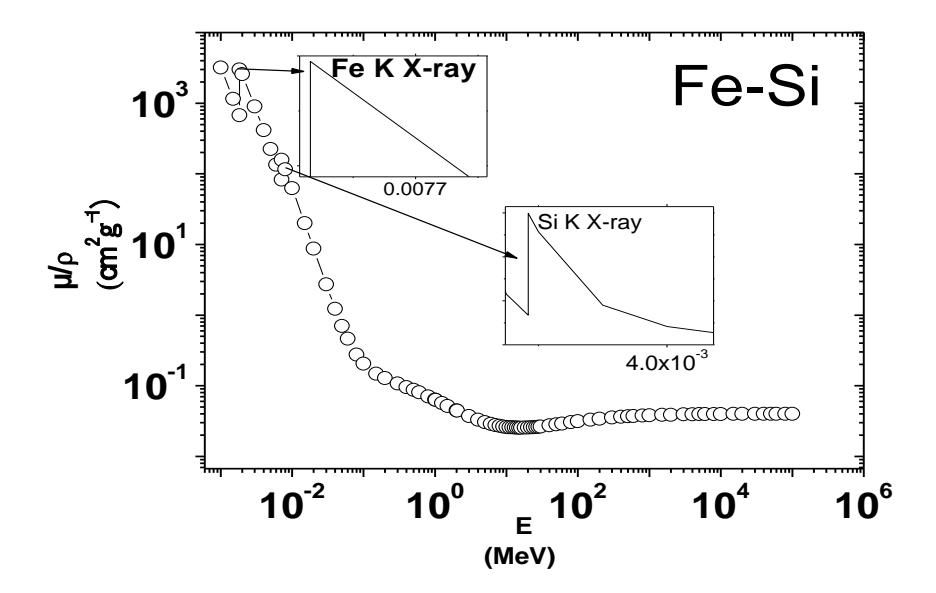


Fig. 3.13 Variation of total mass attenuation coefficient with photon energy for Fe-Si alloy

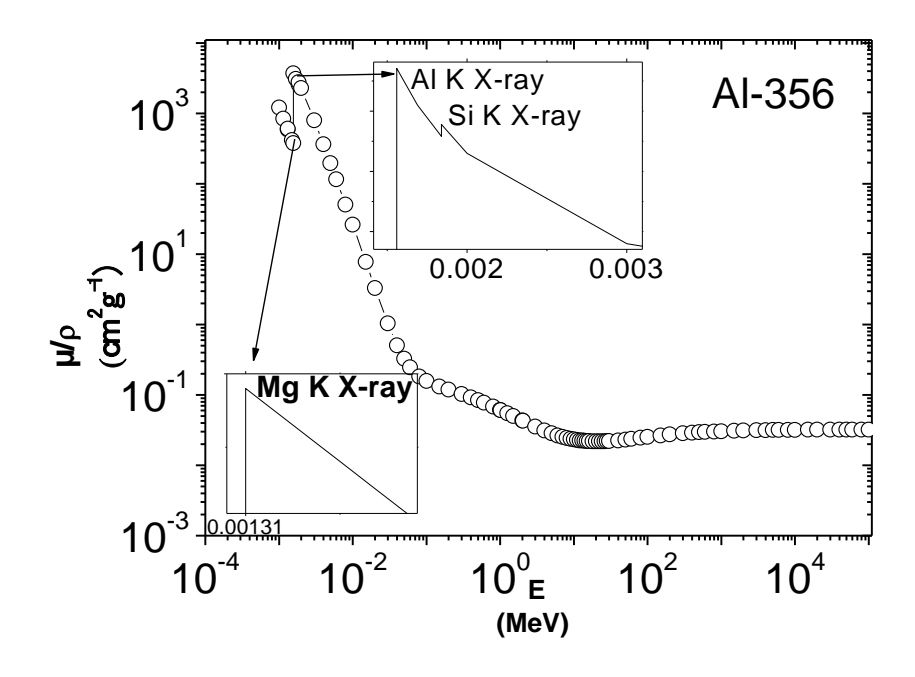


Fig. 3.14 Variation of total mass attenuation coefficient with photon energy for Al 356 alloy

X-ray absorption edges observed in Al-43 those are Al K and Si K X-ray at energies 1.56 and 1.84 keV respectively. The variation of mass attenuation coefficient with photon energy for Fe-Si is as shown in fig 3.13. There are 2 X-ray absorption edges observed in Fe-Si those are Si K and Fe

K X-ray at energies 1.84 and 7.11 keV respectively. The variation of mass attenuation coefficient with photon energy for Al-356 alloy is as shown in fig 3.14. There are 3 X-ray absorption edges are observed in Al 356 those are Mg K, Al K and Si K X-ray at energies 1.31, 1.56 and 1.84 keV respectively.

The variation of mass attenuation coefficient with photon energy for Al-A355 is as shown in

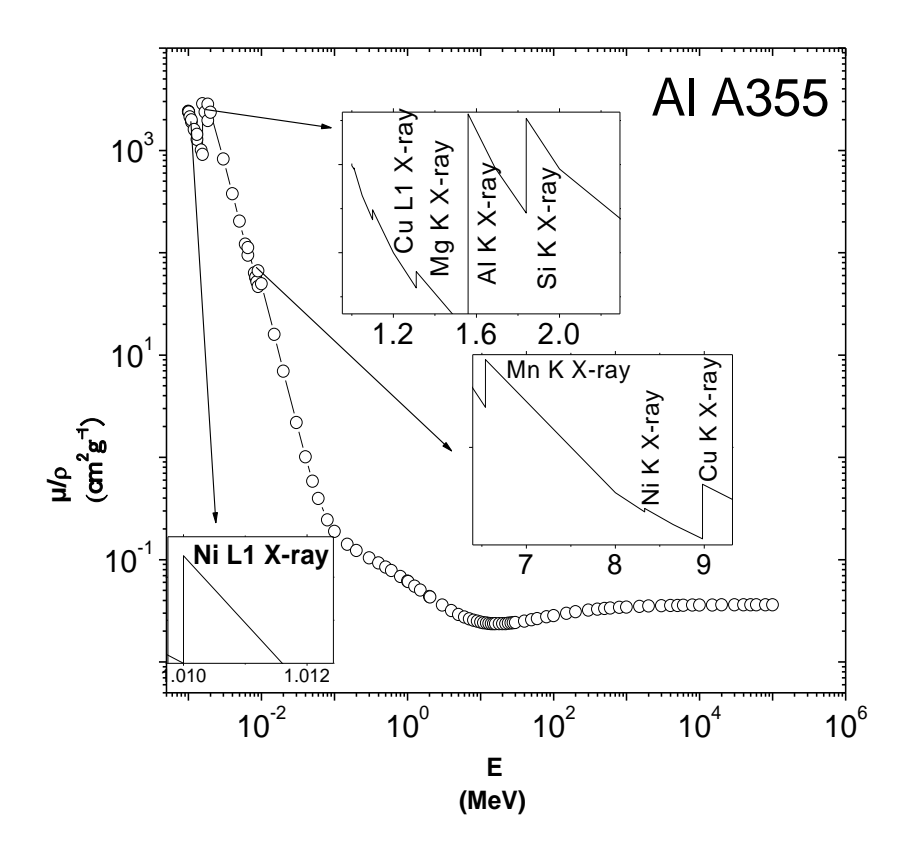


Fig. 3.15 Variation of total mass attenuation coefficient with photon energy for Al- A355 alloy.

fig 3.15. There are 8 X-ray absorption edges observed in Al A355 those are Ni L1, Cu L1, Mg K, Al K, Si K, Mn K, Ni K and Cu K X-ray at energies 1.01, 1.1, 1.31, 1.56, 1.84, 6.54, 8.33 and 8.98 keV respectively. The variation of mass attenuation coefficient with photon energy for Al-355 is as shown in fig 3.16. There are 4 X-ray absorption edges observed in Al 355 those are Cu L1, Al K, Si K and Mo L1 X-ray at energies 1.1, 1.56, 1.84 and 2.87 keV respectively.

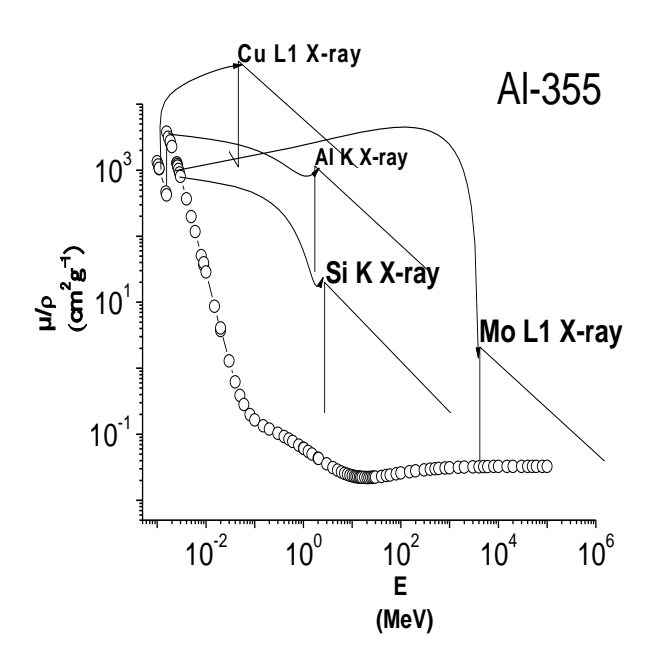


Fig. 3.16 Variation of total mass attenuation coefficient with photon energy for Al- 355 alloy.

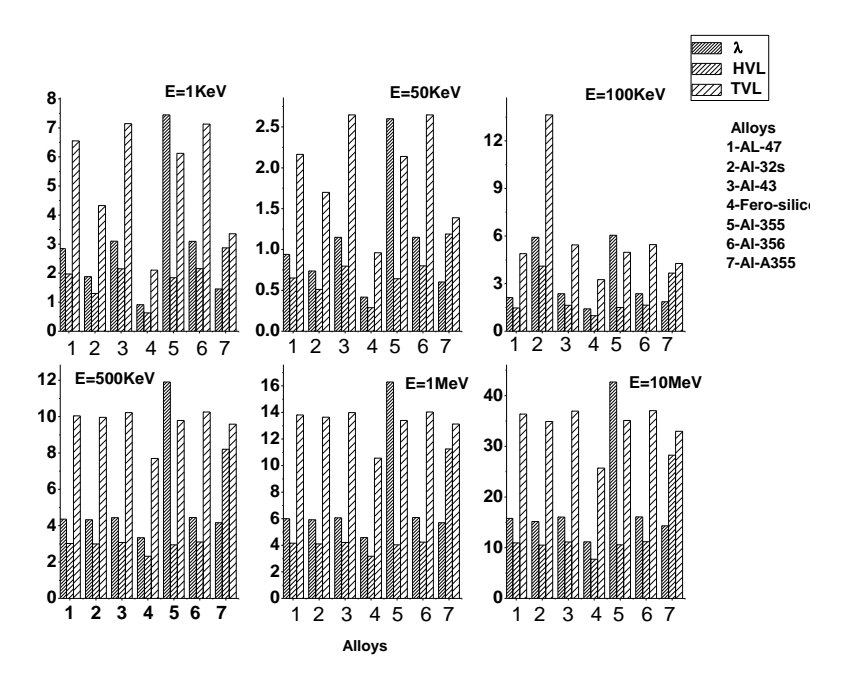


Fig. 3.17 Comparison of Half value layer (HVL), Tenth value layer (TVL) and mean free path(λ) for aluminium silicon alloys (1.Al-47, 2.Al-32s, 3.Al-43, 4-Ferro Silicon, 5.Al-355, 6. Al-356 and 7.Al A-355).

3.2.2.2 Gamma/X-ray interaction parameters

The HVL, TVL and λ for different aluminium silicon alloys have been calculated. The comparison of HVL, TVL and λ for different aluminium silicon alloys are as shown in Fig. 3.17. From

this comparison, it is clear that the HVL and TVL are small for ferro silicon alloy than the other aluminium silicon alloys. It means gamma/X-ray penetrates less in ferro silicon alloy than the other aluminum silicon alloys. It means ferro-silicon is good absorber of gamma/X-ray radiation. The variation of effective atomic number and effective electron density with energy for different aluminium silicon alloys are as shown in Fig 3.18. These parameters for aluminium silicon alloys

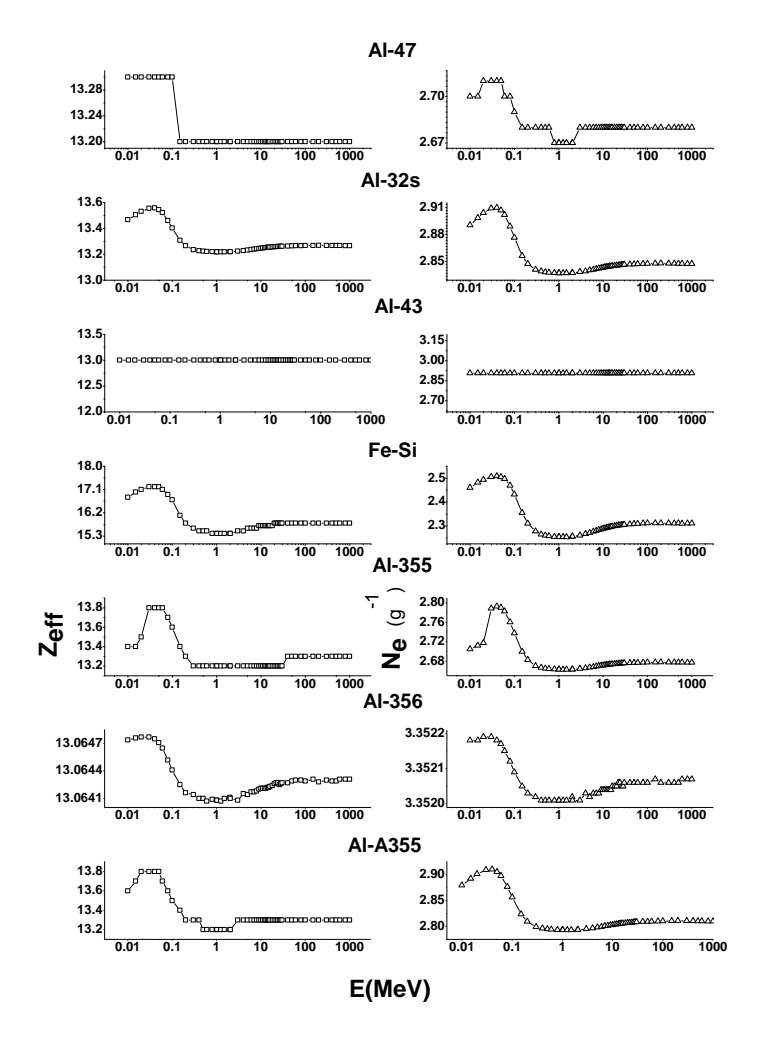


Fig. 3.18 Variation of effective atomic number and effective electron density with energy for different aluminium silicon alloys.

are large in the low energy region (due to photo electric effect) and decreases progressively, There after increases and becomes constant for high energy (due to pair production). It is also observed that effective atomic number and effective electron density are almost constant for the alloy Al-43.

3.2.2.3 Variation of energy exposure buildup factors (B_{ex}) with the energy

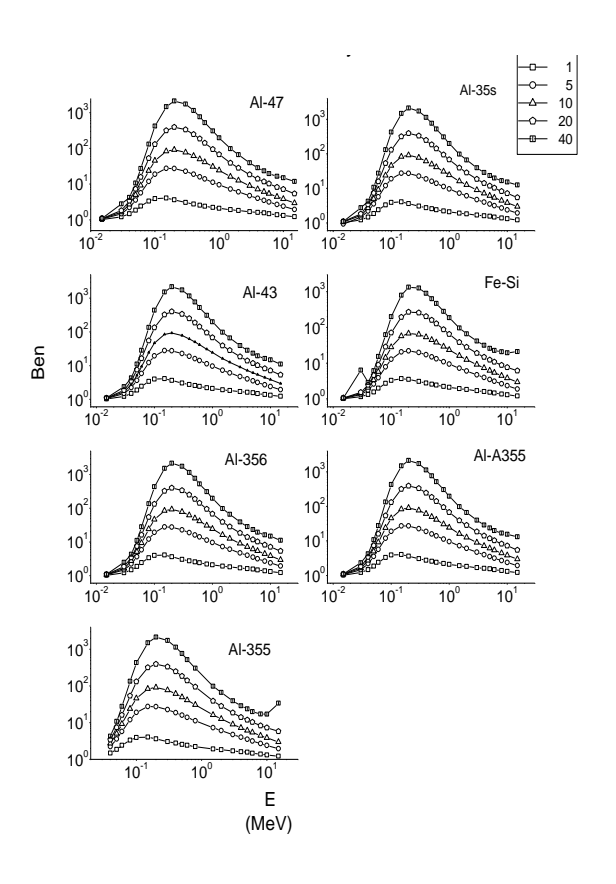


Fig. 3.19 Variation of exposure buildup factors with energy for different mean free paths for aluminum silicon alloys.

The variation of exposure buildup factors with energy at different mean free paths are as shown in Fig 3.19. The variation of exposure buildup factors with mean free path at various energies (0.1, 0.5, 1.5, 5 and 15 MeV) for different aluminium silicon alloys are as shown in Fig3.20. From this figure it is clear that B_{ex} values increases with increase in the target thickness. This is due to the reason that with increase in the target thickness, scattering events in the medium increases. The comparison of exposure buildup factors with energy for different aluminium silicon alloys are as shown in Fig3.21. It is observed that B_{ex} value is larger for ferro silicon alloy among the studied aluminium silicon alloys at different energies. It also reveals that scattering and absorption is larger in ferro-silicon than the other studied alloys. Ferro silicon can be used for the shielding for gamma/X-ray radiations.

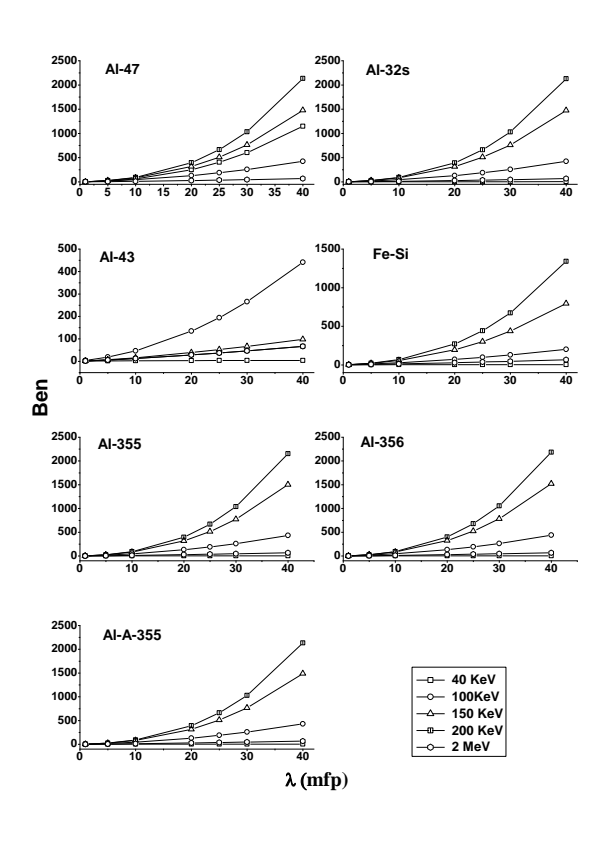


Fig. 3.20 Variation of exposure buildup factors with mean free path at different energies for different aluminium silicon alloys.

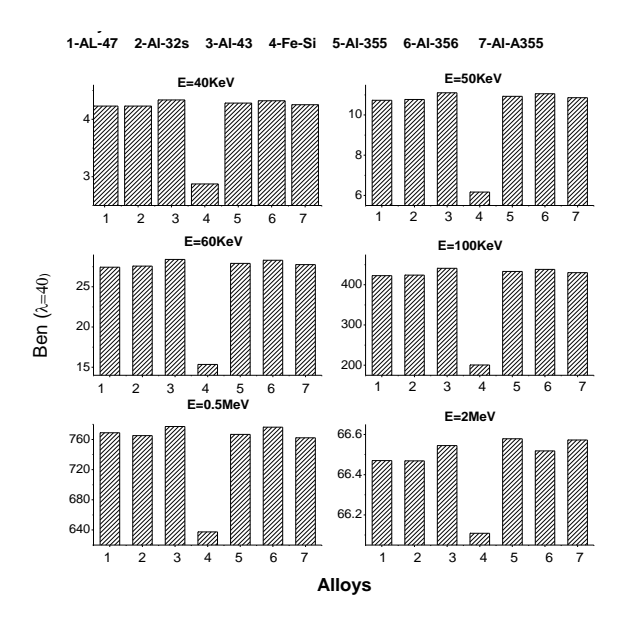


Fig. 3.21 Comparison of exposure buildup factors with energy for different aluminium silicon alloys (1-Al-47, 2-Al-32S, 3-Al-43, 4-Ferro silicon, 5-Al-355, 6-Al-356, 7-Al-A355).

3.2.2.4 **Neutron shielding Properties**

Neutron scattering length and cross sections such as coherent neutron scattering length, incoherent neutron scattering lengths, coherent neutron scattering cross section, incoherent neutron scattering cross sections, total neutron scattering cross section and neutron absorption cross sec-

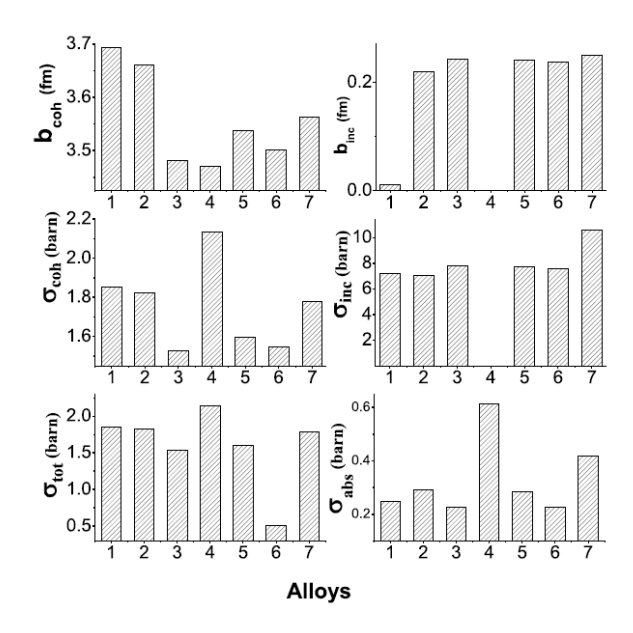


Fig. 3.22 Comparison of evaluated coherent neutron scattering length (λ_{nc}), incoherent neutron scattering lengths (λ_{inc}), coherent neutron scattering cross section (σ_{nc}), incoherent neutron scattering cross sections (σ_{inc}), total neutron scattering cross section (σ_{tot}) and neutron absorption cross sections (σ_a) for different aluminium silicon alloys (1-Al-47, 2-Al-32S, 3-Al-43, 4-Ferro silicon, 5-Al-355, 6-Al-356, 7-Al-A355).

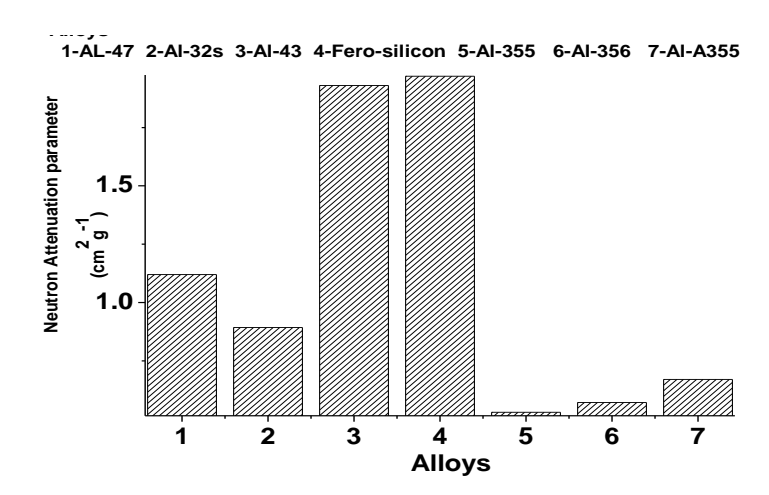


Fig. 3.23 Comparison of neutron attenuation parameters among the studied aluminium silicon alloys (1-Al-47, 2-Al-32S, 3-Al-43, 4-Ferro silicon, 5-Al-355, 6-Al-356, 7-Al-A355).

tions are related to shielding capability of the medium. Hence in the present work, these parameters has been considered as shielding parameters. The attenuation parameter is evaluated using the total cross section. The comparison of evaluated coherent neutron scattering length, incoherent neutron scattering lengths, coherent neutron scattering cross section, incoherent neutron scattering lengths.

ing cross sections, total neutron scattering cross section and neutron absorption cross sections for different Al–Si alloys are as shown in Fig 3.22. From this figure, it is clear that coherent neutron scattering length and incoherent neutron scattering lengths are smaller for Ferro silicon alloy than that of the other studied alloys. Coherent and total neutron scattering cross sections are large for Ferro silicon alloy. The neutron absorption cross section is high for Ferro silicon alloy. From the study of above parameters suggest that neutron scattering and absorption is larger in ferro-silicon alloy than that of the other studied alloys. The comparison of evaluated neutron attenuation parameter (cm^2/g) for the studied Al–Si alloys is shown in Fig 3.23.From this fig, it is clear that the total neutron attenuation parameter is larger for ferro silicon alloy than that of the other studied alloys. Hence attenuation of neutrons are larger for ferro silicon alloy than that of the other studied alloys Ferro-silicon alloy may be used for the shielding of neutrons also.

3.2.3 **Gallium alloys**

The variation of energy exposure buildup factors (B_{ex}) with energy for the studied gallium alloys at different mean free paths is shown in figure 3.24. It is found that B_{ex} increases up to the

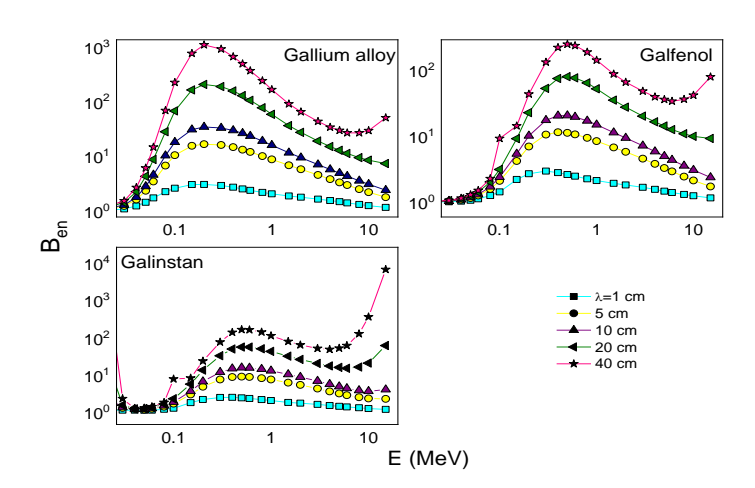


Fig. 3.24 Variation of energy exposure buildup factors with energy for the studied gallium alloys at different mean free

Epe and then decreases. Here Epe is the energy value at which the photo electric interaction coef-

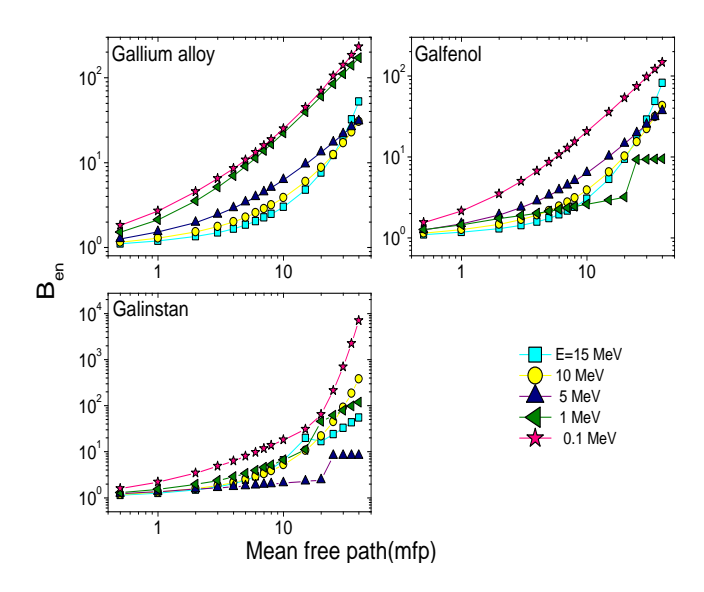


Fig. 3.25 Variation of energy exposure buildup factors with mean free path for the studied gallium alloys at different energies

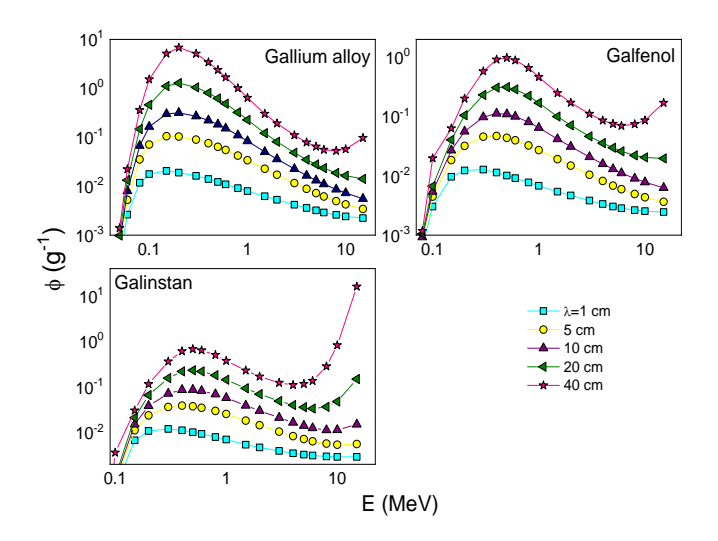


Fig. 3.26 Variation of φ with energy for the studied gallium alloys at different mean free paths.

ficients match with Compton interaction coefficients for a given value of effective atomic number (Z_{eff}) . With the increase in mean free path, deposition of energy in the medium increases. Hence, energy absorption buildup factor increases with mean free path. Among the studied gallium alloys, galinstan alloy is found to have larger energy absorption buildup factor compared to that of other two alloys.

The variation of B_{ex} with mean free path for the studied gallium alloys at different energies is shown in figure 3.25. From this figure it is clear that B_{ex} values increases with increase in the

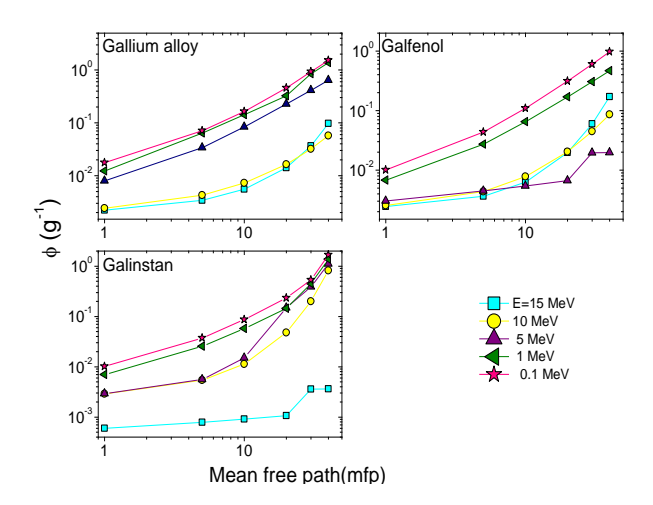


Fig. 3.27 Variation of φ with mean free path for the studied gallium alloys at different energies.

target distance. This is due to the reason that with increase in the target distance, scattering events in the medium increases. B_{ex} values increases up to the Epe and then decreases. Here Epe is the energy value at which the photo electric interaction coefficients match with Compton interaction coefficients for a given value of effective atomic number (Z_{eff}). Among the studied alloys B_{ex} is larger for Galinstan for the given energies.

Variation of specific absorbed fractions of energy (φ) with different mean free paths is shown in figure 3.26. φ is large for larger mean free paths, with the increase in mean free paths, B_{ex} increases and hence φ also increases. Variation of φ with mean freepaths at different energies for the studied gallium alloys is shown in figure 3.27. It is observed that φ is larger for smaller energies.

Comparison of B_{ex} and φ among the studied gallium alloys at different energies is shown in figure 3.28. From this figure it is found that the values of B_{ex} and φ is large for Galinstan [Ga-68.5%, In-21.5%, Sn-10%] among the studied gallium alloys. On comparison of B_{ex} and φ among the studied gallium alloys it is found that the alloy Galinstan is having larger values of B_{ex} and φ than that of others. This may be due to the fact that the effective atomic number and mass attenuation coefficient are larger for Galinstan alloy than that of others.

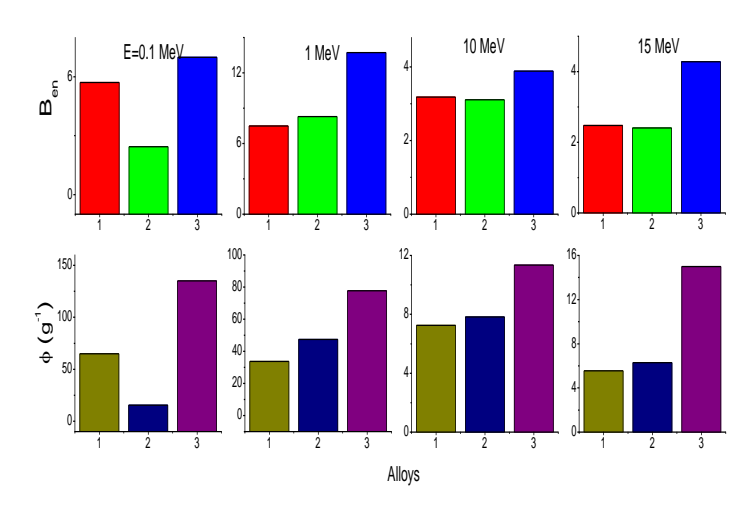


Fig. 3.28 Comparison of EBF and SAF among the studied alloys for 10 mfp (1- Gallium alloy, 2- Galfenol and 3- Galinstan) at different energies.

To validate the present work we have evaluated the mass attenuation coefficient for Arsenic oxide for which experimental values are available. The comparison of values produced by the present work with that of experiments is shown in table. From this table it is clear that present work is close to the experiments.

3.2.4 Lead Alloys

Theoretically, X-ray / gamma, neutron shielding parameters of lead based binary / tertiary/Quaternary alloys viz., Foundary type, Lino type, Molybdochalkos, Monotype, Stereo type, Tune, Type metal and Wood's metal alloy were studied.

3.2.4.1 Gamma / X-ray shielding parameters of lead Alloys

Variation of μ/ρ with Gamma energy for all the selected binary / tertiary / quaternary alloys - Foundary type(FD), Lino type(LT), Molybdochalkos(MC), Monotype(MT), Stereo type(ST), Tune(Tu), Type metal(TM) and Wood's metal(WM) are graphically represented in Fig 3.29(a-d) and Fig 3.30(e-h) respectively. In all the selected binary / tertiary / quaternary alloys, the variation clearly shows the rapid decrease in μ/ρ value with increase in gamma energy along with few X-ray

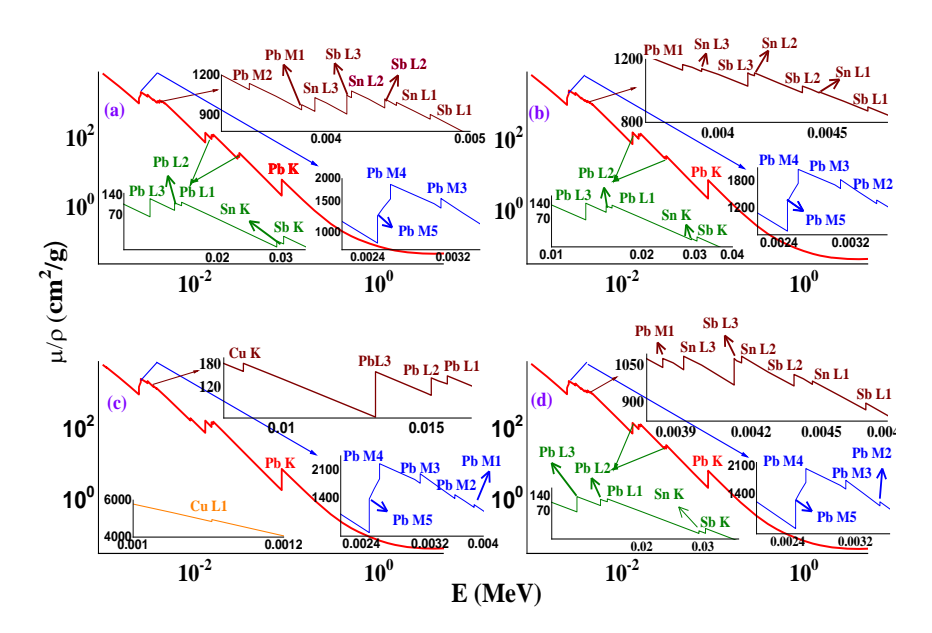


Fig. 3.29 Variation of mass attenuation coefficient with gamma energy for the (a) FD, (b) LT, (c) MC and (d) MT binary / tertiary / quaternary alloys respectively

absorption edges. The rapid decrease in μ/ρ at lower energy is mainly due to the photoelectric process which gets dominated at lower energy. When gamma rays interact with corresponding binary / tertiary / quaternary alloys, it exhibits X-ray absorption edges at particular photon energy. These X-ray absorption edges are the characteristics of the elements present in the chosen binary / tertiary / quaternary alloys. FD type tertiary alloy gives four absorption peaks observed in the range 2-3 keV, 3-5 keV, 13-32 keV and 88 keV, which are the characteristics of the elements present in the alloy (Fig 3.29(a)). Each absorption peak is expanded and given in the inset of Fig 3.29(a). The first absorption peak (2-3 keV) is associated with three minor X-ray absorption edges at 2.48, 2.59 and 3.07 keV corresponding to Pb M5-X-ray, Pb M4-X-ray and Pb M3-X-ray respectively. The second X-ray absorption peak is associated with eight minor peaks at 3.55 keV, 3.85 keV, 3.93 eV, 4.13 keV, 4.16 keV, 4.38 keV, 4.5 keV and 4.7 keV corresponding to Pb M2-X-ray, Pb-M1-X-ray, Sn-L3-X-ray, Sb-L3-X-ray, Sn-L2-X-ray, Sn-L1-X-ray and Sb-L1-X-ray respectively. The third X-ray absorption peak consists five minor absorption edges at 13 keV, 15.2 keV, 15.9 keV, 29.2 keV and 30.5 keV corresponding to Pb-L3-X-ray, Pb-L2-X-ray, Pb-L1-X-ray, Sn-K-X-ray and Sb-K-X-ray respectively. The fourth absorption peak appearing at 88 keV corre-

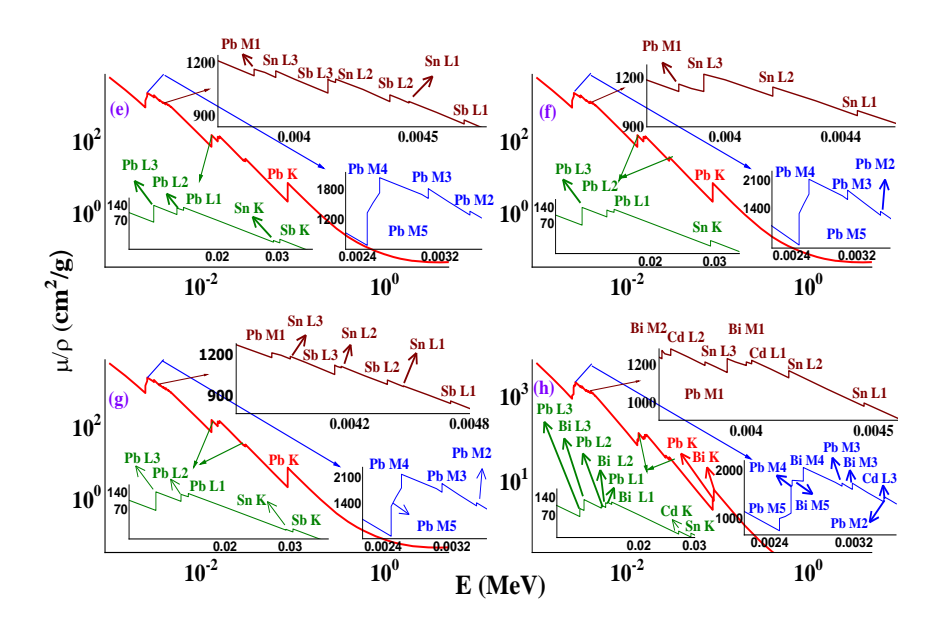


Fig. 3.30 Variation of mass attenuation coefficient with gamma energy for the (e) ST, (f) TU, (g) TM and (h) WM binary / tertiary / quaternary alloys respectively

sponds to Pb-K-X-ray.

Similar trend is observed for the remaining binary/ tertiary/ quaternary alloys. LT, MT, ST and TM alloy gives the characteristic X-ray absorption peaks of Pb, Sn and Sb elements. Fig 3.29(b, d) Fig 3.30(e and g) and inset figure clearly depicts the Pb-M5-X-ray, Pb-M4-X-ray, Pb-M3-X-ray, Pb-M2-X-ray, Pb-M1-X-ray, Sn-L3-X-ray, Sb-L3-X-ray, Sn-L2-X-ray, Sb-L2-X-ray, Sn-L1-X-ray, Sb-L1-X-ray, Pb-L3-X-ray, Pb-L3-X-ray, Pb-L1-X-ray, Sn-K-X-ray, Sb-K-X-ray and Pb-K-X-ray absorption peaks observed for LT, MT, ST and TM alloys. For MC, TU and Wm binary, tertiary quaternary alloys, Pb-M5-X-ray, Pb-M4-X-ray, Pb-M3-X-ray, Pb-M2-X-ray, Pb-M1-X-ray, Pb-L3-X-ray, Pb-L2-X-ray, Pb-L1-X-ray and Pb-K-X-ray absorption peaks observed at 2.48, 2.59, 3.07, 3.55, 3.85, 13, 15.2, 15.9 and 88 keV respectively. Further, characteristic peaks of copper Cu-L1-X-ray and Cu-K-X-ray are observed at 1.1 and 8.98 keV respectively for MC whereas Sn-L3-X-ray, Sn-L2-X-ray, Sn-L1-X-ray and Sn-K-X-ray absorption peaks are observed at 3.93, 4.16, 4.46 and 29.2 keV respectively for TU binary alloy. In case of WM quaternary alloy, Bi-M5-X-ray, Bi-M4-X-ray, Bi-M3-X-ray, Cd-L3-X-ray, Bi-M2-X-ray, Bi-M1-X-ray, Cd-L1-X-ray, Sn-L2-X-ray, Sn-L3-X-ray, Bi-M3-X-ray, Bi-L1-X-ray, Bi-K-X-ray, Sn-K-ray, Sn-K

Bi-K-X-ray are observed at 2.58, 2.69, 3.18, 3.54, 3.70, 3.73, 3.93, 4, 4.02, 4.16, 4.46, 13.4, 15.7, 16.4, 26.7, 29.2 90.5 keV respectively (Fig 3.29c and Fig 3.30(f and h)).

In general, reduction in the intensity of the beam was affected by the atomic number of the

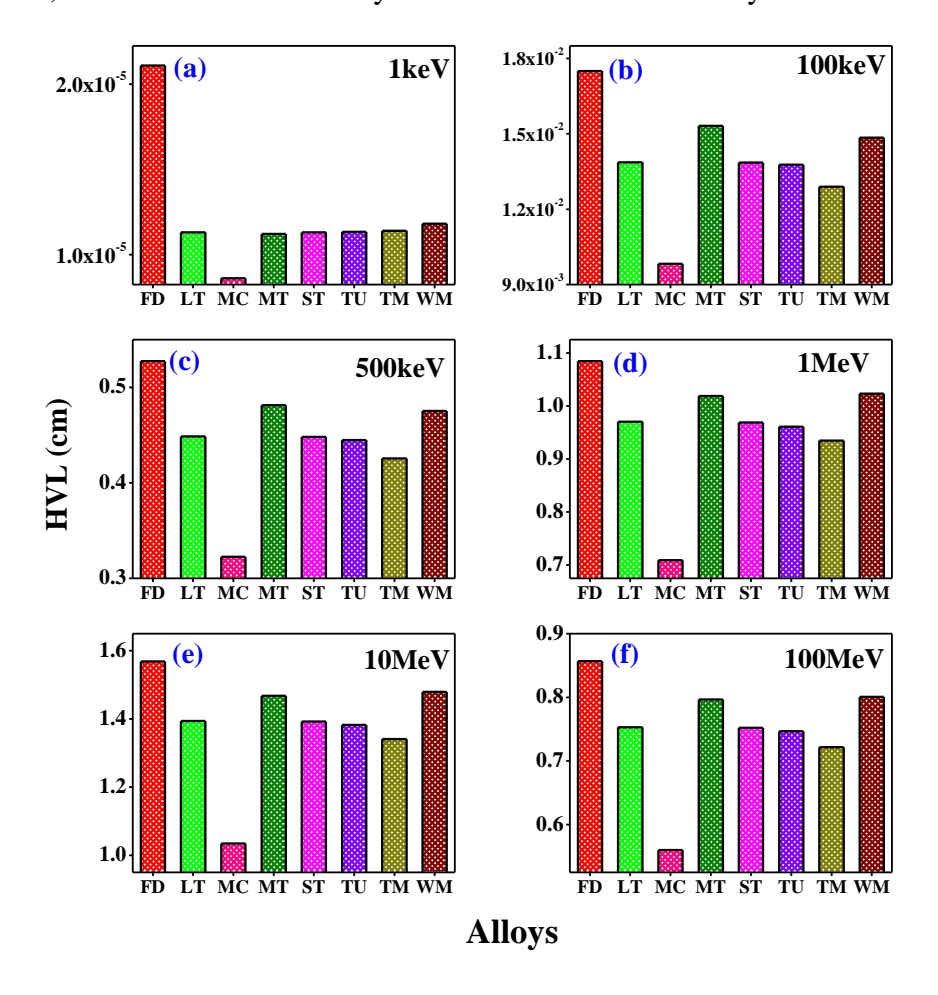


Fig. 3.31 Comparison of HVL of FD, LT, MC, MT, ST, TU, TM and WM binary / tertiary / quaternary alloys at different photon energies

absorbing material or beam energy. The HVL of gamma,X-ray beam is the thickness of absorbing material needed to reduce the beam to half of its original potential. HVL is (i) indirect measure of photon energy or beam hardness, (ii) an important quality control test as it is used to measure whether or not there is sufficient filtration in the x-ray beam to remove low energy radiation, which can be damaging and (iii) It also helps to determine the type and thickness of shielding required in the facility. Fig 3.31 shows the comparison of HVL values of selected binary, tertiary, quaternary alloys at different photon energies (1 keV, 100 keV, 500 keV, 1 MeV, 10 MeV and 100 MeV).

Among the selected lead alloys, HVL value was found to be smaller for MC which indicates that it is a good absorber.

In the further investigation, we have studied the variation of other gamma, X-ray shielding

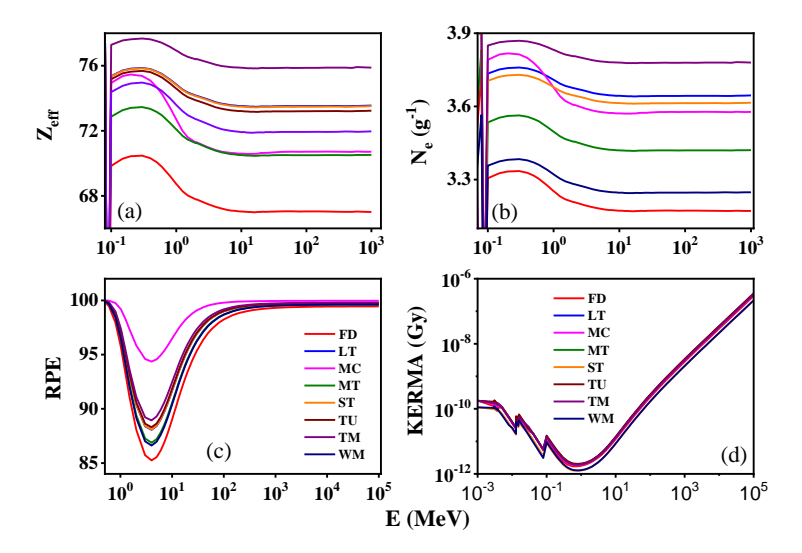


Fig. 3.32 Variation of (a) Z_{eff} , (b) N_e , (c) RPE and (d) Kerma with photon energy for FD, LT, MC, MT, ST, TU, TM and WM binary / tertiary / quaternary alloys

parameter such as Z_{eff} , electron density (N_e) , radiation protection efficiency (RPE) and KERMA for all the selected binary , tertiary , quaternary alloys with gamma energy (Fig 3.32 (a-d)). Both Z_{eff} and N_e follow a similar trend with gamma energy for all the selected alloys (Fig 3.32 (a and b)). For instance, Z_{eff} and N_e value was found to be maximum for WM quarternary alloy and minimum for FD tertiary alloy whereas, RPE was found to be larger for MC compared to other binary / tertiary / quaternary alloys under study as shown in Fig 3.32(c)). The point where both Compton scattering and photoelectric effect dominates simultaneously, dip point is observed and RPE becomes minimum. The other X-ray , gamma-ray shielding parameter, KERMA gives the information about the kinetic energy released in the particular material. All the binary, tertiary , quaternary alloys show three absorption peaks at 2.83, 14.5 and 103 keV except variation in intensity. This KERMA value was found to be larger for MC binary alloy. The maximum RPE and KERMA value indicates the better performance of MC binary alloy as a better shielding material.

Compared to other alloys under study, MC binary alloy is a good absorber. Thus, the remain-

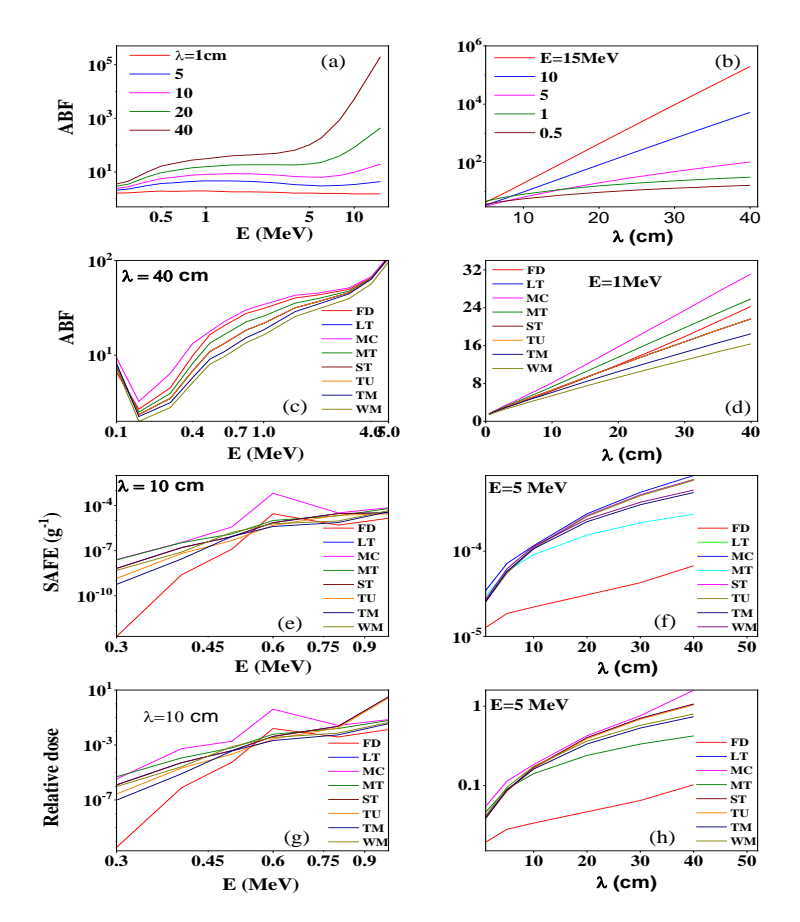


Fig. 3.33 Variation of (a) ABF with photon energy, (b) ABF with λ for MC binary alloy, (c) ABF with photon energy, (d) ABF with λ , (e) SAFE with photon energy, (f) SAFE with λ , (g) Relative dose with photon energy, (h) Relative dose with λ for FD, LT, MC, MT, ST, TU, TM and WM binary / tertiary / quaternary alloys

ing shielding parameters such as Absorption buildup factor (B_{en}) , φ and RD is studied at different photon energy and different penetration depth (λ) (Fig 3.33 a and b). For a particular penetration depth, photoelectric effect and pair production process dominates in the lower and higher energy, whereas Compton scattering dominates at the intermediate energy region. The similar behavior is observed for all the penetration depth except the variation in intensity. However, linear relationship is observed with penetration depth for different photon energy. Fig 3.33c, Fig 3.33 e and Fig 3.33g shows the graphical representation of variation of B_{en} (at λ =40 cm), φ and RD (at λ = 10 cm) with photon energy for all the selected binary,tertiary,quaternary alloys. Fig 3.33d, Fig 3.33f and Fig 3.33h shows the variation of B_{en} (at E = 1 MeV), φ and relative dose (E = 5 MeV) with

penetration depth for all the studied alloys. The B_{en} , φ and RD increases with increase in penetration depth. With increase in penetration depth, thickness of the interacting material increases which results in increasing the scattering events in the interacting medium [108].

Among all the selected alloys, MC binary alloy shows larger B_{en} , φ and RD value and hence

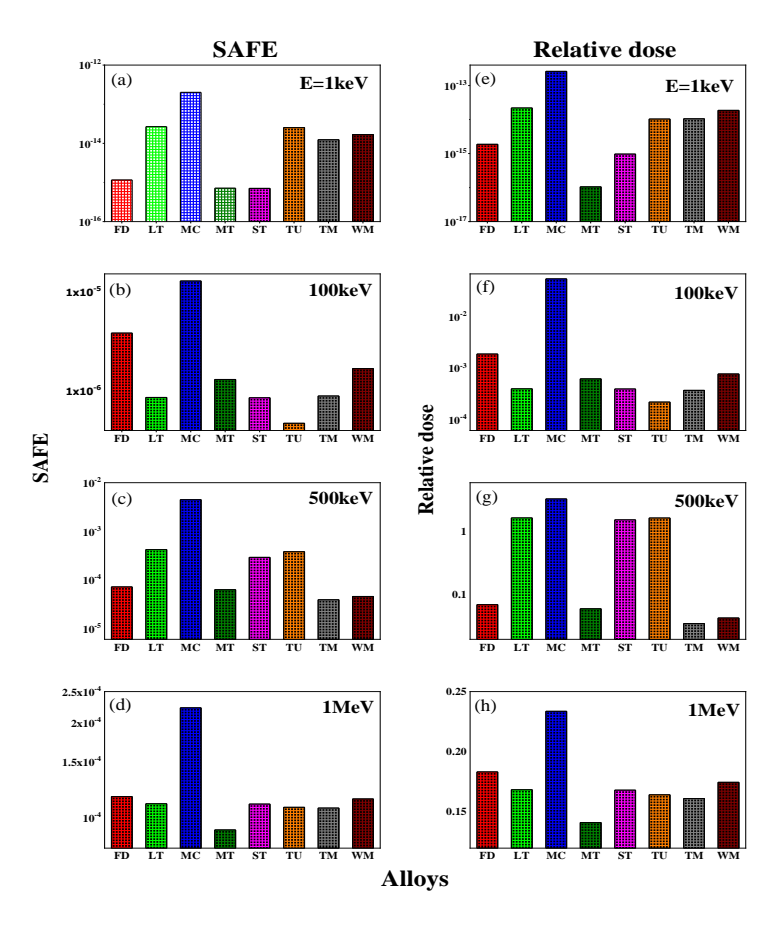


Fig. 3.34 Comparison of SAFE and relative dose for FD, LT, MC, MT, ST, TU, TM and WM binary, tertiary, quaternary alloys at different photon energies

a good absorber. Fig 3.34(a-d) and Fig 3.34 (e-h) shows the comparison of φ and RD at different energies (1 keV, 100 keV, 500 keV, 1 MeV) for all the binary / tertiary / quarternary studied alloys. Fig 3.35 (a and b) depicts the variation of φ and RD of MC binary alloy with thickness. Initially φ value goes on increasing with increase in thickness and reaches the higher value at 0.5 cm thickness and thereafter decreases slowly with increase in the thickness value. As the gamma photon passes through the medium, there is a chance of production of secondary radiation which results in the higher value of φ . As the thickness increases, incident gamma ,X-ray loses its energy and

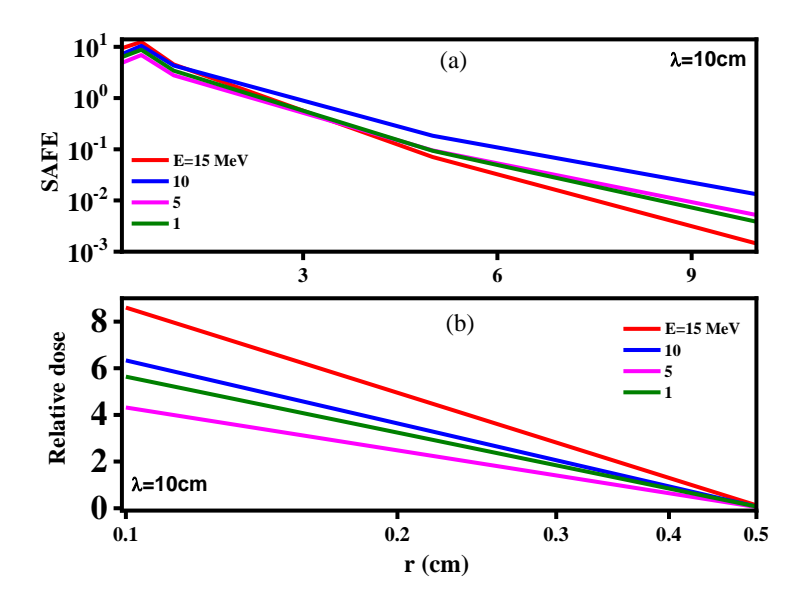


Fig. 3.35 Variation of (a) φ and (b) RD with distance (r) for FD, LT, MC, MT, ST, TU, TM and WM binary / tertiary / quaternary alloys

hence decreases in φ as well as RD.

3.2.4.2 **Neutron shielding parameters**

The comparison of neutron shielding parameters for all the studied binary, tertiary, quarternary alloys is as shown in Fig 3.36 (a-f). This figure compares the (a) coherent neutron scattering length (λ_{co}) , (b) incoherent neutron scattering length (λ_{inc}) (c) coherent neutron scattering cross section (σ_{co}) , (d) incoherent neutron scattering cross sections (σ_{inc}) , (e) total neutron scattering cross section (σ_{tot}) and (f) neutron absorption cross sections (σ_{ab}) for all the selected alloys. Among all the selected alloys, MC binary alloy shows smaller λ_{co} , λ_{inc} , σ_{co} , σ_{inc} . However, larger σ_{tot} and σ_{ab} values are observed. As λ_{co} , λ_{inc} , σ_{co} , σ_{inc} values are less, neutrons collide more frequently in the material. During each such collisions, it loses energy frequently. Further, fig 3.37 shows the comparison of another neutron shielding parameter called Neutron attenuation parameter (NAP) for all the selected alloys. A material which possess smaller λ_{co} , λ_{inc} , σ_{co} , σ_{inc} and high σ_{tot} , σ_{ab} and NAP shows the characteristic behavior of a good absorber. Since MC binary alloy shows all these characteristics and hence it is considered as a good absorber.

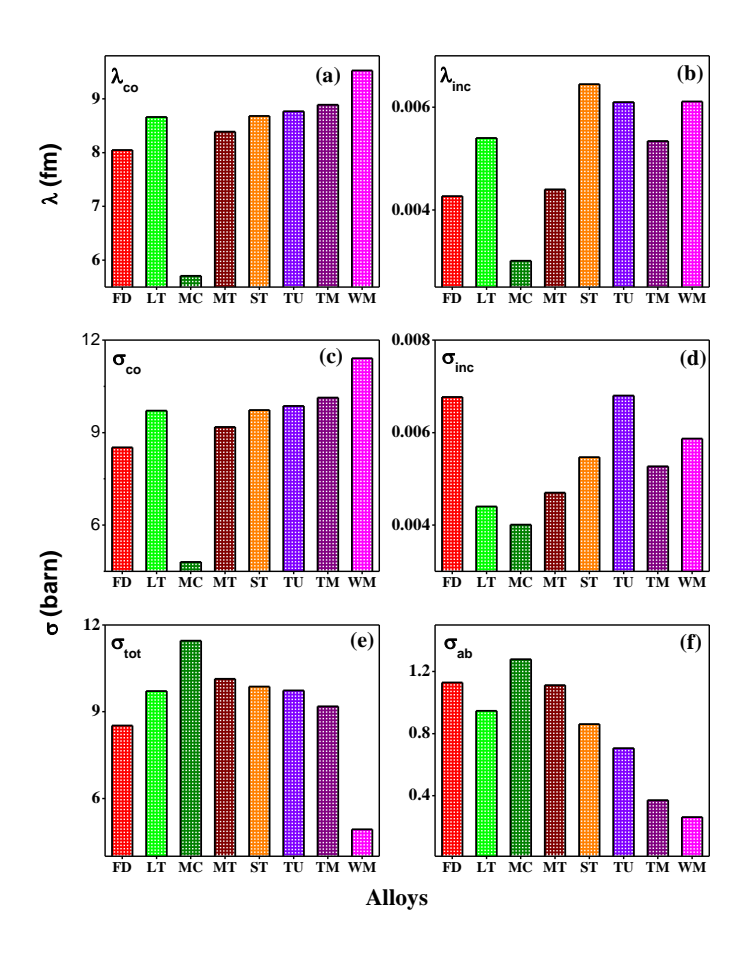


Fig. 3.36 Comparison of neutron shielding parameters for the FD, LT, MC, MT, ST, TU, TM and WM binary / tertiary / quaternary alloys

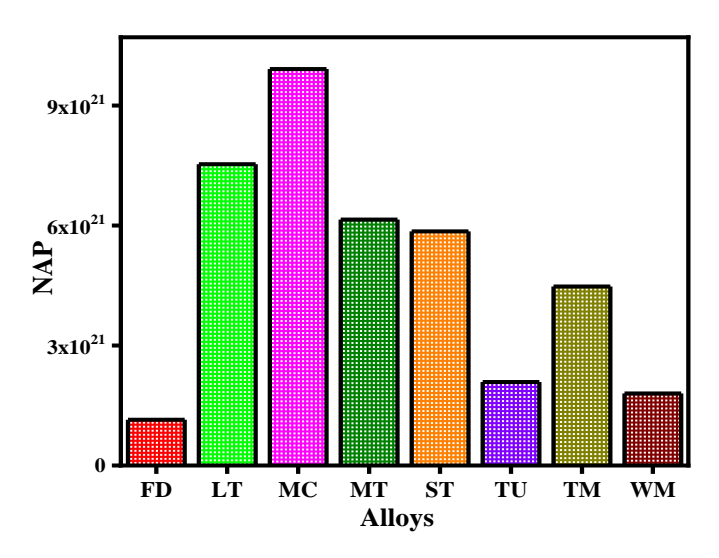


Fig. 3.37 Comparison of neutron attenuation parameters (NAP) for the FD, LT, MC, MT, ST, TU, TM and WM binary / tertiary / quaternary alloys

3.2.5 Aluminium alloys

3.2.5.1 Selection of good shielding material for X-ray,gamma radiation Among Aluminium alloys

The parameters related to X-ray,gamma radiations are studied as explained in theory section. The parameters such as μ/ρ , HVL, λ , n_e , RPE and KERMA coefficient is studied in the selected aluminium alloys such as Aluminium-Lithium(a), Hydronalium(b), Hiduminium(c), Italma(d), Magnalium(e), Nickel-Titanium-Aluminium(f), Duralumin(g) and Y alloy(h) within the energy range 100keV to 100MeV. Figure 3.38(a-h) shows the variation of $\frac{\mu}{\rho}$ as a function of energy E. $\frac{\mu}{\rho}$

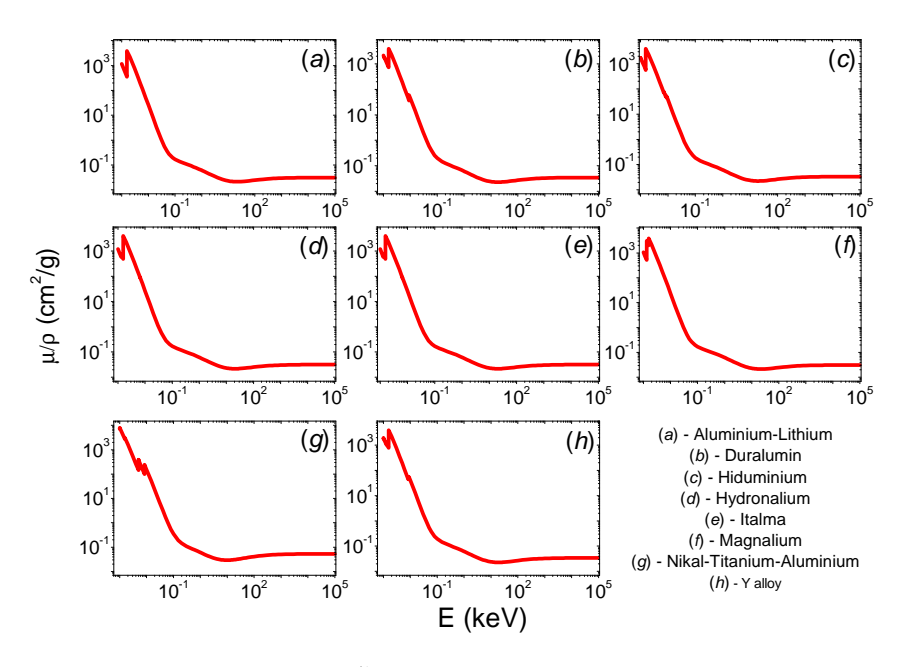


Fig. 3.38 Variation of $\frac{\mu}{\rho}$ versus E for the studied Al alloys.

values are high in the low energy region and exponentially decreases. The photoelectric interaction is more dominant in the lower energy range and Compton scattering becomes dominant in the higher energy range. For an instance, in case of Al-Li (figure 3.38-a) shows a peak at 1.56keV due to photoelectric effect at K-absorption edges of the aluminium. Similarly, in case of Duralium, the K and L_1 absorption edges were absorbed due to Al and Cu. In all the studied aluminium alloys, the K and L absorption edges were observed. The type of alloys studied, corresponding X-ray

Table 3.1 Tabulation of type of alloy, X-ray edge, element and its corresponding energy(MeV).

Type of alloy	X-ray edge	Element	Energy (keV)
Aluminium-Lithium	K	Al	1.56
Duralumin	L1	Cu	1.10
	K	Al	1.56
	K	Cu	8.98
Hiduminium	L1	Ni	1.01
	L1	Cu	1.10
	K	Al	1.56
	K	Fe	7.11
	K	Ni	8.33
	K	Cu	8.98
Hydronalium	K	Mg	1.31
	K	Al	1.56
	K	Mn	6.54
Italma	K	Mg	1.31
	K	Al	1.56
	K	Mn	6.54
Magnalium	K	Mg	1.31
	K	Al	1.56
	L1	Ni	1.01
Nikel-Titanium-	K	Al	1.56
Aluminium	K	Ti	4.97
	K	Ni	8.33
Y alloy	L1	Ni	1.01
	L1	Cu	1.10
	K	Mg	1.31
	K	Al	1.56
	K	Ni	8.33
	K	Cu	8.98

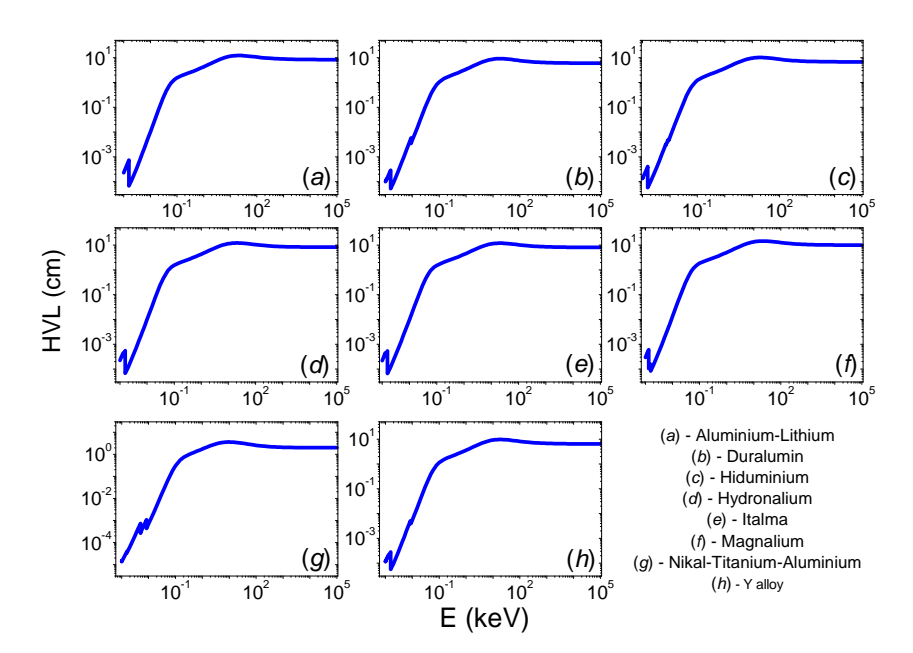


Fig. 3.39 A plot of HVL versus E for the studied Al alloys.

edges with type of element and corresponding energy is tabulated in table 3.1. In all these cases it is noticed that the K absorption edge of Cu is 8.98keV. Similarly, K absorption edge of Al is 1.56keV, L_1 absorption edge of Ni is about 1.01keV, further K-absorption edge of Fe, Mg, Mn and Ti is found to be 7.11keV, 1.31keV, 6.54keV and 4.97keV respectively.

The HVL is the thickness of an absorber that reduces γ radiation to half its original intensity,

whereas, the TVL is the thickness of an absorber that reduces γ radiation to tenth of its original intensity. The HVL and TVL values are extremely valuable for determining the penetration capacity of distinct radiations through specific materials. Thus, the figure 3.39(a-h) shows a plot of HVL as function of energy for different studied alloys. The value of HVL increases with increase in energy and remains almost constant when E>0.1keV. In all these cases, it is clearly visible that sudden dip is observed near the absorption edges which were clearly seen in case of μ/ρ as function of energy (figure 3.38).

Collisions occur as particles travel through a substance, and these collisions might cause their

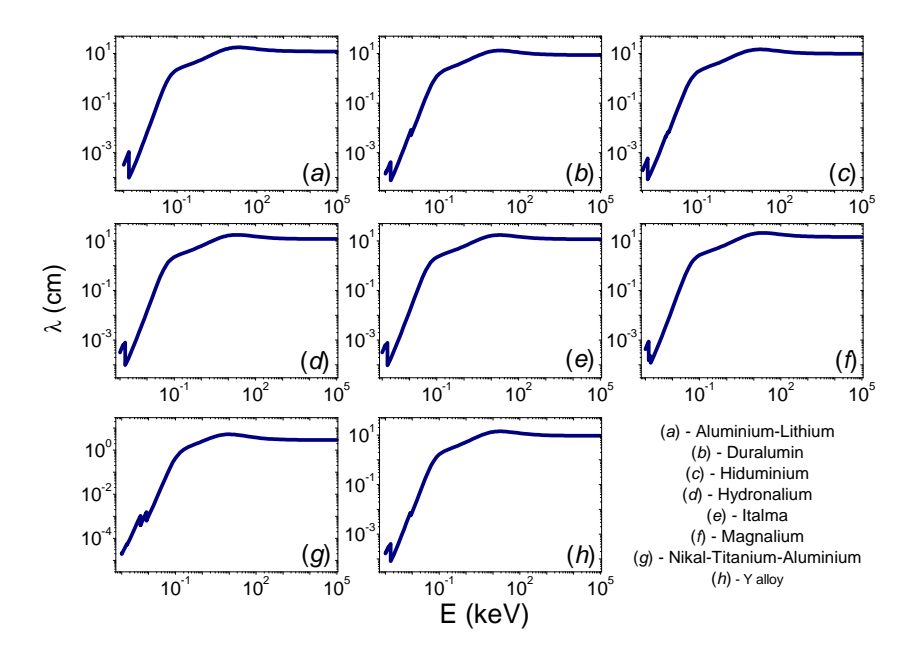


Fig. 3.40 A plot of mean free path (λ) versus energy E for the studied Al alloys.

velocity to alter. As a result, the average distance between these collisions is a measure of the like-lihood of a particular interaction. This distance, commonly referred to as the mean free path. The figure 3.40(a-h) shows a plot of mean free path as a function of energy for different studied alloys. In this case also we have observed a dip similar to HVL which may be due to the absorption edge of element, for an instance in case of Aluminium-Lithium the K-absorption edge was observed for the aluminium element at energy of 1.56keV. Since, photoelectric effect and absorption rate will be more and hence, the mean free path and HVL decreases at this particular energy. Hence,

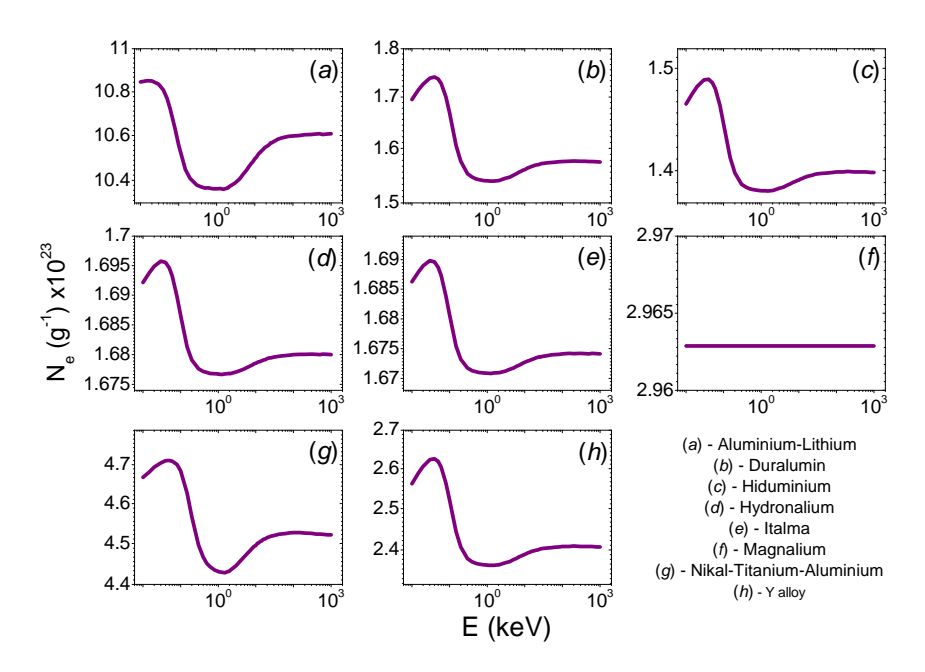


Fig. 3.41 Effective electron density (N_e) versus E for the studied Al alloys.

sudden dip is observed at this energy.

The effective electron per unit of mass of a material is denoted by $N_{el}(g^{-1})$ i.e effective electron density. Figure 3.41(a-h) shows the variation of N_{el} with energy for the investigated aluminium alloys. It is obvious from this diagram that N_e values are high in the low energy region (due to photoelectric effect) and gradually decreases, then it gradually increases and become constant in the high energy region which is due to pair production. However, in case of Magnalium, no variation is observed which may be due to the less effect of photoelectric and pair production in that particular element.

RPE is a critical metric for determining a shielding material's performance. RPE is evaluated at different thickness such as t=1, 10 and 40cm for different studied aluminium alloys.. The figure 3.42 depicts the variation of RPE with energy for the investigated aluminium alloys at various thicknesses. The efficiency of protection of the radiation gradually increase with thickness for all of the investigated aluminium alloys at a given energy and it is maximum for a thickness of 40 cm. However, in each thickness the RPE decreases with increase in energy and remains almost constant above 10keV.

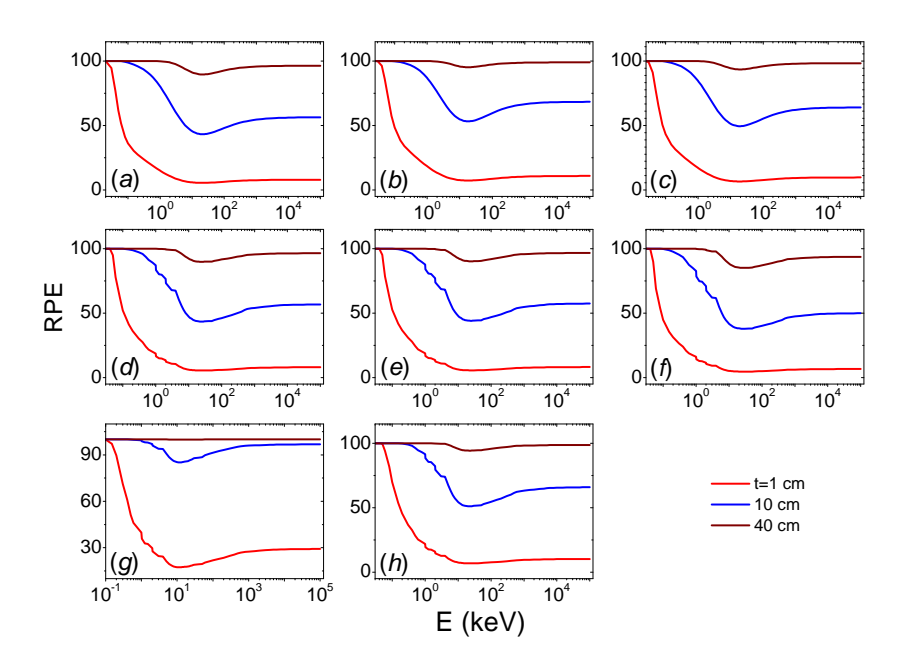


Fig. 3.42 Radiation protection energy (RPE) versus E for the studied Al alloys at different thickness.

Table 3.2 Tabulation of gamma shielding parameters for selected Ni-Ti-Al alloy.

Interaction	Value corresponding
parameter	to the parameter
$\mu/\rho \ (cm^2g^{-1})$	7913.09
$\mu (cm^{-1})$	51765.84
HVL (cm)	3.63
TVL (cm)	12.08
Z_{eff}	24.4
RPE	100.0
λ (cm)	5.24
$N_{el} (electrons g^{-1})$	4.71E+23
KERMA	1.49E-08

Best shielding material is identified by comparing all the studied parameters for X-ray, gamma radiation. Fig 3.43(a-f) shows a comparison of μ/ρ , HVL, λ , N_e , radiation shielding effectiveness and KERMA coefficient for the investigated aluminium alloys at 661 keV. The HVL and photon λ are small for Ni-Ti-Al alloy, whereas μ/ρ , N_e , RPE and KERMA coefficient are highest for Ni-Ti-Al alloy at an energy of 661keV among the studied aluminium alloys. The values corresponding to Ni-Ti-Al for the different parameters is tabulated in table 3.2.

Furthermore, the absorbed dose rate of gamma radiation in different aluminium alloys are

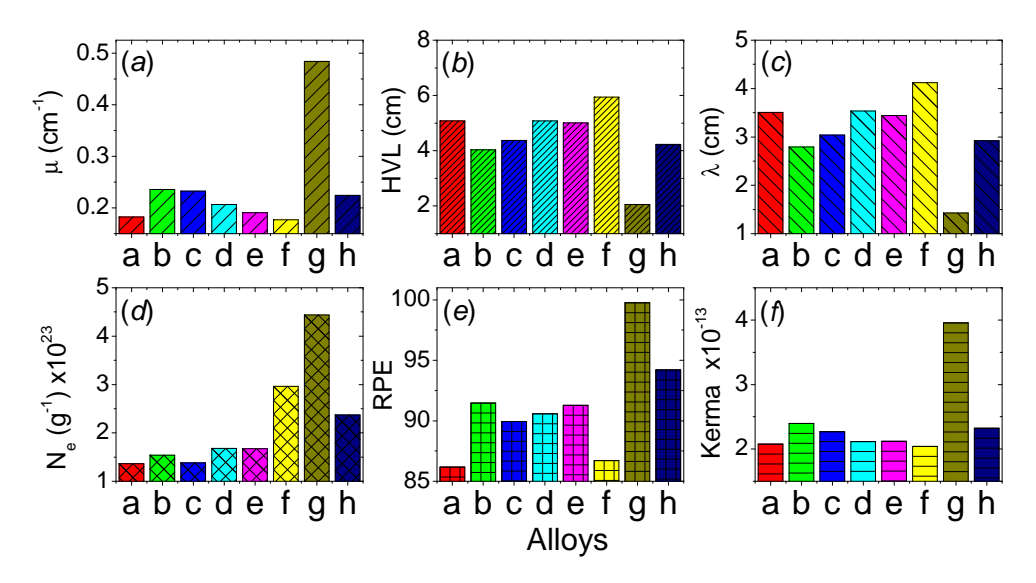


Fig. 3.43 Comparison of different shielding parameters such as (a) μ , (b) HVL, (c) λ , (d) N_e , (e) RPE and (f) KERMA coefficient for the studied Al alloys at an energy of 661 keV. Name of the alloys are given in section 3.2.5.1.

measured from the different sources such as 154 Eu, 22 Na, 137 Cs, 60 Co and 135 I in the energy range of 0.123MeV to 1.33MeV. Figure 3.44(a) shows comparison between all the studied aluminium alloys from 154 Eu source at an energy of 0.123MeV with the longer lifetime of 16years. Among these studied alloys, the Ni-Ti-Al alloy is a good absorber of gamma radiation and Al-Li alloy is a weak absorber of gamma radiation. Similarly, different gamma radiations have been investigated from different sources such as 22 Na, 137 Cs, 60 Co and 135 I and their comparison with aluminium alloys are shown in figure 3.44(b-f). Among all the studied absorbed dose rate of γ -radiation using distinct gamma sources, it is observed that Ni-Ti-Al alloy is a good absorber of gamma radiation. Hence, detail investigation on X-ray and gamma radiation shows good shielding properties for Ni-Ti-Al alloy. As a result, it can deduce that the Ni-Ti-Al alloy will absorb more X-ray/ γ radiations than the other aluminium alloys studied.

3.2.5.2 Selection of good shielding material for neutron shielding parameter

The shielding capability of material also depends on neutron cross sections and scattering lengths. Neutron scattering lengths such as λ_{co} and λ_{inc} , neutron cross sections such as σ_{co} , σ_{inc} ,

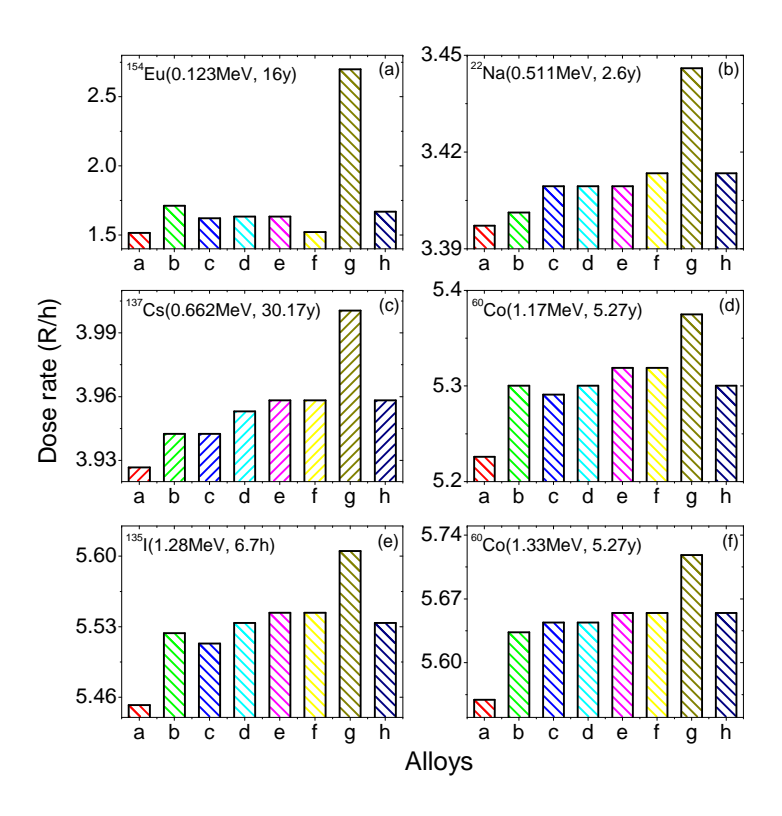


Fig. 3.44 Comparison of gamma dose rate of the studied Al alloys for distinct energies ranging from 0.123MeV to 1.33MeV. Name of the alloys are given in section 3.2.5.1.

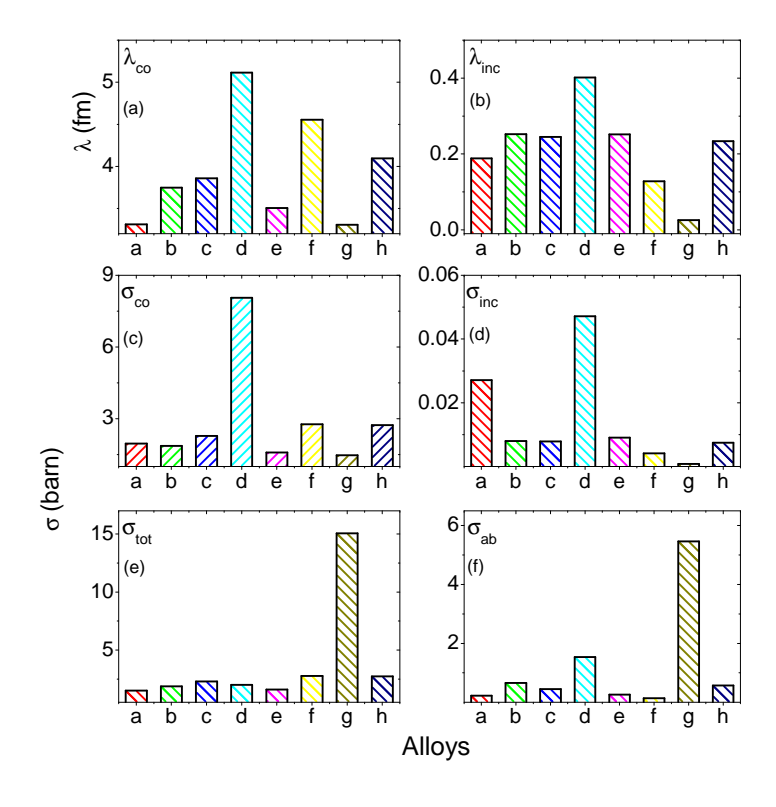


Fig. 3.45 Correlation of studied (a) (λ_{co}) and (b) (λ_{inc}) . A comparison of (c) coherent (σ_{co}) (d) incoherent (σ_{inc}) , (e) total (σ_{tot}) and (f) neutron absorption cross sections (σ_{ab}) for aluminium alloys. Name of the alloys are given in section 3.2.5.1.

 σ_{tot} and σ_{ab} for different aluminium alloys were studied. The figure 3.45(a-f) shows a plot of neutron scattering lengths and cross sections. From figure 3.45(a) and (b) it is clear that Ni-Ti-Al alloy posses smaller coherent and incoherent scattering lengths and larger in case of Hydronalium alloy. However, Al-Li aquires smaller coherent neutron scattering lengths. Similarly, shorter coherent, incoherent and larger total and absorption cross sections. Further, the Hydronalium alloy shows larger value of coherent and incoherent scattering when compared to other studied alloys. The detail investigation shows that smaller neutron scattering lengths, larger total and absorption cross sections in Ni-Ti-Al. Hence, these parameters suggests that Ni-Ti-Al alloy is good material for neutron shielding when compared to other aluminium alloys studied.

3.2.5.3 Selection of good shielding material for electromagnetic shielding parameter Among AL-Alloys.

Further, the electromagnetic shielding parameters for different aluminium alloys have been investigated . Electromagnetic radiations not only depends on wavelengths but also depends on its energy and frequency. A wide range of wavelength from radio waves $(10^4 \text{ to } 10^2) \text{ cm}$ to infrared radiation (IR) 10^{-2}cm were considered. In order to investigate electromagnetic shielding properties of different aluminium alloys, different radiations with different frequencies have been considered . Figure 3.46(a) to (I) shows a comparison of different aluminium alloys at different frequencies. The infrared radiation ranging between near IR, mid IR and far IR with the frequency ranging between $4 \times 10^{14} \text{Hz}$ to $3 \times 10^{12} \text{Hz}$. Further, microwave region with the frequency of $3 \times 10^{11} \text{Hz}$ and radiowave (Rw) frequency ranging from ultra high frequency (UHF) range, very high frequency range (VHF), high frequency (HF), medium frequency (MF), low frequency (LW), very low frequency (VLF), ultra low frequency (ULF) and extreme low frequency (ELF) whose frequencies ranges between $3 \times 10^9 \text{Hz}$ to 30 Hz as seen in figure 3.46. From the figure it is clear

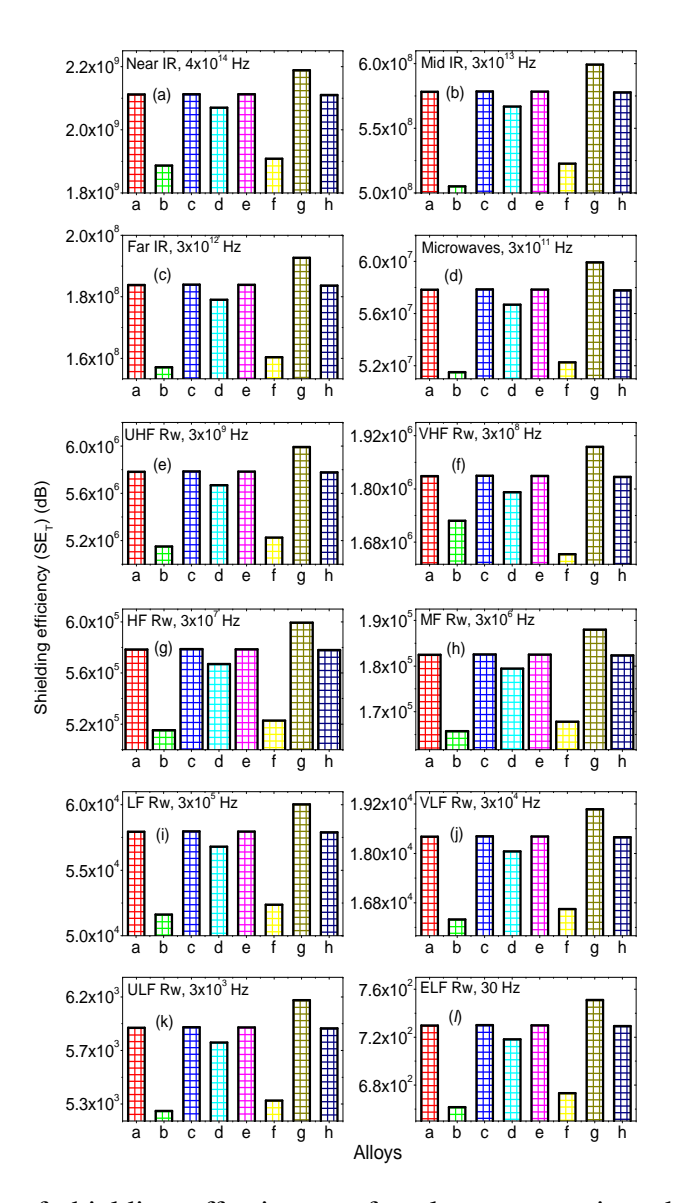


Fig. 3.46 Comparison of shielding effectiveness for electromagnetic radiation at different frequency range from radio waves to infrared radiations in different studied aluminium alloys. Name of the alloys are given in section 3.2.5.1.

that, Ti-Ni-Al alloy shows larger value of shielding efficiency when compared to other studied alloys at all the studied frequencies. Hence, Ti-Ni-Al alloy reveals larger shielding efficiency when compared to other aluminium alloys.

3.2.5.4 Selection of good shielding material for Bremsstrahlung among Aluminium alloy

 β -emitters with energy range 0.6 to 3 MeV were considered during an evaluation. Around 21 β -emitters were considered and these are taken from the table I of available literature [272].

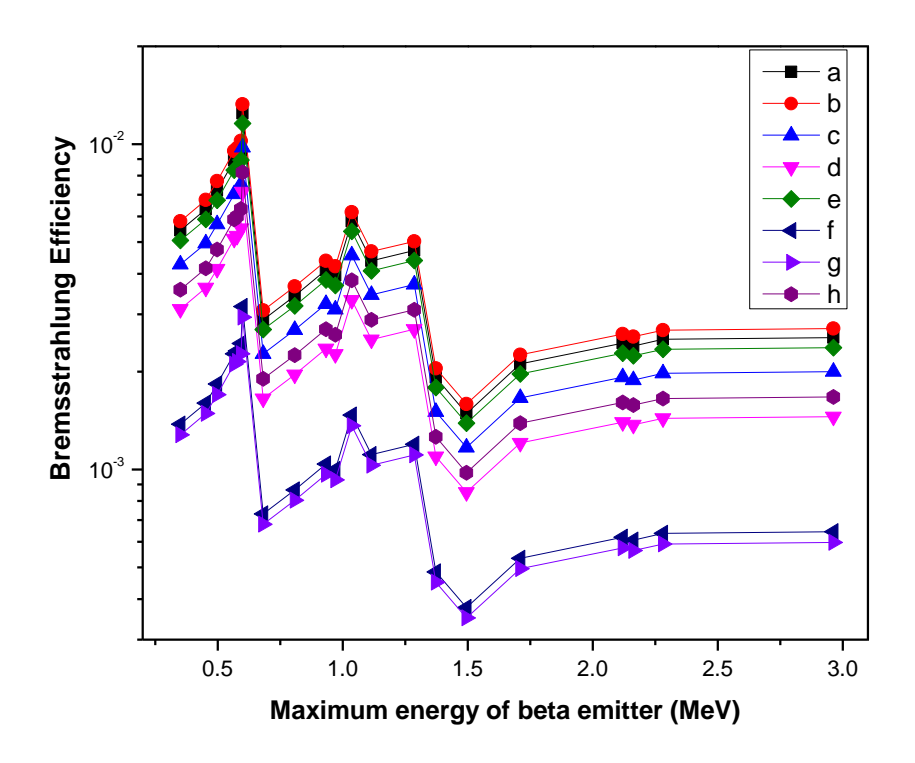


Fig. 3.47 Variation of Bremsstrahlung efficiency as a function of maximum energy of beta emitters for the studied aluminium alloys. Name of the alloys are given in section 3.2.5.1.

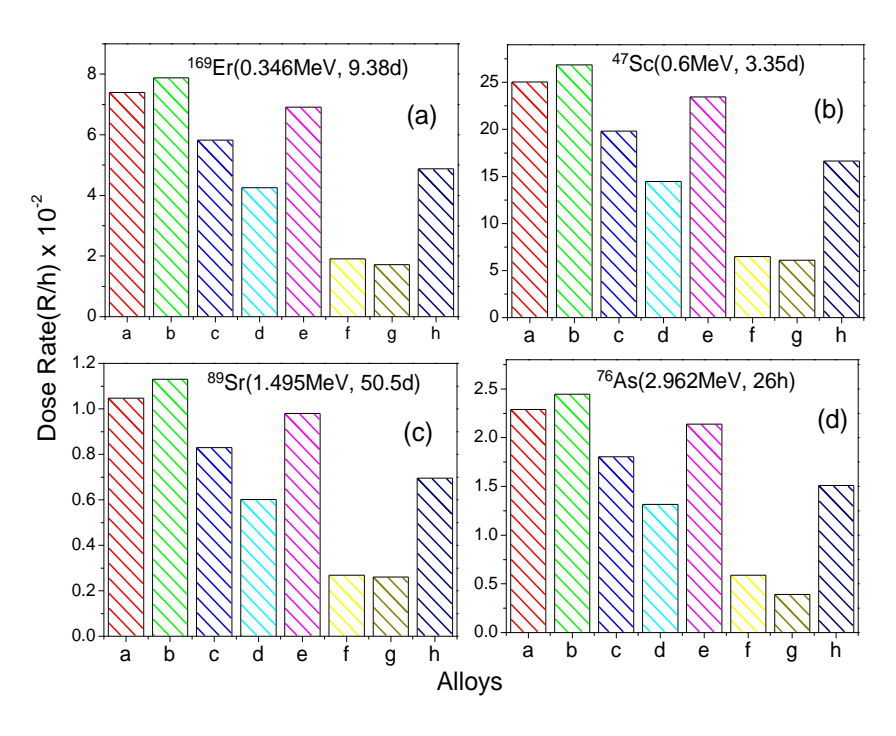


Fig. 3.48 Comparison of Bremsstrahlung dose rate for the different studied aluminium alloys in (a) 169 Er at an energy of 0.351MeV, (b) 47 Sc at an energy of 0.6MeV, (c) 89 Sr at an energy of 1.495MeV and (d) 76 As at an energy of 2.962MeV. Name of the alloys are given in section 3.2.5.1.

Bremsstrahlung efficiency, dose rate and probability of energy loss i.e P_{Br} is evaluated as explained in theory. Fig 3.47 shows a variation of Bremsstrahlung efficiency as a function of maximum.

mum energy of beta emitters for the studied aluminium alloys. It is evident from the figure that no systematic variation is observed for Bremsstrahlung efficiency as a function of energy. It is obvious from the figure that, the Bremsstrahlung efficiency is larger for the ⁴⁷Sc beta emitter at an energy of 0.6MeV and shorter for ⁸⁹Sr beta emitter at 1.495MeV. Among the studied aluminium alloys, Duralium shows larger Bremsstrahlung efficiency and Ni-Ti-Al posses shorter Bremsstrahlung efficiency when compared to other studied aluminium alloys.

The Bremsstrahlung dose rate for the studied aluminium alloys has been compared with ¹⁶⁹Er, ⁴⁷Sc, ⁸⁹Sr and ⁷⁶As at 0.346MeV, 0.6MeV, 1.495MeV and 2.962MeV energies respectively. Figure 3.48(a-d) shows comparison of dose rate for the studied alloys in case of ¹⁶⁹Er, ⁴⁷Sc, ⁸⁹Sr and ⁷⁶As beta emitters. From this comparison it is clear that the Duralium shows larger dose rate when compared to other studied aluminium alloys for the studied beta emitters. Whereas, the Ni-Ti-Al alloy shows shorter dose rate in case of ¹⁶⁹Er, ⁴⁷Sc, ⁸⁹Sr and ⁷⁶As beta emitters. Hence, among the studied different aluminium alloys, the Ni-Ti-Al alloy posses shorter dose rate.

In addition, the probability of energy loss during Bremsstrahlung interaction of β -particle is studied using different beta emitters such as 169 Er, 47 Sc, 89 Sr and 76 As at an energy of 0.346MeV, 0.6MeV, 1.495MeV and 2.962MeV respectively. The figure 3.49(a-d) shows comparison of the $(P_{Br})_{\beta}$ for the different alloys in case of 169 Er, 47 Sc, 89 Sr and 76 As β -emitters. Similar to dose rate, here also we have observed larger $(P_{Br})_{\beta}$ in case of Duralium when compared to other studied aluminium alloys. Whereas, the Ni-Ti-Al alloy shows shorter $(P_{Br})_{\beta}$ in case of 169 Er, 47 Sc, 89 Sr and 76 As beta emitters. Hence, among the studied different aluminium alloys, the Ni-Ti-Al alloy posses shorter probability of energy loss during Bremsstrahlung interaction of β -particle.

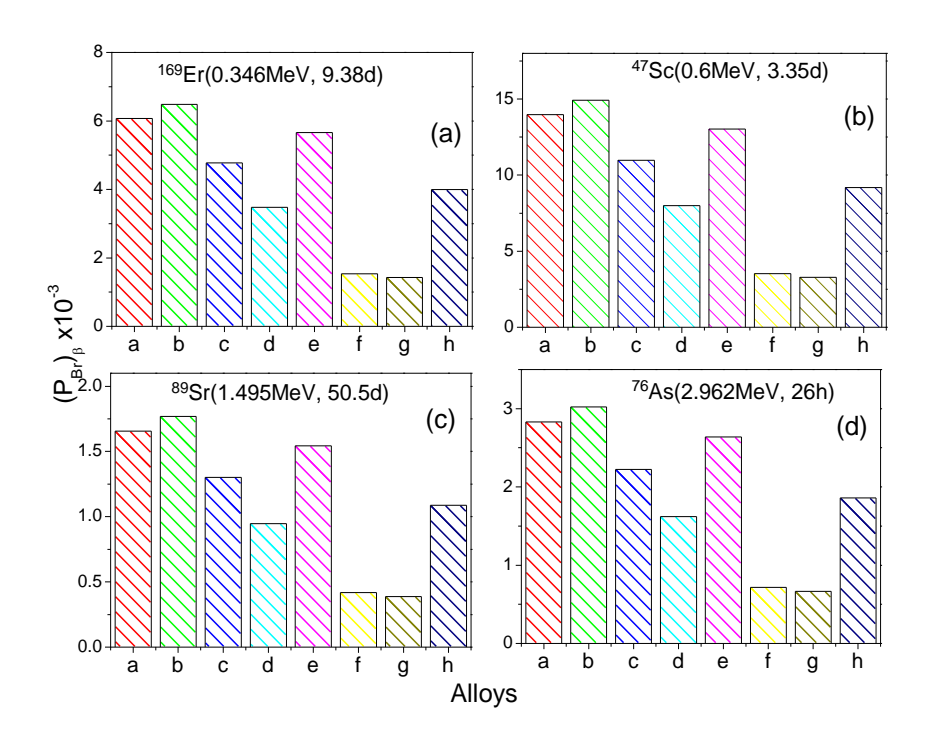


Fig. 3.49 Comparison of probability of energy loss during Bremsstrahlung interaction for the studied aluminium alloys in different beta emitters i.e (a) 169 Er at an energy of 0.351MeV, (b) 47 Sc at an energy of 0.6MeV, (c) 89 Sr at an energy of 1.495MeV and (d) 76 As at an energy of 2.962MeV. Name of the alloys are given in section 3.2.5.1.

3.2.6 Silicon-boron alloys

3.2.6.1 Selection of best X, γ radiation absorber among Si-B alloys

The μ/ρ values are calculated for the selected silicon boron alloys Si_{0.95}B_{0.05}(SB1),Si_{0.9}B_{0.1}(SB2), Si_{0.8}B_{0.2}(SB3), Si_{0.7}B_{0.3}(SB4), Si_{0.6}B_{0.4}(SB5), and Si_{0.5}B_{0.5}(SB6). SB1, SB2, SB3, SB4, SB5 and SB6 from 1keV to 100 GeV enery band 3.50. From the nature of the graph it is found that μ/ρ values for SiB alloys are high in the low energy region ,is due to the dominant photoelectric interaction. In the high energy region, Compton scattering becomes dominant and hence μ/ρ values becomes smaller. Fig. 3.50 (a-f) gives the pictorial representation of μ/ρ with photon energies in the range 1-1.8keV, 1.8-100 keV, 150keV-1MeV, 1-10 MeV, 11-100 MeV and 150MeV-100 GeV respectively. In the energy region 1keV - 10 MeV, the variation of μ/ρ value is almost same where initially μ/ρ is maximum and decreases progressively. In the energy region 11-100 MeV, μ/ρ value starts to increase slowly and remains almost constant in the energy region 150 MeV - 100

GeV. In all the range of energy, SB1 possess larger μ/ρ value whereas SB6 possess smaller value among the studied Si-B alloys.

In addition to μ/ρ , the shielding parameters for the selected Si-B alloys in the energy range

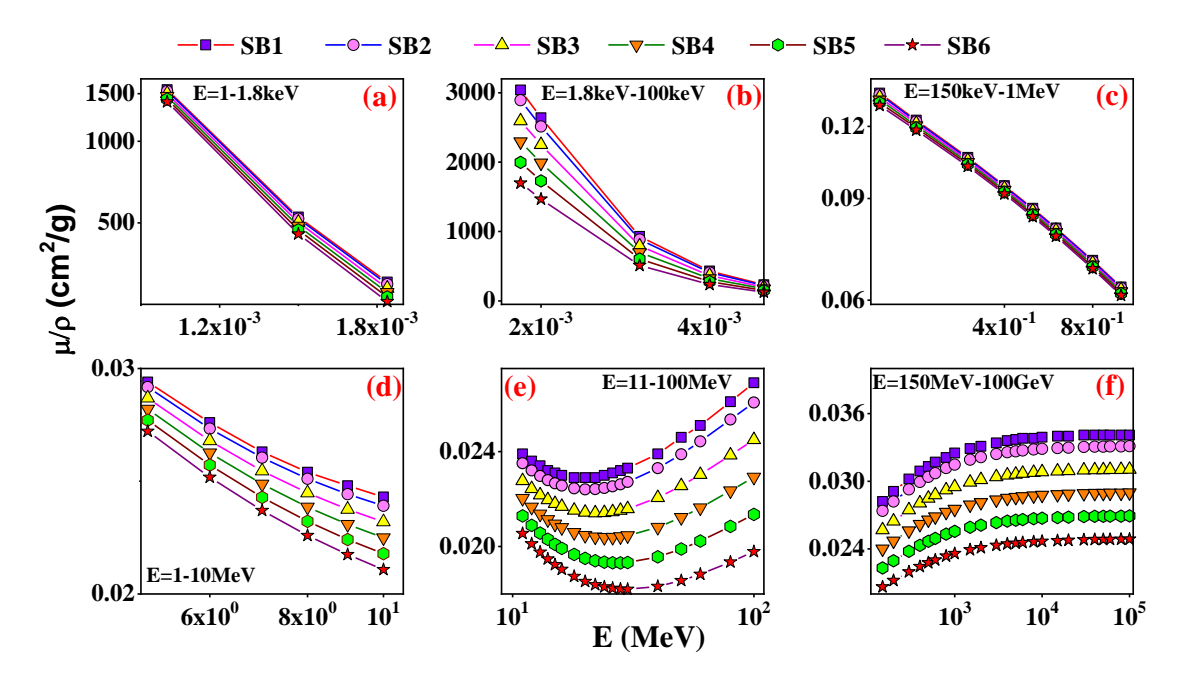


Fig. 3.50 Variation of mass attenuation coefficient (cm^2g^{-1}) as a function of energy (MeV)

1-100 GeV are discussed in detail. Fig. 3.51 (a-f), Fig. 3.52 (a-f) shows the variation of HVT and TVT in the energy range 1-1.8keV, 1.8-100 keV, 150keV-1MeV, 1-10 MeV, 11-100 MeV and 150MeV-100 GeV for all the selected Si-B alloys respectively. Both HVL and TVL shows the linear variation with photon energy upto 10 MeV and thereafter slight variations are observed. The HVL and TVL value remains almost constant in the energy range 150MeV-100 GeV. HVL and TVL found to be smaller for SB1 and larger for SB6.

The material having less penetration depth will be a good absorbing material. 3.53 (a-f) shows the variation of penetration depth with $E_{h\nu}$ of all alloys from 1-1.8keV, 1.8-100 keV, 150keV-1MeV, 1-10 MeV, 11-100 MeV and 150MeV-100 GeV. Among the selected Si-B alloys, SB1 possess smaller penetration depth whereas SB6 possess larger penetration depth. Hence SB1 is a good absorber.

The pictorial representation of \mathbf{Z}_{eff} for selected Si-B alloys in different energy regions is

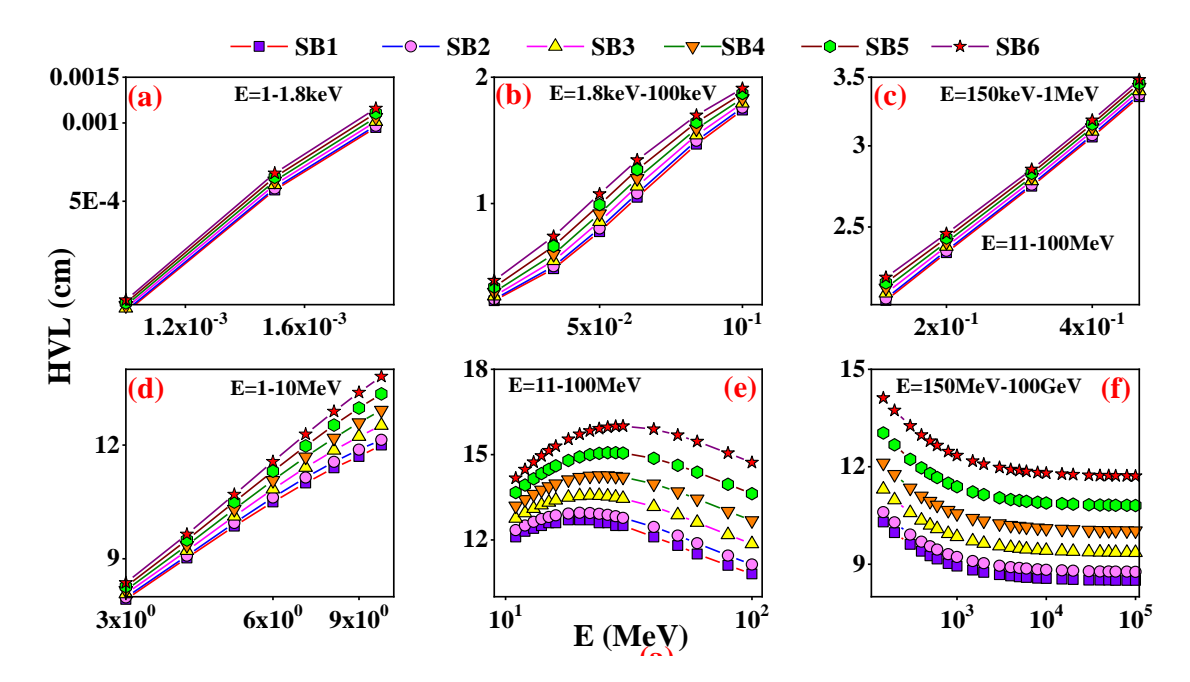


Fig. 3.51 Variation of half value layer (HVL) (cm) as a function of energy (MeV)

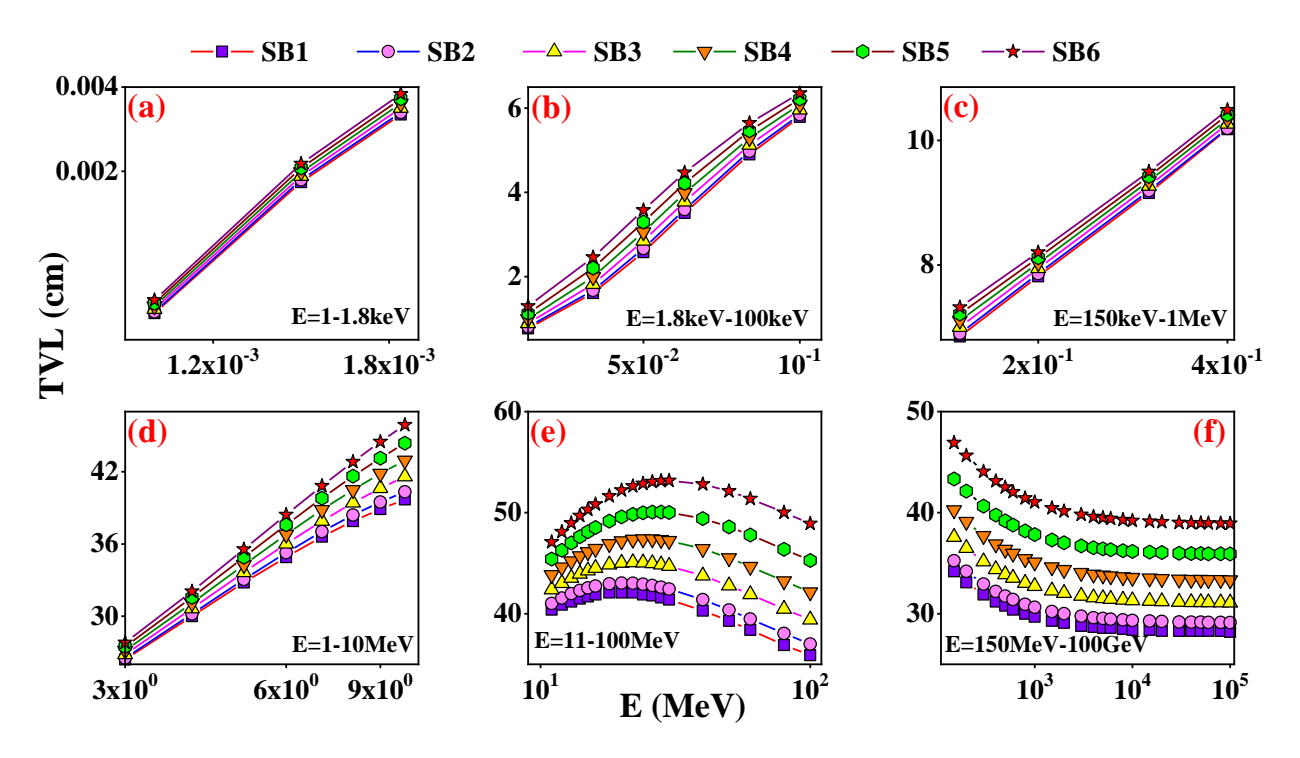


Fig. 3.52 Variation of tenth value layer (TVL) (cm) as a function of energy (MeV)

given in fig 3.54 (a-f). Generally, for any material, Z_{eff} increases with increase in photon energy. The Z-dependence of the radiative process is higher than that of the collisional process. Higher Z_{eff} values in the high energy range are well explained by this condition, especially for materials containing high Z elements as components. As we observed from the fig 3.54 (a-f), since the

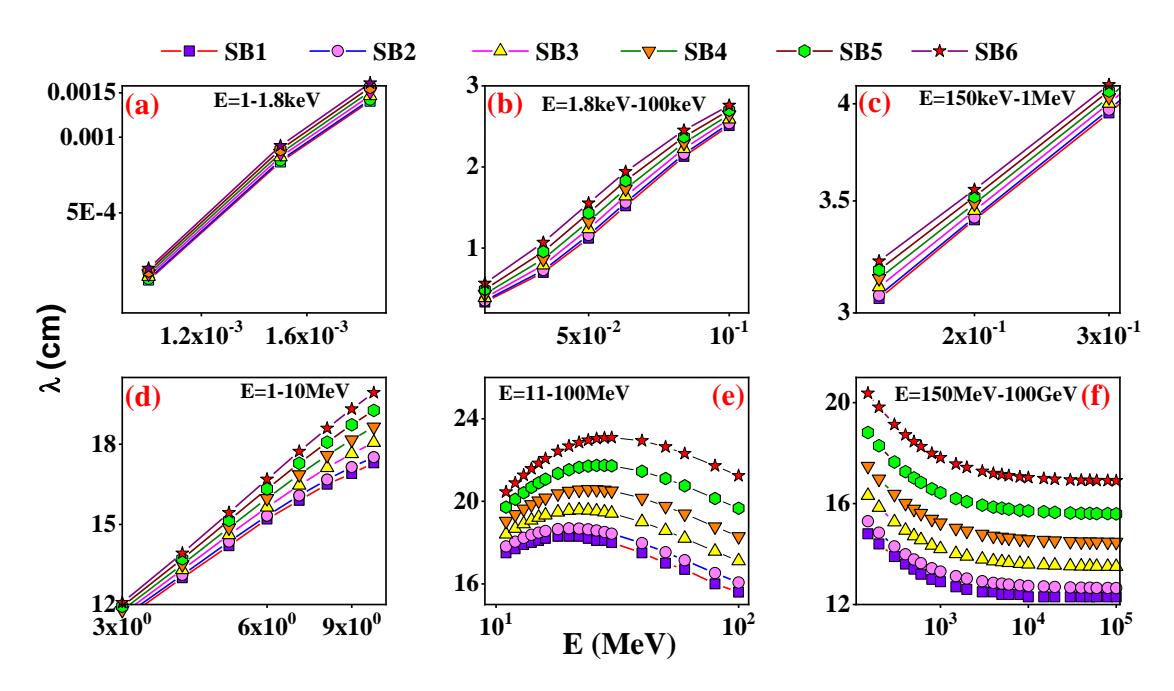


Fig. 3.53 Variation of mean free path (λ) (cm) as a function of energy (MeV)

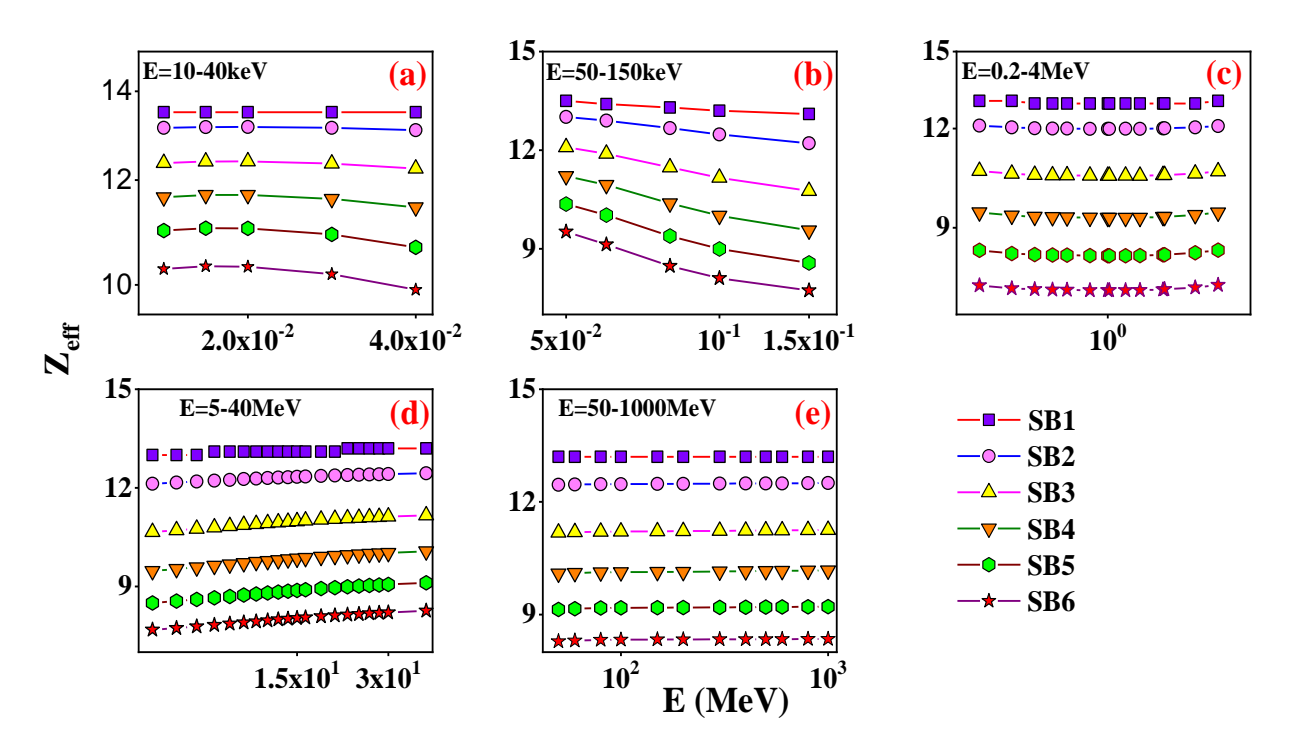


Fig. 3.54 Variation of effective atomic number (Z_{eff}) as a function of energy (MeV)

Si-B alloys consists low Z elements, no such significant variations of Z_{eff} with photon energy are observed.

The dependance of effective electron density with the photon energy as shown in fig 3.55 (a-f). Both Z_{eff} and N_{el} was found to be larger for SB1 and smaller for SB6.

The buildup factor is a function of photon energy and penetration depth[273]. Thus, the

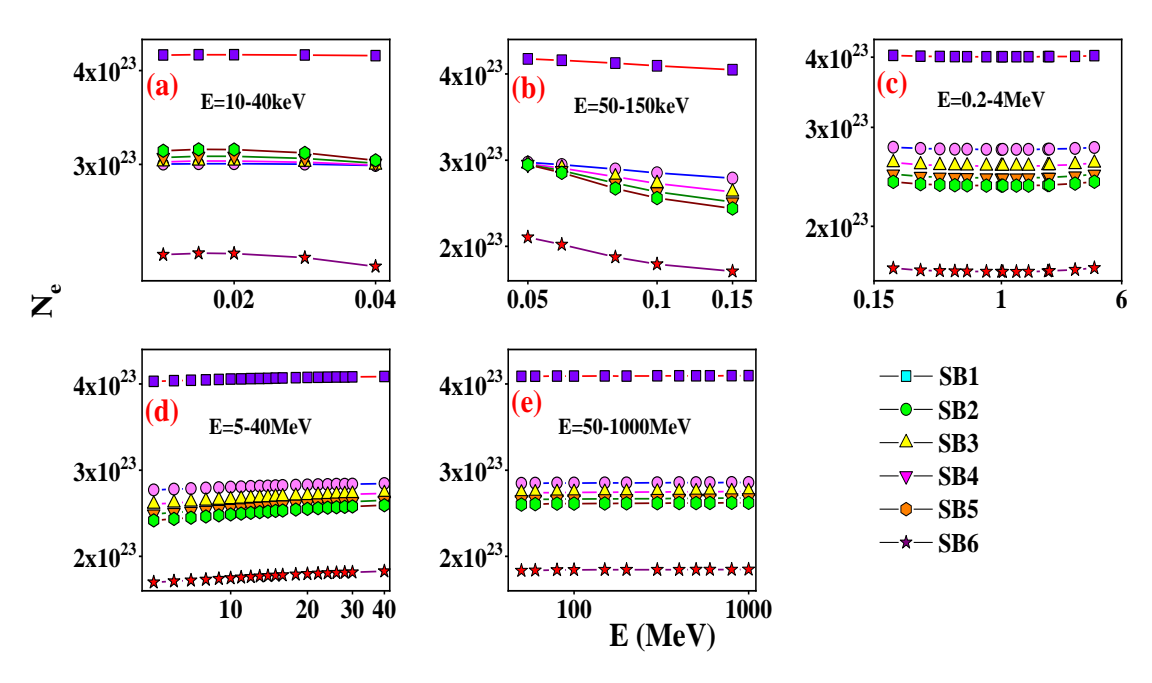


Fig. 3.55 Variation of electron density (N_e) as a function of energy (MeV)

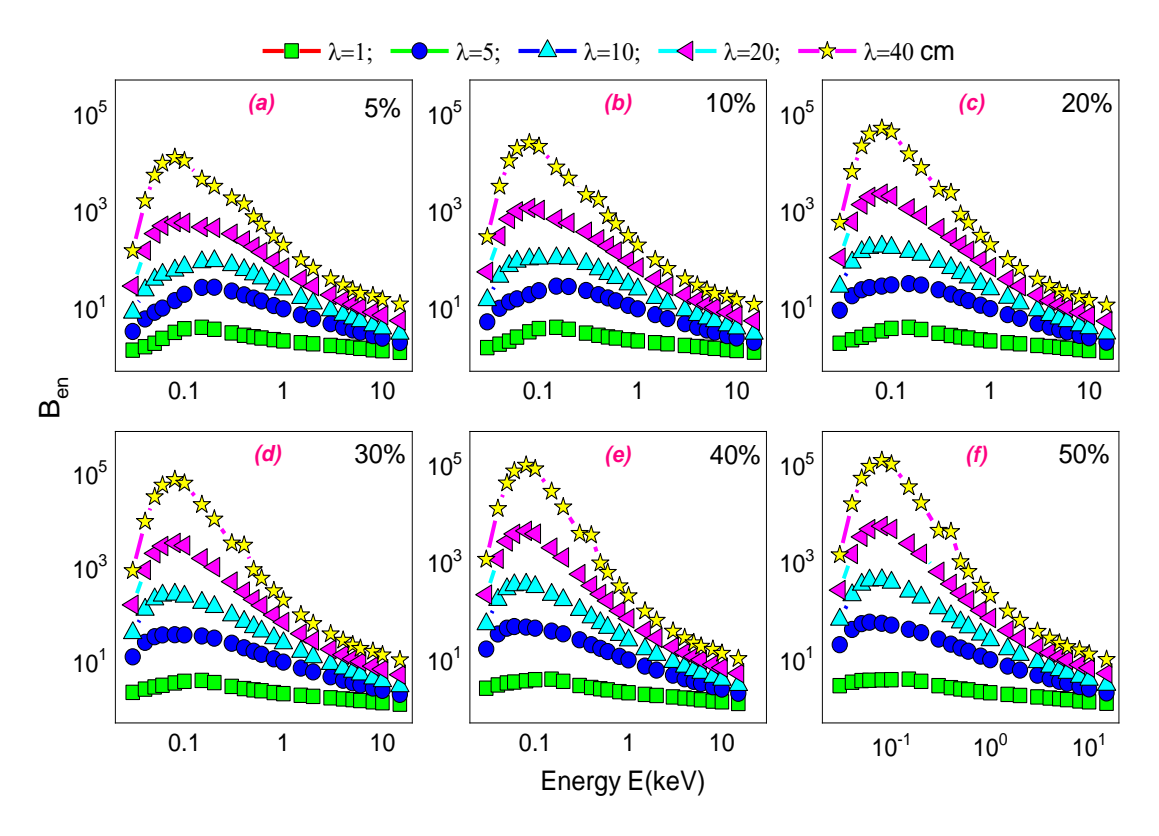


Fig. 3.56 Variation of B_{en} with that of energy for different mean free paths and for different boron concentrations.

variation of buildup factor (B_{en}) was studied as a function of photon energy and penetration depth

(1, 5, 10, 20 and 40 cm) for all the selected alloys. At a particular penetration depth, in the lower energy zone, B_{en} is also low, as the energy increases, B_{en} slowly increases and become maximum at a particular photon energy and further decreases. The photoelectric effects, in which all photons are entirely eliminated from the material in the low energy area, could explain the low B_{en} values. The B_{en} values increases with increasing energy in the intermediate energy zone, possibly due to the dominance of Compton scattering, but pair production dominates in the high energy region and B_{en} value decreases as it is observed in fig 3.56 (a-f)).

The performance of the selected alloys in attenuation of gamma, X-ray photons is also studied

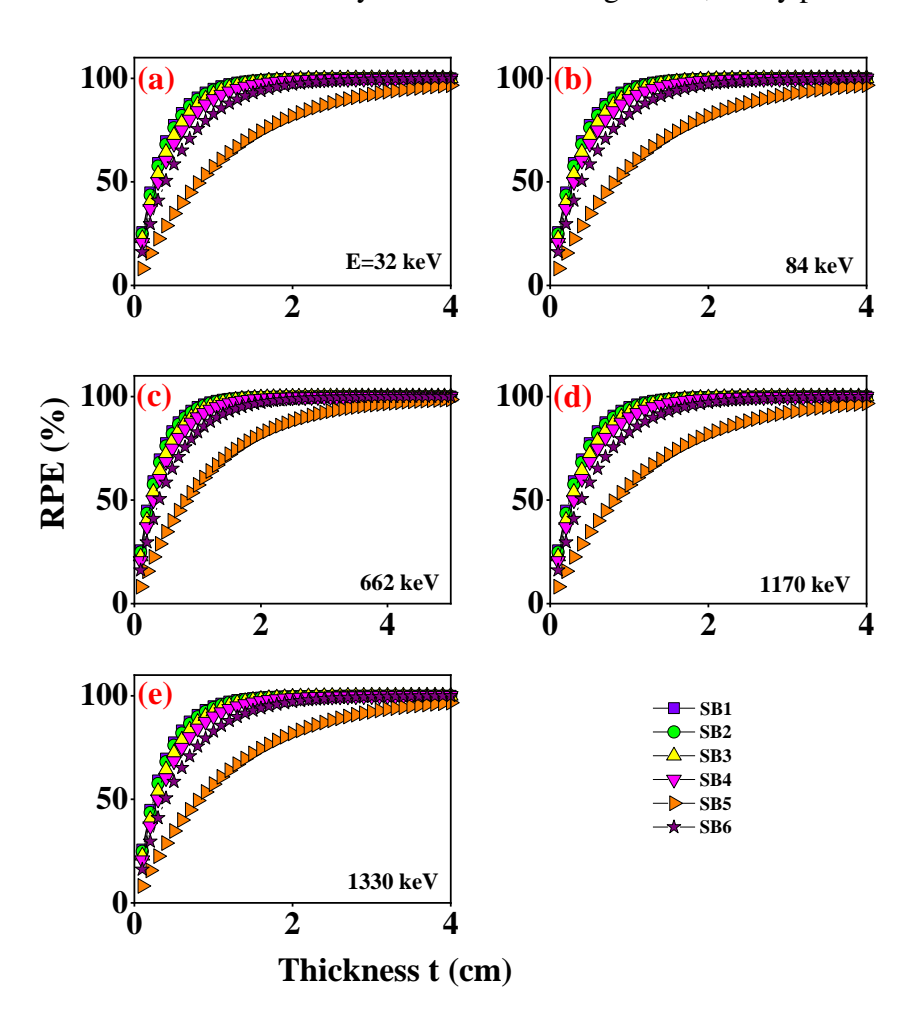


Fig. 3.57 Variation of RPE of various alloys with that of thickness of alloys at different energies in keV.

in terms of radiation protection efficiency (RPE) and kinetic energy released in matter (KERMA). Fig 3.57 (a-e) depicts the variation of RPE with thickness for the selected alloys at the energy 32,

84, 662, 1170 and 1330 keV. As the thickness increases the RPE increases exponentially and thereafter remains constant. The nature of the RPE variation almost remains same for all the selected alloys for the energy under study. Fig 3.58 depicts the variation of KERMA coefficient as a func-

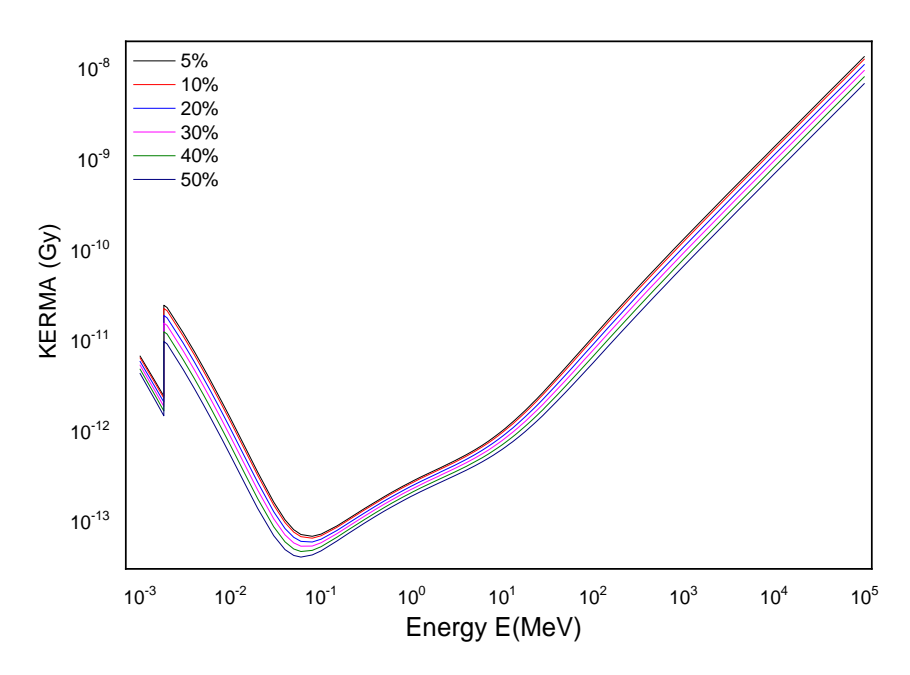


Fig. 3.58 Variation of KERMA with that of energy for different boron concentrations.

tion of energy for the selected alloys. The RPE and KERMA value was found to be larger for SB1 compared to other selected alloys. From the detailed study, it is observed that μ/ρ , HVL, TVL and penetration depth found to be smaller for SB1, whereas RPE, B_{en} and KERMA value found to be maximum for SB1 compared to other selected alloys. This clearly indicates that among the selected Si-B alloys, SB1 might be a good gamma / X-ray radiation absorber. Fig 3.59(a-i) depicts the variation of μ/ρ , TVL, HVL, penetration depth, Z_{eff}, N_{el}, RPE, specific gamma ray constant and KERMA with different Boron concentration at 662, 1170 and 1330 keV photon energy.

In addition to above parameters, lead equivalent thickness (d_{pb}) was calculated for all the selected Si-B alloys at different energies. The variation of d_{pb} as a function of energy for studied alloys are shown in fig3.60. The d_{pb} value increases with increase in photon energy and reaches the maximum at a particular value. At all energies, d_{pb} value was found to be larger for SB1 compared to other selected Si-B alloys as shown in fig. 3.60.

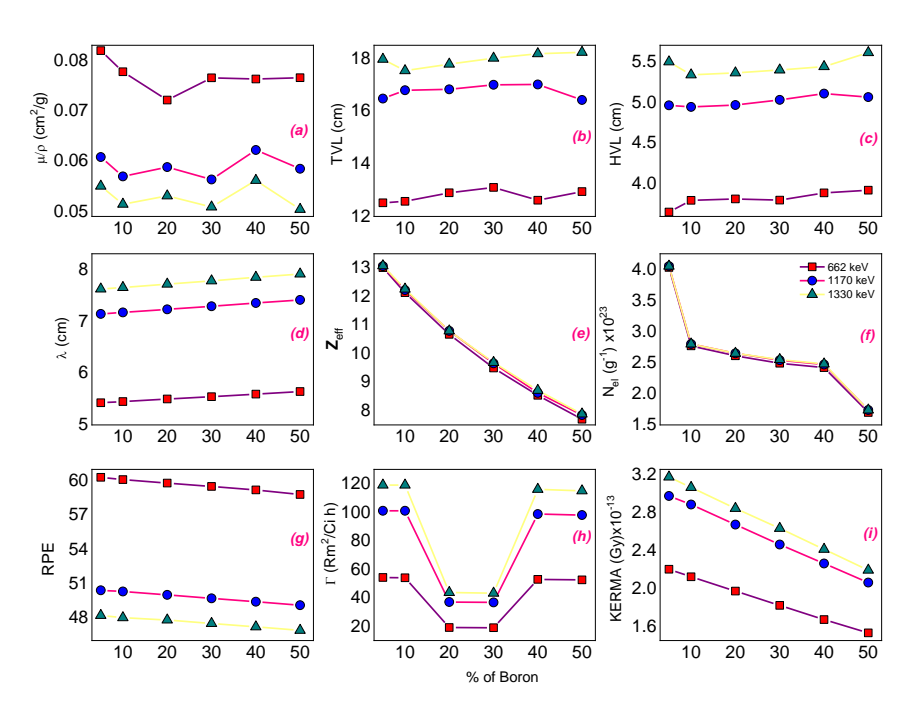


Fig. 3.59 Variation of (a) μ/ρ , (b) TVL, (c) HVL, (d) λ , (e) Z_{eff} , (f) N_e , (g) RPE, (h) SGR (Γ) and (i) KERMA with that of boron concentrations for different energies.

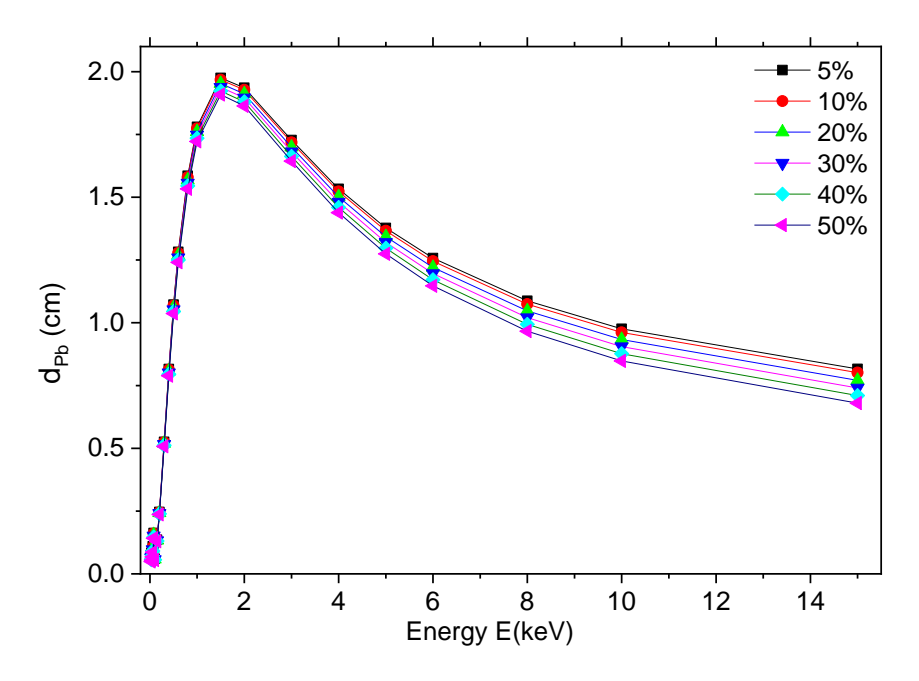


Fig. 3.60 Variation of lead equivalent distance (d_{Pb}) with that of energy for different boron concentrations.

3.2.6.2 EMI shielding properties of Si-B alloys

In the present study, total shielding effectiveness was calculated and compared among the Si-B alloys under study in different regions of electromagnetic spectrum is shown in Fig 3.61. Among

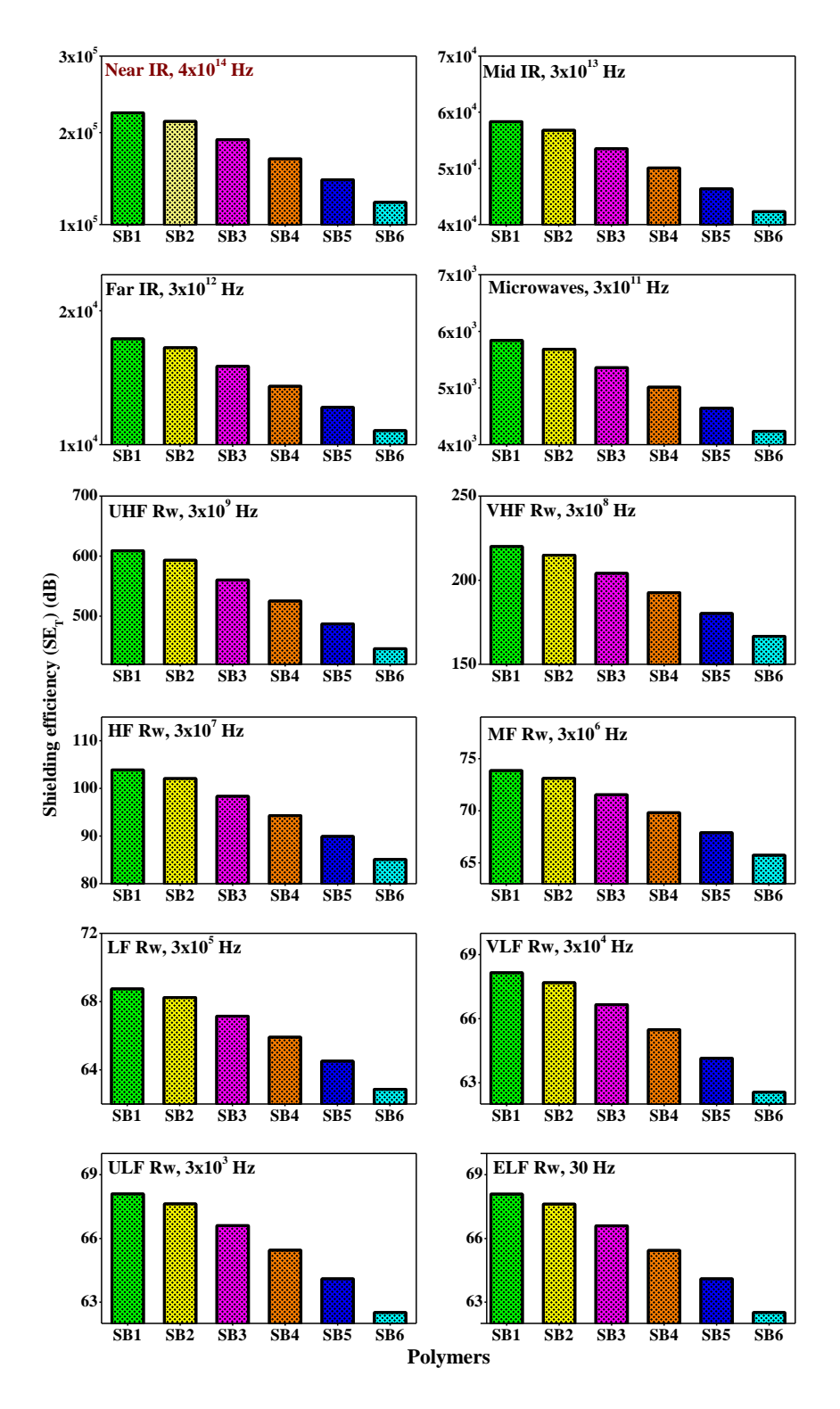


Fig. 3.61 Variation of SET with that of boron concentrations for different frequencies / energies.

all the Si-B alloys under study, SB1 alloy shows larger shielding effectiveness.

3.2.6.3 Neutron shielding parameters of Si-B alloys

The variation of neutron shielding parameters for all the selected Si-B alloys is as shown in Fig 3.62 (a-f). From this figure it is found that SB1 shows smaller λ_{coh} , λ_{incoh} , σ_{coh} , σ_{incoh} . However, larger σ_{tot} and σ_{abs} values are observed. A material which possess smaller b_{coh} , b_{incoh} , σ_{coh} , σ_{incoh} and high σ_{tot} , σ_{abs} shows the characteristic behavior of a good absorber. Since SB1 shows all these characteristics, it is considered as a good absorber.

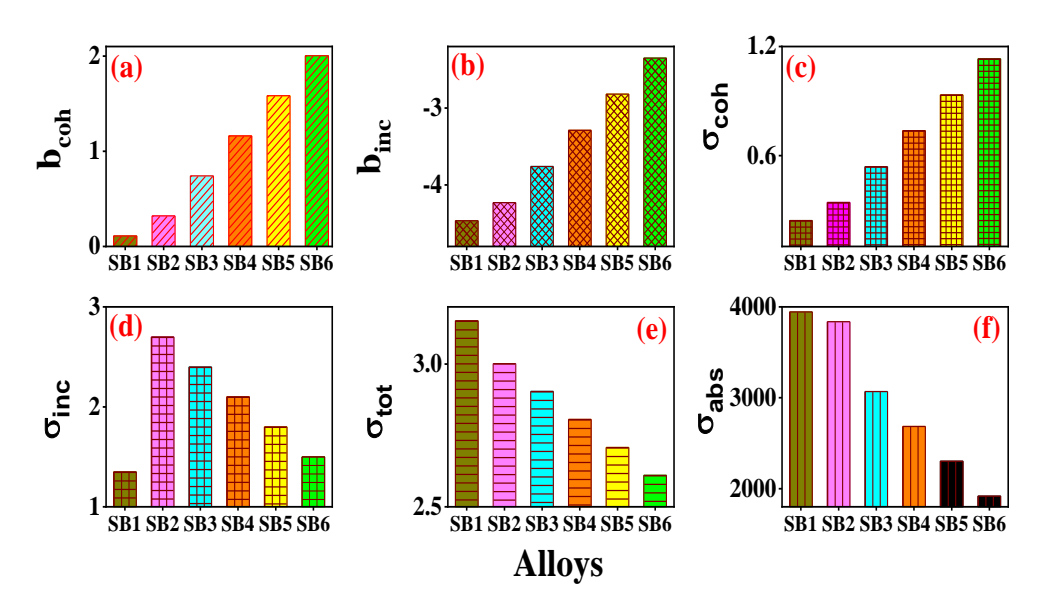


Fig. 3.62 Variation of neutron shielding parameters with different silicon boron alloys (SB1, SB2, SB3, SB4, SB5 and SB6)]

3.2.7 Zinc alloys

For the studied zinc alloys of different composition, the comparison of φ with energy is as shown in figure 3.63. It is observed that among the studied zinc alloys, φ is larger for the alloy of composition (Cu 70 %, Ni 15 %, Zn 15%). The comparison of RD with energy is as shown in figure 3.64. It is found that among the studied zinc alloys, RD is larger for the alloy of composition (Cu 70 %, Ni 15 %, Zn 15%). The variation of φ and RD with energy for the studied alloy of composition (Cu 70 %, Ni 15 %, Zn 15%) is shown in figure 3.65. It is found that φ and RD rises up to E_{pe} and then decreases. φ and RD is maximum at an energy of 0.5 MeV.

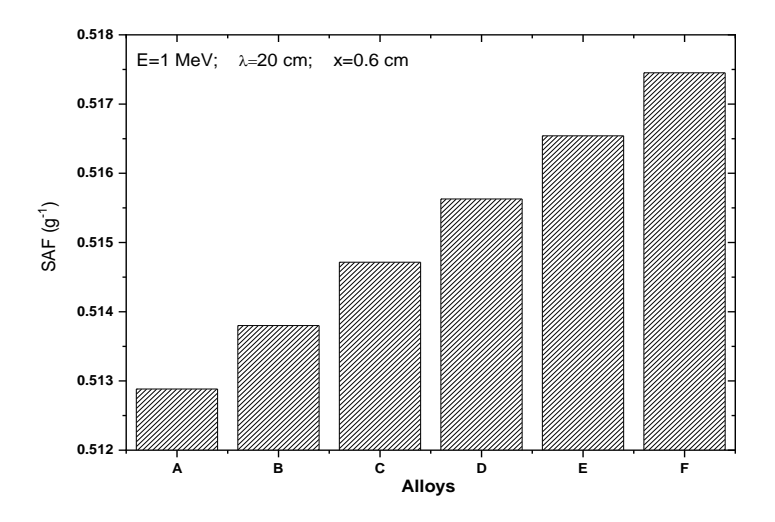


Fig. 3.63 Comparison of SAF(φ) for the studied alloys at a particular energy

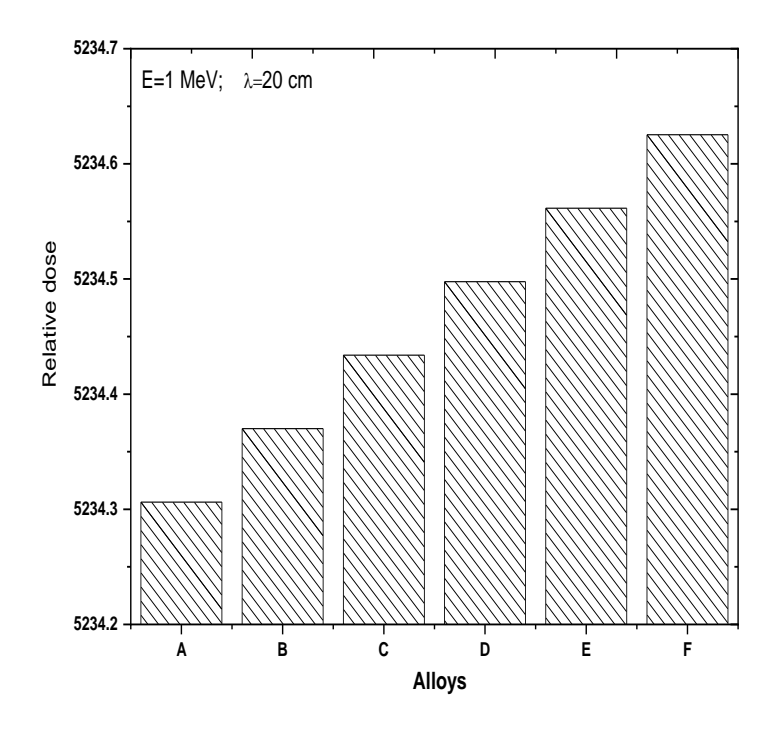


Fig. 3.64 Comparison of RD for the studied alloys at a particular energy

3.3 Silicon Germanium alloys

Theoretically, X-ray/gamma-ray and neutron shielding parameters were studied by considering the different compositions of Si-Ge alloy such as $Si_{0.1}Ge_{0.9}$ (SG1), $Si_{0.2}Ge_{0.8}$ (SG2), $Si_{0.4}Ge_{0.6}$ (SG3), $Si_{0.6}Ge_{0.4}$ (SG4), $Si_{0.8}Ge_{0.2}$ (SG5) and $Si_{0.9}Ge_{0.1}$ (SG6).

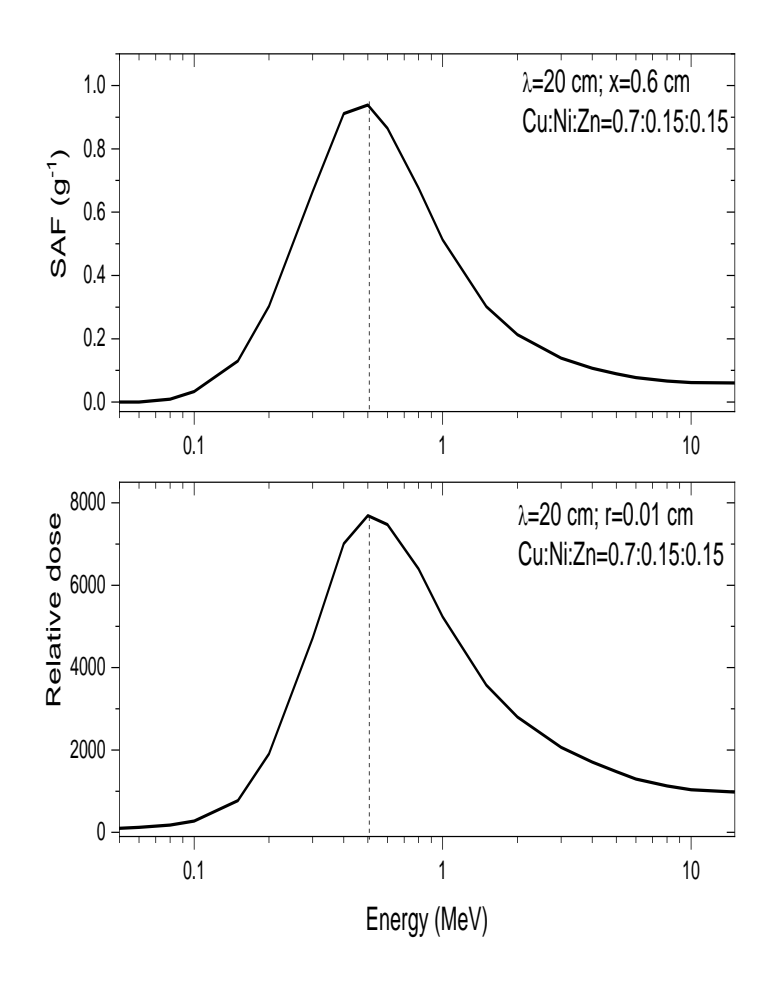


Fig. 3.65 Variation of SAF(φ) and RD with energy for the studied alloy of composition (Cu 70 %, Ni 15 %, Zn 15%)

3.3.0.1 Gamma ray interaction parameters

Variation of μ/ρ with the Gamma energy is graphically represented. Fig. 3.66 shows the variation of μ/ρ of SG1, SG2, SG3, SG4, SG5 and SG6 (a-f) of Si-Ge alloy with photon energy ranging between 1 keV - 100 GeV respectively. Different interaction process are dominant at different energy regions. As observed from the Fig. 3.66, μ/ρ rapidly decreases at lower energies and few X-ray absorption edges were identified. The appearance of absorption edges at lower energy region is due to constituent elements of Si-Ge alloy. When gamma-rays interact with Si-Ge alloy, it exhibits characteristic X-ray absorption edges. Among two absorption edges, first absorption edge appearing at lower photon energy corresponds to Ge L-X-ray (12-14 keV) and Si K-X-ray

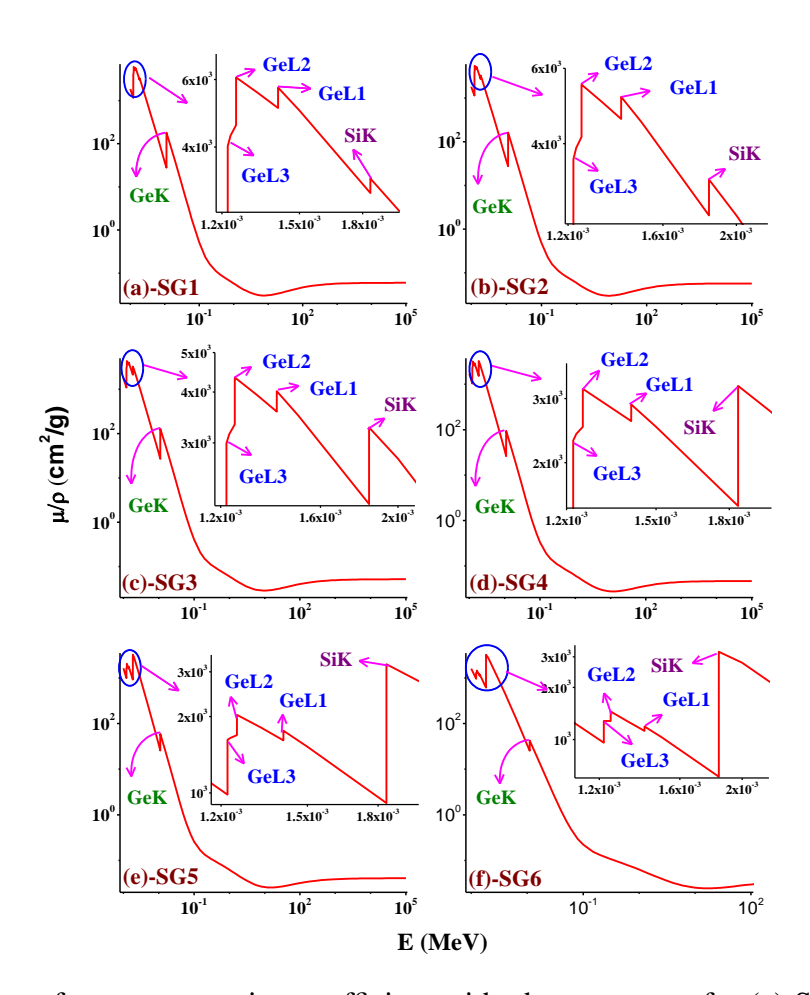


Fig. 3.66 Variation of mass attenuation coefficient with photon energy for (a) SG1, (b) SG2, (c) SG3, (d) SG4, (e) SG5 and (f) SG6 Si-Ge alloys respectively

(18 keV) whereas second absorption edge appeared at slight higher photon energy corresponds to Ge K-X-ray (122 keV). Fig3.66(a) shows the variation of μ/ρ with photon energy (1keV - 100 GeV) of SG1 alloy. Inset of Fig 3.66(a) shows the magnified portion of first absorption edge. First peak in the figure consists four small absorption X-ray edges corresponding to Ge L1-X-ray (14 keV), Ge L2-X-ray (12.5 keV), Ge L3-X-ray (12.3 keV) and Si K-X-ray (18.4 keV).

Similar trend is observed for the other studied Si-Ge alloys with different X-ray absorption edge intensities (Fig. 3.66 (b-f)). The absorption edge intensity corresponding to Ge K-X-ray is for SG1, SG2, SG3, SG4, SG5 and SG6 respectively. Similarly, for the other X-ray absorption edges such as Ge L1-X-ray, Ge L2-X-ray, Ge L3-X-ray and Si K-X-ray are found to be for SG1, SG2, SG3, SG4, SG5 and SG6 respectively. The absorption edge of different intensities corresponding

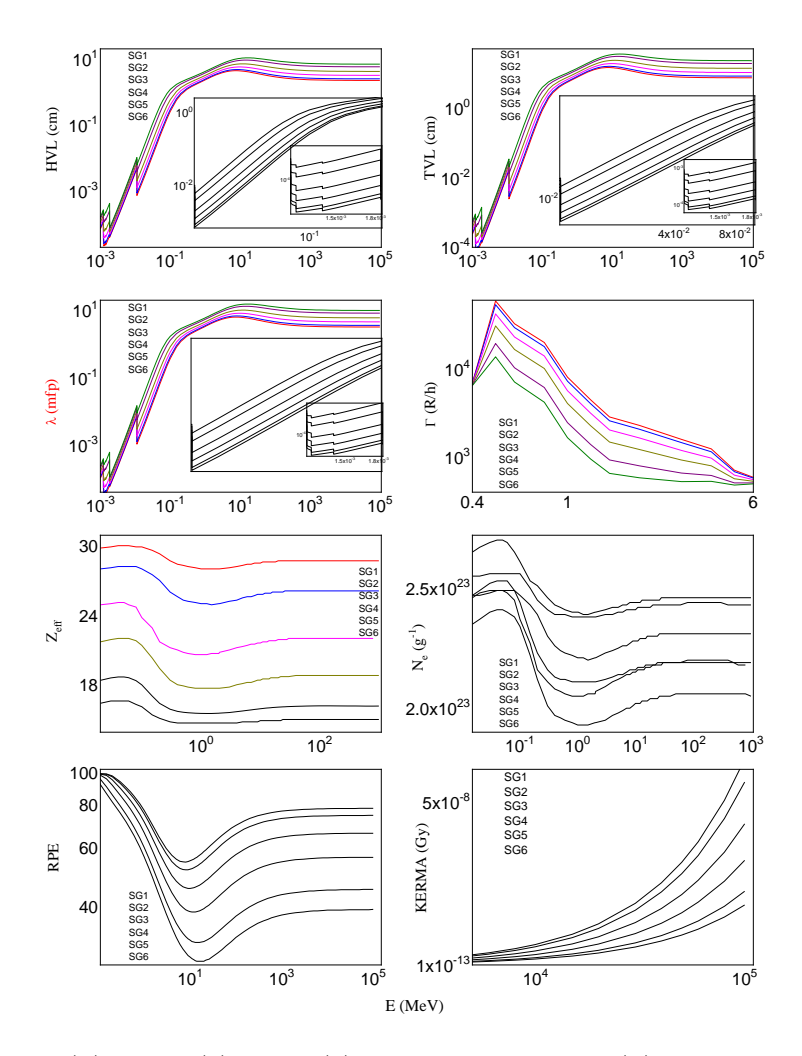


Fig. 3.67 Variation of (a) HVL, (b) TVL, (c) mean free path (λ) , (d) specific gamma ray constant (Γ) , (e) Effective atomic number (Z_{eff}) , (f) effective electron density (N_e) , (g) radiation protection efficiency (RPE) and (h) KERMA with photon energy respectively for SG1, SG2, SG3, SG4, SG5 and SG6 alloys

to Ge K-X-ray, Ge L1-X-ray, Ge L2-X-ray, Ge L3-X-ray and Si K-X-ray follows the order SG6 < SG5 < SG4 < SG3 < SG2 < SG1. Furthermore, the variation in the intensity of X-ray absorption edges represents response of high energetic radiation on given material mainly depends on the composition. Higher the value of μ/ρ , consequences the higher probability of photon . Thus, Among the selected Si-Ge alloys, SG1 has higher values of μ/ρ .

In the further investigation, we have studied the variation of HVL, TVL, mfp, specific gamma ray constant (Γ), Effective atomic number (Z_{eff}), effective electron density (N_{el}), radiation protection efficiency (RPE) and KERMA for SG1, SG2, SG3, SG4, SG5 and SG6 Si-Ge alloys with

photon energy is graphically represented in the Fig. 3.67. The calculated HVL values (Fig. 3.67) (a)) was smaller for SG1 compared to other studied alloys. The first absorption edge is observed at 18 keV whereas another one at 110 keV. Since HVL, TVL and λ are inversely proportional to μ , similar trend with photon energy is observed with slight difference in X-ray absorption edge intensity. For instance, to reduce the intensities to half at 18 keV for SG1, SG2, SG3, SG4, SG5 and SG6 alloys require 30, 34, 48, 79, 143 and 220 μ m. To reduce the intensities to tenth of its value at 18 keV for SG1, SG2, SG3, SG4, SG5 and SG6 alloys require 98, 110, 161, 266, 437 and 679 μ m thickness (Fig. 3.67 (a) and (b)). The variation of λ or penetration depth with photon energy for the SG1, SG2, SG3, SG4, SG5 and SG6 are very small viz., 0.4, 0.5, 0.7, 1.1, 2 and 3 μ m at lower energies respectively and increases with increase in photon energy. At 233 keV, it was found to be 0.2, 0.3, 0.4, 0.7, 1.1, 2 cm for SG1, SG2, SG3, SG4, SG5 and SG6 respectively (Fig. 3.67 (c)). Since the penetration depth is small for SG1, the photon undergoes collision frequently rather than the other selected alloys. If the collision is frequent, the photon loses the energy. As a result, SG1 might be the good absorber. In the case of X-ray/gamma ray involving applications, specific gamma ray constant (Γ) plays an important role [274]. For all the selected alloys, the variation of specific gamma ray constant with photon energy follows the similar trend (Fig. 3.67 (d)). The specific gamma ray constant was found to be larger for SG1 compared to the other studied alloys. The larger specific gamma ray constant indicates the material (SG1) as a good absorber. The other parameters Z_{eff} , N_{el} , RPE and KERMA also depends on the photon energy. Both Z_{eff} and N_{el} shows similar behavior with photon energy for the selected alloys (Fig. 3.67 (e) and (f)). For instance, Z_{eff} was found to be 30, 28, 25, 22, 19 and 17 below 60 keV whereas constant behavior was observed for SG1, SG2, SG3, SG4, SG5 and SG6 respectively above 60 keV. Effective atomic number and electron density was found to be larger for SG1 and smaller for SG6. Since electron density is large for SG1, more number of electrons are available for the photon interaction and hence loses the energy more frequently, hence shows good absorbing properties compared to other selected alloys. Further, the other shielding parameters RPE and KERMA also have been studied for all the selected Si-Ge alloys ,graphically represented in Fig. 3.67 (g) and (h). RPE value slowly decreases and attains the minimum value at 7, 8, 10, 12, 15 and 16 MeV photon energy for SG1, SG2, SG3, SG4, SG5 and SG6 respectively and there after increases slowly with increase in photon energy upto 700 MeV. RPE value was found to be smaller for SG6 and larger for SG1. The another X-ray/gamma-ray shielding parameter, KERMA gives the information about the kinetic energy released in the particular material. This KERMA value was found to be larger for SG1 compared to other selected alloys.

It is found that good shielding material should have small λ , HVL and TVL and high electron density, Z_{eff} , RPE and KERMA value. Since SG1 alloy shows all these characteristics compared to other selected alloys, the absorption buildup factor and φ was studied at different photon energy and at different λ values. Fig. 3.68 (a) depicts the variation of B_{en} with photon energy at different penetration depth for SG1 alloy. B_{en} value was found to be small, both at lower and higher energy regions with a maximum at intermediate energy region. Photoelectric effect and pair production dominates in the lower and higher energy region respectively whereas Compton scattering dominates in the intermediate energy region. Initially, at lower energy B_{en} increases slowly with increase in photon energy until a maximum is reached. At the intermediate energy region, the increase in counts of multiple scattered photons causes higher B_{en} values and thereafter B_{en} decreases with increase in photon energy due to pair production. The B_{en} value was examined for different penetration depth (5, 10, 20, 30 and 40 cm). Even though, the variation was same for the different penetration depths, B_{en} at intermediate region increases with increase in penetration depth. Fig. 3.68 (b) depicts the variation of B_{en} with λ at different photon energies for SG1 alloy. As the penetration depth increases, multiple scattered photons increases with increase in volume

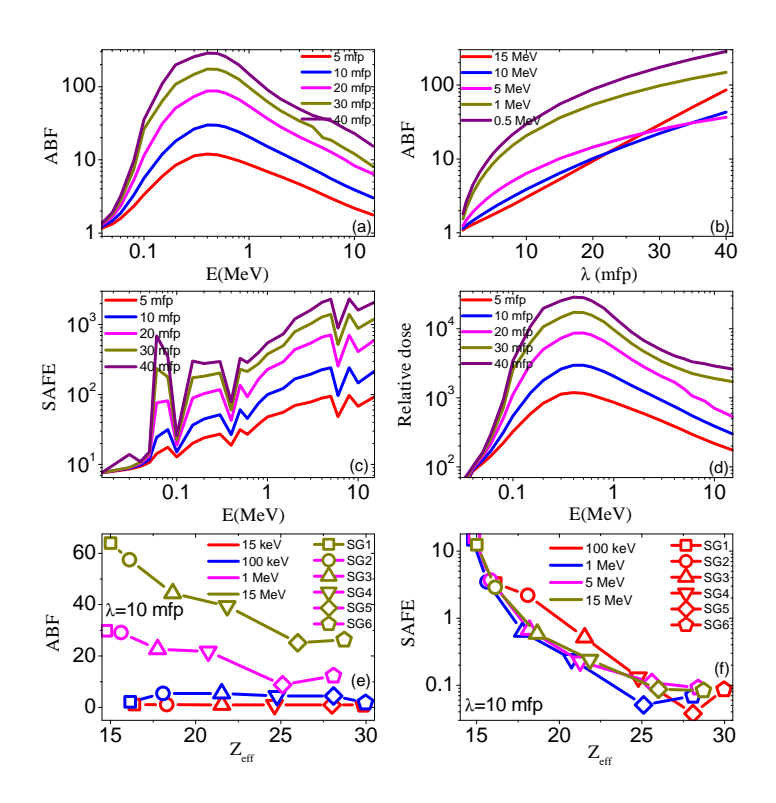


Fig. 3.68 Variation of (a) (B_{en}) with energy at different λ , (b) B_{en} with mean free path (λ) at different energies, (c) SAFE with energy at different λ , (d) relative dose with energy at different λ for SG1 alloy, (e) B_{en} with Z_{eff} at different energies, (f) SAFE with Z_{eff} at different energies for SG1, SG2, SG3, SG4, SG5 and SG6 alloys

and hence linear behaviour was observed. Fig. 3.68 (c) shows the variation of specific absorbed fraction of energy (φ) with photon energy for the different penetration depths. φ gives the information about the energy absorbed by the SG1 alloy which is transferred to electrons by the photon interactions. The material absorbs the radiation only at particular photon energy. Thus maximum absorption peaks are observed at some particular energy. This variation is the characteristic of the material. Larger φ value was observed for the higher penetration depth. Similar trend is observed in the case of relative dose (Fig. 3.68 (d)). Fig. 3.68 (e) and Fig. 3.68 (f) shows the variation of B_{en} and φ with Z_{eff} at the penetration depth of 10 cm for all the selected alloys at different photon energies. Since, Z_{eff} is composition dependent, both the B_{en} and φ were found to be composition dependent.

3.3.0.2 **Neutron shielding parameters**

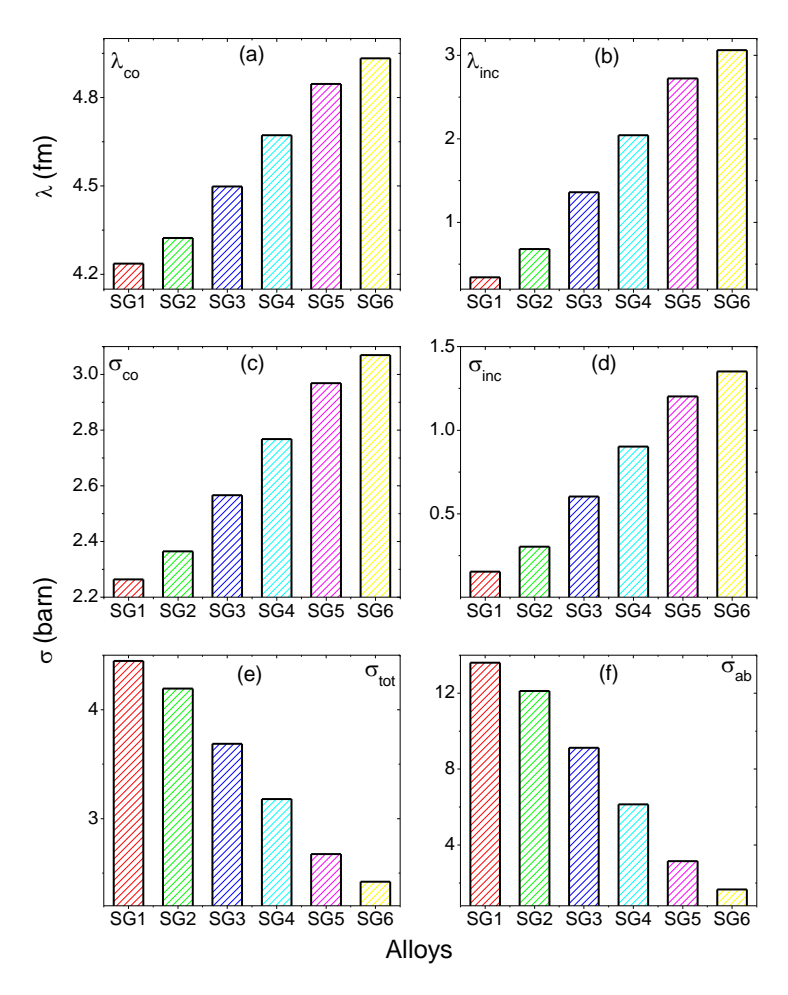


Fig. 3.69 Comparison of neutron shielding parameters for SG1, SG2, SG3, SG4, SG5 and SG6 alloys

The comparison of neutron shielding parameters for the studied alloys is as shown in Fig. 3.69. This figure shows the comparison of (a) coherent neutron scattering length, (b) incoherent neutron scattering length (c) coherent neutron scattering cross section, (d) incoherent neutron scattering cross sections, (e) total neutron scattering cross section and (f) neutron absorption cross sections for the selected alloys. Among all the selected alloys, SG1 shows smaller coherent neutron scattering length, incoherent neutron scattering length, coherent neutron scattering cross section, incoherent neutron scattering cross sections and larger total neutron scattering cross section and neutron absorption cross sections. From this study it is observed that SG1 alloy is a good absorber

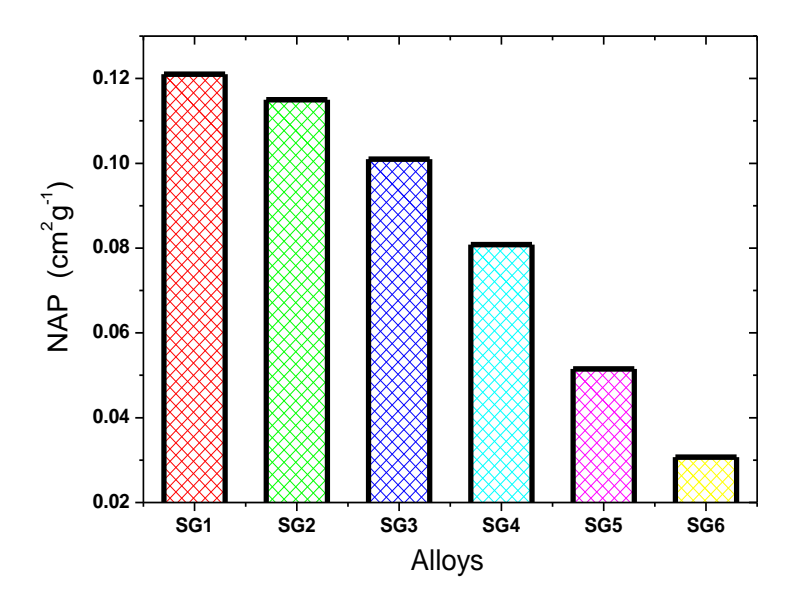


Fig. 3.70 Comparison of neutron attenuation parameters (NAP) for SG1, SG2, SG3, SG4, SG5 and SG6 Si-Ge alloys

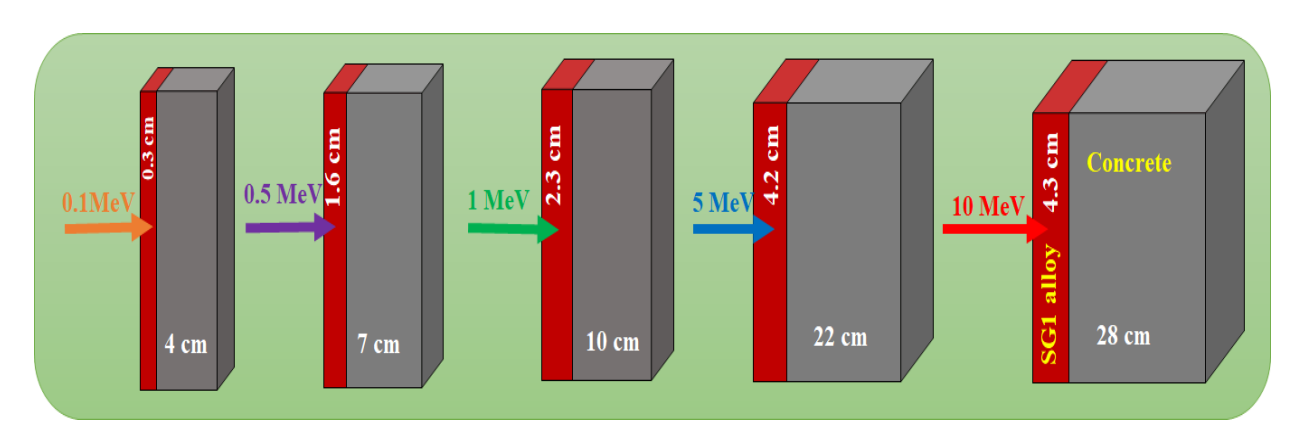


Fig. 3.71 Diagram showing the absorption of radiation by SG1 alloy and ordinary concrete combination at different energies

of neutrons. The evaluated neutron attenuation parameters (NAP) for studied alloys is as shown in Fig. 3.70. From this comparison it is observed that attenuation parameter for SG1 alloy is larger than that of the other studied alloys. Hence it can be concluded that neutrons attenuated will be more in SG1 alloy than the other studied alloys.

The Si-Ge alloy coated on concrete can be used to absorb gamma/X-ray and neutron shielding. For instance, our calculation shows that, to absorb 0.1 MeV gamma/X-ray radiation, 0.15 cm thickness of $Si_{0.1}Ge_{0.9}$ coating reduces 50 % of intensity. Thus 0.3 cm thickness of $Si_{0.1}Ge_{0.9}$ alloy coated on 4 material absorbs almost incident intensity. This 0.3 cm thickness of $Si_{0.1}Ge_{0.9}$ alloy coated on 4

cm concrete block can absorb 0.1 MeV X-ray/gamma-ray radiation without leakage. In the same way, we have designed the other blocks of SG1 alloy coated on concrete for shielding of different X-ray/gamma-ray energy radiation and it is shown in Fig. 3.71.

CHAPTER 4

Synthesis and characterization of nano compounds

4.1 Synthesis

4.1.1 Synthesis of Barium-Nickel-Iron Oxide NanoComposite

In the present studies, for the first time Ba–Fe–Ni oxide nanocomposite (Ba-Fe-Ni) was synthesized by using solution combustion method and calcined at 500° C .Ba(NO₃)₂), Iron(III) nitrate [Fe(NO₃)₃ · 9H₂O], Nickel nitrate [Ni(NO₃)₂ · 6H₂O] and Urea [CH₄N₂O] with 99.9 % purity were obtained from Sd-fine chemicals. All the reagents were of analytical grade and used as such without further purification. Ba-Fe-Ni nanocomposite(BFNONC) was synthesized by solution combustion method using Urea as fuel. All the reagents are taken in a cylindrical crucible, stirred well in order to obtain homogeneity for half an hour at 400 rpm. This crucible was placed in a muffle furnace that had been preheated to a temperature of $500 \pm 10^{\circ}$ C. The resultant solution was first boiled, then dehydrated to remove gases such as carbon dioxide, nitrogen and water vapour before forming the final product. The resulting product was calcined for 3 hours at 500° C, then cooled to ambient temperature and collected. The visual depiction for the synthesis of BFNONC using urea as a fuel is shown in Fig. 4.1

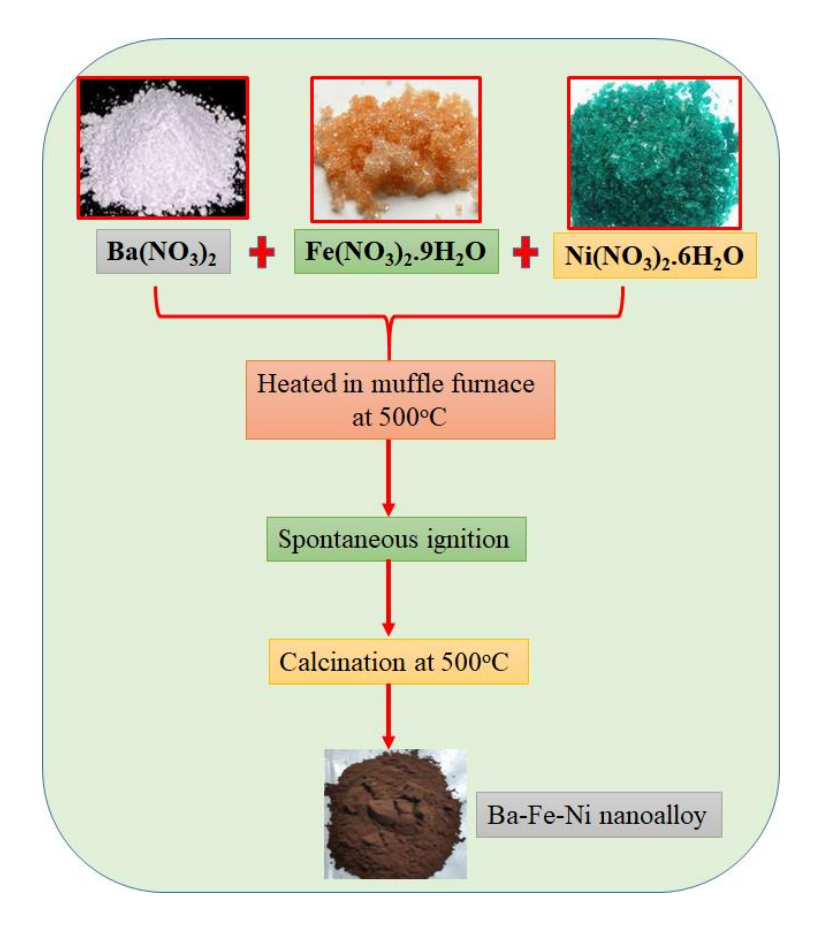


Fig. 4.1 Flowchart for the synthesis of BFNONC

4.1.2 Synthesis of Aluminium-Barium-zinc oxide Nonocomposite

For the first time Aluminium-Barium-Zinc oxide nanocomposite (ZABNONC) were synthesized by Solution Combustion synthesis where calcination was carried out low temperatures 600^{0} C Ba(NO₃)₂, Iron(III) nitrate [Fe(NO₃)₃ · 9H₂O], Aluminium nitrate [Al(NO₃)₃ · 9H₂O] and Urea [CH₄N₂O] as fuel with 99.9 % purity were acquired from Sd-fine chemicals. All the reagents were of AR grade and used as such without further purification. All of the chemicals are placed in a cylindrical crucible and agitated thoroughly for half an hour at 400 rpm to achieve homogeneity. This crucible was put in a muffle furnace that was preheated to $600 \pm 10^{\circ}$ C. Before creating the final product, the resulting solution was boiled, then dehydrated to eliminate gases such as carbon dioxide, nitrogen, and water vapour. The resultant product was calcined at 600° C for 3 hours before being cooled to room temperature and collected. Flowchart for the synthesis of ZABNONC,

urea as a fuel is shown in Fig.4.2

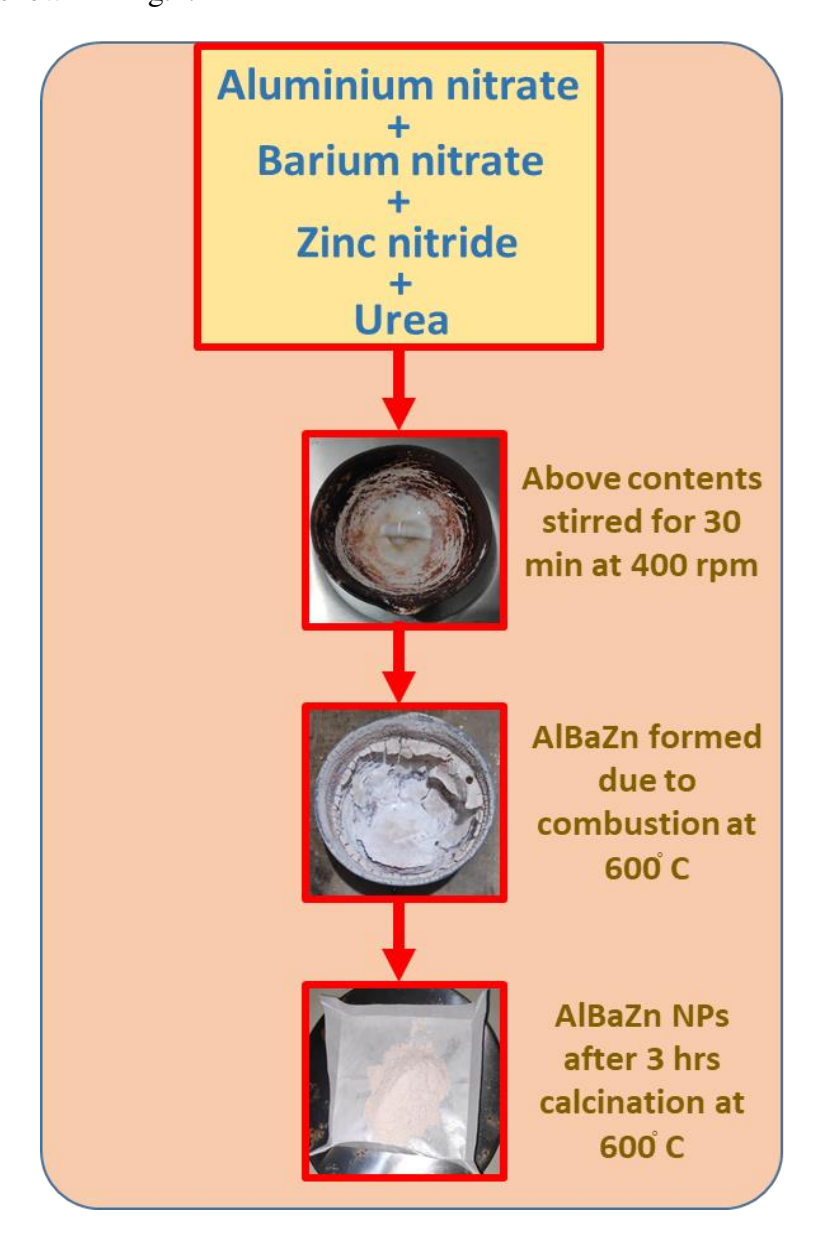


Fig. 4.2 Flowchart for the synthesis of ZABNONC

4.1.3 Synthesis of Leadaluminoborate nanocomposite

For the first time, we are reporting the analysis of X-ray/gamma ray shielding properties of Leadaluminoborate nanocomposite (LABNC) synthesized by solution combustion method using Mint leaves extract as a reducing agent.LABNC was synthesized by solution combustion method using mint leaves extract as a reducing agent. Stoichiometric amount of Aluminium nitrate [Al(NO₃)₃) \cdot 9 H_2O], Lead nitrate [Pb(NO₃)₂], Boron nitride [BN] with 99.9 % purity were

procured from Sd-fine chemicals without any further purification are dissolved in HNO $_3$. Freshly prepared 10 ml Mint leaves extract was mixed thoroughly to the above mixture using a magnetic stirrer for about 1h to obtain homogeneity at 400 rpm. This was placed in a preheated muffle furnace which is at $500 \pm 10^{\circ}$ C followed by calcination for 3 h at 500° C to remove gases such as carbon dioxide, nitrogen and water vapour. The calcinated sample was cooled to ambient temperature and collected. The procedure for the synthesis of LABNC is pictorially represented in Fig.4.3



Fig. 4.3 Pictorial representation for the synthesis of LABNC

4.2 Characterization

4.2.1 Characterization Ba-Fe-Ni Oxide NanoComposite

4.2.1.1 PXRD analysis of Ba-Fe-Ni Oxide NanoComposite

PXRD is one of the most widely utilised characterization techniques which gives information about the crystalline structure, phase nature, lattice parameters and crystalline grain size. Fig.4.4(a) depicts the PXRD pattern of BFNONC synthesized by low temperature solution com-

bustion method calcined at 500°C for 3 hrs. The sample's/NCs high crystallinity is confirmed by the strong diffraction planes. The BFNONC consists of Bragg's reflections (200), (210), (211),

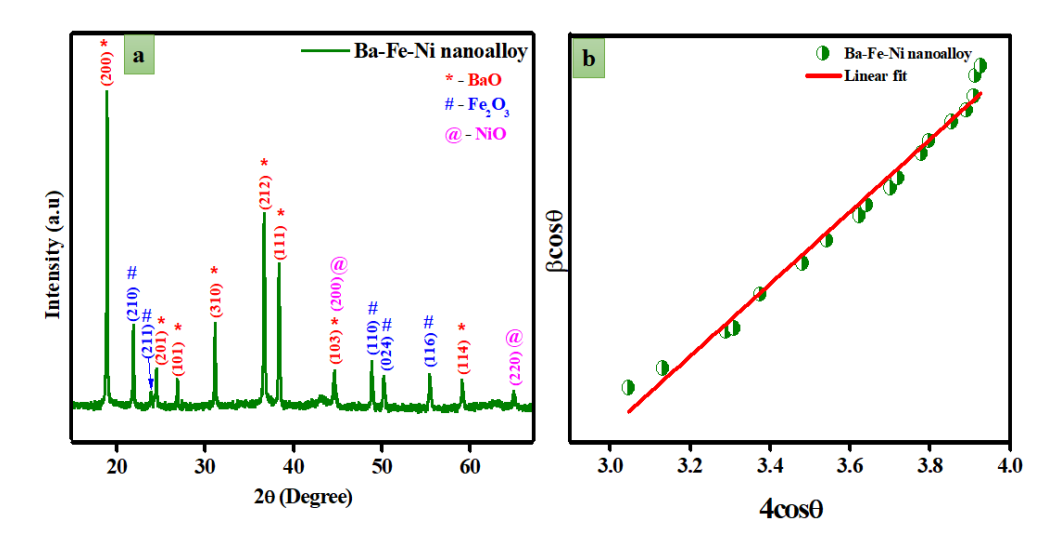


Fig. 4.4 PXRD pattern of BFNONC

(201), (101), (310), (212), (111), (103), (200), (110), (024), (116), (114) and (220) at 18.81, 21.76, 24.03, 24.43, 26.91, 31.11, 36.65, 38.29, 44.55, 48.86, 50.19, 55.33, 59.13 and 64.87° 2θ respectively. Among these reflections, (200), (101), (310), (212), (111), (103) and (114) corresponds to tetragonal phase of BaO [275], (210), (211), (110), (024) and (116) corresponds to γ phase Fe₂O₃ [276] whereas remaining (200) and (220) corresponds to face centred cubic phase of NiO [277]. The presence of Bragg's reflections corresponding to BaO, Fe₂O₃ and NiO clearly confirms the formation of BFNONC. There are no signs of any further peaks relating to other impurities which confirms the purity of the sample.

The average crystallite size of BFNONC was determined by using Debye-Scherrer's equation and the Williamson-Hall (W-h) plot method Fig.4.4(b) and is explained in our previous work [278–280].For (200) plane peak crystal size is found to be 30nm by Debye-Scherrer's equation, and from W-H plot approach it was 32nm. The crystallite size determined from W-H plots was somewhat greater than Debye Scherrer's equation. The modest variations in the numbers were due to the fact that the strain component was assumed to be negligible in Scher-

rer's calculation, the observed widening of the diffraction peak was attributed only to grain size reduction. [281, 282]. Various structural parameters were computed by the formulas given by Vidya et al., [283], values are $1.1 \times 10^{15} \, \text{lin m}^{-2}$, 2.22×10^{-3} and 3.352×10^{-3} respectively.

4.2.1.2 SEM analysis of Barium-Nickel-Iron Oxide NanoComposite

SEM and EDAX analysis can be used to determine the morphology of the surface, distribution of particles and the elemental composition of the synthesised NCs. Fig.4.5(a-c) shows the SEM

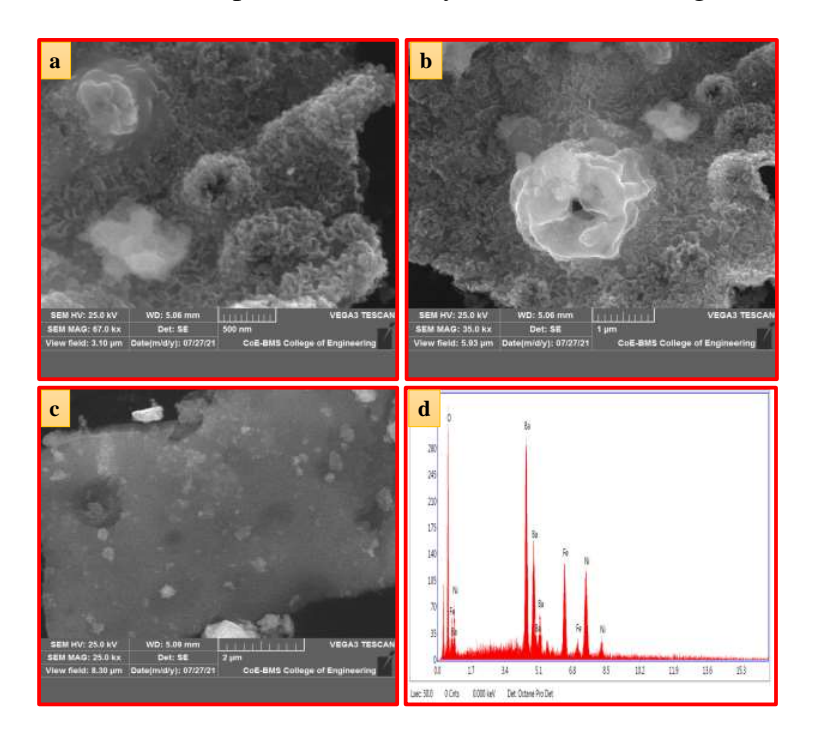


Fig. 4.5 SEM image (a-c) at different magnifications and EDAX spectra (d) of BFNONC

image of BFNONC at different magnification. Since it is a NCs which is the combination of BaO, Fe_2O_3 and NiO oxides, no such regular or irregular shaped nanoparticles are observed. The surface morphology is made up of large number of scaly natured agglomerated flakes which looks as they are placed one above the other as shown in Fig.4.5(a and b). In addition to agglomerated flakes, few Cinder cone volcanoes like voids are observed which is the characteristic of the combustion method. When the pressure is released, the gases explode, like soda spewing out of a bottle can that you shook up and opened suddenly. These types of nanoflakes are highly friable which facilitates

easy grinding to obtain finer particles. At higher magnification, this NCs looks in the form of Ice block Fig.4.5(c). The existence of Ba, O, Fe and Ni atoms in the host matrix, as well as the lack of other contaminants, is confirmed by energy dispersive X-ray spectroscopy analysis (EDAX) Fig.4.5(d).

4.2.1.3 FTIR analysis of Barium-Nickel-Iron Oxide NanoComposite

The absorption of electromagnetic radiation with wavelengths in the mid-infrared range (4000–400 cm⁻¹) is measured using the FTIR technique. The dipole moment of a molecule changes when it absorbs infrared radiation (IR), and the molecule becomes IR active. Fig.4.6(a) exhibits FTIR spectra for BFNONC calcined at 500°C for 3 hours in the range 400 - 4000 cm⁻¹. The sharp

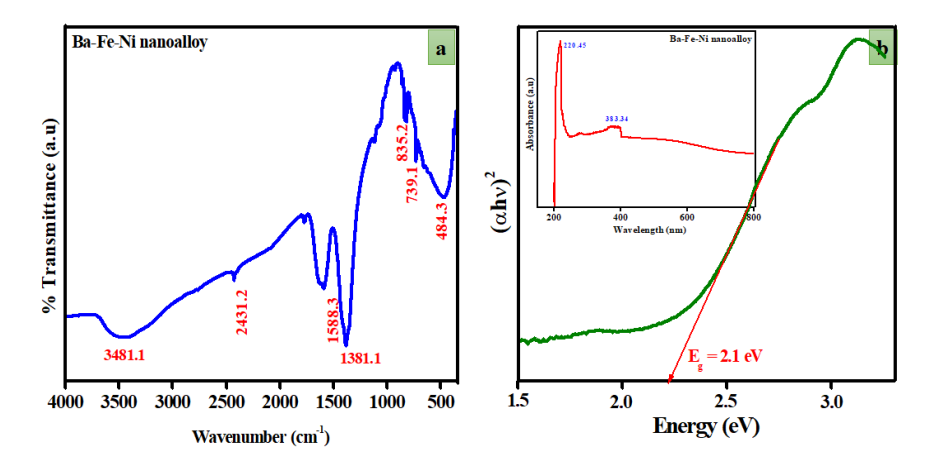


Fig. 4.6 (a) FTIR spectra and (b) Wood and Tauc's plot (UV-Visible absorption spectra) of BFNONC

IR peaks are observed at 484.3, 739.1, 835.2, 1381.1, 1588.3, 2431.2, 3481.1 cm⁻¹. The peaks observed at 484.3 cm⁻¹ attributed to the metallic (M) - oxygen (M = Ba, Fe and Ni) bond vibration [284]. An absorption band observed at 3481.2 cm⁻¹ corresponds to the presence of O-H group. The less intense sharp absorption band observed at 2431.2 cm⁻¹ corresponds to traces of absorbed atmospheric CO₂ [285]. The bands observed at 739.1 and 835.2 cm⁻¹ correspond to the deformation of vibration of C-H group. Furthermore, in the range from 1300 to 1700 cm⁻¹ (1381.1 and 1588.3 cm⁻¹) corresponds to the presence of carboxyl groups related to Urea was noted.

4.2.1.4 UV-Visible analysis of Barium-Nickel-Iron Oxide NanoComposite

Another common characterisation method for nanoscale materials is UV-Visible spectroscopy, which is relatively simple and low-cost. It compares the amount of light reflected or absorbed from a sample to the amount of light reflected or absorbed from a reference material. The optical properties are sensitive to size, shape, concentration, agglomeration state and refractive index near the nanoparticle surface, which makes UV-Visible spectroscopy an important tool to identify, characterize and investigate these materials. Inset of Fig.4.6 (b) shows the UV-Visible absorption spectra of BFNONC in the wavelength range 200-800 nm. Absorption was strong across a wide wavelength range, from ultraviolet to visible light, with an absorption tail extending into the infrared. The spectra shows prominent absorption band with maximum at 220.45 and 383.34 nm. The absorption band appeared at 220.45 nm was assigned to Oxygen to metal ions charge transfer transitions. The electronegativity of the oxygen atoms bonded to the metal centres determines the position of the maximum of this band [286]. Transitions involving extrinsic states such as surface states, defects, and impurities were predicted to cause the other lower intensity peak found at 383.34 nm. [287, 288].

Energy gap calculations were done using standard techniques followed the by previous re-

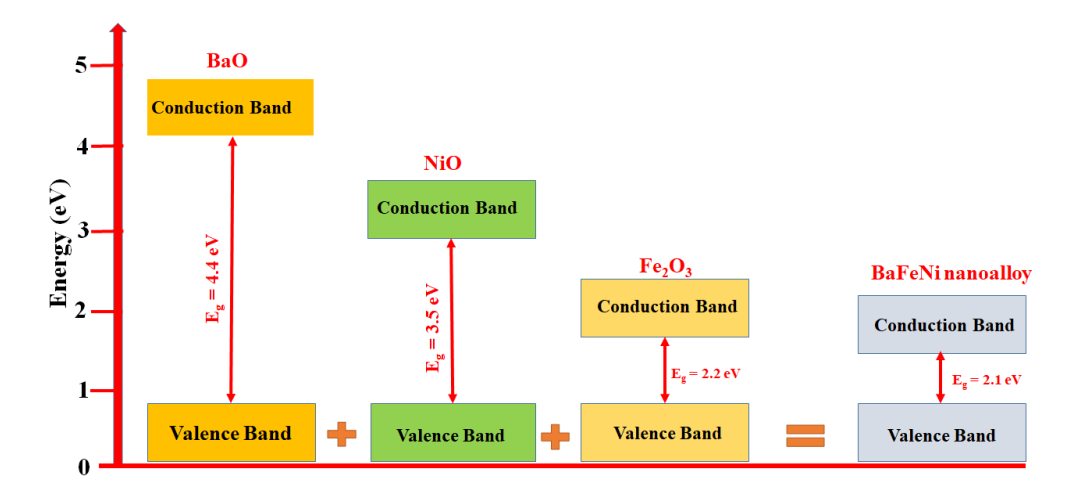


Fig. 4.7 Energy band diagram

searchers [289] was found to be 2.1eV and shown in Fig.4.6(b). Fig.4.7 shows the pictorial representation of energy band diagram. As we observed from the Fig.4.7, as per the literature, the energy band gap of BaO, Fe₂O₃ and NiO lies at 4.4, 2.2 and 3.5 eV respectively [290–292]. The energy band gap of BFNONC lies at 2.1 eV. The amount of band gap has a significant effect on the refractive index and transparency effect of the material. As per the literature, high refractive index and less transparency is observed for the nanomaterials with less energy band gap. Compared to individual oxide materials, the synthesized NCs has less energy band gap. As a result of less transparency and absorption is more [293, 294]. From the literature [295–298], it is observed that there is a effect on the x-ray, gamma absorption properties and optical direct energy band gap. The absorption of gamma rays, X-rays is larger for the material with smaller optical direct energy band gap [295–298]. In radiation shielding, absorption of X-rays/Gamma rays by a material plays an important role. In the present study, compared to Barium Oxide, Iron Oxide and Nickel Oxide, the obtained nanocomposite possesses less energy band gap. As a result, the absorption of X-rays, gamma rays is more in BFNONC compared to that of individual oxide matrices and hence shielding property also. Previous researchers [295] also observed a decrease in the optical energy gap with increasing the gamma absorbed dose.

4.2.2 Characterization of Aluminium-Barium-zinc oxide Nonocomposite

4.2.2.1 PXRD analysis of Aluminium-Barium-zinc oxide Nonocomposite

The crystalline structure of ZABNONC synthesized by SCS were investigated with the PXRD pattern obtained shown in Fig.4.8. During the synthesis, the combination of Aluminium nitrate, Barium nitrate and Zinc nitrate results in the formation of Zinc Aluminate and Barium nitrate (Nitrobarite) complex nanocomposite. The PXRD pattern shows (220), (311), (222), (400), (331), (422) and (511) planes at 30.97, 36.71, 38.37, 44.57, 50.19, 55.23 and 59.10 $^{\circ}$ 2 θ values corre-

sponds to spinel cubic phase of ZnAl₂O4 (JCPDS card No. 05–0669) [299] whereas the remaining (hkl) planes (111), (200), (110), (102), (411), (221) and (113) planes appeared at 18.78, 21.95, 32.02, 34.61, 47.61, 48.90 and 56.65° 2θ values corresponds to cubic Ba(N O_3)₂ (Card Number-3424)[300]. The remaining peaks appeared at 24.41 and 26.99 corresponds to α and γ phase of Al₂ O_3 . The presence of intense and broad diffraction peaks in Fig.4.8 represents high degree of crystallanity of complex nanocomposite.

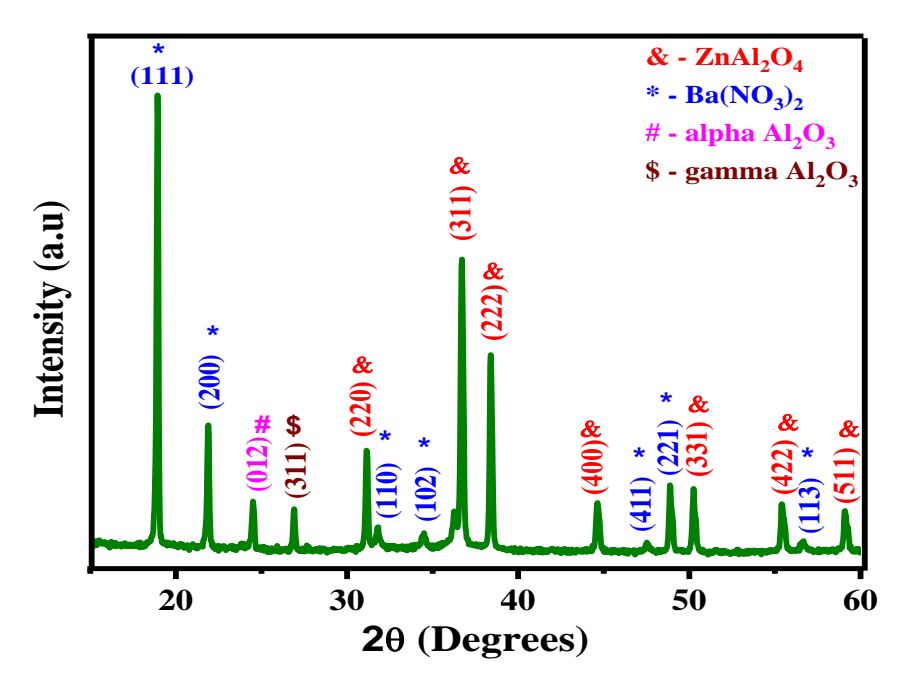


Fig. 4.8 PXRD pattern of ZABNONC

4.2.2.2 SEM analysis of Aluminium-Barium-zinc oxide Nonocomposite

From SEM and EDAX analysis, morphology distribution of particles and the chemical composition of the synthesized ZABNONC can be studied. Fig. 4.9 shows the SEM micrographs of ZABNONC synthesized by the solution combustion method. The tripod structure was observed with various sizes and shapes. Fig. 4.10 shows the EDAX spectrum of $Ba(NO_3)_2$ –ZnO solid solution. From EDAX spectrum elemental composition analysis, it was confirmed that the presence of elements Al, Ba, Zn, and O, which clearly shows the formation of ZABNONC. Further, it also

confirms that there is no missing a constituent element of composite and no addition of impurity if any, during the ZABNONC synthesis process.

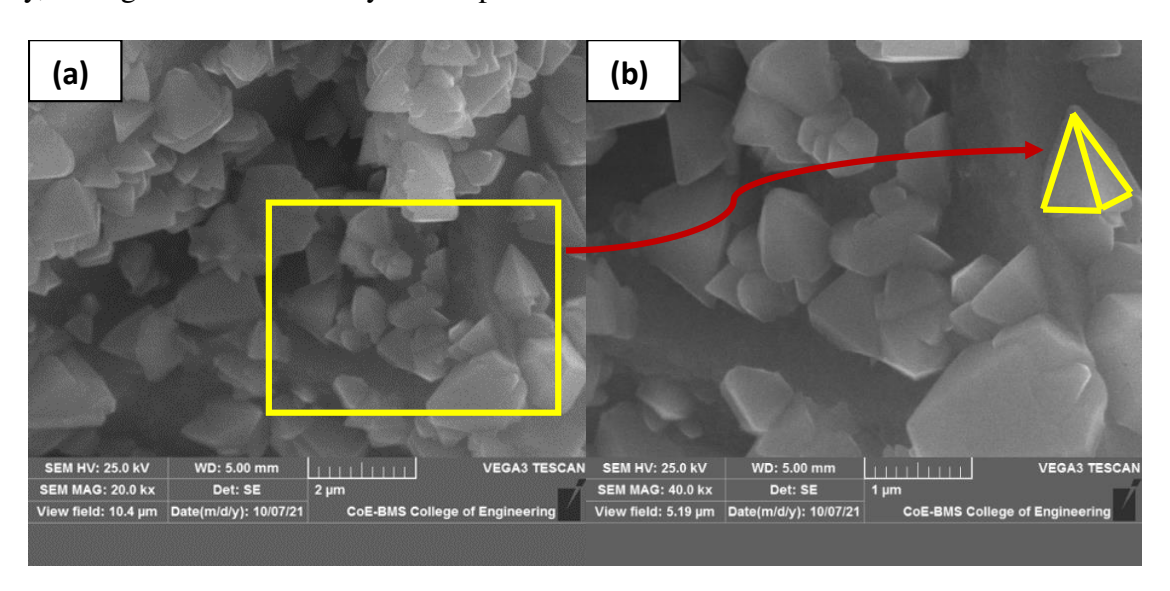


Fig. 4.9 SEM images (a-b) of ZABNONC

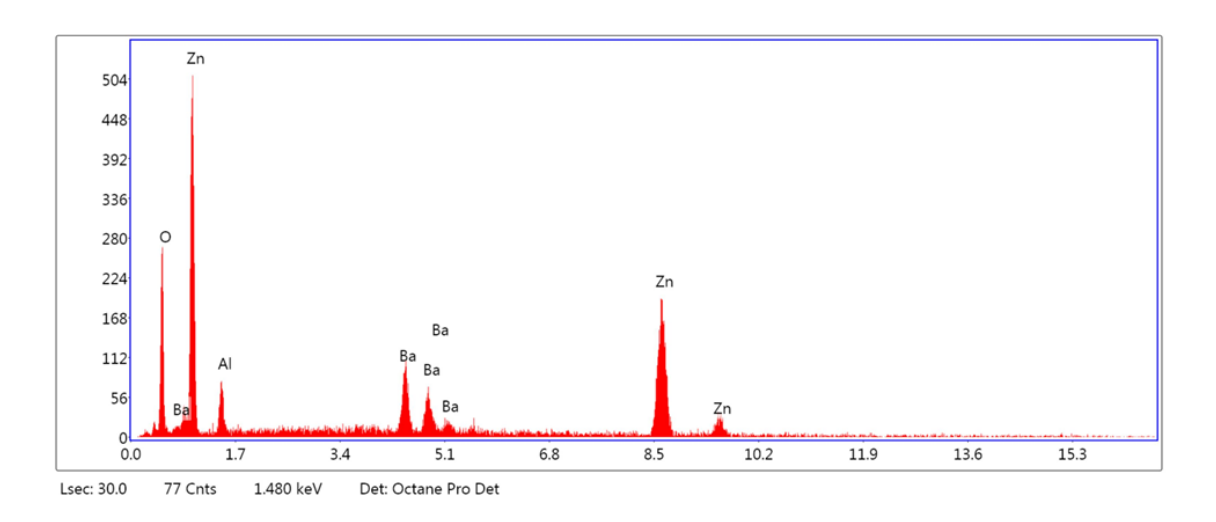


Fig. 4.10 EDAX (Elemental composition) of ZABNONC

4.2.2.3 FTIR analysis of Aluminium-Barium-zinc oxide Nonocomposite

EMW radiation of wave number with in the range (4000–400 cm⁻¹) and their absorption when they interact with the nanomaterials is studied under FTIR study technique and during this procedure when molecules receives infrared radiation (IR), their dipole moment changes, and the molecules turns into IR active. Fig. 4.11 exhibits FTIR spectra for ZABNONC in the Wavenumber

range $400 - 4000 \text{ cm}^{-1}$.

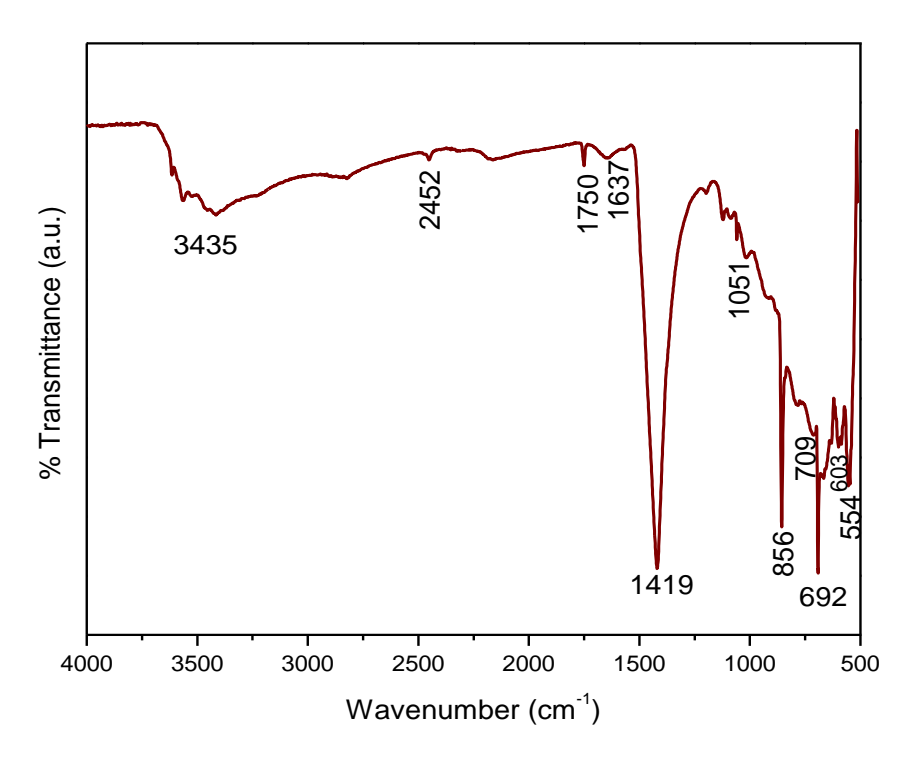


Fig. 4.11 FTIR spectrum of Aluminium-Barium-zinc oxide Nonocomposite

4.2.2.4 UV-Visible analysis of Aluminium-Barium-zinc oxide Nonocomposite

Fig.4.12 shows the UV visible spectrum of ZABNONC. The sample shows a strong absorption peak at 256 nm in the UV region. Based on the literature data, usually nitrates gives the absorption peak between 260-310 nm, since the absorption peak appears at 256 nm, this can be attributed to absorption of NO_2 [301], when occupancy by one electron forms a positively charged with respect to the lattice (F⁺ - center). The other absorption peak appeared at 352 nm corresponds to F⁺ - center [302].

The optical band gap of ZABNONC was calculated by Tauc's relation [303], The Tauc's relation can be given as $(\alpha h \nu) = A(h \nu - Eg)^n$ where α is the optical absorption coefficient, 'h' is plank constant and ν is optical frequency, 'A' is a constant, 'E_g' is the optical band gap energy and 'n' is an exponent value which heavily depends on the nature of the electronic transition causing the light absorption. In order to calculate the direct band gap, we have selected 'n' value which

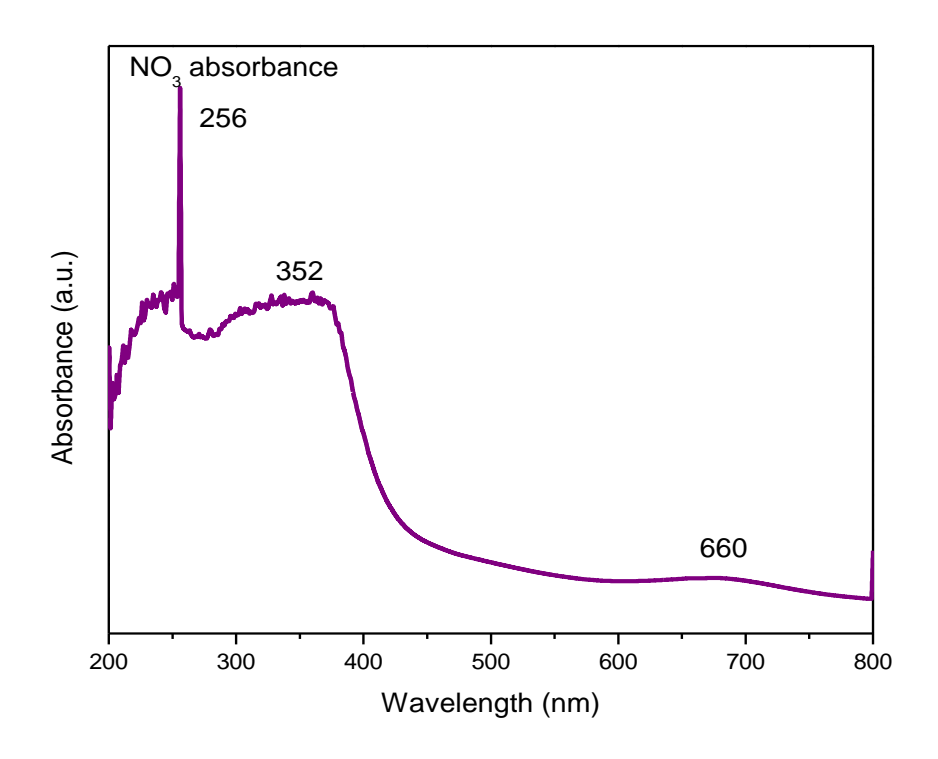


Fig. 4.12 UV-Visible absorption spectrum of ZABNONC

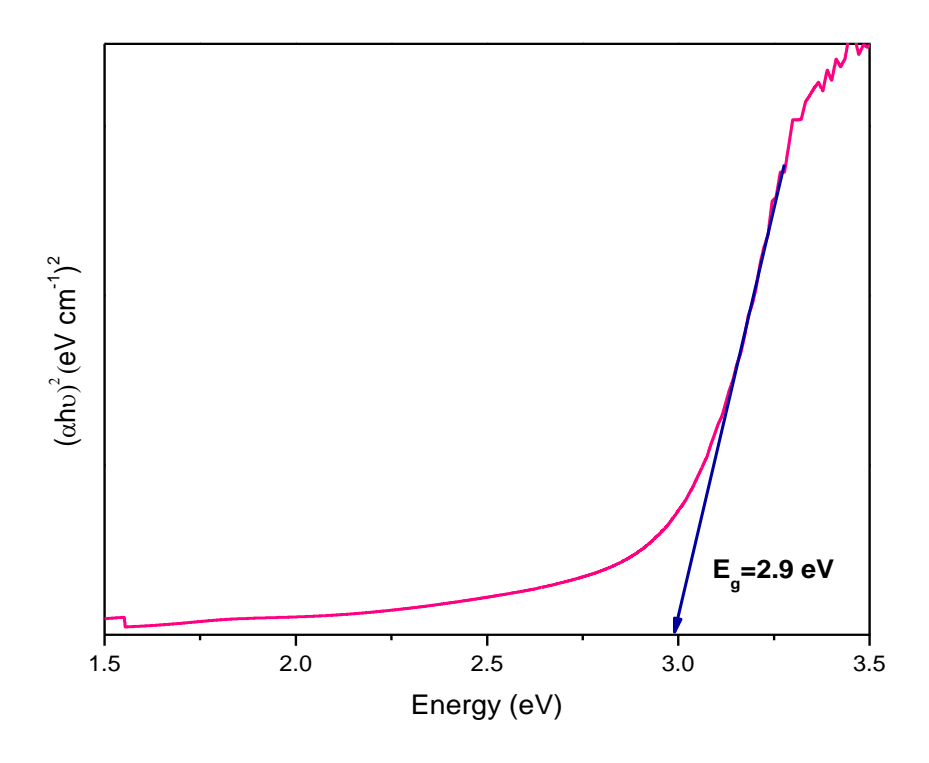


Fig. 4.13 Wood and Tauc's plot of ZABNONC

is equal to 1/2. Fig. 4.13 shows the Tauc's plot for ZABNONC. The plot of $(\alpha \nu)^2$ versus photon energy $(h\nu)$ gives the straight line. From the direct energy band gap was found to be 2.9 eV.

Fig.4.14 shows the pictorial representation of energy band diagram.



Fig. 4.14 Energy band diagram

4.2.3 Characterization of Leadaluminoborate nanocomposite

4.2.3.1 PXRD analysis of Leadaluminoborate nanocomposite

PXRD is one of the most widely utilised characterization techniques which gives information about the crystalline structure, phase nature, lattice parameters and crystallyte size. Fig.4.15(a) depicts the PXRD pattern of LABNC synthesized by green solution combustion method calcined at 500°C for 3 hrs. The PXRD pattern of LABNC clearly indicates the formation of orthorhombic

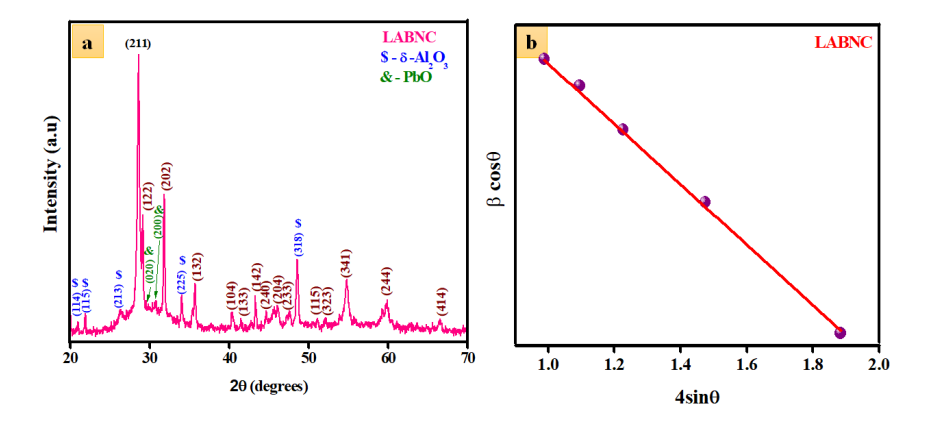


Fig. 4.15 (a) PXRD pattern and (b) W-h plot of LABNC

crystal structure ,where a = 7.0423 Å, b = 9.8989 Å, c = 9.428 Åand space group Pbcn(60). The Bragg's reflections (211), (122), (202), (132), (104), (133), (142), (240), (204), (233), (115), (323), (341), (244) and (414) matches well with the JCPDS card number 00-153-3962 [276]. In addition to these reflections, less intense Bragg's reflections (114), (115), (213), (225) and (318) corresponding to δ -Al₂ O_3 ; (020) and (200) reflections corresponding to PbO were observed.

Average crystal size is calculated by the standard procedures mentioned in chapter 4.2.1.1 and was found to be 62nm Fig.4.15(b). There is a slight variation in the crystal size about 3 nm among W-H plot (62nm) and Debye Scherrer's equations (65nm) due to the reasons mentioned in the chapter 4.2.1.1 [281, 282]. Other crystal parameters are found to be 4.4×10^{14} lin m⁻², 7.4×10^{-2} and 0.501 [283].

4.2.3.2 SEM assessment of Leadaluminoborate nanocomposite

SEM and EDAX analysis can be used to analyze the morphology of the surface, distribution of particles and the elemental composition of the synthesized NCs. Fig.4.16(a-c) shows the SEM

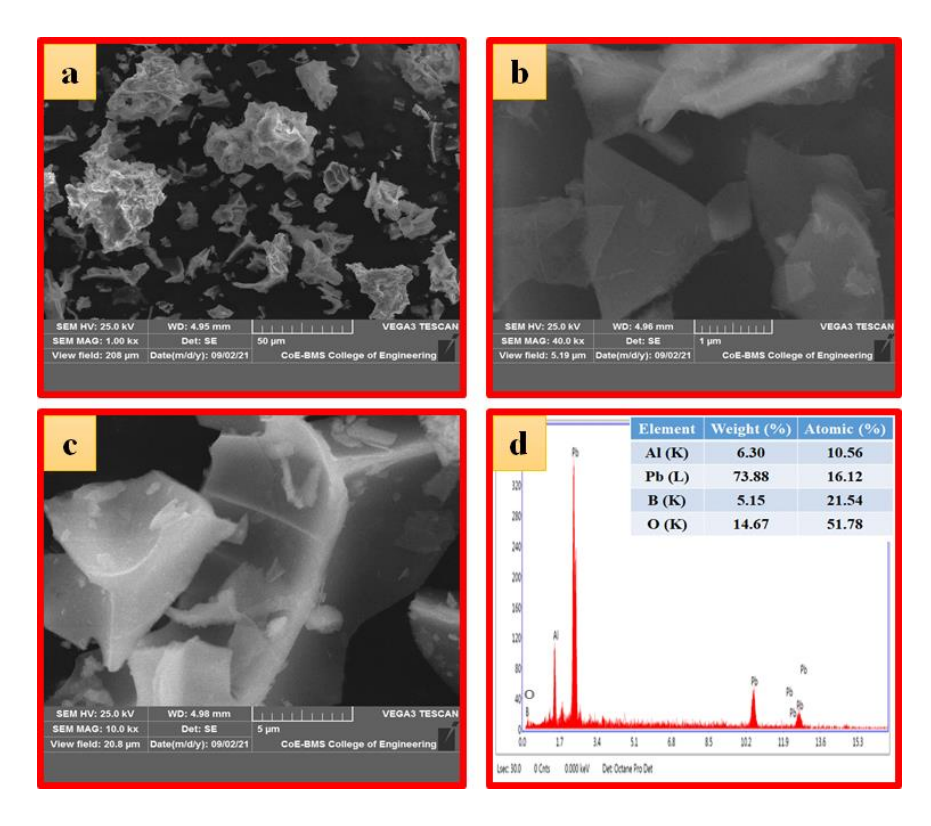


Fig. 4.16 SEM image (a-c) and EDAX (Inset: Elemental composition) (d) of LABNC

image of LABNC at different magnifications. At 50 μ m, the morphology of particles looks in the form of dry leaves Fig.4.16(a). As the magnification changes to 1 μ m, the particles looks in the form of triangular shape Fig.4.16(b). However, the bigger sized particles with irregular shape are observed at 2 μ m magnification Fig.4.16(c). All these changes in morphology from dry

leaves to triangular shape and then to irregular shape was mainly due to the synthesis of NCs with green (mint leaves extract) solution combustion method. Elemental composition is represented by Fig.4.16(d) which confirms that SCS(solution combustion synthesis) method is the most effective method to get surface morphology free from defects.

4.2.3.3 FTIR analysis of Leadaluminoborate nanocomposite

The absorption of electromagnetic radiation with wavelengths in the mid-infrared range (4000–400 cm⁻¹) is measured using the FTIR technique. The dipole moment of a molecule changes when it absorbs infrared radiation (IR), and the molecule becomes IR active. Fig.4.17(a) exhibits FTIR spectra for LABNC in the range 400 - 4000 cm⁻¹. In the FTIR spectra, the broad band ob-

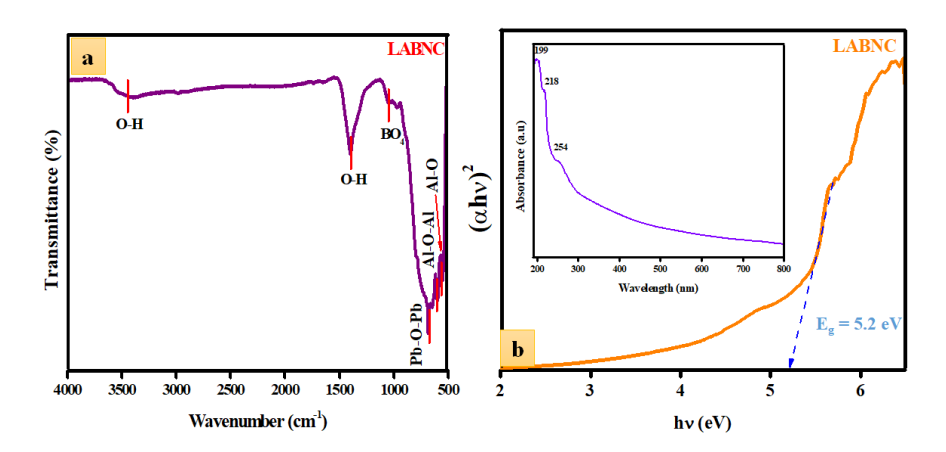


Fig. 4.17 (a) FTIR spectra and (b) Wood and Tauc's plot (Inset: UV-Visible absorption spectra) of LABNC

served at 3445 cm^{-1} is the characteristic of -OH stretching vibration that is bonded to M^{3+} (M = Al/Pb/B) and the band at 1398 cm^{-1} corresponds to physisorbed water [304]. The band which is located at 1045 cm^{-1} corresponds to the BO₄ tetrahedral group [305]. A sharp peak around 687 cm^{-1} represents the asymmetric bending vibration of Pb-O –Pb bond [304]. The stretching modes of Al-O-Al and Al-O linkages were observed at 617 and 573 cm^{-1} respectively [306].

4.2.3.4 UV-Visible analysis of Leadaluminoborate nanocomposite

Another common characterisation method for nanoscale materials is UV-Visible spectroscopy, which is relatively simple and low-cost. It compares the amount of light reflected or absorbed from a sample to the amount of light reflected or absorbed from a reference material. The optical properties are sensitive to size, shape, concentration, agglomeration state and refractive index near the nanoparticle surface, which makes UV-Visible spectroscopy an important tool to identify, characterize and investigate these materials. Inset of Fig.4.17b shows the UV-Visible absorption spectra of LABNC in the wavelength range 200-800 nm. Absorption was strong across a wide wavelength range, from ultraviolet to visible light, with an absorption tail extending into the infrared. The spectra shows prominent absorption band with maximum at 199, 218 and 254 nm. These absorption bands appeared at 199 and 218 nm were assigned to oxygen to metal ions charge transfer transitions. The electronegativity of the oxygen atoms bonded to the metal centres determines the position of maximum of this band [286]. The other less intense peak observed at 254 nm was expected to arise from transitions involving extrinsic states such as surface states/defects/impurities [287, 288].

Energy gap calculations were performed by the standard procedures taken from previous work

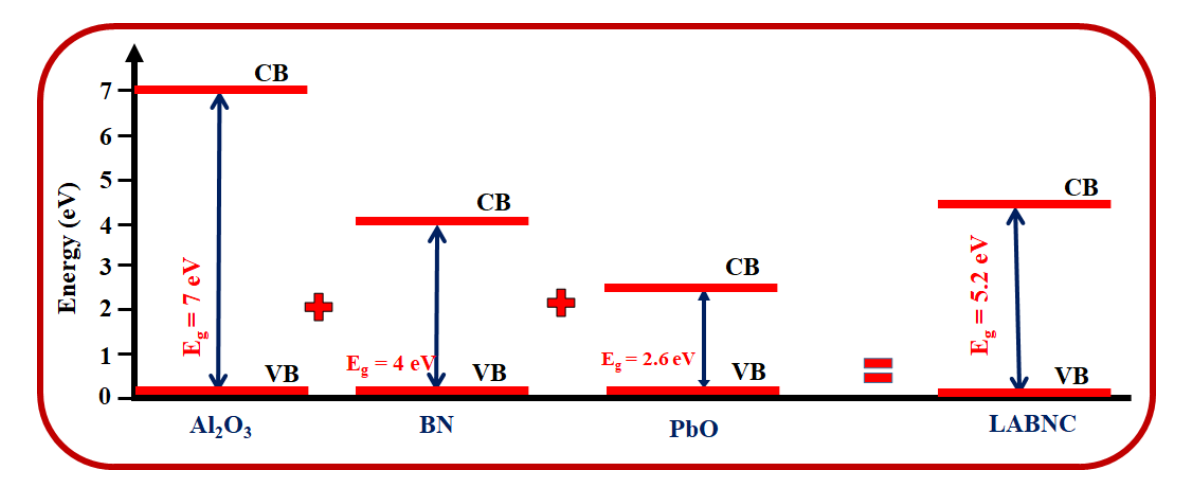


Fig. 4.18 Schematic representation of Energy band diagram of LABNC

[289] was found to be 5.2ev and shown in Fig.4.17(b) Fig.4.18 shows the pictorial representation of energy band diagram. As we observed from the Fig.4.18, as per literature, the energy band gap of Al_2O_3 , PbO and B_2O_3 lies at 7, 2.6 and 4 eV respectively [307–309]. After the formation of NCs, the energy band gap was tuned to 5.2 eV. This decrease in bandgap was mainly due to the introduction of new energy states into the optical band gap [310].

CHAPTER 5

Measurements of shielding values of X, γ radiation of Ba–Ni–Fe oxide, Aluminium-Barium-Zinc oxide and Leadaluminoborate Nanocomposites

5.1 Experiment to measure X, γ radiation shielding dimensions

Standard procedure of radiation shielding parametrs was explained in the previous work[282], same is represented in Fig.5.1.The intensities I_0 and I of the beam before and after passing through the material are measured for sufficient time. The μ/ρ of the material is then estimated using the relation:

$$\left(\frac{\mu}{\rho}\right)_{c} = \left(\frac{1}{t\rho}\right) \ln\left(\frac{I_{o}}{I}\right) \tag{5.1}$$

Where t and ρ are the thickness and density of the material respectively. The spectrum of the γ ray source without target material has been recorded, But when we place the target material above the source there is an interaction between γ rays and target material and produces secondary x-rays. The distinguished spectrum has been recorded that is with target material between the detector and source and spectrum obtained only with source.

Theoretically, μ/ρ are generated using WinXCom program. [263]. Calculation of μ/ρ

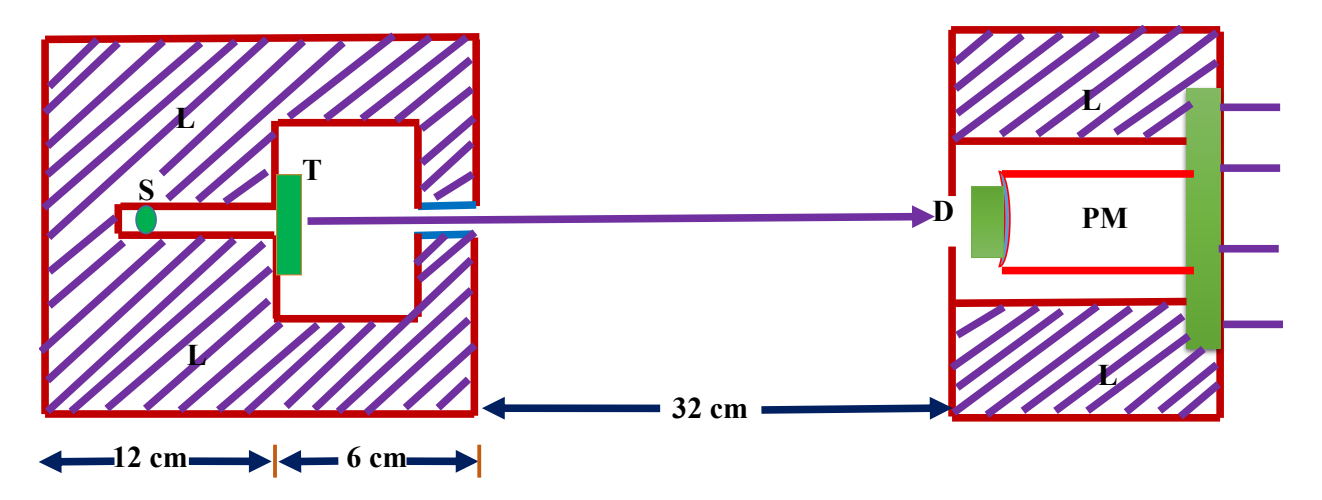


Fig. 5.1 Schematic diagram of the Experimental Setup (S: Source position, T: Target sample, L: Lead shielding, D: Detector, PM: Photomultiplier)

explained in [23]. The HVL, TVL and λ formulas are given below

$$HVL = \frac{ln2}{\mu} = \frac{0.693}{\mu} \tag{5.2}$$

$$TVL = \frac{ln10}{\mu} = \frac{2.303}{\mu} \tag{5.3}$$

$$\lambda = \frac{\int_0^\infty x exp(-\mu x) dx}{\int_0^\infty exp(-\mu x) dx} = \frac{1}{\mu}$$
 (5.4)

In the previous work [26, 196, 197, 263, 265–271] methods have been explained to compute all required parameters

5.2 Analysis

5.2.1 Analysis of measured X-ray / gamma ray shielding properties of Barium-Nickel-Iron oxide Nanocomposites

Gamma sources such as ²²Na (0.511, 0.081 MeV), ⁵⁷Co (1.173, 1.332 MeV), ¹³⁷Cs (0.6615 MeV) and (¹³³Ba (0.276, 0.356 MeV) are used to check the weld defects in industries, medical field, communication system, nuclear reactors, material science, and student research facilities [311]. Thus there is a need to develop the shielding materials for these gamma radiations.

The measured mass attenuation co-efficient compared with the NIST data base and this Comparison is also shown in the table 5.1. In this table, relative difference between the theoretical and experimental values also presented.

Fig.5.2 (a-d) shows the graphical representation of measured gamma ray spectra using differ-**Table 5.1** Comparison of measured mass attenuation co-efficient with that of NIST data.

Energy (MeV)	$(\mu/\rho)_{expt} cm^2/g$	$(\mu/\rho)_{[312]} cm^2/g$	% error
0.276	0.22	0.17774	19.2078
0.365	0.10	0.12274	22.7442
0.511	0.088	0.09202	4.5708
0.662	0.075	0.07676	2.3584
1.173	0.054	0.05485	1.5839
0.511	0.051	0.05249	2.9257

ent sources such as ¹³⁷Cs (0.6615 MeV), ⁶⁰Co (1.173 and 1.332 MeV), ²²Na (0.511, 0.081 MeV) and ¹³³Ba (0.276 and 0.356 MeV) for different thickness 5, 10, 15, 20 and 25 mm of BFNONC. The nature of the gamma ray spectrum is different for different source. For ¹³³Ba gamma ray source, three high intensity peaks are observed at 160.71, 300.37 and 356.75 keV. For ⁶⁰Co source, the gamma ray spectrum consists two peaks at 1174.47 and 1334.3 keV, whereas for ¹³⁷Cs source, single high intense peak is observed at 662.75 keV. Two high intense peaks are observed at 529 and 1287 keV for ²²Na source. As the thickness of BFNONC increases from 5, 10, 15, 20 and

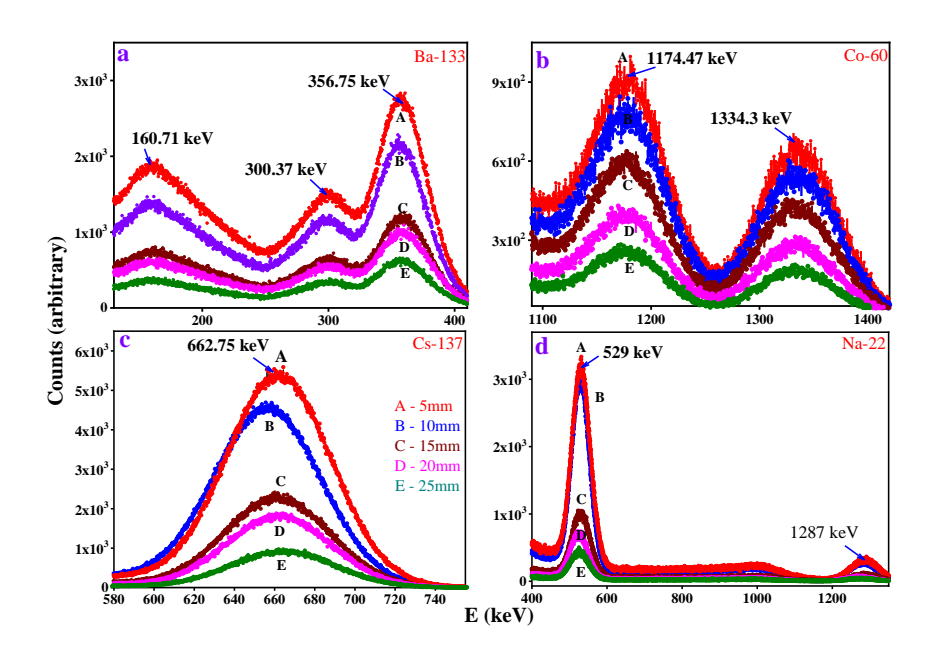


Fig. 5.2 Measured Gamma ray spectra in BFNONC NPs using different sources such as Ba-133, Co-60, Cs-137 and Na-22 for different thickness.

Table 5.2 Comparison of measured X-ray / gamma shielding properties for BFNONC with that of the theory.

SOUR	CE		^{56}Ba		^{22}Na	^{137}Cs	Cs 60Co	
ENERGY	(MeV)	0.081	0.276	0.356	0.511	0.6615	1.173	1.332
$\mu/\rho(cm^2\ g^{-1})$	Th	2.01	0.17	0.11	0.09	0.07	0.06	0.04
	Ex	0.40 ± 0.02	0.22 ± 0.01	0.10 ± 0.01	0.09 ± 0.00	0.08 ± 0.00	0.05 ± 0.00	0.05 ± 0.00
(=1)	Th	9.45	0.78	0.55	0.41	0.37	0.26	0.25
$\mu(cm^{-1})$	Ex	2.16 ± 0.11	0.99 ± 0.05	0.47 ± 0.02	0.42 ± 0.02	0.35 ± 0.02	0.26 ± 0.01	0.25 ± 0.01
HVL (cm)	Th	0.13	1.35	1.82	2.39	2.79	3.88	4.14
HVL (CIII)	Ex	0.65 ± 0.03	1.13 ± 0.06	2.21 ± 0.11	2.37 ± 0.12	2.82 ± 0.14	3.82 ± 0.19	4.14 ± 0.21
TVI (am)	Th	0.08	0.93	1.28	1.67	1.94	2.71	2.86
TVL (cm)	Ex	0.35 ± 0.02	0.75 ± 0.04	1.45 ± 0.07	1.67 ± 0.08	1.93 ± 0.10	2.65 ± 0.13	2.87 ± 0.14
$\lambda(cm)$	Th	0.26	3.13	4.21	5.49	6.47	8.89	9.52
A(CIII)	Ex	1.42 ± 0.07	2.56 ± 0.13	4.87 ± 0.24	5.42 ± 0.27	6.43 ± 0.32	8.93 ± 0.45	9.41 ± 0.47
7	Th	35.57	29.67	26.84	24.26	23.21	21.91	21.87
Z_{eff}	Ex	34.65 ± 1.73	31.13 ± 1.56	28.11 ± 1.41	24.41 ± 1.22	23.18 ± 1.16	22.01 ± 1.10	21.82 ± 1.09
$N_e \times 10^{23}$	Th	4.78	3.98	3.58	3.18	3.15	3.00	2.96
$(electrons g^{-1})$	Ex	4.62 ± 0.23	3.81 ± 0.19	3.65 ± 0.18	3.22 ± 0.16	3.08 ± 0.15	2.92 ± 0.15	2.93 ± 0.15
EABF	Th	43.58	33.88	28.96	24.36	21.39	15.88	14.89
(mfp=10mm)	Ex	21.33 ± 1.07	38.23 ± 1.91	33.54 ± 1.68	24.52 ± 1.23	21.23 ± 1.06	15.84 ± 0.79	14.78 ± 0.74
KERMA	Th	7.01	1.67	1.67	1.67	2.11	2.63	2.63
(MeV)×10 ⁻¹³	Ex	4.69 ± 0.23	2.16 ± 0.11	1.79 ± 0.09	1.95 ± 0.10	2.11 ± 0.11	2.72 ± 0.14	2.88 ± 0.14
SGR	Th	99.65	29.73	28.39	30.17	33.29	42.26	44.94
$(Rm^2 Ci^{-1} h)$	Ex	47.29 ± 2.36	40.44 ± 2.02	28.39 ± 1.42	29.94 ± 1.50	33.12 ± 1.66	42.36 ± 2.12	44.65 ± 2.23
	Th (x=1mm)	3.83×10^{-4}	0.01	0.01	0.01	0.01	0.01	0.01
$SAF(g^{-1})$	Ex (x=1mm)	$(3.00 \pm 0.15) \times 10^{-2}$	0.01 ± 0	0.02 ± 0	0.01 ± 0	0.01 ± 0	0.01 ± 0	0.05 ± 0
(mfp=10mm)	Th (x=5mm)	3.83×10^{-4}	0.06	0.05	0.04	0.04	0.02	0.02
	Ex (x=5mm)	$(3.00 \pm 0.15) \times 10^{-2}$	0.05 ± 0	0.06 ± 0	0.04 ± 0	0.04 ± 0	0.02 ± 0	0.02 ± 0
	Th (t=1)	99.75	53.89	42.55	34.29	29.94	22.81	21.65
RPE	Ex (t=1)	80.13 ± 4.01	50.18 ± 2.51	46.17 ± 2.31	34.45 ± 1.72	30.54 ± 1.53	22.66 ± 1.13	22.13 ± 1.11
	Th (t=5)	99.75	96.97	93.29	87.59	83.24	72.45	70.21
KI L	Ex (t=5)	99.87 ± 4.99	91.19 ± 4.56	88.12 ± 4.41	88.07 ± 4.40	83.83 ± 4.19	72.28 ± 3.61	70.03 ± 3.50
	Th (t=10)	99.75	99.89	99.49	98.54	97.11	92.53	91.02
	Ex (t=10)	99.99 ± 5.00	97.67 ± 4.88	97.15 ± 4.86	98.29 ± 4.91	97.18 ± 4.86	92.21 ± 4.61	90.55 ± 4.53

25 mm, the nature of the gamma ray spectrum remains unaltered except the variation in intensity.

The intensity of the peak increases with decrease in the thickness of the BFNONC. From the ex-

perimental data, the μ/ρ values of BFNONC at different energies are extracted.

Compared to bulk materials nanoparticles significantly improve mechanical properties and

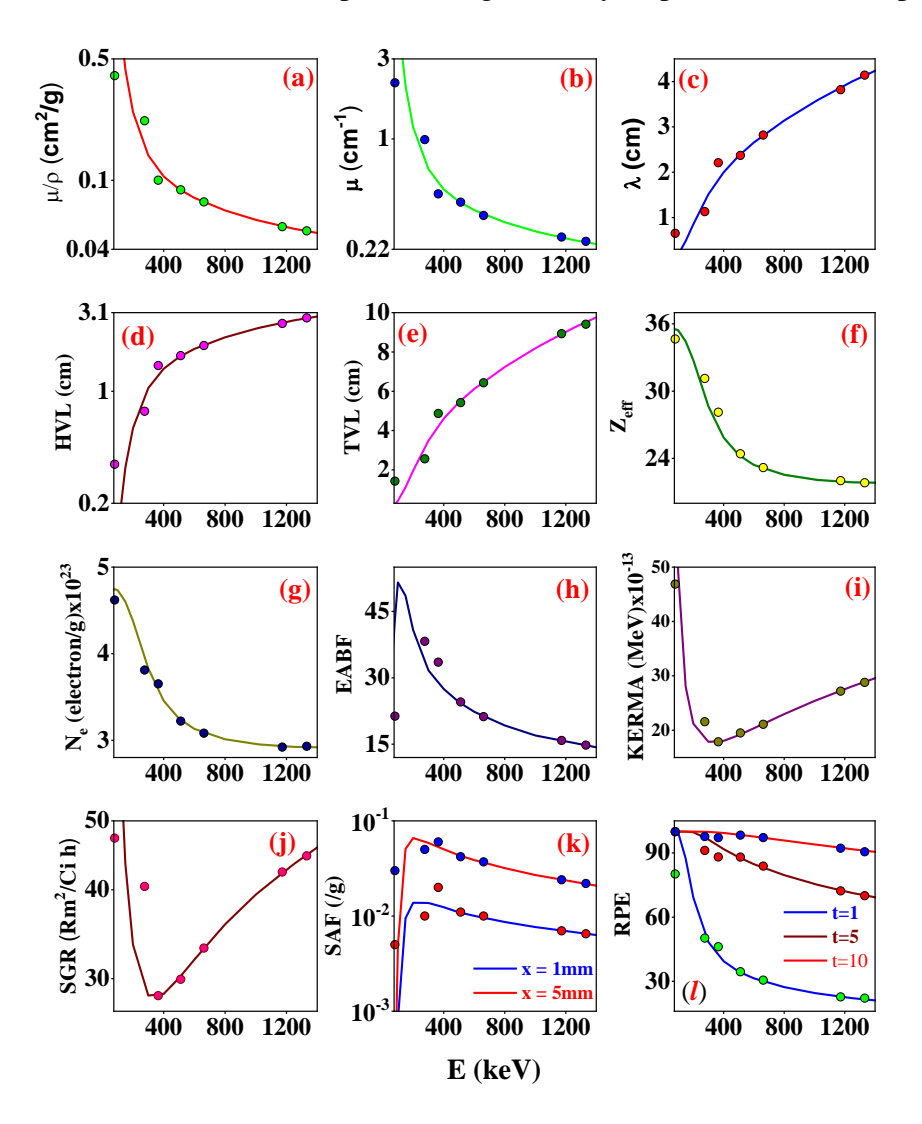


Fig. 5.3 Comparison of measured shielding properties for BFNONC such as (a) μ/ρ , (b) μ , (c) λ , (d)HVL, (e)TVL, (f) Z_{eff} , (g) N_e , (h) EABF, (i) KERMA, (j) SGR, (k) SAF and (l) RPE with that of the theoretical values in the energy range 0.081-1.332 MeV

also shielding to certain extent [313]. One of the radiation shielding parameter μ/ρ is an important parameter for characterizing the penetration and diffusion of X- ray/gamma rays in materials. Higher μ/ρ s means better shielding ability of a material. This radiation shielding property depends on the nature of the material, particle size distribution, energy band gap etc. All these properties of nanoparticles made them to show better shielding property over the bulk material. Fig.5.3 (a-1) and Table 5.2 gives the comparison of measured shielding properties such as μ/ρ , μ ,

HVL, TVL, λ , Z_{eff} , N_e , EABF, KERMA, SGR, SAF and RPE with that of the theoretical values in the energy range 0.081-1.332 MeV . In general, the theoretical values are based on the Hubbel data [74, 314, 315] which is calculated when there is an interaction of X-ray / gamma -ray with the micrometer sized atoms / particles. It is clearly observed from Table 5.2 that above 356 keV X-ray / gamma ray interaction energy, the measured shielding parameters agrees well with the theoretical value whereas slight deviation is observed below 356 keV. The measured shielding parameters agrees well with the theory above 356 keV X-ray/ gamma-ray interaction. Since the crystals / particles are in nano range, the atom / particle size plays a very important role in this deviation. Furthermore, an accurate theory is necessary to explain the X-ray / gamma ray interaction with the NCs.

5.2.2 Analysis of of measured X/ γ ray shielding properties of Aluminium-Barium-Zinc oxide Nanocomposites.

Fig.5.4 (a-d) represents the graphical view of measured γ ray spectra using different radiation

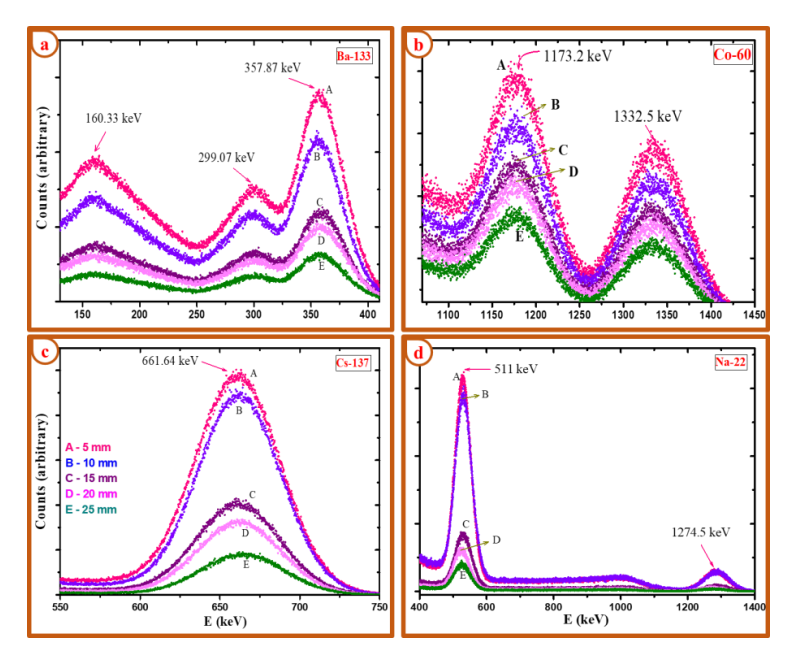


Fig. 5.4 Measured Gamma ray spectra in ZABNONC NPs using different sources such as Ba-133, Co-60, Cs-137 and Na-22 for different thickness.

Table 5.3 Comparison of measured X-ray / gamma shielding properties of ZABNONC with that of the theory.

SOUR	CE		^{56}Ba		^{22}Na	^{137}Cs	^{7}Cs ^{60}Co	
ENERGY	(MeV)	0.081	0.276	0.356	0.511	0.6615	1.173	1.332
/ (2 -1)	Th	0.59	0.23	0.12	0.09	0.08	0.05	0.05
$\mu/\rho(cm^2\ g^{-1})$	Ex	1 ± 0.05	0.32 ± 0.02	0.13 ± 0.01	0.09 ± 0	0.08 ± 0	0.05 ± 0	0.05 ± 0
(-1)	Th	11.43	0.84	0.57	0.39	0.33	0.23	0.21
$\mu(cm^{-1})$	Ex	3.3 ± 0.17	1.2 ± 0.06	0.58 ± 0.03	0.41 ± 0.02	0.34 ± 0.02	0.24 ± 0.01	0.22 ± 0.01
HVI ()	Th	0.06	0.88	1.25	1.69	2.05	2.91	3.12
HVL (cm)	Ex	0.11 ± 0.01	0.56 ± 0.03	1.2 ± 0.06	1.7 ± 0.09	2 ± 0.1	2.9 ± 0.15	3.1 ± 0.16
TVI ()	Th	0.21	2.92	4.13	5.66	6.8	9.66	10.35
TVL (cm)	Ex	0.48 ± 0.02	2 ± 0.1	4.2 ± 0.21	5.7 ± 0.29	6.8 ± 0.34	9.7 ± 0.49	10.3 ± 0.52
1/	Th	0.09	1.27	1.79	2.46	2.94	4.18	4.51
$\lambda(cm)$	Ex	0.15 ± 0.01	1 ± 0.05	1.77 ± 0.09	2.45 ± 0.12	2.95 ± 0.15	4.2 ± 0.21	4.5 ± 0.23
7	Th	42.87	40.52	38.95	36.88	35.77	34.22	34.09
Z_{eff}	Ex	42.2 ± 2.11	40 ± 2	38.9 ± 1.95	36.9 ± 1.85	35.8 ± 1.79	34.2 ± 1.71	34.1 ± 1.71
$N_e \times 10^{23}$	Th	5.82	5.51	5.29	5.01	4.86	4.65	4.63
$(electrons g^{-1})$	Ex	5.62 ± 0.28	5.41 ± 0.27	5.28 ± 0.26	5.02 ± 0.25	4.86 ± 0.24	4.65 ± 0.23	4.63 ± 0.23
EABF	Th	4.59	16.78	17.81	17.86	17.12	14.43	13.75
(mfp=10mm)	Ex	10.1 ± 0.51	16 ± 0.8	17.9 ± 0.9	17.8 ± 0.89	17.2 ± 0.86	14.4 ± 0.72	13.7 ± 0.69
KERMA	Th	7.27	1.71	1.59	1.63	1.78	2.27	2.42
$(MeV) \times 10^{-12}$	Ex	3.87 ± 0.19	1.97 ± 0.1	1.57 ± 0.08	1.65 ± 0.08	1.78 ± 0.09	2.27 ± 0.11	2.42 ± 0.12
SGR	Th	136.27	33.56	30.82	30.68	32.78	42.19	43.6
$(Rm^2 Ci^{-1} h)$	Ex	65.4 ± 3.27	38.5 ± 1.93	30.5 ± 1.53	30.6 ± 1.53	33 ± 1.65	41.5 ± 2.08	43.8 ± 2.19
	Th (x=1mm)	6.71×10^{-5}	0.11	0.10	0.09	0.07	0.05	0.04
$SAF(g^{-1})$	Ex (x=1mm)	0.02 ± 0	0.05 ± 0	0.09 ± 0	0.08 ± 0	0.08 ± 0	0.05 ± 0	0.04 ± 0
(mfp=10mm)	Th (x=5mm)	0.014	4.83	2.47	6.4	9.55	9.94	7.58
	Ex (x=5mm)	0.052 ± 0.0026	5.1 ± 0.26	4.5 ± 0.23	6.3 ± 0.32	6.5 ± 0.33	6.6 ± 0.33	6.8 ± 0.34
	Th (t=1)	99	55.94	43.28	33.47	28.87	21.4	19.97
RPE	Ex (t=1)	90.3 ± 4.52	60.6 ± 3.03	43.7 ± 2.19	33.6 ± 1.68	29.4 ± 1.47	20.7 ± 1.04	20.1 ± 1.01
	Th (t=5)	99	97.56	93.65	87.14	81.44	69.95	67.06
	Ex (t=5)	96.4 ± 4.82	95.5 ± 4.78	94.3 ± 4.72	86.7 ± 4.34	80.6 ± 4.03	69.1 ± 3.46	67.3 ± 3.37
	Th (t=10)	99.89	100.11	99.86	98.46	96.41	90.76	89.33
	Ex (t=10)	98 ± 4.9	98 ± 4.9	99.3 ± 4.97	98.8 ± 4.94	97.2 ± 4.86	90.4 ± 4.52	89.1 ± 4.46

sources viz: 137 Cs (0.6615 MeV), 60 Co (1.173 and 1.332 MeV), 22 Na (0.511, 0.081 MeV) and 133 Ba (0.276 and 0.356 MeV) and this procedure is done with various thickness (shown in graph) of ZABNONC. From the graph it is very clear that the shape of spectrum is different for different source, with the change of thickness, shape of graph remains unchanged but the intensity of the peaks is varying inversely with the thickness, furthermore for different radiation sources different peaks are observed at different energies,namely for 133 Ba , three high intensity peaks at 160.71, 300.37 and 356.75 keV. 60 Co has peaks at 1174.47 and 1334.3 keV, 137 Cs single maximum intense peak at 662.75 keV and finally Two high intense peaks at 528 and 1287 keV for 22 Na source. From the experimental data, the μ/ρ values of ZABNONC of various energy levels are recovered.

Fig.5.5 (a-l), Table 5.3 correlation all measured shielding properties (Mentioned in the keywords) with that of the theoretical values in the energy range 0.081-1.332 MeV. In general, the

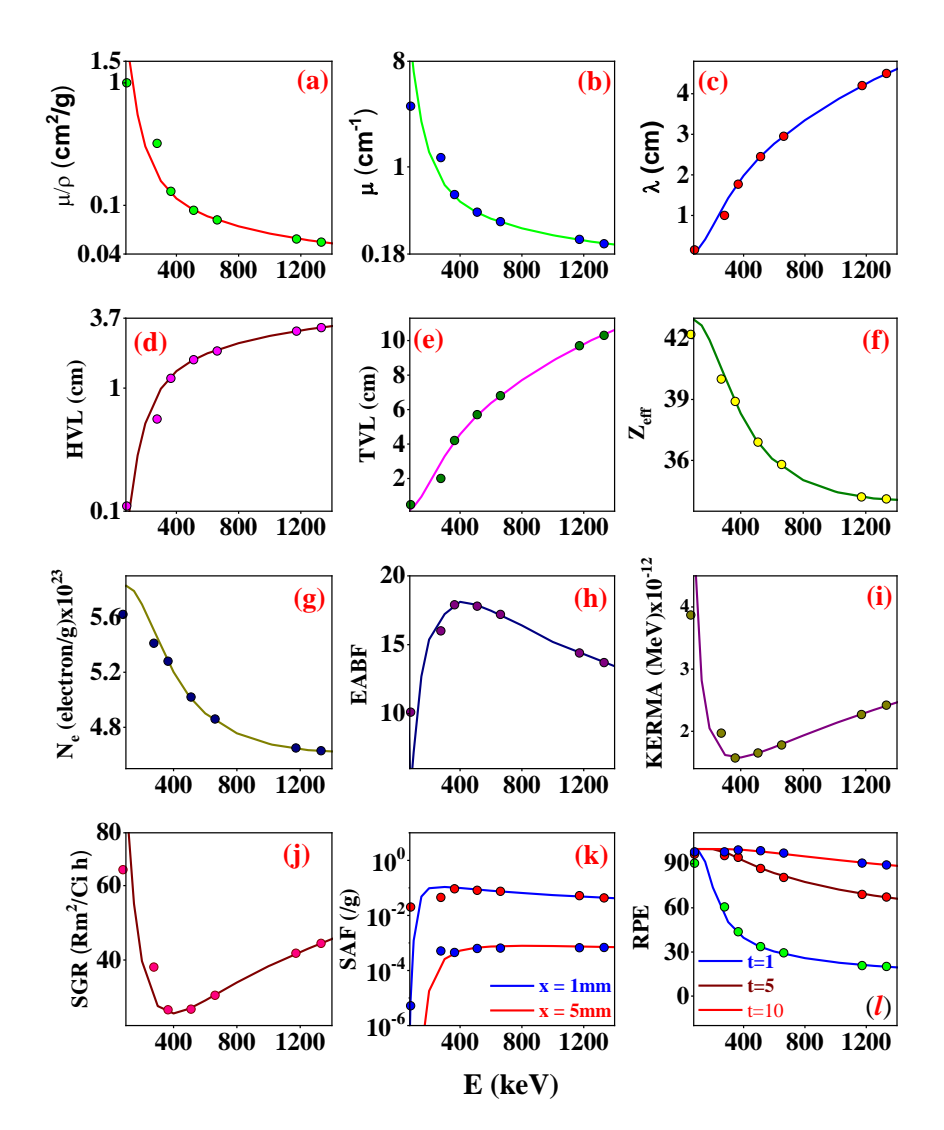


Fig. 5.5 Comparison of measured shielding properties for ZNBNONC such as (a) μ/ρ , (b) μ , (c) λ , (d)HVL, (e)TVL, (f) Z_{eff} , (g) N_{el} , (h) EABF, (i) KERMA, (j) SGR, (k) SAF and (l) RPE with that of the theoretical values in the energy range 0.081-1.332 MeV

theoretical values are based on the Hubbel data [74, 314, 315],these values are extracted when there is an interaction of X/ γ radiation with minute particles/atoms of size in the order 10^{-6} m . It is clearly observed from Table 5.3 that above 356 keV X/ γ ray interaction energy, the measured shielding parameters agrees well with the theoretical value whereas slight deviation is observed below 356 keV due to the crystals are in the order 10^{-9} m , Furthermore, an accurate theory is necessary to explain the X/ γ ray interaction with the NCs.

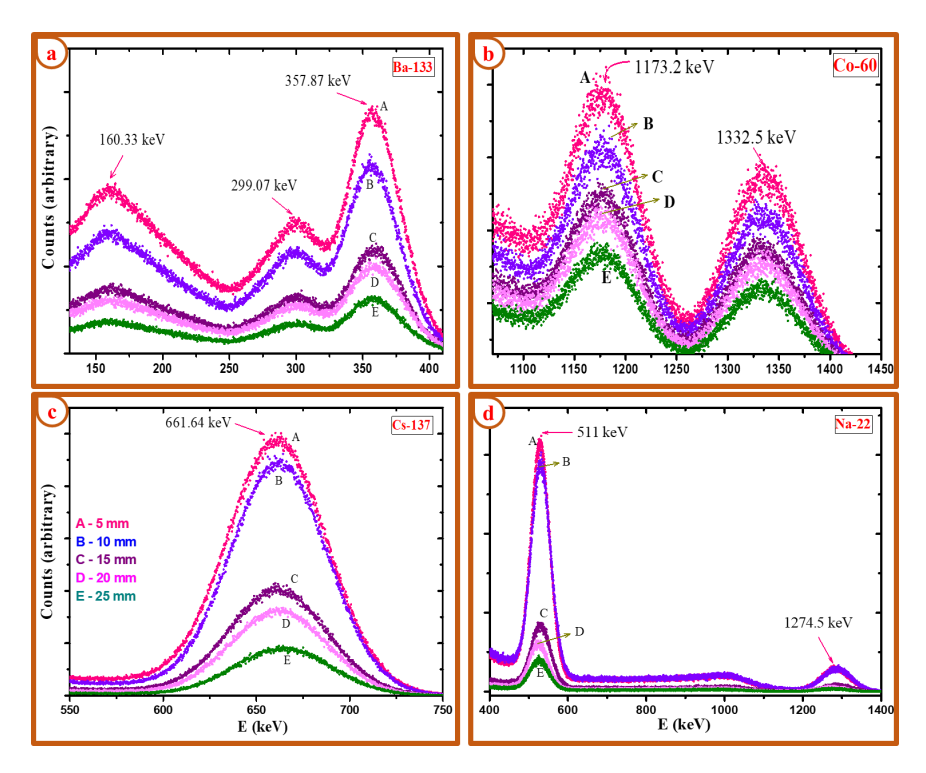


Fig. 5.6 Measured Gamma ray spectra in LABNC using different sources such as Ba-133, Co-60, Cs-137 and Na-22 for different thickness.

5.2.3 Study of shielding properties of X, γ radiation of Leadaluminoborate Nanocomposites

Fig.5.6 (a-d) shows the graphical representation of measured gamma ray spectra using different sources such as 137 Cs (0.6615 MeV), 60 Co (1.173 and 1.332 MeV), 22 Na (0.511, 0.081 MeV) and 133 Ba (0.276 and 0.356 MeV) for different thickness 5, 10, 15, 20 and 25 mm of LABNC. The nature of the gamma ray spectrum is different for different source. For 133 Ba gamma ray source, three high intensity peaks are observed at 160.71, 300.37 and 356.75 keV. For 60 Co source, the gamma ray spectrum consists two peaks at 1174.47 and 1334.3 keV, whereas for 137 Cs source, single high intense peak is observed at 662.75 keV. Two high intense peaks are observed at 528 and 1287 keV for 22 Na source. As the thickness of LABNC increases from 5, 10, 15, 20 and 25 mm, nature of the gamma ray spectrum remains unaltered except the variation in intensity. The intensity of the peak increases with decrease in the thickness of the LABNC. From the experimental data, the μ/ρ values of LABNC at different energies are extracted.

Comparison of measured shielding properties with theoretical was correlated in Table 5.4 and

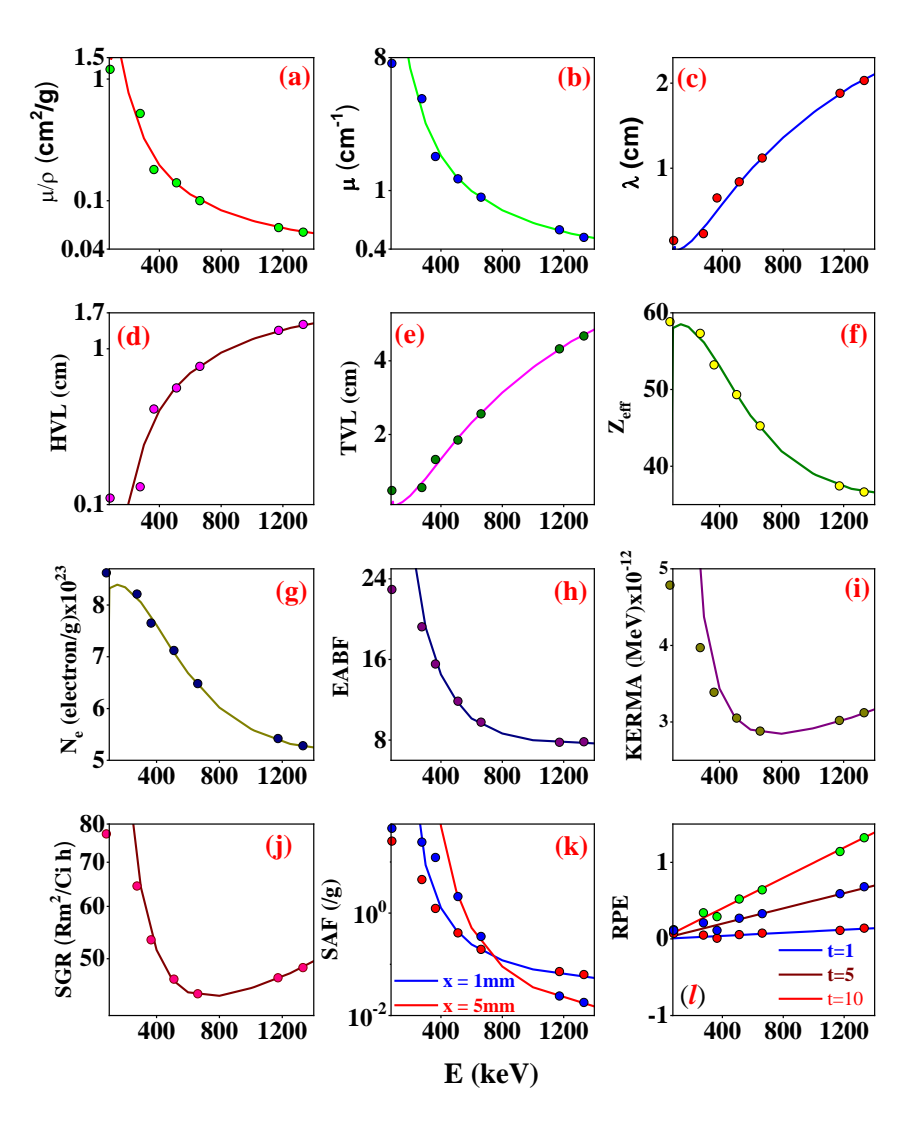


Fig. 5.7 Comparison of measured shielding properties for LABNC of such as (a) μ/ρ , (b) μ , (c) λ , (d)HVL, (e)TVL, (f) Z_{eff} , (g) N_{el} , (h) EABF, (i) KERMA, (j) SGR, (k) SAF and (l) RPE with that of the theoretical values in the energy range 0.081-1.332 MeV

Fig.5.7.The theoretical values are based on the Hubbel data [74, 314, 315]. From Fig.5.7, is is observed that, gamma interaction parameters such as μ/ρ , μ , Z_{eff} , N_e , EABF, KERMA, SGR and SAF increases, whereas HVL, TVL, λ , RPE decreases with increase in energy. These are the properties of good shielding material. Hence, the present nanocomposite might be a good absorbing material. It is clearly observed from Table 5.4 that above 356 keV X-ray/gamma ray interaction energy, the measured shielding parameters agrees well with the theoretical value whereas slight deviation is observed below 356 keV. Since the crystals/particles are in nanorange, the atom/particle

Table 5.4 Comparison of measured X-ray/gamma shielding properties of LABNC with that of the theory.

SOUR	CE		^{56}Ba		^{22}Na	^{137}Cs	60(Co
ENERGY	(MeV)	0.081	0.276	0.356	0.511	0.6615	1.173	1.332
/ / 2 =1\	Th	1.79	0.43	0.25	0.14	0.10	0.06	0.06
$\mu/\rho(cm^2 g^{-1})$	Ex	1.20 ± 0.06	0.52 ± 0.03	0.18 ± 0.01	0.14 ± 0.01	0.10 ± 0.01	0.06 ± 0.00	0.06 ± 0.00
(-1)	Th	15.70	3.80	0.23	1.22	0.91	0.54	0.49
$\mu(cm^{-1})$	Ex	7.30 ± 0.37	4.20 ± 0.21	1.70 ± 0.09	1.20 ± 0.06	0.90 ± 0.05	0.54 ± 0.03	0.48 ± 0.02
11371 ()	Th	0.04	0.21	0.33	0.57	0.78	1.30	1.42
HVL (cm)	Ex	0.11 ± 0.01	0.13 ± 0.01	0.41 ± 0.02	0.56 ± 0.03	0.77 ± 0.04	1.31 ± 0.77	1.43 ± 0.07
TNII ()	Th	0.15	0.69	1.10	1.90	2.57	4.31	4.70
TVL (cm)	Ex	0.48 ± 0.02	0.56 ± 0.03	1.32 ± 0.07	1.85 ± 0.09	2.56 ± 0.13	4.32 ± 0.22	4.67 ± 0.23
1()	Th	0.06	0.30	0.48	0.83	1.12	1.87	2.04
$\lambda(cm)$	Ex	0.15 ± 0.01	0.23 ± 0.01	0.65 ± 0.03	0.84 ± 0.04	1.12 ± 0.06	1.88 ± 0.09	2.03 ± 0.10
7	Th	39.53	56.62	54.42	49.35	45.18	37.67	36.80
Z_{eff}	Ex	58.83 ± 2.94	57.32 ± 2.87	53.21 ± 2.66	49.32 ± 2.47	45.25 ± 2.26	37.42 ± 1.87	36.63 ± 1.83
$N_e \times 10^{23}$	Th	5.67	8.12	7.81	7.08	6.48	5.40	5.28
$(electrons g^{-1})$	Ex	8.62 ± 0.43	8.21 ± 0.41	7.65 ± 0.38	7.12 ± 0.36	6.48 ± 0.32	5.42 ± 0.27	5.28 ± 0.26
EABF	Th	57.46	21.42	16.58	11.75	9.68	7.85	7.73
(mfp=10mm)	Ex	22.94 ± 1.15	19.24 ± 0.96	15.55 ± 0.78	11.86 ± 0.59	9.78 ± 0.49	7.78 ± 0.39	7.83 ± 0.39
KERMA	Th	6.27	5.12	3.85	3.04	2.88	3.01	3.12
(MeV)×10 ⁻¹²	Ex	4.78 ± 0.24	3.97 ± 0.20	3.39 ± 0.17	3.05 ± 0.15	2.88 ± 0.14	3.02 ± 0.15	3.12 ± 0.16
SGR	Th	94.94	73.10	57.10	46.27	44.28	46.78	48.67
$(Rm^2 Ci^{-1} h)$	Ex	77.29 ± 3.86	64.44 ± 3.22	53.39 ± 2.67	46.54 ± 2.33	44.22 ± 2.21	46.76 ± 2.34	48.45 ± 2.42
	Th (x=1mm)	-6.31×10 ⁷⁶	-5.89×10^{10}	-35.10	0.45	0.21	0.07	0.06
$SAF(g^{-1})$	Ex (x=1mm)	$(-25.54 \pm 1.28) \times 10^{76}$	$(-4.53 \pm 0.23) \times 10^{10}$	-1.23 ± 0.06	0.41 ± 0.02	0.20 ± 0.01	0.07 ± 0	0.06 ± 0
(mfp=10mm)	Th (x=5mm)	2.56×10^{78}	8.65×10^{12}	1.45×10^4	2.46	0.39	0.03	0.02
	Ex (x=5mm)	$(45.22 \pm 2.26) \times 10^{78}$	$(24.42 \pm 1.22) \times 10^{12}$	$(12.23 \pm 0.61) \times 10^4$	2.11 ± 0.11	0.35 ± 0	0.02 ± 0	0.02 ± 0
	Th (t=1)	0.008	0.03	0.04	0.05	0.07	0.12	0.13
	Ex (t=1)	0.12 ± 0.01	0.34 ± 0.02	0.29 ± 0.01	0.52 ± 0.03	0.64 ± 0.03	1.14 ± 0.06	1.32 ± 0.07
RPE	Th (t=5)	0.04	0.14	0.18	0.26	0.33	0.58	0.66
	Ex (t=5)	0.07 ± 0	0.05 ± 0	0.01 ± 0	0.06 ± 0	0.08 ± 0	0.11 ± 0.01	0.14 ± 0.01
	Th (t=10)	0.08	0.28	0.36	0.51	0.66	1.17	1.33
	Ex (t=10)	0.11 ± 0.01	0.21 ± 0.01	0.11 ± 0.01	0.27 ± 0.01	0.33 ± 0.02	0.59 ± 0.03	0.68 ± 0.03

size plays a very important role in this deviation.

The medical radiation shield is primarily utilised as a fabric for radiation-shielding aprons. The thickness and weight of the shielding fabric are critical considerations in ensuring user safety. The interaction of radiation with the nanomaterial produces photoelectric and compton effect. Good shielding efficiency is observed in the lower region where photoelectric effect is dominant. At the higher region (Compton effect), shielding efficiency is less because of scattering due to transmission rather than due to absorption. More particles are needed to improve shielding performance by increasing the probability of interaction within the same area. In nanomaterials, the number of particles per unit area is large in the shielding sheet, density is high and uniform dispersion can be achieved. When the particles are in nanoscale, a multilayered structure can be formed in the shielding sheet because of the clustering effect and shielding efficiency can be improved [316].

In the present study, the theory will explain how the gamma/X-ray radiation shielding parameters is going to vary with respect to kinetic energy in the nanoscale range.

CHAPTER 6

Summary and conclusion

6.1 Criteria for selection of good absorber of X-ray/gamma radiation

The material/medium which is having larger values of μ/ρ , Z_{eff} , Γ , RPE, buildup factor, Specific absorbed fraction and relative dose, meanwhile smaller values of mean free path, TVL and HVL are considered as good absorber of X-ray/gamma radiation. In this view, eight different alloys such as Iron-Boron, Iron-Silicon, Gallium alloys, lead alloys, Aluminium alloys, Silicon-Boron alloys, Zinc alloys and Silicon-Germanium were considered during the detail investigations. The selected alloy in each category with the above said criteria is follows;

6.2 Selection of good shielding material

6.2.1 **Iron-Boron alloys**

Earlier researchers [14] studied X-ray and γ -ray shielding properties in six different Iron-Boron alloys such as Fe_{0.95} B_{0.05}, Fe_{0.9} B_{0.1}, Fe_{0.8} B_{0.2}, Fe_{0.7} B_{0.3}, Fe_{0.6} B_{0.4} and Fe_{0.5} B_{0.5}. The shielding parameters were studied. Eventually, it is found that the Fe_{0.95} B_{0.05} satisfies above said criteria. Hence Fe_{0.95} B_{0.05} is good absorber of X-ray/gamma radiation among Iron-Boron alloys. Hence, in the present study the Iron-Boron Fe_{0.95} B_{0.05} alloy has been considered for further investigation.

6.2.2 Silicon alloys

The different types of Silicon alloys such as Al-47 (Al_{0.87} Si_{0.1} Ni_{0.008}, Al-32S(Al_{0.854} Cu_{0.008}Si_{0.12} Mg_{0.001} Ni_{0.008}), Al-43 (Al_{0.95} Si_{0.05}), Ferrosilicon Fe_{0.21} Si_{0.79}, Al-356 (Mg_{0.003} Al_{0.927} Si_{0.07}), Al-355(Al_{0.93} Si_{0.05} Cu_{0.013} Mo_{0.005}) and Al-A355 (Al_{0.92} Cu_{0.014}Si_{0.05} Mn_{0.008}Mg_{0.005} Ni_{0.0075}) [23] were investigated. In addition to shielding parameters, the coherent/incoherent neutron scattering lengths and cross sections were also studied. Again investigations were carried for the scattering/absorption neutron cross sections of silicon alloys. Among the different studied silicon alloys, the Iron-silicon $Fe_{0.21}Si_{0.79}$ alloy possesses good shielding properties. Hence, in further investigations we have used $Fe_{0.21}Si_{0.79}$ alloy.

6.2.3 **Gallium alloys**

The different Gallium alloys such as Galfenol Fe_{0.3} Ga_{0.7}, Galinstan Ga_{0.685} In_{0.215} Sn_{0.1} and Gallium alloy Al_{0.5} Ga_{0.5} [33] were investigated in detail. The detail analysis of shielding properties shows that Galinstan Ga_{0.685} In_{0.215} Sn_{0.1} is a good shielding material with less hazardous and cost-effective material when compared to other Gallium alloys studied. As a result, in subsequent studies, we employed Galinstan alloy ($Ga_{0.685}$ In_{0.215} Sn_{0.1}).

6.2.4 Lead alloys

Literature [3] mainly focuses on lead based alloys shielding properties. The selected alloys are as follows; Foundary type $(Sn_{0.15} Sb_{0.23} Pb_{0.62})$, Molybdochalkos $(Pb_{0.9} Cu_{0.1})$, Lino type $(Sn_{0.04} Sb_{0.16} Pb_{0.8})$, Turne type $(Sn_{0.2} Pb_{0.8})$, Mono type $(Sn_{0.09} Sb_{0.19} PB_{0.72})$, Type metal $(Sn_{0.03} Sb_{0.11} Pb_{0.86})$, Stereo type $(Sn_{0.06} Sb_{0.14} Pb_{0.8})$ and Woods metal $(Cd_{0.1} Sn_{0.13} Pb_{0.27} Bi_{0.5})$. According to detail analysis, the binary alloy Molybdochalkos $(Pb_{0.9} Cu_{0.1})$ has good shielding properties. As a result, in our further research, we chose Molybdochalkos alloy.

6.2.5 **Aluminium alloys**

Around eight aluminium alloys such as Li-Al Li_{0.02} Al_{0.98}, Hydronalium Mg_{0.12} Mn_{0.01} Al_{0.87}, Hiduminium Cu_{0.2} Fe_{0.2} Ni_{0.2} Al_{0.94}, Italma Mg_{0.035} Mn_{0.003} Al_{0.96}, Magnalium Mg_{0.5} Al_{0.5}, Ni-Ti-Al Ti_{0.4} Al_{0.1} Ni_{0.50}, Duralumin Al_{0.9} Cu_{0.1} and Y alloy Cu_{0.04} Ni_{0.04} Mg_{0.04} Al_{0.88} are investigated. Exploration of all these aluminium alloys for shielding properties exhibits good absorber for Ni-Ti-Al alloy. Consequently, we explored $Ti_{0.4}Al_{0.1}Ni_{0.50}$ alloy in further investigations.

6.2.6 Silicon-Boron alloys

About six Silicon-Boron alloys such as $Si_{0.5}$ $B_{0.5}$, $Si_{0.6}$ $B_{0.4}$, $Si_{0.7}$ $B_{0.3}$, $Si_{0.8}$ $B_{0.2}$, $Si_{0.9}$ $B_{0.1}$ and $Si_{0.95}$ $B_{0.05}$ were explored. Using detail analysis of Silicon-Boron alloys, it is observed that the $Si_{0.95}$ $B_{0.05}$ possess good shielding material. As an outcome, we conducted further research on the $Si_{0.95}$ $B_{0.05}$ alloy.

6.2.7 **Zinc alloys**

Zinc alloys can be utilised as biodegradable metals because of their corrosion resistance and biocompatibility [317]. The good shielding material of Zinc alloys were considered using different parameters such as relative dose and SAF in the energy range 15keV to 15MeV. The different composition of Zinc alloys such as $Cu_{0.7}$ $Ni_{0.15}$ $Zn_{0.15}$, $Cu_{0.6}$ $Ni_{0.2}$ $Zn_{0.2}$, $Cu_{0.5}$ $Ni_{0.25}$ $Zn_{0.25}$, $Cu_{0.4}$ $Ni_{0.3}$ $Zn_{0.3}$, $Cu_{0.3}$ $Ni_{0.35}$ $Zn_{0.35}$ and $Cu_{0.2}$ $Ni_{0.4}$ $Zn_{0.4}$ have been studied. The good shielding material is selected in such a way that the comparison of relative dose and specific absorbed fraction (SAF) were found to be larger. In this way the Zinc alloy i.e $Cu_{0.7}$ $Ni_{0.15}$ $Zn_{0.15}$ posses larger SAF and relative dose and in further examinations we used $Cu_{0.7}$ $Ni_{0.15}$ $Zn_{0.15}$ alloy.

6.2.8 Silicon-Germanium alloys

The neutron shielding parameters of around six Silicon-Germanium alloys are studied. The Si-Ge alloys such as $Si_{0.1}$ $Ge_{0.9}$, $Si_{0.2}$ $Ge_{0.8}$, $Si_{0.4}$ $Ge_{0.6}$, $Si_{0.6}$ $Ge_{0.4}$, $Si_{0.8}$ $Ge_{0.2}$ and $Si_{0.9}$ $Ge_{0.1}$ were investigated. Among the studied Silicon-Germanium alloys, the $Si_{0.1}$ $Ge_{0.9}$ alloy posses lesser TVL, HVL and penetration depth and larger values of Γ , Z_{eff} , RPE and kinetic energy released in matter. Then in subsequent studies, we utilised $Si_{0.1}$ $Ge_{0.9}$ alloy.

During the detailed examinations of eight different alloys including Iron-Boron, Silicon, Gallium, lead, Aluminium, Silicon-Boron, Zinc and Silicon-Germanium it is seen that one of the material posses good shielding properties in each category. The selected alloy in each category is based on the aforementioned criteria.

The good absorber of X-ray and Gamma radiation among each category is selected. Among the studied iron-boron alloys, Fe_{0.95} B_{0.05} was found to be best shielding materials. Similarly, Ferro-Silicon (Fe_{0.21} Si_{0.79}), Galinstan (Ga_{0.685} In_{0.215} Sn_{0.1}), Molybdochalkos (Cu_{0.1} Pb_{0.9}), Ni-Ti-Al (Ti_{0.4} Al_{0.1} Ni_{0.50}), Silicon-Boron alloy (Si_{0.95} B_{0.05}), Zinc alloy (Cu_{0.7} Ni_{0.15} Zn_{0.15}) and Silicon-Germanium alloy (Si_{0.1} Ge_{0.9}) are found to be good absorber among the Iron-Silicon, Gallium, lead, Aluminium, Silicon-Boron, Zinc and Silicon-Germanium respectively.

6.3 Comparison of shielding parameter amoung studied alloys

The parameters such as μ/ρ , λ , TVL, Z_{eff} , Γ , RPE and KERMA is studied in the selected alloys such as Iron-Boron alloy (Fe_{0.95} B_{0.05}), Ferro-silicon (Fe-Si) alloy, Galinstan alloy (Ga_{0.685} In_{0.215} Sn_{0.1}), Molybdochalkos alloy (Cu_{0.1} Pb_{0.9}), Aluminium alloy i.e Ni-Ti-Al Ti_{0.4} Al_{0.1} Ni_{0.50} alloy, Silicon-Boron alloy (Si_{0.95} B_{0.05}) alloy, Zinc alloy (Cu_{0.7} Ni_{0.15} Zn_{0.15}) and Silicon-Germanium alloy (Si_{0.1} Ge_{0.9}).

Response of μ/ρ is studied with energy is depicted in figure 6.1(a). The selected eight differ-

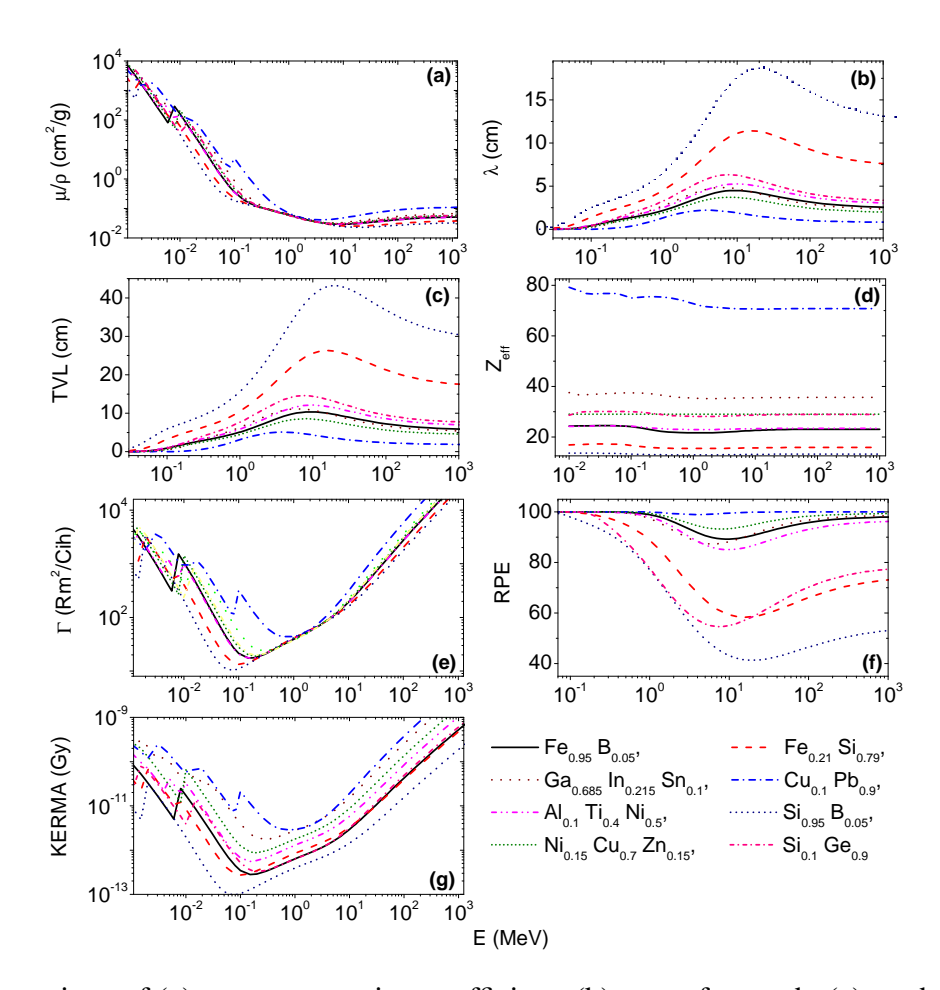


Fig. 6.1 Comparison of (a) mass attenuation coefficient, (b) mean free path, (c) tenth value layer, (d) effective atomic number, (e) specific gamma ray constant, (f) radiation protection efficiency and (g) KERMA with that of energy for the studied alloys.

ent alloys are studied in the energy range 1keV to 100GeV. μ/ρ decreases with increase in energy for the studied alloys. Relatively all alloys decreases with energy, however absorption peaks were observed near 1keV, 10keV and 100keV when these different alloys interact with the γ -rays. The overall behaviour of μ/ρ in lower energy region is due to photo electric effect followed by Compton effect in middle region and higher energy region is mainly due to pair production. Hence, from all the studied alloys it is noticed that Molybdochalkos alloy posses larger μ/ρ value when compared to other studied alloys. Further, λ is investigated as a function of energy as shown in figure 6.1(b). Among all the studied alloys, energy varies inversely proportional to λ where λ is the distance between successive collision reaches a maximum value and again as the larger energy leads to decrease in λ . From the figure it is evident that the Molybdochalkos alloy's peak is shifted

towards left side and on other side Si-B alloy's peak is shifted towards right side. The λ is minimum in case of Molybdochalkos alloy and larger when compared to Si-B alloy. Similar effect is also observed for TVL with that of energy as seen in figure 6.1(c). In addition, the role of effective interaction with photons were studied and it is represented in figure 6.1(d).

The value of Z_{eff} varies between 10 to 80 and among which the Molybdochalkos alloy is having larger value when compared to other studied alloys. The specific gamma ray constant Γ with that of energy is shown in figure 6.1(e). The value of Γ decreases and reaches minimum when energy corresponds to 100keV. However, in case of Molybdochalkos alloy minimum is achieved at 1MeV. In majority of alloys absorption peaks were observed from 1keV to 100keV when these alloys interact with photons. It is noticed that the Molybdochalkos alloy possess larger value when compared to other studied alloys. Later, we have also studied RPE as a function of energy as manifested in figure 6.1(f). The variation observed in this case is reverse as seen in figure 6.1(b) and (c). The larger value of RPE is observed for the Molybdochalkos alloy. KERMA is also studied with the energy in the range 1keV to 100GeV. As similar to figure 6.1(e), the KERMA value also decreases and reaches minimum when energy corresponds to 100keV. In case of Molybdochalkos alloy, the minimum is obtained at 1MeV. In majority of alloys absorption peaks were detected ranging from 1keV to 100keV when these alloys interact with photons. When compared to the other alloys investigated, the Molybdochalkos alloy has a higher value of KERMA.

Furthermore, energy absorption buildup factors are studied for all eight selected alloys. The figure 6.2 shows variation of buildup factors at different penetration depths (λ =5cm, 10cm, 20cm and 40cm) as function of energy. The buildup factor increases gradually and reaches a maximum value when energy ranges between 0.1MeV to 1MeV. Again in all these studied alloys buildup factor decreases with increase in energy. In all the penetration depths the observed maxima is found to be almost at the same position. The X-ray/Gamma radiation absorption is maximum at

the energy where the absorption buildup factor is also maximum.

Furthermore, specific absorption fraction of energy $\varphi(g^{-1})$ is studied in all eight different

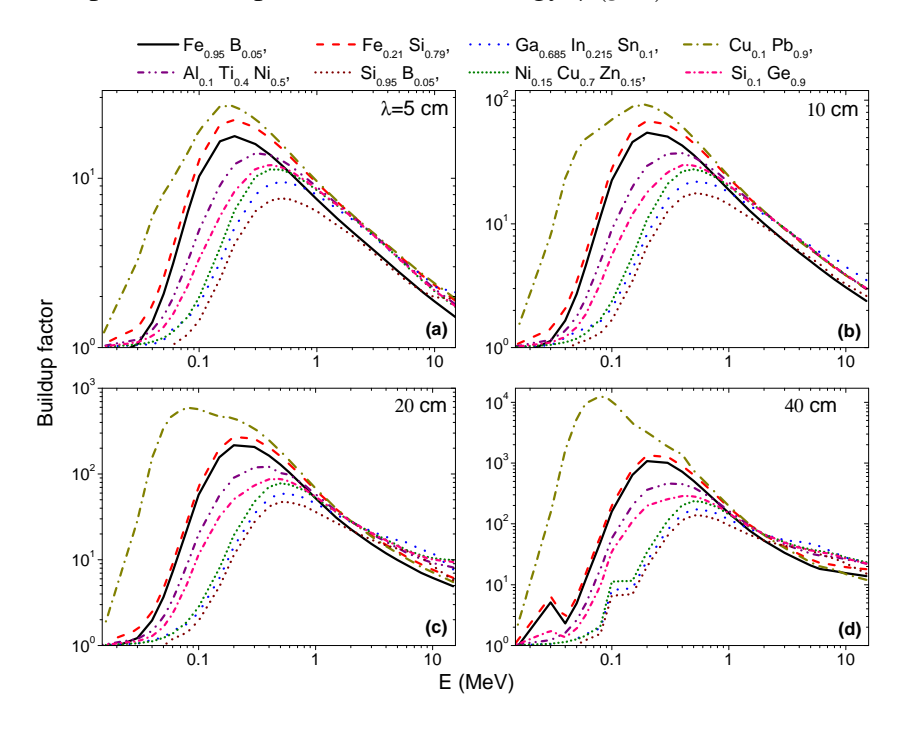


Fig. 6.2 Comparison of buildup factors of the studied alloys with that of photon energy at penetration depths of (a) 5 cm, (b) 10 cm, (c) 20 cm and (d) 40 cm.

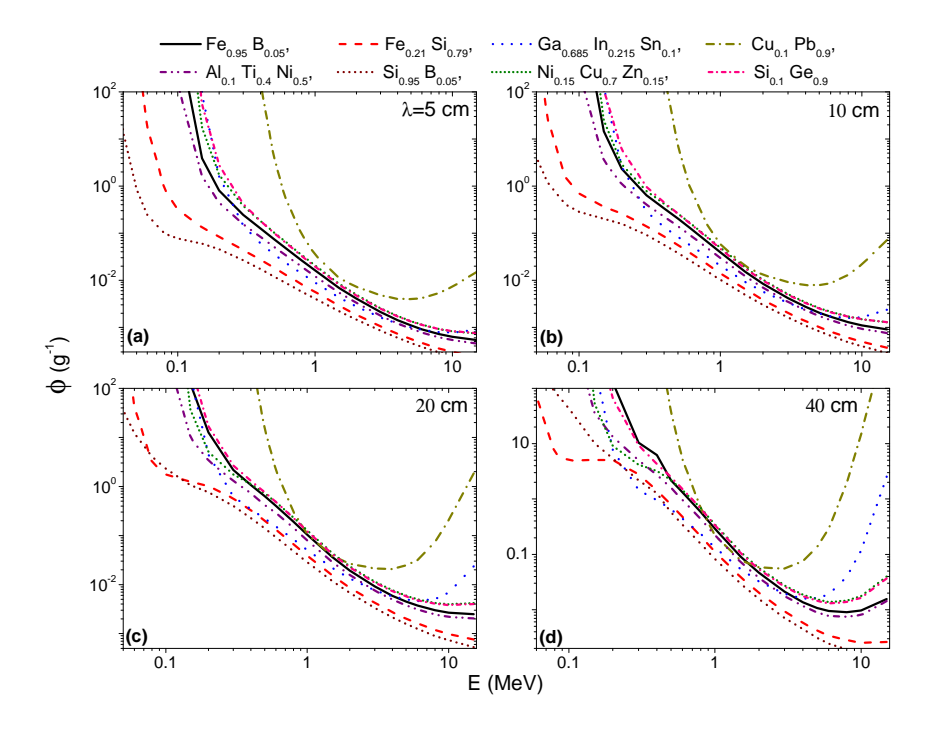


Fig. 6.3 Comparison of specific absorption fraction of energy of the studied alloys as a function of photon energy at penetration depths of (a) 5 cm, (b) 10 cm, (c) 20 cm and (d) 40 cm.

alloys at different penetration depth with the photon energy and it is shown in figure 6.3. The

value of $\varphi(g^{-1})$ decreases with increase in photon energy. A systematic variation is observed for all the studied alloys except Molybdochalkos alloy and Galinstan alloy. In these two cases there is a gradual increase of $\varphi(g^{-1})$ is observed when photon energy is greater than 1MeV particularly when penetrating depth is equal to 20cm and 40cm which is clearly visible in figure 6.3(c) and (d). This may be due to the presence of heavy element like Lead (Pb) which may leads to production of secondary radiations [318].

The relative dose of each alloy studied is defined as the ratio of the target dose rate to the

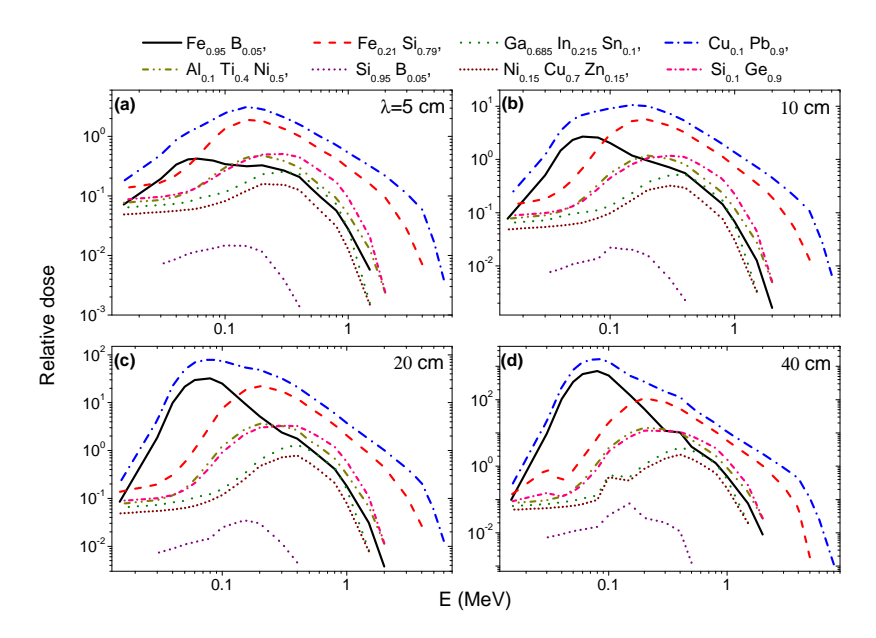


Fig. 6.4 Comparison of relative dose of the studied alloys with that of photon energy at penetration depths of (a) 5 cm, (b) 10 cm, (c) 20 cm and (d) 40 cm.

initial dose rate. A plot of relative dose as a function of photon energy is shown in figure 6.4(a) to (d) at different penetration depths. From the figure 6.4(a) it is seen that the value of relative dose increases and attains a maximum value and again it gradually declines. The peak value is shifted from left for FeB to right in the SiGe alloy. Similarly, larger value of relative dose is also observed when penetration depth is equal to 20cm and 40cm. At penetration depths, the Molybdochalkos alloy posses larger value of relative dose when compared to other studied alloys. Hence, the detail investigation shows that the Molybdochalkos alloy possesses larger value of μ/ρ , Z_{eff} , Γ , RPE, KERMA, buildup factor, specific absorption fraction and relative dose, smaller value of λ and

TVL.

After detail investigation, it is found that λ and TVL are large at one particular energy, mean-**Table 6.1** X-ray/gamma energy at which shielding efficiency becomes minimum (E_m^S) and corresponding λ , Z_{eff} , HVL and RPE (%)

Alloys	$E_m^s({ m MeV})$	λ (cm)	Z_{eff}	HVL(cm)	RPE (%)
$Fe_{0.95}B_{0.05}$	9	4.49	22.5	3.11	89
$Fe_{0.21}Si_{0.79}$	16	11.42	15.73	7.91	58
$Ga_{0.685}In_{0.215}Sn_{0.1}$	6	4.85	35.42	3.36	87
$Cu_{0.1}Pb_{0.9}$	4	2.21	70.82	1.53	99
$Al_{0.1}Ti_{0.4}Ni_{0.5}$	10	5.26	23.24	3.65	85
$Si_{0.95}B_{0.05}$	20	18.74	13.15	12.99	41
$Ni_{0.15}Cu_{0.7}Zn_{0.15}$	8	3.72	28.98	2.58	93
$Si_{0.1}Ge_{0.9}$	8	6.32	28.57	4.38	55

while, Γ , RPE and KERMA coefficients are small at the same energy for all alloys. This energy is referred as E_m^S and at this energy, all the alloys shows poor shielding efficiency than their neighbour energies. The evaluated E_m^S for studied alloys are shown in table 6.1. Among all the studied alloys, Molybdochalkos alloy is having large Z_{eff} when compared to other studied alloys at minimum energy.

The absorption buildup factor and relative dose is maximum at one energy for a given alloy. **Table 6.2** X-ray/gamma energy at which shielding efficiency becomes maximum ($E_{opt.}$) and corresponding Z_{eff} , HVL and RPE (%)

Alloys	$E_{opt.}$ (MeV)	Z_{eff}	HVL(cm)	RPE
$Fe_{0.95}B_{0.05}$	0.06	24.39	0.08	100
$Fe_{0.21}Si_{0.79}$	0.2	15.82	1.58	99
$Ga_{0.685}In_{0.215}Sn_{0.1}$	0.4	36.13	1.09	100
$Cu_{0.1}Pb_{0.9}$	0.15	75.37	0.03	100
$Al_{0.1}Ti_{0.4}Ni_{0.5}$	0.2	23.61	0.74	100
$Si_{0.95}B_{0.05}$	0.1	13.21	1.60	100
$Ni_{0.15}Cu_{0.7}Zn_{0.15}$	0.3	28.99	0.71	99
$Si_{0.1}Ge_{0.9}$	0.3	28.84	1.19	94

At this energy, that alloy can absorb large quantity of radiation when compare to the neighbor energies. This energy we defined as optimal energy ($E_{opt.}$) for absorption of x-ray/gamma radiation of that alloy. At this energy, that alloy/medium can give maximum shielding efficiency. The

evaluated $E_{opt.}$ for studied alloys are shown in table 6.2. The value of Z_{eff} and HVL corresponding to the $E_{opt.}$ is as also tabulated in the table 3.2. This $E_{opt.}$ increase with increase in the Z_{eff} of the medium. It is also evident that the Molybdochalkos alloy shows larger value of Z_{eff} even at energy corresponding to maximum value. Hence, in general Molybdochalkos alloy is having larger Z_{eff} .

6.4 Selected good shielding material among the studied alloys

In current study, we have investigated suitable alloy for X, γ shielding among the studied alloys such as Iron-Boron, Iron-Silicon, Gallium alloys, lead alloys, Aluminium alloys, Silicon-Boron alloys, Zinc alloys and Silicon-Germanium. Various shielding parameters like μ/ρ , λ , TVL, Z_{eff} , Γ , RPE, KERMA, φ and relative dose are studied. From the detail investigations of all alloys, it is clear that Molybdochalkos possesses larger value of μ/ρ , Z_{eff} , Γ , RPE, KERMA, buildup factor, φ and relative dose. Meanwhile, smaller value of λ and TVL. Thus, we may conclude that Molybdochalkos alloy is having good shielding properties. The energies at which radiation protection efficiency is maximum (E_{opt}) and minimum (E_m^s) for a studied alloys is also identified. To use this practically, further mechanical, thermal and structural properties has to be investigated.

6.5 Results on studies of shielding parameters of nano-composites

In summary, BFNONC was synthesized for the first time by using economical solution combustion method using urea as a fuel and calcined at 500° C. The synthesized sample was characterized by different techniques. The PXRD pattern confirms the existence of (hkl) planes corresponding tetragonal phase of BaO, γ phase Fe₂O₃ and cubic NiO which inturn confirms the formation of BFNO nanocomposite. The average crystallite size obtained from the Scherrer's equation and W-H plot method was found to be 30 and 32 nm respectively. The surface morphology made up

large number of piled flakes. The optical energy direct band gap obtained from Wood and Tauc's plot was found to be 2.1 eV. The detailed analysis of measured X-ray / gamma ray shielding properties of BFNONC was measured in the energy range 0.081 -1.332 MeV. Above 356 keV X-ray / gamma ray interaction energy, the measured shielding parameters agrees well with the theoretical values whereas deviation is observed below 356 keV. This variation is mainly due to the impact of crystallite / particle size of the target medium on the X-ray / gamma ray interaction energy. The synthesised BFNONC finds application in the shielding of for X-ray / gamma ray.

ZABNONC was synthesized for the first time by using economical SCS method using urea as a fuel and calcined at 600° C.Mean crystalline size is found to be 17nm (W-h) ,20nm(Scherrer's) and energy gap is found to be 2.9eV using standard methods. X/γ ray shielding properties of ZABNONC were measured in elaborate manner, above 356 keV X/γ ray interaction energy, the measured shielding parameters agrees well with the theoretical value whereas slight deviation is observed below 356 keV due to the crystals are in the nano order. Hence from this conclusions the synthesised ZABNONC finds application in the X/γ ray shielding parameters.

In summary, LABNC was synthesized for the first time by economical solution combustion method using mint leaves extract as a reducing agent and calcined at 500° C. Crystal size measured using methods followed used for ZABNOC, same was found to be 62nm(W-h), 65nm(Scherrer's). The optical energy direct band gap obtained from Wood and Tauc's plot was found to be 5.2 eV. The detailed analysis of X-ray/gamma ray shielding properties of LABNC was measured in the energy range 0.081 -1.332 MeV. Above 356 keV X-ray/gamma ray interaction energy, the measured shielding parameters agrees well with the theoretical values whereas deviation is observed below 356 keV. This variation is mainly due to the impact of crystallite/particle size of the target medium on the X-ray/gamma ray interaction energy. The synthesized LABNC finds application in the shielding of X-ray/gamma ray.

6.6 Scope of research work

The modification in alloys composition or choosing different alloys and comparing them with existing shielding materials becomes fascinating field of research. The selection of suitable alloy for effective radiation shielding will certainly solve the radiation hazardous.

Radiation Physicists are constantly exploring kinds of materials in terms of seeing various radiation shielding factors in order to efficiently use radiations in many domains. In nuclear experiments and radiation related experiments, shielding is one of the most important aspects to be taken care of. In this regard there have been many materials which are being looked into. Amongst which there have been usage of materials which contain heavy elements occupying the front-line. Due to the shortcomings of traditional shielding materials, several researchers have proposed using metallic alloys as an alternative for X-ray/Gamma ray shielding material. Lead and lead based alloys are conventional materials used as a primary shielding material type due to superior attenuation properties against ionizing X-rays/gamma, its high atomic number and density. Combination of one or two other elements with lead, improves certain advanced properties such as hardness. We have proposed suitable alloys and nano composites for X-ray/Gamma ray shielding material. To use this practically, further mechanical, thermal and structural properties has to be investigated.

References

- [1] V. P. Singh and N. M. Badiger. γ -ray interaction characteristics for some boron containing materials. *Vacuum*, 113:24–27, 2015.
- [2] V. P. Singh, M. E. Medhat, N. M. Badiger, and A. Z. M. S. Rahman. Radiation shielding effectiveness of newly developed superconductors. *Radiation Physics and Chemistry*, 106:175–183, 2015.
- [3] K. V. Sathish, H. C. Manjunatha, Y. S. Vidya, B. M. Sankarshan, P. S. Damodara Gupta, L. Seenappa, K. N. Sridhar, and S. A. C. Raj. Investigation on shielding properties of lead based alloys. *Progress in Nuclear Energy*, 137:103788, 2021.
- [4] S. Chen, M. Bourham, and A. Rabiei. Attenuation efficiency of x-ray and comparison to gamma ray and neutrons in composite metal foams. *Radiation Physics and Chemistry*, 117:12–22, 2015.
- [5] M. S. Al-Buriahi, Y. S. M. Alajerami, A. S. Abouhaswa, A. Alalawi, T. Nutaro, and B. Tonguc. Effect of chromium oxide on the physical, optical, and radiation shielding properties of lead sodium borate glasses. *Journal of Non-Crystalline Solids*, 544:120171, 2020.
- [6] S. Kaur, A. Kaur, P. S. Singh, and T. Singh. Scope of pb-sn binary alloys as gamma rays shielding material. *Progress in Nuclear Energy*, 93:277–286, 2016.

- [7] O Agar, M. I. Sayyed, F Akman, H. O. Tekin, and M. R. Kaçal. An extensive investigation on gamma ray shielding features of pd/ag-based alloys. *Nuclear Engineering and Technology*, 51(3):853–859, 2019.
- [8] H. Singh, J. Sharma, and T. Singh. Extensive investigations of photon interaction properties for znxte100-x alloys. *Nuclear engineering and technology*, 50(8):1364–1371, 2018.
- [9] T. Kaur, J. Sharma, and T. Singh. Thickness optimization of sn–pb alloys for experimentally measuring mass attenuation coefficients. *Nuclear Energy and Technology*, 3(1):1–5, 2017.
- [10] B Aygün, E. Şakar, T Korkut, M.I. Sayyed, A. Karabulut, and M. H. M. Zaid. Fabrication of ni, cr, w reinforced new high alloyed stainless steels for radiation shielding applications. *Results in Physics*, 12:1–6, 2019.
- [11] A. E. Ersundu, M Büyükyıldız, M. Çelikbilek Ersundu, Erdem Şakar, and MJPNE Kurudirek. The heavy metal oxide glasses within the wo3-moo3-teo2 system to investigate the shielding properties of radiation applications. *Progress in Nuclear Energy*, 104:280–287, 2018.
- [12] Bünyamin Aygün. High alloyed new stainless steel shielding material for gamma and fast neutron radiation. *Nuclear Engineering and Technology*, 52(3):647–653, 2020.
- [13] S. P. Nikanorov, M. P. Volkov, V. N. Gurin, Y. A. Burenkov, L. I. Derkachenko, B. K. Kardashev, L. L. Regel, and W. R. Wilcox. Structural and mechanical properties of al–si alloys obtained by fast cooling of a levitated melt. *Materials Science and Engineering: A*, 390(1-2):63–69, 2005.
- [14] K. V. Sathish, H. C. Manjunatha, L. Seenappa, K. N. Sridhar, N. Sowmya, and S. A. Raj.

- Gamma, x-ray and neutron shielding properties of iron boron alloys. *Materials Today: Proceedings*, 49:613–619, 2022.
- [15] L. Seenappa, H. C. Manjunatha, K. N. Sridhar, and C. Hanumantharayappa. Gamma, x-ray and neutron shielding properties of polymer concretes. *journal=Defence Technology*, 56(8):631–634, 2018.
- [16] M. Krüger, S. Franz, H. Saage, M. Heilmaier, J. H. Schneibel, P. Jéhanno, M. Böning, and H. Kestler. Mechanically alloyed mo–si–b alloys with a continuous α-mo matrix and improved mechanical properties. *Intermetallics*, 16(7):933–941, 2008.
- [17] Y. Song, C. Chai, Q. Fan, W. Zhang, and Y. Yang. Physical properties of si-ge alloys in c2/m phase: A comprehensive investigation. *Journal of Physics: Condensed Matter*, 31(25):255703, 2019.
- [18] L. He, Y. Liu, J. Li, and B. Li. Effects of hot rolling and titanium content on the microstructure and mechanical properties of high boron fe–b alloys. *Materials and Design* (1980-2015), 36:88–93, 2012.
- [19] R. S. Rana, R. Purohit, and S. Das. Reviews on the influences of alloying elements on the microstructure and mechanical properties of aluminum alloys and aluminum alloy composites. *International Journal of Scientific and research publications*, 2(6):1–7, 2012.
- [20] R. A. Kellogg, A. M. Russell, T. A. Lograsso, A. B. Flatau, A. E. Clark, and M. Wun-Fogle. Mechanical properties of magnetostrictive iron-gallium alloys. In *Smart Structures and Materials 2003: Active Materials: Behavior and Mechanics*, volume 5053, pages 534–543. International Society for Optics and Photonics, 2003.
- [21] S. Cai, T. Lei, N. Li, and F. Feng. Effects of zn on microstructure, mechanical properties and

- corrosion behavior of mg–zn alloys. *Materials Science and Engineering: C*, 32(8):2570–2577, 2012.
- [22] J. Glazer. Microstructure and mechanical properties of pb-free solder alloys for low-cost electronic assembly: a review. *Journal of Electronic Materials*, 23(8):693–700, 1994.
- [23] H. C. Manjunatha, K. V. Sathish, L. Seenappa, D. Gupta, and S. A. c. Raj. A study of x-ray, gamma and neutron shielding parameters in si-alloys. *Radiation Physics and Chemistry*, 165:108414, 2019.
- [24] B. C. Reddy, H. C. Manjunatha, Y. S. Vidya, K. N. Sridhar, U. M. Pasha, L. Seenappa,
 B. Sadashivamurthy, N. Dhananjaya, K. V. Sathish, and P. S. Damodara Gupta. X-ray/gamma ray radiation shielding properties of α-bi2o3 synthesized by low temperature solution combustion method. *Nuclear Engineering and Technology*, 54(3):1062–1070, 2022.
- [25] K. V. Sathish, H. C. Manjunatha, Y. S. Vidya, K. N. Sridhar, L. Seenappa, B. C. Reddy, S. A. C. Raj, and P. S D. Gupta. X-rays/gamma rays radiation shielding properties of barium–nickel–iron oxide nanocomposite synthesized via low temperature solution combustion method. *Radiation Physics and Chemistry*, page 110053, 2022.
- [26] H. C. Manjunatha, B. M. Chandrika, L. Seenappa, and H. C. Study of gamma attenuation properties of tungsten copper alloys. *International Journal of Nuclear Energy Science and Technology*, 10(4):356–368, 2016.
- [27] L. Seenappa, H. C. Manjunatha, K. N. Sridhar, N. Nagaraja, and V. H. Doddamani. A study of dosimetric parameters of new born tissue and adult tissue of some organs. *Materials Today: Proceedings*, 49:878–881, 2022.
- [28] N. Nagaraja, H. C. Manjunatha, L. Seenappa, K. N. Sridhar, H. B. Ramalingam, and

- N. Sowmya. Specific absorbed fraction of energy and relative dose in some polymers. *Materials Today: Proceedings*, 49:898–903, 2022.
- [29] L. Seenappa, Manjumath. H. C., B. M. Chandrika, and K. N. Sridhar. Study of gamma, x-ray and neutron shielding parameters of some alloys. *Indian journal of pure and applied Physic*, 56:631–634, 2018.
- [30] H. C. Manjunatha, L. Seenappa, and K. N. Sridhar. Semi-empirical formula for photon energy absorption buildup factors of elements and compounds. *International Journal of Nuclear Energy Science and Technology*, 13(1):16–26, 2019.
- [31] H. C. Manjunatha, L. Seenappa, B. M. Chandrika, K. N. Sridhar, and C. Hanuman-tharayappa. Gamma, x-ray and neutron shielding parameters for the al-based glassy alloys. *Applied Radiation and Isotopes*, 139:187–194, 2018.
- [32] N. Nagaraja, H. C. Manjunatha, L. Seenappa, K. N. Sridhar, and H. B. Ramalingam. Selection of shielding materials for gamma/x-ray and neutron radiations among the commonly used polymers. *International Journal of Nuclear Energy Science and Technology*, 13(4):325–339, 2019.
- [33] K. V. Sathish, L. Seenappa, H. C. Manjunatha, Y. S. Vidya, K. N. Sridhar, and S. A. C. Raj. Radiation shielding properties of gallium alloys. *Materials Today: Proceedings*, 2022.
- [34] N. Nagaraja, H. C. Manjunatha, L. Seenappa, K. N. Sridhar, and H. B. Ramalingam. Radiation shielding properties of silicon polymers. *Radiation Physics and Chemistry*, 171:108723, 2020.
- [35] L. Gerward, N. Guilbert, K. Bjorn Jensen, and H. Levring. Winxcom—a program for

- calculating x-ray attenuation coefficients. *Radiation physics and chemistry*, 71(3-4):653–654, 2004.
- [36] F. Akman, M. R. Kaçal, M. I. Sayyed, and H. A. Karataş. Study of gamma radiation attenuation properties of some selected ternary alloys. *Journal of Alloys and Compounds*, 782:315–322, 2019.
- [37] S.R. Manohara, S.M. Hanagodimath, L. Gerward, and K.C. Mittal. Exposure buildup factors for heavy metal oxide glass: a radiation shield. *Journal of the Korean Physical Society*, 59(2):2039–2042, 2011.
- [38] Bünyamin Alım, E. Şakar, A. Baltakesmez, İbrahim Han, M. I. Sayyed, and Lütfü Demir. Experimental investigation of radiation shielding performances of some important aisicoded stainless steels: Part i. *Radiation Physics and Chemistry*, 166:108455, 2020.
- [39] A. Wagh, M.I. Sayyed, A Askin, Özgür Fırat Özpolat, E Sakar, G. Lakshminarayana, and S. D. Kamath. Influence of re oxides (eu3+, sm3+, nd3+) on gamma radiation shielding properties of lead fluoroborate glasses. *Solid State Sciences*, 96:105959, 2019.
- [40] H. O. Tekin and O. Kilicoglu. The influence of gallium (ga) additive on nuclear radiation shielding effectiveness of pd/mn binary alloys. *Journal of Alloys and Compounds*, 815:152484, 2020.
- [41] M. S. Al-Buriahi, D. K. Gaikwad, H. H. Hegazy, C. Sriwunkum, and R. Neffati. Fe-based alloys and their shielding properties against directly and indirectly ionizing radiation by using fluka simulations. *Physica Scripta*, 96(4):045303, 2021.
- [42] V. P. Singh, M. E. Medhat, and S. P. Shirmardi. Comparative studies on shielding properties

- of some steel alloys using geant4, mcnp, winxcom and experimental results. *Radiation Physics and Chemistry*, 106:255–260, 2015.
- [43] R. El-Mallawany, M. I. Sayyed, M. G. Dong, and Y. S. Rammah. Simulation of radiation shielding properties of glasses contain pbo. *Radiation Physics and Chemistry*, 151:239– 252, 2018.
- [44] EI-Katab and H. Abdul-hamid. App. Radiat. Isot, 42:303, 1991.
- [45] G. Kaur, K. Singh, B. S. Lark, and H. S. Sahota. Photon interaction studies in solutions of some alkali metal chlorides—i. *Radiation Physics and Chemistry*, 58(4):315–323, 2000.
- [46] K. Singh, G. Kaur, V. Kumar, A. K. Dhami, and B. S. Lark. Measurement of attenuation coefficients of some dilute solutions at 662 kev. *Radiation Physics and Chemistry*, 53(2):123–126, 1998.
- [47] K. Singh, Gagandeep, H. S. Sahota, and B. S. Lark. Interaction of 662-kev photons with some solutions of urea. *Nuclear science and engineering*, 132(1):58–64, 1999.
- [48] C. Q. Tran, C. T. Chantler, and Z. Barnea. X-ray mass attenuation coefficient of silicon: theory versus experiment. *Physical review letters*, 90(25):257401, 2003.
- [49] Shivaramu and V. R. Effective atomic numbers for photon energy absorption and energy dependence of some thermoluminescent dosimetric compounds. *Nuclear Instruments and Methods in Physics Research Section B-beam Interactions With Materials and Atoms*, 168:294–304, 2000.
- [50] J. H. Hubbell. Photon mass attenuation and energy-absorption coefficients. *The International Journal of Applied Radiation and Isotopes*, 33(11):1269–1290, 1982.

- [51] M. J. Berger and J. H. Hubbell. Xcom: Photon cross sections database. web version 1.2. national institute of standards and technology, gaithersburg, md 20899, usa, august 1999 (originally published as nbsir 87-3597, xcom: Photon cross sections on a personal computer (july 1987) 1987–1999), 1999.
- [52] W. Da-Chun, L. Ping-An, and Y. Hua. Measurement of the mass attenuation coefficients for sih4 and si. *Nuclear Instruments and Methods in Physics Research Section B: Beam Interactions with Materials and Atoms*, 95(2):161–165, 1995.
- [53] A. Khanna, S. S. Bhatti, K. J. Singh, and K. S. Thind. Gamma-ray attenuation coefficients in some heavy metal oxide borate glasses at 662 kev. *Nuclear Instruments and Methods in Physics Research Section B: Beam Interactions with Materials and Atoms*, 114(3-4):217–220, 1996.
- [54] I. Orlić, I. Bogdanović, S. Zhou, and J. L. Sanchez. Parametrization of the total photon mass attenuation coefficients for photon energies between 100 ev and 1000 mev. *Nuclear Instruments and Methods in Physics Research Section B: Beam Interactions with Materials and Atoms*, 150(1-4):40–45, 1999.
- [55] M. A. Abdel, R., E. A. Badawi, Y. L. Abdel-Hady, and N. Kamel. Effect of sample thickness on the measured mass attenuation coefficients of some compounds and elements for 59.54, 661.6 and 1332.5 kev γ-rays. *Nuclear Instruments and Methods in Physics Research Section A: Accelerators, Spectrometers, Detectors and Associated Equipment*, 447(3):432–436, 2000.
- [56] M. Angelone, T. Bubba, and A. Esposito. Measurement of the mass attenuation coefficient for elemental materials in the range $6 \le z \le 82$ using x-rays from 13 up to 50 kev. *Applied Radiation and Isotopes*, 55(4):505–511, 2001.

- [57] Ü Turgut, Ö Şimşek, E Büyükkasap, and M. Ertuğrul. X-ray attenuation coefficients at different energies and the validity of the mixture rule for compounds around the absorption edge. *Spectrochimica Acta Part B: Atomic Spectroscopy*, 57(2):261–266, 2002.
- [58] U. Turgut, E Büyükkasap, O. Şimşek, and M. Ertuğrul. X-ray attenuation coefficients of fe compounds in the k-edge region at different energies and the validity of the mixture rule.

 *Journal of Quantitative Spectroscopy and Radiative Transfer, 92(2):143–151, 2005.
- [59] O. Içelli, Salih Erzeneoğlu, and B. Gürbulak. Mass attenuation coefficients for n-type inse, inse: Gd, inse: Ho and inse: Er single crystals. *Journal of Quantitative Spectroscopy and Radiative Transfer*, 90(3-4):399–407, 2005.
- [60] S. Erzeneoğlu, Orhan Icelli, B. Gürbulak, and A. Ateş. Measurement of mass attenuation coefficients for holmium doped and undoped layered semiconductors inse at different energies and the validity of mixture rule for crystals around the absorption edge. *Journal of Quantitative Spectroscopy and Radiative Transfer*, 102(3):343–347, 2006.
- [61] C. Q. Tran, C. T. Chantler, Z. Barnea, M. D. De Jonge, B. B. Dhal, C. Chung, D. Paterson, and J. Wang. Measurement of the x-ray mass attenuation coefficient of silver using the x-ray-extended range technique. *Journal of Physics B: Atomic, Molecular and Optical Physics*, 38(1):89, 2004.
- [62] S. M. Midgley. Measurements of the x-ray linear attenuation coefficient for low atomic number materials at energies 32–66 and 140kev. *Radiation Physics and Chemistry*, 72(4):525–535, 2005.
- [63] M. Rettschlag, R. Berndt, and P. Mortreau. Measurement of photon mass attenuation coefficients of plutonium from 60 to 2615 kev. *Nuclear Instruments and Methods in Physics*

- Research Section A: Accelerators, Spectrometers, Detectors and Associated Equipment, 581(3):765–771, 2007.
- [64] T. Singh, A. Kaur, J. Sharma, and P. S. Singh. Gamma rays' shielding parameters for some pb-cu binary alloys. *Engineering science and technology, an international journal*, 21(5):1078–1085, 2018.
- [65] E. Şakar, M. Büyükyıldız, Bünyamin Alım, Betül Ceviz Şakar, and M. Kurudirek. Leaded brass alloys for gamma-ray shielding applications. *Radiation Physics and Chemistry*, 159:64–69, 2019.
- [66] L. Liu, X. Chen, J. Wang, L. Qiao, S. Gao, K. Song, C. Zhao, X. Liu, D.i. Zhao, and F. Pan. Effects of y and zn additions on electrical conductivity and electromagnetic shielding effectiveness of mg-y-zn alloys. *Journal of Materials Science and Technology*, 35(6):1074–1080, 2019.
- [67] T. Kaur, J. Sharma, and T. Singh. Review on scope of metallic alloys in gamma rays shield designing. *Progress in Nuclear Energy*, 113:95–113, 2019.
- [68] M. R. Kaçal, F. Akman, and M. I. Sayyed. Evaluation of gamma-ray and neutron attenuation properties of some polymers. *Nuclear Engineering and Technology*, 51(3):818–824, 2019.
- [69] M. G. Dong, X. X. Xue, Y. Elmahroug, M. I. Sayyed, and M. H. M. Zaid. Investigation of shielding parameters of some boron containing resources for gamma ray and fast neutron. *Results in Physics*, 13:102129, 2019.
- [70] C. Khobkham, P. Limkitjaroenporn, K. Shimada, J. Kaewkhao, and W. Chaiphaksa. Photon interaction behavior of zirconium alloy materials. *Materials Today: Proceedings*, 5(7):14928–14932, 2018.

- [71] I. Han and L. Demir. Mass attenuation coefficients, effective atomic and electron numbers of ti and ni alloys. *Radiation Measurements*, 44(3):289–294, 2009.
- [72] B. R. Kerur, S. R. Thontadarya, and B. Hanumaiah. A novel method for the determination of x-ray mass attenuation coefficients. *International journal of radiation applications and instrumentation. Part A. Applied radiation and isotopes*, 42(6):571–575, 1991.
- [73] N. M. Nagabhushan, B. R. Kerur, M. T. Lagare, R. Nathuram, M. C. Abani, S. R. Thontadarya, and B. Hanumaiah. Technique for measurement of photon intensity for the determination of μm in the low photon energy region. *Journal of X-ray Science and Technology*, 12(3):161–168, 2004.
- [74] J. H. Hubbell and S. M. Seltzer. Tables of x-ray mass attenuation coefficients and mass energy-absorption coefficients 1 kev to 20 mev for elements z= 1 to 92 and 48 additional substances of dosimetric interest. Technical report, National Inst. of Standards and Technology-PL, Gaithersburg, MD (United ..., 1995.
- [75] M.T. Teli, C.S. Mahajan, and R. Nathuram. Measurement of mass and linear attenuation coefficients of gamma rays for various elements through aqueous solution of salts. *Indian journal of pure and applied physics*, 39:816–824, 2001.
- [76] B. Saritha and A. N. Rao. Z dependence of photon interactions in wood materials. *Canadian Journal of Physics*, 91(3):221–225, 2013.
- [77] S. Gowda, S. Krishnaveni, T. Yashoda, T. K. Umesh, and R. Gowda. Photon mass attenuation coefficients, effective atomic numbers and electron densities of some thermoluminescent dosimetric compounds. *Pramana*, 63(3):529–541, 2004.
- [78] M. D. Jonge, C. Q. Tran, C. T. Chantler, Z. Barnea, B. B. Dhal, D. J. Cookson, W. K.

- Lee, and A. Mashayekhi. Measurement of the x-ray mass attenuation coefficient and determination of the imaginary component of the atomic form factor of molybdenum over the 13.5–41.5- kev energy range. *Physical Review A*, 71(3):032702, 2005.
- [79] M. I. Sayyed, F. Q. Mohammed, K. A. Mahmoud, E. Lacomme, Kawa M. Kaky, M. U. Khandaker, and M. R. I. Faruque. Evaluation of radiation shielding features of co and nibased superalloys using mcnp-5 code: potential use in nuclear safety. *Applied Sciences*, 10(21):7680, 2020.
- [80] M. M. Sadawy and R. M. El Shazly. Nuclear radiation shielding effectiveness and corrosion behavior of some steel alloys for nuclear reactor systems. *Defence Technology*, 15(4):621–628, 2019.
- [81] V. P. Singh and N. M. Badiger. Gamma ray and neutron shielding properties of some alloy materials. *Annals of Nuclear Energy*, 64:301–310, 2014.
- [82] E. Şakar, Özgür Fırat Özpolat, Bünyamin Alım, M.I. Sayyed, and M. Kurudirek. Phy-x/psd: development of a user friendly online software for calculation of parameters relevant to radiation shielding and dosimetry. *Radiation Physics and Chemistry*, 166:108496, 2020.
- [83] T. Korkut, O. Gencel, E. Kam, and W. Brostow. X-ray, gamma, and neutron radiation tests on epoxy-ferrochromium slag composites by experiments and monte carlo simulations. *International journal of polymer analysis and characterization*, 18(3):224–231, 2013.
- [84] M.I. Sayyed, G. Lakshminarayana, M. G. Dong, M. Çelikbilek Ersundu, A.E. Ersundu, and I.V. Kityk. Investigation on gamma and neutron radiation shielding parameters for bao/sro-bi2o3-b2o3 glasses. *Radiation Physics and Chemistry*, 145:26–33, 2018.
- [85] E. Kobayashi, S. Matsumoto, H. Doi, T. Yoneyama, and H. Hamanaka. Mechanical prop-

- erties of the binary titanium-zirconium alloys and their potential for biomedical materials. *Journal of biomedical materials research*, 29(8):943–950, 1995.
- [86] R. D. Prengaman. Secondary batteries—lead—acid systems— lead alloys. *Encyclopedia of Electrochemical Power Sources*, pages 648–654, 2009.
- [87] S. Tekumalla, S. Seetharaman, A. Almajid, and M. Gupta. Mechanical properties of magnesium-rare earth alloy systems: a review. *Metals*, 5(1):1–39, 2015.
- [88] D. Sariyer, R. Küçer, and N. Küçer. Neutron shielding properties of concretes containing boron carbide and ferro–boron. *Procedia-Social and Behavioral Sciences*, 195:1752–1756, 2015.
- [89] C. Harrison, S. Weaver, C. Bertelsen, E. Burgett, N. Hertel, and E. Grulke. Polyethylene/boron nitride composites for space radiation shielding. *Journal of applied polymer science*, 109(4):2529–2538, 2008.
- [90] E. Kavaz, H. O. Tekin, N. Y.ıldız Yorgun, ÖF Özdemir, and M. I. Sayyed. Structural and nuclear radiation shielding properties of bauxite ore doped lithium borate glasses: experimental and monte carlo study. *Radiation Physics and Chemistry*, 162:187–193, 2019.
- [91] X. Li, J. Wu, C. Tang, Z. He, P. Yuan, Y. Sun, W. Lau, K. Zhang, J. Mei, and Y. Huang. High temperature resistant polyimide/boron carbide composites for neutron radiation shielding. *Composites Part B: Engineering*, 159:355–361, 2019.
- [92] A.ç Levet, E. Kavaz, and Yüksel Özdemir. An experimental study on the investigation of nuclear radiation shielding characteristics in iron-boron alloys. *Journal of Alloys and Compounds*, 819:152946, 2020.

- [93] J. H. Hubbell. Compilation of photon cross-sections: some historical remarks and current status. *X-Ray Spectrometry*, 28(4):215–223, 1999.
- [94] D. Yılmaz and P Önder. Effect of an external magnetic field on the mass attenuation coefficients of p-si and n-si. *Nuclear Instruments and Methods in Physics Research Section B:*Beam Interactions with Materials and Atoms, 423:72–74, 2018.
- [95] T. A. A. Junior, M. S. Nogueira, V. Vivolo, M. P. A. Potiens, and LL Campos. Mass attenuation coefficients of x-rays in different barite concrete used in radiation protection as shielding against ionizing radiation. *Radiation. Physics and Chemistry*, 140:349–354, 2017.
- [96] S. M. Vahabi, M. Bahreinipour, and M. S. Zafarghandi. Determining the mass attenuation coefficients for some polymers using mcnp code: a comparison study. *Vacuum*, 136:73–76, 2017.
- [97] A. M. El-Khayatt. Semi-empirical determination of gamma-ray kerma coefficients for materials of shielding and dosimetry from mass attenuation coefficients. *Progress in Nuclear Energy*, 98:277–284, 2017.
- [98] M. A. Koehl, R. S. Rundberg, and J. C. Braley. Experimental and monte carlo investigation of mass attenuation coefficients of fission product isotopes in molecular precipitates.

 Applied Radiation and Isotopes, 122:148–152, 2017.
- [99] S. S. Obaid, M. I. Sayyed, D. K. Gaikwad, and P. P. Pawar. Attenuation coefficients and exposure buildup factor of some rocks for gamma ray shielding applications. *Radiation Physics and Chemistry*, 148:86–94, 2018.
- [100] Z. Dehghani, A. V. Noghreiyan, M. Nadafan, and M. H. M. Ara. Investigation of gamma-

- ray irradiation on molecular structure, optical properties and mass attenuation coefficients of colloidal gold nanoparticles. *Optical Materials*, 70:99–105, 2017.
- [101] R. Mirji and B. Lobo. Computation of the mass attenuation coefficient of polymeric materials at specific gamma photon energies. *Radiation Physics and Chemistry*, 135:32–44, 2017.
- [102] U. A. Tarim, O. Gurler, E. N. Ozmutlu, and S. Yalcin. Monte carlo calculations for gammaray mass attenuation coefficients of some soil samples. *Annals of nuclear energy*, 58:198–201, 2013.
- [103] L. Seenappa, H. C. Manjunatha, K. N. Sridhar, and C. Hanumantharayappa. Gamma, x-ray and neutron shielding properties of polymer concretes. *journal=Defence Technology*, 56(5):383–391, 2018.
- [104] M. R. Kacal, F. Akman, and M. I. Sayyed. Investigation of radiation shielding properties for some ceramics. *Radiochimica Acta*, 107(2):179–191, 2019.
- [105] A. Ripin, F. Mohamed, T. F. Choo, M. R. Yusof, S. Hashim, and d. S. K. Ghoshal. X-ray shielding behaviour of kaolin derived mullite-barites ceramic. *Radiation Physics and Chemistry*, 144:63–68, 2018.
- [106] H.C. Manjunatha. A dosimetric study of beta induced bremsstrahlung in bone. *Applied Radiation and Isotopes*, 94:282–293, 2014.
- [107] H. C. Manjunatha and B. Rudraswamy. Beta induced bremsstrahlung exposure in dna and rna. *Physica Medica*, 27(4):188–193, 2011.
- [108] H. C. Manjunatha and B. Rudraswamy. A study of thickness and penetration depth de-

- pendence of specific absorbed fraction of energy in bone. *Annals of Nuclear Energy*, 38(10):2271–2282, 2011.
- [109] J. H. Hubbell. A power-series buildup factor formulation. application. *Journal of Research* of the National Bureau of Standards: Engineering and instrumentation. C, 67:291, 1963.
- [110] A. B. Chilton, C. M. Eisenhauer, and G. L. Simmons. Photon point source buildup factors for air, water, and iron. *Nuclear Science and Engineering*, 73(1):97–107, 1980.
- [111] Y. Sakamoto, S-i. Tanaka, and Y. Harima. Interpolation of gamma-ray buildup factors for point isotropic source with respect to atomic number. *Nuclear Science and Engineering*, 100(1):33–42, 1988.
- [112] G. S. Brar, A. K. Sandhu, M. Singh, and G. S. Mudahar. Exposure buildup factors for bakelite, perspex and magnox-a12 up to 40 mfp using the interpolation method. *Radiation Physics and Chemistry*, 44(5):459–466, 1994.
- [113] G. S. Brar and G. S. Mudahar. Energy and effective atomic number dependence of the exposure buildup factor in soils—a study. *Nuclear geophysics*, 9(5):471–480, 199.
- [114] G. S. Sidhu, P. S. Singh, and G. S. Mudahar. A study of energy and effective atomic number dependence of the exposure build-up factors in biological samples. *Journal of Radiological Protection*, 20(1):53, 2000.
- [115] D. Rezaei-O and S. Azimkhani. Investigation of gamma-ray shielding properties of concrete containing different percentages of lead. *Applied Radiation and Isotopes*, 70(10):2282–2286, 2012.
- [116] I. Akkurt, H. Akyildirim, B Mavi, S. Kilincarslan, and C. Basyigit. Gamma-ray shielding

- properties of concrete including barite at different energies. *Progress in Nuclear Energy*, 52(7):620–623, 2010.
- [117] I. Akkurt, S. Kilincarslan, and C Basyigit. The photon attenuation coefficients of barite, marble and limra. *Annals of Nuclear Energy*, 31(5):577–582, 2004.
- [118] T. Kaur, J. Sharma, and T. Singh. Gamma rays shielding parameters for white metal alloys. In *AIP Conference Proceedings*, volume 1953, page 140123. AIP Publishing LLC, 2018.
- [119] N. Ekinci, E. Kavaz, Bünyamin Aygün, and U. Perişanoğlu. Gamma ray shielding capabilities of rhenium-based superalloys. *Radiation Effects and Defects in Solids*, 174(5-6):435–451, 2019.
- [120] F. Akman, M.I. Sayyed, M. R. Kaçal, and H. O. Tekin. Investigation of photon shielding performances of some selected alloys by experimental data, theoretical and mcnpx code in the energy range of 81 kev–1333 kev. *Journal of Alloys and Compounds*, 772:516–524, 2019.
- [121] J. Kaewkhao, J. Laopaiboon, and W. Chewpraditkul. Determination of effective atomic numbers and effective electron densities for cu/zn alloy. *Journal of Quantitative Spectroscopy and Radiative Transfer*, 109(7):1260–1265, 2008.
- [122] S. R. Manohara, S. M. Hanagodimath, K. S. Thind, and L. Gerward. On the effective atomic number and electron density: a comprehensive set of formulas for all types of materials and energies above 1 kev. *Nuclear Instruments and Methods in Physics Research Section B:*Beam Interactions with Materials and Atoms, 266(18):3906–3912, 2008.
- [123] R. Sharma, V. Sharma, P. S. Singh, and T. Singh. Effective atomic numbers for some calcium–strontium-borate glasses. *Annals of Nuclear Energy*, 45:144–149, 2012.

- [124] N. Ekinci and N. Astam. Measurement of mass attenuation coefficients of biological materials by energy dispersive x-ray fluorescence spectrometry. *Radiation measurements*, 42(3):428–430, 2007.
- [125] A. Akar, H. Baltaş, U. Çevik, F. Korkmaz, and N. T. Okumuşoğlu. Measurement of attenuation coefficients for bone, muscle, fat and water at 140, 364 and 662 kev γ -ray energies. *Journal of Quantitative Spectroscopy and Radiative Transfer*, 102(2):203–211, 2006.
- [126] Y. Elmahroug, B. Tellili, C. Souga, and K. Manai. Parshield: a computer program for calculating attenuation parameters of the gamma rays and the fast neutrons. *Annals of Nuclear Energy*, 76:94–99, 2015.
- [127] M. M. Hosamani and N. M. Badiger. Determination of effective atomic number of composite materials using backscattered gamma photons—a novel method. *Chemical Physics Letters*, 695:94–98, 2018.
- [128] M. M. Hosamani, A. Vinayak, S. Mangeshkar, S. Malode, S. Bhajantri, V. Hegde, G. B. Hiremath, and N. M. Badiger. Determination of effective atomic number of multifunctional materials using backscattered beta particles—a novel method. *Spectroscopy Letters*, 53(2):132–139, 2020.
- [129] Y. Harima, Y. Sakamoto, and Shun-ichi. Tanaka. Applicability of geometrical progression approximation (gp method) of gamma-ray buildup factors. Technical report, Japan Atomic Energy Research Inst., 1986.
- [130] C. Suteau and M. Chiron. An iterative method for calculating gamma-ray build-up factors in multi-layer shields. *Radiation protection dosimetry*, 116(1-4):489–492, 2005.
- [131] M. M. Rafiei and H. Tavakoli-Anbaran. Calculation of the exposure buildup factors for

- x-ray photons with continuous energy spectrum using monte carlo code. *Journal of Radiological Protection*, 38(1):207, 2018.
- [132] N. Nagaraja, L. Manjunatha, H. C.and Seenappa, K. N. Sridhar, H. B. Ramalingam, et al. Comparison of radiation shielding properties of some coordination polymers. *Radiation Protection and Environment*, 42(4):150, 2019.
- [133] M. Kurudirek, B. Doğan, M. İngeç, N. Ekinci, and Yüksel Özdemir. Gamma-ray energy absorption and exposure buildup factor studies in some human tissues with endometriosis.

 Applied Radiation and Isotopes, 69(2):381–388, 2011.
- [134] M. Kurudirek and Yüksel Özdemir. A comprehensive study on energy absorption and exposure buildup factors for some essential amino acids, fatty acids and carbohydrates in the energy range 0.015–15 mev up to 40 mean free path. *Nuclear Instruments and Methods in Physics Research Section B: Beam Interactions with Materials and Atoms*, 269(1):7–19, 2011.
- [135] O. İçelli, K. S. Mann, Zeynel Yalçın, S. Orak, and V. Karakaya. Investigation of shielding properties of some boron compounds. *Annals of Nuclear Energy*, 55:341–350, 2013.
- [136] B. Ahmed, G. B. Shah, A. H. Malik, M. Rizwan, et al. Gamma-ray shielding characteristics of flexible silicone tungsten composites. *Applied Radiation and Isotopes*, 155:108901, 2020.
- [137] H. O. Tekin, E. E. Altunsoy, E. Kavaz, M. I. Sayyed, O. Agar, and M. Kamislioglu. Photon and neutron shielding performance of boron phosphate glasses for diagnostic radiology facilities. *Results in Physics*, 12:1457–1464, 2019.
- [138] C. Lobascio, M. B., R. D., M. Faraud, G. Gialanella, G. Grossi, V. Guarnieri, L. Manti,

- M. Pugliese, A. Rusek, et al. Accelerator-based tests of radiation shielding properties of materials used in human space infrastructures. *Health physics*, 94(3):242–247, 2008.
- [139] S. A. Tijani, S. M. Kamal, Y. A.Hadeethi, Mehenna A., M. A. Hussein, S. Wageh, and L. A. Dim. Radiation shielding properties of transparent erbium zinc tellurite glass system determined at medical diagnostic energies. *Journal of Alloys and Compounds*, 741:293– 299, 2018.
- [140] A. B. Azeez, K. S. Mohammed, M. M. A. Bakri A., A. V. Sandhu, A. Rahmat, H. Kamarudin, and L. Jamaludin. Replacement of lead by green tungsten-brass composites as a radiation shielding material. In *Applied Mechanics and Materials*, volume 679, pages 39–44. Trans Tech Publ, 2014.
- [141] Z. Caner and M. Tufan. Investigation of attenuation coefficients of some stainless steel and aluminum alloys. In AIP Conference Proceedings, volume 1935, page 180002. AIP Publishing LLC, 2018.
- [142] A. H. E.Kateb and A. S. Abdul. H. Photon attenuation coefficient study of some materials containing hydrogen, carbon and oxygen. *International journal of radiation applications and instrumentation. Part A. Applied radiation and isotopes*, 42(3):303–307, 1991.
- [143] K. Singh, G. Kaur, V. Kumar, A. K. Dhami, and B.S. Lark. Measurement of attenuation coefficients of some dilute solutions at 662 kev. *Radiation Physics and Chemistry*, 53(2):123–126, 1998.
- [144] B Saritha and A. N. Rao. A study on photon attenuation coefficients of different wood materials with different densities. In *Journal of Physics: Conference Series*, volume 662, page 012030. IOP Publishing, 2015.

- [145] A. B. Azeez, K. S. Mohammed, A. V. Sandu, A. M. M. Bakri, H. Kamarudin, and I. G. Sandu. Evaluation of radiation shielding properties for concrete with different aggregate granule sizes. *Rev. Chim*, 64:899–903, 2013.
- [146] I Akkurt, H Akyildirim, B Mavi, S. Kilincarslan, and C Basyigit. Photon attenuation coefficients of concrete includes barite in different rate. *Annals of Nuclear Energy*, 37(7):910– 914, 2010.
- [147] A. B. Azeez, K. S. Mohammed, A. M. A.l. Bakri, H. I. Hasan, and O. A. Abdulkareem. Radiation shielding characteristics of concretes incorporates different particle sizes of various waste materials. In *Advanced Materials Research*, volume 925, pages 190–194. Trans Tech Publ, 2014.
- [148] Yüksel Özdemir and M. Kurudirek. A study of total mass attenuation coefficients, effective atomic numbers and electron densities for various organic and inorganic compounds at 59.54 kev. *Annals of Nuclear Energy*, 36(11-12):1769–1773, 2009.
- [149] J. H. Hubbell. Photon cross sections, attenuation coefficients and energy absorption coefficients. *National Bureau of Standards Report NSRDS-NBS29*, *Washington DC*, 1969.
- [150] P. Limkitjaroenporn, J. Kaewkhao, and S. Asavavisithchai. Determination of mass attenuation coefficients and effective atomic numbers for inconel 738 alloy for different energies obtained from compton scattering. *Annals of Nuclear Energy*, 53:64–68, 2013.
- [151] R. Vijayakumar, L. Rajasekaran, N. Ramamurthy, et al. Effective atomic numbers for photon energy absorption of some low-z substances of dosimetric interest. *Radiation Physics and Chemistry*, 62(5-6):371–377, 2001.

- [152] D. F. Jackson and D. J. Hawkes. X-ray attenuation coefficients of elements and mixtures.

 Physics Reports, 70(3):169–233, 1981.
- [153] M. P. Singh, B. S. Sandhu, and B. Singh. Measurement of the effective atomic number of composite materials using rayleigh to compton scattering of 279 kev gamma rays. *Physica Scripta*, 76(4):281, 2007.
- [154] S. R. Manohara, S. M. Hanagodimath, and L. Gerward. Studies on effective atomic number, electron density and kerma for some fatty acids and carbohydrates. *Physics in Medicine and Biology*, 53(20):N377, 2008.
- [155] I. Han and L. Demir. Determination of mass attenuation coefficients, effective atomic and electron numbers for cr, fe and ni alloys at different energies. *Nuclear Instruments and Methods in Physics Research Section B: Beam Interactions with Materials and Atoms*, 267(1):3–8, 2009.
- [156] O. İçelli, S. Erzeneoğlu, İsmail H Karahan, and Güven Çankaya. Effective atomic numbers for cocuni alloys using transmission experiments. *Journal of Quantitative Spectroscopy and Radiative Transfer*, 91(4):485–491, 2005.
- [157] M. Kurudirek, M. Büyükyıldız, and Yüksel Özdemir. Effective atomic number study of various alloys for total photon interaction in the energy region of 1 kev–100 gev. *Nuclear Instruments and Methods in Physics Research Section A: Accelerators, Spectrometers, Detectors and Associated Equipment*, 613(2):251–256, 2010.
- [158] D. C. Creagh and J. H. Hubbell. Problems associated with the measurement of x-ray attenuation coefficients. i. silicon. report of the international union of crystallography x-ray attenuation project. *Acta Crystallographica Section A: Foundations of Crystallography*, 43(1):102–112, 1987.

- [159] A. Baştuğ, Ali Gürol, Orhan İçelli, and Yusuf Şahin. Effective atomic numbers of some composite mixtures including borax. *Annals of Nuclear Energy*, 37(7):927–933, 2010.
- [160] V. Manjunathaguru and T. K. Umesh. Simple parametrization of photon mass energy absorption coefficients of h-, c-, n-and o-based samples of biological interest in the energy range 200–1500 kev. *Pramana*, 72(2):375–387, 2009.
- [161] S. Prasanna Kumar and T. K. Umesh. Effective atomic number of composite materials for compton effect in the gamma ray region 280–1115 kev. *Applied Radiation and Isotopes*, 68(12):2443–2447, 2010.
- [162] T. K. Kumar and K V. Reddy. Effective atomic numbers for materials of dosimetric interest.

 *Radiation Physics and Chemistry, 50(6):545–553, 1997.
- [163] H. P. Schätzler. Basic aspects on the use of elastic and inelastic scattered gamma radiation for the determination of binary systems with effective atomic numbers of less than 10. *The International Journal of Applied Radiation and Isotopes*, 30(2):115–121, 1979.
- [164] U. r. Cevik, H. Baltaş, Ahmet Çelik, and E. Bacaksız. Determination of attenuation coefficients, thicknesses and effective atomic numbers for cuinse2 semiconductor. *Nuclear Instruments and Methods in Physics Research Section B: Beam Interactions with Materials and Atoms*, 247(2):173–179, 2006.
- [165] H Baltaş, Ş Çelik, U Cevik, and E. Yanmaz. Measurement of mass attenuation coefficients and effective atomic numbers for mgb2 superconductor using x-ray energies. *Radiation measurements*, 42(1):55–60, 2007.
- [166] S. G. Gounhalli, A. Shantappa, and S. M. Hanagodimath. Studies on effective atomic

- numbers and electron densities of some chemical explosives in the energy range 1kev–100 gev. *Journal of Chemical and Pharmaceutical Research*, 4(5):2545–2563, 2012.
- [167] A. N. Eritenko, A. L. Tsvetiansky, and A. A. Polev. Analytical dependence of effective atomic number on the elemental composition of matter and radiation energy in the range 10–1000 kev. *Nuclear Instruments and Methods in Physics Research Section B: Beam Interactions with Materials and Atoms*, 414:107–112, 2018.
- [168] C. Möhler, P. Wohlfahrt, C. Richter, and S. Greilich. On the equivalence of image-based dual-energy ct methods for the determination of electron density and effective atomic number in radiotherapy. *Physics and Imaging in Radiation Oncology*, 5:108–110, 2018.
- [169] D. Sakata, A. Haga, S. Kida, T. Imae, S. Takenaka, and K. Nakagawa. Effective atomic number estimation using kv-mv dual-energy source in linac. *Physica Medica*, 39:9–15, 2017.
- [170] P. Sathiyaraj, E. J. J. Samuel, C. C. S. Valeriano, and M. Kurudirek. Effective atomic number and buildup factor calculations for metal nano particle doped polymer gel. *Vacuum*, 143:138–149, 2017.
- [171] W. G. J. Langeveld. Effective atomic number, mass attenuation coefficient parameterization, and implications for high-energy x-ray cargo inspection systems. *Physics Procedia*, 90:291–304, 2017.
- [172] R. Sharma, J. K. Sharma, T. Kaur, T. Singh, J. Sharma, and P. S. Singh. Experimental investigation of effective atomic numbers for some binary alloys. *Nuclear Engineering and Technology*, 49(7):1571–1574, 2017.
- [173] Aytaç Levet and Yüksel Özdemir. Determination of effective atomic numbers, effective

- electrons numbers, total atomic cross-sections and buildup factor of some compounds for different radiation sources. *Radiation Physics and Chemistry*, 130:171–176, 2017.
- [174] V. P. Singh and N. M. Badiger. Study of mass attenuation coefficients, effective atomic numbers and electron densities of carbon steel and stainless steels. *Radioprotection*, 48(3):431–443, 2013.
- [175] S. Seven, I. H. Karahan, and Ömer F Bakkaloglu. The measurement of total mass attenuation coefficients of cocuni alloys. *Journal of Quantitative Spectroscopy and Radiative Transfer*, 83(2):237–242, 2004.
- [176] Ertuğrul O Bursalıoğlu, F. A Alkan, Ümit B Barutçu, M. Demir, Yaşar Karabul, Begüm Balkan, Ersoy Öz, and O. İçelli. Prediction of electron density and trace element concentrations in human blood serum following radioiodine therapy in differentiated thyroid cancer patients. *Measurement*, 100:19–25, 2017.
- [177] F. Akman, Ridvan Durak, M. F. Turhan, and M. R. Kaçal. Studies on effective atomic numbers, electron densities from mass attenuation coefficients near the k edge in some samarium compounds. *Applied Radiation and Isotopes*, 101:107–113, 2015.
- [178] M. Kurudirek and T. Onaran. Calculation of effective atomic number and electron density of essential biomolecules for electron, proton, alpha particle and multi-energetic photon interactions. *Radiation Physics and Chemistry*, 112:125–138, 2015.
- [179] C. V. More, R. M. Lokhande, and P. P. Pawar. Effective atomic number and electron density of amino acids within the energy range of 0.122–1.330 mev. *Radiation Physics and Chemistry*, 125:14–20, 2016.

- [180] D. L. Wu. New global electron density observations from gps-ro in the d-and e-region ionosphere. *Journal of Atmospheric and Solar-Terrestrial Physics*, 171:36–59, 2018.
- [181] A. Laith. Al-ani, "measured buildup factor for gamma rays in shielding materials". *Journal of Saddam University*, 5(1):181–191, 2001.
- [182] M. Kurudirek, DARİOUS S.i, NAVİD Khaledi, C Çakır, and K.S. Mann. Investigation of x-and gamma ray photons buildup in some neutron shielding materials using gp fitting approximation. *Annals of Nuclear Energy*, 53:485–491, 2013.
- [183] V. P. Singh and N. M. Badiger. Energy absorption buildup factors, exposure buildup factors and kerma for optically stimulated luminescence materials and their tissue equivalence for radiation dosimetry. *Radiation Physics and Chemistry*, 104:61–67, 2014.
- [184] K. S. Mann, M. S. Heer, and A. Rani. Gamma-ray double-layered transmission exposure buildup factors of some engineering materials, a comparative study. *Radiation Physics and Chemistry*, 125:27–40, 2016.
- [185] C. J. Park and H. Y. Jeong. Uncertainty analysis for the weighted least square fitted buildup factors in the point kernel module. *Annals of Nuclear Energy*, 92:312–316, 2016.
- [186] N. Kucuk, S.R. Manohara, S. M. Hanagodimath, and L. Gerward. Modeling of gamma ray energy-absorption buildup factors for thermoluminescent dosimetric materials using multi-layer perceptron neural network: A comparative study. *Radiation Physics and Chemistry*, 86:10–22, 2013.
- [187] S. R. Manohara, S. M. Hanagodimath, and L. Gerward. Energy absorption buildup factors for thermoluminescent dosimetric materials and their tissue equivalence. *Radiation Physics and Chemistry*, 79(5):575–582, 2010.

- [188] K. S. Mann, J. Singla, V. Kumar, and G. S. Sidhu. Investigations of mass attenuation coefficients and exposure buildup factors of some low-z building materials. *Annals of Nuclear Energy*, 43:157–166, 2012.
- [189] H. Atak, O. Şahin Çelikten, and M. Tombakoğlu. Finite and infinite system gamma ray buildup factor calculations with detailed physics. *Applied Radiation and Isotopes*, 105:11–14, 2015.
- [190] P. S. Singh, T. Singh, and P. Kaur. Variation of energy absorption buildup factors with incident photon energy and penetration depth for some commonly used solvents. *Annals of Nuclear Energy*, 35(6):1093–1097, 2008.
- [191] K. S. Mann and T. Korkut. Gamma-ray buildup factors study for deep penetration in some silicates. *Annals of Nuclear Energy*, 51:81–93, 2013.
- [192] E. Kavaz, N. Ahmadishadbad, and Yüksel Özdemir. Photon buildup factors of some chemotherapy drugs. *Biomedicine and Pharmacotherapy*, 69:34–41, 2015.
- [193] F. Hernández and F. El-Daoushy. Semi-empirical method for self-absorption correction of photons with energies as low as 10 kev in environmental samples. *Nuclear Instruments and Methods in Physics Research Section A: Accelerators, Spectrometers, Detectors and Associated Equipment*, 484(1-3):625–641, 2002.
- [194] H. Hirayama. Exposure buildup factors of high-energy gamma rays for water, concrete, iron, and lead. *Nuclear Technology*, 77(1):60–67, 1987.
- [195] E. E. Morris, A. B. Chilton, and A. F. Vetter. Tabulation and empirical representation of infinite-medium gamma-ray buildup factors for monoenergetic, point isotropic sources in water, aluminum, and concrete. *Nuclear Science and Engineering*, 56(2):171–178, 1975.

- [196] H. C. Manjunatha and B. Rudraswamy. Computation of ct-number and zeff in teeth. *Health Physics*, 100(5):S92–S99, 2011.
- [197] H. C. Manjunatha and B. Rudraswamy. Energy absorption and exposure build-up factors in hydroxyapatite. *Radiation measurements*, 47(5):364–370, 2012.
- [198] Jeffrey F Williamson. Brachytherapy technology and physics practice since 1950: a half-century of progress. *Physics in Medicine and Biology*, 51(13):R303, 2006.
- [199] M. F. Tsiakalos, S. Stathakis, G. A. Plataniotis, C. Kappas, and K. Theodorou. Monte carlo dosimetric evaluation of high energy vs low energy photon beams in low density tissues. *Radiotherapy and oncology*, 79(1):131–138, 2006.
- [200] Y. Harima. An approximation of gamma-ray buildup factors by modified geometrical progression. *Nuclear Science and Engineering*, 83(2):299–309, 1983.
- [201] J. K. Shultis and R. E. Faw. Radiation shielding technology. *Health Physics*, 88(4):297–322, 2005.
- [202] A. Shimizu, T. Onda, and Y. Sakamoto. Calculation of gamma-ray buildup factors up to depths of 100 mfp by the method of invariant embedding,(iii) generation of an improved data set. *Journal of nuclear science and technology*, 41(4):413–424, 2004.
- [203] V. P. Singh, M. E. Medhat, and N. M. Badiger. Assessment of exposure buildup factors of some oxide dispersion strengthened steels applied in modern nuclear engineering and designs. *Nuclear Engineering and Design*, 270:90–100, 2014.
- [204] O. Chibani. New photon exposure buildup factors. *Nuclear science and engineering*, 137(2):215–225, 2001.

- [205] Gladys R White. The penetration and diffusion of co 60 gamma-rays in water using spherical geometry. *Physical Review*, 80(2):154, 1950.
- [206] U. Fano. Gamma-ray attenuation. part ii. analysis of penetration. *Nucleonics (US) Ceased publication*, 11, 1953.
- [207] H. Hirayama and D. K. Trubey. Effects of incoherent and coherent scattering on the exposure buildup factors of low-energy gamma rays. *Nuclear Science and Engineering*, 99(2):145–156, 1988.
- [208] Y. Namito, S. Ban, and H. Hirayama. Effects of linear polarization and doppler broadening on the exposure buildup factors of low-energy gamma rays. *Nuclear science and engineering*, 120(3):199–210, 1995.
- [209] H. Hirayama. Effects of the photon cross sections and energy-absorption coefficients of air to the gamma-ray point isotropic exposure buildup factors. *Nuclear science and engineering*, 124(2):258–270, 1996.
- [210] G. S. Brar, G. S. Sidhu, P. S. Singh, and G. S. Mudahar. Buildup factor studies of hoomaterials as a function of weight fraction of constituent elements. *Radiation Physics and Chemistry*, 54(2):125–129, 1999.
- [211] A. B Chilton, J. K enneth Shultis, and R. E. Faw. Principles of radiation shielding. 1984.
- [212] J. H. Hubbell. Review of photon interaction cross section data in the medical and biological context. *Physics in Medicine and Biology*, 44(1):R1, 1999.
- [213] M. I. Sayyed, M. Y. AlZaatreh, K. A. Matori, H. Sidek, and M. H. M. Zaid. Comprehensive study on estimation of gamma-ray exposure buildup factors for smart polymers as a potent application in nuclear industries. *Results in Physics*, 9:585–592, 2018.

- [214] A. Shimizu. Calculation of gamma-ray buildup factors up to depths of 100 mfp by the method of invariant embedding,(i) analysis of accuracy and comparison with other data.

 *Journal of nuclear science and technology, 39(5):477–486, 2002.
- [215] merican national standard (ans). merican National Standard (ANS)(125), 1991.
- [216] Y. Harima, Y. Sakamoto, S. Tanaka, and M. Kawai. Validity of the geometric-progression formula in approximating gamma-ray buildup factors. *Nuclear Science and Engineering*, 94(1):24–35, 1986.
- [217] G. S. Sidhu, P. S. Singh, and G. S. Mudahar. Energy absorption buildup factor studies in biological samples. *Radiation protection dosimetry*, 86(3):207–216, 1999.
- [218] M. Kurudirek and S. Topcuoglu. Investigation of human teeth with respect to the photon interaction, energy absorption and buildup factor. *Nuclear Instruments and Methods in Physics Research Section B: Beam Interactions with Materials and Atoms*, 269(10):1071–1081, 2011.
- [219] R. Khabaz. A new approach to examine the exposure and dose buildup factors for multienergy radioisotopic gamma sources with gp analytical expression. *Radiation Physics and Chemistry*, 151:53–58, 2018.
- [220] E. Kavaz and N. Yıldız Yorgun. Gamma ray buildup factors of lithium borate glasses doped with minerals. *Journal of Alloys and Compounds*, 752:61–67, 2018.
- [221] L. A. Al-Ani and H. M. Jawad. Pair production contribution effect on the calculation of gamma ray dose buildup factor for water and graphite in the energy range (4–10) mev. *Journal of Radiation Research and Applied Sciences*, 11(3):177–181, 2018.

- [222] R. M. Lokhande, C. V. More, B. S. Surung, and P. P. Pawar. Determination of attenuation parameters and energy absorption build-up factor of amine group materials. *Radiation Physics and Chemistry*, 141:292–299, 2017.
- [223] J. M. Sharaf and H. Saleh. Gamma-ray energy buildup factor calculations and shielding effects of some jordanian building structures. *Radiation Physics and Chemistry*, 110:87–95, 2015.
- [224] G. C. Bakos and N. F. Tsagas. Angular exposure dose build up factors for combined energies source of disc geometry. *Annals of Nuclear Energy*, 22(8):553–558, 1995.
- [225] R. M. Lokhande, V. Vinayak, S. V. Mukhamale, and P. P. Khirade. Gamma radiation shielding characteristics of various spinel ferrite nanocrystals: a combined experimental and theoretical investigation. *RSC Advances*, 11(14):7925–7937, 2021.
- [226] A. M. El-Khayatt. Calculation of photon shielding properties for some neutron shielding materials. *Nuclear Science and Techniques*, 28(5):1–7, 2017.
- [227] K. S. Mann. γ -ray shielding behaviors of some nuclear engineering materials. *Nuclear Engineering and Technology*, 49(4):792–800, 2017.
- [228] M.I. Sayyed. Investigation of shielding parameters for smart polymers. *Chinese journal of physics*, 54(3):408–415, 2016.
- [229] S. M. Badawy and A. A. Abd El-L. Synthesis and characterizations of magnetite nanocomposite films for radiation shielding. *Polymer Composites*, 38(5):974–980, 2017.
- [230] T. Hayashi, K. Tobita, Y. Nakamori, and S. Orimo. Advanced neutron shielding material using zirconium borohydride and zirconium hydride. *Journal of Nuclear Materials*, 386:119–121, 2009.

- [231] K. S. Mann, A. Rani, and M. S. Heer. Shielding behaviors of some polymer and plastic materials for gamma-rays. *Radiation Physics and Chemistry*, 106:247–254, 2015.
- [232] O. Gurler and U. A. Tarim. Determination of radiation shielding properties of some polymer and plastic materials against gamma-rays. *Acta Phys. Pol. A*, 130:236–238, 2016.
- [233] K. Srinivasan and E. James J. Samuel. Evaluation of radiation shielding properties of the polyvinyl alcohol/iron oxide polymer composite. *Journal of medical physics*, 42(4):273, 2017.
- [234] T. Kaur, J. Sharma, and T. Singh. Feasibility of pb-zn binary alloys as gamma rays shielding materials. *Int. J. Pure Appl. Phys.*, 13(1):222–225, 2017.
- [235] T. Singh, S. Kaur, P. Kaur, H. Kaur, and P. S. Singh. Variation of photon interaction parameters with energy for some cu-pb alloys. In *AIP Conference Proceedings*, volume 1675, page 020057. AIP Publishing LLC, 2015.
- [236] Krzysztof W Fornalski. Simple empirical correction functions to cross sections of the photoelectric effect, compton scattering, pair and triplet production for carbon radiation shields for intermediate and high photon energies. *Journal of Physics Communications*, 2(3):035038, 2018.
- [237] L. Sabbatucci and F. Salvat. Theory and calculation of the atomic photoeffect. *Radiation Physics and Chemistry*, 121:122–140, 2016.
- [238] R. H. Pratt, R. D. Levee, R. L. Pexton, and W. Aron. K-shell photoelectric cross sections from 200 kev to 2 mev. *Physical Review*, 134(4A):A898, 1964.
- [239] J. J. DeMarco, R. E. Wallace, and K. Boedeker. An analysis of mcnp cross-sections and tally

- methods for low-energy photon emitters. *Physics in Medicine and Biology*, 47(8):1321, 2002.
- [240] H. Brysk and C. D. Zerby. Photoelectric cross sections in the kev range. *Physical Review*, 171(2):292, 1968.
- [241] M. F. Smith, C. E Floyd J. r., and R. J. Jaszczak. A vectorized monte carlo code for modeling photon transport in spect. *Medical physics*, 20(4):1121–1127, 1993.
- [242] H. Zaidi, A. H. Scheurer, and C. Morel. An object-oriented monte carlo simulator for 3d cylindrical positron tomographs. *Computer methods and programs in biomedicine*, 58(2):133–145, 1999.
- [243] H. Zaidi. Comparative evaluation of photon cross-section libraries for materials of interest in pet monte carlo simulations. *IEEE Transactions on Nuclear Science*, 47(6):2722–2735, 2000.
- [244] N. Bhattacharyya, N. Chaudhury, and S. C. Roy. Measurement of total and photoelectric cross sections in the vicinity of absorption edges of heavier atoms. *Applied radiation and isotopes*, 46(6-7):419–420, 1995.
- [245] W. F. Titus. Total photoelectric cross sections of copper, molybdenum, silver, tantalum, and gold at 662 kev. *Physical Review*, 115(2):351, 1959.
- [246] T. J. Bethell and E. A. Bergin. Photoelectric cross-sections of gas and dust in protoplanetary disks. *The Astrophysical Journal*, 740(1):7, 2011.
- [247] F. Legarda, M. Herranz, and O. M. De Lafuente. A semiempirical formula for the photoelectric cross-section for photon energies up to 1 mev. *International Journal of Radiation*

- Applications and Instrumentation. Part A. Applied Radiation and Isotopes, 40(1):85–88, 1989.
- [248] L. Storm and H. I. Israel. Photon cross sections from 1 kev to 100 mev for elements z= 1 to z= 100. *Atomic Data and Nuclear Data Tables*, 7(6):565–681, 1970.
- [249] J. H. Hubbell, H. A. Gimm, and I O/verbo/. Pair, triplet, and total atomic cross sections (and mass attenuation coefficients) for 1 mev-100 gev photons in elements z= 1 to 100. *Journal of physical and chemical reference data*, 9(4):1023–1148, 1980.
- [250] W. Dachun, Y. Hua, L. Pingan, and D. Xunliang. Measurements of mass attenuation coefficients of yttrium with characteristic lines from elements excited by energetic protons.

 Nuclear Instruments and Methods in Physics Research Section B: Beam Interactions with

 Materials and Atoms, 71(3):249–254, 1992.
- [251] O. Gurler, C. H. Oktar, S. Yalcin, and G. Kaynak. Analytical formulas for calculating photoelectric attenuation coefficients. *Radiation Effects and Defects in Solids*, 167(12):895–902, 2012.
- [252] M. Ashoor, A. Asgari, A. Khorshidi, and A. Rezaei. Evaluation of compton attenuation and photoelectric absorption coefficients by convolution of scattering and primary functions and counts ratio on energy spectra. *Indian journal of nuclear medicine: IJNM: the official journal of the Society of Nuclear Medicine, India*, 30(3):239, 2015.
- [253] L. Gerward. X-ray attenuation coefficients and atomic photoelectric absorption cross sections of silicon. *Journal of physics B: Atomic and molecular physics*, 14(18):3389, 1981.
- [254] S. A. Moszkowski and R. E. Meyerott. Photoelectric k and 1 shell absorption coefficients for highly ionized atoms. *The Astrophysical Journal*, 124:537, 1956.

- [255] A. M. El-Khatib, M. I. Abbas, M. Abd Elzaher, M. S. Badawi, M. T. Alabsy, G. A. Alharshan, and D. A. Aloraini. Gamma attenuation coefficients of nano cadmium oxide/high density polyethylene composites. *Scientific reports*, 9(1):1–11, 2019.
- [256] K. S. R. Sarma, K. L. Narasimham, K. Premchand, S. B. Reddy, K. Parthasaradhi, and V. Lakshminarayana. Photoelectric cross-sections of light elements and compounds at low photon energies. *Pramana*, 18(6):485–494, 1982.
- [257] R. Nathuram, I. S. Sundara Rao, and M. K. Mehta. Photoelectric cross sections for 6–20-kev photons in beryllium, carbon, magnesium, aluminum, silicon, copper, silver, and lead. *Physical Review A*, 37(12):4978, 1988.
- [258] B. Roy, B. K. Chatterjee, S. C. Roy, N. Bhattacharya, and N. Choudhury. Photoelectric cross-sections derived from measured total attenuation coefficient of photons near absorption edges of heavier atoms. *Applied radiation and isotopes*, 48(6):785–788, 1997.
- [259] B. Al-Aaraj. Calculation of the photoelectric cross-section for subshells p-compounds.

 *Tishreen University Journal for Studies and Scientific Research, 24(12):225–232, 2002.
- [260] W Heitler. Oxford press, 3rd:21, 1954.
- [261] B. Crasemann, P. E. Koblas, T. C. Wang, H. E. Birdseye, and M. H. Chen. Measurement of the photoelectric cross section of h₂ at 5.4 and 8.4 kev. *Phys. Rev. A*, 9:1143–1151, Mar 1974.
- [262] M. J. Berger and J. H. Hubbell. Xcom: Photon cross sections on a personal computer. Technical report, National Bureau of Standards, Washington, DC (USA). Center for Radiation . . . , 1987.

- [263] H. C. Manjunatha. Influence of gamma irradiation on conductivity of yba2cu3o7. *Radiation Physics and Chemistry*, 113:24–27, 2015.
- [264] S. R. Manohara, S. M. Hanagodimath, and L. Gerward. Photon interaction and energy absorption in glass: a transparent gamma ray shield. *Journal of Nuclear materials*, 393(3):465–472, 2009.
- [265] L. Seenappa, H. C. Manjunatha, B. M. Chandrika, and H. Chikka. A study of shielding properties of x-ray and gamma in barium compounds. *Journal of Radiation Protection and Research*, 42(1):26–32, 2017.
- [266] H. C. Manjunatha. A study of gamma attenuation parameters in poly methyl methacrylate and kapton. *Radiation Physics and Chemistry*, 137:254–259, 2017.
- [267] H. C. Manjunatha. A study of gamma attenuation parameters in poly methyl methacrylate and kapton. *Radiation Physics and Chemistry*, 137:254–259, 2017.
- [268] B. Rudraswamy, N. Dhananjaya, and H. C. Manjunatha. Measurement of absorbed dose rate of gamma radiation for lead compounds. *Nuclear Instruments and Methods in Physics Research Section A: Accelerators, Spectrometers, Detectors and Associated Equipment*, 619(1-3):171–173, 2010.
- [269] H. C. Manjunatha. A study of photon interaction parameters in lung tissue substitutes.

 **Journal of Medical Physics/Association of Medical Physicists of India, 39(2):112, 2014.
- [270] H. C. Manjunatha and B. Rudraswamy. Study of effective atomic number and electron density for tissues from human organs in the energy range of 1 kev–100 gev. *Health physics*, 104(2):158–162, 2013.

- [271] K. C. Suresh, H. C. Manjunatha, and B. Rudraswamy. Study of z eff for dna, rna and retina by numerical methods. *Radiation protection dosimetry*, 128(3):294–298, 2008.
- [272] H. C. Manjunatha. Bremsstrahlung dosimetric parameters of beta-emitting therapeutic radionuclides. *Radiation Effects and Defects in Solids*, 171(3-4):316–327, 2016.
- [273] M. I. Sayyed. Half value layer, mean free path and exposure buildup factor for tellurite glasses with different oxide compositions. *Journal of Alloys and Compounds*, 695:3191–3197, 2017.
- [274] M. R. Ioan, V. Fugaru, S. Bercea, A. Celarel, L. C. Tugulan, and C. Cimpeanu. Co-60 specific gamma-ray constant (γ) determinations for various biological materials involved in radiotherapy procedures, by using geant4 and nist xcom. *Romanian Journal of Physics*, 63:701, 2018.
- [275] M. A. Ansari and N. Jahan. Structural and optical properties of bao nanoparticles synthesized by facile co-precipitation method. *Materials Highlights*, 2(1-2):23–28, 2021.
- [276] S. Hei, Y. Jin, and F. Zhang. Fabrication of γ -fe2o3 nanoparticles by solid-state thermolysis of a metal-organic framework, mil-100 (fe), for heavy metal ions removal. *Journal of Chemistry*, 2014, 2014.
- [277] H. Yan, D. Zhang, J. Xu, Y. Lu, Y. Liu, K. Qiu, Y. Zhang, and Y. Luo. Solution growth of nio nanosheets supported on ni foam as high-performance electrodes for supercapacitors.

 Nanoscale research letters, 9(1):1–7, 2014.
- [278] Y. S. Vidya, K. S. Anantharaju, H. Nagabhushana, S. C. Sharma, H. P. Nagaswarupa,S. C. Prashantha, C. Shivakumara, et al. Combustion synthesized tetragonal zro2: Eu3+

- nanophosphors: structural and photoluminescence studies. *Spectrochimica Acta Part A: Molecular and Biomolecular Spectroscopy*, 135:241–251, 2015.
- [279] K. Gurushantha, K. S. Anantharaju, S. C. Sharma, H. P. Nagaswarupa, S. C. Prashantha, K. R. Vishnu Mahesh, L. Renuka, Y. S. Vidya, and H. Nagabhushana. Bio-mediated sm doped nano cubic zirconia: Photoluminescent, judd–ofelt analysis, electrochemical impedance spectroscopy and photocatalytic performance. *Journal of Alloys and Compounds*, 685:761–773, 2016.
- [280] J. Malleshappa, H. Nagabhushana, B. Daruka Prasad, S. C. Sharma, Y. S. Vidya, and K. S. Anantharaju. Structural, photoluminescence and thermoluminescence properties of ceo2 nanoparticles. *Optik*, 127(2):855–861, 2016.
- [281] J. B.Prasanna Kumar, G. Ramgopal, Y. S. Vidya, K. S. Anantharaju, B. Daruka Prasad, S. C. Sharma, S. C. Prashantha, H. P. Nagaswarupa, D. Kavyashree, and H. Nagabhushana. Green synthesis of y2o3: Dy3+ nanophosphor with enhanced photocatalytic activity. *Spectrochimica Acta Part A: Molecular and Biomolecular Spectroscopy*, 149:687–697, 2015.
- [282] B. C. Reddy, H. C. Manjunatha, Y. S. Vidya, K. N. Sridhar, U. M. Pasha, L. Seenappa, C. Mahendrakumar, B. Sadashivamurthy, N. Dhananjaya, B. M. Sankarshan, et al. Synthesis and characterization of multi functional nickel ferrite nano-particles for x-ray/gamma radiation shielding, display and antimicrobial applications. *Journal of Physics and Chemistry of Solids*, 159:110260, 2021.
- [283] Y. S. Vidya, K. Gurushantha, H. Nagabhushana, S. C. Sharma, K. S. Anantharaju, C. Shivakumara, D. Suresh, H. P. Nagaswarupa, S. C. Prashantha, and M. R. Anilkumar. Phase transformation of zro2: Tb3+ nanophosphor: Color tunable photoluminescence and photocatalytic activities. *Journal of Alloys and Compounds*, 622:86–96, 2015.

- [284] W. Qin, C. Yang, R. Yi, and G. Gao. Hydrothermal synthesis and characterization of single-crystalline [alpha]-fe2o3 nanocubes. *Journal of Nanomaterials*, 2011, 2011.
- [285] Q. A. Drmosh, M. A. Gondal, Z. H. Yamani, and T. A. Saleh. Spectroscopic characterization approach to study surfactants effect on zno2 nanoparticles synthesis by laser ablation process. *Applied Surface Science*, 256(14):4661–4666, 2010.
- [286] V. Dellarocca, L. Marchese, M. L. Pena, F. Rey, A. Corma, and S. Coluccia. Surface properties of mesoporous ti-mcm-48 and their modifications produced by silylation. In *Oxide-based Systems at the Crossroads of Chemistry. Second International Workshop*, volume 140, pages 209–220, 2001.
- [287] S. Das, C. Yang, and C. Lu. Structural and optical properties of tunable warm-white light-emitting zro 2: Dy3+–eu 3+ nanocrystals. *Journal of the American Ceramic Society*, 96(5):1602–1609, 2013.
- [288] H. Q. Cao, X. Q. Qiu, B. Luo, Y. Liang, Y. H. Zhang, R. Q. Tan, M. J. Zhao, and Q. M. Zhu. Synthesis and room-temperature ultraviolet photoluminescence properties of zirconia nanowires. *Advanced Functional Materials*, 14(3):243–246, 2004.
- [289] Y. S. Vidya, K. S. Anantharaju, H. Nagabhushana, and S. C. Sharma. Euphorbia tirucalli mediated green synthesis of rose like morphology of gd2o3: Eu3+ red phosphor: Structural, photoluminescence and photocatalytic studies. *Journal of Alloys and Compounds*, 619:760–770, 2015.
- [290] X. Yang, Y. Wang, Y. Chen, and H. Yan. The structural and electronic properties of bao under epitaxial strains: First-principles calculations. *Acta Phys Polon A*, 129:64–68, 2016.
- [291] P. Mallick and B. N. Dash. X-ray diffraction and uv-visible characterizations of α -fe2o3

- nanoparticles annealed at different temperature. *Nanosci. Nanotechnol*, 3(5):130–134, 2013.
- [292] M. D. Irwin, D. B. Buchholz, A. W. Hains, R. P. H. Chang, and T. J. Marks. p-type semi-conducting nickel oxide as an efficiency-enhancing anode interfacial layer in polymer bulk-heterojunction solar cells. *Proceedings of the National Academy of Sciences*, 105(8):2783–2787, 2008.
- [293] A. I Khodadadi and R. Taherian. Investigation on the radiation shielding properties of lead silicate glasses modified by zno and bao. *Materials Chemistry and Physics*, 251:123136, 2020.
- [294] R. Peymanfar, M. Yektaei, S. Javanshir, and E. Selseleh-Zakerin. Regulating the energy band-gap, uv–vis light absorption, electrical conductivity, microwave absorption, and electromagnetic shielding effectiveness by modulating doping agent. *Polymer*, 209:122981, 2020.
- [295] M. F. Zaki. Gamma-induced modification on optical band gap of cr-39 ssntd. *Brazilian Journal of Physics*, 38:558–562, 2008.
- [296] M. A. El-Shahawy. Spectral changes of cr-39 induced by irradiation and heat treatment. Polymer degradation and stability, 57(2):157–161, 1997.
- [297] A. F. Saad, S. T. Atwa, R. Yokota, and M. Fujii. Radiation-induced modifications on spectroscopic and thermal properties of cr-39 and sr-90 nuclear track detectors. *Radiation measurements*, 40(2-6):780–784, 2005.
- [298] T. Sharma, S. Aggarwal, S. Kumar, V. K. Mittal, P. C. Kalsi, and V. K. Manchanda. Effect of

- gamma irradiation on the optical properties of cr-39 polymer. *Journal of materials science*, 42(4):1127–1130, 2007.
- [299] S-F. Wang, G-Z. Sun, L. M. Fang, L. Lei, X. Xiang, and X-T. Zu. A comparative study of znal 2 o 4 nanoparticles synthesized from different aluminum salts for use as fluorescence materials. *Scientific reports*, 5(1):1–12, 2015.
- [300] M. Nishi, S-Y. Chen, and H. Takagi. Mild ammonia synthesis over ba-promoted ru/mpc catalysts: Effects of the ba/ru ratio and the mesoporous structure. *Catalysts*, 9(5):480, 2019.
- [301] N. L. Aluker, M. E. Herrmann, and Y. M. Suzdaltseva. A spectrophotometric study of nitrate and nitrite salts and their aqueous solutions. *Optics and Spectroscopy*, 127(6):991– 996, 2019.
- [302] N. Alves, W. B. Ferraz, and L. Faria. Carbon doped lanthanum aluminate (laalo_3: C) synthesized by solid state reaction for application in uv thermoluminescent dosimetry. *International Nuclear Atlantic Conference*, 2015.
- [303] W. Muhammad, N. Ullah, M. Haroon, and B. H. Abbasi. Optical, morphological and biological analysis of zinc oxide nanoparticles (zno nps) using papaver somniferum l. *RSC Adv.*, 9:29541–29548, 2019.
- [304] K. T. Arulmozhi and N. Mythili. Studies on the chemical synthesis and characterization of lead oxide nanoparticles with different organic capping agents. *AIP advances*, 3(12):122122, 2013.
- [305] J. Cha, H. Jeong, and B. Ryu. Changes in the electrical conductivity and catalytic prop-

- erty of vanadium iron borophosphate glasses with crystallization. *Journal of the Korean Physical Society*, 72(10):1221–1227, 2018.
- [306] J. Roy, N. Bandyopadhyay, S. Das, and S. Maitra. Role of cr2o3 on the mullittization of di-phasic al2o3-sio2 gel. *Cerâmica*, 56:273–278, 2010.
- [307] Rafał Lewandków, Miłosz Grodzicki, P. Mazur, and A. Ciszewski. Interface formation of al2o3 on n-gan (0001): Photoelectron spectroscopy studies. *Surface and Interface Analysis*, 53(1):118–124, 2021.
- [308] N. Mythili and K. T. Arulmozhi. Characterization studies on the chemically synthesized α and β phase pbo nanoparticles. *Int. J. Sci. Eng. Res.*, 5(1):412–416, 2014.
- [309] G. P. Singh, P. Kaur, S. Kaur, R. Kaur, and D. P. Singh. Conversion of ce3+ to ce4+ ions after gamma ray irradiation on ceo2–pbo–b2o3 glasses. *Physica B: Condensed Matter*, 408:115–118, 2013.
- [310] S. A. Hussen. Structural and optical characterization of pure and snzro3 doped ps based polymer nanocomposite. *Materials Research Express*, 7(10):105302, 2020.
- [311] I. Boukhris, I. Kebaili, M. S. Al-Buriahi, and M. I. Sayyed. Radiation shielding properties of tellurite-lead-tungsten glasses against gamma and beta radiations. *Journal of Non-Crystalline Solids*, 551:120430, 2021.
- [312] https://physics.nist.gov/PhysRefData/Xcom/html/xcom1.html.
- [313] G. Tyagi, A. Singhal, S. Routroy, D. Bhunia, and M. Lahoti. Radiation shielding concrete with alternate constituents: An approach to address multiple hazards. *Journal of Hazardous Materials*, 404:124201, 2021.

- [314] M. Berger. Xcom: photon cross sections database. http://www. nist. gov/pml/data/xcom/index. cfm, 2010.
- [315] L. Gerward, N. Guilbert, K. Bjørn Jensen, and H. Levring. X-ray absorption in matter. reengineering xcom. *Radiation Physics and Chemistry*, 60(1-2):23–24, 2001.
- [316] S. Kim. Analysis of shielding performance of radiation-shielding materials according to particle size and clustering effects. *Applied Sciences*, 11(9):4010, 2021.
- [317] K. V. Sathish, L. Seenappa, H. C. Manjunatha, K. N. Sridhar, and S. A. C. Raj. Specific absorbed fraction of energy and relative dose in zinc alloys. In *Proceedings of the DAE Symp. on Nucl. Phys*, volume 65, page 832, 2021.
- [318] H. C. Manjunatha and B. Rudraswamy. Exposure of bremsstrahlung from beta-emitting therapeutic radionuclides. *Radiation measurements*, 44(2):206–210, 2009.

LIST OF PUBLICATIONS

Journal publications

- [1] K.V.Sathish, H.C. Manjunatha, Y.S.Vidya, B.M. Sankarshan, P.S. Damodara Gupta, L. Seenappa, K.N. Sridhar and S.Alfred Cecil Raj. Investigation on shielding properties of lead based alloys. *Progress in Nuclear Energy* 137(2021)103788
- [2] K.V. Sathish, H.C. Manjunatha, Y.S. Vidya, K.N. Sridhar, L. Seenappa, B. Chinnappa Reddy, S. Alfred Cecil Raj and P.S. Damodara Gupta. X-rays/gamma rays radiation shielding properties of Barium–Nickel–Iron oxide nanocomposite synthesized via low temperature solution combustion method. *Radiation Physics and Chemistry* 194(2022) 110053.
- [3] H.C. Manjunatha, K.V. Sathish, L. Seenappa, P.S. Damodara Gupta, S.Alfred Cecil Raj, A study of X-ray, gamma and neutron shielding parameters in Si-alloys. *Radiation Physics and Chemistry* 165(2019)108414.
- [4] K.V. Sathish, H.C. Manjunatha, L. Seenappa, K.N. Sridhar, N. Nagaraj and S. Alfred Cecil Raj. Specific absorbed fraction of energy of silicon-boron alloys. NISCAIR-CSIR, *Indian Journal of Pure and Applied Physics* Vol. 58 (April 2020)213-217.
- [5] K.V. Sathish, H.C. Manjunatha, L. Seenappa, K.N. Sridhar, N. Sowmya, S. Alfred Cecil Raj. Gamma, X-ray and neutron shielding properties of iron boron alloys. *Materials Today Proceedings Volume* 49, Part 3,(2022) 613-619.

[6] K.V. Sathish, L. Seenappa, H.C. Manjunatha, Y.S. Vidya, K.N. Sridhar, S. Alfred Cecil Raj. Radiation shielding properties of gallium alloys. *Materials Today Proceedings Volume* 57,(2022) 295-299.

Full papers in conference proceedings

- [1] K.V. Sathish, H.C. Manjunatha, L. Seenappa, P.S. Damodara Gupta and S. Alfred Cecil Raj. XRay and Gamma Shielding Properties of Al-Si alloy. *The Proceedings of National Conference on Environmental Monitoring Impact Assessment and Management* (NCEMIAM-2019) were published having ISBN. (978-93-88680-09-7).
- [2] K.V. Sathish, L. Seenappa, H.C. Manjunatha, K.N. Sridhar, S. Alfred cecil Raj. Specific absorbed fraction of energy and relative dose in Zinc alloys. *Proceedings of the DAE symp.on*Nucl. Phys. 65 (2021).
- [3] K.V. Sathish, H.C. Manjunatha, L. Seenappa, K.N. Sridhar, N.Nagaraj, S. Alfred Cecil Raj.

 A study of Si-B alloys for radiation shielding. *The Proceedings of international Conference on Indian Society for Radiation Physics*(JNU) 2019.
- [4] N. Nagaraja, H.C. Manjunatha, L. Seenappa, K.N. Sridhar, Ramalingam, H.B, N.Sowmya, and K.V. Sathish, Specific absorbed fraction of energy and relative dose in silicon boron 14 polymers. *The Proceedings of international Conference on Indian Society for Radiation Physics (JNU)* 2019.
- [5] K.V. Sathish, H.C. Manjunatha, L. Seenappa, K.N. Sridhar, N.Nagaraja and S. Alfred Cecil Raj, Specific absorbed fraction of energy Silicon-Boron alloys. *The Proceedings of international Conference on New Frontiers in Nuclear Physics. (ICNFNP2019)* Department of physics Banaras Hindu University, Varanasi, India October14-17,2019

[6] N.Nagaraja, K.N. Sridhar, H.C. Manjunatha, L. Seenappa, K.V. Sathish, Ramalingam.H.B and A study of Boron polymers for radiation shielding. *The Proceedings of international Conference on New Frontiers in Nuclear Physics. (ICNFNP2019)* Department of physics Banaras Hindu University, Varanasi, India October14-17, 2019.



Contents lists available at ScienceDirect

Radiation Physics and Chemistry

journal homepage: www.elsevier.com/locate/radphyschem



A study of X-ray, gamma and neutron shielding parameters in Si- alloys

H.C. Manjunatha^{a,*}, K.V. Sathish^a, L. Seenappa^a, Damodara Gupta^b, S. Alfred Cecil Raj^c

- ^a Department of Physics, Government College for Women, Kolar, 563101, Karnataka, India
- ^b Department of Physics, Government First Grade College, Hoskote, 562114, Karnataka, India
- ^c Department of Physics, St. Joseph's College, Trichy, 620020, Tamil Nadu, India

ARTICLE INFO

Keywords: Gamma X-ray Neutron

Shielding



We have studied the X-ray and gamma radiation shielding parameters such as mass attenuation coefficient, linear attenuation coefficient, half value layer, tenth value layer, effective atomic numbers, exposure buildup factors and specific gamma ray constant in aluminum silicon alloys (Al-47, Al- 32S, Al-43, Fe-Si, Al-356, Al-355 and Al-A355). We have also studied the neutron shielding properties such as coherent neutron scattering length, incoherent neutron scattering lengths, coherent neutron scattering cross section, incoherent neutron scattering cross sections, total neutron scattering cross section and neutron absorption cross sections in aluminium silicon alloys. It has been compared the shielding properties among the studied aluminium silicon alloys. From the detail study it is found that mean free path, HVL and TVL is minimum and exposure buildup factor is maximum for ferro-silicon alloy. Hence it is clear that ferro-silicon alloy is good absorber for X-ray and gamma radiation. The attenuation parameters for neutron are large for ferro silicon alloy. Hence, we suggest ferro silicon alloy is the best shielding materials for X-ray, gamma and neutrons.

1. Introduction

It is important to replace the lead shielding material by nontoxic and low cost materials. Seenappa et al. (Seenappaet al., 2018a), studied the X-ray, gamma radiation shielding parameters and neutron shielding parameters in some alloys such as AL-6XN, nicrosil, nisil, terfenol-D, elektron and ferro-boron. Singh et al. (TejbirSinghet al., 2018), reported the physical properties and gamma rays shielding parameters for some lead-copper binary alloys. Akman et al. (Akmanet al., 2019), investigated the gamma ray shielding performance of ternary alloys. Şakar et al. (ErdemŞakaret al., 2019), determined the radiation shielding properties of leaded brasses using a HPGe detector and a ¹³³Ba radioactive source. Agar et al. (Agaret al., 1016), studied the photon interaction features for some alloys containing palladium and silver alloys to use it as an alternative gamma radiations shielding material. Manjunatha et al. (Manjunatha et al., 2018), studied the X-ray and gamma radiation shielding parameters for the Al-based glassy alloys. Liu et al. (Liuet al., 1016), investigated the effects of Yittrium and Zinc additions on electrical conductivity and electromagnetic shielding effectiveness of Mg-Y-Zn alloys.

Kaur et al. (TaranjotKaur and TejbirSingh, 2019), made an attempt to summarize the various investigations made so far on visualizing the feasibility of alloys as radiation shielding material. Kaçal et al.

(Kaçalet al., 1016), determined the gamma-ray attenuation characteristics of eight different polymers using high resolution HPGe detector and different radioactive sources. Dong et al. (Donget al., 1016), calculated the shielding parameters of some boron containing resources for gamma ray and fast neutron. Aygün et al. (Aygünet al., 2019), studied the fabrication of Nickel alloys, Chromium and Tungsten reinforced new alloyed stainless steels for radiation shielding applications. Khobkham et al. (Khobkhamet al., 2018), studied the photon interaction behavior of zirconium alloy materials by using WinXCom program in the energy range 1 keV-100 MeV. Seenappa et al. (Seenappaet al., 2018b), studied the X-ray and gamma radiation shielding and neutron shielding properties of polymer concretes. Kacal et al. (Kacalet al., 2018), carried out the experimental studies of radiation shielding properties for some ceramics. Ripin et al. (Ripinet al., 2018), studied the x-ray shielding behavior of kaolin derived mullitebarites ceramics. Shielding of radiation means protection from harmful radiation such as alpha, beta, gamma and neutrons. It is easy to stop the alpha and beta radiation but stopping of gamma and neutrons are difficult. Neutrons are released during the nuclear reactions in nuclear reactors. Shielding against the neutrons is also important. While selecting the shielding material for nuclear reactor, there is a need study the shielding properties of neutrons along with the gamma radiation. In the present work, we have studied the X-ray and gamma radiation

E-mail address: manjunathhc@rediffmail.com (H.C. Manjunatha).

^{*} Corresponding author.

Table 1
Elemental composition.

Name of the alloy	Element	composition	
Al-47	AL	0.867	
	Si	0.125	
	Ni	0.008	
Al-32s	Al	0.854	
	Cu	0.008	
	Si	0.12	
	Mg	0.001	
	Ni	0.008	
Al- Silicon-43	Al	0.950	
	Si	0.050	
Ferrosilicon	Si	0.79	
	Fe	0.21	
Al-355	Al	0.932	
	Cu	0.013	
	Si	0.05	
	Mo	0.005	
Al-356	Al	0.927	
	Si	0.07	
	Mg	0.003	
Al-A355	Al	0.916	
	Cu	0.014	
	Si	0.05	
	Mn	0.0075	
	Mg	0.005	
	Ni	0.0075	

shielding parameters such as mass attenuation coefficient, linear attenuation coefficient, half value layer, tenth value layer, effective atomic numbers, electron density, exposure buildup factors, and specific gamma ray constant in aluminium silicon alloys. We have also studied the neutron shielding properties in silicon alloys. We have also evaluated the mechanical properties of silicon alloys.

2. Theory

2.1. Gamma/X-ray interaction parameters

In the present work, the mass attenuation coefficients (MAC) and photon interaction cross sections in the energy range from 1 keV to 100 GeV are generated using WinXCom (Gerward et al., 2004) and its composition (http://www5.csudh.edu/oli) (Table 1). Al-47 alloy is a mixture of Al (86.7%), Si(12.5%) and Ni(0.8%). Al–32S is a mixture of Al (85.4%), Si(12%), Cu (0.8%), Mg (0.1%) and Ni(0.8%). Al-Silicon-43 is a mixture of Al (95%) and Si(5%). Ferrosilicon is a mixture of Fe (21%) and Si(79%). Al-355 is mixture of Al (93.2%), Cu(1.3%), Si(5%) and Mo (0.5%), Al-356 is mixture of Al (92.7%), Si(7%) and Mg (0.3%). Al-A355 is a mixture of Al (91.6%), Cu(1.4%), Si(5%), Mn (0.75%), Mg (0.5%) and Ni (0.75%). The total linear attenuation coefficient (μ) can be evaluated by multiplying density of compounds to mass attenuation coefficients (Manjunatha and Rudraswamy, 2011a, 2013; Suresh et al., 2008; Manjunatha, 2014).

 Table 2

 Comparison of measured mass attenuation coefficient with present work.

Name of the alloy	$E = 662 \mathrm{keV}$		E = 1170 keV		E = 1330 keV	
	Expt	Present work	Expt	Present work	Expt	Present work
AL 47	0.0693 ± 0.0041	0.0732	0.0554 ± 0.0032	0.0584	0.0497 ± 0.0032	0.0526
AL 32S	0.0711 ± 0.0042	0.0756	0.0559 ± 0.0036	0.0592	0.0512 ± 0.0029	0.0546
Al Si 43	0.0709 ± 0.0049	0.0756	0.0550 ± 0.0039	0.0586	0.0504 ± 0.0039	0.0536
Ferrosilicon	0.0735 ± 0.0054	0.0786	0.0570 ± 0.0038	0.0608	0.0525 ± 0.0036	0.0552
Al 355	0.0700 ± 0.0056	0.0752	0.0559 ± 0.0037	0.0596	0.0502 ± 0.0039	0.0532
Al 356	0.0648 ± 0.0054	0.0696	0.0552 ± 0.0037	0.0589	0.0500 ± 0.0031	0.0532
Al A 355	0.0690 ± 0.0049	0.0742	0.0561 ± 0.0034	0.0595	0.0496 ± 0.0036	0.0528

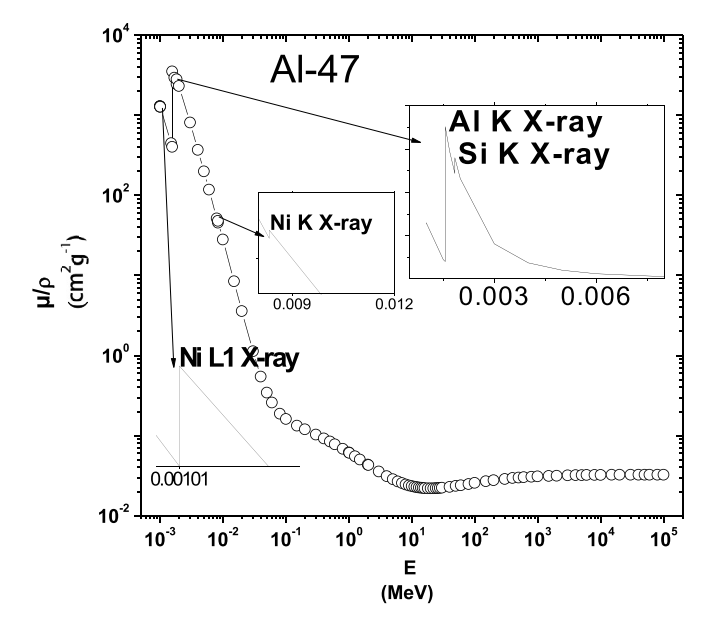


Fig. 1. Variation of total mass attenuation coefficient with photon energy for Al-47 alloy.

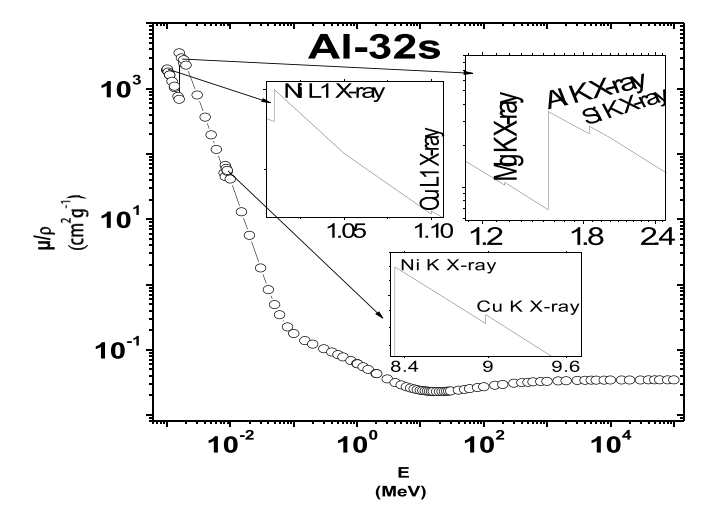


Fig. 2. Variation of total mass attenuation coefficient with photon energy for Al-32s alloy.

$$\mu = \left(\frac{\mu}{\rho}\right)_c \times \rho \tag{1}$$

The total linear attenuation coefficient (μ) is used in the calculation of Half Value Layer (HVL). HVL is the thickness of an interacting medium that reduces the radiation level by a factor of 2 that is to half the initial level and is calculated by the following equation

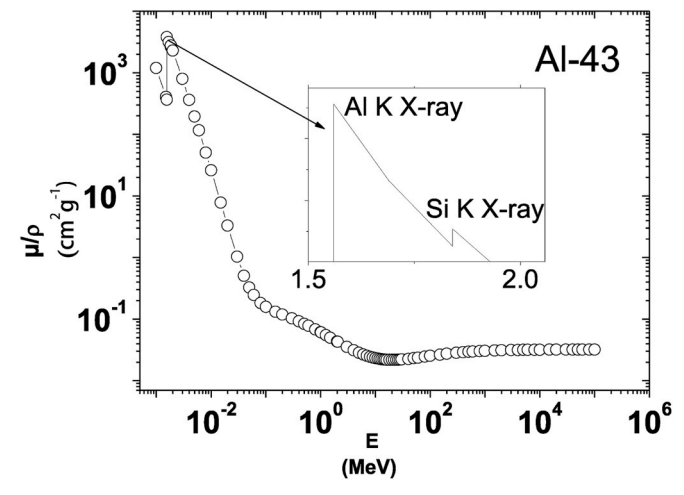


Fig. 3. Variation of total mass attenuation coefficient with photon energy for Al-43 alloy.

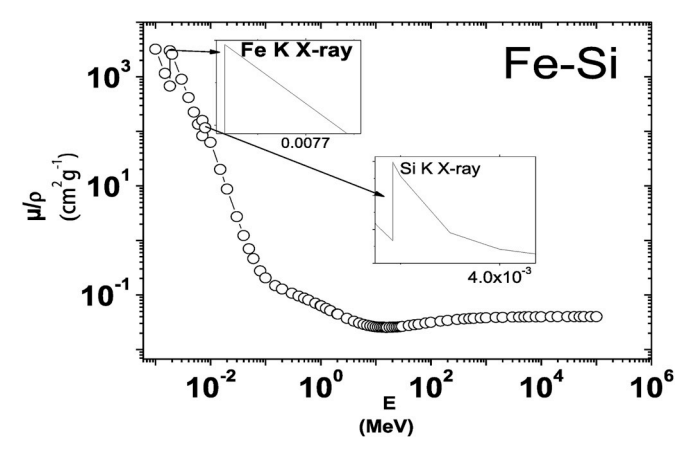
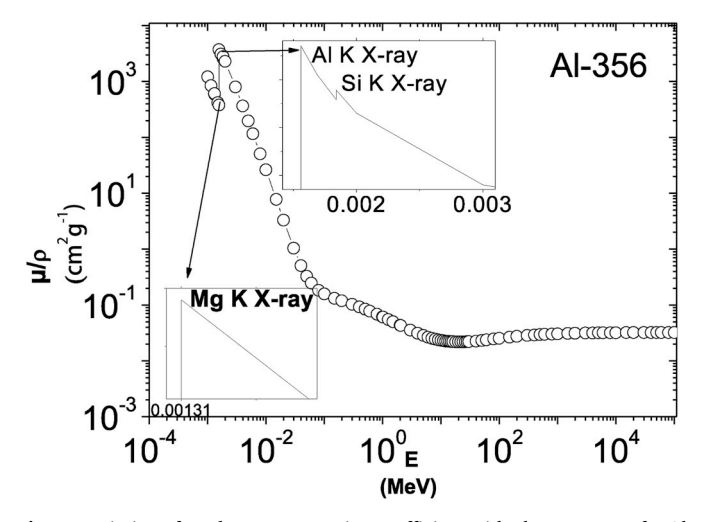


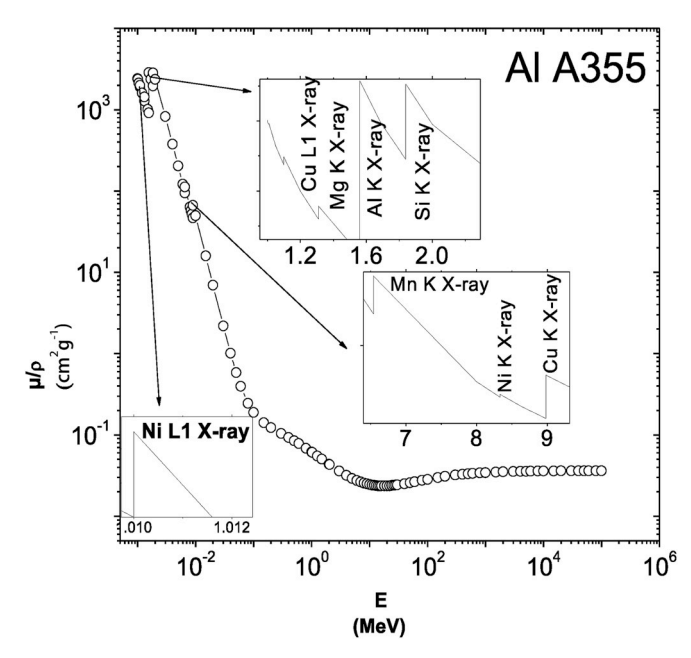
Fig. 4. Variation of total mass attenuation coefficient with photon energy for Fe–Si alloy.



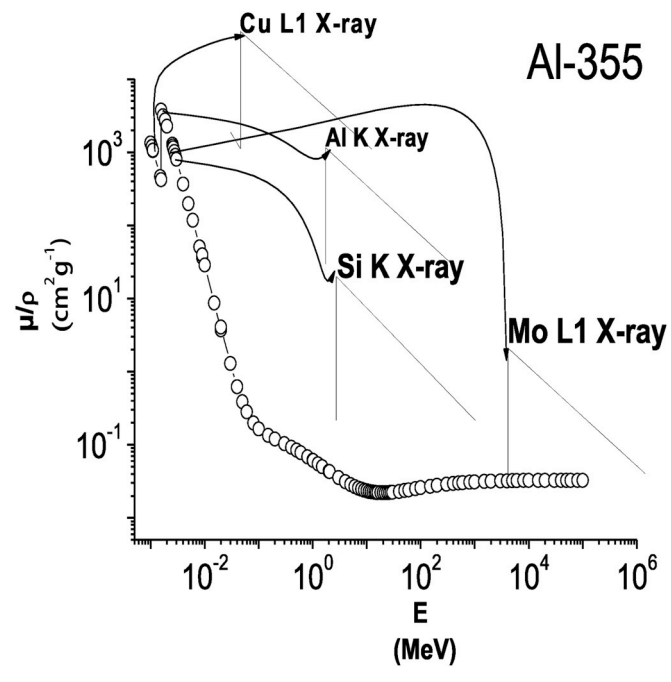
 $\begin{tabular}{ll} {\bf Fig.~5.~Variation~of~total~mass~attenuation~coefficient~with~photon~energy~for~Al~356~alloy. \end{tabular}$

(Manjunatha and Rudraswamy, 2011a, 2013; Suresh et al., 2008; Manjunatha, 2014)

$$HVL = \frac{\ln 2}{\mu} = \frac{0.693}{\mu}$$
 (2)



 $\textbf{Fig. 6.} \ \ \text{Variation of total mass attenuation coefficient with photon energy for Al-A355 alloy.}$



 $\textbf{Fig. 7.} \ \ \text{Variation of total mass attenuation coefficient with photon energy for Al- 355 alloy. }$

The total linear attenuation coefficient (μ) is also used in the calculation of Tenth Value Layer (TVL). It is the thickness of an interacting medium for attenuating a radiation beam to 10% of its radiation level and is computed by

$$TVL = \frac{ln10}{\mu} = \frac{2.303}{\mu} \tag{3}$$

The average distance between two successive interactions is called the relaxation length (λ) . It is also called the photon mean free path which is determined by the equation

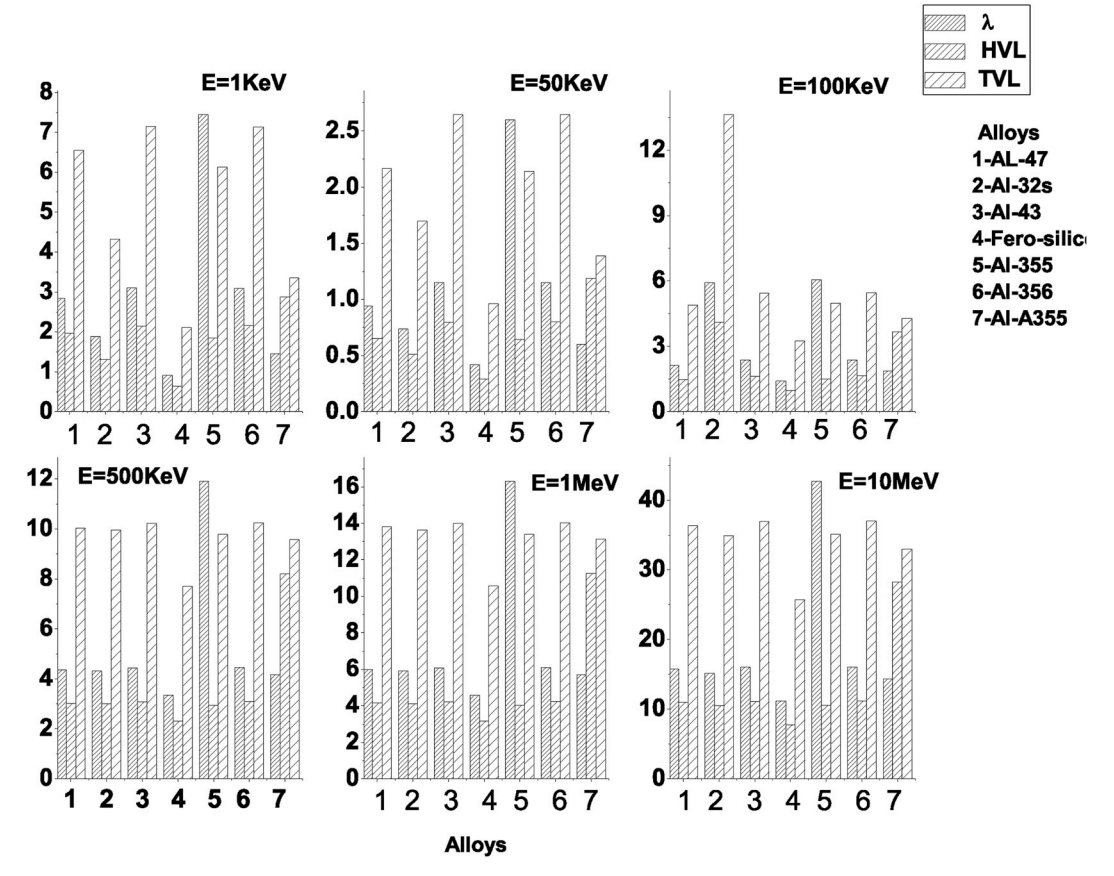


Fig. 8. Comparison of Half value layer (HVL), Tenth value layer (TVL) and mean free path(λ) for aluminium silicon alloys (1.Al-47, 2.Al-32s, 3.Al-43, 4-Ferro Silicon, 5.Al-355, 6. Al-356 and 7.Al A-355).

$$\lambda = \frac{\int\limits_{0}^{\infty} x exp(-\mu x) dx}{\int\limits_{0}^{\infty} exp(-\mu x) dx} = \frac{1}{\mu}$$
(4)

The gamma interaction parameters such as linear attenuation coefficients $\mu(\text{cm}^{-1})$, HVL (in cm), TVL (in cm) and mean free path λ are calculated using above equations (1)–(4). The total molecular cross section σ_m [milli barn] is computed from the following equation using the values of mass attenuation coefficients $[(\mu/\rho)_c]$ (Manjunatha and Rudraswamy, 2011a, 2013; Suresh et al., 2008; Manjunatha, 2014)

$$\sigma_m(E) = \left(\frac{1}{N}\right) \left(\frac{\mu}{\rho}(E)\right)_c \sum_i n_i A_i \tag{5}$$

where n_i is the number of atoms of ith element in a given molecule, $(\mu/\rho)_c$ is the mass attenuation coefficient of compound, N is the Avogadro's number and A_i is the atomic weight of element i. The effective (average) atomic cross section for a particular atom in the compound σ_a [milli barn] is estimated using the equation (Manjunatha and Rudraswamy, 2011a, 2013; Suresh et al., 2008; Manjunatha, 2014),

$$\sigma_{\alpha}(E) = \frac{\sigma_{m}}{\sum_{i} n_{i}} = \frac{\left(\frac{1}{N}\right)\left(\frac{\mu}{\rho}(E)\right)_{c} \sum_{i} n_{i} A_{i}}{\sum_{i} n_{i}}$$
(6)

The effective electronic cross section σ e [milli barn] is computed from mass attenuation coefficient (μ/ρ)i of ith element in the given molecule using following equation (Manjunatha and Rudraswamy, 2011a, 2013; Suresh et al., 2008; Manjunatha, 2014)

$$\sigma_{e}(E) = \left(\frac{1}{N}\right) \sum_{i} \left\{ \left(\frac{f_{i} A_{i}}{z_{i}}\right) \left(\frac{\mu}{\rho}(E)\right)_{i} \right\}$$
(7)

where, f_i is the fractional abundance (a mass fraction of the ith element in the molecule) and Z_i is the atomic number of the ith element in a molecule. Finally the $Z_{\rm eff}$ is estimated as

$$z_{eff} = \frac{\sigma_a}{\sigma_e} \tag{8}$$

The effective electron density (N_e) , expressed in terms of number of electrons per unit mass is closely related to the effective atomic number. For an element, the electron density is given by

 $N_e = NZ/A$ [electrons/g]. This expression can be generalized for a compound,

$$N_e(g^{-1}) = \frac{N}{\sum_i n_i A_i} Z_{eff} \sum_i n_i$$
(9)

2.2. Secondary radiation during the interaction of gamma/X-ray

During the interaction of gamma/X-ray with the medium, it degrade their energy and produces secondary radiations through the different interaction process. The quantity of secondary radiations produced in the medium and energy deposited/absorbed in the medium is studied by calculating buildup factors. In the present work, we have estimated energy exposure build up factors ($B_{\rm en}$) using GP fitting method (Manjunatha and Rudraswamy, 2011b, 2012a, 2012b). We have evaluated the G-P fitting parameters (b, c, a, X_k and d) for different aluminium silicon alloys using following expression which is based on Lagrange's interpolation technique (Manjunatha and Rudraswamy, 2012a)

$$P_{z_{eff}} = \sum \left(\frac{\prod_{Z' \neq Z} (Z_{eff} - Z)}{\prod_{z \neq Z} (z - Z)} \right) P_z$$
(10)

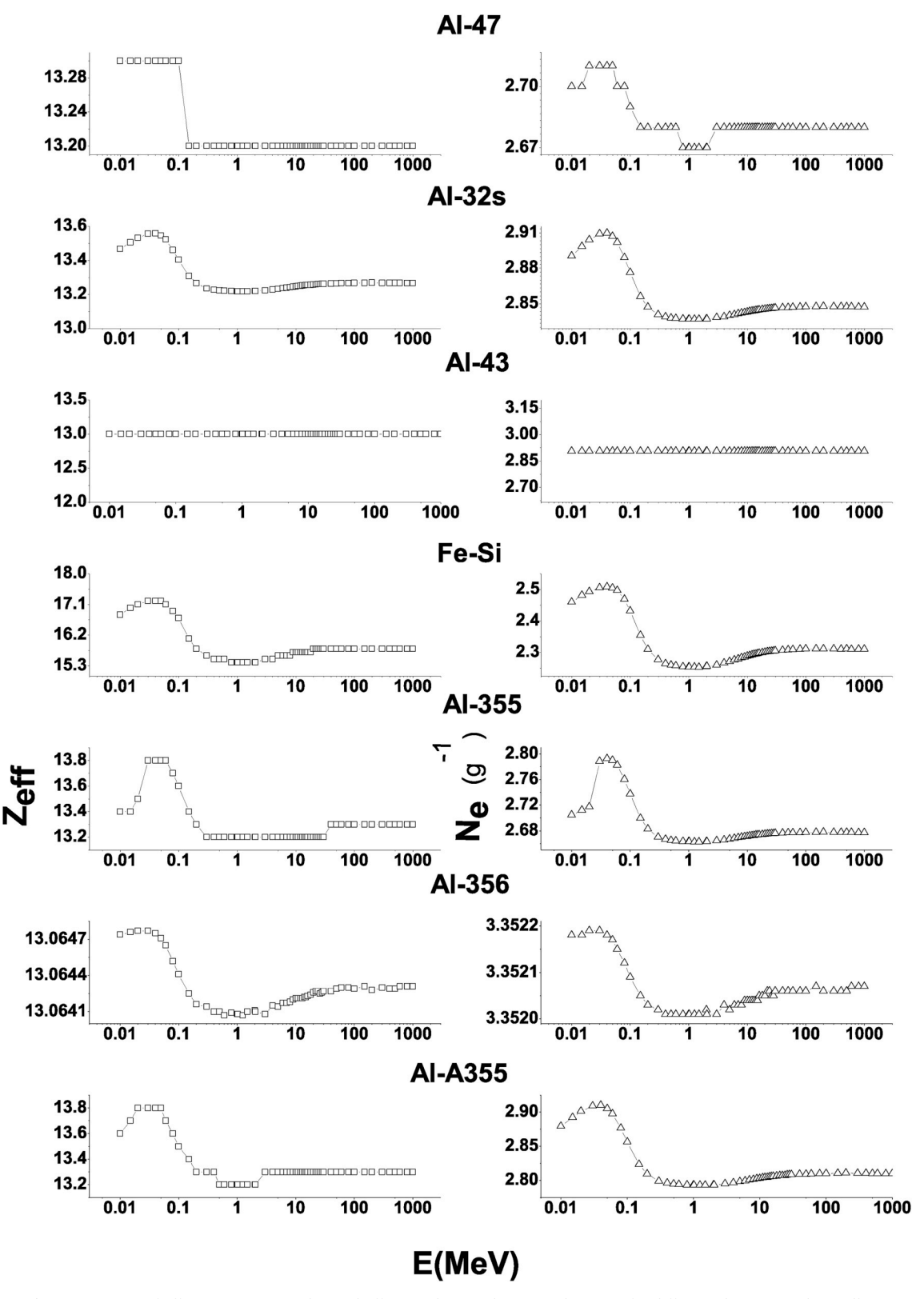


Fig. 9. Variation of effective atomic number and effective electron density with energy for different aluminium silicon alloys.

where lower case z is the atomic number of the element of known G-P fitting parameter P_z adjacent to the effective atomic number ($Z_{\rm eff}$) of the given material whose G-P fitting parameter $P_{Z_{\rm eff}}$ is desired and upper case Z are atomic numbers of other elements of known G-P fitting parameter adjacent to $Z_{\rm eff}$. GP fitting parameters (b, c, a, X_k and d) for element adjacent to $Z_{\rm eff}$ are provided by the standard data available in

literature (Manjunatha). The computed G-P fitting parameters (b, c,a, X_k and d) were then used to compute the EABF in the energy range 0.015MeV–15MeV up to a penetration depth of 40 mean free path with the help of G-P fitting formula, as given by the equations (Manjunatha and Rudraswamy, 2011b, 2012a, 2012b)

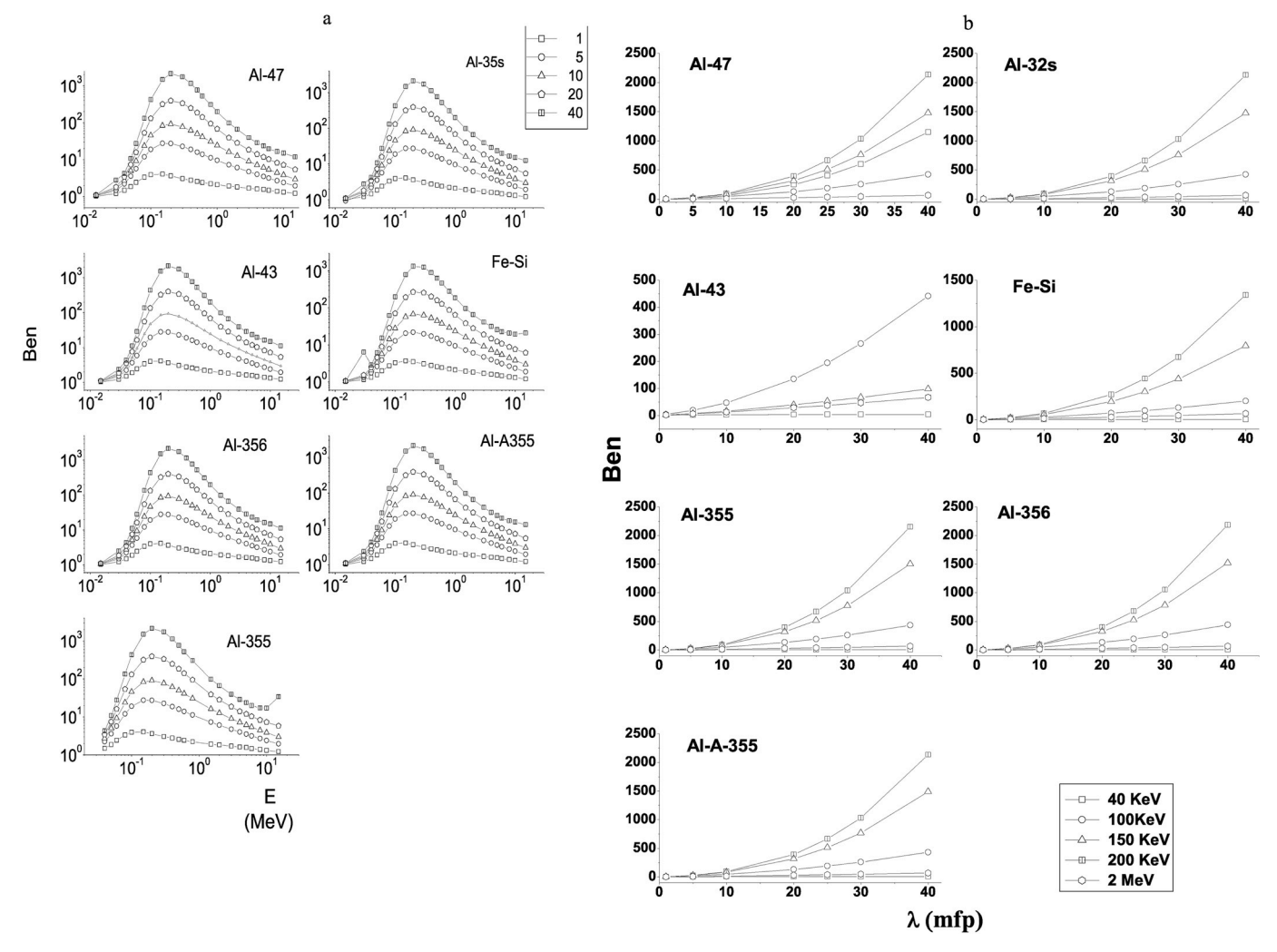


Fig. 10. a: Variation of exposure buildup factors with energy for different mean free paths for aluminum silicon alloys. b: Variation of exposure buildup factors with mean free path at different energies for different aluminium silicon alloys.

$$B(E, X) = 1 + \frac{b-1}{K-1}(K^X - 1)$$
 for $K \neq 1$ (11)

$$B(E, X) = 1 + (b - 1)X$$
 for $K = 1$ (12)

$$K(E, X) = CX^{a} + d \frac{\tanh\left(\frac{X}{X_{K}} - 2\right) - \tanh(-2)}{1 - \tanh(-2)}$$
For penetration depth (X)

$$\leq 40 \text{mfp}$$
 (13)

Where X is the source-detector distance for the medium in mean free paths (mfp) and b is the value of build-up factor at 1mfp. K (E,X) is the dose multiplication factor and b, c,a, X_k and d are computed G-P fitting parameters that depend on attenuating medium and source energy.

2.3. Neutron shielding parameters

The neutron shielding properties (NSP) such as coherent neutron scattering length $[b_{coh}],$ incoherent neutron scattering lengths $[b_{inc}],$ coherent neutron scattering cross section $[\sigma_{coh}],$ incoherent neutron scattering cross sections $[\sigma_{inc}],$ total neutron scattering cross section $[\sigma_{tot}]$ and neutron absorption cross sections $[\sigma_{abs}]$ in aluminum silicon alloys are calculated using following mixture rule

$$(NSP)_{Compound} = \sum f_i (NSP)_i \tag{14}$$

here (NSP) $_i$ is neutron shielding parameter of ith element (Manjunatha) in the concrete and f_i is the fractional abundance (a mass fraction of the

ith element in the molecule). From the computed neutron cross sections, attenuation parameter of neutron is evaluated using the relation;

$$attenuation parameter = \frac{\sigma \times N_A}{A}$$
 (15)

Where N_A and A are Avogadro number and atomic weight respectively. σ is evaluated cross section in barn.

2.4. Measurement of mass attenuation coefficient

To validate the present wok, we have measured mass attenuation coefficient of Aluminum silicon alloys such as Al-47, Al– 32S, Al-43, Fe–Si, Al-356, Al-355 and Al-A355 at different energies. The narrow geometry experimental setup used in the present measurement is explained in the reference [(Manjunatha et al., 2017; Seenappa et al., 2017)]. We have used a NaI(Tl) crystal detector mounted on a photomultiplier tube housed in a lead chamber and a sophisticated PC based MCA for a detection purpose, Gamma sources such as ^{137}Cs (0.662 MeV) and ^{60}Co (1.170, 1.330 MeV) are used. Aluminum silicon alloys such as Al-47, Al– 32S, Al-43, Fe–Si, Al-356, Al-355 and Al-A355 are used as target samples. The sample was directly attached to the opening of the lead shield where source is placed. The integral intensities, I_0 & I of the beam before and after passing through the sample are measured for sufficient time. $(\mu/\rho)_c$ of the sample is then estimated using the relation.

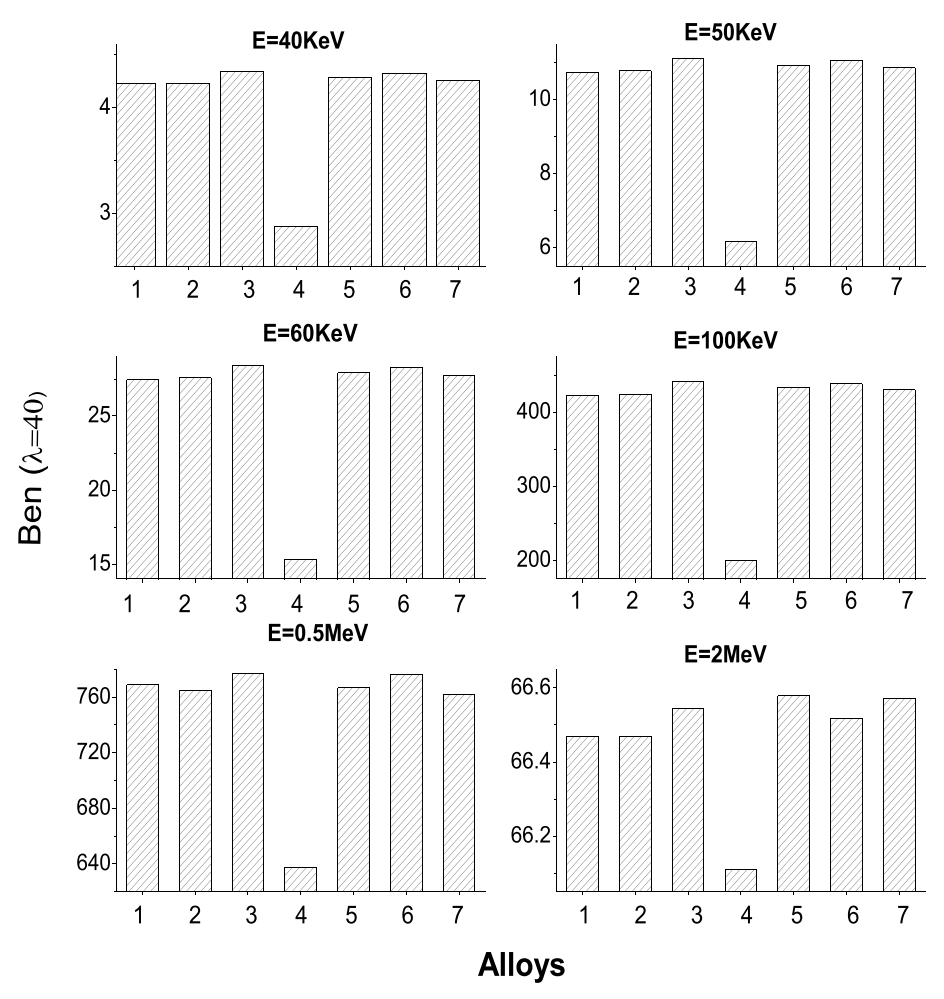


Fig. 11. Comparison of exposure buildup factors with energy for different aluminium silicon alloys (1-Al-47, 2-Al-32S, 3-Al-43, 4-Ferro silicon, 5-Al-355, 6-Al-356, 7-Al-A355).

$$\left(\frac{\mu}{\rho}\right)_{c} = \left(\frac{1}{t\rho}\right) \ln\left(\frac{I_{o}}{I}\right) \tag{16}$$

Where, t and ρ are the thickness and density of the sample respectively. Comparison of present work with experiments is as shown in Table 2.

3. Results and discussions

3.1. Variation of mass attenuation coefficient with photon energy

We have studied the X-ray and gamma radiation shielding parameters in aluminum silicon alloys (Al-47, Al- 32S, Al-43, Fe-Si, Al-356, Al-355 and Al-A355). The calculated mass attenuation coefficient for aluminium silicon alloys is graphically represented. There are two values of mass attenuation coefficients at same energies due to the presence of X-ray absorption edges. The variation of mass attenuation coefficient with photon energy for Al-47 alloy is as shown in Fig. 1. In case of Al 47 alloy, there are 4 X-ray absorption edges those are Ni L3, Al K, Si K and Ni K X ray at energies 1.01, 1.56, 1.84 and 8.33 keV respectively. These identified X-ray absorption edges are highlighted in the Fig. 1. Mass attenuation coefficient values of aluminium silicon alloys are large in the low energy region and decreases progressively. In the low energy region, mass attenuation coefficient is observed to be maximum, because of dominant photoelectric interaction which depends on atomic number as Z^{4-5} . In the intermediate energy region (0.8 < E < 5 MeV), Compton scattering becomes dominant which depends linearly with atomic number. Hence, mass attenuation

coefficient values become minimum. In the high energy region (> 10 MeV), mass attenuation coefficient values again increases because of pair production which is proportional to Z^2 . The variation of mass attenuation coefficient with photon energy for Al– 32S is as shown in Fig. 2. There are 5 X-ray absorption edges are observed in Al 32S those are Ni L1, Cu L1, Mg K, Al K and Si K X ray at energies 1.01, 1.10, 1.31, 1.56 and 1.84 keV respectively.

The variation of mass attenuation coefficient with photon energy for Al-43 alloy is as shown in Fig. 3. There are 2 X-ray absorption edges are observed in Al-43those are Al K and Si K X-ray at energies 1.56 and 1.84 keV respectively. The variation of mass attenuation coefficient with photon energy for Fe–Si is as shown in Fig. 4. There are 2 X-ray absorption edges are observed in Fe–Si those are Si K and Ce K X-ray at energies 1.84 and 7.11 keV respectively. The variation of mass attenuation coefficient with photon energy for Al-356 alloy is as shown in Fig. 5. There are 3 X-ray absorption edges are observed in Al 356 those are Mg K, Al K and Si K X-ray at energies 1.31, 1.56 and 1.84 keV respectively.

The variation of mass attenuation coefficient with photon energy for Al-A355 is as shown in Fig. 6. There are 8 X-ray absorption edges are observed in Al A355 those are Ni L1, Cu L1, Mg K, Al K, Si K, Mn K, Si K and Cu K X-ray at energies 1.01, 1.1, 1.31, 1.56, 1.84, 6.54, 8.33 and 8.98 keV respectively. The variation of mass attenuation coefficient with photon energy for Al-355 is as shown in Fig. 7. There are 4 X-ray absorption edges are observed in Al 355 those are Cu L1, Al K, Si K and Mo L1 X-ray at energies 1.1, 1.56, 1.84 and 2.87 keV respectively.

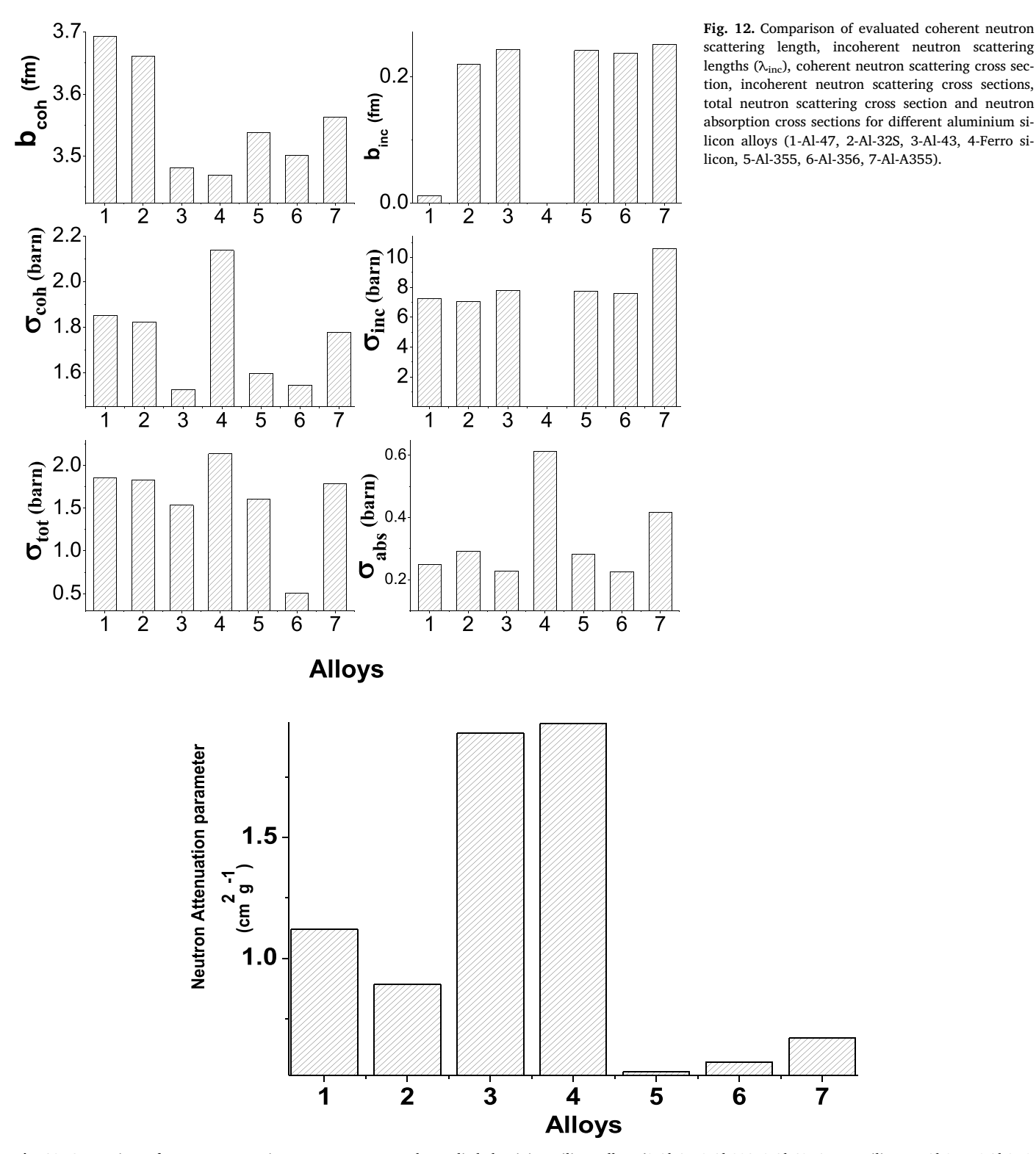


Fig. 13. Comparison of neutron attenuation parameters among the studied aluminium silicon alloys (1-Al-47, 2-Al-32S, 3-Al-43, 4-Ferro silicon, 5-Al-355, 6-Al-356, 7-Al-A355).

3.2. Gamma/X-ray interaction parameters

We have calculated the half value layer, tenth value layer and mean free path for different aluminium silicon alloys. The comparison of half value layer, tenth value layer and mean free path for different aluminium silicon alloys are as shown in Fig. 8. From this comparison, it is clear that the half value layer and tenth value layer are small for ferro

silicon alloy than the other aluminium silicon alloys. It means gamma/X-ray penetrates less in ferro silicon alloy than the other aluminum silicon alloys. It means ferro-silicon is good absorber of gamma/X-ray radiation.

The variation of effective atomic number and effective electron density with energy for different aluminium silicon alloys are as shown in Fig. 9. These parameters for aluminium silicon alloys are large in the

low energy region (due to photo electric effect) and decreases progressively, there after increases and becomes constant for high energy (due to pair production). It is also observed that effective atomic number and effective electron density almost constant for the alloy Al-43.

3.3. Variation of energy exposure buildup factors (EBF) with the energy

The variation of exposure buildup factors with energy at different mean free paths are as shown in Fig. 10a. The variation of exposure buildup factors with mean free path at various energies (0.1, 0.5, 1.5, 5 and 15 MeV) for different aluminium silicon alloys are as shown in Fig. 10b. From this figure it is clear that EBF values increases with increase in the target thickness. This is due to the reason that with increase in the target thickness, scattering events in the medium increases. The comparison of exposure buildup factors with energy for different aluminium silicon alloys are as shown in Fig. 11. It is observed that EBF value is larger for ferro silicon alloy among the studied aluminium silicon alloys at different energies. It is also reveals that scattering and absorption is larger in ferro-silicon than the other studied alloys. Ferro silicon can be used for the shielding for gamma/X-ray radiations.

3.4. Neutron shielding properties

Neutron scattering length and cross sections such as coherent neutron scattering length, incoherent neutron scattering lengths, coherent neutron scattering cross section, incoherent neutron scattering cross sections, total neutron scattering cross section and neutron absorption cross sections are related to shielding capability of the medium. Hence in the present work, we have considered these parameters as shielding parameters. The attenuation parameter is evaluated using the total cross section. The comparison of evaluated coherent neutron scattering length, incoherent neutron scattering lengths, coherent neutron scattering cross section, incoherent neutron scattering cross sections, total neutron scattering cross sections and neutron absorption cross sections for different Al–Si alloys are as shown in Fig. 12.

From this figure, it is clear that coherent neutron scattering length and incoherent neutron scattering lengths are smaller for Ferro silicon alloy than that of the other studied alloys. Coherent and total neutron scattering cross sections are large for Ferro silicon alloy. The neutron absorption cross section is high for Ferro silicon alloy. From the study of above parameters suggest that neutron scattering and absorption is larger in ferro-silicon alloy than that of the other studied alloy. The comparison of evaluated neutron attenuation parameter (cm $^2/\mathrm{g}$) for the studied Al–Si alloys is shown in Fig. 13. From this figure, it is clear that the total neutron attenuation parameter is larger for ferro silicon alloy than that of the other studied alloy. Hence attenuation of neutrons are large in larger for ferro silicon alloy than that of the other studied alloy.

Ferro-silicon alloy may be used for the shielding for neutrons also.

4. Conclusion

We have studied the X-ray, gamma and neutron shielding parameters in Al–Si alloys. From the detail study, it is clear that Ferro silicon alloy is good absorber for X-ray, gamma radiation and neutron. The attenuation parameters for neutron is large for Hence, we suggest that Ferro silicon alloy is best shielding material for X-ray, gamma and neutrons.

Appendix A. Supplementary data

Supplementary data to this article can be found online at https://doi.org/10.1016/j.radphyschem.2019.108414

References

Agar et al., Nucl. Engin. and Tech. doi.org/10.1016/j.net.2018.12.014.
Akman, et al., 2019. J. Alloy. Comp. 782, 315–322.
Aygün, B., et al., 2019. Results in Physics 12, 1–6.
M.G.Dong et al., Results in Physics, doi.org/10.1016/j.rinp.2019.02.065.
ErdemŞakar, et al., 2019. Radiat. Phys. Chem. 159, 64–69.
Gerward, L., Guilbert, N., Jensen, K.B., Levring, H., 2004. Radiat. Phys. Chem. 71,

Kacal, Mustafa R., et al., 2018. Radiochim. Acta 107 (2).

M.R.Kaçal et al., Nucl. Eng. and Tech. doi.org/10.1016/j.net.2018.11.011.

Khobkham, C., et al., 2018. Materialstoday proceedings 5 (7), 14928–14932. Lizi Liu et al., J. Mater. Sci. Technol.. doi.org/10.1016/j.jmst.2018.12.010.

H.C.Manjunatha, A study of gamma dosimetric parameters in some skeletal muscle relaxants, Pramana - J. Phys. 89:42.

Manjunatha, H.C., 2014. A study of photon interaction parameters in lung tissue substitutes. J. of med. Phy. 39 (2), 112.

Manjunatha, H.C., Rudraswamy, B., 2011a. Computation of CT-number and Zeff in teeth. Healt.phy. 100 (5), S92–S99.

Manjunatha, H.C., Rudraswamy, B., 2011b. Computation of exposure build-up factors in teeth. Radiat. Phys. Chem. 80 (1), 14–21.

Manjunatha, H.C., Rudraswamy, B., 2012a. Energy absorption and exposure build-up factors in hydroxyapatite. Rad.Meas. 47 (5), 364–370.

Manjunatha, H.C., Rudraswamy, B., 2012b. Energy absorption build-up factors in teeth. Jour.Radio .Nucl.Chem. 294 (2), 251–260.

Manjunatha, H.C., Rudraswamy, B., 2013. Study of effective atomic number and electron density for tissues from human organs in the energy range of 1 keV–100 GeV. Health Phys. (Tokyo) 104 (2), 158–162.

Manjunatha, H.C., Seenappa, L., Chandrika, B.M., Hanumantharayappa, Chikka, 2017. Ann. Nucl. Energy 109, 310–317.

Manjunatha, et al., 2018. Appl. Radiat. Isot. 139, 187-194.

Ripin, A., et al., 2018. Radiat. Phys. Chem. 144, 63-68.

Seenappa, L., Manjunatha, H.C., Chandrika, B.M., Chikkahanumantharayappa, 2017. J. of Rad. Protec. and Resear. 42 (1), 26–32.

Seenappa, et al., 2018a. Indian J. Pure Appl. Phys. 56 (08).

Seenappa, L., et al., 2018b. IJPAP 56 (05).

Suresh, K.C., Manjunatha, H.C., Rudraswamy, B., 2008. Study of Zeff for DNA, RNA and retina by numerical methods. Radiat. Prot. Dosim. 128 (3), 294–298.

TaranjotKaur, JeewanSharma, TejbirSingh, 2019. Prog. Nucl. Energy 113, 95–113. TejbirSingh, et al., 2018. Eng. Sci. and Tech. 21 (5), 1078–1085.



Indian Journal of Pure & Applied Physics Vol. 58, April 2020, pp. 213-217



Specific absorbed fraction of energy of silicon-boron alloys

KV Sathish^a, H C Manjunatha^{a*}, L Seenappa^a, K N Sridhar^b, N Nagaraj^b & S Alfred Cecil Raj^c

^aDepartment of Physics, Government College for Women, Kolar 563 101, India

^bDepartment of Physics, Government First Grade College, Kolar 563 101, India

^cDepartment of Physics, St. Joseph's College, Trichy 620 020, India

Received 17 February 2020

We have studied the energy absorption buildup factors and specific absorbed fraction of energy for the silicon-boron alloys of different composition such as alloy $A-Si_{0.95}-B_{0.05}$, alloy $B-Si_{0.9}-B_{0.1}$, alloy $C-Si_{0.8}-B_{0.2}$, alloy $D-Si_{0.7}-B_{0.3}$, alloy $E-Si_{0.6}-B_{0.4}$ and alloy $F-Si_{0.5}-B_{0.5}$ for wide energy range (0.015–15 MeV) up to the penetration depth of 40 mfp using geometric progression fitting method. Buildup factors increase with the increase in the penetration depth. It has been found that the shielding parameters such as mass attenuation coefficient, effective atomic number and buildup factor values are larger for the silicon-boron alloy $Si_{0.95}-B_{0.05}$ than the other studied silicon-boron alloys. Specific absorbed fraction of energy is maximum for the silicon-boron alloy $Si_{0.95}-B_{0.05}$. Hence, we can conclude that the silicon-boron alloy $Si_{0.95}-B_{0.05}$ is a good absorber of X-rays, gamma and neutrons among the studied alloys. The present study is useful in the field of radiation shielding.

Keywords: Energy absorption, Buildup factor, Silicon-boron alloys, Radiation shielding

1 Introduction

When gamma and X-rays enter the medium, they degrade their energy through scattering with the medium, giving rise to secondary radiation which can be estimated by a factor which is called the "buildup factor." Manjunatha and Rudraswamy studied energy absorption and exposure buildup factors in hydroxyapatite, and these are helpful in dosimetry and diagnostics. The same group^{2,3} computed the buildup factors and photon relative dose distribution in different regions of teeth, which is useful in dental science. Previous researchers⁴ also computed buildup factors for the estimation of specific absorbed fractions of energy in the biological samples. Previous researchers used exposure buildup factors for the calculations of secondary radiation dose such as bremsstrahlung^{5,6}. Steel is used for shielding of gamma radiation.

Calculations of the energy absorbed in a medium include not only the contribution of uncollided photons from the source but also the contributions from the collided and secondary photons. In practice, this is done by multiplying the contribution of uncollided photons with the energy absorption buildup factor^{7,8}. The buildup factor is an important

*Corresponding author (E-mail: manjunathhc@rediffmail.com)

parameter in the distribution of photon flux in every object. In brnchytherapy, radioactive seeds are implanted into the patient's body to destroy the cancerous tumor^{9,10}. Thus, it is important to consider the photon buildup factor in the calculation of radiation dose received by the cancer cells. The buildup factor data were computed by different codes such as PALLAS-PL11, RADHEAT-V412, ADJMOM-1¹³ and ASFIT¹⁴. Several authors have provided different buildup factor data for extensive utilization of design in radiation shields and other purposes¹⁵⁻¹⁹. ANSI/ANS 6.4.3 used the geometric progression (GP) fitting method²⁰ and provided buildup factor data for 23 elements, water, air, and concrete at 25 standard energies in the energy range 0.015-15 MeV with suitable interval up to the penetration depth of 40 mfp.

Previous studies²¹ compared the computed buildup factors using the GP fitting method with the PALLAS code. Good agreement was observed for penetration depth up to 40 mfp. Shimizu *et al.*²² compared the buildup factors obtained by three different methods (GP fitting, invariant embedding, and Monte Carlo method), and only small discrepancies were observed for low-Z elements up to 10 mfp. Singh *et al.*²³ studied the variation of energy absorption buildup factors with incident photon energy and penetration

depth for some solvents. Sidhu et al.²⁴ computed the exposure buildup factors in biological samples and studied the variation of exposure buildup factors with incident photon energy and effective atomic number. Previous researchers²⁵ studied X-ray and gamma radiation shielding parameters in silicon alloys. Silicon appears as coarse polyhedral particles and its hardness goes on increasing with increase in the number of silicon particles²⁶. The influence of the Si content in the alloys have better wear resistance and mechanical properties²⁷. The alloys with Boron content are used for the neutron shielding purpose²⁸. The alloys with Boron content are possess good mechanical properties²⁹. In the present study, we have studied the energy absorption buildup factors of the silicon-boron alloys of different composition such as alloy A-Si0.95-B0.05, alloy B- Si0.9-B0.1, alloy C-Si0.8-B0.2, alloy D- Si0.7-B0.3, alloy E- Si0.6-B0.4 and alloy F- Si0.5-B0.5 for wide energy range (0.015– 15 MeV) up to the penetration depth of 40 mfp using GP fitting method. The consideration of the primary photons interaction in the target medium is not sufficiently accurate for the estimation of absorbed dose in other various organs from a source of photons. An accurate absorbed dose calculation needs specific absorbed fraction of energy (U). It is defined as the ratio of the energy absorbed by the target to the energy emitted by the source. In the present work, we have also studied the specific absorbed fraction of energy for the silicon-boron alloys of different composition such as alloy A-Si_{0.95}-B_{0.05}, alloy B- Si_{0.9}- $B_{0.1}$, alloy C- $Si_{0.8}$ - $B_{0.2}$, alloy D- $Si_{0.7}$ - $B_{0.3}$, alloy E- Si_{0.6}-B_{0.4} and alloy F- Si_{0.5}-B_{0.5} for wide energy range (0.015-15 MeV) up to the penetration depth of 40 mfp.

2 Theory

Three methods are used to calculate the specific absorbed fraction of energy for a given source organ target organ pair at a given initial photon energy: (i) ϕ is calculated from the target to source to with the Monte Carlo radiation transport computer program; (ii) ϕ is calculated from source to target with the Monte Carlo computer program and this value is used to estimate target to source and (iii) ϕ is calculated from the target to source with the point source kernel method. In this method, the specific absorbed fraction of energy at distance x from the point source mono energetic photon emitter is given by:

$$\Phi(x) = \frac{\mu_{en} \exp(-\mu x) B_{en}}{4\pi R^2 \rho} \qquad \dots (1)$$

Here, μ_{en} is linear absorption coefficient of photons of given energy, μ is linear attenuation coefficient of photons of given energy, B_{en} is energy absorption build up factor; ρ is density of the medium. The energy absorption build up factors are computed and are used to evaluate ϕ for the distance up to 10 mm and penetration depth up to 40 mean free paths.

In the present work, we have estimated energy absorption build up factor (B_{en}) using GP fitting method³⁰⁻³⁷. We have evaluated the G-P fitting parameters (b, c, a, X_k and d) for different alloys using following expression which is based on Lagrange's interpolation technique

$$P_{Z_{eff}} = \sum \left(\frac{\prod_{Z' \neq Z} (Z_{eff} - Z)}{\prod_{z \neq Z} (z - Z)} \right) P_{z} \qquad \dots (2)$$

where lower case z is the atomic number of the element of known G-P fitting parameter P_z adjacent to the effective atomic number ($Z_{\rm eff}$) of the given material whose G-P fitting parameter $P_{Z_{\rm eff}}$ is desired and upper case Z are atomic numbers of other elements of known G-P fitting parameter adjacent to $Z_{\rm eff}$. For the computation of $Z_{\rm eff}$, the values of mass attenuation coefficients were computed from WinXCom computer program³⁰. $Z_{\rm eff}$ is computed from the following equations:

$$Z_{eff} = \frac{\frac{1}{N} \left(\frac{\mu}{\rho}\right) \sum n_i A_i}{\frac{1}{N} \sum \left(\frac{f_i A_i}{Z_i}\right) \left(\frac{\mu}{\rho}\right)} \qquad \dots (3)$$

Where n_i is the number of atoms of i^{th} element in a given molecule, (μ/ρ) is the mass attenuation coefficient of silicon-boron alloys, N is the Avogadro's number, A_i is the atomic weight of element i. $(\mu/\rho)_{st}$ was estimated based on the chemical composition and f_i is the fractional abundance.

GP fitting parameters (b, c, a, X_k and d) for element adjacent to Z_{eff} are provided by the standard data available in literature³⁷. The computed G-P

fitting parameters (b, c, a, X_k and d) were then used to compute the EABF in the energy range 0.015MeV-15MeV up to a penetration depth of 40 mean free path with the help of G-P fitting formula, as given by the equations³⁰⁻³⁷:

$$B(E, X) = 1 + \frac{b-1}{K-1}(K^{X} - 1)$$
; for $K \neq 1$... (4)

$$B(E, X) = 1 + (b-1)X$$
; for K=1 ... (5)

$$K(E, X) = CX^{a} + d \frac{\tanh(\frac{X}{X_{K}} - 2) - \tanh(-2)}{1 - \tanh(-2)};$$

For penetration depth $(X) \le 40 \text{mfp}$... (6)

Where X is the source-detector distance for the medium in mean free paths (mfp) and b is the value of build-up factor at 1mfp. K(E,X) is the dose multiplication factor and b, c, a, X_k and d are computed G-P fitting parameters that depend on attenuating medium and source energy.

3 Results and Discussion

We have calculated energy absorption buildup factors using GP fitting method. The calculated energy absorption buildup factors are graphically represented. The variation of energy absorption buildup factors with incident photon energy for silicon-boron alloys is shown in Fig. 1. From this figure, it is observed that energy absorption increases

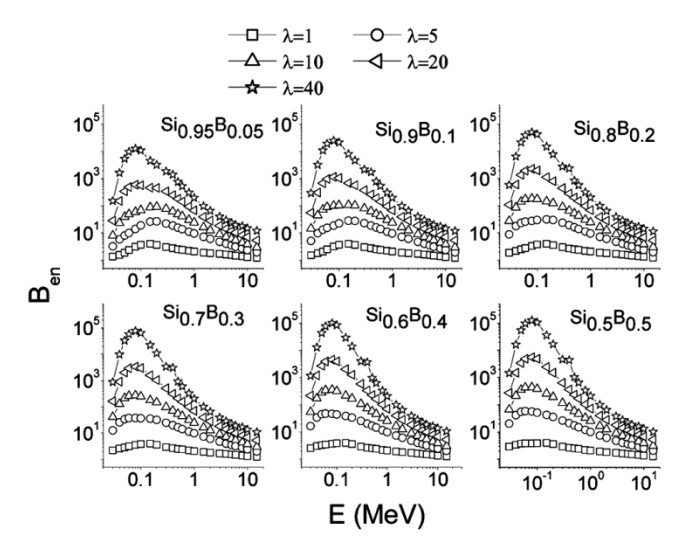


Fig. 1 – Variation of buildup factors (Ben) of different siliconboron alloys with energy (MeV) for different mean free paths (Alloy A-Si_{0.95}-B_{0.05}, Alloy B- Si_{0.9}-B_{0.1}, Alloy C- Si_{0.8}-B_{0.2}, Alloy D- Si_{0.7}-B_{0.3}, Alloy E- Si_{0.6}-B_{0.4} and Alloy F- Si_{0.5}-B_{0.5}.)

up to the E_{pe} (0.1 MeV) and then decreases. Here, E_{pe} is the energy value at which the photoelectric interaction coefficients match with Compton interaction coefficients for a given value of effective atomic number (Z_{eff}). The variation of buildup factors with energy is due to the dominance of photoelectric absorption in the lower end and the dominance of pair production in the higher photon energy region. As the energy of incident photon increases, Compton scattering overtakes the photoelectric absorption. It results in multiple Compton scattering events, which increases the energy absorption buildup factor up to the E_{pe} , and it becomes maximum at E_{pe} . Thereafter (above E_{pe}), pair production starts dominating (absorption process) which reduces the energy absorption buildup factor to a minimum value. The variation of energy absorption buildup factors with the penetration depth at 0.1 MeV, 1 MeV, 5 MeV, 10 MeV and 15 MeV is shown in Fig. 2. The buildup factor increases with the penetration depth.

The variation of specific absorbed fractions (ϕ) as a function of energy for silicon boron alloys are as shown in Fig. 3. It is observed that specific absorbed fractions increases up to the E_{pe} and then decreases. Here E_{pe} is the energy value at which the photo electric interaction coefficients matches with Compton interaction coefficients for a given value of effective atomic number (Z_{eff}). The variation of specific absorbed fractions with mean free path at various energies (0.05, 0.1, 0.5, 1.0, 5.0, 10 and 15 MeV) for different silicon boron alloys are as shown in Fig. 4. From this Figure it is clear that specific absorbed fractions value increases with

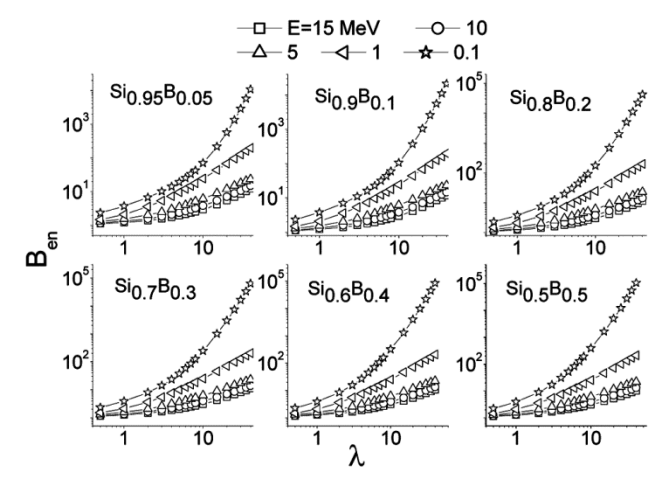


Fig. 2 – Variation of buildup factors (Ben) of different siliconboron alloys with mean free path at different energies (MeV). (Alloy A-Si $_{0.95}$ -B $_{0.05}$, Alloy B- Si $_{0.9}$ -B $_{0.1}$, Alloy C- Si $_{0.8}$ -B $_{0.2}$, Alloy D- Si $_{0.7}$ -B $_{0.3}$, Alloy E- Si $_{0.6}$ -B $_{0.4}$ and Alloy F- Si $_{0.5}$ -B $_{0.5}$.)

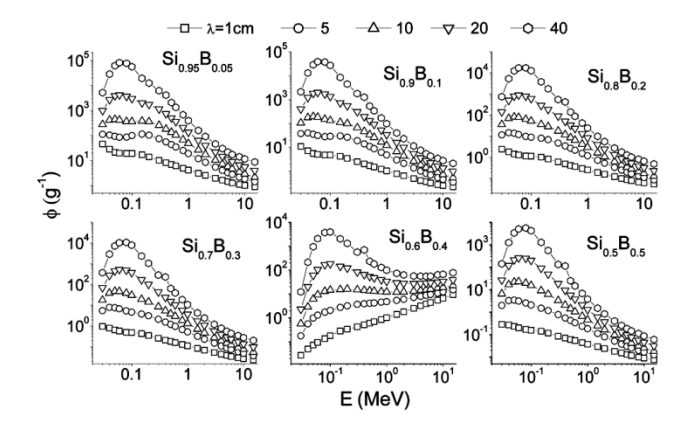


Fig. 3 – Variation of specific absorbed fractions (ϕ) (g⁻¹) as a function of energy (MeV). (Alloy A-Si_{0.95}-B_{0.05}, Alloy B- Si_{0.95}-B_{0.1}, Alloy C- Si_{0.8}-B_{0.2}, Alloy D- Si_{0.7}-B_{0.3}, Alloy E- Si_{0.6}-B_{0.4} and Alloy F- Si_{0.5}-B_{0.5})

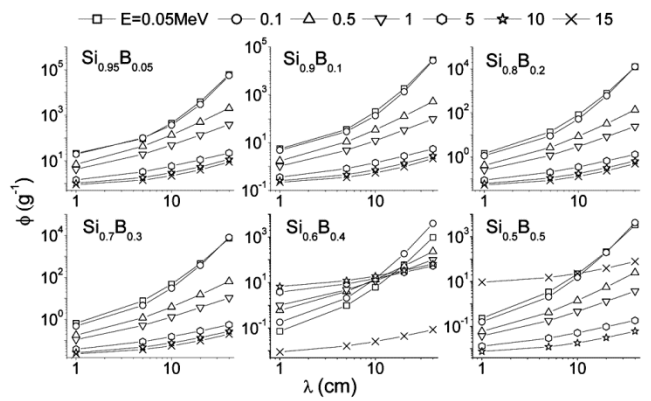


Fig. 4 – Variation of specific absorbed fractions (ϕ) (g⁻¹) as a function of mean free path (λ). (Alloy A-Si_{0.95}-B_{0.05}, Alloy B-Si_{0.9}-B_{0.1}, Alloy C-Si_{0.8}-B_{0.2}, Alloy D-Si_{0.7}-B_{0.3}, Alloy E-Si_{0.6}-B_{0.4} and Alloy F-Si_{0.5}-B_{0.5}.)

increase in the target distance. This is due to the reason that with increase in the target distance, scattering events in the medium increases.

Variation of effective electron density and specific absorbed fractions (φ) as a function effective atomic number for silicon boron alloys are as shown in Figs 5 and 6. The effective electron density and specific absorbed fractions for boron polymers is large in the low energy region (due to photo electric effect) and decreases progressively, there after increases and becomes constant for high energy (due to pair production). Figure 7 shows the comparison of specific absorbed fraction of energy among the studied silicon boron alloys at different energies for mean free paths corresponding to 20 and 40. From this comparison, it is clear that the silicon boron alloy $Si_{0.95}$ - $B_{0.05}$ is having larger value of specific absorbed fractions than the other studied alloys.

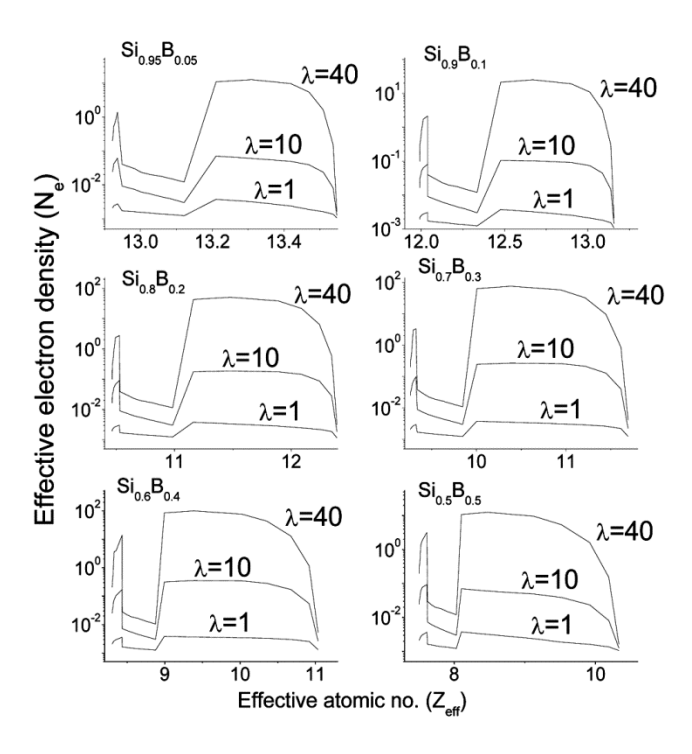


Fig. 5 – Variation of effective electron density as a function of effective atomic number. (Alloy A-Si $_{0.95}$ -B $_{0.05}$, Alloy B- Si $_{0.9}$ -B $_{0.1}$, Alloy C- Si $_{0.8}$ -B $_{0.2}$, Alloy D- Si $_{0.7}$ -B $_{0.3}$, Alloy E- Si $_{0.6}$ -B $_{0.4}$ and Alloy F- Si $_{0.5}$ -B $_{0.5}$.)

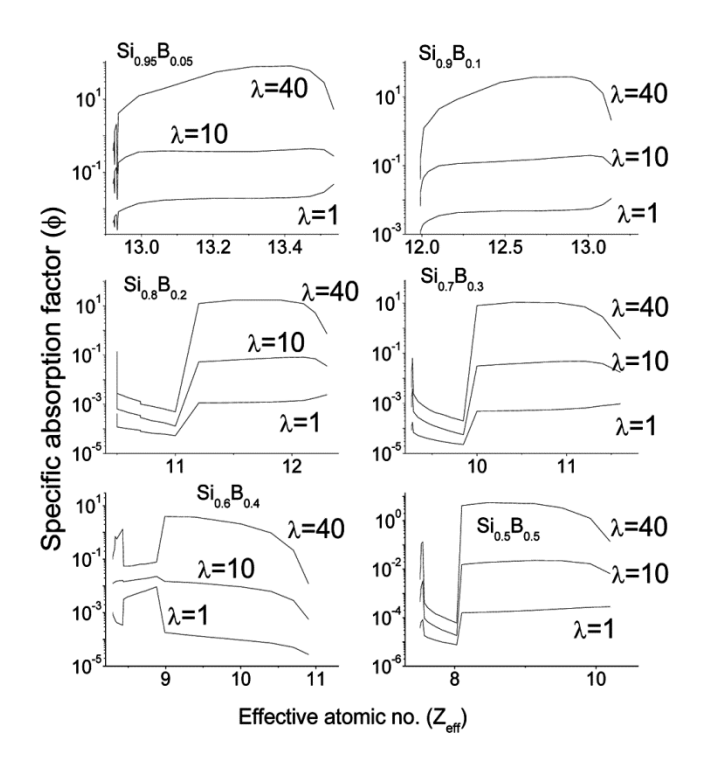


Fig. 6 – Variation of specific absorption factor as a function of effective atomic number. (Alloy A-Si $_{0.95}$ -B $_{0.05}$, Alloy B- Si $_{0.9}$ -B $_{0.1}$, Alloy C- Si $_{0.8}$ -B $_{0.2}$, Alloy D- Si $_{0.7}$ -B $_{0.3}$, Alloy E- Si $_{0.6}$ -B $_{0.4}$ and Alloy F- Si $_{0.5}$ -B $_{0.5}$.)

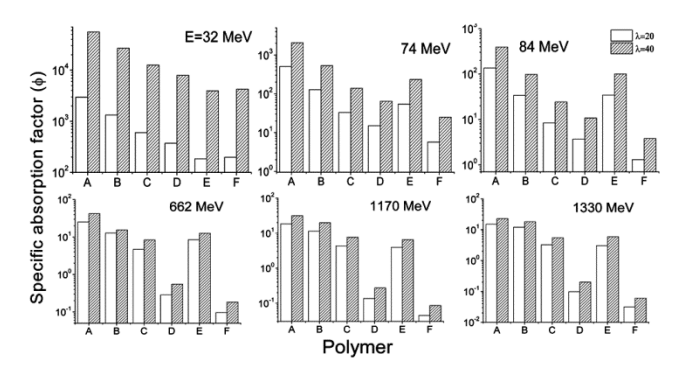


Fig.7 – Comparison of specific absorption factor with siliconboron alloys at different energies for mean free path corresponding to 20 and 40. (Alloy A-Si $_{0.95}$ -B $_{0.05}$, Alloy B- Si $_{0.9}$ -B $_{0.1}$, Alloy C- Si $_{0.8}$ -B $_{0.2}$, Alloy D- Si $_{0.7}$ -B $_{0.3}$, Alloy E- Si $_{0.6}$ -B $_{0.4}$ and Alloy F- Si $_{0.5}$ -B $_{0.5}$.).

4 Conclusions

We have studied the energy absorption buildup factors and specific absorbed fraction of energy for the silicon-boron alloys of different composition. From this study, we can suggest that the silicon boron alloy Si_{0.95}-B_{0.05} is the good absorber of X-ray, gamma and it can be used for shielding purpose.

References

- Manjunatha H C & Rudraswamy B, Radiat Meas, 47 (2012)
- 2 Manjunatha H C & Rudraswamy B, Radiat Phys Chem, 80 (2011) 14.
- 3 Manjunatha H C & Rudraswamy B, *J Radio Nucl Chem*, 294 (2012) 251.
- 4 Manjunatha H C & Rudraswamy B, Ann Nucl Energy, 38 (2011) 2271.
- 5 Manjunatha H C, Appl Rad Isotopes, 94 (2014) 282.
- Manjunatha H C & Rudraswamy B, *Phys Med*, 27 (2011) 188.
- 7 Harima Y, Nucl Sci Eng, 83 (1983) 299.
- 8 Shultis J K & Faw R E, *Health Phys*, 88 (2005) 587.
- 9 Chibani O, Med Phys, 32 (2005) 3688.
- 10 Tsiakalos M F, Radio Ther Oncol, 79 (2006) 131.
- 11 Takeuchi K & Pallas-Pl S P, Ship Res Inst, 42 (1973).
- 12 Yamano N, Minami K, Koyama K & Naito Y, Atom Energy Res Inst Rep Jpn, 1316 (1989).

- 13 Simmons G L, National Bureau of Standards Technical Note, (1973) 748.
- 14 Gopinath D V & Samthanam K, Nucl Sci Eng, 43 (1971) 186.
- 15 Hubbell J H, J Res, 67C (1963) 291.
- 16 Chilton A B, Eisenhauer C M & Simmons G L, Nucl Sci Eng, 73 (1980) 97.
- 17 Sakamoto Y, Tanaka S & Harima Y, Nucl Sci Eng, 100 (1988) 33.
- 18 Brar G S, Sandhu A K, Makhan S & Mudahar G S, *Radiat Phys Chem*, 44 (1994) 459.
- 19 Brar G S & Mudahar G S, Nucl Geophys, 9 (1995) 471.
- 20 American National Standard (ANS). (1991).
- 21 Harima Y, Sakamoto Y, Tanaka S & Kawai M, Nucl Sci Eng, 94 (1986) 24.
- 22 Shimizu A, Onda T & Sakamoto Y, J Nucl Sci Technol, 41 (2004) 413.
- 23 Singh P S, Tejbir S & Paramajeet K, Ann Nucl Energy, 35 (2008) 1093.
- 24 Sidhu G S, Singh P S & Mudahar G S, J Radiol Prot, 20 (2000) 53.
- 25 Manjunatha H C, Sathish K V & Seenappa L, *Radiat Phys Chem*, 165 (2019) 108414.
- 26 Torabian H, Pathak J P & Tiwari S N, Wear, 177 (1994) 47.
- 27 Singh M, Prasad B K, Mondal D P & Jha A K, Tribol Int, 34 (2001) 557.
- 28 Nakaidze, Gharibashvili, Antadze M & Tsagareishvili, J Solid State Chem, 177 (2004) 592.
- 29 Zhang S, Song J, Liao H & Liu Y, Materials, 12 (2019) 1100
- 30 Leif G, Guilbert N, Jensen K B & Leving H, Radiat Phys Chem, 71 (2004) 653.
- 31 Manjunatha H C & Rudraswamy B, *Radiat Meas*, 47 (2012) 364
- 32 Manjunatha H C & Rudraswamy B, Radiat Phys Chem, 80 (2011) 14.
- 33 Manjunatha H C & Rudraswamy B, *J Radio Nucl Chem*, 294 (2012) 251.
- 34 Manjunatha H C & Rudraswamy B, *Health Phys*, 104 (2013)
- 35 Suresh K C, Manjunatha H C & Rudraswamy B, Radiat Prot Dosimetry, 128 (2007) 294.
- 36 Manjunatha H C & Rudraswamy B, *Health Phys*, 100 (2011) 892
- 37 Manjunatha H C, *J Med Phys*, 39 (2014) 112.
- 38 American National Standard, ANSI/ANS 6.4.3. Oak Ridge, TN 37831-6362 (1991).

Specific absorbed fraction of energy and relative dose in Zinc alloys

K.V. Sathish^{1,3}, L. Seenappa¹, H.C. Manjunatha^{1*}, K.N. Sridhar², S. Alfred Cecil Raj³

¹Department of Physics, Government College for Women, Kolar-563101, Karnataka, India ³Department of Physics, Government First Grade College, Kolar-563101, Karnataka, India ³Department of Physics, St. Joseph's College, Trichy-620020 Tamil Nadu, India Corresponding authors: seenappakolar@gmail.com, manjunathhc@rediffmail.com

I. Introduction

Due to the desirable corrosion characteristics and biocompatibility, Zinc alloys can be used as the biodegradable metals. In the present work we have investigated the specific absorbed fraction (SAF) of energy, energy absorption buildup factors (ABFs) and relative dose (RD) in the energy range 15keV-15 MeV for zinc alloys of different composition such as alloy A (Cu 20 %, Ni 40 %, Zn 40 %), alloy B (Cu 30 %, Ni 35 %, Zn 35%), alloy C (Cu 40 %, Ni 30 %, Zn 30%), alloy D (Cu 50 %, Ni 25 %, Zn 25%), alloy E (Cu 60 %, Ni 20 %, Zn 20%) and alloy F (Cu 70 %, Ni 15 %, Zn 15%) up to the penetration depth (PD) of 40 mfp using GP fitting method. It is found that both SAF and RD are larger for alloy F (Cu 70 %, Ni 15 %, Zn 15%) than the other studied zinc alloys. Hence, we can conclude that the alloy F (Cu 70 %, Ni 15 %, Zn 15%) is a good absorber of X-rays, neutrons and gamma among the investigated zinc alloys. This work finds its usefulness in the radiation dosimetry and shielding of radiation.

On entering a medium, X-rays and gamma rays undergo scattering and the energy gets degraded, due to which secondary radiation are produced. secondary radiations can be calculated using buildup factor. Manjunatha and Rudraswamy [1-2] evaluated the photon relative dose distribution and buildup factors in various parts of teeth. Manjunatha and Rudraswamy [3] studied energy absorption buildup factors as well as exposure buildup factors in hydroxyapatite. Previous researchers used exposure buildup factors for the investigation of secondary radiation dose like bremsstrahlung [4-5]. By injecting radioactive seeds into the patient's body, cancerous tumors can be destroyed in brachytherapy [6-7]. Cancerous tumors can be destroyed by multiplying the contribution of uncollided photons with the energy absorption buildup factors [8-9]. For designing the shielding of radiation, previous researchers gave the data for buildup factors [10-14]. In the computations of radiation dose absorbed by the cancer cells it is necessary to assume photon buildup factors.

To estimate the absorbed dose in certain organs using photons, the interaction of the primary photons in the target medium is not much accurate. Hence specific absorbed fraction of energy is required for the accurate estimation of absorbed dose. Specific absorbed fraction of energy is defined as the ratio of the energy absorbed

by the target to the energy emitted by the source. In the present work, we have estimated the energy corresponds to SAF and RD up to the penetration depth of 40 mfp in energy range 15keV–15 MeV in zinc alloys of different composition.

I. Theory

II.1. Specific absorbed fraction of energy

The procedure for the determination of the specific absorbed fraction of energy is explained in detail in our previous work [15]. It is given by the expression

$$\Phi(x) = \frac{\exp(-\mu x)\mu_{en}B_{en}}{4\pi r^2\rho} \tag{1}$$

II.2. Relative dose

The procedure for the determination of the Relative dose is explained in detail in our previous work [1]. It is given by the expression

$$\frac{D_r}{D_0} = \frac{B}{r}e^{-\mu r} \tag{2}$$

III. Results and discussions

For the studied zinc alloys of different composition, the comparison of SAF with energy is as shown in figure 1. It is observed that among the studied zinc alloys, SAF is larger for the alloy of composition (Cu 70 %, Ni 15 %, Zn 15%). The comparison of RD with energy is as shown in figure 2. It is found that among the studied zinc alloys, RD is larger for the alloy of composition (Cu 70 %, Ni 15 %, Zn 15%). The variation of SAF and RD with energy for the studied alloy of composition (Cu 70 %, Ni 15 %, Zn 15%) is shown in figure 3. It is found that SAF and RD rises up to the E_{pe} and then decreases. SAF and RD is maximum at an energy of 0.5 MeV. E_{pe} is the value of energy at which the Compton interaction coefficients matches with photo electric interaction coefficients

IV. Conclusion

We have investigated the EABFs, SAF of energy and RD for zinc alloys. From this study, it is clear that for the alloy of composition (Cu 70 %, Ni 15 %, Zn 15%), the SAF of energy and RD is maximum among all the studied zinc alloys. From this study we can suggest that the zinc alloy of composition (Cu 70 %, Ni 15 %, Zn 15%) can be used as a good absorber of gamma rays, neutrons and X-rays

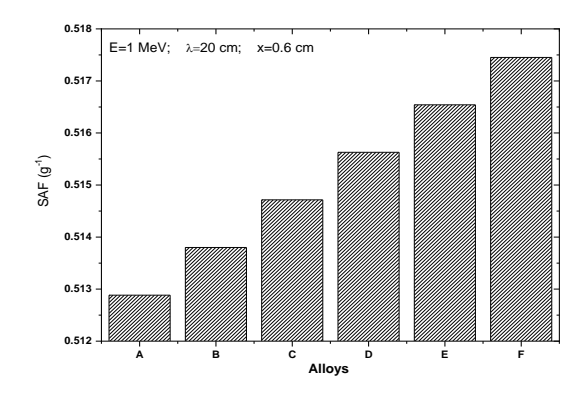


Fig 1. Comparison of SAF for the studied alloys at a particular energy

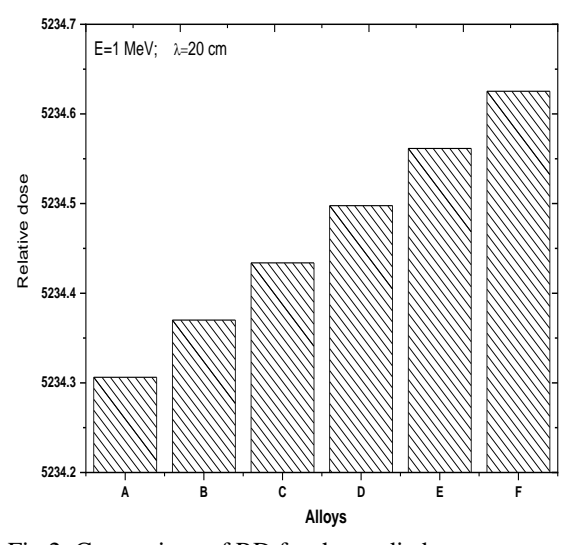


Fig 2. Comparison of RD for the studied alloys at a particular energy

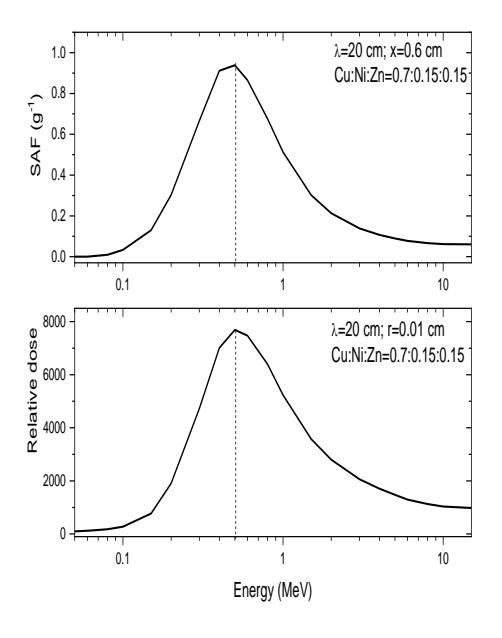


Fig 3. Variation of SAF and RD with energy for the studied alloy of composition (Cu 70 %, Ni 15 %, Zn 15%)

References

[1] H.C. Manjunatha and B. Rudraswamy, Rad. Phy. Chem, 80 (2011) 14-21.

[2] H.C. Manjunatha and B. Rudraswamy, J. Radio. Nucl. Chem, 294 (2012) 251-260.

[3] H.C. Manjunatha and B. Rudraswamy, Rad. Meas. 47 (2012) 364-370.

[4] H.C. Manjunatha, Appl. Rad. Isotopes, 94 (2014) 282-293.

[5] H.C. Manjunatha and B. Rudraswamy, Phys. Med, 27 (2011) 188-193.

[6] O. Chibani, Med Phys, 32 (2005) 3688-98.

[7] M.F. Tsiakalos, Radio. Ther. Oncol. 79 (2006) 131-138

[8] Y. Harima, Nucl. Sci. Eng. 83 (1983) 299-309.

[9] J.K. Shultis and R.E. Faw, Health Phys 88 (2005) 587-612

[10] J.H. Hubbell, J. Res. 67C (1963) 291-306.

[11] A.B. Chilton, C.M. Eisenhauer and G.L. Simmons, Nucl. Sci. Eng. 73 (1980) 97-107.

[12] Y. Sakamoto, S. Tanaka and Y. Harima, Nucl. Sci. Eng. 100 (1988) 33-42.

[13] G.S. Brar, A.K. Sandhu, S. Makhan and G.S.

Mudahar, Rad. Phys. Chem. 44 (1994) 459-465.

[14] G.S. Brar and G.S. Mudahar, Nucl. Geophys. 9 (1995)471-480.

[15] H.C. Manjunatha and B. Rudraswamy, Annals of Nuclear Energy 38(10) ([2011) 2271-2282 ELSEVIER

Contents lists available at ScienceDirect

Materials Today: Proceedings

journal homepage: www.elsevier.com/locate/matpr



Radiation shielding properties of gallium alloys

K.V. Sathish ^{a,d}, L. Seenappa ^{a,*}, H.C. Manjunatha ^a, Y.S. Vidya ^b, K.N. Sridhar ^c, S. Alfred Cecil Raj ^d

- ^a Department of Physics, Government College for Women, Kolar-563101, Karnataka, India
- ^b Department of Physics, Lal Bahadur Shastri Government First Grade College, RT Nagar, Bangalore–560032, Karnataka, India
- ^c Department of Physics, Government First Grade College, Kolar-563101, Karnataka, India
- ^d Department of Physics, St. Joseph's College, Trichy-620020, Tamil Nadu, India

ARTICLE INFO

Article history:

Available online 12 March 2022

Keywords: Interaction Scattering Radiation Galfenol Penetration

ABSTRACT

Consideration of the photon interaction in the target medium is not sufficient for the estimation of absorbed dose in the different organs from a source of photons. For the accurate absorbed dose calculation specific absorbed fraction of energy is required. It is defined as the ratio of the energy absorbed by the target to the energy emitted by the source. The calculation of specific absorbed fraction of energy depends on the buildup factor values and the interaction of secondary electrons. X-rays and gamma rays undergo scattering on entering a medium, thus the energy gets degraded, due to which secondary radiation are produced. These secondary radiations can be calculated using buildup factor. Gallium alloys are less toxic and cost effective material compared to lead. Due to the importance of Gallium alloys in radiation shielding, the study of an interaction of X-rays and gamma radiation in these alloys becomes important

In the present work we have investigated the energy exposure buildup factors (EBF) and specific absorbed fraction (SAF) of energy for some gallium alloys such as Gallium alloy [Al-50%, Ga-50%], Galfenol [Fe-30%, Ga-70%] and Galinstan [Ga-68.5%, In-21.5%, Sn-10%]. With the increase in the penetration depth, the value of buildup factors increases. It is observed that the values of exposure buildup factors and Specific absorbed fraction of energy are larger for the gallium alloy Galinstan than the other studied gallium alloys. From this work it is clear that among the studied gallium alloys, in Galinstan absorption of X-rays and gamma radiations more compared to other studied alloys. Hence, we can conclude that the gallium alloy Galinstan is a good absorber of X-rays and gamma radiation among the studied gallium alloys. This work is useful in the shielding of radiation.

Copyright © 2022 Elsevier Ltd. All rights reserved.

Selection and peer-review under responsibility of the scientific committee of the International Symposium on Materials of the Millennium: Emerging Trends and Future Prospects.

1. Introduction:

Consideration of the photon interaction in the target medium is not sufficient for the estimation of absorbed dose in the different organs from a source of photons. For the accurate absorbed dose calculation specific absorbed fraction of energy is required. It is defined as the ratio of the energy absorbed by the target to the energy emitted by the source. The calculation of specific absorbed fraction of energy depends on the buildup factor values and the interaction of secondary electrons. X-rays and gamma rays undergo scattering on entering a medium, thus the energy gets

degraded, due to which secondary radiation are produced. These secondary radiations can be calculated using buildup factor.

Manjunatha and Rudraswamy [1–2] evaluated the photon relative dose distribution and buildup factors in various parts of teeth. The Lambert Beer law determines the strength of X-ray / gamma ray beam passing through a medium. A corrective factor known as the "build up factor" is employed to apply the law. It gives the information on the quantity of secondary radiations produced in the medium and energy deposited/absorbed in the medium. Previous researchers studied the secondary radiation dose like bremsstrahlung used exposure buildup factors [3–4]. Earlier workers [5] studied the biological samples to compute their specific absorbed fraction of energy. A number of researchers gave the data for buildup factor for designing the shielding of radiation and other

E-mail address: seenappakolar@gmail.com (L. Seenappa).

^{*} Corresponding author.

such applications [6–10]. Sidhu et al., [11] investigated how exposure buildup factors varies with the energy of incident photon and effective atomic number ($Z_{\rm eff}$) in biological samples.

Shimizu et al., [12] observed small discrepancies for elements of lower atomic numbers up to 10 mfp when the buildup factors obtained by three methods viz., Monte Carlo method, invariant embedding, and GP fitting are compared. Singh et al., [13] investigated how exposure buildup factors varies with the energy of incident photon. The present work focusses on the estimation of buildup factor as explained by Manjunatha et al., [14] and specific

absorbed fractions in some gallium alloys such as Gallium alloy [Al-50%, Ga-50%], Galfenol [Fe-30% , Ga-70%] and Galinstan [Ga-68.5% , In-21.5%, Sn-10%].

2. Material and Methods:

In this work, we have evaluated the energy absorption build-up factor (B_{en}) using GP fitting method [15–22]. WinXCom computer program [18] gives mass attenuation coefficients values, from which we can evaluate Z_{eff} , from the following equation:

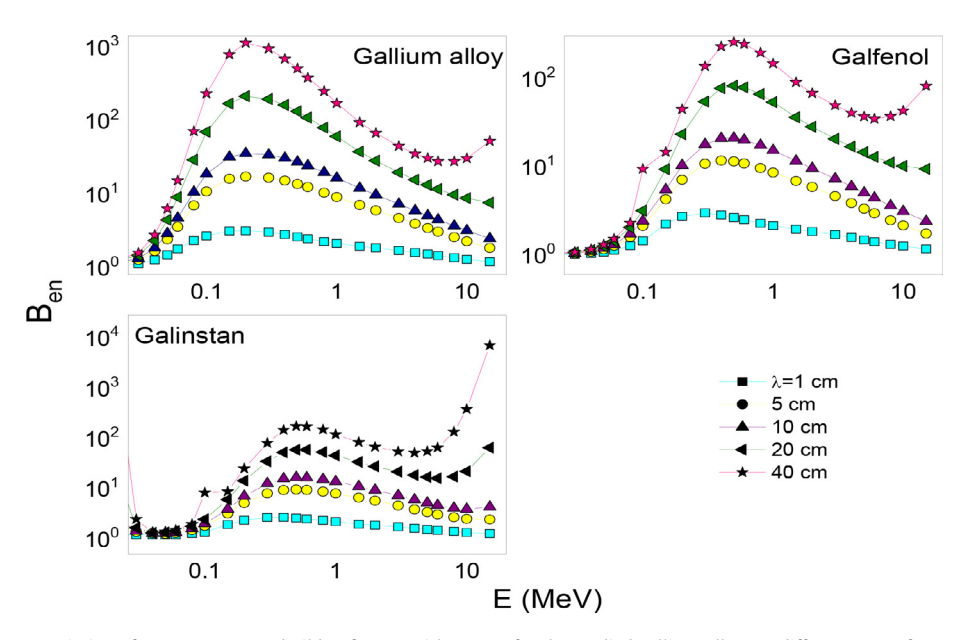


Fig. 1. Variation of energy exposure buildup factors with energy for the studied gallium alloys at different mean free paths.

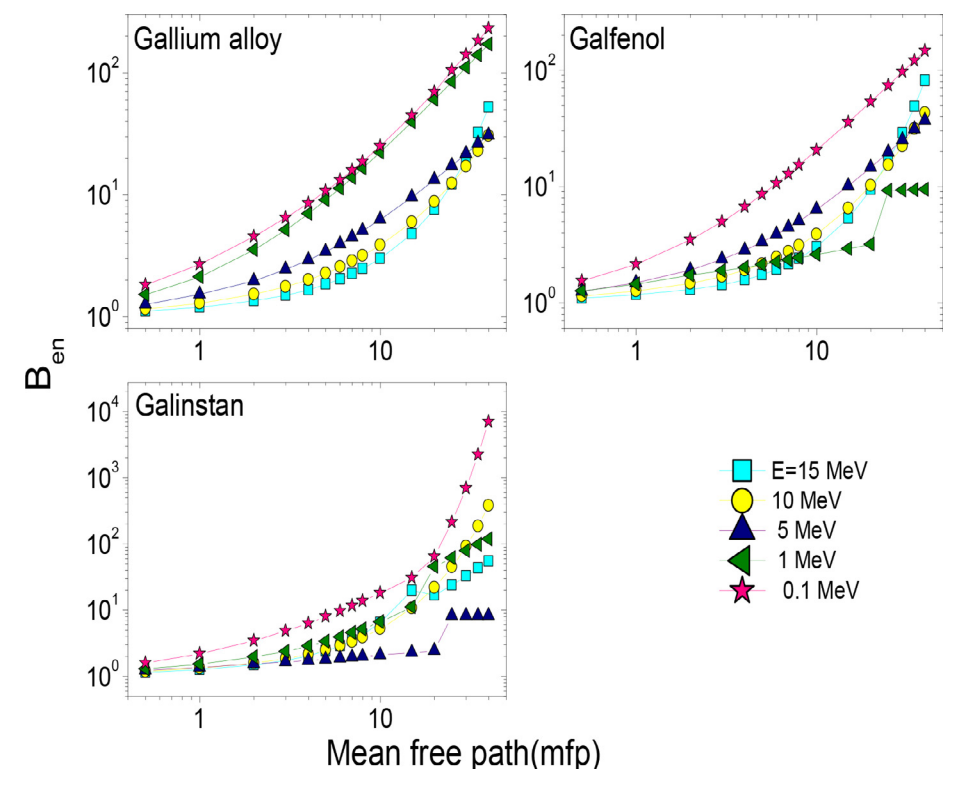


Fig. 2. Variation of energy exposure buildup factors with mean free path for the studied gallium alloys at different energies.

$$Z_{eff} = \frac{\frac{\frac{1}{N}\binom{\mu}{\rho}}{\sum n_i} n_i A_i}{\frac{1}{N} \sum \left(\frac{f_i A_i}{Z_i}\right) \left(\frac{\mu}{\rho}\right)} \tag{1}$$

Where (μ/ρ) is the mass attenuation coefficient, n_i is the number of atoms of ith element in a given molecule, A_i is the atomic weight of element i, N is the Avogadro's number. From the standard data

available in literature [23], GP fitting parameters (a, b, c, d & X_k) are provided for element adjacent to $Z_{\rm eff}$. The evaluated G-P fitting parameters were then used to estimate the energy absorption buildup factor up to a depth of 40 mfp in the energy range 15 keV-15 MeV using G-P fitting relations [16–22]

$$B(X,E) = \frac{1-b}{1-K}(K^{X}-1) + 1 \text{ for } K \neq 1$$
 (2)

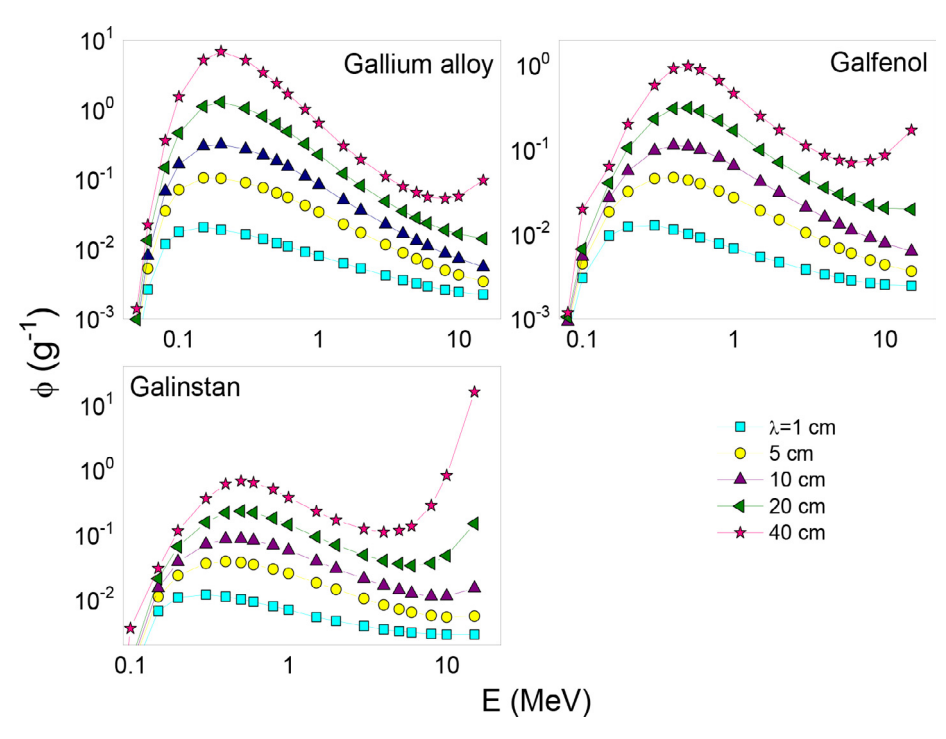


Fig. 3. Variation of SAF with energy for the studied gallium alloys at different mean free paths.

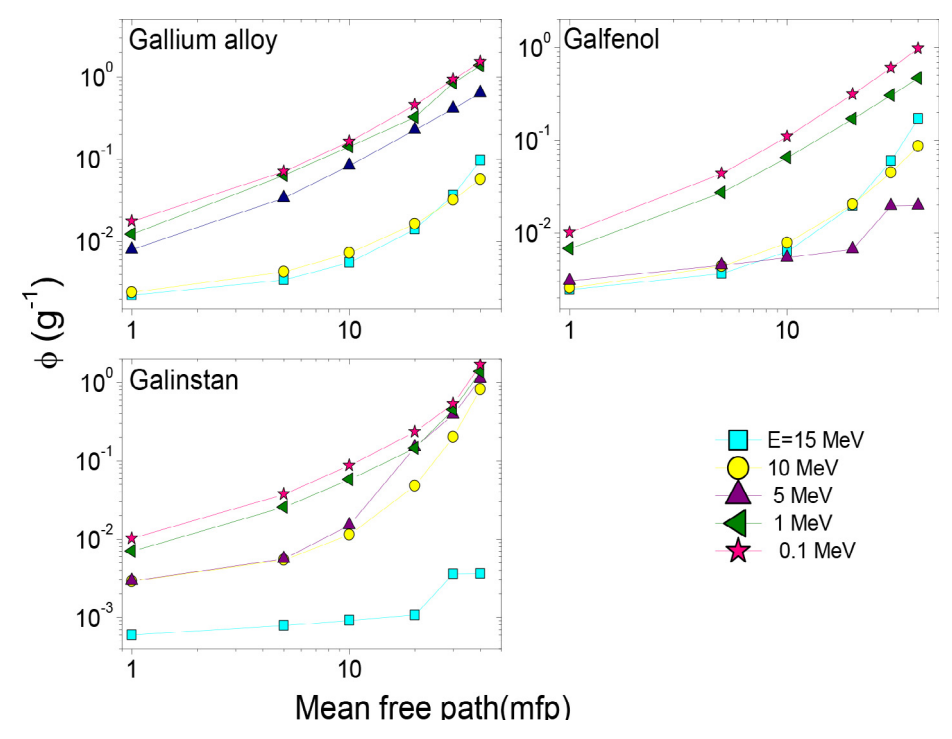


Fig. 4. Variation of SAF with mean free path for the studied gallium alloys at different energies.

$$B(X, E) = 1 - X(1 - b)$$
 for $K = 1$ (3)

$$K(X,E) = \frac{\left[\tanh\left(\frac{X}{X_K} - 2\right) - \tanh(-2)\right]d}{1 - \tanh(-2)} + CX^a \text{ For penetration depth } (X) \le 40\text{mfp}$$
(4)

Where b is the value of buildup factor at 1mfp & X is the distance between source & detector for the medium in mfps. a, b, c, d & X_k are estimated using G-P fitting parameters which depends on source energy & attenuating medium and K(E, X) is the dose multiplication factor.

To estimate the energy corresponding to or a given pair of organ-source & organ-target at a given energy of initial photon three different techniques are employed: (i) SAF is estimated from source to target using Monte Carlo computer program and this value is used to estimate target to source, (ii) SAF is investigated from the target to source using Monte Carlo radiation transport computer program and (iii) SAF is estimated from the target to source with the point source kernel method. In this method, the energy corresponding to SAF at distance × from the point source of mono energetic photon emitter is given by

$$\Phi(x) = \frac{\exp(-\mu x)\mu_{en}B_{en}}{4\pi r^2 \rho} \tag{5}$$

Here μ_{en} is photon linear absorption coefficient at a given energy, μ is photon linear attenuation coefficient at a given energy, B_{en} is the build-up factor corresponding to energy absorption, ρ is density of the medium. To evaluate specific absorbed fraction, estimated energy absorption build up factors up to a penetration depth of 40 mfp & distance up to 10 mm are required.

3. Results and Discussion:

The variation of energy exposure buildup factors (EBF) with energy for the studied gallium alloys at different mean free paths is shown in Fig. 1. It is found that EBF increases up to the E_{pe} and then decreases. Here E_{pe} is the energy value at which the photo electric interaction coefficients match with Compton interaction coefficients for a given value of effective atomic number (Z_{eff}) . With the increase in mean free path, deposition of energy in the medium

increases. Hence, energy absorption buildup factor increases with mean free path. Among the studied gallium alloys, galinstan alloy is found have larger energy absorption buildup factor compared to that of other two alloys.

The variation of EBF with mean free path (mfp) for the studied gallium alloys at different energies is shown in Fig. 2. From this figure it is clear that EBF values increases with increase in the target distance. This is due to the reason that with increase in the target distance, scattering events in the medium increases. EBF values increases up to the $E_{\rm pe}$ and then decreases. Here $E_{\rm pe}$ is the energy value at which the photo electric interaction coefficients match with Compton interaction coefficients for a given value of effective atomic number ($Z_{\rm eff}$). Among the studied alloys EBF is larger for Galinstan for the given energies.

Variation of specific absorbed fractions (SAF) with energy at different mean free paths is shown in Fig. 3. SAF is large for larger mean free paths, with the increase in mean free paths, EBF increases and hence SAF also increases. Variation of specific absorbed fractions (SAF) with mean free at different energies for

Table 1Comparison of experimental values with that produced by Wincom program for Arsenic oxide.

As203				
E keV	(μ/ρ) expt	(μ/ρ)winXcom		
5.411	222.17 ± 3.99	181.9714		
5.895	175.72 ± 3.17	140.9716		
6.404	140.40 ± 2.54	117.3126		
6.925	113.64 ± 2.05	98.5678		
7.472	92.49 ± 2.78	79.121		
8.041	76.19 ± 1.38	59.604		
8.631	62.28 ± 1.13	51.3198		
9.572	45.76 ± 0.83	38.7532		
9.876	43.20 ± 0.82	34.6111		
10.986	32.33 ± 0.59	26.2567		
11.21	30.64 ± 0.58	24.8526		
11.907	191.42 ± 3.34	136.1275		
12.502	158.71 ± 2.86	124.2628		
13.299	135.59 ± 2.46	108.3263		
14.142	112.48 ± 2.03	91.6175		
140,933	100.63 ± 1.82	76.3128		
15.859	85.28 ± 1.54	67.7478		
16.766	74.17 ± 1.35	61.0081		

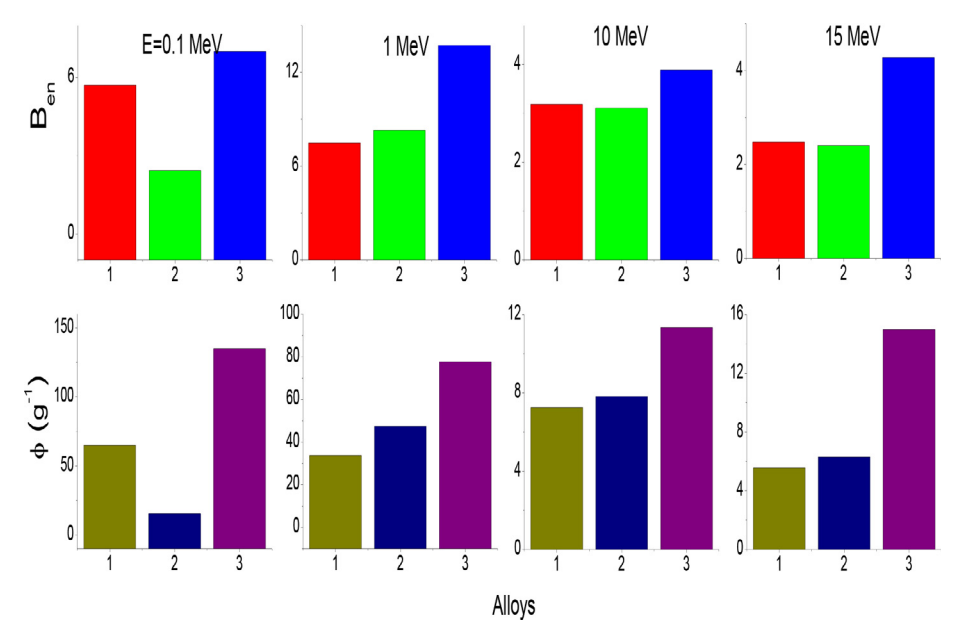


Fig. 5. Comparison of EBF and SAF among the studied alloys for 10 mfp (1- Gallium alloy, 2- Galfenol and 3- Galinstan) at different energies.

the studied gallium alloys is shown in Fig. 4. It is observed that SAF is larger for smaller energies.

Comparison of EBF and SAF among the studied gallium alloys at different energies is shown in Fig. 5. From this figure it is found that the values of EBF and SAF is large for Galinstan [Ga-68.5%, In-21.5%, Sn-10%] among the studied gallium alloys. On comparison of EBF and SAF among the studied gallium alloys it is found that the alloy Galinstan is having larger values of EBF and SAF than that of others. This may be due to the fact that the effective atomic number and mass attenuation coefficient are larger for Galinstan alloy than that of others.

To validate the present work we have evaluated the mass attenuation coefficient for Arsenic oxide for which experimental values are available. The comparison of values produced by the present work with of experiments is shown in Table 1.. From this table it is clear that present work is close to the experiments.

4. Conclusion

We have evaluated the energy absorption build up factors and specific absorbed fraction of energy in some gallium alloys such as Gallium alloy [Al-50%, Ga-50%], Galfenol [Fe-30%, Ga-70%] and Galinstan [Ga-68.5%, In-21.5%, Sn-10%]. From the comparison of EBF and SAF among the studied gallium alloys at different energies it is clear that for the gallium alloy Galinstan [Ga-68.5%, In-21.5%, Sn-10%] the EBF and SAF is maximum for all energies among all the studied gallium alloys. From this study we can suggest that the gallium alloy Galinstan [Ga-68.5%, In-21.5%, Sn-10%] can be used as a good absorber of X-rays and gamma rays.

Declaration of Competing Interest

The authors declare that they have no known competing financial interests or personal relationships that could have appeared to influence the work reported in this paper.

Funding

The authors did not receive support from any organization for the submitted work.

Availability of data and material

Yes.

Code availability

The authors did not use any codes for the submitted work.

Authors' contributions

The corresponding author state that all the authors are part of the work and equally contributed for the manuscript in the present form.

Ethics approval

We abide the rules and guidelines of ethics.

Consent to participate

All listed authors have approved the manuscript before submission, including the names and order of authors.

Consent for publication

We are submitting the manuscript entitled "Radiation shielding properties of Gallium alloys" for kind publication in your esteem Journal Kindly acknowledge the receipt of the manuscript.

References

- [1] H.C. Manjunatha, B. Rudraswamy, Computation of exposure build-up factors in teeth, Rad. Phy. Chem 80 (2011) 14–21.
- [2] H.C. Manjunatha, B. Rudraswamy, Energy absorption build-up factors in teeth, J. Radio. Nucl. Chem 294 (2012) 251–260.
- [3] H.C. Manjunatha, A dosimetric study of Beta induced bremsstrahlung in bone, Appl. Rad. Isotopes 94 (2014) 282–293.
- [4] H.C. Manjunatha, B. Rudraswamy, Beta induced Bremsstrahlung exposure in DNA and RNA, Phys. Med 27 (2011) 188–193.
- [5] H.C. Manjunatha, B. Rudraswamy, A study of thickness and penetration depth dependence of specific absorbed fraction of energy in bone, Ann. Nucl. Energy 38 (2011) 2271–2282.
- [6] J.H. Hubbell, A power series buildup factor formulation, J. Res. 67C (1963) 291–
- [7] A.B. Chilton, C.M. Eisenhauer, G.L. Simmons, Photon Point Source Buildup Factors for Air, Water and Iron, Nucl. Sci. Eng. 73 (1980) 97–107.
- [8] Y. Sakamoto, S. Tanaka, Y. Harima, Nucl. Sci. Eng. 100 (1988) 33-42.
- [9] G.S. Brar, A.K. Sandhu, S. Makhan, G.S. Mudahar, Interpolation of gamma-ray buildup factors for point isotropic source with respect to atomic number, Rad. Phys. Chem. 44 (1994) 459–465.
- [10] G.S. Brar, G.S. Mudahar, Energy and effective atomic number dependence of the exposure buildup factor in soils—a study, Nucl. Geophys. 9 (1995) 471– 480
- [11] G.S. Sidhu, P.S. Singh, G.S. Mudahar, A study of energy and effective atomic number dependence of the exposure build-up factors in biological samples, J. Radiol. Prot. 20 (2000) 53–68.
- [12] A. Shimizu, T. Onda, Y. Sakamoto, Calculation of gamma-ray buildup factors up to depths of 100 mfp by the method of invariant embedding, (III) generation of an improved data set, J. Nucl. Sci. Technol. 41 (2004) 413–424.
- [13] P.S. Singh, S. Tejbir, K. Paramajeet, Variation of energy absorption buildup factors with incident photon energy and penetration depth for some commonly used solvents, Ann. Nucl. Energy. 35 (2008) 1093–1097.
- [14] H.C. Manjunatha, K.V. Sathish, L. Seenappa, et al., A study of x-ray, gamma and neutron shielding parameters in Si-alloys, Rad. Phy. and Chem. 165 (2019).
- [15] H.C. Manjunatha, B. Rudraswamy, Energy absorption build-up factors in teeth, J. Radio. Nucl. Chem. 294 (2012) 251–260.
- [16] K.C. Suresh, H.C. Manjunatha, B. Rudraswamy, Study of Zeff for DNA, RNA and retina by numerical methods, Rad. Prot. Dosimetry 128 (2007) 294–298.
- [17] H.C. Manjunatha, A study of photon interaction parameters in lung tissue substitutes, J. Med. Phys. 39 (2014) 112–115.
- [18] N. Gerward Leif, K.B Jensen Guilbert, H. Leving, WinXCom a program for calculating x-ray attenuation coefficients, Rad. Phy. Chem. 71 (2004) 653–654.
- [19] H.C. Manjunatha, B. Rudraswamy, Energy absorption and exposure build-up factors in hydroxyapatite, Rad. Meas. 47 (2012) 364–370.
- [20] H.C. Manjunatha, B. Rudraswamy, Computation of CT-number and Zeff in Teeth, Health Phys 100 (2011) S92–S99.
- [21] H.C. Manjunatha, B. Rudraswamy, Computation of exposure build-up factors in teeth, Rad. Phys. Chem. 80 (2011) 14–21.
- [22] H.C. Manjunatha, B. Rudraswamy, Study of effective atomic number and electron density for tissues from human organs in the energy range of 1 keV– 100 GeV. Health Phys. 104 (2013) 158–162.
- [23] American National Standard. ANSI/ANS 6.4.3. Oak Ridge, TN 37831-6362 (1991).

ARTICLE IN PRESS

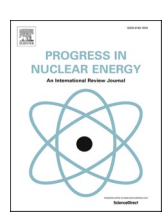
Progress in Nuclear Energy xxx (xxxx) xxx



Contents lists available at ScienceDirect

Progress in Nuclear Energy

journal homepage: www.elsevier.com/locate/pnucene



Investigation on shielding properties of lead based alloys

K.V. Sathish ^{a,b}, H.C. Manjunatha ^{a,**}, Y.S. Vidya ^{c,*}, B.M. Sankarshan ^d, P.S. Damodara Gupta ^a, L. Seenappa ^a, K.N. Sridhar ^a, Alfred Cecil Raj ^b

- ^a Department of Physics, Government College for women, Kolar, 563101, Karnataka, India
- ^b Department of Physics, St. Joseph's college, Thiruchirapalli, 620002, Tamil Nadu, India
- ^c Department of Physics, Lal Bahadur Shastri Government First Grade College, RT Nagar, Bangalore, 560032, Karnataka, India
- ^d Department of Physics, The National institute of Engineering, Mysuru, 570008, Karnataka, India

ARTICLE INFO

Keywords: Gamma / X-ray shielding parameters Mechanical properties Relative dose Lead based alloys

ABSTRACT

The current study involves the X-ray/gamma and neutron shielding properties of selected lead based binary/ tertiary/quaternary alloys such as Foundary type, Lino type, Molybdochalkos, Mono type, Stereo type, Turne type, Type metal and Woods metal. The X-ray/gamma and neutron shielding parameters are studied in detail for all the selected alloys. Among all the selected alloys, Molybdochalkos shows larger values of mass attenuation coefficient (MAC), absorption buildup factor (ABF), Z_{eff} , N_e , specific absorbed fractions of energy (SAFE), radiation protection efficiency (RPE), kinetic energy released in matter (KERMA) and relative dose. Furthermore, neutron total interaction cross section (σ_{tot}) and absorption cross section (σ_{tot}) values are also larger. This clearly indicates that Molybdochalkos binary alloy is the good absorber of both X-ray/gamma and neutrons.

1. Introduction

In nuclear experiments and radiation related experiments, shielding is one of the most important aspects to be taken care of. In this regard there have been many materials which are being looked into. Amongst which there have been usage of materials which contain heavy elements occupying the front-line. The materials used for radiation shielding vary from flexible materials Intom et al. (2020); Turhan et al. (2020) to that of glasses Sayved et al. (2020); Sopapan et al. (2020). Traditionally elements with higher atomic numbers and concrete were used for shielding. There have been investigations on concrete with different amounts of lead Rezaei-Ochbelagh and Azimkhani (2012). Lead in different proportions with other materials including that of other metals is an important candidate for radiation shielding. Many studies have been conducted to find out the alternatives such as alloys, polymers, glasses etc., to improve the shielding efficiency. Among the alternative shielding materials, alloys/binary-alloys/tertiary alloys have gained the major importance in literature Agar et al. (2019); Akman et al. (2019).

The X-ray/gamma and neutron shielding effectiveness can be examined on the basis of certain parameters such as MAC (mass attenuation coefficient), penetration depth (mean free path), HVT (half value thickness), TVT (tenth value thickness), Z_{eff} (effective atomic number),

Ne (effective electron number) and EBF (exposure buildup factor), coherent neutron scattering length, coherent neutron scattering cross section, incoherent neutron scattering cross sections, total neutron scattering cross section, neutron absorption cross sections etc. Enormous work has been reported on shielding parameters of alloys Al-Buriahi and Tonguc (2020); Alavian and Tavakoli-Anbaran (2020); Babu et al. (1984); Islam et al. (2020); Manjunatha (2017); Manjunatha et al. (2016a); Manjunatha and Rudraswamy (2006); Manjunatha et al. (2019a,b, 2018a,b); Nagaraja et al. (2019); Rudraswamy et al. (2010); Seenappa et al. (2017, 2018a,b); Shafka et al. (2015); Shah and Wasim (2020); Yılmaz et al. (2011). Limkitjaroenporn et al., Limkitjaroenporn et al. (2013) determined the MAC and $Z_{\it eff}$ for Inconel 738 alloy for different energies obtained from Compton scattering. Singh et al., Singh and Badiger (2013) computed the MAC, Zeff and effective electron density of carbon steel and stainless steels by using the WinXcom program. Seven et al., Seven et al. (2004) measured the total MAC for Co, Cu, Ni elements and Co-Cu, Co-Cu-Ni alloys at different energies using transmission arrangement. However, lead and lead based alloys are conventional materials used as a primary shielding material type due to superior attenuation properties against ionizing X-rays/gamma, its high atomic number and density. Combination of one or two other elements with lead, improves certain advanced properties such as hardness,

E-mail addresses: manjunathhc@rediffmail.com (H.C. Manjunatha), vidyays.phy@gmail.com (Y.S. Vidya).

https://doi.org/10.1016/j.pnucene.2021.103788

Received 10 February 2021; Received in revised form 28 April 2021; Accepted 17 May 2021 0149-1970/© 2021 Elsevier Ltd. All rights reserved.

^{*} Corresponding author.

^{**} Corresponding author.

K.V. Sathish et al.

corrosion resistance, tensile strength etc. Agar et al. (2019). Kaur et al., Kaur et al. (2016, 2017) studied the scope of Pb-Sn and Pb-Zn binary alloy in gamma ray shielding. Further the physical properties and shielding parameters were discussed in detail. Singh et al., Singh et al. (2015) computed various photon interaction parameters for different compositions of Cu-Pb binary alloys in the wide energy regime of 1 keV-100 GeV. Tekin and Kilicoglu investigated the gamma-ray and neutron shielding properties of different type of Ga additive in Pd-Mn binary alloys Tekin and Kilicoglu (2020). Issa et al., Issa et al. (2020) utilized MCNPX code, XCOM and XMuDat to compute the nuclear radiation parameters of fabricated five different glasses based on PbO. In addition to nuclear radiation parameters, numerous physical and mechanical parameters were discussed in detail. Mahmoud et al. (2018) fabricated, characterized and studied the gamma ray shielding parameters of nano and micro lead oxide dispersed high density polyethylene composites. As lead based alloys are easily available and low in cost, many research workers carried out extensive work in this area by exploring the gamma/X-ray radiation shielding parameters El-Toony et al. (2020); Kaur et al. (2019); Manohara et al. (2011); Zhang et al. (2020).

The investigations of mechanical properties of the alloys place a very important role to reveal their possible use for alloy design through a hardness test and a tensile test Kobayashi et al. (1995). The alloys are easy to process on relatively unsophisticated machinery because of their low melting points and relatively high mechanical properties soon after casting Prengaman (2009). Alloys posses good mechanical properties Kobayashi et al. (1995). Studies on mechanical properties are also important when these are used for the purpose of shielding Prengaman (2009); Tekumalla et al. (2015).

Present work investigates the X-ray/gamma, neutron shielding properties of lead based alloys such as Foundary type $(Sn_{0.15}\text{-}Sb_{0.23}\text{-}Pb_{0.62})$ (FD), Lino type $(Sn_{0.04}\text{-}Sb_{0.16}\text{-}Pb_{0.8})$ (LT), Molybdochalkos $(Cu_{0.1}\text{-}Pb_{0.9})$ (MC), Mono type $(Sn_{0.09}\text{-}Sb_{0.19}\text{-}Pb_{0.72})$ (MT), Stereo type $(Sn_{0.06}\text{-}Sb_{0.14}\text{-}Pb_{0.8})$ (ST), Turne type $(Sn_{0.2}\text{-}Pb_{0.8})$ (TU), Typemetal $(Sn_{0.03}\text{-}Sb_{0.11}\text{-}Pb_{0.86})$ (TM) and Woods metal $(Cd_{0.1}\text{-}Sn_{0.133}\text{-}Pb_{0.267}\text{-}Bi_{0.5})$ (WM) which are less toxic than the lead. Hence we felt it worthwhile to study these lead based alloys.

2. Theory

2.1. Gamma/X-ray shielding parameters

2.1.1. Mass attenuation coefficient, Half Value Layer, mean free path, effective atomic number and electron density

Theoretically, mass attenuation coefficient (MAC) (μ_m) in the energy range from 1 keV to 100 GeV are produced for FD, LT, MC, MT, ST, TU, TM and WM alloy by using WinXCom Gerward et al. (2004); Manjunatha (2015); Manjunatha et al. (2019b). For shielding purposes, the optimum thickness of the material plays a very important role. It is necessary to have the knowledge of Half Value Layer (HVL) which depends on the energy of the photon radiation and the type of material/alloy. The average distance travelled by the photon in the target material before it can be absorbed or scattered is called a photon mean free path (λ) or penetration depth. The ratio of total atomic cross section (σ_a) to the total electronic cross section (σ_e) gives effective atomic number (Z_{eff}). The σ_a can be derived from the values of the MAC. The number of electrons per unit mass gives another interaction parameter called electron density (N_e) and is calculated from the measured Z_{eff} . Larger the electron density value, more are the chances of photon interaction Manohara et al. (2009). Our Previous work Manjunatha (2014, 2015, 2017); Manjunatha et al. (2016b); Manjunatha and Rudraswamy (2013); Manjunatha et al. (2017); Rudraswamy et al. (2010); Seenappa et al. (2017); Suresh et al. (2008); clearly demonstrates the method and equations used in estimating the atomic, electronic cross section, effective atomic number and effective electron density.

2.1.2. Specific gamma ray constant (Γ) and radiation protection efficiency. The gamma ray constant is an exposure rate (in R/h) due to photons at a distance of 1 m from a source with an activity of 1 Ci which can be determined by the relation

$$\Gamma = 657.68 \times E_{\gamma} \left(\frac{\mu_{en}}{\rho}\right) \frac{R.m^2}{Ci.hr} \tag{1}$$

The radiation protection efficiency (RPE) is evaluated using the following equation

$$\left(1 - \frac{I}{I_0}\right) \times 100\% = (1 - e^{-\mu t}) \times 100\% \tag{2}$$

where μ is the measure of linear attenuation coefficient. I and I_0 are the intensities of the radiation for thickness t and t = 0 respectively.

2.1.3. Absorption buildup factor

The interaction of γ ray with material depends upon photon energy and element compositions of binary/tertiary/quaternary alloy. The strength of γ ray beam through the medium depends on Lambert Beer law under three conditions: (i) monochromatic rays, (ii) thin absorbing material and (iii) narrow beam geometry. If the conditions set out above are not satisfied, then the law is no longer applicable. In order to apply the law, a correction factor called "build up factor" is used. It gives the information on the quantity of secondary radiations produced in the medium and energy deposited/absorbed in the medium. In the present work, we have estimated energy absorption build up factors (ABF) using geometric progression (GP) fitting method for FD, LT, MC, MT, ST, TU, TM and WM binary/tertiary/quaternary alloys as explained by Manjunatha et al., Manjunatha et al. (2019b) for different penetration depth and photon energy.

2.2. Neutron shielding parameters

The neutron shielding parameters such as the coherent neutron scattering length (λ_{inc}), incoherent neutron scattering length (λ_{inc}), coherent neutron scattering cross section (σ_{co}), incoherent neutron scattering cross sections (σ_{inc}), total neutron scattering cross section (σ_{tot}), neutron absorption cross sections (σ_{ab}) in the FD, LT, MC, MT, ST, TU, TM and WM binary/tertiary/quaternary alloys were calculated using the equation as explained in Manjunatha et al., Manjunatha et al. (2019b). From the computed neutron cross sections, attenuation parameter of neutron is evaluated using the relation

Attenuation parameter =
$$\frac{\sigma_{abs} \times N_A}{A} cm^2 / g$$
 (3)

where N_A and A are Avogadro number, atomic weight respectively and σ_{abs} is the evaluated absorption cross section.

2.3. Kerma coefficients from partial photon interactions

For the energy fluence Φ of uncharged radiation of energy E, the Kerma K is given by El-Khayatt (2017).

$$K = \Phi E(\mu_{tr} / \rho) \tag{4}$$

where (μ_{tr}/ρ) is the mass energy transfer coefficient of the material for this radiation. The Kerma coefficient k is given by El-Khayatt (2017).

$$k = K/\Phi = E(\mu_n/\rho) \tag{5}$$

To determine the Kerma coefficient k(E) at certain photon energy E we need a) The partial cross section for the photoelectric process, Compton scattering and pair production and b) The energy deposition fraction from each of the partial photon interaction. γ -ray Kerma coefficient is given by

K.V. Sathish et al.

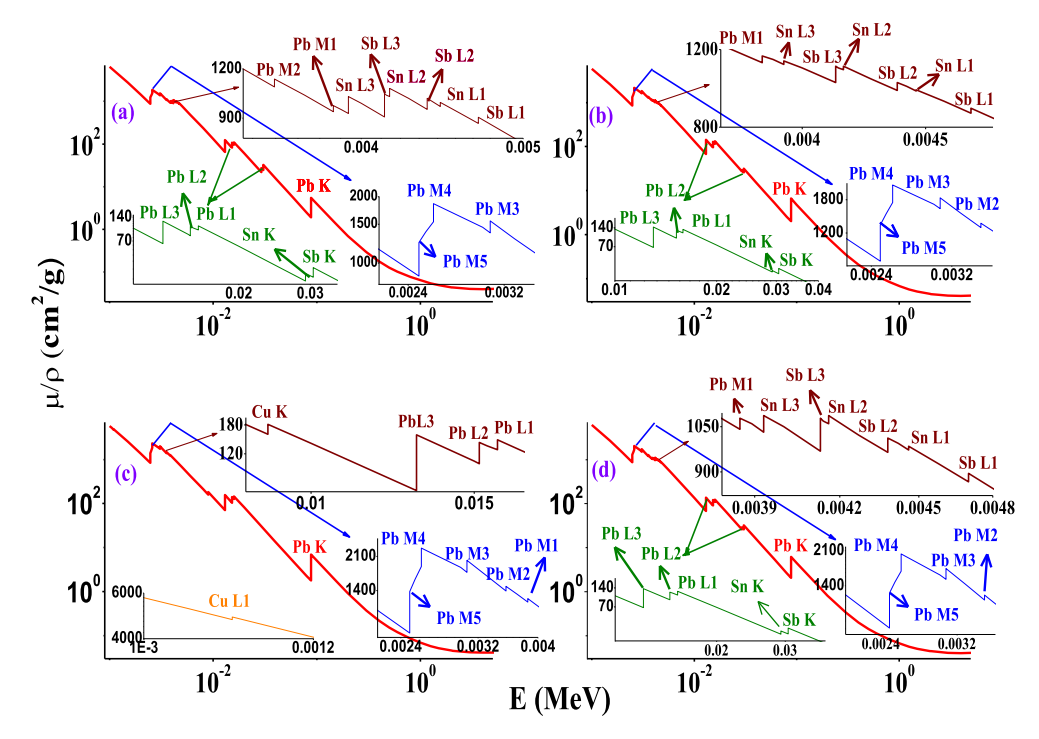


Fig. 1. Variation of MAC with gamma energy for the (a) FD, (b) LT, (c) MC and (d) MT binary/tertiary/quaternary alloys respectively.

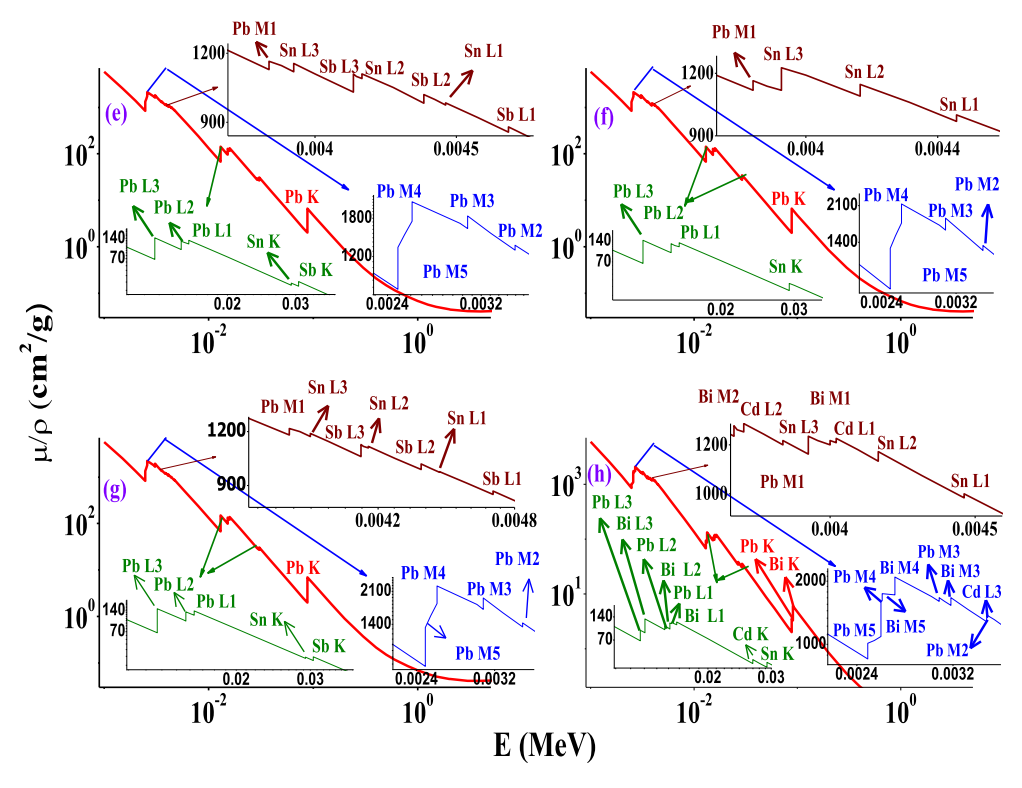


Fig. 2. Variation of MAC with gamma energy for the (e) ST, (f) TU, (g) TM and (h) WM binary/tertiary/quaternary alloys respectively.

$$k(E) = k_D \Sigma_i w^i [\sigma_r^i E + \sigma_{ca}^i E + \sigma_k^i (E - 1.022)]$$

$$Gycm^2 / photon$$
(6)

where k(E) is the photon Kerma coefficient at energy E, σ_r^i , σ_k^i and σ_{Ca}^i are photoelectric, pair production and Compton energy absorption cross sections (cm^2/g) for the ith element at photon energy E respectively, w^i is the weight fraction of the ith element and k_D is the energy conversion

coefficient from MeV to Gy.

2.4. Relative dose

The ratio of dose rate in target to initial dose rate is termed as relative dose intensity. Dose distribution at a distance ${\bf r}$ is given by

$$D_r = D_0 e^{-\mu r} B/r \tag{7}$$

K.V. Sathish et al.

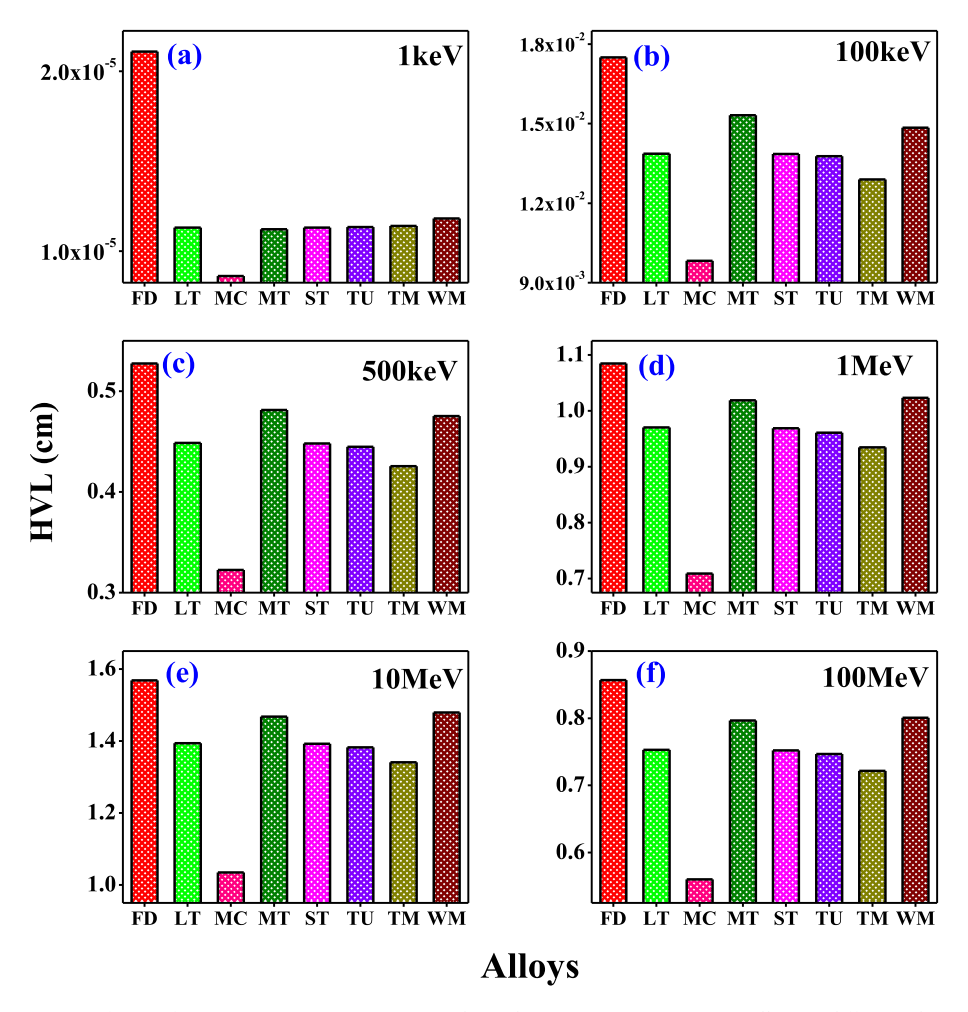


Fig. 3. Comparison of HVL of FD, LT, MC, MT, ST, TU, TM and WM binary/tertiary/quaternary alloys at different photon energies.

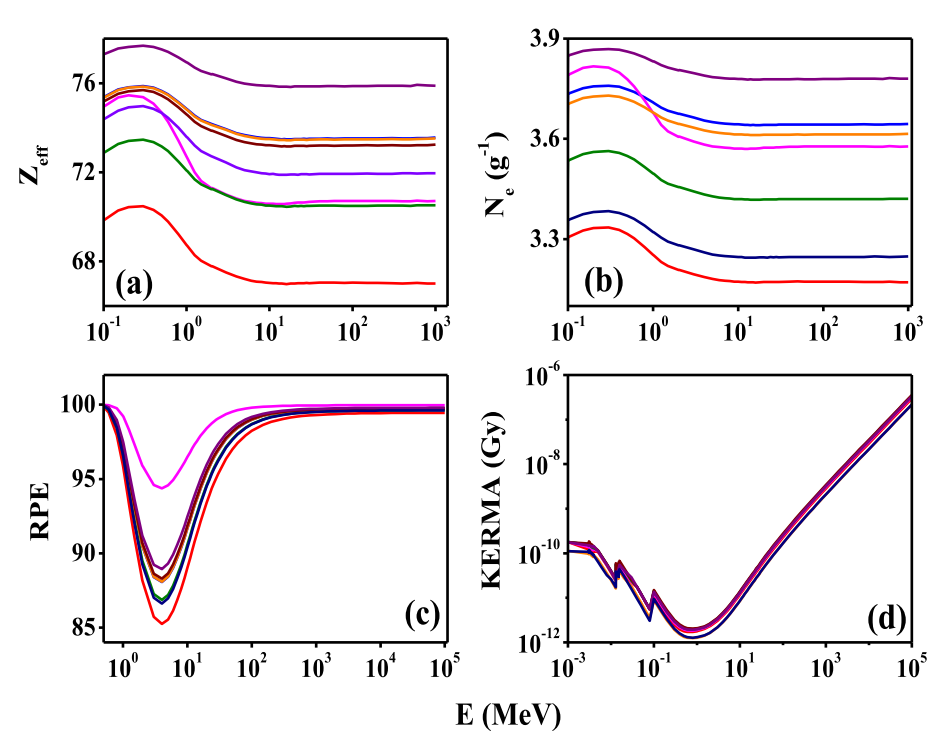


Fig. 4. Variation of (a) Z_{eff} , (b) N_e , (c) RPE and (d) Kerma with photon energy for FD, LT, MC, MT, ST, TU, TM and WM binary/tertiary/quaternary alloys.



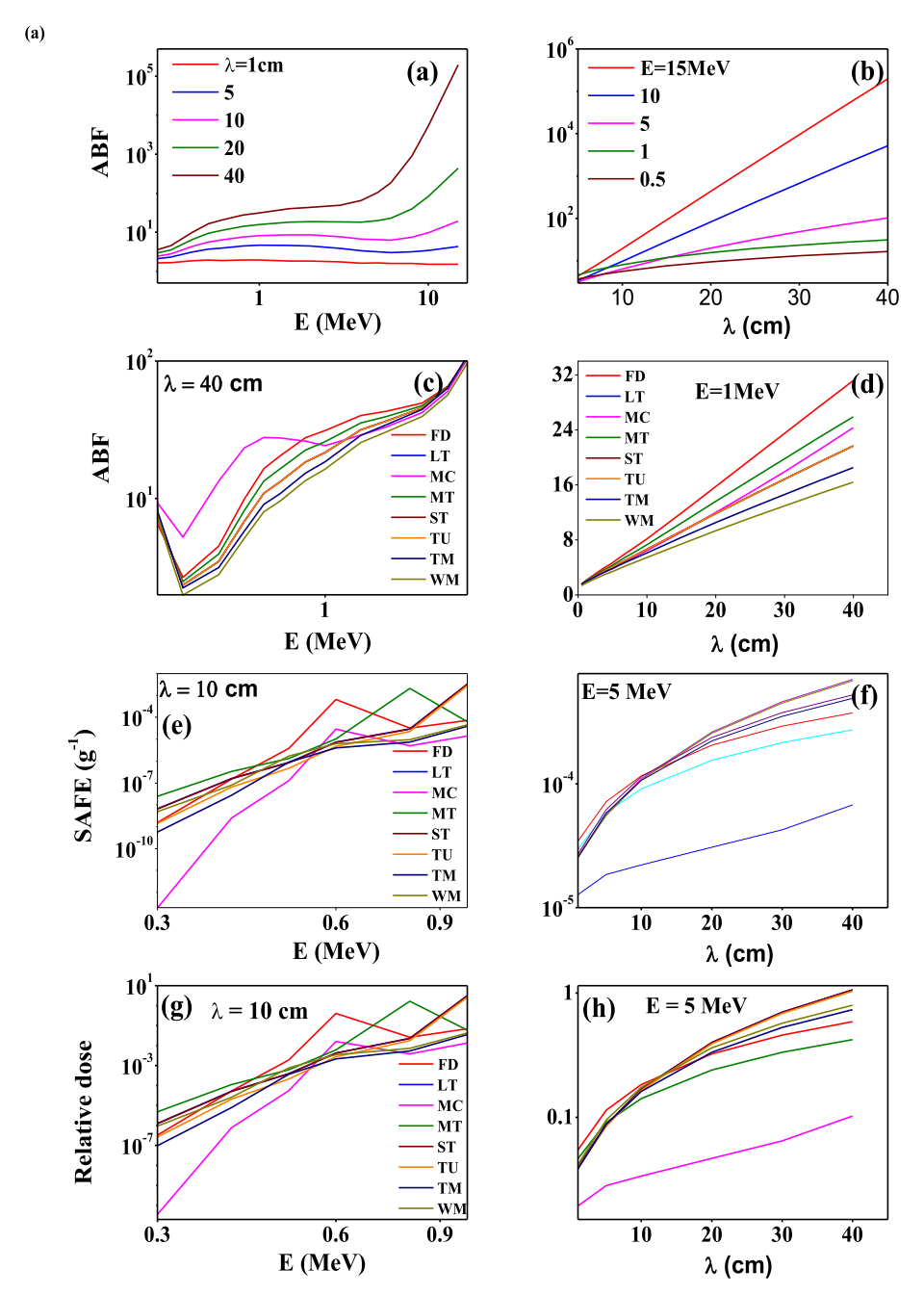


Fig. 5. Variation of (a) *ABF* with photon energy, (b) *ABF* with λ for MC binary alloy, (c) *ABF* with photon energy, (d) *ABF* with λ , (e) *SAFE* with photon energy, (f) *SAFE* with λ , (g) *Relative* dose with photon energy, (h) *Relative* dose with λ for FD, LT, MC, MT, ST, TU, TM and WM binary/tertiary/quaternary alloys.

where μ denotes the linear attenuation coefficient for the appropriate photon energy and B is the exposure build-up factor. D_0 is the initial dose delivered by the gamma ray source. The relative dose distribution at a distance r is

$$\frac{D_r}{D_0} = e^{-\mu r} B / r \tag{8}$$

The relative dose distribution can be calculated by using the estimated exposure build-up for different penetration depths.

2.5. Specific absorbed fraction of energy

The specific absorbed fraction of energy (SAFE) is the fraction of emitted energy from the source organ that is absorbed by the target organ per unit mass of target organ. The specific absorbed fraction of energy at distance x from the point source is given by

$$\Phi(x) = \frac{\mu_{en} \exp(-\mu x) B_{en}}{4\pi r^2 \rho} \tag{9}$$

Here μ_{en} is linear absorption coefficient of photons of given energy, μ is linear attenuation coefficient of photons of given energy, B_{en} is energy absorption build up factor; ρ is density of the medium. The energy absorption build up factors are computed and are used to evaluate Φ for various distances.

3. Results and discussion

Theoretically, X-ray/gamma, neutron shielding parameters of lead based binary/tertiary/quaternary alloys viz., FD, LT, MC, MT, ST, TU,

K.V. Sathish et al.

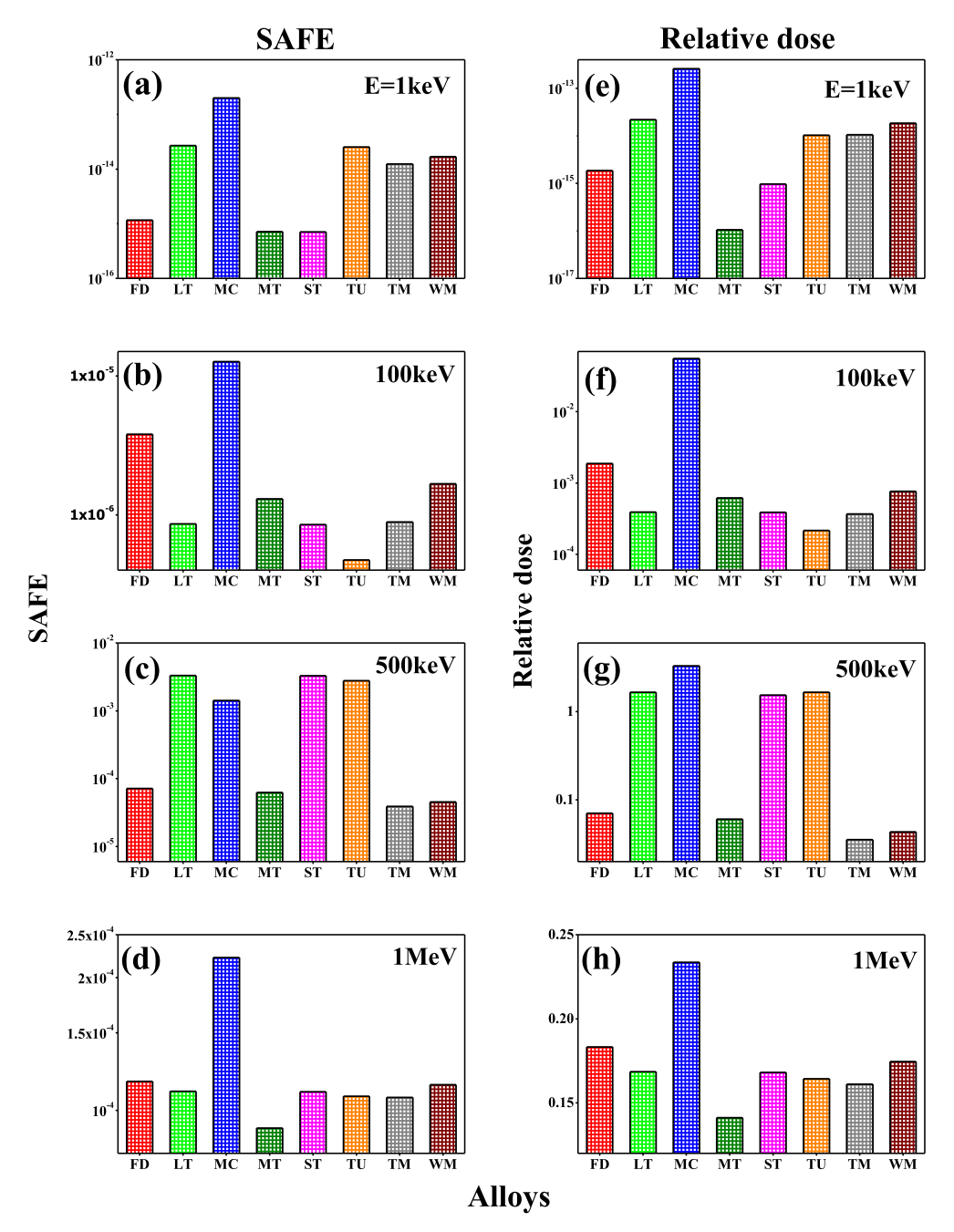


Fig. 6. Comparison of SAFE and relative dose for FD, LT, MC, MT, ST, TU, TM and WM binary/tertiary/quaternary alloys at different photon energies.

TM and WM alloy were studied.

3.1. Gamma/X-ray shielding parameters

Variation of MAC with Gamma energy for all the selected binary/tertiary/quaternary alloys - FD, LT, MC, MT, ST, TU, TM and WM are graphically represented in Fig. 1(a–d) and Fig. 2(e–h) respectively. In all the selected binary/tertiary/quaternary alloys, the variation clearly shows the rapid decrease in MAC value with increase in gamma energy along with few X-ray absorption edges. The rapid decrease in MAC at lower energy is mainly due to the photoelectric process which gets dominated at lower energy. When gamma rays interact with corresponding binary/tertiary/quaternary alloys, it exhibits X-ray absorption edges at particular photon energy. These X-ray absorption edges are the characteristics of the elements present in the chosen binary/tertiary/quaternary alloys. FD type tertiary alloy gives four absorption peaks

observed in the range 2-3 keV, 3-5 keV, 13-32 keV and 88 keV, which are the characteristics of the elements present in the alloy (Fig. 1(a)). Each absorption peak is expanded and given in the inset of Fig. 1(a). The first absorption peak (2-3 keV) is associated with three minor X-ray absorption edges at 2.48, 2.59 and 3.07 keV corresponding to Pb M5-Xray, Pb M4-X-ray and Pb M3-X-ray respectively. The second X-ray absorption peak is associated with eight minor peaks at 3.55 keV, 3.85 keV, 3.93eV, 4.13 keV, 4.16 keV, 4.38 keV, 4.5 keV and 4.7 keV corresponding to Pb M2-X-ray, Pb-M1-X-ray, Sn-L3-X-ray, Sb-L3-X-ray, Sn-L2-X-ray, Sb-L2-X-ray, Sn-L1-X-ray and Sb-L1-X-ray respectively. The third X-ray absorption peak consists five minor absorption edges at 13 keV, 15.2 keV, 15.9 keV, 29.2 keV and 30.5 keV corresponding to Pb-L3-X-ray, Pb-L2-X-ray, Pb-L1-X-ray, Sn-K-X-ray and Sb-K-X-ray respectively. The fourth absorption peak appearing at 88 keV corresponds to Pb-K-X-ray. Similar trend is observed for the remaining binary/tertiary/ quaternary alloys. LT, MT, ST and TM alloy gives the characteristic X-ray

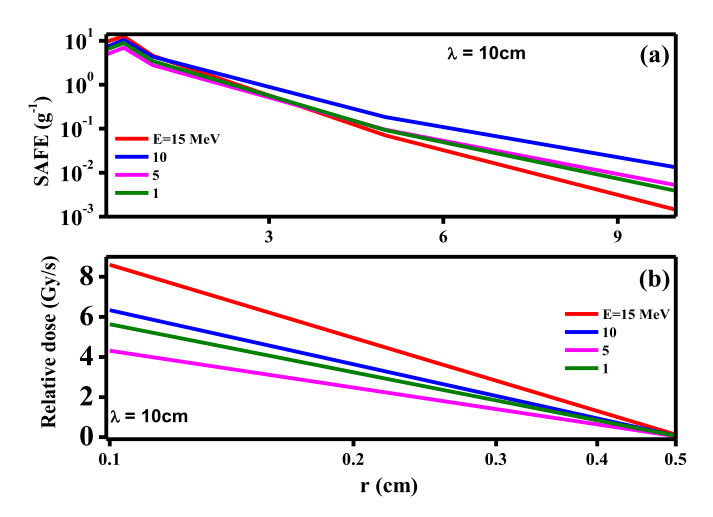


Fig. 7. Variation of (a) SAFE and (b) relative dose with distance (r) for FD, LT, MC, MT, ST, TU, TM and WM binary/tertiary/quaternary alloys.

absorption peaks of Pb, Sn and Sb elements. Fig. 1(b, d) Fig. 2(e and g) and inset figure clearly depicts the Pb-M5-X-ray, Pb-M4-X-ray, Pb-M3-Xray, Pb-M2-X-ray, Pb-M1-X-ray, Sn-L3-X-ray, Sb-L3-X-ray, Sn-L2-X-ray, Sb-L2-X-ray, Sn-L1-X-ray, Sb-L1-X-ray, Pb-L3-X-ray, Pb-L2-X-ray, Pb-L1-X-ray, Sn-K-X-ray, Sb-K-X-ray and Pb-K-X-ray absorption peaks observed for LT, MT, ST and TM alloys. For MC, TU and WM binary/ tertiary/quaternary alloys, Pb-M5-X-ray, Pb-M4-X-ray, Pb-M3-X-ray, Pb-M2-X-ray, Pb-M1-X-ray, Pb-L3-X-ray, Pb-L2-X-ray, Pb-L1-X-ray and Pb-K-X-ray absorption peaks observed at 2.48, 2.59, 3.07, 3.55, 3.85, 13, 15.2, 15.9 and 88 keV respectively. Further, characteristic peaks of copper Cu-L1-X-ray and Cu-K-X-ray are observed at 1.1 and 8.98 keV respectively for MC whereas Sn-L3-X-ray, Sn-L2-X-ray, Sn-L1-X-ray and Sn-K-X-ray absorption peaks are observed at 3.93, 4.16, 4.46 and 29.2 keV respectively for TU binary alloy. In case of WM quaternary alloy, Bi-M5-X-ray, Bi-M4-X-ray, Bi-M3-X-ray, Cd-L3-X-ray, Bi-M2-X-ray, Bi-M1-X-ray, Cd-L1-X-ray, Sn-L2-X-ray, Sn-L3-X-ray, Bi-L3-X-ray, Bi-L2-X-ray, Bi-L1-X-ray, Bi-K-X-ray, Sn-K-ray, Bi-K-X-ray are observed at 2.58, 2.69, 3.18, 3.54, 3.70, 3.73, 3.93, 4, 4.02, 4.16, 4.46, 13.4, 15.7, 16.4, 26.7, 29.2 90.5 keV respectively (Figs. 1(c) and 2(f and h)).

In general, reduction in the intensity of the beam was affected by the atomic number of the absorbing material or beam energy. The HVL of gamma/X-ray beam is the thickness of absorbing material needed to

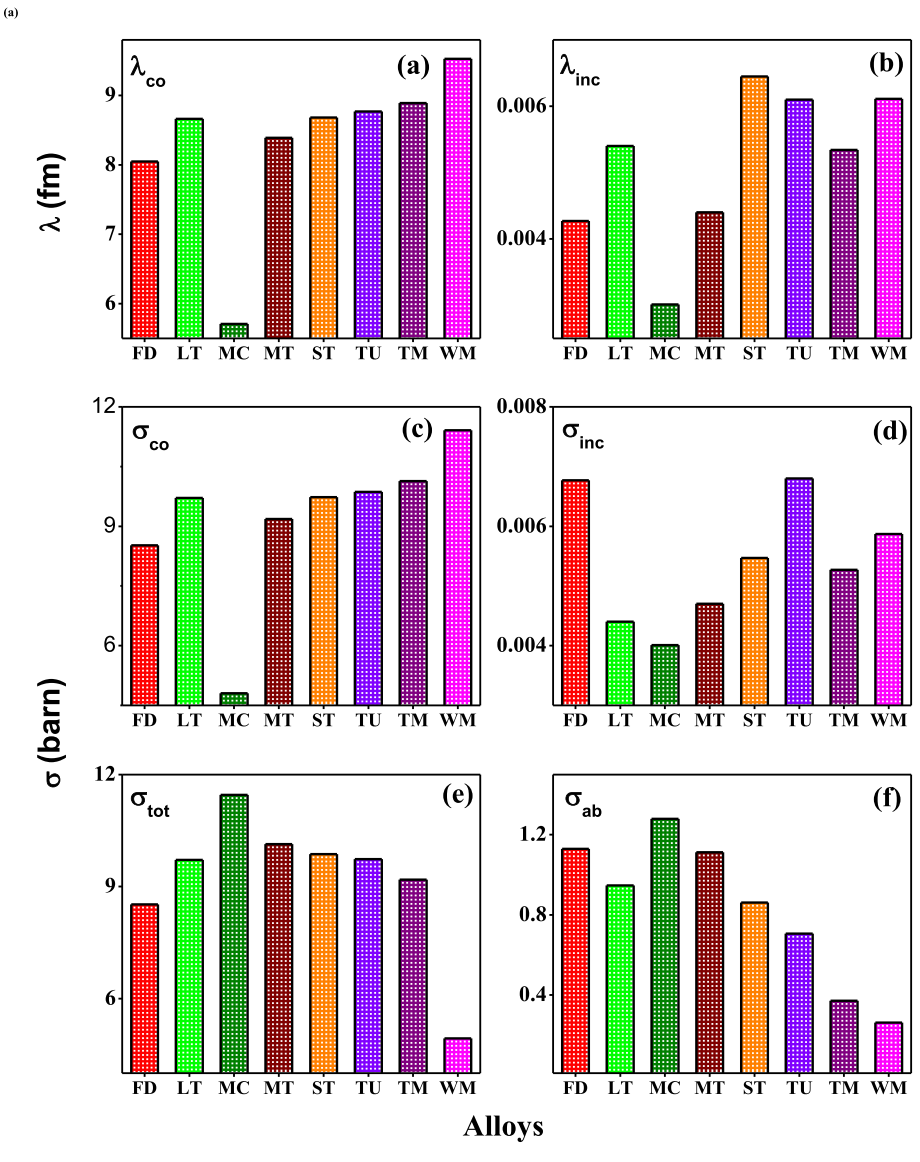


Fig. 8. Comparison of neutron shielding parameters for the FD, LT, MC, MT, ST, TU, TM and WM binary/tertiary/quaternary alloys.

K.V. Sathish et al.

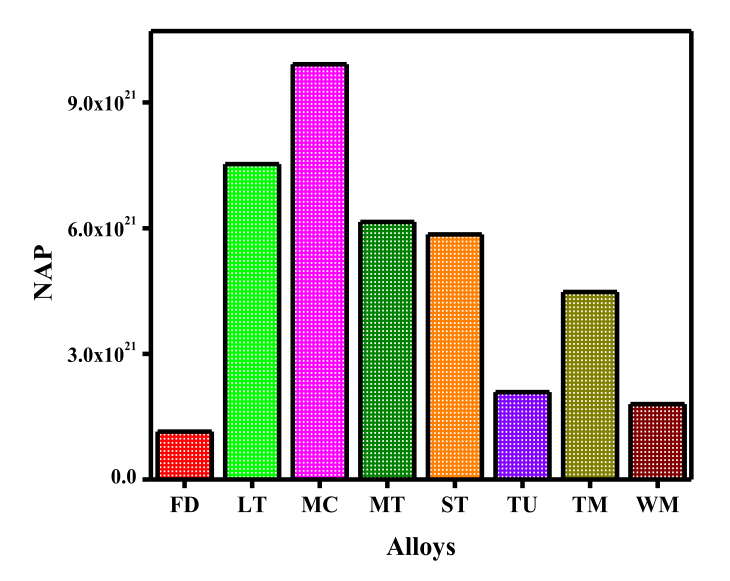


Fig. 9. Comparison of neutron attenuation parameters (*NAP*) for the FD, LT, MC, MT, ST, TU, TM and WM binary/tertiary/quaternary alloys.

reduce the beam to half of its original potential. HVL is (i) indirect measure of photon energy or beam hardness, (ii) an important quality control test as it is used to measure whether or not there is sufficient filtration in the x-ray beam to remove low energy radiation, which can be damaging and (iii) it also helps to determine the type and thickness of shielding required in the facility. Fig. 3 shows the comparison of HVL values of selected binary/tertiary/quaternary alloys at different photon energies (1 keV, 100 keV, 500 keV, 1 MeV, 10 MeV and 100 MeV). Among the selected lead alloys, HVL value was found to be smaller for MC which indicates that it is a good absorber.

In the further investigation, we have studied the variation of other gamma/X-ray shielding parameter such as Z_{eff} , electron density (N_e), radiation protection efficiency (RPE) and KERMA for all the selected binary/tertiary/quaternary alloys with gamma energy (Fig. 4(a-d)). Both Z_{eff} and N_e follow a similar trend with gamma energy for all the selected alloys (Fig. 4 (a and b)). For instance, Z_{eff} and N_e value was found to be maximum for WM quaternary alloy and minimum for FD tertiary alloy whereas, RPE was found to be larger for MC compared to other binary/tertiary/quaternary alloys under study as shown in Fig. 4 (c)). The point where both Compton scattering and photoelectric effect dominates simultaneously, dip point is observed and RPE becomes minimum. The other X-ray/gamma-ray shielding parameter, KERMA gives the information about the kinetic energy released in the particular material. All the binary/tertiary/quaternary alloys show three absorption peaks at 2.83, 14.5 and 103 keV except variation in intensity. This KERMA value was found to be larger for MC binary alloy. The maximum RPE and KERMA value indicates the better performance of MC binary alloy as a better shielding material.

Compared to other alloys under study, MC binary alloy is a good absorber. Thus, the remaining shielding parameters such as Absorption buildup factor (ABF), SAFE and relative dose is studied at different photon energy and different penetration depth (λ) (Fig. 5 a and b) For a particular penetration depth, photoelectric effect and pair production process dominates in the lower and higher energy, whereas Compton scattering dominates at the intermediate energy region. The similar behavior is observed for all the penetration depth except the variation in intensity. However, linear relationship is observed with penetration depth for different photon energy. Fig. 5(c), (e) and Fig. 5(g) shows the graphical representation of variation of ABF (at $\lambda = 40$ cm), SAFE and Relative dose (at $\lambda = 10$ cm) with photon energy for all the selected binary/tertiary/quaternary alloys. Fig. 5(d), (f) and (h) shows the variation of ABF (at E = 1 MeV), SAFE and relative dose (E = 5 MeV) with penetration depth for all the studied alloys. The ABF, SAFE and

relative dose increases with increase in penetration depth. With increase in penetration depth, thickness of the interacting material increases which results in increasing the scattering events in the interacting medium Manjunatha and Rudraswamy (2011). Among all the selected alloys, MC binary alloy shows larger ABF, SAFE and relative dose value and hence a good absorber. Fig. 6(a-d) and Fig. 6(e-h) shows the comparison of SAFE and relative dose at different energies (1 keV, 100 keV, 500 keV, 1 MeV) for all the binary/tertiary/quaternary studied alloys. Fig. 7 (a and b) depicts the variation of SAFE and relative dose of MC binary alloy with thickness. Initially SAFE value goes on increasing with increase in thickness and reaches the higher value at 0.5 cm thickness and thereafter decreases slowly with increase in the thickness value. As the gamma photon passes through the medium, there is a chance of production of secondary radiation which results in the higher value of SAFE. As the thickness increases, incident gamma/X-ray loses its energy and hence decreases in SAFE as well as Relative dose.

3.2. Neutron shielding parameters

The comparison of neutron shielding parameters for all the studied binary/tertiary/quaternary alloys is as shown in Fig. 8(a-f). This figure compares the (a) coherent neutron scattering length (λ_{co}), (b) incoherent neutron scattering length (λ_{inc}) (c) coherent neutron scattering cross section (σ_{co}), (d) incoherent neutron scattering cross sections (σ_{inc}), (e) total neutron scattering cross section (σ_{tot}) and (f) neutron absorption cross sections (σ_{ab}) for all the selected alloys. Among all the selected alloys, MC binary alloy shows smaller $\lambda_{co},\,\lambda_{inc},\,\sigma_{co},\,\sigma_{inc}.$ However, larger σ_{tot} and σ_{ab} values are observed. As λ_{co} , λ_{inc} , σ_{co} , σ_{inc} values are less, neutrons collide more frequently in the material. During each such collisions, it loses energy frequently. Further, Fig. 9 shows the comparison of another neutron shielding parameter called Neutron attenuation parameter (NAP) for all the selected alloys. A material which possess smaller λ_{co} , λ_{inc} , σ_{co} , σ_{inc} and high σ_{tot} , σ_{ab} and NAP shows the characteristic behavior of a good absorber. Since MC binary alloy shows all these characteristics and hence it is considered as a good absorber

4. Summary

In summary, X-rays/gamma and neutron shielding parameters of the FD, LT, MC, MT, ST, TU, TM and WM binary/tertiary/quaternary lead based alloys are studied in detail. The larger values of gamma shielding parameters such as MAC, ABF, Z_{eff} , N_e , SAFE, RPE, KERMA and relative dose. Furthermore neutron shielding parameters such as σ_{tot} and σ_{ab} values clearly indicates Molybdochalkos binary alloy is the good absorber of X-rays/gamma ray and neutron.

Declaration of competing interest

The authors declare that they have no known competing financial interests or personal relationships that could have appeared to influence the work reported in this paper.

References

Agar, O., Sayyed, M., Akman, F., Tekin, H., Kaçal, M., 2019. An extensive investigation on gamma ray shielding features of pd/ag-based alloys. Nuclear Engineering and Technology 51 (3), 853–859.

Akman, F., Sayyed, M., Kaçal, M., Tekin, H., 2019. Investigation of photon shielding performances of some selected alloys by experimental data, theoretical and mcnpx code in the energy range of 81 kev–1333 kev. J. Alloys Compd. 772, 516–524.

Al-Buriahi, M.S., Tonguc, B.T., 2020. Mass attenuation coefficients, effective atomic numbers and electron densities of some contrast agents for computed tomography. Radiat. Phys. Chem. 166, 108507.

Alavian, H., Tavakoli-Anbaran, H., 2020. Comparative study of mass attenuation coefficients for ldpe/metal oxide composites by Monte Carlo simulations. The European Physical Journal Plus 135 (1), 82.

Babu, K.S., Lingam, S.C., Reddy, D.K., 1984. Gamma-ray cross sections and effective atomic numbers in some alloys in the energy range 32 to 662 kev. Can. J. Phys. 62 (2), 178–182.

K.V. Sathish et al.

- El-Khayatt, A.M., 2017. Semi-empirical determination of gamma-ray kerma coefficients for materials of shielding and dosimetry from mass attenuation coefficients. Prog. Nucl. Energy 98, 277–284.
- El-Toony, M., Eid, G., Algarni, H., Alhuwaymel, T., Abel-hady, E., 2020. Synthesis and characterisation of smart poly vinyl ester/pb2o3 nanocomposite for gamma radiation shielding. Radiat. Phys. Chem. 168, 108536.
- Gerward, L., Guilbert, N., Jensen, K.B., Levring, H., 2004. Winxcom—a program for calculating x-ray attenuation coefficients. Radiat. Phys. Chem. 71 (3–4), 653–654.
- Intom, S., Kalkornsurapranee, E., Johns, J., Kaewjaeng, S., Kothan, S., Hongtong, W., Chaiphaksa, W., Kaewkhao, J., 2020. Mechanical and radiation shielding properties of flexible material based on natural rubber/bi2o3 composites. Radiat. Phys. Chem. 172, 108772.
- Islam, S., Mahmoud, K., Sayyed, M., Alim, B., Rahman, M.M., Mollah, A., 2020. Study on the radiation attenuation properties of locally available bees-wax as a tissue equivalent bolus material in radiotherapy. Radiat. Phys. Chem. 172, 108559.
- Issa, S.A., Ali, A.M., Susoy, G., Tekin, H., Saddeek, Y.B., Elsaman, R., Somaily, H., Algarni, H., 2020. Mechanical, physical and gamma ray shielding properties of xpbo-(50-x) moo3–50v2o5 ($25 \le x \le 45$ mol%) glass system. Ceram. Int. 46 (12), 20251–20263.
- Kaur, P., Singh, D., Singh, T., 2019. Sm3+ and gd3+ co-doped lead phosphate glasses for γ-rays shielding and sensing. J. Lumin. 209, 74–88.
- Kaur, S., Kaur, A., Singh, P.S., Singh, T., 2016. Scope of pb-sn binary alloys as gamma rays shielding material. Prog. Nucl. Energy 93, 277–286.
- Kaur, T., Sharma, J., Singh, T., 2017. Feasibility of pb-zn binary alloys as gamma rays shielding materials. Int. J. Pure Appl. Phys. 13 (1), 222–225.
- Kobayashi, E., Matsumoto, S., Doi, H., Yoneyama, T., Hamanaka, H., 1995. Mechanical properties of the binary titanium-zirconium alloys and their potential for biomedical materials. J. Biomed. Mater. Res. 29 (8), 943–950.
- Limkitjaroenporn, P., Kaewkhao, J., Asavavisithchai, S., 2013. Determination of mass attenuation coefficients and effective atomic numbers for inconel 738 alloy for different energies obtained from compton scattering. Ann. Nucl. Energy 53, 64–68.
- Mahmoud, M.E., El-Khatib, A.M., Badawi, M.S., Rashad, A.R., El-Sharkawy, R.M., Thabet, A.A., 2018. Fabrication, characterization and gamma rays shielding properties of nano and micro lead oxide-dispersed-high density polyethylene composites. Radiat. Phys. Chem. 145, 160–173.
- Manjunatha, H.C., 2014. A study of photon interaction parameters in lung tissue substitutes. Journal of Medical Physics/Association of Medical Physicists of India 39 (2), 112.
- Manjunatha, H.C., 2015. Influence of gamma irradiation on conductivity of yba2cu3o7. Radiat. Phys. Chem. 113, 24–27.
- Manjunatha, H.C., 2017. A study of gamma attenuation parameters in poly methyl methacrylate and kapton. Radiat. Phys. Chem. 137, 254–259.
- Manjunatha, H.C., Chandrika, B.M., Seenappa, L., Hanumantharayappa, C., 2016a. Study of gamma attenuation properties of tungsten copper alloys. Int. J. Nucl. Energy Sci. Technol. 10 (4), 356–368.
- Manjunatha, H.C., Chandrika, B.M., Seenappa, L., Hanumantharayappa, C., 2016b. Study of gamma attenuation properties of tungsten copper alloys. Int. J. Nucl. Energy Sci. Technol. 10 (4), 356–368.
- Manjunatha, H.C., Rudraswamy, B., 2006. Theoretical method for external bremsstrahlung cross section of reactor shielding materials and other compounds. In: Proceedings of the Sixteenth National Symposium on Radiation Physics: Radiation Transport-Experiments, Computations and Theory.
- Manjunatha, H.C., Rudraswamy, B., 2011. A study of thickness and penetration depth dependence of specific absorbed fraction of energy in bone. Ann. Nucl. Energy 38 (10), 2271–2282
- Manjunatha, H.C., Rudraswamy, B., 2013. Study of effective atomic number and electron density for tissues from human organs in the energy range of 1 kev–100 gev. Health Phys. 104 (2), 158–162.
- Manjunatha, H.C., Sathish, K.V., Seenappa, L., Damodara Gupta, P.S., Raj, S.A.C., 2019a.
 A study of x-ray, gamma and neutron shielding parameters in si-alloys. Radiat. Phys. Chem. 165, 108414.
- Manjunatha, H.C., Sathish, K.V., Seenappa, L., Gupta, D., Raj, S.A.C., 2019b. A study of x-ray, gamma and neutron shielding parameters in si-alloys. Radiat. Phys. Chem. 165, 108414.
- Manjunatha, H.C., Seenappa, L., Chandrika, B.M., Sridhar, K.N., Hanumantharayappa, C., 2018a. Gamma, x-ray and neutron shielding parameters for the al-based glassy alloys. Appl. Radiat. Isot. 139, 187–194.

- Manjunatha, H.C., Seenappa, L., Sridhar, K.N., 2018b. Study of gamma/x-ray interaction in kondo insulators. X Ray Spectrom. 47 (1), 34–45.
- Manjunatha, H.C., Seenappa, L., Sridhar, K.N., Hanumantharayappa, C., 2017. Study of gamma/x-ray interaction in some diodes and transistors. Int. J. Nucl. Energy Sci. Technol. 11 (4), 377–389.
- Manohara, S., Hanagodimath, S., Gerward, L., 2009. Photon interaction and energy absorption in glass: a transparent gamma ray shield. J. Nucl. Mater. 393 (3), 465-472
- Manohara, S., Hanagodimath, S., Gerward, L., Mittal, K., 2011. Exposure buildup factors for heavy metal oxide glass: a radiation shield. J. Kor. Phys. Soc. 59 (2), 2039–2042.
- Nagaraja, N., Sridhar, K.N., Manjunatha, H.C., Seenappa, L., Ramalingam, H.B., Srinivas, M.G., 2019. A study of gamma, x-ray and neutron radiation shielding parameters in some polymers. In: Proceedings of the Fourteenth Biennial DAE-BRNS Symposium on Nuclear and Radiochemistry: Book of Abstracts.
- Prengaman, R.D., 2009. Secondary Batteries_Lead_Acid Systems Lead Alloys. Encyclopedia of Electrochemical Power Sources, pp. 648–654.
- Rezaei-Ochbelagh, D., Azimkhani, S., 2012. Investigation of gamma-ray shielding properties of concrete containing different percentages of lead. Appl. Radiat. Isot. 70 (10), 2282–2286.
- Rudraswamy, B., Dhananjaya, N., Manjunatha, H.C., 2010. Measurement of absorbed dose rate of gamma radiation for lead compounds. Nuclear Instruments and Methods in Physics Research Section A Accelerators, Spectrometers, Detectors and Associated Equipment 619 (1–3), 171–173.
- Sayyed, M., Ati, A.A., Mhareb, M., Mahmoud, K., Kaky, K.M., Baki, S., Mahdi, M., 2020. Novel tellurite glass (60-x) teo2–10geo2-20zno–10bao-xbi2o3 for radiation shielding. J. Alloys Compd. 844, 155668.
- Seenappa, L., Manjunatha, H.C., Chandrika, B.M., Chikka, H., 2017. A study of shielding properties of x-ray and gamma in barium compounds. Journal of Radiation Protection and Research 42 (1), 26–32.
- Seenappa, L., Manjunatha, H.C., Chandrika, B.M., Sridhar, K.N., Hanumantharayappa, C., 2018a. Study of gamma, x-ray and neutron shielding parameters of some alloys. Indian J. Pure Appl. Phys. 56 (5), 631–634.
- Seenappa, L., Manjunatha, H.C., Sridhar, K.N., Hanumantharayappa, C., 2018b. Gamma x-ray and neutron shielding properties of polymer concretes. Indian J. Pure Appl. Phys. 56 (5), 383–391.
- Seven, S., Karahan, I.H., Bakkaloglu, Ö.F., 2004. The measurement of total mass attenuation coefficients of cocuni alloys. J. Quant. Spectrosc. Radiat. Transf. 83 (2), 237–242.
- Shafka, Z., Hannora, A.E., Sherif, M.M., 2015. Preparation of lead-polymer nano composite for nuclear shielding applications. Int. J. Res. Appl. Sci. Eng. Technol. 3, 1046–1049.
- Shah, S., Wasim, M., 2020. Mass attenuation coefficients of iaea soil standards at different gamma-ray energies. Nucleus 57 (2), 62–66.
- Singh, T., Kaur, S., Kaur, P., Kaur, H., Singh, P.S., 2015. Variation of photon interaction parameters with energy for some cu-pb alloys. In: AIP Conference Proceedings, vol. 1675. AIP Publishing LLC. 020057.
- Singh, V., Badiger, N., 2013. Study of mass attenuation coefficients, effective atomic numbers and electron densities of carbon steel and stainless steels. Radioprotection 48 (3), 431–443.
- Sopapan, P., Laopaiboon, J., Jaiboon, O., Yenchai, C., Laopaiboon, R., 2020. Feasibility study of recycled crt glass on elastic and radiation shielding properties used as x-ray and gamma-ray shielding materials. Prog. Nucl. Energy 119, 103149.
- Suresh, K.C., Manjunatha, H.C., Rudraswamy, B., 2008. Study of z {subeff} for dna, rna and retina by numerical methods. Radiat. Protect. Dosim. 43 (294–298).
- $Tekin, H., Kilicoglu, O., 2020. \ The influence of gallium (ga) additive on nuclear radiation shielding effectiveness of pd/mn binary alloys. J. Alloys Compd. 815, 152484.$
- Tekumalla, S., Seetharaman, S., Almajid, A., Gupta, M., 2015. Mechanical properties of magnesium-rare earth alloy systems: a review. Metals 5 (1), 1–39.
- Turhan, M.F., Akman, F., Polat, H., Kaçal, M.R., Demirkol, İ., 2020. Gamma-ray attenuation behaviors of hematite doped polymer composites. Prog. Nucl. Energy 129, 103504.
- Yılmaz, E., Baltas, H., Kırıs, E., Ustabas, İ., Cevik, U., El-Khayatt, A., 2011. Gamma ray and neutron shielding properties of some concrete materials. Ann. Nucl. Energy 38 (10), 2204–2212.
- Zhang, Q.-P., Xu, Y.-C., Li, J.-L., Liu, A.-J., Xu, D.-G., Wei, M., Zhou, Y.-L., 2020. Hunting for advanced low-energy gamma-rays shielding materials based on pbwo4 through crystal defect engineering. J. Alloys Compd. 822, 153737.

\$ SUPER

Contents lists available at ScienceDirect

Radiation Physics and Chemistry

journal homepage: www.elsevier.com/locate/radphyschem





X-rays/gamma rays radiation shielding properties of Barium–Nickel–Iron oxide nanocomposite synthesized *via* low temperature solution combustion method

K.V. Sathish^{a,b}, H.C. Manjunatha^{a,*}, Y.S. Vidya^{c,**}, K.N. Sridhar^d, L. Seenappa^a, B. Chinnappa Reddy^e, S. Alfred Cecil Raj^b, P.S. Damodara Gupta^a

- ^a Department of Physics, Government College for Women, Kolar, 563101, Karnataka, India
- ^b Department of Physics, St.Joseph's College, Affiliated To Bharathidasan University, Tiruchirappalli, 620002, TamilNadu, India
- ^c Department of Physics, Lal Bahadur Shastri Government First Grade College, RT Nagar, Bangalore, 560032, Karnataka, India
- ^d Department of Physics, Government First Grade College, Kolar, 563101, Karnataka, India
- ^e Department of Physics, Government First Grade College, Srinivasapur, 563135, Karnataka, India

ARTICLE INFO

Keywords: Ba-Fe-Ni oxide Nanocomposite Solution combustion method Radiation shielding

ABSTRACT

In the present communication, for the first time Ba–Fe–Ni oxide nanocomposite (BFNONC) was synthesized by using solution combustion method and calcined at 500^{o} C. The synthesized sample was characterized using the techniques such as powder X-ray diffraction (PXRD), scanning electron microscopy (SEM), Fourier transmission infrared spectroscopy (FTIR) and UV–Visible spectrophotometer to determine phase purity, functional group, surface morphology, structural analysis and energy band gap. The presence of diffraction peaks corresponding to BaO, Fe₂O₃ and NiO clearly confirms the formation of BFNONC. The average crystallite size was found to be 30 nm. The direct energy band gap determined by using Wood and Tauc's relation was found to be 2.1 eV. Further, the X-ray/gamma ray shielding properties of BFNONC in the energy range 0.081–1.332 MeV using NaI (TI) detector and multi channel analyser (MCA) were measured. The measured shielding parameters are compared with the theory. Above 356 keV energy of X-ray/gamma ray, the measured shielding parameters agrees well with the theory, whereas slight deviation is observed below 356 keV. This deviation is mainly due to the influence of atomic/crystallite size of the BFNONC. This BFNONC finds an application as a shielding material in radiation shielding.

1. Introduction

Nowadays, nanocomposites (NCs) initiate important development in nanotechnologies due to specific chemical and physical properties (Omanović-Mikličanin et al., 2020). Modification of the compositions, mixing of two or more elements adds to the possibility of tuning the properties at the nanoscale (Calvo, 2020). Many researchers have been captivated by the extraordinary level of novelty and unique possibilities for primarily new technologies that can be expected from combining size and composition effects, which has sparked a flurry of work. The NCs possess different structural, electronic, dielectric, magnetic, optical and chemical properties compared to those of corresponding bulk metals (Lewin et al., 2006). The combining of two or more metallic elements in

clusters or bigger nanoparticles results in even more complexity and uniqueness. The main purpose of the field of NCs is to investigate and characterize the wide range of composite properties at the nanoscale as a function of size and composition both elemental and percentile. Presently, efforts of researchers are well underway to attain this goal.

NCs combine and enhance a wide variety of size effects with a wide range of composition effects, resulting in a multitude of novel features and characteristics that could not be acquired by just changing the size of pure metallic systems or the composition of bulk materials (Lewin et al., 2006). Recently, NCs have received much attention with respect to their application in engineering, aerospace, medicine, plastics, rubber, coatings, adhesives, and electronic, optic materials, science and nuclear industry, (Ates et al., 2020). Barrera et al. (2019), reviewed the

E-mail addresses: manjunathhc@rediffmail.com (H.C. Manjunatha), vidyays.phy@gmail.com (Y.S. Vidya).

^{*} Corresponding author.

^{**} Corresponding author.

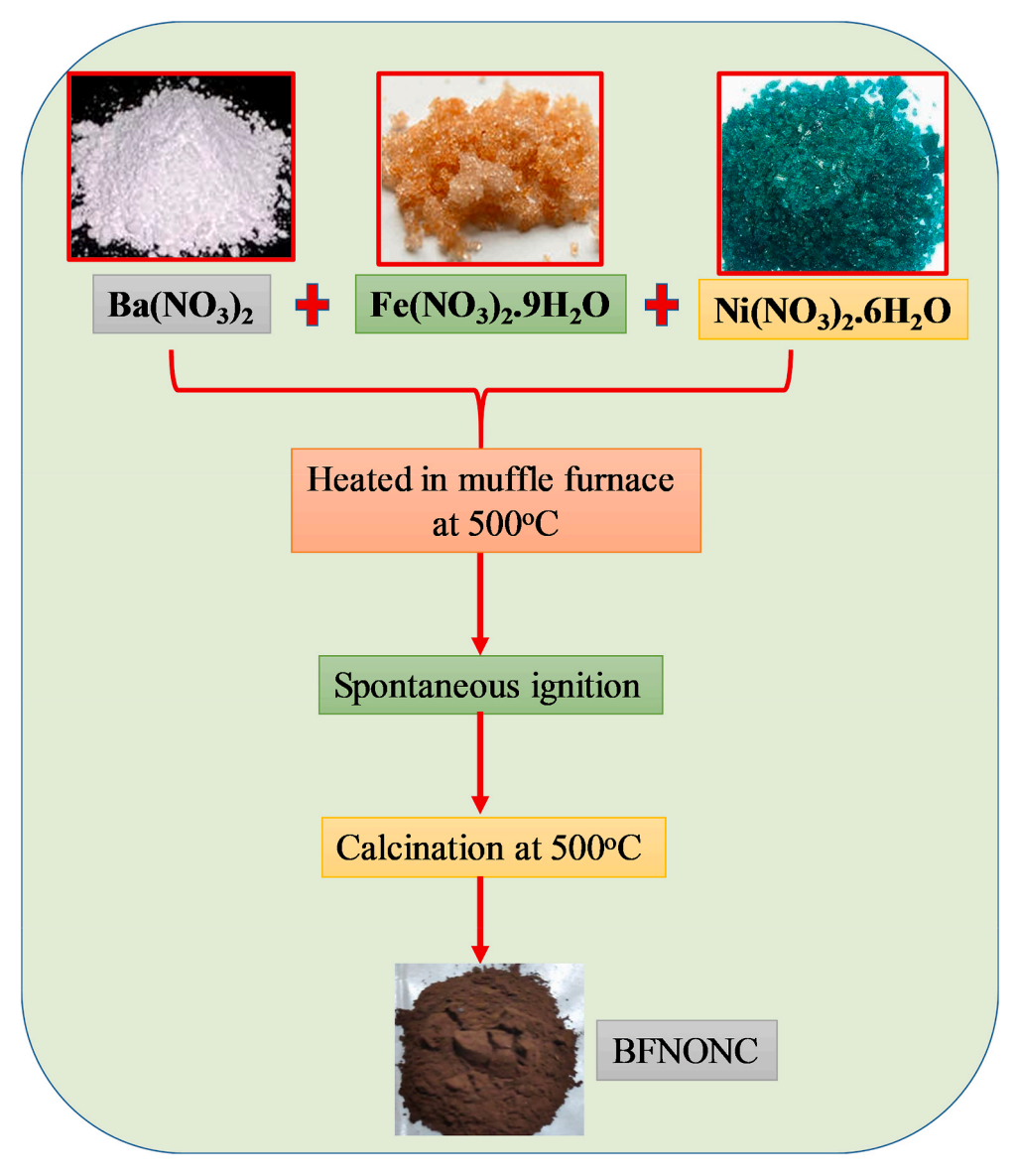


Fig. 1. Flowchart for the synthesis of BFNONC.

magnetic properties of various families of NC materials containing nanoparticles of transition metals or transition-metal compounds. Tishkevich et al. (DI Tishkevich et al., 2020), calculated the Linear and mass paths of protons and Ar $^+$ ions in Al, Al_2O_3 , Bi, and W_{77} , $_7Cu_2O_3$ composite shields using a SRIM software package and discussed the dependence of threshold energy on the serial number of these particles. The variety of the NCs such as Nd₂Fe₁₄B/ α -Fe (Cui et al., 2005), polymers NCs (Novakova et al., 2003), (CoFeZr)_x(Al₂O₃)_{(1-x)} (Zhukowski-Julia Sidorenko et al., 2010) etc., nanocomposites are explored. In contrast to extensive studies on the optical, magnetic and electrical properties of NCs, however X-ray/gamma ray radiation shielding properties have not yet been explored (El-Gendy et al., 2016; Wu and Kim, 2007; Niu et al., 2019).

Prolonged exposure to high-energy X-ray and gamma rays, as well as high penetrating neutrons, can result in major health issues. New materials are continually being developed to remove these risks, and various researches are being conducted (Levet et al., 2020). Generally, high-atomic-number materials, such as lead and steel are frequently employed to absorb radiation in high-radiation environments (Singh et al., 2015). Determining the most appropriate material for shielding is the most challenging in the research field. NCs are the most common and favoured radiation shielding material because of their high shielding

efficacy (Akman et al., 2019). In comparison with the traditional metal-based materials/composites/polymer/polymer composites, NCs have recently become popular as radiation shielding materials due to their low cost, high corrosion resistance, lightweight, simple and great processability and broad absorption and bandwidth capabilities (Sirin, 2020; Tellili et al., 2017). Sayyed et al. (2021), investigated the role of Bi₂O₃ on the mechanical and radiation shielding properties of Bi₂O₃ -ZnO - TiO₂ - Na₂O - TeO₂ glass system. Tishkevich et al. (2019), studied the shielding and attenuation properties of Tungsten and copper composite materials. The transition metal oxide NCs are interesting from fundamental and technological points of view where the bonding involves valence d orbitals (De Almeida and Ahuja, 2006). Only few rare earth/transition metal NCs have been produced so far (Hu et al., 2019; Feng et al., 2018). Compared to lead, Barium, Iron and Nickel are less toxic, which has been proposed as a substitute. Already researchers carried out number of research work on Barium Oxide (Kaur et al., 2019; Zezulova et al., 2017), Iron oxide (Ganguly et al., 2021; Shahboub et al., 2021) and Nickel oxide (Tekin et al., 2019; Kamil et al., 2022) as a shielding material. Compared to individual oxides, nanocomposite formed by these oxides shows better optical, thermal and mechanical properties which is required for a better shielding material. In this regard, an attempt was done and shielding properties of newly synthesized

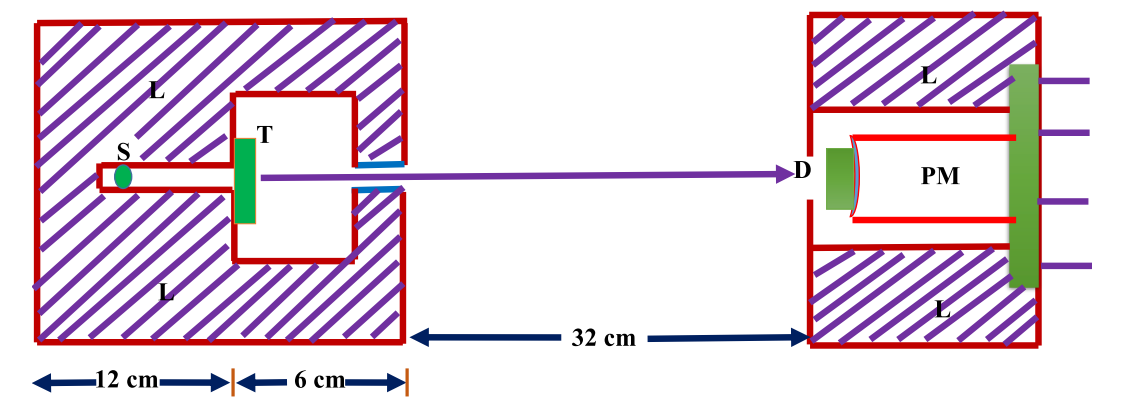


Fig. 2. Schematic diagram of the Experimental Setup of BFNONC (S: Source position, T:BFNONC sample, L: Lead shielding, D: Detector, PM: Photomultiplier).

 ${\rm BaO-Fe_2}O_3$ and NiO nanocomposite was discussed in detail to explore a shielding material an alternative to replace the toxic lead material.

A barium compound has a comparably large density of 4.5 g/cm³, good mechanical properties and environmentally-friendly properties (Akkurt et al., 2005). Compounds which contain Nickel have cost-effective, good thermal, mechanical and structural properties. Meanwhile, compounds with iron have good mechanical strength, ductility and thermal stability (Hamad et al., 2021). The compound which is having the combination of Barium, Nickel and Iron is expected to be good radiation shielding material. Various techniques for the synthesis of NCs have been proposed, including mechanical alloying (Phong et al., 2015), mechanochemical processing (Azizi et al., 2011), electrospinning (Jing et al., 2016), solution-phase chemical synthesis (Karipoth et al., 2016), electrochemical deposition (Tishkevich et al., 2018) etc. Tishkevich et al. (2018), has discussed the bismuth coatings on the non-lead materials production by the electrochemical deposition method and investigation of the shielding efficiency from electron radiation. Inhomogeneity of the end product, limited surface area, development of large agglomerated particles, and presence of different flaws (surface, impurities) are all characteristics of the conventional techniques. The solution combustion method was used to solve these issues. This approach creates a consistent product with a large surface area and small particles, as well as a shorter processing time and a lower cost. Among all these techniques, solution combustion synthesis has been successfully employed to the preparation of BFNONC. Solution combustion method is a time-and energy-saving approach for the synthesis of NCs that can be easily scaled up. It includes the use of basic instruments, low-cost raw materials, the absence of surfactant and the ease with which chemical compositions can be designed. Solution combustion method produces high purity products permits stabilization of metastable phases, and allows the formation of virtually any size and shape products. Furthermore, aqueous combustion reaction facilitates the mixture of raw materials at molecular level. However, till to date, there are no literatures to report the preparation of BFNONC.

In the present study, an attempt was done by synthesizing BFNONC which is a mixture of alkaline earth metal and transition metal using low temperature solution combustion method using urea as a fuel. One of the motives to synthesize NCs of these compounds and investigating their properties is the desire to control the energy band gap and to study the X-rays/Gamma rays shielding parameters, which provides the base for achieving optimal range over which a shielding material can design. The study of BFNONC, due to lack of an efficient synthesis approach, shielding properties are not yet explored. In the present work, we have synthesized BFNONC and studied the X-ray/gamma radiation shielding and anti-microbial properties. Present work consist of two parts, In the first part, we have synthesized and characterized the BFNONC. In the second part, we have measured the radiation shielding properties and antimicrobial properties. To the best of our knowledge, for the first time, low temperature solution combustion synthesis was demonstrated to be

a versatile and energy efficient method for preparing BFNONC. The obtained nano powders were characterized using X-ray diffraction (XRD), scanning electron microscopy (SEM), Fourier transmission infrared spectroscopy (FTIR) and UV–Visible absorption spectroscopy. In addition to the gamma ray shielding and antimicrobial properties of synthesized BFNONC are studied in detail.

2. Materials and methods

2.1. Synthesis of BFNONC

 $Ba(NO_3)_2$, Iron(III) nitrate [Fe(NO₃)₃ · 9H₂O], Nickel nitrate [Ni (NO₃)₃ · 6H₂O] and Urea [CH₄N₂O] with 99.9 % purity were obtained from Sd-fine chemicals. All the reagents were of analytical grade and used as such without further purification. BFNONC was synthesized by solution combustion method using Urea as fuel. All the reagents are taken in a cylindrical crucible, stirred well in order to obtain homogeneity for half an hour at 400 rpm. This crucible was placed in a muffle furnace that had been preheated to a temperature of $500 \pm 10^{\circ}$ C. The resultant solution was first boiled, then dehydrated to remove gases such as carbon dioxide, nitrogen and water vapour before forming the final product. The resulting product was calcined for 3 h at 500° C, then cooled to ambient temperature and collected. The visual depiction for the synthesis of BFNONC using urea as a fuel is shown in Fig. 1.

2.2. Characterization of BFNONC

The final products were characterized using Shimadzu Powder X-ray diffractometer (PXRD). The diffraction patterns were recorded at room temperature using Cu K_{α} (1.541 Å) radiation with nickel filter in the 2h range 20–50^o at a scan rate of 2^o min⁻¹. The morphological features and particle size were studied by scanning electron microscopy (SEM, Hitachi-3000) and transmission electron microscopy (TECNAIF-30) respectively. FTIR studies of the NPs were performed with a PerkinElmer Forntier FTIR spectrometer. The UV-Visible absorption spectrum was recorded on PerkinElmer UV-Visible Spectrophotometer. Further, measurement of X-ray/gamma ray shiedling properties of BFNONC and its theoritical evaluation was explained briefly in our previous work (Reddy et al., 2021). Theoretically, X-ray/gamma ray shielding parameters such as Mass attenuation coefficient (μ/ρ), Half Value Layer (HVL), Tenth Value Layer (TVL), Mean free path (λ), Effective atomic number (Z_{eff}) , Electron density (N_e) , Energy Absorption Buildup Factor (EABF), kinetic energy released in matter (KERMA), Specific gamma ray constant (SGR), specific absorbed fraction of energy (SAF) and Radiation protection efficiency (RPE) are also discussed in detail. The schematic view of the experimental set up used for the measurement of X-ray/gamma ray shiedling properties of BFNONC is displayed in Fig. 2.

The errors in the experiment came from two major sources; the counting rate error and the uncertainties on the thickness of target. The

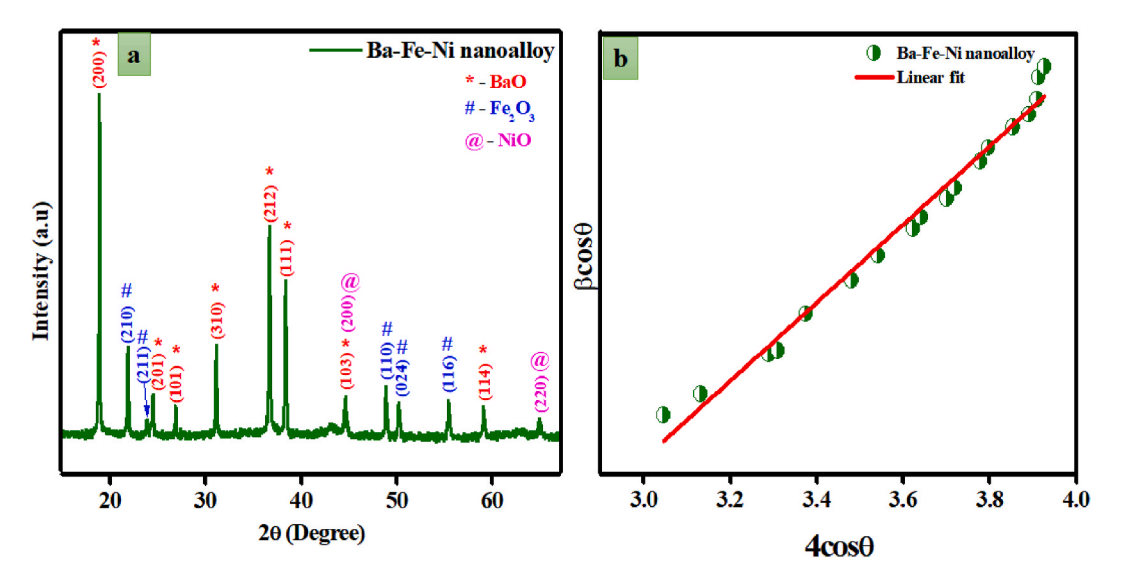


Fig. 3. (a) PXRD pattern of BFNONC and (b) W-h plot of BFNONC.

maximum errors in the total mass attenuation coefficients were calculated from errors in incident (I_0) and transmitted (I) intensities and areal density (t) by using the propagation of error formula,

$$\Delta\left(\frac{\mu}{\rho}\right) = \frac{1}{t}\sqrt{\left(\frac{\Delta I_0}{I_0}\right)^2 + \left(\frac{\Delta I}{I}\right)^2 + \left(\ln\frac{\Delta I}{I}\right)^2 + \left(\frac{\Delta t}{t}\right)^2} \tag{1}$$

where ΔI_0 , ΔI and Δt are the errors in the intensities I_0 , I and thickness t of the sample respectively.

3. Theory

3.1. Gamma/X-ray shielding parameters

determined by the relation:

3.1.1. Mass attenuation coefficient, Half Value Layer, mean free path, effective atomic number and electron density

Theoretically, mass attenuation coefficient (MAC) (μ/ρ) in the energy range from 1 keV to 100 GeV are produced for BFNONC by using WinXCom (Manjunatha, 2015; Manjunatha et al., 2019). For shielding purposes, the optimum thickness of the material plays a very important role. It is necessary to have the knowledge of the Half Value Layer (HVL) which depends on the energy of the photon radiation and the type of material. The average distance travelled by the photon in the target material before it can be absorbed or scattered is called a photon mean free path (λ) or penetration depth. The ratio of total atomic cross section (σ_a) to the total electronic cross section (σ_e) gives effective atomic number (Z_{eff}). The σ_a can be derived from the values of the MAC. The number of electrons per unit mass gives the another interaction parameter called electron density (N_e) and is calculated from the measured Z_{eff} . Larger the electron density value, more are the chances of photon interaction (Manohara et al., 2009). Our Previous work (Manjunatha, 2014, 2015, 2017; Seenappa et al., 2017; Manjunatha et al., 2016, 2017; Rudraswamy et al., 2010; Manjunatha and Rudraswamy, 2013; Suresh et al., 2008) clearly demonstrates the method and equations used in estimating the atomic, electronic cross section, effective atomic number and effective electron density.

3.1.2. Specific gamma ray constant (Γ) and radiation protection efficiency The gamma ray constant is an exposure rate (in R/h) due to photons at a distance of 1 m from a source with an activity of 1 Ci which can be

$$\Gamma = 657.68 \times E_{\gamma} \left(\frac{\mu_{en}}{\rho}\right) \frac{R.m^2}{Ci.hr} \tag{2}$$

The radiation protection efficiency (RPE) is evaluated using the following equation:

$$\left(1 - \frac{I}{I_0}\right) \times 100\% = (1 - e^{-\mu t}) \times 100\% \tag{3}$$

where μ is the measure of linear attenuation coefficient. I and I_0 are the intensities of the radiation for thickness t and t = 0 respectively.

4. Results and discussion

BFNONC was synthesized by utilizing an inexpensive solution combustion process with urea as a fuel and calcined at 500°C. The synthesized sample was evaluated utilizing techniques such as PXRD, SEM, EDAX, FTIR, and UV–Visible spectrophotometer to determine phase purity, functional group, surface morphology, structural analysis, and energy band gap. To our knowledge, this is the first time that an attempt has been made to build an effective and a good X-ray/gamma ray material. As a result, the X-ray/Gamma ray shielding capabilities of synthesized BFNONC are thoroughly explored.

4.1. PXRD analysis of BFNONC

PXRD is one of the most widely utilised characterization techniques which gives information about the crystalline structure, phase nature, lattice parameters and crystalline grain size. Fig. 3a depicts the PXRD pattern of BFNONC synthesized by low temperature solution combustion method calcined at 500° C for 3 h. The sample's/NCs high crystallinity is confirmed by the strong diffraction planes.

The BFNONC consists of Bragg's reflections (200), (210), (211), (201), (101), (310), (212), (111), (103), (200), (110), (024), (116), (114) and (220) at 18.81, 21.76, 24.03, 24.43, 26.91, 31.11, 36.65, 38.29, 44.55, 48.86, 50.19, 55.33, 59.13 and 64.87° 2θ respectively. Among these reflections, (200), (101), (310), (212), (111), (103) and (114) corresponds to tetragonal phase of BaO (Ansari and Jahan, 2021), (210), (211), (110), (024) and (116) corresponds to γ phase Fe₂O₃ (Hei et al., 2014) whereas remaining (200) and (220) corresponds to face centred cubic phase of NiO (Yan et al., 2014). The presence of Bragg's reflections corresponding to BaO, Fe₂O₃ and NiO clearly confirms the formation of BFNONC. There are no signs of any further peaks relating to other impurities which confirms the purity of the sample. The average crystallite size of BFNONC was determined by using Debye-Scherrer's equation and the Williamson-Hall (W-h) plot method (Fig. 3b) and is explained in our previous work (Vidya et al., 2015a; Gurushantha et al.,

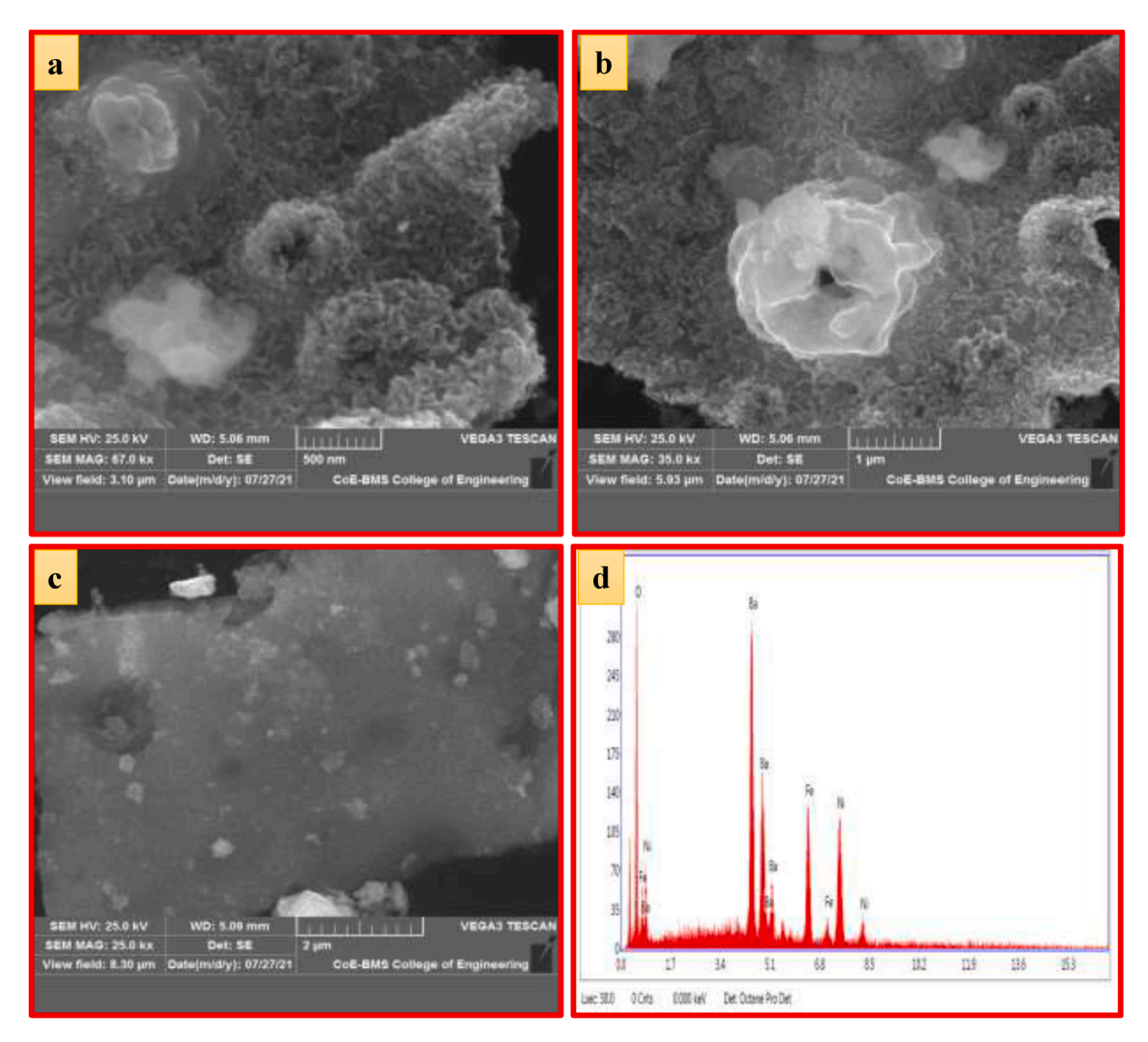


Fig. 4. SEM image (a-c) at different magnifications and EDAX spectra (d) of BFNONC.

Table 1
Weight fraction and atomic fraction of synthesized nanocomposite obtained from the EDAX measurement

Element	Weight %	Atomic %
ОК	19.05	56.22
Ba L	47.62	16.38
Fe K	14.45	12.21
Ni K	18.88	15.19

2016; Malleshappa et al., 2016). In Debye-Scherrer's equation crystallite size was calculated using high intense (200) peak and was found to be 30 nm whereas in W–h plot method the crystallite size was found to be 32 nm. When compared to Debye Scherrer's equation, the crystallite size calculated from W–h plots was somewhat larger. The slight differences in the numbers were owing to the fact that in Scherrer's calculation, the strain component was believed to be negligible and the observed broadening of the diffraction peak was attributed only to grain size reduction (Reddy et al., 2021; Prasanna Kumar et al., 2015). The other structural parameters such as dislocation density, strain and stacking fault was calculated using the relation given in vidya et al. (Vidya et al., 2015b), which was found to be $1.1 \times 10^{15} \, \text{lin m}^{-2}$, 2.22×10^{-3} and 3.352×10^{-3} respectively.

4.2. Morphological analysis of BFNONC

SEM and EDAX analysis can be used to determine the morphology of the surface, distribution of particles and the elemental composition of the synthesized NCs.

Fig. 4a-c shows the SEM image of BFNONC at different magnification. Since it is a NCs which is the combination of BaO, Fe₂O₃ and NiO oxides, no such regular or irregular shaped nanoparticles are observed. The surface morphology is made up of large number of scaly natured agglomerated flakes which looks as they are placed one above the other as shown in Fig. 4(a and b). In addition to agglomerated flakes, few Cylinder cone volcanoes like voids are observed which is the characteristic of the combustion method. When the pressure is released, the gases explode, like soda spewing out of a bottle can that you shook up and opened suddenly. These type of nanoflakes are highly friable which facilitates easy grinding to obtain finer particles. At higher magnification, this NCs looks in the form of Ice block (Fig. 4c). The existence of Ba, O, Fe and Ni atoms in the host matrix, as well as the lack of other contaminants, is confirmed by energy dispersive X-ray spectroscopy analysis (EDAX) (Fig. 4d). The atomic percentages and weight percentages of the elements present in the synthesized BFNONC are listed in the Table 1. Generally, there is a large influence of particle size distribution on radiation shielding ability. The uniform and small sized particles increases the interaction of X-ray/gamma ray with nanoparticles which inturn increases the absorption (Li et al., 2017). The Particle size distribution of synthesized nano particles as shown in Fig. 5.

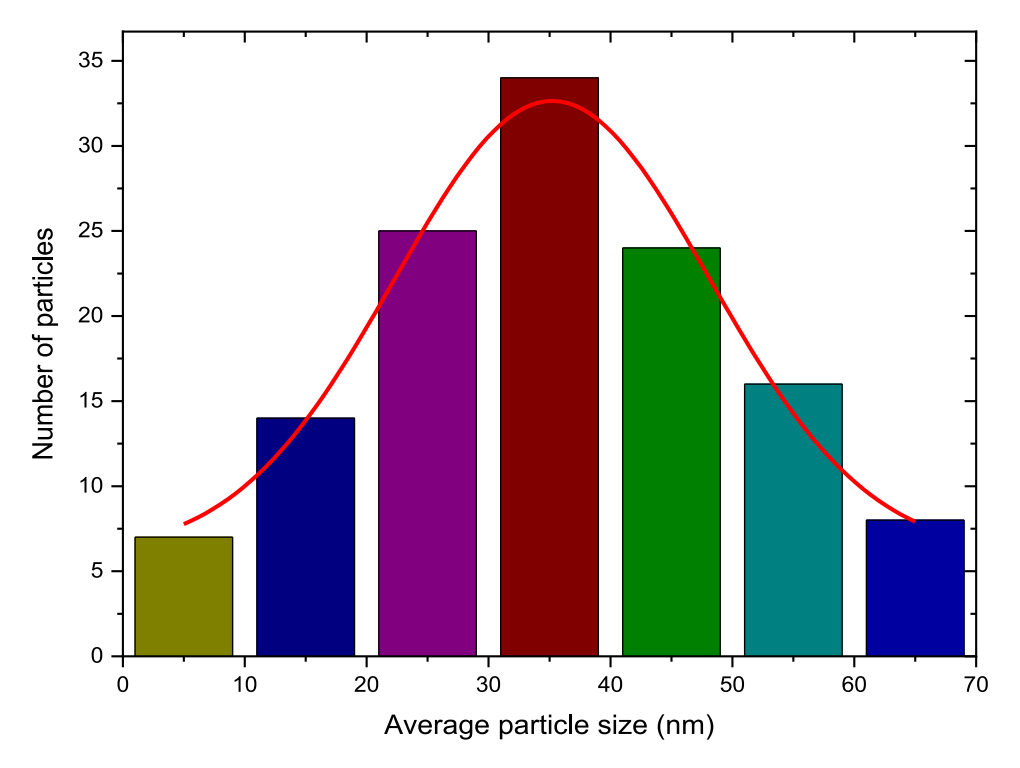


Fig. 5. Particle size distribution.

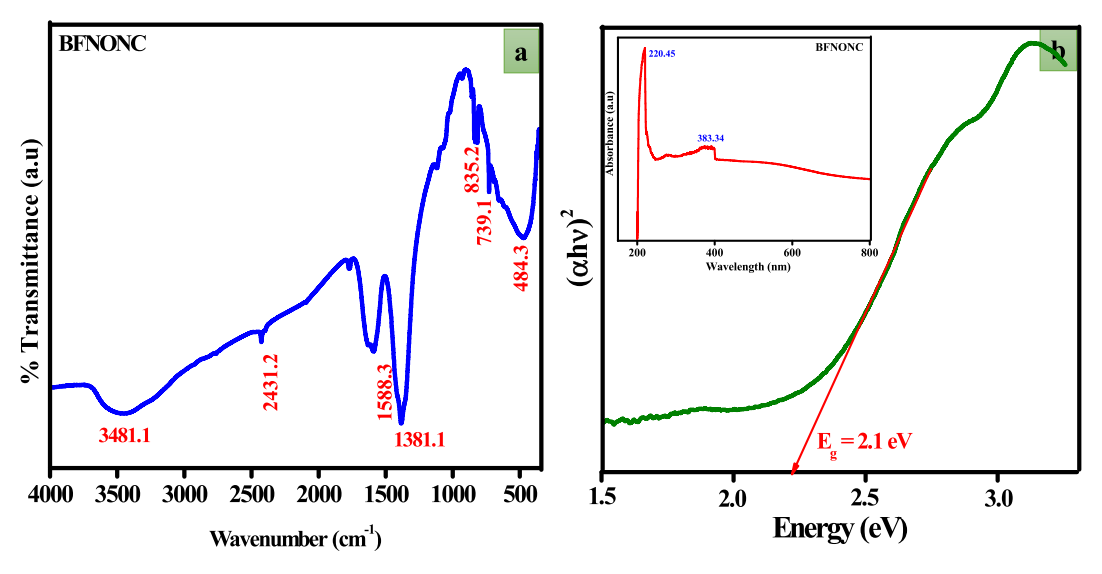


Fig. 6. (a) FTIR spectra and (b) Wood and Tauc's plot (Inset: UV-Visible absorption spectra) of BFNONC.

4.3. FTIR analysis of BFNONC

The absorption of electromagnetic radiation with wavelengths in the mid-infrared range ($4000-400~\text{cm}^{-1}$) is measured using the FTIR technique. The dipole moment of a molecule changes when it absorbs infrared radiation (IR), and the molecule becomes IR active. Fig. 6a exhibits FTIR spectra for BFNONC calcined at 500°C for 3 h in the range $400-4000~\text{cm}^{-1}$. The sharp IR peaks are observed at 484.3, 739.1, 835.2, 1381.1, 1588.3, 2431.2, $3481.1~\text{cm}^{-1}$. The peaks observed at $484.3~\text{cm}^{-1}$ attributed to the metallic (M) - oxygen (M = Ba, Fe and Ni) bond vibration (Qin et al., 2011). An absorption band observed at $3481.2~\text{cm}^{-1}$ corresponds to the presence of O–H group. The less intense sharp absorption band observed at $2431.2~\text{cm}^{-1}$ corresponds to traces of absorbed atmospheric CO₂ (Drmosh et al., 2010). The bands observed at

739.1 and 835.2 cm⁻¹ correspond to the deformation of vibration of C–H group. Furthermore, in the range from 1300 to 1700 cm⁻¹ (1381.1 and 1588.3 cm⁻¹) corresponds to the presence of carboxyl groups related to Urea was noted.

4.4. UV-visible spectroscopic analysis and direct energy band gap calculation of BFNONC

Another common characterization method for nanoscale materials is UV–Visible spectroscopy, which is relatively simple and low-cost. It compares the amount of light reflected or absorbed from a sample to the amount of light reflected or absorbed from a reference material. The optical properties are sensitive to size, shape, concentration, agglomeration state and refractive index near the nanoparticle surface, which

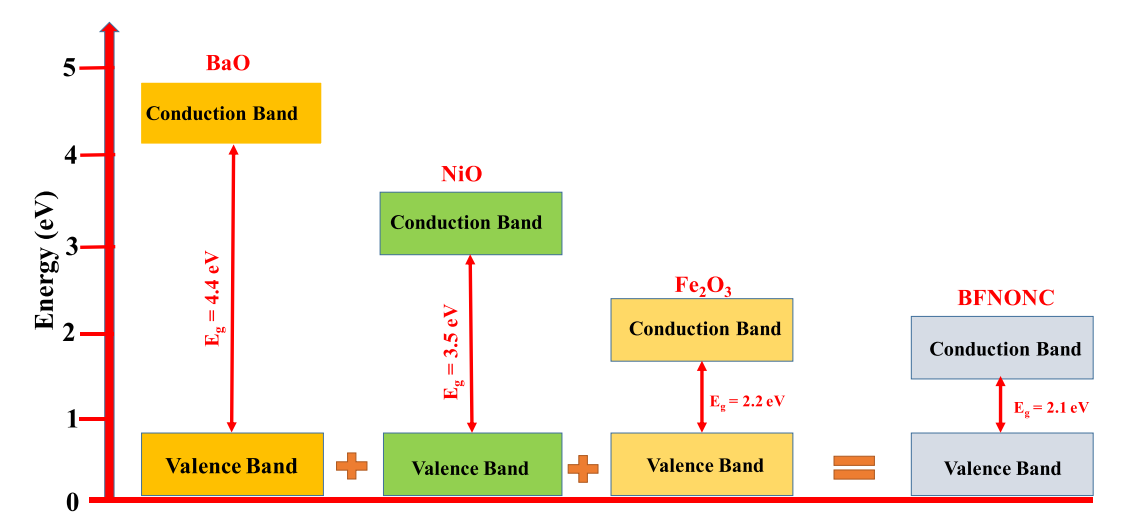


Fig. 7. Energy band diagram.

 Table 2

 Comparison of measured mass attenuation co-efficient with that of NIST data.

Energy (MeV)	$(\mu/\rho)_{expt}$ cm ² /g	$(\mu/\rho)_{[73]} cm^2/g$	% error
0.276	0.22	0.177 74	19.207 8
0.365	0.10	0.122 74	22.744 2
0.511	0.088	0.092 02	4.570 8
0.662	0.075	0.076 76	2.358 4
1.173	0.054	0.054 85	1.583 9
0.511	0.051	0.052 49	2.925 7

makes UV–Visible spectroscopy an important tool to identify, characterize and investigate these materials. Inset of Fig. 6b shows the UV–Visible absorption spectra of BFNONC in the wavelength range 200–800 nm. Absorption was strong across a wide wavelength range, from ultraviolet to visible light, with an absorption tail extending into the infrared. The spectra shows prominent absorption band with maximum at 220.45 and 383.34 nm. The absorption band appeared at 220.45 nm was assigned to Oxygen to metal ions charge transfer transitions. The electronegativity of the oxygen atoms bonded to the metal centres determines the position of the maximum of this band (Dellarocca et al., 2001). The other less intense peak observed at 383.34 nm was expected to arise from transitions involving extrinsic states such as surface states/defects/impurities (Das et al., 2013; Cao et al., 2004).

Wood and Tauc's relation was used to estimate the direct energy

band gap (Vidya et al., 2015c). The energy gap is determined by plotting $(\alpha h \nu)^2$ versus $h \nu$ and finding the intercept on the $h \nu$ axis by extrapolating the plot to $(\alpha h\nu)^2 = 0$. Fig. 6b shows the Wood and Tauc's plot from which the direct band gap is obtained and was found to be 2.1 eV. Fig. 7 shows the pictorial representation of energy band diagram. As we observed from the Fig. 7, as per the literature, the energy band gap of BaO, Fe₂O₃ and NiO lies at 4.4, 2.2 and 3.5 eV respectively (Yang et al., 2016; Mallick and Dash, 2013; Irwin et al., 2008). The energy band gap of BFNONC lies at 2.1 eV. The amount of bandgap has a significant effect on the refractive index and transparency effect of the material. As per the literature, high refractive index and less transparency is observed for the nanomaterials with less energy bandgap. Compared to individual oxide materials, the synthesized NCs has less energy bandgap. As a result less transparency and absorption is more (Khodadadi and Taherian, 2020; Peymanfar et al., 2020). From the literature (Zaki, 2008; El-Shahawy, 1997; Saad et al., 2005; Sharma et al., 2007), it is observed that there is a effect on the x-ray/gamma absorption properties and optical direct energy band gap. the absorption of gamma rays/X-rays is larger for the material with smaller optical direct energy band gap (Zaki, 2008; El-Shahawy, 1997; Saad et al., 2005; Sharma et al., 2007). In radiation shielding, absorption of X-rays/Gamma rays by a material plays an important role. In the present study, compared to Barium Oxide, Iron Oxide and Nickel Oxide, the obtained nanocomposite possesses less energy band gap. As a result, the absorption of X-rays/gamma rays is more in BFNONC compared to that of individual oxide matrices and

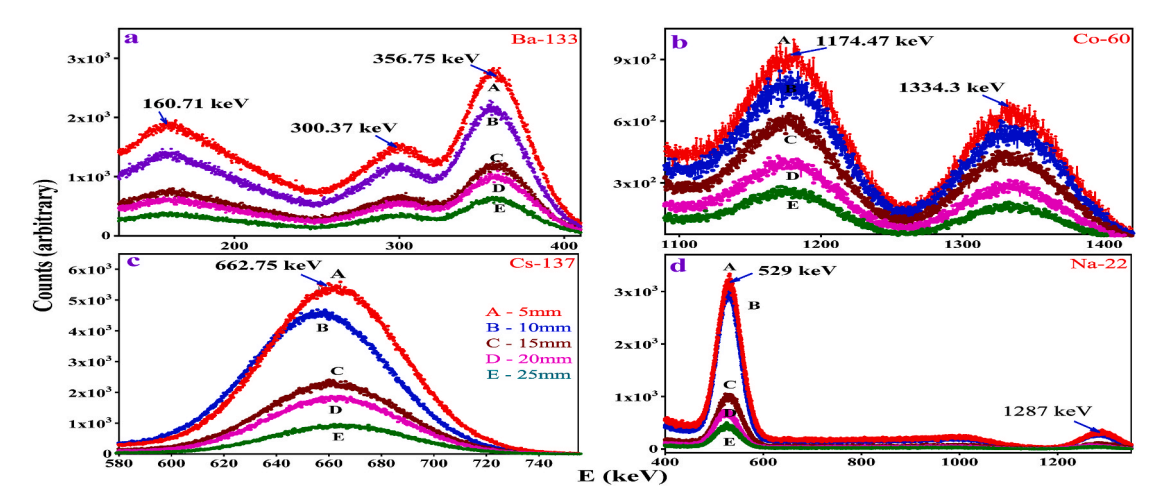


Fig. 8. Measured Gamma ray spectra in BFNONC NPs using different sources such as Ba-133, Co-60, Cs-137 and Na-22 for different thickness.

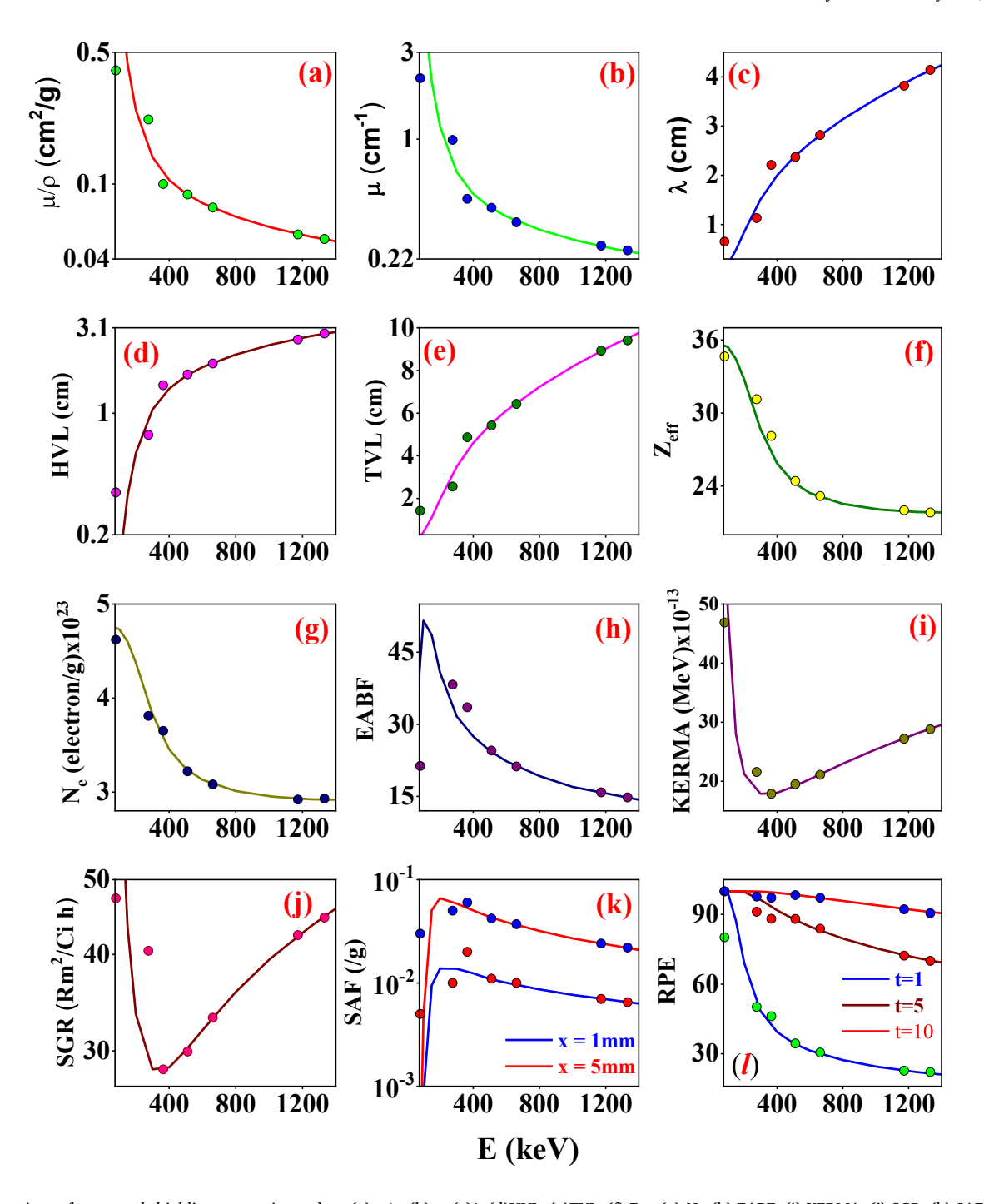


Fig. 9. Comparison of measured shielding properties such as (a) μ/ρ , (b) μ , (c) λ , (d)HVL, (e)TVL, (f) Z_{eff} , (g) N_e , (h) EABF, (i) KERMA, (j) SGR, (k) SAF and (l) RPE with that of the theoretical values in the energy range 0.081–1.332 MeV.

hence shielding property also. Previous researcher (Zaki, 2008) also observed a decrease in the optical energy gap with increasing the gamma absorbed dose.

4.5. Analysis of measured X-ray/gamma ray shielding properties of BFNONC

Gamma sources such as 22 Na (0.511, 0.081 MeV), 57 Co (1.173, 1.332 MeV), 137 Cs (0.6615 MeV) and (133 Ba (0.276, 0.356 MeV) are used to check the weld defects in industries, medical field, communication system, nuclear reactors, material science, and student research facilities (Boukhris et al., 2021). Thus there is a need to develop the shielding

materials for these gamma radiations. The measured mass attenuation co-efficient compared with the NIST data base and this Comparison is also shown in the Table 2. In this table, relative difference between the theoretical and experimental values also presented.

Fig. 8(a–d) shows the graphical representation of measured gamma ray spectra using different sources such as 137 Cs (0.6615 MeV), 60 Co (1.173 and 1.332 MeV), 22 Na (0.511, 0.081 MeV) and 133 Ba (0.276 and 0.356 MeV) for different thickness 5, 10, 15, 20 & 25 mm of BFNONC. The nature of the gamma ray spectrum is different for different source. For 133 Ba gamma ray source, three high intensity peaks are observed at 160.71, 300.37 and 356.75 keV. For 60 Co source, the gamma ray spectrum consists two peaks at 1174.47 and 1334.3 keV, whereas for 137 Cs

Table 3
Comparison of measured X-ray/gamma shielding properties with that of the theory.

SOURCE		⁵⁶ Ba			²² Na	¹³⁷ Cs	⁶⁰ Co	
ENERGY (MeV)		0.081	0.276	0.356	0.511	0.661 5	1.173	1.332
$\mu/\rho \ (cm^2 \ g^{-1})$	Th	2.01	0.17	0.11	0.09	0.07	0.06	0.04
	Ex	0.40 ± 0.02	0.22 ± 0.01	0.10 ± 0.01	0.09 ± 0.00	0.08 ± 0.00	0.05 ± 0.00	0.05 ± 0.00
μ (cm ⁻¹)	Th	9.45	0.78	0.55	0.41	0.37	0.26	0.25
	Ex	2.16 ± 0.11	0.99 ± 0.05	0.47 ± 0.02	0.42 ± 0.02	0.35 ± 0.02	0.26 ± 0.01	0.25 ± 0.01
HVL (cm)	Th	0.13	1.35	1.82	2.39	2.79	3.88	4.14
	Ex	0.65 ± 0.03	1.13 ± 0.06	2.21 ± 0.11	2.37 ± 0.12	2.82 ± 0.14	3.82 ± 0.19	4.14 ± 0.21
TVL (cm)	Th	0.08	0.93	1.28	1.67	1.94	2.71	2.86
	Ex	0.35 ± 0.02	0.75 ± 0.04	1.45 ± 0.07	1.67 ± 0.08	1.93 ± 0.10	2.65 ± 0.13	2.87 ± 0.14
λ (cm)	Th	0.26	3.13	4.21	5.49	6.47	8.89	9.52
	Ex	1.42 ± 0.07	2.56 ± 0.13	4.87 ± 0.24	5.42 ± 0.27	6.43 ± 0.32	8.93 ± 0.45	9.41 ± 0.47
Z_{eff}	Th	35.57	29.67	26.84	24.26	23.21	21.91	21.87
	Ex	34.65 ± 1.73	31.13 ± 1.56	28.11 ± 1.41	24.41 ± 1.22	23.18 ± 1.16	22.01 ± 1.10	21.82 ± 1.09
$N_e \times 10^{23}$	Th	4.78	3.98	3.58	3.18	3.15	3.00	2.96
(electrons g^{-1})	Ex	4.62 ± 0.23	3.81 ± 0.19	3.65 ± 0.18	3.22 ± 0.16	3.08 ± 0.15	2.92 ± 0.15	2.93 ± 0.15
EABF	Th	43.58	33.88	28.96	24.36	21.39	15.88	14.89
(mfp = 10 mm)	Ex	21.33 ± 1.07	38.23 ± 1.91	33.54 ± 1.68	24.52 ± 1.23	21.23 ± 1.06	15.84 ± 0.79	14.78 ± 0.74
KERMA	Th	7.01	1.67	1.67	1.67	2.11	2.63	2.63
$(\text{MeV})\times 10^{-13}$	Ex	4.69 ± 0.23	2.16 ± 0.11	$\textbf{1.79} \pm \textbf{0.09}$	1.95 ± 0.10	2.11 ± 0.11	$\textbf{2.72} \pm \textbf{0.14}$	2.88 ± 0.14
SGR	Th	99.65	29.73	28.39	30.17	33.29	42.26	44.94
$(Rm^2 Ci^{-1} h)$	Ex	47.29 ± 2.36	40.44 ± 2.02	28.39 ± 1.42	29.94 ± 1.50	33.12 ± 1.66	42.36 ± 2.12	44.65 ± 2.23
SAF (g^{-1})	Th $(x = 1 mm)$	3.83×10^{-4}	0.01	0.01	0.01	0.01	0.01	0.01
(mfp = 10 mm)	Ex $(x = 1 \text{ mm})$	$(3.00 \pm 0.15) \times 10^{-2}$	0.01 ± 0	0.02 ± 0	0.01 ± 0	0.01 ± 0	0.01 ± 0	0.05 ± 0
(IIII)	Th $(x = 5 \text{ mm})$	3.83×10^{-4}	0.06	0.05	0.04	0.04	0.02	0.02
	Ex (x = 5 mm)	$(3.00 \pm 0.15) \times 10^{-2}$	0.05 ± 0	0.06 ± 0	0.04 ± 0	0.04 ± 0	0.02 ± 0	0.02 ± 0
RPE	Th $(t = 1)$	99.75	53.89	42.55	34.29	29.94	22.81	21.65
	$\operatorname{Ex}(t=1)$	80.13 ± 4.01	50.18 ± 2.51	46.17 ± 2.31	34.45 ± 1.72	30.54 ± 1.53	22.66 ± 1.13	22.13 ± 1.11
	Th $(t = 5)$	99.75	96.97	93.29	87.59	83.24	72.45	70.21
	Ex (t = 5)	99.87 ± 4.99	91.19 ± 4.56	88.12 ± 4.41	88.07 ± 4.40	83.83 ± 4.19	72.28 ± 3.61	70.03 ± 3.50
	Th $(t = 3)$	99.75	99.89	99.49	98.54	97.11	92.53	91.02
	Ex (t = 10)	99.99 ± 5.00	97.67 ± 4.88	97.15 ± 4.86	98.29 ± 4.91	97.11 97.18 ± 4.86	92.21 ± 4.61	90.55 ± 4.53
	(t — 10)	77.77 ± 0.00	27.07 ± 1.00	>7.10 ± 1.00	70.27 ± 1.71	>7.10 ± 1.00	>2.21 ± 1.01	70.00 ± 1.00

source, single high intense peak is observed at $662.75~{\rm keV}$. Two high intense peaks are observed at $528~{\rm and}~1287~{\rm keV}$ for $^{22}{\rm Na}$ source. As the thickness of BFNONC increases from 5, 10, 15, 20 & 25 mm, the nature of the gamma ray spectrum remains unaltered except the variation in intensity. The intensity of the peak increases with decrease in the thickness of the BFNONC. From the experimental data, the MAC values of BFNONC at different energies are extracted.

Compared to bulk materials Nanoparticles significantly improve mechanical properties and also shielding to certain extent (Tyagi et al., 2021). One of the radiation shielding parameter MAC is an important parameter for characterizing the penetration and diffusion of X-ray/gamma rays in materials. Higher MACs means better shielding ability of a material. This radiation shielding property depends on the nature of the material, particle size distribution, energy band gap etc. All these properties of nanoparticles made them to show better shielding property over the bulk material. Fig. 9(a-l) and Table 3 gives the comparison of measured shielding properties such as μ/ρ , μ , HVL, TVL, λ , Z_{eff} , N_e , EABF, KERMA, SGR, SAF and RPE with that of the theoretical values in the energy range 0.081-1.332 MeV. In general, the theoretical values are based on the Hubbel data (Hubbell and Seltzer, 1995; Berger, 2010; Gerward et al., 2001) which is calculated when there is an interaction of X-ray/gamma -ray with the micrometer sized atoms/particles. It is clearly observed from Table 3 that above 356 keV X-ray/gamma ray interaction energy, the measured shielding parameters agrees well with the theoretical value whereas slight deviation is observed below 356 keV. The measured shielding parameters agrees well with the theory above 356 keV X-ray/gamma-ray interaction. Since the crystals/particles are in nanorange, the atom/particle size plays a very important role in this deviation. Furthermore, an accurate theory is necessary to explain the X-ray/gamma ray interaction with the NCs.

4.6. Summary

In summary, BFNONC was synthesized for the first time by using economical solution combustion method using urea as a fuel and calcined at 500° C. The synthesized sample was characterized by different techniques. The PXRD pattern confirms the existence of (hkl) planes corresponding tetragonal phase of BaO, γ phase Fe₂O₃ and cubic NiO which inturn confirms the formation of BFNO nanocomposite. The average crystallite size obtained from the Scherrer's equation and W-H plot method was found to be 30 and 32 nm respectively. The surface morphology made up large number of piled flakes. The optical energy direct band gap obtained from Wood and Tauc's plot was found to be 2.1 eV. The detailed analysis of measured X-ray/gamma ray shielding properties of BFNONC was measured in the energy range 0.081-1.332 MeV. Above 356 keV X-ray/gamma ray interaction energy, the measured shielding parameters agrees well with the theoretical values whereas deviation is observed below 356 keV. This variation is mainly due to the impact of crystallite/particle size of the target medium on the X-ray/gamma ray interaction energy. The synthesized BFNONC finds application in the shielding of for X-ray/gamma ray.

Author contribution statement

K.V. Sathish, Y. S. Vidya, H. C. Manjunatha, K. N. Sridhar, L. Seenappa, B. Chinnappa Reddy, S. Alfred Cecil Raj and P. S. Damodara Gupta conceived and planned the experiments. K.V. Sathish, Y. S. Vidya, H. C. Manjunatha, K. N. Sridhar, L. Seenappa, B. Chinnappa Reddy, and P. S. Damodara Gupta designed the model and the computational framework and analyzed the data. K.V. Sathish, H. C. Manjunatha, K. N. Sridhar, L. Seenappa, B. Chinnappa Reddy, S. Alfred Cecil Raj and P. S. Damodara Gupta synthesised and characterized the material. H. C. Manjunatha, L. Seenappa, B. Chinnappa Reddy and S. Alfred Cecil Raj

conducted attenuation measurements with the help of other authors. Y. S. Vidya and H. C. Manjunatha wrote the manuscript with the help of all authors

Declaration of competing interest

The authors declare that they have no known competing financial interests or personal relationships that could have appeared to influence the work reported in this paper.

References

- Akkurt, I., Basyigit, Celalettin, Kilincarslan, S., Mavi, B., 2005. The shielding of γ-rays by concretes produced with barite. Prog. Nucl. Energy 46 (1), 1–11.
- Akman, F., Kaçal, M.R., Sayyed, M.I., Karataş, H.A., 2019. Study of gamma radiation attenuation properties of some selected ternary alloys. J. Alloys Compd. 782, 315–322.
- Ansari, Manauwar Ali, Jahan, Nusrat, 2021. Structural and optical properties of bao nanoparticles synthesized by facile co-precipitation method. Mater. Highlights 2 (1–2), 23–28.
- Ates, Burhan, Koytepe, Suleyman, Ulu, Ahmet, Gurses, Canbolat, Thakur, Vijay Kumar, 2020. Chemistry, structures, and advanced applications of nanocomposites from biorenewable resources. Chem. Rev. 120 (17), 9304–9362.
- Azizi, A., Yourdkhani, A., Koohestani, H., Sadrnezhaad, S.K., Asmatulu, R., 2011. Fe50co50 nanoparticles via self-propagating high-temperature synthesis during milling. Powder Technol. 208 (3), 623–627.
- Barrera, Gabriele, Tiberto, Paola, Allia, Paolo, Bonelli, Barbara, Esposito, Serena, Marocco, Antonello, Pansini, Michele, Leterrier, Yves, 2019. Magnetic properties of nanocomposites. Appl. Sci. 9 (2), 212.
- Berger, M.J.O.K., 2010. Xcom: photon cross sections database. http://www.nist.gov/pml/data/xcom/index.cfm.
- Boukhris, Imed, Kebaili, Imen, Al-Buriahi, M.S., Sayyed, M.I., 2021. Radiation shielding properties of tellurite-lead-tungsten glasses against gamma and beta radiations. J. Non-Cryst. Solids 551, 120430.
- Calvo, Florent, 2020. Nanoalloys: from Fundamentals to Emergent Applications. Elsevier. Cao, H.Q., Qiu, X.Q., Luo, Bin, Liang, Yu, Zhang, Y.H., Tan, R.Q., Zhao, M.J., Zhu, Q.M., 2004. Synthesis and room-temperature ultraviolet photoluminescence properties of zirconia nanowires. Adv. Funct. Mater. 14 (3), 243–246.
- Cui, B.Z., Han, K., Garmestani, H., Su, J.H., Schneider-Muntau, H.J., Liu, J.P., 2005. Enhancement of exchange coupling and hard magnetic properties in nanocomposites by magnetic annealing. Acta Mater. 53 (15), 4155–4161.
- Das, Subrata, Yang, Che-Yuan, Lu, Chung-Hsin, 2013. Structural and optical properties of tunable warm-white light-emitting zro 2: Dy3+–eu 3+ nanocrystals. J. Am. Geram. Soc. 96 (5), 1602–1609.
- De Almeida, J.S., Ahuja, R., 2006. Electronic and optical properties of ru o 2 and ir o 2. Phys. Rev. B 73 (16), 165102.
- Dellarocca, V., Marchese, L., Pena, M.L., Rey, F., Corma, A., Coluccia, Salvatore, 2001. Surface properties of mesoporous ti-mcm-48 and their modifications produced by silylation. In: Oxide-based Systems at the Crossroads of Chemistry. Second International Workshop, vol. 140, pp. 209–220.
- Tishkevich, D.I., Grabchikov, S.S., Grabchikova, E.A., Vasin, D.S., Lastovskiy, S.B., Yakushevich, A.S., Vinnik, D.A., Zubar, T.I., Kalagin, I.V., Mitrofanov, S.V., et al., 2020. Modeling of paths and energy losses of high-energy ions in single-layered and multilayered materials. In: IOP Conference Series: Materials Science and Engineering, vol. 848. IOP Publishing, 012089.
- Drmosh, Q.A., Gondal, M.A., Yamani, Z.H., Saleh, T.A., 2010. Spectroscopic characterization approach to study surfactants effect on zno2 nanoparticles synthesis by laser ablation process. Appl. Surf. Sci. 256 (14), 4661–4666.
- El-Gendy, Ahmed A., Hampel, Silke, Büchner, Bernd, Klingeler, Rüdiger, 2016. Tuneable magnetic properties of carbon-shielded nipt-nanoalloys. RSC Adv. 6 (57), 52427–52433.
- El-Shahawy, Magda A., 1997. Spectral changes of cr-39 induced by irradiation and heat treatment. Polym. Degrad. Stabil. 57 (2), 157–161.
- Feng, Jicheng, Geutjens, Ruben, Thang, Nguyen V., Li, Junjie, Guo, Xiaoai, keri, Albert, Basak, Shibabrata, Galbacs, Gabor, Biskos, George, Nirschl, Hermann, et al., 2018. Magnetic phase transition in spark-produced ternary lafesi nanoalloys. ACS Appl. Mater. Interfaces 10 (7), 6073–6078.
- Ganguly, Sayan, Kanovsky, Naftali, Das, Poushali, Gedanken, Aharon, Margel, Shlomo, 2021. Photopolymerized thin coating of polypyrrole/graphene nanofiber/iron oxide onto nonpolar plastic for flexible electromagnetic radiation shielding, strain sensing, and non-contact heating applications. Adv. Mater. Interfac. 8 (23), 2101255.
- Gerward, L., Guilbert, N., Jensen, K Bjørn, Levring, H., 2001. X-ray absorption in matter. reengineering xcom. Radiat. Phys. Chem. 60 (1–2), 23–24.
- Gurushantha, K., Anantharaju, K.S., Sharma, S.C., Nagaswarupa, H.P., Prashantha, S.C., Vishnu Mahesh, K.R., Renuka, L., Vidya, Y.S., Nagabhushana, H., 2016. Biomediated sm doped nano cubic zirconia: photoluminescent, judd-ofelt analysis, electrochemical impedance spectroscopy and photocatalytic performance. J. Alloys Compd. 685, 761–773.
- Hamad, R.M., Mhareb, M.H.A., Alajerami, Y.S., Sayyed, M.I., Saleh, Gameel, Hamad, M Kh, Ziq, KhA., 2021. A comprehensive ionizing radiation shielding study of fexse0. 5te0. 5 alloys with various iron concentrations. J. Alloys Compd. 858, 157636.

- Hei, Shengtao, Jin, Yan, Zhang, Fumin, 2014. Fabrication of γ-fe2o3 nanoparticles by solid-state thermolysis of a metal-organic framework, mil-100 (fe), for heavy metal ions removal. J. Chem. 2014.
- Hu, Yang, Jensen, Jens Oluf, Cleemann, Lars Nilausen, Brandes, Benedikt Axel, Li, Qingfeng, 2019. Synthesis of pt-rare earth metal nanoalloys. J. Am. Chem. Soc. 142 (2), 953–961.
- Hubbell, John H., Seltzer, Stephen M., 1995. Tables of X-Ray Mass Attenuation
 Coefficients and Mass Energy-Absorption Coefficients 1 Kev to 20 Mev for Elements
 Z= 1 to 92 and 48 Additional Substances of Dosimetric Interest.
- Irwin, Michael D., Buchholz, D Bruce, Hains, Alexander W., Chang, Robert PH., Marks, Tobin J., 2008. p-type semiconducting nickel oxide as an efficiencyenhancing anode interfacial layer in polymer bulk-heterojunction solar cells. Proc. Natl. Acad. Sci. Unit. States Am. 105 (8), 2783–2787.
- Jing, Panpan, Du, Jinlu, Wang, Jianbo, Zhu, Zentai, Feng, Hongmei, Liu, Zhenlin, Liu, Qingfang, 2016. Synthesis, microstructure and magnetic performance of feco alloy nanoribbons. Mater. Lett. 162, 176–179.
- Kamil, Sarah M., Abul-Magd, Ashraf A., El-Gammal, W., Saudi, H.A., 2022. Impact of the Structural Changes on the Attenuation Properties of Some Nickel Borate-Based Glasses Containing Lead and Lanthanum Cations for Gamma-Ray Shielding Applications.
- Karipoth, Prakash, Thirumurugan, Arun, Velaga, Srihari, Greneche, Jean-Marc, Joseyphus, R Justin, 2016. Magnetic properties of feco alloy nanoparticles synthesized through instant chemical reduction. J. Appl. Phys. 120 (12), 123906.
- Kaur, Parminder, Singh, K.J., Thakur, Sonika, Singh, Prabhjot, Bajwa, B.S., 2019. Investigation of bismuth borate glass system modified with barium for structural and gamma-ray shielding properties. Spectrochim. Acta Mol. Biomol. Spectrosc. 206, 367–377.
- Khodadadi, Abolfazl, Taherian, Reza, 2020. Investigation on the radiation shielding properties of lead silicate glasses modified by zno and bao. Mater. Chem. Phys. 251, 123136.
- Levet, Aytaç, Kavaz, Esra, Özdemir, Yüksel, 2020. An experimental study on the investigation of nuclear radiation shielding characteristics in iron-boron alloys. J. Alloys Compd. 819, 152946.
- Lewin, Menachem, Pearce, E.M., Levon, Kalle, Mey-Marom, Abraham, Zammarano, Mauro, Wilkie, Charles A., Jang, Bok Nam, 2006. Nanocomposites at elevated temperatures: migration and structural changes. Polym. Adv. Technol. 17 (4), 226–234.
- Li, Ran, Gu, Yizhuo, Wang, Yidong, Yang, Zhongjia, Li, Min, Zhang, Zuoguang, 2017. Effect of particle size on gamma radiation shielding property of gadolinium oxide dispersed epoxy resin matrix composite. Mater. Res. Express 4 (3), 035035.
- Malleshappa, J., Nagabhushana, H., Prasad, B Daruka, Sharma, S.C., Vidya, Y.S., Anantharaju, K.S., 2016. Structural, photoluminescence and thermoluminescence properties of ceo2 nanoparticles. Optik 127 (2), 855–861.
- Mallick, P., Dash, B.N., 2013. X-ray diffraction and uv-visible characterizations of α-fe2o3 nanoparticles annealed at different temperature. Nanosci. Nanotechnol. 3 (5), 130–134.
- Manjunatha, H.C., 2014. A study of photon interaction parameters in lung tissue substitutes. J. Med. Phys./Assoc. Med. Phys. India 39 (2), 112.
- Manjunatha, H.C., 2015. Influence of gamma irradiation on conductivity of yba2cu3o7. Radiat. Phys. Chem. 113, 24–27.
- Manjunatha, H.C., 2017. A study of gamma attenuation parameters in poly methyl methacrylate and kapton. Radiat. Phys. Chem. 137, 254–259.
- Manjunatha, H.C., Rudraswamy, B., 2013. Study of effective atomic number and electron density for tissues from human organs in the energy range of 1 kev–100 gev. Health Phys. 104 (2), 158–162.
- Manjunatha, H.C., Chandrika, B.M., Seenappa, L., Hanumantharayappa, Chikka, 2016. Study of gamma attenuation properties of tungsten copper alloys. Int. J. Nucl. Energy Sci. Technol. 10 (4), 356–368.
- Manjunatha, H.C., Seenappa, L., Sridhar, K.N., Hanumantharayappa, Chikka, 2017. Study of gamma/x-ray interaction in some diodes and transistors. Int. J. Nucl. Energy Sci. Technol. 11 (4), 377–389.
- Manjunatha, H.C., Sathish, K.V., Seenappa, L., Gupta, Damodara, Alfred Cecil Raj, S., 2019. A study of x-ray, gamma and neutron shielding parameters in si-alloys. Radiat. Phys. Chem. 165, 108414.
- Manohara, S.R., Hanagodimath, S.M., Gerward, Leif, 2009. Photon interaction and energy absorption in glass: a transparent gamma ray shield. J. Nucl. Mater. 393 (3), 465–472.
- Niu, Fang-xu, Wang, Yan-xiang, Ma, Lian-ru, Xie, Zi-yi, Wang, Yao-yao, Wang, Chengguo, Mao, Yan-peng, 2019. Achieving enhanced dielectric property via growing coni-p nano-alloys on sic nanowires with 3d conductive network. J. Alloys Compd. 778, 933–941.
- Novakova, A.A., Lanchinskaya, V Yu, Volkov, A.V., Gendler, T.S., Kiseleva, T Yu, Moskvina, M.A., Zezin, S.B., 2003. Magnetic properties of polymer nanocomposites containing iron oxide nanoparticles. J. Magn. Magn Mater. 258, 354–357.
- Omanović-Mikličanin, Enisa, Badnjević, Almir, Kazlagić, Anera, Hajlovac, Muhamed, 2020. Nanocomposites: a brief review. Health Technol. 10 (1), 51–59.
- Peymanfar, Reza, Yektaei, Mona, Javanshir, Shahrzad, Selseleh-Zakerin, Elnaz, 2020. Regulating the energy band-gap, uv-vis light absorption, electrical conductivity, microwave absorption, and electromagnetic shielding effectiveness by modulating doping agent. Polymer 209, 122981.
- Phong, P.T., Phong, L.T.H., Dai, N.V., Nam, D.N.H., Phuc, N.X., et al., 2015. Structural and magnetic properties of mechanically alloyed fe50co50 nanoparticles. J. Alloys Compd. 640, 34–38.
- Prasanna Kumar, J.B., Ramgopal, G., Vidya, Y.S., Anantharaju, K.S., Prasad, B Daruka, Sharma, S.C., Prashantha, S.C., Nagaswarupa, H.P., Kavyashree, D., Nagabhushana, H., 2015. Green synthesis of y2o3: Dy3+ nanophosphor with

- enhanced photocatalytic activity. Spectrochim. Acta Mol. Biomol. Spectrosc. 149, 687–697.
- Qin, Wenqing, Yang, Congren, Yi, Ran, Gao, Guanhua, 2011. Hydrothermal synthesis and characterization of single-crystalline [alpha]-fe2o3 nanocubes. J. Nanomater.
- Reddy, B Chinnappa, Manjunatha, H.C., Vidya, Y.S., Sridhar, K.N., Pasha, U Mahaboob, Seenappa, L., Mahendrakumar, C., Sadashivamurthy, B., Dhananjaya, N., Sankarshan, B.M., et al., 2021. Synthesis and characterization of multi functional nickel ferrite nano-particles for x-ray/gamma radiation shielding, display and antimicrobial applications. J. Phys. Chem. Solid. 110260.
- Rudraswamy, B., Dhananjaya, N., Manjunatha, H.C., 2010. Measurement of absorbed dose rate of gamma radiation for lead compounds. Nucl. Instrum. Methods Phys. Res. Sect. A Accel. Spectrom. Detect. Assoc. Equip. 619 (1–3), 171–173.
- Saad, A.F., Atwa, S.T., Yokota, R., Fujii, M., 2005. Radiation-induced modifications on spectroscopic and thermal properties of cr-39 and sr-90 nuclear track detectors. Radiat. Meas. 40 (2–6), 780–784.
- Sayyed, M.I., Askin, Ali, Zaid, M.H.M., Olukotun, S.F., Khandaker, Mayeen Uddin, Tishkevich, Daria I., Bradley, D.A., 2021. Radiation shielding and mechanical properties of bi2o3-na2o-tio2-zno-teo2 glass system. Radiat. Phys. Chem. 186, 109556.
- Seenappa, L., Manjunatha, H.C., Chandrika, B.M., Chikka, Hanumantharayappa, 2017.
 A study of shielding properties of x-ray and gamma in barium compounds. J. Radiat. Protect. Res. 42 (1), 26–32.
- Shahboub, A., El Damrawi, G., Saleh, A., 2021. A new focus on the role of iron oxide in enhancing the structure and shielding properties of ag2o-p2o5 glasses. Eur Phys. J. Plus 136 (9), 1-17.
- Sharma, Tanu, Aggarwal, Sanjeev, Kumar, Shyam, Mittal, V.K., Kalsi, P.C., Manchanda, V.K., 2007. Effect of gamma irradiation on the optical properties of cr-39 polymer. J. Mater. Sci. 42 (4), 1127–1130.
- Singh, Vishwanath P., Medhat, M.E., Badiger, N.M., Saliqur Rahman, Abu Zayed Mohammad, 2015. Radiation shielding effectiveness of newly developed superconductors. Radiat. Phys. Chem. 106, 175–183.
- Sirin, M., 2020. The effect of titanium (ti) additive on radiation shielding efficiency of al25zn alloy. Prog. Nucl. Energy 128, 103470.
- Suresh, K.C., Manjunatha, H.C., Rudraswamy, B., 2008. Study of z {subeff} for dna, rna and retina by numerical methods. Radiat. Protect. Dosim. 43 (294–298).
- Tekin, H.O., Kavaz, Esra, Altunsoy, E.E., Kilicoglu, O., Agar, O., Erguzel, T.T., Sayyed, M. I., 2019. An extensive investigation on gamma-ray and neutron attenuation parameters of cobalt oxide and nickel oxide substituted bioactive glasses. Ceram. Int. 45 (8), 9934–9949.
- Tellili, Borhan, Elmahroug, Youssef, Souga, Chedly, 2017. Investigation on radiation shielding parameters of cerrobend alloys. Nucl. Eng. Technol. 49 (8), 1758–1771.

- Tishkevich, Daria I., S Grabchikov, Sergey, Lastovskii, Stanislav B., Trukhanov, Sergey V., Zubar, Tatyana I., Vasin, Denis S., Trukhanov, Alex V., Kozlovskiy, Artem L., Zdorovets, Maxim M., 2018. Effect of the synthesis conditions and microstructure for highly effective electron shields production based on bi coatings. ACS Appl. Energy Mater. 1 (4), 1695–1702.
- Tishkevich, D.I., Grabchikov, S.S., Lastovskii, S.B., Trukhanov, S.V., Vasin, D.S., Zubar, T. I., Kozlovskiy, A.L., Zdorovets, M.V., Sivakov, V.A., Muradyan, T.R., et al., 2019. Function composites materials for shielding applications: correlation between phase separation and attenuation properties. J. Alloys Compd. 771, 238–245.
- Tyagi, Gaurav, Singhal, Anupam, Routroy, Srikanta, Bhunia, Dipendu, Lahoti, Mukund, 2021. Radiation shielding concrete with alternate constituents: an approach to address multiple hazards. J. Hazard Mater. 404, 124201.
- Vidya, Y.S., Anantharaju, K.S., Nagabhushana, H., Sharma, S.C., Nagaswarupa, H.P., Prashantha, S.C., Shivakumara, C., et al., 2015a. Combustion synthesized tetragonal zro2: Eu3+ nanophosphors: structural and photoluminescence studies. Spectrochim. Acta Mol. Biomol. Spectrosc. 135, 241–251.
- Vidya, Y.S., Gurushantha, K., Nagabhushana, H., Sharma, S.C., Anantharaju, K.S., Shivakumara, C., Suresh, D., Nagaswarupa, H.P., Prashantha, S.C., Anilkumar, M.R., 2015b. Phase transformation of zro2: Tb3+ nanophosphor: color tunable photoluminescence and photocatalytic activities. J. Alloys Compd. 622, 86–96.
- Vidya, Y.S., Anantharaju, K.S., Nagabhushana, H., Sharma, S.C., 2015c. Euphorbia tirucalli mediated green synthesis of rose like morphology of gd2o3: Eu3+ red phosphor: structural, photoluminescence and photocatalytic studies. J. Alloys Compd. 619, 760–770.
- Wu, Jun Hua, Kim, Young Keun, 2007. Synthesis and microwave properties of highly permeable feco-based nano-alloys. Phys. Status Solidi 204 (12), 4087–4090.
- Yan, Hailong, Zhang, Deyang, Xu, Jinyou, Lu, Yang, Liu, Yunxin, Qiu, Kangwen, Zhang, Yihe, Luo, Yongsong, 2014. Solution growth of nio nanosheets supported on ni foam as high-performance electrodes for supercapacitors. Nanoscale Res. Lett. 9 (1), 1–7.
- Yang, Xiong, Wang, Ying, Chen, Yifei, Yan, Huiyu, 2016. The structural and electronic properties of bao under epitaxial strains: first-principles calculations. Acta Phys. Pol., A 129, 64–68.
- Zaki, M.F., 2008. Gamma-induced modification on optical band gap of cr-39 ssntd. Braz. J. Phys. 38, 558-562.
- Zezulova, Anezka, Stanek, Theodor, Opravil, T.O.M.Á.Š., 2017. Influence of barium oxide additions on portland clinker. Ceramics 61 (1), 20–25.
- Zhukowski, Pawel, Julia Sidorenko, Koltunowicz, T., Fedotova, J., Larkin, A., 2010.
 Magnetic properties of nanocomposites (cofezr) x (al2o3) 1-x. Przeglad Elektrotechniczny 86 (7), 296–298.

ARTICLE IN PRESS

Materials Today: Proceedings xxx (xxxx) xxx



Contents lists available at ScienceDirect

Materials Today: Proceedings

journal homepage: www.elsevier.com/locate/matpr



Gamma, X-ray and neutron shielding properties of iron boron alloys

K.V. Sathish a,c, H.C. Manjunatha a,*, L. Seenappa , K.N. Sridhar , N. Sowmya a,*, S. Alfred Cecil Raj c

- ^a Department of Physics, Government College for Women, Kolar 563101, Karnataka, India
- ^b Department of Physics, Government First Grade College, Kolar 563101, Karnataka, India
- ^c Department of Physics, St. Joseph's College, Trichy 620020, Tamil Nadu, India

ARTICLE INFO

Article history: Received in revised form 4 February 2021 Accepted 29 April 2021 Available online xxxx

Keywords:
Mass attenuation coefficient
Shielding
Incoherent
Electron density
Gamma radiation
Radiation protection efficiency

ABSTRACT

The present study focusses on the shielding parameters (X-ray and gamma radiation) such as mass attenuation coefficient (MAC), linear attenuation coefficient (LAC), Tenth Value Layer (TVL), Half Value Layer (HVL), electron density, effective atomic number, specific gamma ray constant and radiation protection efficiency in some iron boron alloys such as $Fe_{0.95}B_{0.05}$ (A), $Fe_{0.9}B_{0.1}$ (B), $Fe_{0.8}B_{0.2}$ (C), $Fe_{0.7}B_{0.3}$ (D), $Fe_{0.6}B_{0.4}$ (E) and $Fe_{0.5}B_{0.5}$ (F). We also investigated the neutron shielding properties (NSP) such as coherent and incoherent neutron scattering length and cross section. Then the total neutron scattering and absorption cross sections were evaluated along with the radiation protection efficiency in the iron boron alloys. The shielding properties of the various iron boron alloys were compared. It is clear from the detailed study that the iron boron alloy $Fe_{0.95}B_{0.05}$ is a perfect absorber for x-ray, gamma and neutron radiation. We therefore suggest that the iron boron alloy $Fe_{0.95}B_{0.05}$ is a good shielding material for gamma, neutrons and x-rays.

© 2021 Elsevier Ltd. All rights reserved.

Selection and peer-review under responsibility of the scientific committee of the Web International Conference on Accelerating Innovations in Material Science – 2020.

1. Introduction

Nuclear shielding for X-rays, gamma and neutrons is an important concern in the field of radiation physics. The mass attenuation coefficient (MAC) and its derivable are fundamental parameters for the collection of shielding materials for X-ray and gamma radiation. Hayashi et al., [1] have shown that the capability of neutron shielding is increased by the combination of steel and Zr (BH₄)₄. Tekina et al., [2] were studied the MAC and calculated shielding parameters (for example: effective atomic number (Zeff), HVL, TVL, effictive electron density (Nel), average free path, and photon transport factors). Kurudirek et al., [3] have inferred from the findings that the build-up of photons was smaller in case of NaCl relative to other materials at lower penetration depths. Earlier researchers [4–7] were studied the gamma and neutron shielding and γ -ray interaction properties in alloys, polymers and boron containing elements. The synthesis and characterization of nanocomposite magnetite films were effectively used [8].

E-mail addresses: manjunathhc@rediffmail.com (H.C. Manjunatha), sowmyaprakash8@gmail.com (N. Sowmya). 2.1. Gamma/X-ray interaction parameters

In the present research, the MAC and the photon interaction cross-sections in the energy range from 1 keV to 100 GeV are produced using WinXCom [15] and its composition.

The polymers, plastic materials and polyvinyl alcohol / iron oxide polymer composite were extensively used to measure

radiation shielding properties [9-14]. In the current paper, we

studied the parameters of X-ray and Gamma radiation safety such

as MAC and LAC, HVL and TVL, Z_{eff} , N_{el} and specific γ -ray constant.

We also studied the neutron shielding properties in the iron boron

The total LAC can be calculated by multiplying the density of the compounds to the MAC. By multiplying density of compounds to the MAC, the overall LAC can be estimated. By using the total LAC, the corresponding HVL is evaluated. HVL is the thickness of the interactive medium which reduces the radiation level by a factor of 2. Therefore, it is half the initial level and is determined by a ratio of 0.693 to the LAC. Again, the total LAC is also used in the TVL estimation. It is the interactive media's thickness used to attenuate

https://doi.org/10.1016/j.matpr.2021.04.516

 $2214\text{-}7853/\text{\circledcirc}\ 2021$ Elsevier Ltd. All rights reserved.

Selection and peer-review under responsibility of the scientific committee of the Web International Conference on Accelerating Innovations in Material Science – 2020.

alloys.

2. Theory

Please cite this article as: K.V. Sathish, H.C. Manjunatha, L. Seenappa et al., Gamma, X-ray and neutron shielding properties of iron boron alloys, Materials Today: Proceedings, https://doi.org/10.1016/j.matpr.2021.04.516

^{*} Corresponding authors.

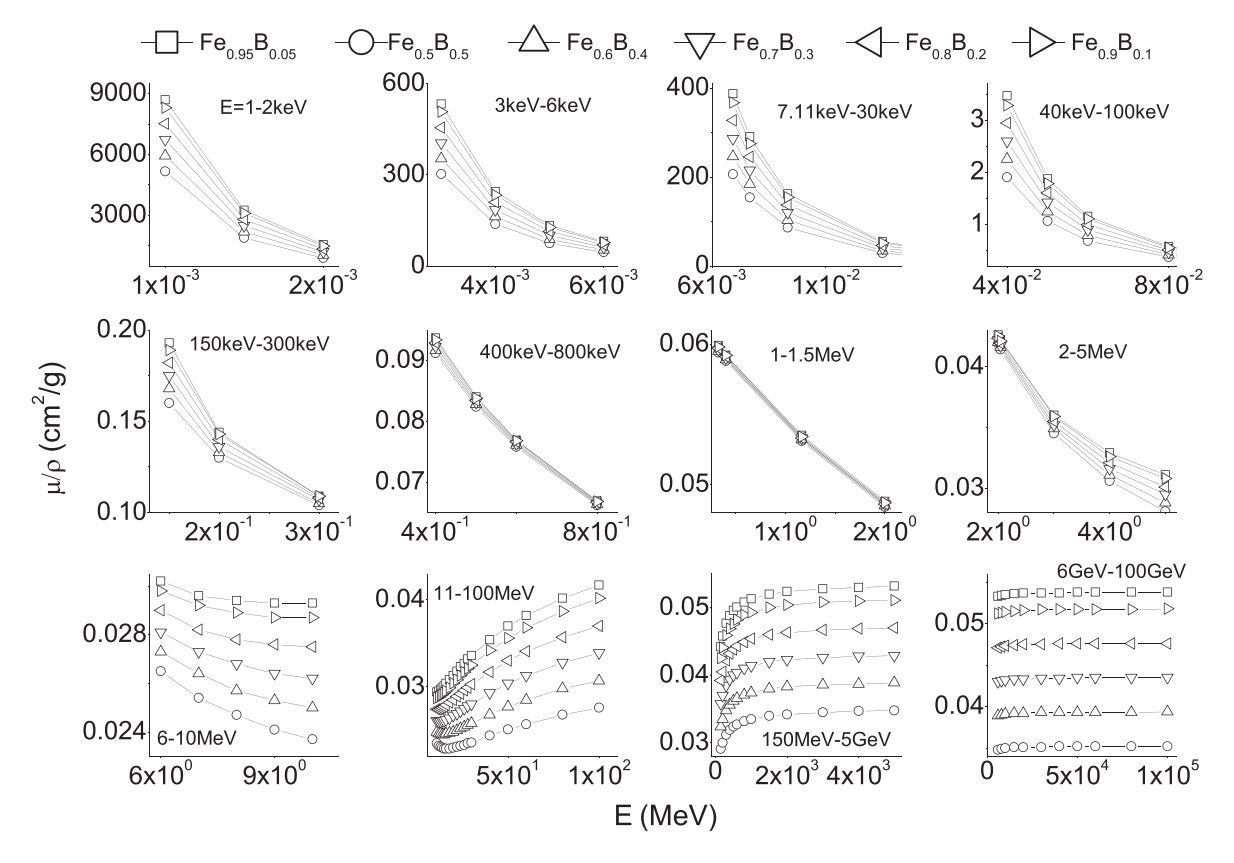


Fig. 1. Variation of mass attenuation coefficient with energy for the studied iron boron alloys.

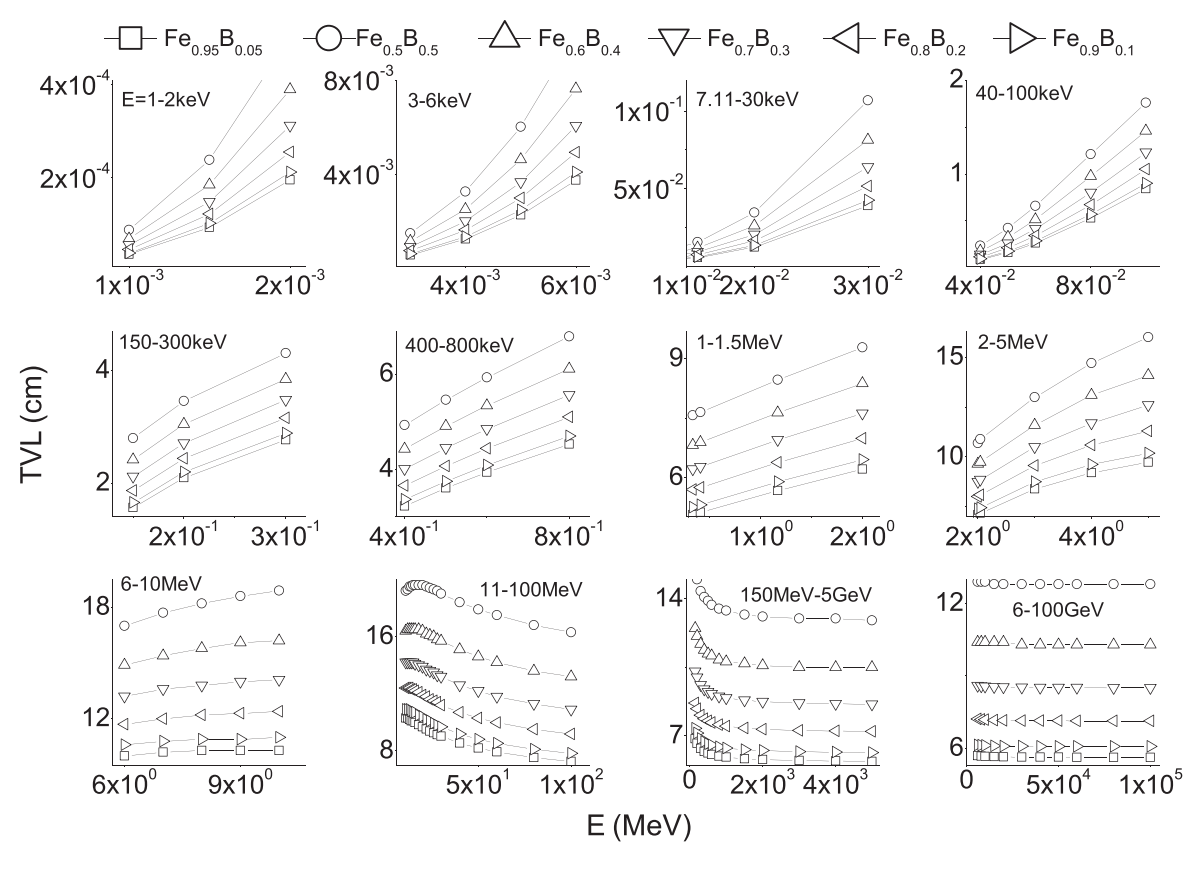


Fig. 2. Variation of tenth value layer (TVL) with energy for the studied iron boron alloys.

K.V. Sathish, H.C. Manjunatha, L. Seenappa et al.

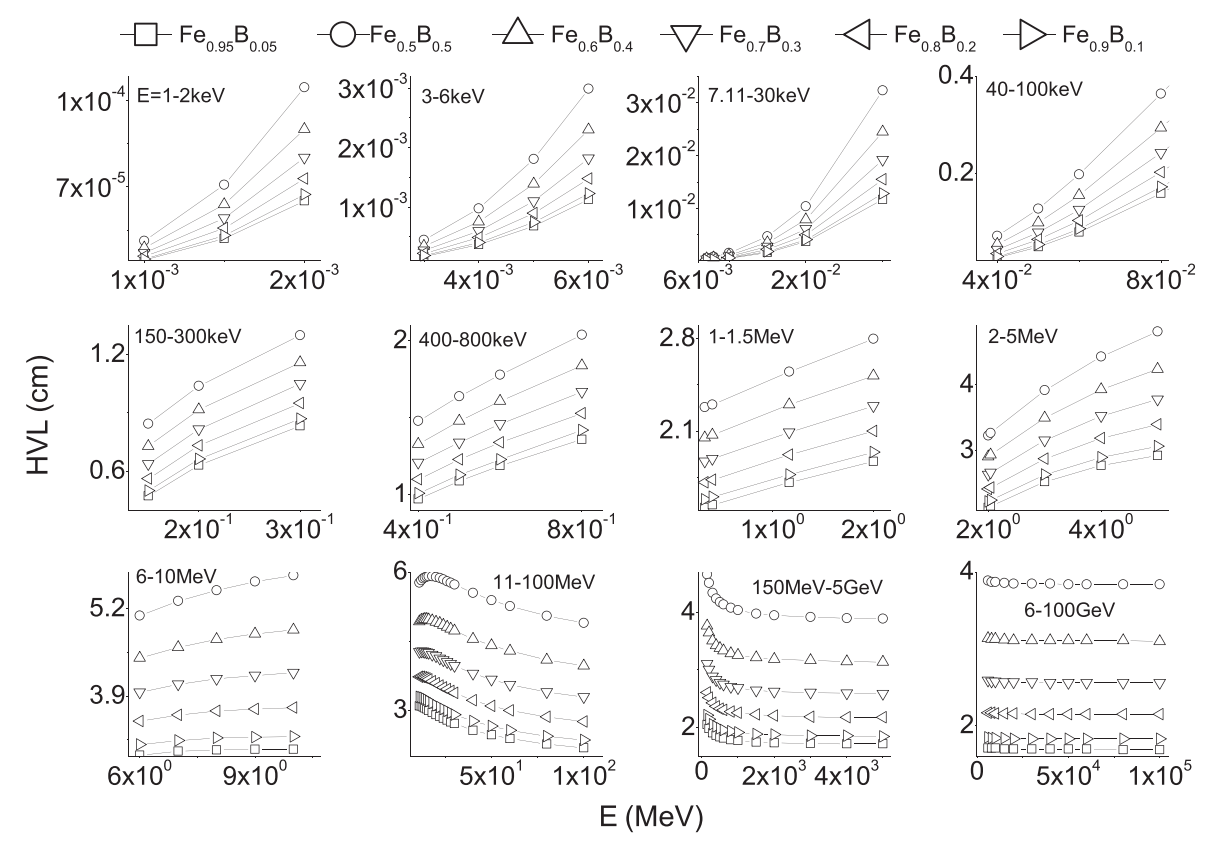


Fig. 3. Variation of half value layer (HVL) with energy for the studied iron boron alloys.

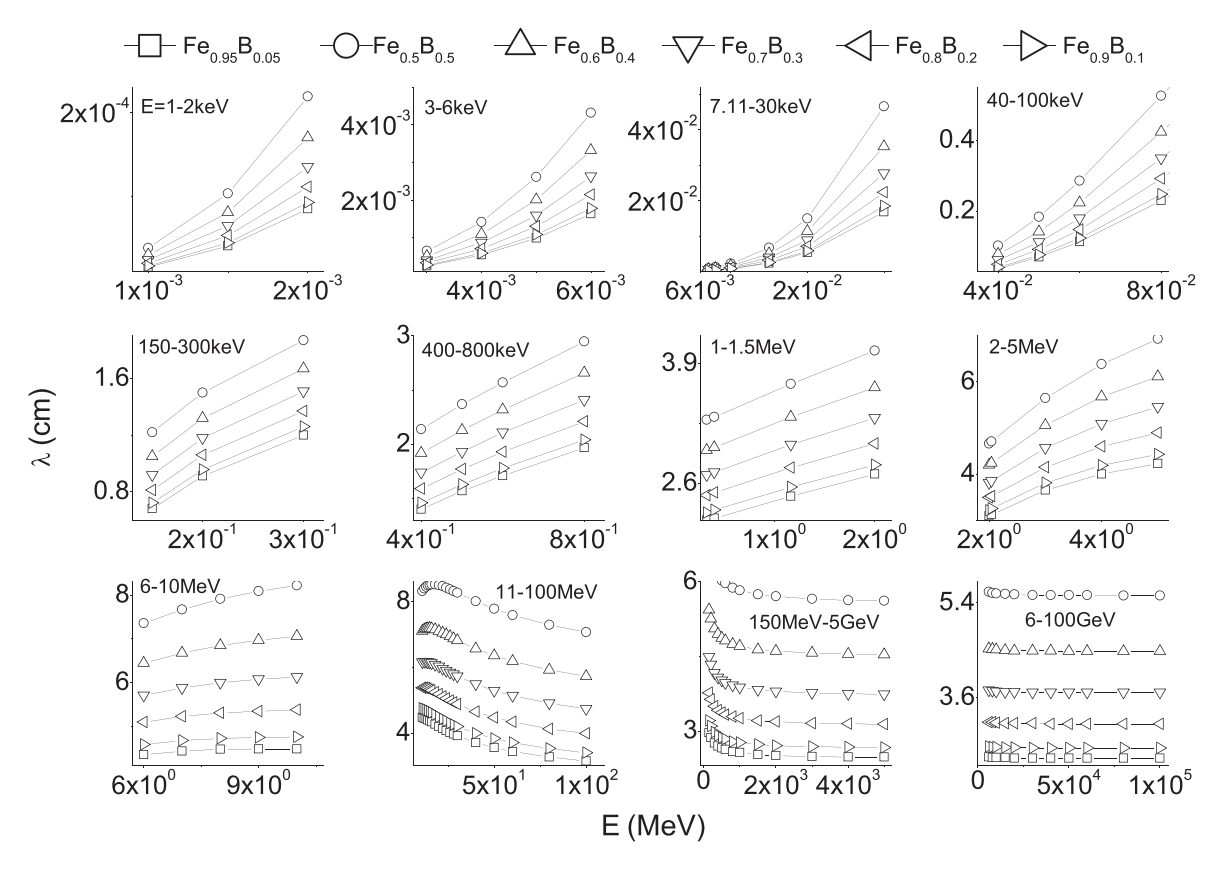


Fig. 4. Variation of mean free path with energy for the studied iron boron alloys.

K.V. Sathish, H.C. Manjunatha, L. Seenappa et al.

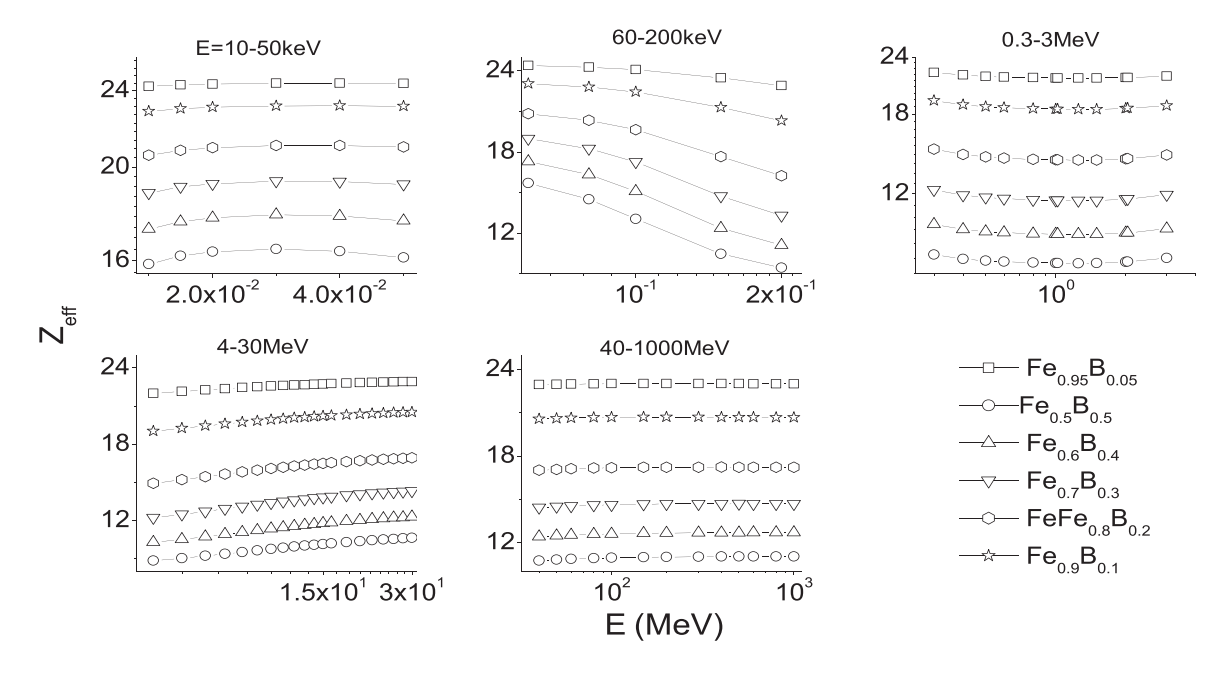


Fig. 5. Variation of effective atomic number with energy for the studied iron boron alloys.

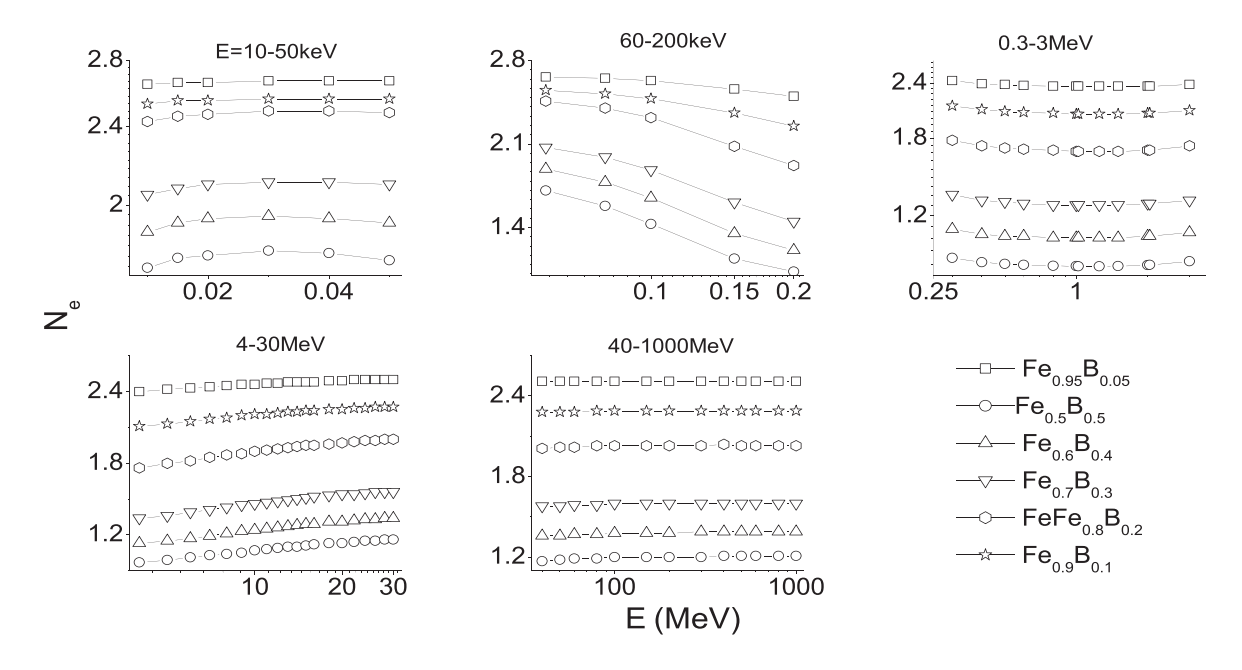


Fig. 6. Variation of effective electron density versus the energy for the studied iron boron alloys.

the radiation beam to 10% of its radiation level. The TVL is evaluated by a ratio of 2.303 to the LAC. The mean free path (λ) is the average interval between the consecutive encounters. The λ is evaluated by the reciprocal of LAC.

The $Z_{\rm eff}$ is estimated by using the ratio between atomic and electronic cross section. Previous researchers [15–25] describe in detail the method for estimating the atomic and electronic cross section. The electron density is defined as the number of electrons/unit mass. The effective density of electrons is calculated

from the atomic number measured. The earlier researchers [15–25] explained the method for the measurement of effective electron density is described.

2.2. Specific gamma ray constant (Γ)

The Γ is a photon emission and it is expressed as follows;

$$\Gamma = 657.68 \times E_{\gamma} \left(\frac{\mu_{en}}{\rho} \right) \frac{R \cdot m^2}{Ci \cdot hr} \tag{1}$$

K.V. Sathish, H.C. Manjunatha, L. Seenappa et al.

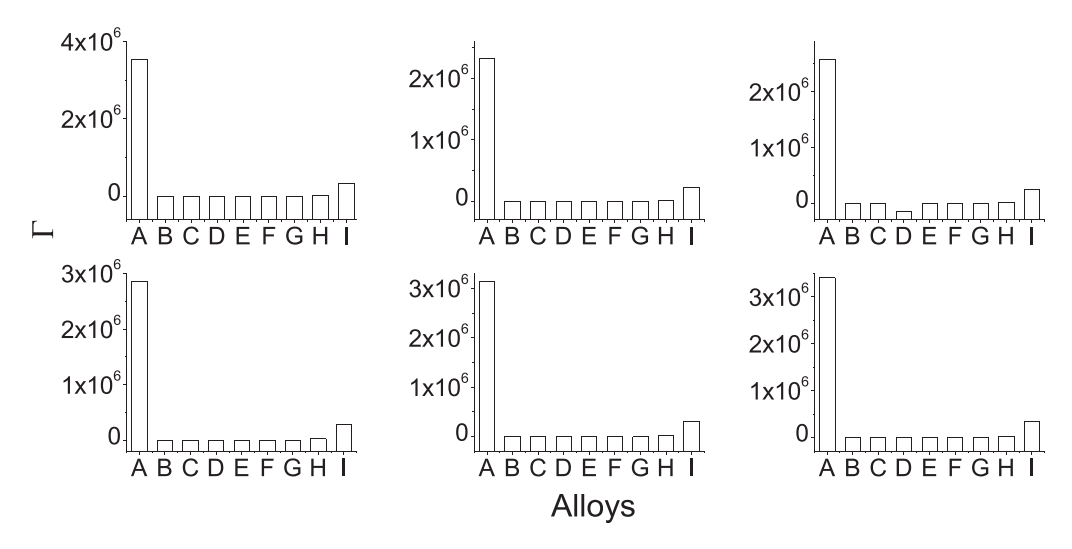


Fig. 7. Comparison of specific gamma ray constant for the studied iron boron alloys, Fe_{0.95}B_{0.05} (A), Fe_{0.95}B_{0.1} (B), Fe_{0.8}B_{0.2} (C), Fe_{0.7}B_{0.3} (D), Fe_{0.6}B_{0.4} (E) and Fe_{0.5}B_{0.5} (F).

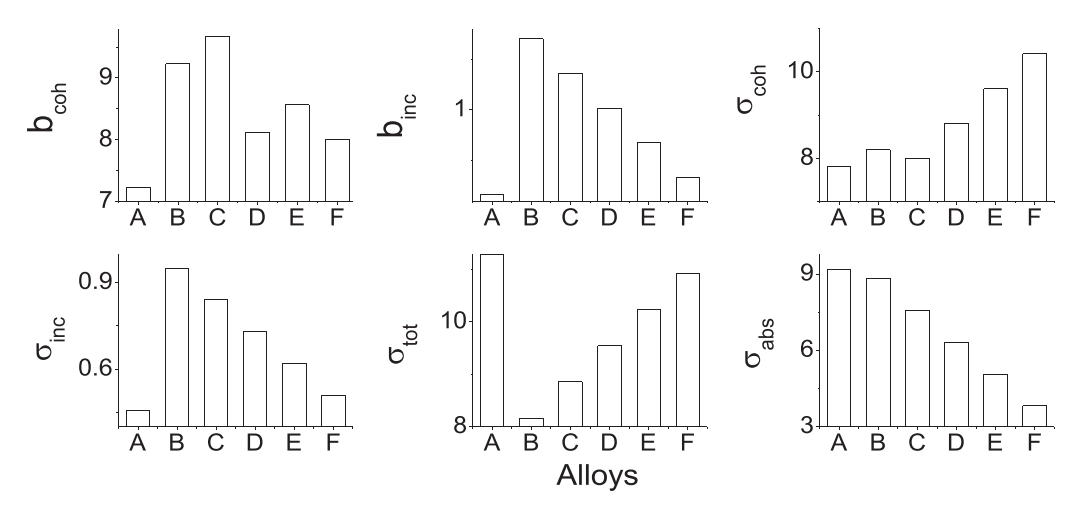


Fig. 8. Comparison of neutron shielding parameters for the studied iron boron alloys, Fe0.95B0.05 (A), Fe0.9B0.1 (B), Fe0.8B0.2 (C), Fe0.7B0.3 (D), Fe0.6B0.4 (E) and Fe0.5B0.5 (F).

2.3. Neutron shielding parameters (NSP)

The NSP such as scattering length and scattering cross sections in iron boron alloys are determined by using following mixture rule:

here $(NSP)_i$ and f_i are the NSP of ith element of the iron boron alloys and the fractional abundance [26].

$$(\textit{NSP}) compound = \sum fi(\textit{NSP}) \tag{2}$$

2.4. Radiation protection efficiency (RPE):

The RPE is evaluated by using the following expression;

$$[I - I/I_0] \times 100\% = (1 - e^{-\mu t}) \times 100\%$$
 (3)

where μ is the measure of LAC. I and I_0 are the intensities of the radiation for thickness t and t = 0 respectively.

3. Results and discussions

3.1. Variation of mass attenuation coefficient with photon energy.

The Fig. 1 shows the variation of MAC values for various iron boron alloys in the energy range 1 keV-100 GeV. MAC values for iron boron alloys are larger in the low energy region and decreases gradually. Because of the dominant photoelectric interaction, the MAC is observed to be high in the low energy region. Again, the Compton scattering is dominant in the high-energy field, which is linearly dependent on nuclear numbers. Hence, MAC value becomes minimum value.

3.2. Gamma/X-ray interaction parameters

For various iron boron alloys, we have measured HVL, TVL and mean free path. The variation of TVL is presented in Fig. 2.

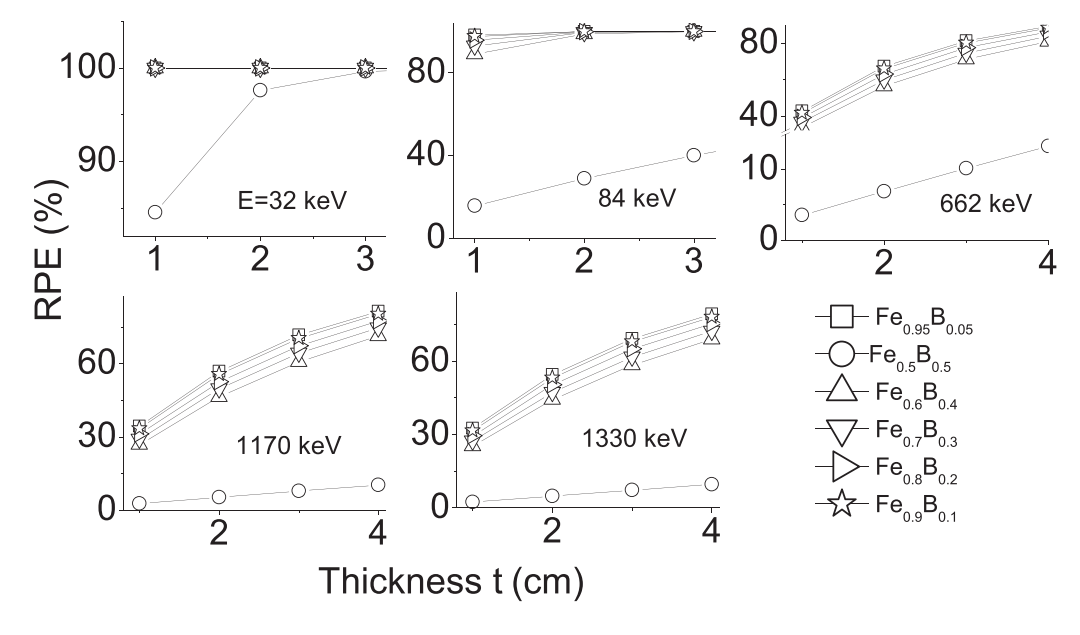


Fig. 9. Variation of radiation protection efficiency of the studied iron boron alloys with that of thickness of the studied alloys at different energies in keV.

Similarly, HVL and mean free path for different iron boron alloys with that of energy are as shown in Figs. 3 and 4 respectively. From the figure, it is observed that the iron boron alloy $Fe_{0.95}B_{0.05}$ is having maximum TVL, HVL and mean free path values when compared to all other alloys studied. Which indicates that the iron boron alloy $Fe_{0.95}B_{0.05}$ will have less penetration for the gamma / X ray than the other iron boron alloys studied. The Figs. 5 and 6 shows the variation of $Z_{\rm eff}$ and $N_{\rm el}$ with energy for the studied iron boron alloys. The studied parameters for iron boron alloys are large in the low energy region (due to photo electric effect) and decreases gradually with energy.

3.3. Specific gamma ray constant

The evaluation of Γ for studied iron boron alloys, Fe_{0.95}B_{0.05} (A), Fe_{0.9}B_{0.1} (B), Fe_{0.8}B_{0.2} (C), Fe_{0.7}B_{0.3} (D), Fe_{0.6}B_{0.4} (E) and Fe_{0.5}B_{0.5} (F) are depicted in Fig. 7. From this comparison, it confirms that Γ is higher for the iron boron alloy Fe_{0.95}B_{0.05} than the other studied alloys.

3.4. Neutron shielding properties

The Fig. 8 shows the comparison of b_{coh} , b_{inc} , σ_{coh} , σ_{inc} , σ_{tot} and σ_{abs} for different iron boron alloys. From the figure, it is evident that the b_{coh} and b_{inc} are minimum for the iron boron alloy Fe_{0.95}B_{0.05}. Then the other studied iron boron alloys. The σ_{coh} and σ_{tot} are minimum for the iron boron alloy Fe_{0.95}B_{0.05}. From the figure it is also observed that the σ_{abs} is maximum for the iron boron alloy Fe_{0.95}B_{0.05} when compared to all other alloys studied.

3.5. Radiation protection efficiency(RPE)

The studied RPE for iron boron alloys at different thickness for different energies (32 keV, 84 keV, 662 keV, 1170 keV and 1330 keV) are shown in Fig. 9. From the figure it is observed that the RPE is maximum for the iron boron alloy $Fe_{0.95}B_{0.05}$ than the other studied iron boron alloys.

4. Conclusion

We studied the shielding parameters for X-rays, gamma and neutrons in iron boron alloys. From the analysis of the different iron boron alloy, it is clear that the iron boron alloy $Fe_{0.95}B_{0.05}$ is good absorber for X-ray, gamma radiation and neutron. The attenuation parameters for neutron is large for the iron boron alloy $Fe_{0.95}B_{0.05}$. Hence, the iron boron alloy $Fe_{0.95}B_{0.05}$ is good absorbing material for X-ray, gamma and neutrons.

Declaration of Competing Interest

The authors declare that they have no known competing financial interests or personal relationships that could have appeared to influence the work reported in this paper.

References

- [1] T. Hayashi, K. Tobita, Y. Nakamori, S. Orimo, et al., J. Nucl. Mat. 386–388 (2009) 119–121.
- [2] H.O. Tekina, E.E. Altunsoyb, E. Kavazd, M.I. Sayyede, et al., Res. Phys. 12 (2019) 1457–1464.
- [3] M. Kurudirek, D. Sardari, N. Khaledi, C. Çakır, K.S. Mann, Ann. Nucl. Ene. 53 (2013) 485–491.
- [4] V.P. Singh, N.M. Badiger Annal, Nucl. Energy 64 (2014) 301-310.
- [5] V.P. Singh, N.M. Badiger, Vacuum 113 (2015) 24–27.
- [6] K.S. Mann, Nucl. Eng. Tech. 49 (4) (2017) 792–800.[7] M.I. Sayyed Chin. J. Phy. 54(3) (2016) 408-415.
- [8] Badawy, Abd Latif, Polymer Composites-38 (5) (2015) 974-980.
- [9] K.S. Mann, A. Rani, M.S. Heer, Rad. Phy. and Chem. 106 (2015) 247–254.
- [10] O. Gurler, U.A. Tarim, Acta Phys. Polo. A 130 (2016) 236–238.
- [11] K. Srinivasan, E.J.J. Samuel, J. Med. Phys. 42 (4) (2017) 273–278.
- [12] L. Seenappa, H.C. Manjunatha, K.N. Sridhar, C., Hanumantharayappa Ind, J. Pure App. Phys. 56 (2018) 383–391.
- [13] H.C. Manjunatha, L. Seenappa, Inter. J. Nucl. Ener. Sci. Tech. 12 (3) (2018) 294–311.
- [14] L. Gerward, N. Guilbert, K.B. Jensen, H. Levring, Rad. Phys. and Chem. 71 (2004) 653–654.
- [15] H.C. Manjunatha, Rad. Phy. and Chem. 113 (2015) 24–27.
- 16] L. Seenappa, H.C. Manjunatha, B.M. Chandrika, C. Hanumantharayappa, J. Rad. Prot. Res. 42 (1) (2017) 26–32.
- [17] H.C. Manjunatha, Rad. Phy. Chem. 137 (2016) 254-259.
- [18] H.C. Manjunatha, L. Seenappa, B.M. Chandrika, C. Hanumantharayappa, Ann. Nucl. Ener. 109 (2017) 310–317.

ARTICLE IN PRESS

K.V. Sathish, H.C. Manjunatha, L. Seenappa et al.

Materials Today: Proceedings xxx (xxxx) xxx

- [19] B. Rudraswamy, N. Dhananjaya, H.C. Manjunatha, Nucl. Ins. Meth. Phy. Res. Sec. A. 619 (1) (2010) 171–173.
 [20] H.C. Manjunatha, B.M. Chandrika, L. Seenappa, C. Hanumantharayappa, I., J. Nucl. Ener. Sci. Tech. 10 (4) (2016) 356–368.
 [21] H.C. Manjunatha, J. med. Phy. 39 (2) (2014) 112.
 [22] H.C. Manjunatha, B. Rudraswamy, Health Phy. 104 (2) (2013) 158–162.

- [23] K.C. Suresh, H.C. Manjunatha, B. Rudraswamy, Rad. Prot. Dos. 128 (3) (2008) 294–298.
 [24] H.C. Manjunatha, B. Rudraswamy, Healt. phy. 100 (5) (2011) S92–S99.
 [25] H.C. Manjunatha, B. Rudraswamy, Rad. Meas. 47 (5) (2012) 364–370.
 [26] V.F. Sears, Neutron News 3 (3) (1992) 26–37.